Mid-Frequency Acoustic Backscattering From Finite Cylindrical Shells and The Influence of Helical Membrane Waves

Charles N. Corrado Jr.

B. S. Webb Institute of Naval Architecture (1983)
S. M. Massachusetts Institute of Technology (1986)

Submitted in Partial Fulfillment
of the Requirements for the Degree of

Doctor of Philosophy

at the

Massachusetts Institute of Technology

January 1993

Signature of Author _____
Department of Ocean Engineering
January 22, 1993

Certified by _____
Professor Ira Dyer
Thesis Supervisor

Accepted by _____
Professor A. Douglas Carmichael
Chairman, Department Graduate Committe

Mid-Frequency Acoustic Backscattering From Finite Cylindrical Shells and The Influence of Helical Membrane Waves

by Charles N. Corrado Jr.

Submitted to the Department of Ocean Engineering in partial fulfillment of the requirements for the degree of Doctor of Philosophy

Abstract

In this thesis I study the mid-frequency scattering properties of cylindrical shells in water to evaluate the influence of helical membrane waves, resiliently mounted internal structures, and typical structural discontinuities. Scattering measurements of an empty shell, an unequally spaced ring stiffened shell, and a ring stiffened shell with resiliently mounted, wave bearing internal structures are interpreted. I also study the specularly directed scatter of infinite cylindrical shells to investigate the properties of membrane wave excitation and reradiation. In addition, scattering of a helical structural wave at an eccentric ring of mass is studied to estimate the influence of the impedance discontinuity located at a ring stiffener.

The measurements and analyses were conducted over a mid-frequency range of $2 < ka < 12$ corresponding to about 1/2 to 3 times the ring frequency of the empty shell. The measurements were all conducted with the use of wide-band pulses yielding good time resolution of propagating waves. Various time and frequency domain representations of the scattered field are presented to illustrate the evolution of observed backscattering processes. Although the field measured at all aspect angles is reviewed, emphasis is placed on interpretation of the backscatter observed over a range within 30 degrees of beam aspect where phase matched (coincident) excitation of membrane waves occurs.

Coincident shear wave radiation is the dominant source of backscatter generated by the empty shell at oblique angles of incidence within 30° of beam aspect. Peak levels of backscatter are generally found at combinations of aspect angle and frequency where coincidence and peak levels of length-scale modulation coexist. Coincident back radiation of shear waves remains evident in the backscatter of the ring stiffened shell, but the backscatter is smeared in time and frequency because the rings directly scatter energy to the acoustic medium, as well as from one membrane wave type to another, and to subsonic flexural waves. The decay rate of the empty shell backscatter exceeds that of the ring stiffened shell by a factor of $2 - 3$ because the rings scatter energy to poorly radiating waves. Although details of the backscatter produced by the empty and ring stiffened shells differ, peak levels of target strength consistently fall within a range of -20 to -15 dB re 1 m. The internal loading further impairs coincident radiation but increases the target strength by about 2 dB for $ka > 5.5$. The damping provided by the resilient mounts increases backscatter decay rates by roughly 1.2 to 1.4 relative to those of the ring stiffened shell.

Bistatic measurements of the internally loaded shell also demonstrate important backscattering aperture effects. Interaction between the shell, ring stiffeners, and internal loading produces a distribution of scattering sources that varies over the

length of the shell. Hence, while the specularly directed scatter exhibits beam patterns similar to that of a uniform line array, the field observed near the monostatic direction is characterized by high side lobes with little roll off.

Thesis Supervisor: Dr. Ira Dyer
Title: Weber-Shaughness Professor of Ocean Engineering, M.I.T.

To Sandra Lou,

for all your love,

for the joy that is Abigail Rebecca.

Acknowledgments

Long before I actually started this thesis I had begun to think about the acknowledgments, but it seems more difficult now to appropriately thank all those who helped get me through this place. First I would like to thank my advisor Dr. Ira Dyer who made it all possible. I must admit that I cursed your name many times in recent months, but looking back I really enjoyed my time here. Thanks for the great opportunity you have given me. I would also like to thank my thesis advisors Dr. Yueping Guo and Dr. Leo Felsen. I could have never made it through without your help Yueping and I hope MIT is smart enough to make you a professor as you deserve. You will make a great teacher. Fortunately for me, Leo dragged me into the world of asymptotics kicking and screaming. None of it would have made much sense without their use. While not official advisors of record, I would also like to thank Dr. Henrik Schmidt and Dr. Rob Fricke for all their help and advice over the years. It was greatly appreciated. I would also like to thank Sabina Rataj and her crew for smoothing the way.

This work was funded by the Office of Naval Research and I gratefully acknowledge their support. I would also like to extend special thanks to all those at the Naval Research Laboratory in Washington, D.C. who made the data acquisition possible. I would especially like to thank Dr. Brian Houston and Jon Spanier who had to put up with my endless stream of questions.

I never would have begun this venture had I not enjoyed my work at BBN so much. All of those who worked with me in the New London office contributed to the atmosphere of camaraderie, but I would like to give special thanks to those who really made it fun, namely Tim Boyd, Mike Dignan, Jimmy Clift, Doug Hanna, Bob Haberman, Ed Lowe, Frank Marafrioti, George Abe, Harry Davis, Mike Coughlin, and Trish Moody. I will miss working and traveling with you guys and wish you all the best. I would also like to thank Bob Gorman, Mark and Kim Clifton, and Vince Godino who I will rejoin in the land of paychecks, but at ETC.

Many friends and classmates here at MIT helped me with my work and were

always entertaining, even when His Crankiness was brooding. Special thanks to Joe Bondaryk for helping out the "Vax Killer" and basically keeping me on my toes, and to Tarun Kapoor for making like the devil and dragging me to the pub at every possible opportunity. I also want to thank Matt Conti for well, being the "Hammer", and I hope you end up designing quiet milking machines out there in Wisconsin with Karen. Many, many thanks to Kevin LePage who has managed to remain a constant source of fun distraction since our days way back at Webb. I know that we will continue to see you, Amy, and Mr. T. often. You know, of course, that one day I am going to pass you and duck jibe in your face. Many thanks to that master fisherman Dan McCarthy and his cohort Pamela for all the fun. Many thanks to Dan Diperna and Chris Howell for those totally out of control days that invigorated the spirit, but pickled the brain. Dave Ricks, Clem Karl, Van Gurley, D.J. Tang, and Gopal all made it fun. I can't imagine what it would have been like without you guys.

Many thanks to the Johnson family: Sue and Frank, Paula and Gerry, and Mom for making me feel welcome. Special thanks to my late father-in-law Dr. Howard K. Johnson for all you taught me. Your warm spirit will always inspire me and we miss you.

Many thanks to my own family: Dave and Joy, my grandparents, and Mom and Dad for the trips, dinners, loans, and moral support that meant so much to Sandy and me. Mom and Dad, I cannot thank you enough for all you have given me. I can only offer to try to do the same for my own children.

Finally, and most importantly, I want to thank my wife Sandy and daughter Abigail. Lou, you sacrificed so much for me to pursue this strange dream and yet you managed to smile through it all. You are simply amazing. My little Abigail, if I never do anything else of worth in my life, I had the good fortune of helping to bring you into this world and knowing that will always make me smile.

Contents

Table of Contents 7

List of Tables 10

List of Figures 11

1 Introduction 22
- 1.1 Research Motivation and Context 22
- 1.2 Shell Designs 24
- 1.3 Previous Research 25
- 1.4 Approach and Overview of Thesis 26

2 Plane Wave Scattering from Infinite Cylinders at Oblique Incidence 41
- 2.1 Introduction 41
- 2.2 Normal Mode Series Solution 43
- 2.3 Asymptotic Formulation 49
  - 2.3.1 Use of Debye Expansions of Hankel Functions 52
  - 2.3.2 Contribution of the Geometric Field 53
  - 2.3.3 Contributions of The Residues 55
  - 2.3.4 Geometric and Membrane Wave Scattering Contributions in the Specular Direction 57
  - 2.3.5 Membrane Wave Helix Properties and the Origin of Coincidence Conditions 59
  - 2.3.6 Detailed Evaluation of Example Form Functions and Time Domain Representations 63
- 2.4 Role of Structural Damping 73
- 2.5 The Free Modes of Propagation 74

3 Empty Shell Backscatter - Measurements and Interpretation 104
- 3.1 Introduction 104
- 3.2 Backscattering at Beam Aspect 105
  - 3.2.1 Interpretation of the Backscatter Features 105
  - 3.2.2 Beam Aspect and Other Specular Target Strength Corrections 107
  - 3.2.3 The Measured Target Strength at Beam Aspect 109
- 3.3 Monostatic Field Properties Observed at Oblique Angles of Incidence 110

3.3.1 The Initial Scatter From the Empty Shell 110
3.3.2 Time Domain Features of the Monostatic Signals 112
3.3.3 Frequency Dependence of the Total Target Strength 113
3.4 Interpretation of the Field Observed Over the Range of Aspect Angles of 60-90 Degrees 114
3.4.1 The Monostatic and Specularly Directed Fields Measured at an Aspect Angle of 75 degrees 119
3.4.2 The Monostatic Field Measured at an Aspect Angle of 66 degrees 132
3.4.3 Evaluation of the Monostatic Signals Measured at Other Representative Aspect Angles 134
3.4.4 Summary 139

4 Scattering of a Structural Wave at a Ring **174**
4.1 Introduction 174
4.2 Interaction of the Ring and Shell 177
4.2.1 Displacements of the Shell 177
4.2.2 Displacements of the Ring 182
4.2.3 Interaction Forces 183
4.3 The Scattered Pressure 184
4.4 Reflection and Transmission Coefficients 188
4.5 Summary of Important Results 191

5 Ring Stiffened and Internally Loaded Shells - Measurements and Interpretation **204**
5.1 Introduction 204
5.2 Influence of Roll Angle 205
5.3 Backscattering at Beam Aspect 206
5.3.1 Aperture Effects 207
5.3.2 Monostatic Time and Frequency Domain Representations . . . 209
5.4 Monostatic Field Properties Observed at Oblique Angles of Incidence 214
5.4.1 The Initial Scatter 214
5.4.2 Time Domain Features of the Monostatic Signals 216
5.4.3 Frequency Dependence of the Total Target Strength 219
5.5 Interpretation of Backscatter Measured Over the Range of Aspect Angles of 60-90 Degrees 221
5.5.1 Introduction 221
5.5.2 Time Evolution and Decay Rates 225
5.5.3 Coincidence Effects and Target Strength 230
5.5.4 Aperture Effects 232
5.6 Summary 235

6 Conclusion **290**
6.1 Summary and Conclusions 290
6.2 Future Work 293

Appendix 296

A Data Acquisition and Signal Processing 296
A.1 Introduction 296
A.2 Test Procedure 301
A.2.1 Test Configuration 301
A.2.2 The Source and Incident Field Properties 303
A.2.3 Scattering Data Measurement 303
A.3 Influence of the Clutter Subtraction Process 305
A.4 Signal Processing Methods 307
A.4.1 Spectral Density Estimates 307
A.4.2 Target Strength Calculations 308
A.4.3 Method of Deconvolution 309
A.4.4 Calculation of Signal Envelopes 311
A.4.5 Bistatic Aperture Imaging 312
A.4.6 The $\tau - p$ Transform 313
A.4.7 Wigner Distribution Analysis 315

B Generation of Membrane Wave Caustics at the Endcaps 327

List of Tables

1.1 Summary of Model Design Parameters 36

2.1 Critical Aspect Angles for Membrane Wave Excitation 60
2.2 Computed Membrane Wave Decay Rates and Form Function Values at Beam Aspect 72
2.3 Computed Membrane Wave Decay Rates and Form Function Values at a 75 degree Aspect Angle 72
2.4 Computed Membrane Wave Decay Rates and Form Function Values at a 66 degree Aspect Angle 72

3.1 Comparison of Measured and Predicted Decay Rates at Beam Aspect 107

5.1 Comparison of the Target Strengths of the Peak Initial Scatter Produced by Different Infinite Cylinders at Beam Aspect 211
5.2 Bow Aspect Time Delays of the First Reflections of Compressional Waves at the Structural Discontinuities 217
5.3 Comparison of the Measured Backscatter Decay Rates of the Shells at an Aspect Angle of 75 Degrees 227
5.4 Comparison of the Measured Backscatter Decay Rates of the Shells at an Aspect Angle of 66 Degrees 230

A.1 Summary of Tests Performed 298
A.2 Scattering Measurement Parameters - July 1991 299
A.3 Scattering Measurement Parameters - October 1991 299
A.4 Empty Shell Scattering Measurement Parameters - May 1992 300
A.5 Complex Shell Scattering Measurement Parameters - June 1992 . . . 300
A.6 Bandpass Filter Parameters Used 311
A.7 Axial Resolution of Beamforming Operations 313

List of Figures

1.1 Illustration of the Orientation of the Monostatic and Specularly Directed Fields, and the Aspect θ and Observation θ_o Angle Reference Conventions 37
1.2 The Design Configuration of the Empty Shell Model and the Exterior Shell of the Ring Stiffened and Complex Models 37
1.3 The Locations of the Ring Stiffeners Comprising the Ring Stiffened and Complex Models 38
1.4 The Internal Loading Configuration of the Complex Model 38
1.5 Illustration of Fundamental Leaky Wave Scattering Processes for Plane Wave Insonification of a Finite Shell 39
1.6 Gaussian Bandpass Filter Impulse Response - $2.75 < ka < 10.0$ 40

2.1 Spatial variable reference conventions of the infinite cylinder analyses 43
2.2 The Backscattering Form Function Magnitude of an Infinite Cylinder at Normal Incidence 78
2.3 Specular Direction Form Function of Infinite Cylinder at a 75 deg Aspect Angle 78
2.4 Specular Direction Form Function of Infinite Cylinder at a $\theta = 66$ deg Aspect Angle 79
2.5 Watson Transform Contour C and Deformed Contour $C\prime$ Used to Determine Asymptotic Solutions 79
2.6 Typical Pole Locations in Complex Azimuthal Wavenumber ν Plane for Plane Wave Excitation of a Fluid Loaded Thin Cylindrical Shell . 80
2.7 Illustration of Phase Matched Launching and Detachment of a Propagating Helical Wave on an Infinite Cylinder 80
2.8 Membrane Wave Launch and Detachment Angles ϕ_{l_m} as a Function of Aspect Angle θ 81
2.9 Membrane Wave Helix Angle ψ_m, Relative to the Axis of the Cylinder, as a Function of Aspect Angle θ 81
2.10 Loci of Aspect Angle θ and Frequency ka Where Conditions of Circumferential Spatial Coincidence Exist for Membrane Wave Excitation 82
2.11 Period of Circumferential Component of Phase Matched Helical Membrane Waves 82
2.12 Gaussian Bandlimited Time Domain Representation of Backscattered Form Function of an Infinite Cylindrical Shell at Normal Incidence . . 83

2.13 Gaussian Bandlimited Time Domain Representation of Backscattered Form Function of an Infinite Pressure Release Cylinder at Normal Incidence 84
2.14 Gaussian Bandlimited Time Domain Representation of Backscattered Form Function of an Infinite Rigid Cylinder at Normal Incidence . . . 84
2.15 Comparison of Normal Mode Series and Asymptotic Solutions for the Backscattered Field Form Function Magnitude and Phase at Normal Incidence 85
2.16 Phase of Specularly Reflected Component of the Backscattered Field Form Function at Normal Incidence 86
2.17 Magnitude of Coupling Coefficient A_m Associated with Compressional Wave Excitation at Normal Incidence 86
2.18 Real and Imaginary Components of Azimuthal Wavenumber Poles ν_m Associated with Compressional Wave Propagation and Excitation at Normal Incidence 87
2.19 Magnitude and Phase of Compressional Leaky Wave Component of Backscattered Field Form Function at Normal Incidence 88
2.20 Gaussian Bandlimited Time Domain Representation of Specularly Directed Scattered Field Form Function of an Infinite Cylindrical Shell at a 75 deg Aspect Angle 89
2.21 Comparison of Normal Mode Series and Asymptotic Solutions for Specular Directed Scattered Field Form Function Magnitude and Phase at a 75 deg Aspect Angle 90
2.22 Phase of Specularly Reflected Component of Scattered Field Form Function at a 75 deg Aspect Angle 91
2.23 Magnitude of Coupling Coefficients A_m Associated with Compressional and Transverse Shear Wave Excitation at a 75 deg Aspect Angle 91
2.24 Real and Imaginary Components of Azimuthal Wavenumber Poles ν_m Associated with Compressional and Transverse Shear Wave Propagation and Excitation at a 75 deg Aspect Angle 92
2.25 Magnitude and Phase of Compressional and Transverse Shear Leaky Wave Component of Specularly Directed Scattered Field Form Function at a 75 deg Aspect Angle 93
2.26 Gaussian Bandlimited Time Domain Representation of Specularly Directed Scattered Field Form Function of an Infinite Cylindrical Shell at a 66 deg Aspect Angle 94
2.27 Comparison of Normal Mode Series and Asymptotic Solutions for Specular Directed Scattered Field Form Function Magnitude and Phase at a 66 deg Aspect Angle 95
2.28 Phase of Specularly Reflected Component of Scattered Field Form Function at a 66 deg Aspect Angle 96
2.29 Magnitude of Coupling Coefficient A_m Associated with Transverse Shear Wave Excitation at a 66 deg Aspect Angle 96

2.30 Real and Imaginary Components of Azimuthal Wavenumber Poles v_m Associated with Transverse Shear Wave Propagation and Excitation at a 66 deg Aspect Angle 97
2.31 Magnitude and Phase of Transverse Shear Leaky Wave Component of Specularly Directed Scattered Field Form Function at a 66 deg Aspect Angle 98
2.32 Comparison of The Backscattering Form Function Magnitude of an Infinite Cylinder at Normal Incidence with Structural Damping Loss Factors of $\eta_d = 0$, 0.01, 0.05, and 0.10 99
2.33 Gaussian Bandlimited Time Domain Representation of Backscattered Form Function of an Infinite Cylindrical Shell at Normal Incidence with a Structural Loss Factor of $\eta_d = 0.1$ 99
2.34 Real Part of Axial Wavenumber Roots $k_z a_r$ Associated with Free Compressional Wave Propagation 100
2.35 Imaginary Part of Axial Wavenumber Roots $k_z a_i$ Associated with Free Compressional Wave Propagation 100
2.36 Real Part of Axial Wavenumber Roots $k_z a_r$ Associated with Free Transverse Shear Wave Propagation 101
2.37 Imaginary Part of Axial Wavenumber Roots $k_z a_i$ Associated with Free Transverse Wave Propagation 101
2.38 Phase and Group Velocities Associated with Free Compressional Wave Propagation 102
2.39 Phase and Group Velocities Associated with Free Transverse Shear Wave Propagation 102
2.40 Real Part of Axial Wavenumber Roots $k_z a_r$ Associated with Free Transverse Flexural Wave Propagation 103
2.41 Phase and Group Velocities Associated with Free Flexural Wave Propagation 103

3.1 Comparison of the Measured Empty Shell and Infinite Cylinder Predicted Beam Aspect Form Functions 142
3.2 Measured Gaussian Bandlimited Monostatic Impulse Response of the Empty Shell at Beam Aspect 142
3.3 Logarithm of the Magnitude of the Envelope of the Gaussian Bandlimited Impulse Response of the Empty Shell at Beam Aspect 143
3.4 Beam Aspect Target Strength Correction 143
3.5 Corrected Target Strength of the Empty Shell as Measured at Beam Aspect 144
3.6 Measured Propagation Delay of the Peak Value of the Initial Return from the Empty Shell 144
3.7 Target Strength of the Peak Initial Return from the Empty Shell Model $T_{initial}(\theta)$ 145
3.8 Comparison Target Strength Values Computed Using the Peak Initial Return and the Time Integral of the Squared Pressure $p_s^2(t)$ 145

3.9 Analytic Signal Envelope of the Gaussian Bandlimited Monostatic Impulse Response of the Empty Shell for the Frequency Range $2.75 < ka < 10.0$ and $0 \leq \theta \leq 90$ deg 146
3.10 Predicted Arrival Times for Scattering from the Slope Discontinuities of the Two Endcaps 147
3.11 Illustration of Propagation Paths of of Scattering from the Slope Discontinuities of the Two Endcaps of the Shell Models 147
3.12 Measured Target Strength $T(\omega, \theta)$ of the Empty Shell Model over $0 \leq \theta \leq 90$ deg 148
3.13 Measured Target Strength $T(\omega, \theta)$ of the Empty Shell Model over $60 \leq \theta \leq 90$ deg 149
3.14 Analytic Signal Envelope of the Gaussian Bandlimited Monostatic Impulse Response of the Empty Shell for the Frequency Range $2.75 < ka < 10.0$ and $60 \leq \theta \leq 90$ deg 150
3.15 Predicted Time Delays of the First 5 Leaky Wave Arrivals Associated with the First Round Trip of the Induced Structural Waves 151
3.16 Loci of Aspect Angle and Frequency Where Conditions of Membrane Wave Spatial Coincidence and Axial Resonance Conditions Exist . . . 152
3.17 Analytic Signal Envelope of the Gaussian Bandlimited Bistatic Impulse Response of the Empty Shell for the Frequency Range of $2.75 < ka < 10.0$ and Observation Angles $50 \leq \theta_o \leq 130$ deg 153
3.18 Effective Axial Distribution of Back and Specular Directed Scattered Field of the Empty Shell Model at an Aspect Angle of 75 degrees . . 154
3.19 Effective Axial Distribution of Back Directed Scattered Field of the Empty Shell Model at an Aspect Angle of 75 degrees 155
3.20 Interpretation of the Scatter Produced by the Empty Shell Model at an Aspect Angle of 75 degrees 156
3.21 $\tau - p$ Transform of the Effective Axial Distribution of the Back Directed Scattered Field of the Empty Shell Model at an Aspect Angle of 75 degrees 157
3.22 Gaussian Bandlimited Monostatic Impulse Response of the Empty Shell at an Aspect Angle of 75 deg 158
3.23 Illustration of Phase Matched, Back Directed Ray Paths for Insonification of the Shell at an Aspect Angle of 75 Degrees 159
3.24 Illustration of the Origins of the Variation of Peak Shear Radiation Observed at Observation Angles Near the Monostatic Receiver 159
3.25 Target Strength of the Empty Shell Monostatic Signal Measured Over $200 < t < 800$ μsec and an Aspect Angle of 75 deg 160
3.26 Magnitude of Shear and Compressional Leaky Wave Components of Specularly Directed Target Strength of an Infinite Cylinder at a 75 deg Aspect Angle 160
3.27 Target Strength of the Empty Shell Monostatic Signal Measured at an Aspect Angle of 75 deg 161

3.28 Analytic Signal Envelope of the Bandlimited Bistatic Impulse Response Signal of the Empty Shell Measured over the Range of Observation Angles $100 \leq \theta_o \leq 180$ deg 162
3.29 Magnitude of the Analytic Signal - Gaussian Bandlimited Monostatic Time Domain Representation of the Empty Shell at an Aspect Angle of 75 deg 163
3.30 Gaussian Bandlimited Specularly Directed Impulse Response of the Empty Shell at an Aspect Angle of 75 deg 164
3.31 Comparison of the Measured Empty Shell and Infinite Cylinder Specularly Directed Form Functions for an Aspect Angle of 75 deg 164
3.32 Smoothed Wigner Distribution of Gaussian Bandlimited Monostatic Impulse Response of the Empty Shell at an Aspect Angle of $\theta = 75$ deg 165
3.33 Gaussian Bandlimited Monostatic Impulse Response of the Empty Shell at an Aspect Angle of 66 deg 166
3.34 Magnitude of the Analytic Signal - Gaussian Bandlimited Monostatic Time Domain Representation of the Empty Shell at an Aspect Angle of 66 deg 166
3.35 Target Strength of the Empty Shell Monostatic Signal Measured Over $300 < t < 900$ μsec and an Aspect Angle of 66 deg 167
3.36 Magnitude of Transverse Shear Leaky Wave Component of Specularly Directed Target Strength of an Infinite Cylinder at a 66 deg Aspect Angle 167
3.37 Target Strength of the Empty Shell Monostatic Signal Measured at an Aspect Angle of 66 deg 168
3.38 Gaussian Bandlimited Monostatic Impulse Response of the Empty Shell at an Aspect Angle of 72 deg 168
3.39 Target Strength of the Empty Shell Monostatic Signal Measured Over $225 < t < 825$ μsec and an Aspect Angle of 72 deg 169
3.40 Magnitude of Transverse Shear Leaky Wave Component of Specularly Directed Target Strength of an Infinite Cylinder at 72 deg Aspect Angle 169
3.41 Target Strength of the Empty Shell Monostatic Signal Measured at an Aspect Angle of 72 deg 170
3.42 Gaussian Bandlimited Monostatic Impulse Response of the Empty Shell at an Aspect Angle of 80 deg 170
3.43 Target Strength of the Empty Shell Monostatic Signal Measured Over $150 < t < 1150$ μsec and an Aspect Angle of 80 deg 171
3.44 Magnitude of Shear and Compressional Leaky Wave Components of Specularly Directed Target Strength of an Infinite Cylinder at a 80 deg Aspect Angle 171
3.45 Target Strength of the Empty Shell Monostatic Signal Measured at an Aspect Angle of 80 deg 172
3.46 Gaussian Bandlimited Monostatic Impulse Response of the Empty Shell at an Aspect Angle of 85 deg 172

3.47 Target Strength of the Empty Shell Monostatic Signal Measured at an Aspect Angle of 85 deg 173
3.48 Magnitude of Shear and Compressional Leaky Wave Components of Specularly Directed Target Strength of an Infinite Cylinder at an 85 deg Aspect Angle 173

4.1 Illustration of the Orientation of the Ring Stiffener and the Coordinate System Used to Determine the Scattered Pressure 175
4.2 The Contour of Integration Used to Determine the Transmission Coefficients for an Incident Wave Propagating in the Positive z Direction 189
4.3 The Magnitude of the Far Field Pressure $p_{s_1}(R, \pi/2)$ Scattered at the Ring by an Incident Shear Wave Mode of Unit Radial Amplitude . . 194
4.4 The Magnitude of the Far Field Pressure $p_{s_1}(R, \pi/2)$ Scattered at the Ring by an Incident Compressional Wave Mode of Unit Radial Amplitude 194
4.5 The Magnitude of the Far Field Pressure $p_{s_1}(R, \pi/2)$ Scattered at the Ring by an Incident Flexural Wave Mode of Unit Radial Amplitude . 195
4.6 The Magnitude of the Integrand Defining the Radial Displacement Produced at the Ring by an Incident Free Shear Wave with Mode $n = 1$ at $ka = 7.06$ 195
4.7 The Reflection Coefficients of an Incident Free Shear Wave with Mode $n = 1$ 196
4.8 The Transmission Coefficients of an Incident Free Shear Wave with Mode $n = 1$ 196
4.9 The Reflection Coefficients of an Incident Free Compressional Wave with Mode $n = 1$ 197
4.10 The Transmission Coefficients of an Incident Free Compressional Wave with Mode $n = 1$ 197
4.11 The Magnitude of the Reflection Coefficient r_{ff} of an Incident Free Flexural Wave with Mode $n = 1$ 198
4.12 The Magnitude of the Transmission Coefficient t_{ff} of an Incident Free Flexural Wave with Mode $n = 1$ 198
4.13 The Coupled Wave Reflection Coefficients of an Incident Free Flexural Wave with Mode $n = 1$ 199
4.14 The Coupled Wave Transmission Coefficients of an Incident Free Flexural Wave with Mode $n = 1$ 199
4.15 The Reflection Coefficients of an Incident Free Shear Wave with Mode $n = 2$ 200
4.16 The Transmission Coefficients of an Incident Free Shear Wave with Mode $n = 2$ 200
4.17 The Reflection Coefficients of an Incident Free Compressional Wave with Mode $n = 2$ 201
4.18 The Transmission Coefficients of an Incident Free Compressional Wave with Mode $n = 2$ 201

4.19 The Magnitude of the Reflection Coefficient r_{ff} of an Incident Free Flexural Wave with Mode $n = 2$ 202
4.20 The Transmission Coefficient t_{ff} of an Incident Free Flexural Wave with Mode $n = 2$ 202
4.21 The Coupled Wave Reflection Coefficients of an Incident Free Flexural Wave with Mode $n = 2$ 203
4.22 The Coupled Wave Transmission Coefficients of an Incident Free Flexural Wave with Mode $n = 2$ 203

5.1 Comparisons of the Measured Target Strength $T(\omega, \theta)$ of the Complex, Internally Loaded Shell at Roll Angles of 0, 22.5, and 45 degrees and Aspect Angle of 66, 75, and 90 degrees 237
5.2 Effective Axial Distribution of Back Directed Scattered Field of the Complex Shell at Beam Aspect 238
5.3 Bistatic Target Strength $T(\omega, \theta_o)$ of the Complex Shell Measured for Beam Aspect over $60 \leq \theta_o \leq 120$ deg 239
5.4 Predicted Beam Pattern of the Empty Shell at Beam Aspect and a Distance $r = 2\ m$ 240
5.5 Measured Beam Pattern of the Complex Shell at Beam Aspect and a Distance $r = 2\ m$ 241
5.6 Measured Beam Pattern of the Complex Shell at Beam Aspect in the Absence of the Initial Scatter 242
5.7 Amplitude and Phase Taper of the Complex Shell at Beam Aspect in the Absence of the Initial Scatter 243
5.8 Gaussian Bandlimited Monostatic Impulse Response of the Complex Shell at Beam Aspect 244
5.9 Logarithm of the Magnitude of the Envelope of the Gaussian Bandlimited Impulse Response of the Complex Shell at Beam Aspect . . 244
5.10 Gaussian Bandlimited Monostatic Impulse Response of the Ring Stiffened Shell at Beam Aspect 245
5.11 Logarithm of the Magnitude of the Envelope of the Gaussian Bandlimited Impulse Response of the Ring Stiffened Shell at Beam Aspect 245
5.12 Comparison of the Measured Target Strengths $T(\omega, \theta)$ of the Empty, Ring Stiffened, and Complex Shells at Beam Aspect 246
5.13 Comparison of the Target Strengths Associated with the Peak Initial Return $T_{initial}(\theta)$ from the Empty, Ring Stiffened, and Complex Shells 246
5.14 Analytic Signal Envelope of the Gaussian Bandlimited Monostatic Impulse Response of the Ring Stiffened Shell for the Frequency Range $2.75 < ka < 10.0$ and $0 \leq \theta \leq 90$ deg 247
5.15 Analytic Signal Envelope of the Gaussian Bandlimited Monostatic Impulse Response of the Complex Shell for the Frequency Range $2.75 < ka < 10.0$ and $0 \leq \theta \leq 90$ deg 248
5.16 Predicted Arrival Times for the First Incidence of Scattering from the Ring Stiffeners and Endcaps of the Shell Models 249

5.17 Illustration of Propagation Paths of the First Incidence of Scattering from the Ring Stiffeners and Endcaps of the Shell Models 250
5.18 Comparison of the Target Strengths Associated with the Integrated Squared Pressure $p_s^2(t,\theta)$ from the Empty, Ring Stiffened, and Complex Shells 250
5.19 Comparison Target Strength Values Computed Using the Measured Peak Initial Return and the Time Integral of the Squared Pressure $p_s^2(t,\theta)$ of the Ring Stiffened Shell 251
5.20 Comparison Target Strength Values Computed Using the Peak Initial Return and the Time Integral of the Squared Pressure $p_s^2(t,\theta)$ of the Complex Shell 251
5.21 Measured Target Strength $T(\omega,\theta)$ of the Ring Stiffened Shell Model over $0 \leq \theta \leq 90$ deg 252
5.22 Measured Target Strength $T(\omega,\theta)$ of the Complex Shell Model over $0 \leq \theta \leq 90$ deg 253
5.23 Comparison of the Measured Target Strengths $T(\omega,\theta)$ of the Complex and Ring Stiffened Shell Models over $0 \leq \theta \leq 90$ deg 254
5.24 Spatial Average of Mean Square Pressure $|P_s(\omega,\theta)|^2$ over the Full Range of Aspect Angles $0 \leq \theta \leq 180$ 255
5.25 Spatial Average of Mean Square Pressure $|P_s(\omega,\theta)|^2$ over the Range of Aspect Angles $61 \leq \theta \leq 81$ and $99 \leq \theta \leq 119$ 255
5.26 Spatial Average of Spatial Average of Mean Square Pressure $|P_s(\omega,\theta)|^2$ over the Range of Aspect Angles within 60 degrees of the Bow and Stern Endcaps. The average is normalized by the mean square pressure of the incident field $|P_{ref}(\omega)|^2$ and 4π steradians. 256
5.27 Measured Target Strength $T(\omega,\theta)$ of the Ring Stiffened Shell Model over $60 \leq \theta \leq 90$ deg 257
5.28 Measured Target Strength $T(\omega,\theta)$ of the Complex Shell Model over $60 \leq \theta \leq 90$ deg 258
5.29 Beam Pattern Produced by Simulated Array at a Distance of 2 m When Steered to $\theta_o = 92$ deg at $ka = 8.5$ 259
5.30 Comparisons of the Frequency Spacing Δka of Measured Backscatter at Aspect Angles of 66, 72, 75, and 80 deg. 260
5.31 Loci of Aspect Angle and Frequency Where Axial Resonance Would Occur for the Different Lengths Between Pairs of Perfectly Reflecting Stiffeners 261
5.32 Measured Target Strength $T(\omega,\theta)$ of the Ring Stiffened Shell Model over $60 \leq \theta \leq 120$ deg 262
5.33 Measured Target Strength $T(\omega,\theta)$ of the Complex Shell Model over $60 \leq \theta \leq 120$ deg 263
5.34 Comparison of Total Backscatter Levels Measured at Complementary Aspect Angles for the Ring Stiffened Shell 264
5.35 Comparison of Total Backscatter Levels Measured at Complementary Aspect Angles for the Complex Shell 264

5.36 Analytic Signal Envelope of the Gaussian Bandlimited Monostatic Impulse Response of the Ring Stiffened Shell for the Frequency Range $2.75 < ka < 10.0$ and $60 \leq \theta \leq 90$ deg 265
5.37 Analytic Signal Envelope of the Gaussian Bandlimited Monostatic Impulse Response of the Complex Shell for the Frequency Range $2.75 < ka < 10.0$ and $60 \leq \theta \leq 90$ deg 266
5.38 Effective Axial Distribution of the Back and Specularly Directed Scatter Sources of the Complex Shell Model at an Aspect Angle of 75 degrees 267
5.39 Comparison of Bandlimited Monostatic Impulse Response Signatures of the Three Shells at an Aspect Angle of 75 deg 268
5.40 Comparison of the Envelopes of the Bandlimited Impulse Response Signatures of the Three Shells at an Aspect Angle of 75 deg 269
5.41 Gaussian Bandlimited Specularly Directed Impulse Response of the Complex Shell at an Aspect Angle of 75 deg 270
5.42 Effective Axial Distribution of the Back and Specularly Directed Scatter Sources of the Complex Shell Model at an Aspect Angle of 66 degrees 271
5.43 Effective Axial Distribution of the Back Directed Scatter Sources of the Complex Shell Model at an Aspect Angle of 66 degrees 272
5.44 Comparison of Bandlimited Monostatic Impulse Response Signatures of the Three Shells at an Aspect Angle of 66 deg 273
5.45 Comparison of the Envelopes of the Bandlimited Impulse Response Signatures of the Three Shells at an Aspect Angle of 66 deg 274
5.46 Gaussian Bandlimited Specularly Directed Impulse Response of the Complex Shell at an Aspect Angle of 66 deg 275
5.47 Target Strength of the Ring Stiffened Shell Monostatic Signal Measured Over $30 < t < 1150 \mu sec$ and an Aspect Angle of 75 deg 276
5.48 Target Strength of the Complex Shell Monostatic Signal Measured Over $30 < t < 1150 \mu sec$ and an Aspect Angle of 75 deg 276
5.49 Target Strength of the Ring Stiffened Shell Monostatic Signal Measured Over $30 < t < 1150 \mu sec$ and an Aspect Angle of 66 deg 277
5.50 Target Strength of the Complex Shell Monostatic Signal Measured Over $30 < t < 1150 \mu sec$ and an Aspect Angle of 66 deg 277
5.51 Comparison of the Measured Target Strength of the Three Shells at an Aspect Angle of 75 deg 278
5.52 Comparison of the Measured Target Strength of the Three Shells at an Aspect Angle of 66 deg 279
5.53 Comparison of the Measured Specularly Directed Target Strength of the Complex and Empty Shells for an Aspect Angle of 75 deg 280
5.54 Comparison of the Measured Complex Shell and Infinite Cylinder Specularly Directed Form Functions for an Aspect Angle of 66 deg . . 280
5.55 Target Strength of the Complex Shell Back Directed Scatter Measured Over $700 < t < 2700 \mu sec$ and an Aspect Angle of 75 deg 281
5.56 Target Strength of the Complex Shell Specularly Directed Scatter Measured Over $700 < t < 2700 \mu sec$ and an Aspect Angle of 75 deg . . 281

5.57 Target Strength of the Complex Shell Back Directed Scatter Measured Over $500 < t < 2500\mu sec$ and an Aspect Angle of 66 deg 282
5.58 Target Strength of the Complex Shell Specularly Directed Scatter Measured Over $500 < t < 2500\mu sec$ and an Aspect Angle of 66 deg . . 282
5.59 Representative Complex Shell Beam Patterns Measured at an Aspect Angle of 75 Degrees 283
5.60 Beam Pattern of Discrete Uniform/Hanning Array Steered to $\theta_o = 105\ deg$ 284
5.61 Representative Complex Shell Beam Patterns Measured at an Aspect Angle of 66 Degrees 285
5.62 Beam Pattern of Discrete Uniform/Hanning Array Steered to $\theta_o = 114\ deg$ 286
5.63 Amplitude and Phase Taper of the Complex Shell at an Aspect Angle of 66 degrees at $ka = 3.9$ 287
5.64 Amplitude and Phase Taper of the Complex Shell at an Aspect Angle of 66 degrees at $ka = 6.2$ 288
5.65 Amplitude and Phase Taper of the Complex Shell at an Aspect Angle of 66 degrees at $ka = 9.25$ 289

A.1 Roll Angle and Aspect Angle Reference Conventions 297
A.2 NRL Building 71 Scattering Measurement Tank 302
A.3 Energy Spectral Density of the Reference Source Signal used for July 1991 Measurements 318
A.4 Measured Reference Source Signal of the July 1991 Measurements . . 318
A.5 Variation of the Source Pressure Field Generated at 30 kHz Along a Line Parallel to the Source at the Target Center 319
A.6 Measured Average Clutter Signal of 17 April, 1991 320
A.7 Clutter Signal Power Spectral Density Measured 17 April, 1991 . . . 320
A.8 Typical Clutter Subtraction Process Results, Ring Stiffened Shell at 75 degree Aspect Angle 321
A.9 Comparison of 'True' Backscattered Signal and Clutter Signal Envelopes, Ring Stiffened Shell at 30 deg Aspect Angle 322
A.10 Comparison of 'True' Backscattered Signal and Clutter Signal Envelopes - Ring Stiffened Shell at Beam Aspect 322
A.11 Typical Levels Clutter Signal Reduction 323
A.12 Typical Residual Clutter Signal Power Spectral Density 323
A.13 Typical Residual Clutter Signal Envelope Magnitude 324
A.14 Ambient Noise Power Spectral Density Measured on 17 July, 1991, 100 Averages 324
A.15 Statistical Properties of the Spectral Magnitude of 100 Shot Ensemble Measurement of the Ring Stiffened Shell at Beam Aspect 325
A.16 Standard Deviation of the Phase of a 100 Shot Ensemble Measurement of the Ring Stiffened Shell at Beam Aspect 325

A.17 Illustration of Classical Beamforming of Bistatic Data for Analysis of the Complex Shell at an Aspect Angle of 75 degrees 326

B.1 Illustration of Helix Wavenumber Components on the Conical Section of the Endcaps Used on All Three Shell Models 331
B.2 Location of Caustic on Endcap for Transverse Shear and Compressional Waves 331
B.3 Illustration of Gaussian Pulse Waveform Before and After Interaction with Caustic at Endcap, $2.75 < ka < 10.0$ 332

Chapter 1

Introduction

1.1 Research Motivation and Context

The scattered pressure field of a cylindrical shell in water is significantly influenced by membrane wave propagation and induced dynamic interaction between the exterior shell and internal structures. The influence of internal structures is of particular interest at intermediate frequencies where wavelengths are comparable to characteristic discontinuity lengths of the submerged structure. In this thesis I interpret the experimentally measured scattering of three different cylindrical shell models to study the influence of helical membrane waves, resiliently mounted internal structures, and typical structural discontinuities such as endcaps and transverse stiffeners. The models consist of an empty shell, an unequally spaced ring stiffened shell, and an internally loaded shell. I also study the specularly directed scattering of infinite cylindrical shells to determine the origins of helical membrane wave excitation and reradiation. In addition, I estimate the scattering to other wave types and to the surrounding acoustic medium that is generated by an incident structural wave at an eccentric ring of mass. The scattering measurements and supporting analyses that I present have been conducted over a frequency range of $2 < ka < 12$. This frequency range corresponds to about 1/2 to 3 times the ring frequency of the empty shell, where k is the acoustic wavenumber and a the shell radius.

This research is motivated by an interest in the acoustic properties of ship and submarine hulls. Internal machinery and platform structures are often resiliently mounted to the hull to inhibit the local transmission of vibratory energy from machinery and supporting structure to the hull. The presence of resiliently mounted structures and structural discontinuities imposed by hull stiffeners must influence the acoustic scattering properties of the hull. An internal structure to hull mass ratio of 3 to 5 is typical of submarine designs. Given such large mass [illegible] typical impedance properties of hull stiffeners, the influences of internal structures may be significant. The shells studied here are not intended to illustrate the behavior of actual ship structures, but rather to demonstrate fundamental scattering processes of finite thin shells at normal and oblique angles of incidence. It is also intended that the data presented here may serve as a benchmark for comparison with developing three dimensional numerical codes.

I review the properties of the backscattered field observed over the full range of aspect angles from bow to stern aspect to delineate the frequency and aspect angle regimes where the influence of the ring stiffeners and internal structures is significant. However, evaluation of the field observed within ± 30 degrees of beam aspect (normal incidence) is the primary focus of this research. This range of aspect angles constitutes the angular regime where transverse shear (torsional) and compressional membrane waves can be excited by phase matching of the incident plane wave as it travels over the cylindrical portions of the shell. I have found excitation of helical membrane waves, and subsequent reradiation and interaction with the constituent structural components of the models, to be the dominant source of backscattered energy over much of this range of aspect angles.

The data presented primarily result from the analysis of monostatic measurements. Some bistatic data are also presented to contrast the monostatic and specularly directed fields, and to illustrate the effective axial source distribution producing the measured backscatter. The physical orientation of the monostatic and specularly directed fields, as well as the aspect (θ) and observation (θ_o) angle reference conven-

tions I employ are illustrated in Figure 1.1. The reference angle $\theta = 0$ defines a polar axis coaligned with the shell's longitudinal axis. All of the measurements that I discuss were conducted in a horizontal plane defined by the axis of the shell and the center of the receiver. The scattering measurements have all been conducted with the use of broadband pulses yielding good time resolution of propagating waves. Hence, I make significant use of time domain representations of the backscattered signatures of the models to demonstrate group delay, decay rate, and other scattering properties.

1.2 Shell Designs

All three shells evaluated here were designed by Conti and Dyer [15] and were constructed from a nickel alloy to high tolerances at the Naval Research Laboratory (NRL). The design parameters of the three shells are summarized in Table 1.1. The design of the empty shell serves as the base exterior shell design for the other two shells and is illustrated in Figure 1.2. All three shells are air filled and have an overall length of 0.86 m and a radius of $a = 0.05537$ m providing an aspect ratio of $L/2a = 7.75$. Each shell has a thickness to radius ratio of 0.0096. At beam aspect, I have observed that the empty shell exhibits a compressional wave radiation period of 66 μsec that corresponds to a fluid loaded compressional wave speed of $c_p = 5270$ m/sec. The two endcaps that enclose the cylindrical portions of the shells consist of a conical section adjoining the cylinder and a spherical hemisphere as illustrated in Figure 1.2. All welds were ground smooth on the exterior surface to prohibit the effects of surface discontinuities.

The ring stiffened shell is comprised of the same exterior shell design configuration, but is stiffened by four large nickel rings that are unequally spaced along the axis of cylinder as illustrated in Figure 1.3. The total mass of the rings equals the mass of the exterior shell and they provide structural impedance discontinuities to waves propagating on the shell. The rings were located with unequal spacing to

provide a means of studying the features of the scatter produced in the absence of pronounced structural periodicity as commonly studied.

The internally loaded, complex shell was designed to provide a means of evaluating the effects of resiliently mounted wave bearing structures. The internal structures are supported from a ring stiffened shell of the same configuration discussed above and illustrated in Figure 1.3. The internal structures consist of a quadrant symmetric arrangement of one inch diameter general purpose Delrin rods interconnected by cylindrical stainless steel masses as illustrated in Figure 1.4. The four wave bearing rods are individually supported from the ring stiffeners by independent, triangular shaped rubber blocks. The various internal components are all secured to one another with an epoxy compound. The Delrin rods were selected to provide a slow longitudinal wave speed relative to the plate speed of the surrounding shell. I have measured the quasi-longitudinal speed of a sample Delrin rod and found that it exhibited a speed of $c_l = 1625\ m/s$. This speed is 30% of the observed compressional wave speed of the shell. The total mass of the internal structures and ring stiffeners is approximately 3 times greater than the mass of the shell, as is representative of conventional submarine designs. The rubber is EAR C1002 Isodamp rubber, and was selected to provide a natural frequency of the suspended masses that is less than 1/3 of the ring frequency of the shell $ka < 1.2$. However, this has not been confirmed experimentally.

1.3 Previous Research

Experimental and analytic studies of the scatter generated by plane wave insonification of simple spherical shells and infinite cylindrical shells have been presented in a variety of references. For example, the effects of induced elastic waves and the azimuthal dependence of the scattered field have been studied by Feit [31] and Marston [62, 63, 32]. These references all emphasize scattering of plane waves at normal angles of incidence where the significance of compressional wave excitation is

revealed. Similar analytic studies of plane wave scattering from infinite cylindrical shells at oblique incidence, and the influence of helical elastic waves, have been studied by Felsen and Ho [19, 20, 21]. Using bistatic measurements of the scattered field of a thick cylindrical shell, Maze et al [36] identified spatial coincidence conditions found at oblique angles of incidence as induced by compressional and whispering gallery waves.

While the significance of the influence of helical membrane wave scattering processes has been recognized in the past, experimental confirmation of the importance of transverse shear waves and the influence of internal structures is limited at best. Relatively few experimental or analytic studies of acoustic scattering from finite cylindrical shells, particularly at oblique angles of incidence, or internally loaded shells are contained in the literature. Maze et al [40] conducted experimental and theoretical studies of the influence of resonant excitation of elastic waves on finite solid cylinders at normal and axial angles of incidence. Talmant and Quentin [52] identified the importance of generated compressional waves on thin cylindrical shells, but only at normal incidence. Guo [25, 26] and Achenbach [2] have analytically studied the scattering effects of infinite cylinders internally loaded with two dimensional mass-spring systems or elastic plates. These studies were all conducted at normal incidence and demonstrate significant scattering effects induced by the interaction of the shell with the internal structures. Resonant excitation of the internal structures and scattering of subsonic flexural waves at the attachment points of the internal structures were found to be significant scattering processes. Similar effects were noted by Klauson and Metsaveer [35] for an infinite shell with axially orientated stiffeners.

1.4 Approach and Overview of Thesis

The time evolution of fundamental helical membrane wave scattering processes for plane wave insonification of a simple finite cylindrical shell with *perfectly reflecting* truncations is illustrated in Figure 1.5. The shell has a length L and radius a,

and is submerged in water with a sound speed c_o. The shell is insonified with a well resolved planar pulse at an aspect angle θ. At time t_0 the incident wave front impacts the bow truncation producing a scattered acoustic pulse that travels back to the receiver along a direct ray path. The incident wave front continues to propagate along the shell with an axial trace velocity $c_z = c_o/\cos\theta$. As the incident wave front passes over the shell, selective membrane waves are excited along its length. At time $t_1 = t_0 + L/c_z$ the incident wave front has passed to the far edge of the shell and the geometric scatter, effectively a specularly reflected wave front, is fully detached from the shell and propagates off in the specular direction. In addition, the induced membrane waves (leaky waves) radiate a specularly directed field that lags the specularly reflected wave front by a time delay $\Delta t_m + \Delta t_{l_m}$ defined as shown below:

$$\Delta t_m = \left(\frac{\pi - \phi_{l_m}}{\pi}\right) T_m \tag{1.1}$$

$$\Delta t_{l_m} = a(1 - \cos\phi_{l_m})/(c_z \tan\theta) \tag{1.2}$$

The variable T_m represents the circumferential period of the excited helical membrane wave of type 'm'. The variable ϕ_{l_m} is the azimuthal angle along the shell surface where both the circumferential and axial phase speeds of the membrane wave helix and incident field are matched. Therefore, ϕ_{l_m} defines the regions, or launch lines, where the membrane waves are excited. A structural wave launched at $+\phi$ will radiate in the specular direction at $-\phi$ following a circumnavigation of the shell. The delay Δt_m is the time required for the induced structural wave to complete the first circumnavigation of the shell. The delay Δt_{l_m} is the additional propagation delay required for the incident phase front to travel to the launch lines of the excited membrane wave type.

At time $t_2 = t_0 + L/c_z + \Delta t_{l_m}$ the incident wave front has passed over the entire length of the shell and launch lines. The incident wave front then continues to prop-

agate away from the shell and the induced structural wave begins to propagate in the opposite direction having experienced an interaction with the endcap. Radiation from the induced membrane wave (leaky) field cannot be observed in the back, or monostatic direction, until this interaction has take place. The propagating structural waves then attenuate with time as they continually radiate into the surrounding acoustic medium. A back directed leaky wave front generated by a structural wave traveling down the shell axis at the forced wave speed would be fully detached from the shell at time $t_3 = t_0 + 2L/c_s + \Delta t_m + \Delta t_{l_m}$. The resulting back directed leaky wave field would then propagate away from the shell and additional distinct leaky wave arrivals would be subsequently observed with a period T_m. At time t_3, the structural wave would also begin to propagate towards the stern radiating with the same axial wavenumber orientation. I have observed that the time evolution of scattering from the empty shell is, with some important exceptions, approximated by this simple scenario.

I begin this thesis with a detailed study of plane wave scattering from infinite cylindrical shells to determine helical membrane wave scattering properties that may influence the processes described above. These studies evaluate the field in the specular direction and are presented in Chapter 2. Clearly, detailed comparisons of the specular field of an infinite shell and the backscatter of a finite shell are inappropriate. Among other differences, the pressure levels of the geometric field initially scattered at the shell truncations cannot be predicted from the specularly "reflected" field of an infinite cylinder. However, given certain assumptions, one can surmise that the evolution of the leaky wave fields would be similar over some period of time beyond the time required for the incident wave front to travel to the far end of the shell ($t > t_2$). The magnitude of the corresponding contribution of the leaky wave fields would also be similar or are at least worthy of comparison. These assumptions include:

- The truncations of the shell do not induce significant dispersive time delays or mode conversion of the incident structural membrane waves.

- The shell truncations do not significantly alter the dispersion relation of the shell, i.e. the membrane wave speeds remain essentially unchanged.

- The time required for membrane waves to traverse the length of the cylinder (or an appropriate shell segment located between a pair of stiffeners) must exceed the characteristic decay time of the wave. If this condition is not met, significant energy will be lost to radiation with the opposite axial orientation ($+k_z$ vs. $-k_z$).

These assumptions appear to be sufficiently well incorporated in the scattering response of the empty shell to allow meaningful comparison of coincidence frequencies, bandwidths and decay rates, and leaky wave pressure levels. Of equal importance, differences demonstrated by the comparisons illuminate the effects of the shell truncations and discontinuities. Subsequent comparisons of the measurements of the ring stiffened and complex shells with corresponding empty shell data illuminate the influence of the stiffeners and the internal loading.

I begin Chapter 2 with the derivation of a simple normal mode series solution to the obliquely incident plane wave scattering problem. I later use normal mode solutions to evaluate the accuracy of asymptotic results and to synthesize broadband time domain representations of the field. I employ a Sommerfeld-Watson Transform technique to derive asymptotic solutions to the problem. The resulting asymptotic expressions provide considerable physical insight into the physical origins of membrane wave excitation and radiation. The asymptotic formulation is used to derive the simple relation shown below that approximately quantifies the magnitude of the form function of the membrane wave field at coincidence:

$$\left|\frac{p_{sm}}{p_o}\right| \sqrt{\frac{2r}{a}} e^{-ik_r r} e^{-ik_z z} \approx \frac{4}{(1+\pi\delta_m)\sqrt{\pi k a_{coin} \sin\theta}}, \quad \delta_m \ll 1 \qquad (1.3)$$

where p_o is the amplitude of the incident field, ka_{coin} is the coincidence frequency of interest, and δ_m is the corresponding imaginary component of the azimuthal wavenumber variable. I have found that both transverse shear and compressional

membrane wave fields meet the δ_m smallness criteria of this expression. Therefore, both shear and compressional wave field contributions to the total scattered field are shown to be surprisingly comparable. Recognizing that membrane waves are essentially non-dispersive on the shell, I also formulate simple approximations for the frequencies and helix properties of the coincident fields. I then present example frequency and time domain representations of the fields computed at three different aspect angles, as well as their corresponding wavenumber roots, coupling coefficients, and leaky wave spectral levels. Throughout most of this thesis I present computational results that assume zero structural damping, because I have found that radiation losses constitute the dominant damping mechanism of the empty and ring stiffened shells. However, in Chapter 2 I present example results of computations of the scattered field generated at normal incidence with different levels of structural damping of the shell to illustrate the fundamental influences of structural damping. Finally, I conclude Chapter 2 with a presentation of the the free modes of propagation of an infinite fluid loaded cylindrical shell.

The measured backscatter of the empty shell is examined in Chapter 3. Many fundamental scattering process that are common to the more complicated shells turn out to be remarkably similar, so that the empty shell is good preparation for results to be shown in later chapters. I begin Chapter 3 with an examination of the backscatter measured at beam aspect. Near beam aspect, I have found that the scatter compares well with that of an infinite cylindrical shell. In this case, the field was measured at a radius where the field experiences cylindrical spreading consistent with the near field of a uniform line array. (Away from beam aspect, the effective radiation length of the scatterer is smaller and the measurement distance corresponds to a region of a spherically spreading far field.) Surprisingly, the measured decay rate for the empty shell at beam aspect is only 56% of that computed for the infinite cylinder, which I argue is due to radiation losses smaller than those of the shell alone. This indicates that radiation is the dominant damping mechanism of the measured system. More importantly, it indicates that the finite shell response incorporates additional energy

storage mechanisms that must include less efficient radiating wave types such as flexural waves.

I then briefly examine the monostatic field measured at oblique angles of incidence ranging from bow to beam aspect to contrast the field with that measured within 30 degrees of beam aspect which is the focus of the ensuing discussions. Within 30 degrees of beam aspect, peak levels of target strength were measured at combinations of frequency and aspect angle where shear wave coincidence conditions and peak length-scale modulation levels coexist. The coincidence frequencies are well approximated by the relations derived in Chapter 2. Frequency and time domain representations of the monostatic field measured at several oblique angles of incidence are next examined. Although details of the time domain features measured at different aspect angles differ significantly, peak levels of target strength $T(\omega, \theta)$ consistently fall within a range of -20 to -15 dB re 1 m.

Interpretation of bistatic data measured with the empty shell insonified at an aspect angle of $\theta = 75$ degrees is also presented in Chapter 3. I use beamforming techniques to determine the effective axial source distribution producing the specular and back directed scatter. The resulting time domain description of the backscatter shows that a strong periodic shear wave field is excited that propagates back towards the bow with an axial group speed that is slower than the trace speed of the incident field. Propagation of this type is shown to take place after the forced wave has interacted with the stern endcap at a time analogous to t_2 as discussed above. I also contrast the frequency and time domain representations of the specularly directed and monostatic measurements. The essential features of the specular field of an infinite cylinder, namely the constructive and destructive interference of the geometric and leaky wave fields, are also exhibited by the finite shell in the specular direction. At this aspect angle, the peak level of the backscattered compressional wave field is 9 dB less than the corresponding peak levels of the shear wave field. However, in the case of an infinite cylinder, peak shear wave levels would exceed compressional wave levels by only 2.5 dB. I believe that the smaller levels of compressional wave backscat-

ter observed result because energy is lost via direct and elastic wave scattering of the field at the stern endcap. The decay rate of the backscatter at times following the observation of peak leaky wave radiation levels is a factor 3 smaller than the infinite cylinder predictions. This decay rate is more indicative of a subsonic flexural wave scattering process generated at the two endcaps. Moreover, at this aspect angle coincidently excited compressional waves will scatter energy to noncoincident shear waves at a structural discontinuity such as the slope discontinuity of the endcaps, but coincident shear waves cannot scatter to compressional waves because they are cutoff. Evidence of large levels of compressional wave radiation are also observed over a range of bistatic observation angles $\cdots < \theta_o < 150$ that appears to originate at the endcap.

The scattering of a structural wave at an eccentric ring of mass is studied in Chapter 4 to estimate the scattering to other wave types and to the surrounding acoustic medium. I make use of asymptotic techniques to compute the reflection and transmission coefficients, as well as the scattered pressure, generated by an incident flexural, shear, or compressional wave of integer azimuthal order when it encounters a single ring. Significant scattering from one membrane wave type to the other, and to flexural waves is predicted. Scattering produced at a series of rings will thus smear the backscatter in the frequency and time domains and inhibit strong coincident radiation. Scattering to the acoustic medium is demonstrated to be a frequency selective process that produces a directive field with peak pressure levels found away from the axis of the shell. The scattered pressure levels generated by an incident membrane wave are comparable to the radiated field of the incident wave, while flexural wave scattering may be significant if its radial displacement amplitude is sufficiently large.

The backscatter measurements of the ring stiffened and complex shells are interpreted in Chapter 5. Both shells employ the same configuration of ring stiffeners, and the same external shell design as that used for the empty shell. I have found that in many ways, the details of the monostatic signatures of the two shells are

remarkably similar. However, the internal loading of the complex shell represents an additional energy storage system and transmission path that produces important differences.

Even at beam aspect, interaction between the shell, stiffeners, and internal loading produces scatter sources that vary significantly over the length of the shell. I use beamforming analysis of the bistatic data measured with the complex shell at beam aspect to demonstrate decreased compressional wave radiation near individual stiffeners. Similar behavior was first demonstrated by Bondaryk [3]. The resulting axially distributed field is analogous to a complicated phase and amplitude tapered array that produces a directive field different from that of the empty shell. The geometric scatter initially observed produces the field of a uniform array and interferes with the directive field produced by the subsequent scattering sources. In particular, a strong null is seen at an observation angle of $\theta_o = 83$ and the ring frequency $ka = 3.6$ that is the result of this type of interference. I also use the beamforming results to estimate the amplitude and phase tapers of the delayed scatter components.

I then briefly examine the monostatic fields measured at oblique angles of incidence ranging from bow to beam aspect and compare the features of the three shells. Comparisons of time domain representations of the monostatic fields demonstrate the existence of structural wave scattering at the ring stiffeners. As a result, large amplitude backscatter components other than the initial scatter is observed much earlier in the evolution of the field than was observed for the empty shell. A comparison of backscattered energy levels demonstrates that the ring stiffeners and internal loading increases the backscatter by more than 3 dB at aspect angles $\theta < 63$ degrees where coincident helical membrane waves are not excited on the cylinder. However, the addition of the ring stiffeners does not significantly increase backscattered energy levels at greater aspect angles of $63 < \theta < 90$ degrees. Interaction of the shell and internal loading is shown to increase backscattering levels at many discrete combinations of frequency and aspect angle. This increase is most prominent above a threshold frequency of $ka = 5.5$. Unfortunately, I know little of the specifics of

the interaction between the shell and the internal structures, the specifics residing outside the domain of my research.

I then use focused beamforming to illustrate the time evolution and axial scattering source distribution of the back and specularly directed scatter produced by the complex shell at aspect angles of 66 and 75 degrees. These results show significant scattering and reflection of elastic waves at the rings. As a result, backscatter decay rates of the three shells are shown to be different at these aspect angles. In particular, I show that the decay rates of packets of leaky wave backscatter observed for the empty shell exceed the decay rate of the ring stiffened shell by a factor of 2-3. This decrease appears to be a result of scattering of the supersonic membrane waves to flexural waves at the rings. The flexural waves energized at the rings will not radiate until they scatter directly to the fluid or into a shear or compressional wave at another ring and these scattering events occur at a lesser rate than for membrane waves because flexural waves propagate with slow group speeds. The decay rates of the complex shell are shown to exceed those of the ring stiffened shell by a factor of roughly 1.2 to 1.4 which I attribute to additional damping provided by the resilient mounts supporting the internal structures.

I also examine the measured beampattern of the complex shell at these same aspect angles. A comparison of back and specularly directed target strength computed for the scatter observed later in time is used to show that aperture effects must be important. In addition, I show that the beampattern found near the specular direction is well approximated by a uniform line array with hanning amplitude taper at the ends. The beampattern observed near the monostatic receiver exhibits high side lobe levels with little roll off that is caused by complicated phase and amplitude tapers of the scattering source distribution.

Finally, conclusions and recommendations for future research are made in Chapter 6 while the data acquisition and signal processing methods used are presented in Appendix A. I also employ a high frequency approximation in Appendix B to explain the generation of caustics at the endcaps.

Although the base frequency range of interest here is $2 < ka < 12$, a frequency range of $2.75 < ka < 10.0$ constitutes the limiting range of the different measurement series conducted. Therefore, all of the time domain representations presented in Chapters 2-5 have been bandlimited over this limiting frequency range so that different measurements can be appropriately compared with one another. The bandpass filter used is defined below and I refer to it as a "Gaussian" bandpass filter:

$$G(\omega) = e^{-(\omega_o - |\omega|)^2 / 2\sigma_\omega^2} \tag{1.4}$$

where ω_o is the center frequency at which $G(\omega) = 1$, and σ_ω is a bandwidth parameter selected to provide a signal reduction of 6 dB at the band edges as discussed further in Appendix A. The impulse response of the filter is shown in Figure 1.6.

Table 1.1: **Summary of Model Design Parameters**

Configuration	
Shell & Ring Material	Ni-200
Length Overall, L	0.86 m
Shell Radius, a	0.05537 m
Shell Thickness, h	0.000532 m
Aspect Ratio, $L/2a$	7.75
Thickness Ratio, h/a	0.0096
Mass Ratio, *Rings/Shell*	1
Mass Ratio, (*Internals & Rings*)/*Shell*	3
Longitudinal Wave Speed Ratio, *Rods/Shell*	1/4
Aprox. Shell Material Properties	
Young's Modulus, E_s	2.2 x 10^{11} N/m^2
Density, ρ_s	8900 kg/m^3
Poisson's Ratio, ν	0.31
Compressional Plate Wave Speed	5270 m/s
Transverse Shear Wave Speed	3100 m/s
Aprox. Delrin Material Properties	
Measured Dynamic Modulus, E_{rod}	3.7 x 10^9 N/m^2
Density, ρ_{rod}	1400 kg/m^3
Poisson's Ratio, ν_{rod}	0.35
Measured Compressional Speed of Rod	1625 m/s

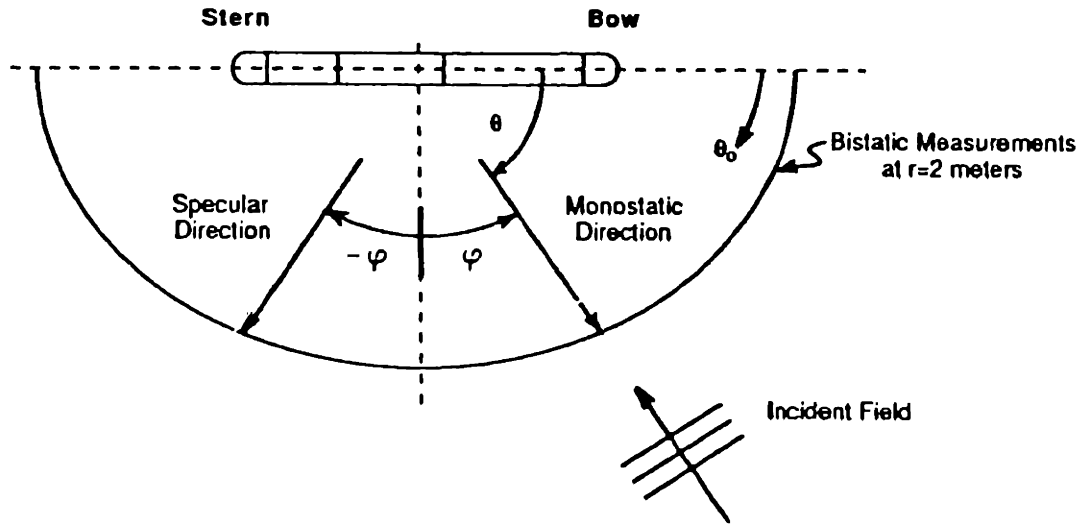

Figure 1.1: Illustration of the Orientation of the Monostatic and Specularly Directed Fields, and the Aspect θ and Observation θ_o Angle Reference Conventions

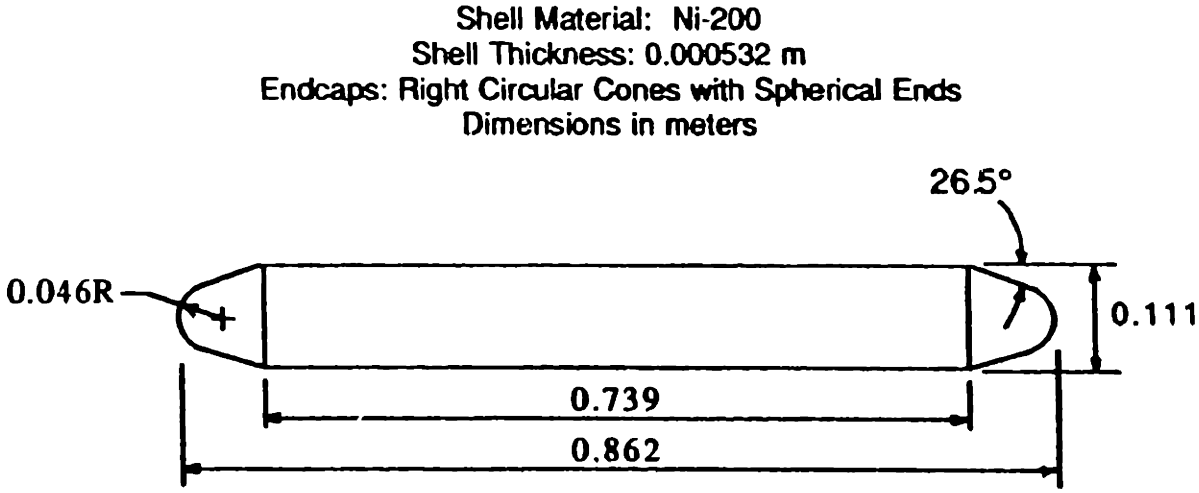

Figure 1.2: The Design Configuration of the Empty Shell Model and the Exterior Shell of the Ring Stiffened and Complex Models

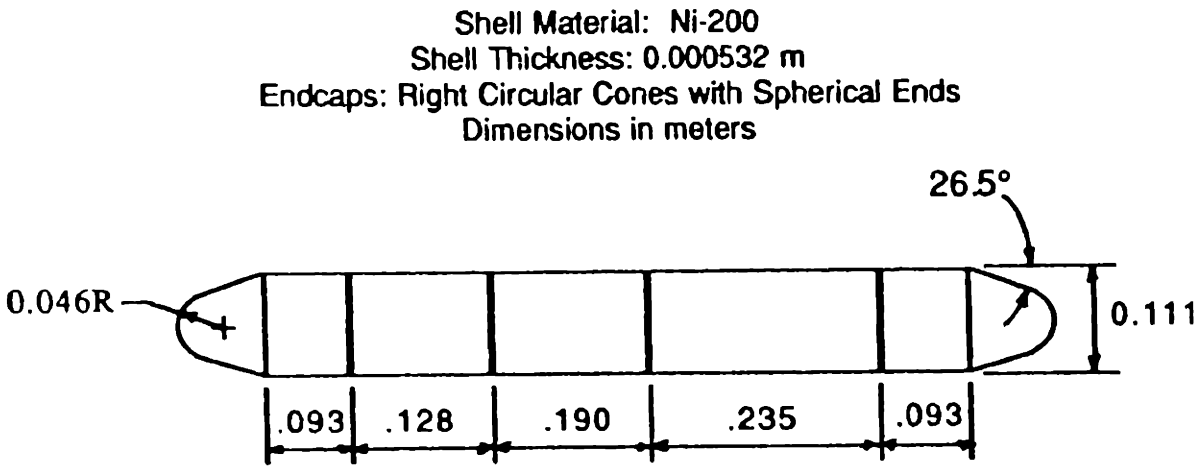

Figure 1.3: The Locations of the Ring Stiffeners Comprising the Ring Stiffened and Complex Models

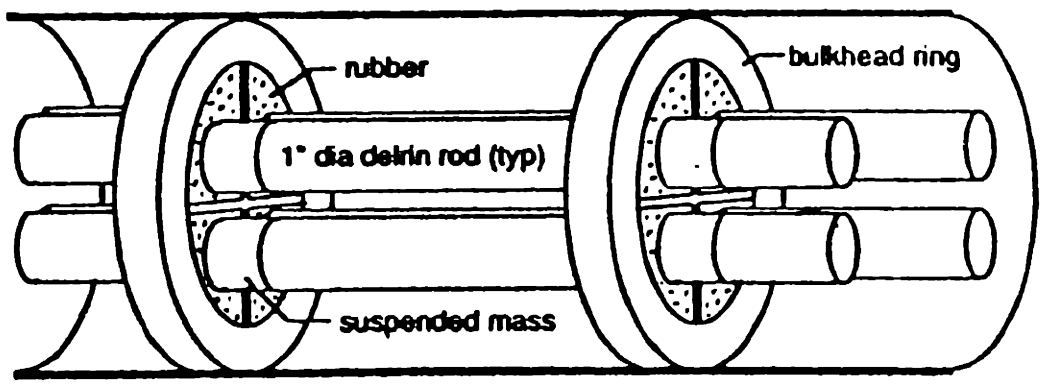

Figure 1.4: The Internal Loading Configuration of the Complex Model (From M. Conti)

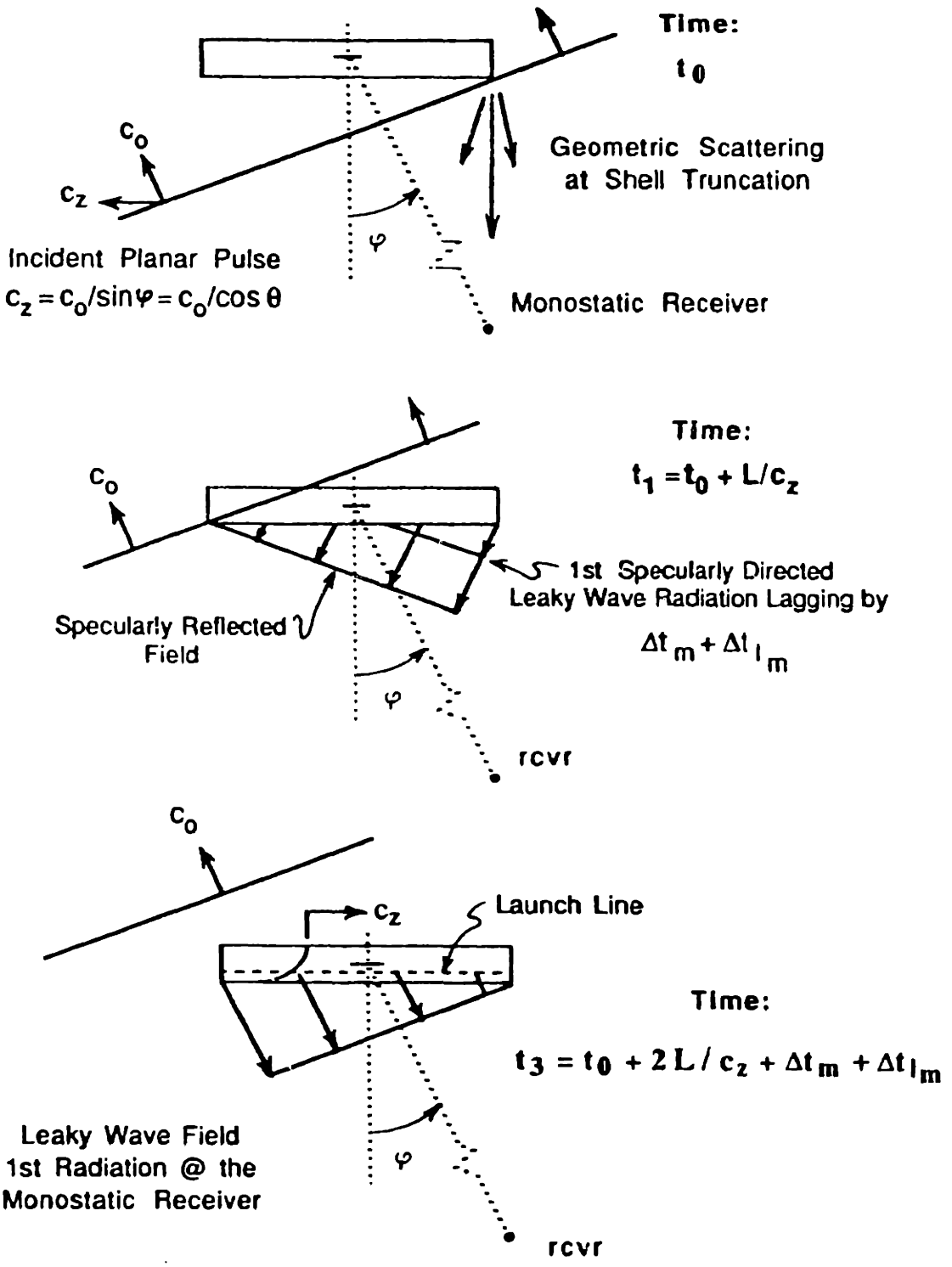

Figure 1.5: Illustration of Fundamental Leaky Wave Scattering Processes for Plane Wave Insonification of a Finite Shell with Perfectly Reflecting Truncations and Monostatic Observation

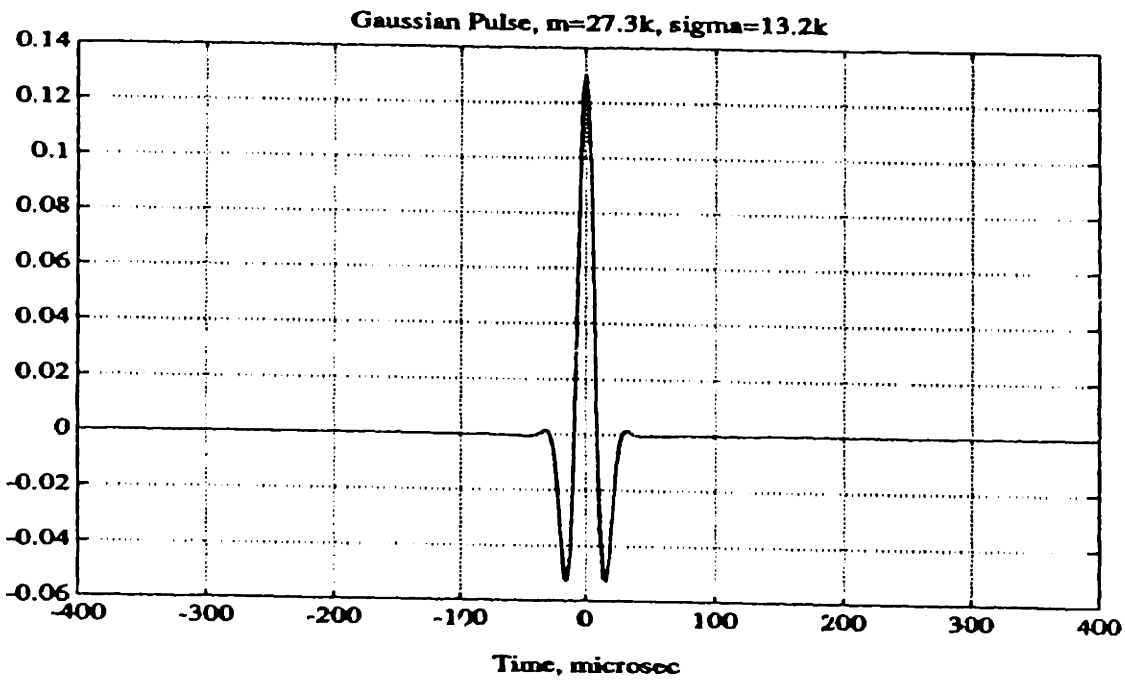

Figure 1.6: Gaussian Bandpass Filter Impulse Response, 6 dB down at Band Edges of the Frequency Range $2.75 < ka < 11.7$

Chapter 2

Plane Wave Scattering from Infinite Cylinders at Oblique Incidence

2.1 Introduction

I have studied the scattering response of thin infinite cylindrical shells to investigate the origins of coincidence conditions and the influence of membrane waves. The analyses presented are limited to angles of incidence within $\pm$ 27 degrees of normal incidence where membrane wave coincidence takes place. The infinite cylinder results presented evaluate the field in the specular direction, rather than in the monostatic direction which is the focus of the experimental studies of this thesis. However, these studies of the scatter produced by an infinite cylinder illustrate important aspects of the membrane wave transduction process found in finite cylindrical shells. Many of the properties highlighted by these analyses are readily observed in the response of the finite empty shell studied experimentally. Differences between the monostatic experimental and specular theoretical results can be attributed to complex gain effects and mode conversion induced by the endcaps, ring stiffeners, and internal loading comprising the finite shells.

I have employed a normal mode series solution technique to provide exact frequency domain solutions to the problem, and asymptotic methods to approximate the solutions and distinguish the different contributions of the geometric and membrane wave fields. Broadband time domain representations of the scattered field are also presented and were numerically computed using discrete inverse transforms of the series solutions. Normal mode solutions, also commonly referred to as partial wave or angular harmonic series solutions, to the plane wave scattering problem are first presented in Section 2.2. Asymptotic solutions to the problem are formulated in Section 2.3 using the Sommerfeld-Watson Transform (SWT) technique. The asymptotic solutions provide physical insight more readily than the normal mode series solutions. The analyses presented in Sections 2.2 and 2.3 all assume zero structural damping and the influences of structural damping are briefly addressed in Section 2.4. Finally, the free modes of propagation of a fluid loaded infinite cylindrical shell are presented Section 2.5. In all cases, I have employed Donnell thin shell theory to describe the equations of motion of the cylinder. The appropriate material and geometric properties listed in Table 1.1 have been used to compute all of the results presented.

Consider an infinitely long, thin cylindrical shell of mean radius a that is submerged in an inviscid fluid of density ρ_o and sound speed c_o as illustrated in Figure 2.1. The axis of the cylinder coincides with the axis of a cylindrical coordinate system (r, ϕ, z). The corresponding midsurface displacements of the shell are (w, v, u). The shell is insonified by a time harmonic plane wave with a time dependence $e^{-i\omega t}$, where ω is the radian frequency of the field and t is time. Linear theory is assumed throughout these studies and the time dependence $e^{-i\omega t}$ is attributed to all response parameters. The time dependence has been suppressed in the equations that follow accordingly. The shell is characterized by its material properties: density ρ_s, Young's modulus E_s, Poisson's ratio ν, and sound speed c_p, where $c_p = \sqrt{E_s/\rho_s(1-\nu^2)}$ is the quasi-longitudinal plate wave speed. The shell has a thickness h, and terms proportional to the ratio $\beta^2 = h^2/12a^2$ represent the

contribution of bending stresses.

The shell is insonified by a plane wave characterized by its amplitude p_o, wavenumber $k = \omega/c_o$, and its aspect angle θ, where θ is a polar angle defined with respect to the z axis and $\theta = 90$ degrees is normal incidence. Alternatively, one can define the direction of the field using the angle φ which is defined relative to a plane normal to the axis of the shell as shown in Figure 2.1. The axial and radial components of the incidence wavenumber, k_z and k_r, are defined by the following relations

$$k_z = k\cos\theta = k\sin\varphi \tag{2.1}$$

$$k_r = \sqrt{k^2 - k_z^2} \tag{2.2}$$

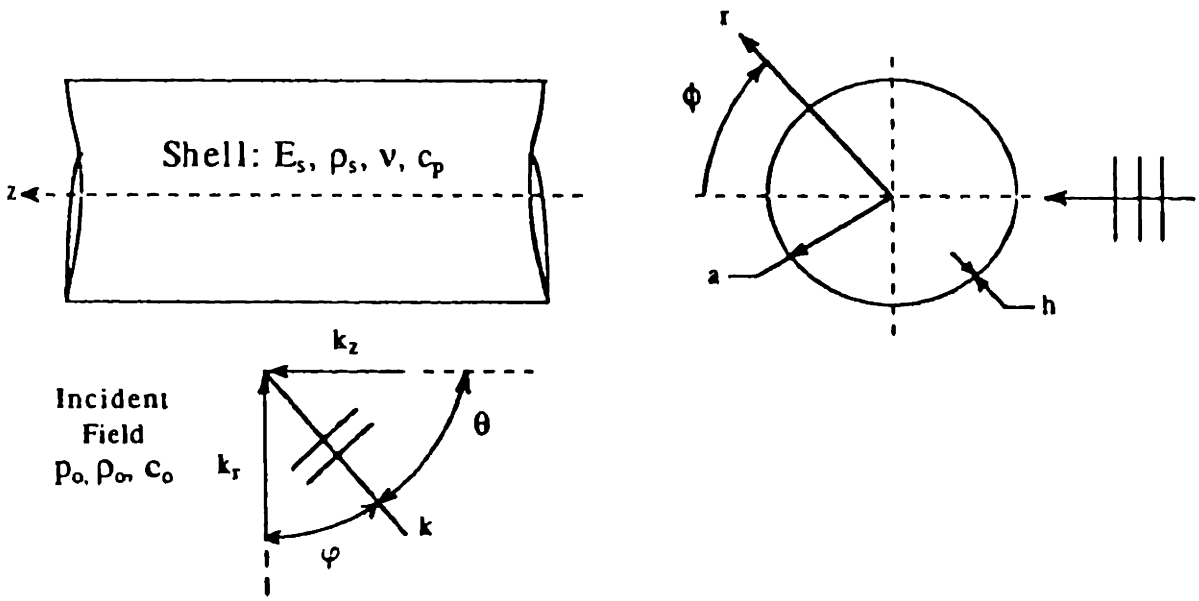

Figure 2.1: Spatial variable reference conventions of the infinite cylinder analyses

2.2 Normal Mode Series Solution

Series solutions to the problem of scattering of an incident plane wave by a cylindrical shell have been presented in numerous references. The separable geometry of

the problem allows one to synthesize the solution as a summation of integer order azimuthal (ϕ) response functions. Scattering of a normally incident plane wave by an empty shell has been studied by Junger and Feit [31] using thin shell theory. Scattering of an obliquely incident plane wave has been presented, with limited interpretation, by Veksler et al [56] using full elastic theory. I have similarly adopted the normal mode series solution approach to provide an exact solution to the problem of oblique incidence, but I have made use of thin shell theory.

The incident plane wave can be expressed as a summation of weighted angular harmonics of the azimuthal coordinate ϕ as shown below:

$$\begin{aligned} p_i &= p_o e^{ik_z z} e^{-ik_r r\cos\phi} \\ &= p_o e^{ik_z z} \sum_{n=0}^{\infty} \varepsilon_n i^n J_n(k_r r)\cos n\phi \end{aligned} \tag{2.3}$$

where

$$\varepsilon_n = \begin{cases} 1 & n = 0 \\ 2 & n > 0 \end{cases}$$

The total pressure p_t in the field consists of the linear summation of the incident field p_i and the field scattered from the cylinder p_s. The scattered pressure must satisfy the Helmholtz equation $\nabla^2 p_s + k^2 p_s = 0$ and boundary conditions that include continuity of radial velocity and zero shear stress at the shell surface, and continuity of normal stress at the shell midplane. Given these constraints, the scatter must be represented by solutions of the form

$$p_s = e^{ik_z z} \sum_{n=0}^{\infty} C_n H_n^{(1)}(k_r r)\cos n\phi \tag{2.4}$$

where the nth-order Hankel function of the first kind is used to represent outgoing waves. The amplitude terms C_n quantify the coupling of the incident field and the cylindrical shell as established by the boundary conditions and the equations of motion of the shell. The coupling of the pressure field and the radial displacements of the shell is quantified, in part, by the linearized momentum equation

$$-\omega^2 \rho_o w = -\frac{\partial (p_i + p_s)}{\partial r} \quad @\ r = a \tag{2.5}$$

The scatter produced by a rigid or pressure release cylinder provides a useful contrast with that produced by an elastic shell and is easily determined from the series expression of the incident plane wave and the momentum equation shown above. Later in Section 2.3.6 I will show example time domain representations of the field produced by rigid and pressure release cylinders at normal incidence to demonstrate the important influences of the shell elasticity. In the case of a rigid cylinder, the radial displacement equals zero ($w = 0$ and $\partial p_i/\partial r = -\partial p_s/\partial r$) and the scattered pressure equals [31]

$$p_s = -p_o e^{ik_z z} \sum_{n=0}^{\infty} \epsilon_n i^n \frac{J_n'(k_r a)}{H_n^{(1)\prime}(k_r a)} H_n^{(1)}(k_r r) \cos n\phi \tag{2.6}$$

Similarly, the total pressure at the outer radius of a pressure release cylinder equals zero and the radial velocity is continuous, or $p_i = -p_s$, and the scattered pressure equals

$$p_s = -p_o e^{ik_z z} \sum_{n=0}^{\infty} \epsilon_n i^n \frac{J_n(k_r a)}{H_n^{(1)}(k_r a)} H_n^{(1)}(k_r r) \cos n\phi \tag{2.7}$$

The remaining information needed to determine the unknown coefficients C_n that quantify the scatter of an elastic shell is provided by the equations of motion of the shell. Vibrations of thin cylindrical shells are studied in a number of references, see for example Cremer, Heckl and Ungar [11], Fahy [18], Pierce [45], or Warburton [59]. The dynamic counterpart of Donnell's static thin shell theory, as presented by Junger and Feit [31], is employed here. The assumptions of this formulation are consistent with the plane stress assumptions of Love-Kirchoff theory and consist of the following:

- Right angles to constituent planes are preserved during deformation.

- Radial acting normal stresses are applied at the shell midplane.
- The radius of curvature of the shell is large compared to the thickness of the shell.
- Displacements are small compared to the wavelength of vibration and thickness of the shell, and vary linearly over its thickness.

Implementation of these assumptions is equivalent to the omission of a variety of linear bending stress terms and results in the following equations presented by Junger and Feit [31]:

$$\frac{\partial^2 u}{\partial z^2} + \frac{1-\nu}{2a^2}\frac{\partial^2 u}{\partial \phi^2} + \frac{1+\nu}{2a}\frac{\partial^2 \vartheta}{\partial z \partial \phi} + \frac{\nu}{a}\frac{\partial w}{\partial z} - \frac{1}{c_p^2}\frac{\partial^2 u}{\partial t^2} = 0 \tag{2.8}$$

$$\frac{1+\nu}{2a}\frac{\partial^2 u}{\partial z \partial \phi} + \frac{1-\nu}{2}\frac{\partial^2 u}{\partial z^2} + \frac{1}{a^2}\frac{\partial^2 \vartheta}{\partial \phi^2} + \frac{1}{a^2}\frac{\partial w}{\partial \phi} - \frac{1}{c_p^2}\frac{\partial^2 \vartheta}{\partial t^2} = 0 \tag{2.9}$$

$$\frac{\nu}{a}\frac{\partial u}{\partial z} + \frac{1}{a^2}\frac{\partial \vartheta}{\partial \phi} + \frac{w}{a^2} + \beta^2\left(a^2\frac{\partial^4 w}{\partial z^4} + 2\frac{\partial^4 w}{\partial z^2 \partial \phi^2} + \frac{1}{a^2}\frac{\partial^4 w}{\partial \phi^4}\right) + \frac{1}{c_p^2}\frac{\partial^2 \vartheta}{\partial t^2} = -\frac{p_s + p_i}{c_p^2 h \rho_s} \tag{2.10}$$

Finally, the displacements of an infinite shell can be described by the orthogonal components shown below

$$\begin{aligned} u &= \sum_{n=0}^{\infty} U_n \cos n\phi \; e^{ik_z z} \\ \vartheta &= \sum_{n=0}^{\infty} V_n \sin n\phi \; e^{ik_z z} \\ w &= \sum_{n=0}^{\infty} W_n \cos n\phi \; e^{ik_z z} \end{aligned} \tag{2.11}$$

Substitution of the series expressions for the shell displacements and pressure fields into the three Donnell equations of motion and the momentum equation provides a system of four linear equations that define solutions for U_n, V_n, W_n, and C_n. I have solved the resulting system of equations to express the scattered pressure as

$$p_s = -p_o e^{ik_z z} \sum_{n=0}^{\infty} \varepsilon_n i^n \cos n\phi \, \frac{N_{s_n}}{D_n} \frac{J_n'(k_r a)}{H_n^{(1)\prime}(k_r a)} H_n^{(1)}(k_r r) \tag{2.12}$$

The term D_n represents the dispersion relation of the fluid loaded shell and is defined as

$$\begin{aligned} D_n &= \left[\Omega^2 - \beta^2 \bar{k}^4 - \vec{F}_\mu E_f k^2 a^2\right]\left[\Omega^2 - \bar{k}^2\right]\left[\Omega^2 - \frac{1-\nu}{2}\bar{k}^2\right] - \Omega^4 \\ &+ \frac{1-\nu}{2}\left[\Omega^2 n^2 + (2\nu+3)\Omega^2\alpha^2 - \left(1-\nu^2\right)\alpha^4\right] \end{aligned} \tag{2.13}$$

where $\Omega = \omega a/c_p$ and $\alpha = k_z a$ are the non-dimensional wavenumbers corresponding to the equivalent plate wave speed of the shell and the axial component of the incident field, respectively. The frequency corresponding to $\Omega = 1$ corresponds to the ring frequency of the shell. The term $\bar{k} = \sqrt{\alpha^2 + n^2}$ represents the non-dimensional wavenumber of an elastic wave traveling along a helical path on the shell. The dispersion relation is consistent with that of Pierce [45] for a thin shell in vacuo. The fluid loading parameters E_f and $\vec{F}_\mu$ are related to the specific acoustic impedances of the shell and the water, and the radiation (outgoing wave) impedance $\vec{Z}_n$, respectively. They are defined as

$$E_f = \frac{c_o^2 \rho_o a}{c_p^2 \rho_s h} \tag{2.14}$$

$$\vec{F}_\mu = \frac{H_n^{(1)}(k_r a)}{k_r a H_n^{(1)\prime}(k_r a)} = \frac{-i}{\rho_o \omega a}\vec{Z}_n \tag{2.15}$$

The numerator term N_{s_n} is of the same form as D_n as expressed in equation 2.13, but with $\vec{F}_\mu$ replaced with $\tilde{F}_\mu$

$$\tilde{F}_\mu = \frac{J_n(k_r a)}{k_r a J_n'(k_r a)} \tag{2.16}$$

The scattered pressure solution of equation 2.12 and the dispersion relation of equation 2.13 simplify to the following at normal incidence

$$p_{s_{norm}} = -p_o \sum_{n=0}^{\infty} \varepsilon_n i^n \cos n\phi \, \frac{Re\left\{D_{n_{norm}} H_n^{(1)\prime}(ka)\right\}}{D_{n_{norm}} H_n^{(1)\prime}(ka)} H_n^{(1)}(kr) \qquad (2.17)$$

$$D_{n_{norm}} = 1 - \Omega^2 + \beta^2 n^4 + \frac{n^2}{\Omega^2 - n^2} + k^2 a^2 E_f \, \vec{F}_\mu \qquad (2.18)$$

The form function, $f_f(\omega, \theta, \phi)$, quantifies the farfield scattered pressure as a function of frequency, aspect angle, and azimuthal angle ϕ. It is defined by the relation

$$f_f(\omega, \theta, \phi) = \frac{p_s(r, \phi)}{p_o} \sqrt{\frac{2r}{a}} e^{-ik_r r} e^{-ik_z z} \qquad (2.19)$$

The magnitude of the form function in the specular direction $f_f(\phi = \pi)$ is shown as a function of the frequency of the incident field $ka = \omega a / c_o$ in Figures 2.2, 2.3, and 2.4 for three representative angles of incidence. I have calculated the solutions shown in these figures with a summation over the first 50 modes. For the frequency range studied here, sufficient convergence is generally apparent following the summation of approximately 20 modes. Zero structural damping has been assumed in these analyses. Membrane waves excited in the shell determine the predominant features of the form function found at these angles. Radiation from induced membrane waves as they travel along helical paths on the shell interferes with a geometric field originating at the illuminated surface of the shell. The field that results consists of alternating frequencies where constructive and destructive interference takes place. The features shown in Figure 2.2 for normal incidence are predominantly produced by the interference of the geometric portion of the field with the field radiated from induced compressional waves as they circumnavigate the shell. Similarly, the features shown in Figure 2.3 for an aspect angle of 75 degrees are produced by interference with induced compressional and torsional wave radiation, while those shown in Figure 2.4 for an aspect angle of 66 degrees are produced by interference with torsional wave radiation only. Detailed discussions of the scatter produced in the specular direction are presented in Section 2.3 where the asymptotic solutions can be better related to the observed features.

2.3 Asymptotic Formulation

Asymptotic solutions to the scattering problem of interest can be formulated using general spectral integral representations or Sommerfeld-Watson transformations (SWT) of an azimuthal harmonic series solution. Felsen et al [19, 20] formulated the solution for phased line source excitation of infinite cylindrical shells using direct spectral synthesis of the appropriate Green's Function. Using these results, Felsen et al [21] reduced the incident field to that of a plane wave by moving the line source out to infinity and renormalizing its amplitude. However, I have found several errors in their formulated equations of the leaky wave contributions presented in Reference [21]. The SWT has also been employed by Felsen [22] and Junger and Feit [31] to formulate asymptotic solutions to a variety of high frequency problems with separable geometries. Williams and Marston [63, 64] used the SWT to rewrite partial wave series solutions as contour integrals for the analysis of backscattering from elastic spheres. Rumerman [49], as well as Ugincius and Uberall [55], employed the SWT to construct a spectral continuum in azimuthal wavenumber as required to derive asymptotic expressions of the field scattered from an infinite cylindrical shell at normal incidence.

I have used the SWT approach of Rumerman [49] to take advantage of the normal mode series solution already derived in Section 2.2. I first modify the scattered pressure series solution of Section 2.2 to express the total pressure in the acoustic medium as a related series of angular harmonics. I then impart the SWT and convert the resulting discrete series representation $\upsilon = n$ into an azimuthal spectral continuum υ. When given a contour path of integration that encloses the real axis, the series expression for the total pressure can be shown to be equivalent to the sum of the residues of a related integrand $f(\upsilon)$ that locates poles on the real axis at $\upsilon = n$. The resulting integral form of the total pressure allows one to take advantage of Cauchy's integral and residue theorems and deform the contour about a different set of poles without changing the value of the integral [49, 20, 21, 29]. The second set of poles is defined by the dispersion relation of the fluid loaded shell

and the associated residues quantify the influence of elastic waves traveling on the shell. The contribution of the geometric field is formulated with saddle point analysis. The asymptotic solutions that result provide considerable physical insight into the predominant scattering processes. They could potentially be used to produce approximate analyses of similar geometries using the geometric theory of diffraction (GTD) as demonstrated by Marston [39]. I will make use of them in the next chapter to evaluate the measured empty shell data.

I apply the SWT to an angular harmonic series expression for the total pressure p_t in the acoustic medium. The total acoustic pressure is the sum of incident pressure p_i, as expressed in equation 2.3, and the scattered pressure p_s shown in equation 2.12. Before applying the SWT, I first modified the equations to express them as a series summation over positive and negative azimuthal orders $e^{in\phi}$ to later take advantage of a contour path of integration that encloses the entire real axis. After combining the resulting equations, and making use of the properties of Hankel and Bessel functions of opposite order [1], the total pressure p_t can be expressed as:

$$p_t = -\frac{p_o}{2} e^{ik_z z} \sum_{n=-\infty}^{\infty} i^n e^{in\phi} \left\{ H_n^{(2)}(k_r r) - \frac{N_{t_n} H_n^{(2)\prime}(k_r a)}{D_n H_n^{(1)\prime}(k_r a)} H_n^{(1)}(k_r r) \right\} \qquad (2.20)$$

where the numerator term N_{t_n} is now a function of the fluid loading term $\overleftarrow{F}_\mu$ associated with the incoming wave impedance $\overleftarrow{Z}_n$ of a cylinder (note the opposite arrow)

$$\begin{aligned} N_{t_n} &= \left[\Omega^2 - \beta^2 \bar{k}^4 - \overleftarrow{F}_\mu E_f k^2 a^2\right] \left[\Omega^2 - \bar{k}^2\right] \left[\Omega^2 - \frac{1-\nu}{2}\bar{k}^2\right] - \Omega^4 \\ &+ \frac{1-\nu}{2} \left[\Omega^2 n^2 + (2\nu+3)\Omega^2 \alpha^2 - \left(1-\nu^2\right)\right] \end{aligned} \qquad (2.21)$$

$$\overleftarrow{F}_\mu = \frac{H_n^{(2)}(k_r a)}{k_r a H_n^{(2)\prime}(k_r a)} = \frac{i}{\rho_o \omega a} \overleftarrow{Z}_n \qquad (2.22)$$

The SWT is then imparted to express the total pressure as a contour integral of a continuous function $f(v)$ of the azimuthal propagation variable v evaluated in the complex plane:

$$f(\upsilon) = \left\{ H_\upsilon^{(2)}(k_r r) - \frac{N_{t_\upsilon} H_\upsilon^{(2)\prime}(k_r a)}{D_\upsilon H_\upsilon^{(1)\prime}(k_r a)} H_\upsilon^{(1)}(k_r r) \right\} \tag{2.23}$$

$$p_t = \frac{p_o i}{4} e^{ik_z z} \oint_C \frac{e^{-i\pi\upsilon/2} e^{i\upsilon\phi} f(\upsilon)}{\sin \pi\upsilon} d\upsilon \tag{2.24}$$

where the terms N_{t_υ} and D_υ are now evaluated as continuous functions of the complex variable υ, rather than at the discrete values n, and C is a clockwise contour that encloses the real axis as shown in Figure 2.5. For real and nonzero values of $k_r a$, the derivative of the Hankel function $H_\upsilon^{(1)\prime}$ only has roots for complex values of υ. Therefore, the residues of the contour integral of equation 2.24 are located on the real axis at the roots of $\sin \pi\upsilon$ corresponding to $\upsilon = n$. The resulting summation of residues yields the series solution of equation 2.20:

$$p_t = \frac{p_o i}{4} e^{ik_z z} \left\{ -2\pi i \sum_{n=-\infty}^{\infty} \frac{e^{i\pi\upsilon/2} e^{i\upsilon(\phi-\pi)} f(\upsilon)}{d(\sin \pi\upsilon)/d\upsilon} \right\} \Bigg|_{\upsilon=n} \tag{2.25}$$

The contour C can be deformed into an equivalent contour $C\prime$ that excludes the real axis and encloses the roots $\upsilon = \upsilon_m$ of the dispersion relation D_υ that are located in the upper half of the complex plane. The original contour C consists of two semicircles of vanishing radius at $\upsilon = \pm\infty$ that do not contribute to the value of the integral, and two line integrals just above and below the real axis, $\mathcal{I}_{A_+}$ and $\mathcal{I}_{A_-}$, as shown in Figure 2.5. The contour integral of equation 2.24 can be expressed solely as a line integral over $\mathcal{I}_{A_+}$ by setting $\upsilon = -\upsilon$ for the integral over $\mathcal{I}_{A_-}$ and taking advantage of the properties of Hankel functions and the even terms N_{t_υ} and D_υ as before:

$$p_t = \frac{p_o i}{2} e^{ik_z z} \int_{A_+} \frac{e^{-i\pi\upsilon/2} \cos \upsilon\phi \; f(\upsilon)}{\sin \pi\upsilon} d\upsilon \tag{2.26}$$

The final contour $C\prime$ can now be constructed to include an integral along the semicircle B_+ as shown in Figure 2.5 that vanishes as the radius $|\upsilon|$ approaches infinity.

$$p_t = \frac{p_o i}{2} e^{ik_z z} \oint_{C_t} \frac{e^{-i\pi v/2} \cos v\,\phi f(v)}{\sin \pi v} dv \tag{2.27}$$

The trigonometric identity employed by Rumerman [49] is also used here to facilitate extraction of the geometric and surface guided field components.

$$\cos v\phi = e^{i\pi v} \left\{ \cos v\,(\pi - \phi) - ie^{-iv\phi} sin\,(v\pi) \right\} \tag{2.28}$$

Substitution of this identity into equation 2.27 yields the total pressure expressed as the sum of a line integral having no poles on the real axis, and a contour integral

$$p_t = \frac{p_o}{2} e^{ik_z z} \left\{ \int_{-\infty}^{\infty} e^{i\pi v/2} e^{-iv\phi} f(v) dv + i \oint_{C_t} \frac{e^{i\pi v/2} \cos v\,(\pi - \phi)\, f(v)}{\sin \pi v} dv \right\} \tag{2.29}$$

The line integral of equation 2.29 can be readily evaluated using saddle point asymptotics to determine the geometric portion of the scattered field, while the residues of the contour integral can be evaluated to determine the contributions of surface guided waves.

2.3.1 Use of Debye Expansions of Hankel Functions

Consideration of the continuous azimuthal propagation wavenumber variable v in the complex plane requires the evaluation of Hankel functions of non-integer complex order that have been represented using Debye asymptotic expansions as presented in references [19, 1, 49]. The Debye expansions shown below include the use of a higher order term as recommended by Rumerman [49] to provide accurate field calculations at lower values of $k_\tau a$.

$$H_v^{(1,2)}(k_\tau a) \approx \sqrt{\frac{2}{\pi k_\tau a \sin \gamma}} \left(1 \mp \frac{i}{8 k_\tau a \sin \gamma} \right) e^{\pm i k_\tau a (\sin \gamma - \gamma \cos \gamma) \mp i\pi/4} \tag{2.30}$$

$$H_v^{(1,2)\prime}(k_r a) \approx \pm\sqrt{\frac{2\sin\gamma}{\pi k_r a}}\left(1 \pm \frac{3i}{8k_r a\sin\gamma}\right) e^{\pm ik_r a(\sin\gamma - \gamma\cos\gamma)\mp i\pi/4} \qquad (2.31)$$

In these equations, the upper sign corresponds to kind 1, the lower sign to kind 2. The parameter γ relates the complex order v of the Hankel function to its argument $k_r a$ as shown below

$$\gamma = \cos^{-1}(v/k_r a) = \pi/2 - \tilde{\phi}_m \qquad (2.32)$$

Using the Debye expansions, the ratio of the derivatives of the Hankel functions shown in equation 2.23 can be expressed as follows

$$\frac{H_v^{(2)\prime}(k_r a)}{H_v^{(1)\prime}(k_r a)} = -i\,\frac{(8k_r a\sin\phi/2 - 3i)}{(8k_r a\sin\phi/2 + 3i)}\, e^{-2ik_r a\cos\tilde{\phi}_m} e^{iv(\pi - 2\tilde{\phi}_m)} \qquad (2.33)$$

2.3.2 Contribution of the Geometric Field

The geometric portion of the scattered field can be determined by conventional first order saddle point asymptotic analysis (SDP) of the second term of the function $f(v)$ contained in the line integral of equation 2.29.

$$p_{spec} = -\frac{p_o}{2}\int_{SDP} e^{i\pi v/2} e^{-iv\phi}\frac{N_{t_v}}{D_v}\frac{H_v^{(2)\prime}(k_r a)}{H_v^{(1)\prime}(k_r a)} H_v^{(1)}(k_r r)\,dv \qquad (2.34)$$

Substitution of the Debye asymptotic expansions yields

$$p_{spec} = i\,\frac{p_o}{2}\sqrt{\frac{2}{\pi k_r r}} e^{i(k_r r - \pi/4)}\int_{SDP}\frac{N_{t_v}}{D_v}\frac{8k_r a\sin\gamma - 3i}{8k_r a\sin\gamma + 3i} e^{-i\Phi(v)}dv \qquad (2.35)$$

where the phase function $\Phi(v)$ is given by the following equation:

$$\Phi(v) = v\phi + 2k_r a\sin\gamma - 2v\gamma \qquad (2.36)$$

As discussed in references [6, 20], the asymptotic form of the solution of equation 2.35 is

$$\int_{SDP} g(v)e^{i\Phi(v)}dv \approx \sqrt{\frac{2\pi}{|d^2\Phi/dv^2|_{v_s}}}g(v_s)e^{i\Phi(v_s)-i\pi/4} \tag{2.37}$$

where v_s is the stationary phase point $d\Phi(v_s)/dv = 0$. For the phase function Φ of interest here, the stationary phase point is defined as

$$v_s = k_r a \cos(\phi/2) \tag{2.38}$$

Finally, substitution of the phase function and its second derivative at the point of stationary phase yields the following contribution to the geometric field:

$$p_{spec} = p_o\sqrt{\frac{a\sin\phi/2}{2r}}R_s(v_s, k_z a)\left(\frac{8k_r a\sin\phi/2 - 3i}{8k_r a\sin\phi/2 + 3i}\right)e^{ik_r(r-2a\sin\phi/2)} \tag{2.39}$$

where

$$R_s(v_s, k_z a) = \frac{N_{t_v}}{D_v}\Big|_{v=v_s, k_z a} \tag{2.40}$$

Although not fully equivalent, the geometric portion of the field p_{spec} may be considered to be the result of an effective plane wave reflection from the surface of the cylinder. The phase and divergence of this contribution are the same as the geometric acoustic results for a perfectly reflecting shell [13, 54]. Moreover, the complex amplitude of this contribution is quantified by an effective specular reflection coefficient R_s. I later refer to this component as the "geometric" or "specularly reflected" component of the field accordingly. The "reflection" from the shell surface occurs at an angle $\phi/2$ producing a phase shift of $k_r(r - 2a\sin\phi/2)$ that corresponds to the waterborne path length to and from the point of reflection. The associated field experiences cylindrical divergence with an apparent focal point at $a/2\sin(\phi/2)$ as defined by the second derivative of the phase $d^2\Phi/dv^2 = -2/k_r a\sin(\phi/2)$.

I have neglected the effects of poles located near the stationary phase point when evaluating the line integral of equation 2.34. These effects were evaluated by Rumerman [49] for insonification at normal incidence. Rumerman indicates that these corrections include a term that can be interpreted as radiation due to the launching of supersonic waves. This term provides continuity of the solution with respect to azimuthal angle ϕ, but equals zero in the specular direction $\phi = \pi$ which is the only angle of interest here. The remaining terms provide further corrections that account for elastic wave excitation and improve the accuracy of the asymptotic approximation of the geometric field contribution. In general, neglecting these corrections for solutions at $\phi = \pi$ generates predictions of the magnitude of the field that exceed the corresponding exact values. However, the resulting errors are small and decrease with increasing frequency as I will demonstrate with example calculations shown in Section 2.3.6. The errors do not hinder the evaluation of the finite shell data because I am primarily interested in the leaky wave field contributions provided by the residues of the contour integral.

2.3.3 Contributions of The Residues

The residues associated with the roots of the dispersion relation D_υ represent the scattering contributions of the various wave types that can be excited on the cylinder. The field associated with each root can be expressed as follows:

$$p_{s_m} = p_o A_m \sqrt{\frac{2\pi}{k_r r}} e^{i(k_z z - \omega t)} e^{i(k_r r - \pi/4)} \frac{\cos \upsilon_m (\pi - \phi)}{\sin \pi \upsilon_m} \frac{H_{\upsilon_m}^{(2)\prime}(k_r a)}{H_{\upsilon_m}^{(1)\prime}(k_r a)} \tag{2.41}$$

where the residues are further quantified by the complex launching, or coupling coefficients A_m, that are computed for each pole υ_m

$$A_m = \frac{N_{t_r}}{\partial (D_\upsilon)/\partial \upsilon} \Bigg|_{\upsilon = \upsilon_m} \tag{2.42}$$

The poles υ_m of the the dispersion relation D_υ are characterized by three types of waves, namely: leaky, creeping, and trapped waves. The scattering contributions of

the three wave types are determined by their locations in the complex plane relative to the radial component of the incident acoustic field $k_r a$, and the real v axis as shown in Figure 2.6. Leaky waves $Re\{v_m\} < k_r a$ are comprised of supersonic elastic waves that radiate as they propagate along helical paths on the shell. Leaky wave radiation represents the predominant shell guided wave contribution to the scatter. For the frequency range of interest here, leaky wave contributions are limited to transverse shear and compressional membrane waves. Creeping waves are heavily damped waves with phase speeds approaching the value of the surrounding medium $Re\{v_m\} \simeq k_r a$. Creeping wave behavior is also to be expected for rigid cylinders where they induce a surface guided contribution to the forward scattered field or shadow region. Given their rapid decay rate, creeping waves provide weak contributions to the field scattered in the specular direction ($\phi = \pi$). Finally, trapped waves consist of subsonic elastic waves $Re\{v_m\} > k_r a$ that contribute to the scatter only via evanescent tunneling. For the frequency range and bending stiffness of the shells studied here, trapped waves are comprised of flexural waves. The various traveling wave contributions to the scatter (leaky, creeping, and trapped) are made evident if the trigonometric terms of equation 2.41 are expressed as a series of complex exponentials as shown below.

$$\frac{\cos v_m(\pi - \phi)}{\sin \pi v_m} = -i\left\{e^{iv_m\phi}\sum_{q=0}^{\infty} e^{iv_m 2\pi q} + e^{-iv_m\phi}\sum_{q=1}^{\infty} e^{iv_m 2\pi q}\right\} \qquad (2.43)$$

The complex exponentials shown in equation 2.43 each represent the phase accumulation of waves circumnavigating the shell with the parameter q effectively representing the number of circumnavigations encountered. The first summation shown in equation 2.43 represents waves circumnavigating the shell in one direction while the second summation represents travel in the opposite direction. The poles v_m quantify the radiation loss δ_m, and circumferential wavenumber component k_{ϕ_m} of the traveling waves.

$$\delta_m = Im\{v_m\} \qquad (2.44)$$

$$k_{\phi_m} = Re\{\upsilon_m\}/a = \Upsilon_m/a \tag{2.45}$$

where

$$Re\{\upsilon_m\} = \Upsilon_m \tag{2.46}$$

2.3.4 Geometric and Membrane Wave Scattering Contributions in the Specular Direction

In the equations and analyses that follow, I describe the scatter produced in the specular direction at $\phi = \pi$. In addition, only the contributions of the geometric field and the leaky wave fields induced by membrane waves will be included. These contributions capture the essential features of the field found in the specular direction over the mid-frequency range of interest.

$$p_s \approx \left(p_{specular} + \sum_m p_{leaky_m} \right) \sqrt{\frac{a}{2r}} e^{ik_z z} e^{ik_r r} \tag{2.47}$$

where $p_{specular}$ and p_{leaky_m} are the asymptotic contributions of the geometric and leaky wave fields to the total form function of the specularly directed scatter. Also, the form function is obviously

$$f_f(\omega, \theta, \phi = \pi) \approx p_{specular} + \sum_m p_{leaky_m} \tag{2.48}$$

The contribution of the specular reflection is defined by the saddle point $\upsilon_s = 0$ and the axial wavenumber of the incident plane wave. Substitution of the saddle point in the expression for the specular field of equation 2.39 yields

$$p_{specular} = p_o R_s \Big|_{\upsilon_s = 0, k_z a} \left(\frac{8k_r a - 3i}{8k_r a + 3i} \right) e^{-i2k_r a} \tag{2.49}$$

The geometric portion of the field is induced by an effective plane wave reflection coefficient R_s imposed by the shell, and experiences cylindrical divergence consistent with a focal point located at a distance $a/2$ from the shell surface.

Substitution of the traveling wave series expression of equation 2.43, and the Debye expansion results of equation 2.33, into equation 2.41 yields the following expression for the leaky wave field in the specular direction:

$$p_{leaky_m} = -2p_o A_m \sqrt{\frac{\pi}{k_r a}} e^{-i2k_r a} e^{i\eta_m}$$
$$\left\{ e^{(i\Upsilon_m - \delta_m)(2\pi - 2\phi_{l_m})} \sum_{q=0}^{\infty} e^{2\pi q(i\Upsilon_m - \delta_m)} + e^{-2(i\Upsilon_m - \delta_m)\phi_{l_m}} \sum_{q=1}^{\infty} e^{2\pi q(i\Upsilon_m - \delta_m)} \right\} \quad (2.50)$$

Phase matched excitation and reradiation from supersonic elastic waves is evident in equation 2.50. The incident plane wave in the water excites an elastic wave on the cylinder in the region of two axial launch lines located such that the launch angle ϕ_{l_m} obeys the phase velocity matching condition:

$$\phi_{l_m} = \sin^{-1}\left(\frac{Re\{\upsilon_m\}}{k_r a}\right) \simeq \tilde{\phi}_m \quad (2.51)$$

where the complex parameter $\tilde{\phi}_m$ approximately equals the launch angle ϕ_{l_m} given the small imaginary components of the membrane wave roots υ_m considered here.

The incident wave couples to a structural wave in the region of either launch line and propagates around the cylinder in a helical path while radiating into the surrounding acoustic medium. Sound is radiated continuously, but it is only radiated in the specular direction when the propagating structural wave encounters the complementary launch line as illustrated in Figure 2.7. The induced structural wave continues to circumnavigate the shell and attenuates at a rate of $8.686\delta_m$ $dB/radian$ or $8.686\delta_m\omega/\Upsilon_m$ dB/sec. Specularly directed waves are launched (detached) from both launch lines as waves circumnavigate the shell in both clockwise and counterclockwise directions. The first series summation shown in equation 2.50 represents the field generated by clockwise traveling waves launched at $+\phi_{l_m}$, while the second summation represents counterclockwise waves launched at $-\phi_{l_m}$. The phase and attenuation terms $-2(i\Upsilon_m - \delta_m)\phi_{l_m}$ that precede the two summations of equation 2.50

account for the decreased azimuthal propagation path length of the first circumnavigation. The phase term η_m provides the phase correction needed to accommodate the additional waterborne path to and from the launch point $2k_r a(1 - \cos\phi_{l_m})$, as well as the $\pi/4$ phase term that is characteristic of Hankel functions:

$$\eta_m = 2k_r a\,(1 - \cos\phi_{l_m}) - \pi/4 \tag{2.52}$$

The axial phase speed of the scattered field equals the axial trace velocity of the incident acoustic field and the induced elastic waves.

The phase accumulation and launching criteria established in equation 2.50 are consistent with the ray formulations of Marston et al [62, 63, 64, 32, 33, 39]. The specular directed wave appears to have been generated from two coaligned axial phased line arrays located at a distance b_m from the plane normal to the incoming wave front that passes through the center of the cylinder:

$$b_m = a\sin\phi_{l_m} \tag{2.53}$$

This would provide an axial focused field similar to that observed for backscattering from spheres by Marston et al [62]. However, I have not been able to experimentally evaluate axial focusing effects because all of the measurements were conducted within a single horizontal plane as discussed in Appendix A.

2.3.5 Membrane Wave Helix Properties and the Origin of Coincidence Conditions

The phase speeds of membrane waves propagating on thin cylindrical shells are only weakly frequency dependent and are effectively dispersionless. Vekaler [56, 57] and Muzychencko et al [42] have found that the membrane wave speeds can be approximated by the transverse shear and compressional phase speeds of a plate of the same thickness and material properties. Given these approximations, one can easily

obtain accurate estimates of phase matched helix properties and coincidence conditions. More accurate values could be obtained from computation of the roots of the dispersion relation, but I have found the errors associated with the use of the plate approximations to be minimal.

The smallest aspect angle at which the incident plane wave can excite a phase matched supersonic structural wave of speed c_m corresponds to an axial orientated structural wave with a zero launch angle $\phi_{l_m} = 0$ and zero azimuthal wavenumber $v = 0$. The critical aspect angle for phase matched excitation is therefore given as

$$\theta_c \simeq \cos^{-1}(c_o/c_m) \tag{2.54}$$

Phased matched excitation can occur over a range of aspect angles $\theta_c \leq \theta \leq \pi - \theta_c$. The critical aspect angles for membrane wave excitation of the cylindrical portions of the shells tested here are listed in Table 2.1.

Table 2.1: **Critical Aspect Angles for Membrane Wave Excitation**

Membrane Wave Type	Phase Speed c_m	Aspect Angle θ_c
Transverse Shear	3100	61.3
Compressional	5270	73.6

The launch angles ϕ_{l_m} required to excite a helical structural wave of speed c_m vary with incident aspect angle θ as shown below:

$$\phi_{l_m} \simeq \sin^{-1}\sqrt{\frac{c_o^2/c_m^2 - \cos^2\theta}{\sin^2\theta}} \tag{2.55}$$

The launch angles associated with the membrane wave speeds of the shells studied here are plotted as a function of aspect angle in Figure 2.8. The corresponding helix angles ψ_m are shown relative to the axis of the cylinder in Figure 2.9, and are defined by the following relation:

$$\psi_m \simeq \cos^{-1}\left(\frac{c_m \cos\theta}{c_o}\right) \tag{2.56}$$

The residues associated with leaky wave propagation become large when the term $\sin \pi v_m \rightarrow 0$, or when the $\Upsilon = Re\{v_m\} \rightarrow n$, where n is any integer, and $\delta_m = Im\{v_m\} \rightarrow 0$. The leaky membrane wave poles of interest here are characterized by small imaginary wavenumber components $\delta_m \ll 1$. Hence, at frequencies where the leaky wave poles meet these conditions, an integer number of circumferential wavelengths subtend the circumference of the cylinder $\lambda_\phi = 2\pi a/n$. The incident field is spatially coincident with a characteristic mode of the shell. Leaky wave returns associated with different circumnavigations of the shell are then observed in phase with one another as made evident by the sum of complex exponentials with phase terms $2\pi qn$.

Although the residues become large at spatial coincidence, their total magnitude is also influenced by the coupling coefficient A_m. Felsen and Ho [21, 23] demonstrated that the coupling coefficient and imaginary component of wavenumber roots δ_m are related by the approximation $|A_m| \approx 2\delta_m$. I have confirmed this result numerically as will be demonstrated with specific examples in Section 2.3.6. Both parameters quantify the coupling of acoustic pressure in the fluid and the shell displacements. With the use of the Felsen and Ho asymptotic expression for the coupling coefficient, the magnitude of the leaky wave form function at coincidence can be shown to be

$$|p_{leaky_m}| \approx \frac{4}{(1+\pi\delta_m)\sqrt{\pi k a_{coin}\sin\theta}}, \quad \delta_m \ll 1 \tag{2.57}$$

I have found the imaginary component of the wavenumber to exhibit values $\delta_m < 0.15$ for both membrane wave types and for the full range of frequencies and aspect angles that are of interest here as is demonstrated in Section 2.3.6. Therefore, this approximation is fully valid for these studies. Specific values of the magnitude of the leaky wave field at coincidence, as well as corresponding decay rates, are listed in Tables 2.2, 2.3, and 2.4 for aspect angles of θ = 90, 75, and 66 (φ = 0, 15,

and 24) degrees. Equation 2.57 and the results of Table 2.3 demonstrate that both transverse shear and compressional waves exhibit surprisingly comparable scattered pressure spectral levels. The similar field contributions of both wave types, as well as their small imaginary wavenumber components δ_m, can be attributed to their small radial displacements (as opposed to flexural waves) and to their supersonic speeds. The radiation resistance imposed by the fluid loading of a given angular order n rapidly approaches a constant value of $\rho_o c_o$ for all supersonic disturbances $k_r a \gg n^2 + 1$ [31]. Hence, the small radial displacement fields of both wave types generate similar pressure levels provided their coupling coefficients are similar. This is often the case as I will demonstrate at an aspect angle of 75 degrees in Section 2.3.6. The different wave speeds of the two wave types, together with phase matching criteria, determine the spatial coincidence frequencies ka_{coin}. Therefore, the wave speeds influence spectral levels via the $1/\sqrt{ka}$ term of equation 2.57. The radiation loss parameter δ_m also influences spectral levels, though less prominently, and serves to control spectral bandwidths and the rate at which energy is stripped off to the surrounding acoustic medium.

The transverse shear wave field induced at normal incidence is uncoupled from the acoustic medium because its radial displacement field equals zero, and $\delta_m = 0$ accordingly. However, the asymptotic formulation of equation 2.57 would erroneously predict a nonzero leaky wave field spectral level. In this case, the wavenumber root ν_m is not a pole of the integrand of the SWT. This anomaly is easily accommodated by ignoring the shear wave root at normal incidence.

Spatial coincidence occurs at combinations of aspect angle θ and frequency ka where appropriate phase matching conditions exist such that $\nu_m(ka, \theta) = n$. For a given frequency and integer order n, the aspect angle θ_{coin} where coincidence conditions exist can be approximated using the following relation for effectively dispersionless wave types:

$$\theta_{coin}(ka, n) \simeq \cos^{-1} \sqrt{c_o^2/c_m^2 \; - \; n^2/k^2a^2} \tag{2.58}$$

The coincidence loci of the membrane waves of interest are plotted in Figure 2.10.

The fundamental period of the circumferential component of a phase matched helical wave is expressed as a function of incident aspect angle in equation 2.59 shown below and is plotted in Figure 2.11 for the shell parameters of interest here.

$$T_m(\theta) \simeq \frac{2\pi a}{c_m}\sqrt{1-(c_m^2/c_o^2)\cos^2\theta} \tag{2.59}$$

The fundamental period T_m corresponds to an estimated azimuthal group velocity of $c_{\phi_g} = c_m/\sqrt{1-(c_m^2/c_o^2)\cos^2\theta}$. This estimate is frequency independent and I demonstrate its accuracy in the discussions that follow where the real part of the roots ν_m are shown to be nearly linear functions of frequency ka.

2.3.6 Detailed Evaluation of Example Form Functions and Time Domain Representations

I have computed time domain representations of the specularly directed scatter and corresponding asymptotic values of the form function for the three representative angles of incidence studied in Section 2.2, namely normal incidence, 75, and 66 ($\varphi = 0$, 15, and 24) degrees. The time domain representations illustrate the evolution of the field and provide a useful comparison with the measured data of the finite shells. The aysmptotic computations approximate the frequency domain details of the field. Zero structural damping has been assumed in these analyses. The material properties and radial dimensions of the finite shells studied experimentally have been used throughout these computations and are listed in Table 1.1.

The time domain representations were computed using a discrete inverse transform of the corresponding "exact" normal mode series solution to exclude the errors of the asymptotic solution. A Gaussian bandpass filter with a bandwidth of $2.75 < ka < 10.0$ was employed as discussed in Appendix A to limit the signal to the frequency range studied experimentally.

Asymptotic values of the form function have been computed over a frequency

range of $2 < ka < 12$. Use of the asymptotic solutions requires computation of the complex roots of the dispersion relation D_v and I have computed them using Muller's method as discussed in reference [47]. Complex, non-integer order Hankel function values were computed using the Debye expansions. The contributions of the geometric and membrane leaky wave fields are the predominant constituents of the acoustic field and are the only ones included.

Normal Incidence

The time domain representation produced at normal incidence ($\theta = 90$ degrees) is shown in Figure 2.12. This corresponds to the form function whose magnitude is shown in Figure 2.2. Contrasting time domain representations of the scatter produced by a pressure release and a rigid cylinder are shown in Figures 2.13 and 2.14, respectively. In all three cases, a bandlimited pulse is initially observed that corresponds to the geometric portion of the field that can effectively be considered a specularly reflected component as discussed in Sections 2.3.2 and 2.3.4. In each case, I have located the peak value of the initial return at a reference time $t = 0$. The initial return from the elastic shell has a negative sense that is consistent with the pressure release cylinder, but its peak amplitude is smaller because a portion of the incident energy is transferred to elastic waves that propagate on the shell. The scatter produced by the pressure release cylinder consists solely of the geometric field initially observed, while the scatter produced by the rigid cylinder consists of an initial geometric return and a highly damped series of creeping wave returns. The signal component shown near $t = 200\ \mu/sec$ in Figure 2.14 corresponds to the first return from a creeping wave launched near $\phi = \pi$ and propagating at a speed $c_m \simeq c_o$. In contrast, the initial return from the elastic shell is followed by a series of exponentially decaying broadband returns with a period of 64 μsec that are produced by radiation from induced compressional waves. At this angle of incidence, transverse shear waves propagate with no radial displacement component and do not contribute to the scatter. The observed period corresponds to the time required for

the compressional wave field to circumnavigate the shell and is well approximated by equation 2.59. These leaky wave returns are of opposite sense with respect to the geometric portion of the field initially observed, but are of the same sense as the incident field. Destructive interference of these returns with the initial scatter produces the characteristic nulls shown in the frequency domain representations of Figure 2.2. The observed decay is a manifestation of radiation losses that occur as the leaky structural wave circumnavigates the shell.

The properties of the asymptotic representations of the form function of the scatter produced by the elastic shell at normal incidence are shown in Figures 2.15 - 2.19. As shown in Figure 2.15, the asymptotic solutions for the magnitude and phase of the form function compare well with the normal mode series solutions. The accuracy of the asymptotic solutions improves with increasing frequency ka as the accuracy of the Debye expansions and the saddle point analyses increase. The low frequency accuracy of the asymptotic prediction could be improved, particularly near the first null of the form function, with the incorporation of the corrective terms to the geometric portion of the field that were derived by Rumerman [49]. The contributions of creeping and trapped wave excitation are unimportant over this range of frequencies.

The predicted contribution of the specularly reflected field is quantified by an effective reflection coefficient of unity magnitude $|R_s| = 1$. However, this approximation does not appropriately account for the initial transfer of energy from the incident, to the elastic wave field. This error is small and not of particular interest to me, because I am particularly interested in the leaky wave contributions to the field that would be observed in the back direction. The phase of the predicted reflection coefficient and the total phase of the geometric portion of the form function are shown in Figure 2.16. The specularly reflected component includes a frequency dependent phase term that is induced by the reflection coefficient, as well as a linear phase term $-2k_e a$ that is associated with waterborne propagation to and from the shell's surface.

The magnitudes of the coupling coefficient A_m and the imaginary component of the azimuthal wavenumber root $Im\{\upsilon_m\} = \delta_m$, shown in Figures 2.17 and 2.18, are related by the approximation $|A_m| \approx 2\delta_m$. This relationship was suggested by Felsen and Ho in references [21, 23]. However, I have found that the relation $A_m \approx i2\delta_m$ of Felsen and Ho does not approximate the phase of the coupling coefficient sufficiently well enough for accurate use over most of the frequency range of interest here. Both the coupling and radiation loss coefficients decrease with increasing frequency in contrast with the experimental results of Talmant and Quentin [52]. Their results demonstrate increasing attenuation with increasing frequency for $ka > 50$, but the predominant attenuation process they observed may be structural, rather than radiation damping.

The real part of the azimuthal wavenumber roots $Re\{\upsilon_m\} = \Upsilon_m$ are also shown in Figure 2.18 as a function of frequency ka. These roots of the dispersion relation correspond to compressional wave propagation on the shell. The real part of the roots is a nearly linear function of frequency which indicates that the induced compressional waves are nearly dispersionless as required for accurate use of the approximations I presented in Section 2.3.5.

The form function contributions of the scatter induced by compressional wave excitation and reradiation at normal incidence are shown in Figure 2.19. The peak levels of the leaky wave field are located at spatial coincidence frequencies which are imposed by the compressional wave speed of the shell and essentially correspond to harmonics of the ring frequency $ka = 3.54$. The form function magnitudes and decay rates computed at the first three coincidence frequencies are listed in Table 2.2. Peak levels decrease with increasing frequency. The decreased peak levels observed are primarily imposed by the $1/\sqrt{k_r a}$ term of the Hankel function that describes the cylindrical leaky wave field. As shown in Figure 2.19, the phase of the compressional wave field decreases by 90 degrees over the half-power bandwidth of each coincidence frequency in a fashion typical of a system resonance. This phase change is imposed by the $1/\sin \pi\upsilon_m$ term of equation 2.41. A linear phase component is also evident as

imposed by the incremental waterborne path length to and from the launch lines on the shell as shown in equation 2.52. The spatially coincident compressional wave field is the source of the large amplitude, periodic radiation shown in the time domain representation of Figure 2.12.

The peaks and minima of the form function shown in Figures 2.2 and 2.15 are produced by the interaction of the leaky wave radiated field with the geometric (specularly reflected) field. The minima occur near the spatial coincidence frequencies where the leaky wave contributions are out of phase with the geometric portion of the field. This is confirmed by a comparison of Figures 2.16 and 2.19 where the specularly reflected and leaky wave fields are shown to be 180 degrees out of phase with one another at the frequencies where the minima are located. The decrease in peak levels of the leaky wave form function with increasing frequency produces larger minimum values (shallower nulls) of the total form function as shown. Peak levels of the form function occur at frequencies near the nulls where the leaky wave contributions are in phase with the geometric field.

75 Degree Aspect Angle (φ=15)

The bandlimited time domain representation of the exact normal mode solution computed at an aspect angle of $\theta = 75$ degrees is illustrated in Figure 2.20. The magnitude of the corresponding normal mode form function solution is shown in Figure 2.3. I evaluate the field at this aspect angle as an example of an angle of incidence where both torsional and compressional membrane waves can be excited in the shell. Once again, a bandlimited pulse is initially observed that corresponds to the geometric or specularly reflected portion of the field. As noted at normal incidence, the peak amplitude of this return has a negative sense as is consistent with a pressure release surface. The initial return from the cylinder is followed by two series of exponentially decaying returns with different periods and decay rates. One series of returns has a period of $T = 94\ \mu sec$ that corresponds to the time required for the induced helical shear wave field to circumnavigate the shell. The second series of

returns exhibit a period of $T = 26\ \mu sec$ corresponding to helical compressional wave radiation. The period of both wave types is well approximated by equation 2.59. Both series of leaky wave returns are again of opposite sense with respect to the geometric portion of the field initially observed. The compressional wave field can be seen to decay at a significantly faster rate than the shear wave field. Shear wave radiation remains clearly evident at times $t > 400\ \mu sec$. Although compressional wave radiation still exists, it cannot be seen over this later time duration. I have experimentally observed a similar persistence of shear wave backscatter over longer time durations at aspect angles ranging from 74 to 85 degrees as will be discussed in the Chapters that follow. Constructive and destructive interference of the leaky wave radiation with the field initially scattered produces the nulls and peaks shown in the frequency domain representation of Figure 2.3. The different decay rates shown are manifestations of radiation losses that occur as the two membrane wave types circumnavigate the shell with different levels of coupling to the acoustic field.

The form function properties at an aspect angle of 75 deg are shown in Figures 2.21 - 2.25. The leaky wave contributions associated with both wave types have been included in the asymptotic computation of the form function. Except at low ka, the asymptotic solution again compares well with the normal mode series solution as shown in Figure 2.21.

The predicted contribution of the specularly reflected field is again quantified by an effective reflection coefficient of unity magnitude $|R_s| = 1$. The phase of the predicted reflection coefficient and the total phase of the geometric portion of the form function are shown in Figure 2.22. Once again, the specularly reflected component includes a frequency dependent phase term that is induced by the reflection coefficient, as wells as a linear phase term that is associated with waterborne propagation to and from the shell's surface.

The magnitudes of the coupling coefficients A_m, and the wavenumber roots υ_m, associated with both membrane wave types are compared in Figures 2.23 and 2.24, respectively. The magnitudes of the coupling coefficient and the imaginary wavenum-

ber component δ_m are again related by the approximation $|A_m| \approx 2\delta_m$. The coupling coefficients and imaginary wavenumber components of both wave types decrease with increasing frequency as was noted for compressional waves at normal incidence. Although values of A_m and δ_m associated with both wave types are comparable, those associated with shear wave excitation and radiation are larger than those of compressional waves at all frequencies of interest here. The coupling coefficient and imaginary wavenumber components associated with compressional wave excitation decrease as the aspect angle approaches the critical value of $\theta = 73.6$ degrees. This may be seen by comparing Figures 2.23 and 2.24 with Figures 2.17 and 2.18. In contrast, shear wave values increase as the aspect angle approaches the critical value of $\theta = 61.3$ degrees.

The real components of the azimuthal wavenumber roots Υ_m are also shown in Figure 2.24 and can be seen to be nearly linear functions of frequency for both wave types. Therefore, both membrane wave types are nearly dispersionless.

The form function contributions of the scattered field induced by membrane wave excitation and reradiation at this aspect angle are shown in Figure 2.25. The peak levels of both the shear and compressional leaky wave fields are located at their respective spatial coincidence frequencies. The form function magnitudes and decay rates computed at the coincidence frequencies shown in Figure 2.25 are listed in Table 2.3. The magnitudes of the peak leaky wave contributions are comparable for both wave types as is to be expected given the comparable coupling coefficient and imaginary wavenumber roots exhibited. However, the magnitude of the form function contribution associated with shear wave leakage at the lowest coincidence frequency is 5 dB larger than the corresponding contribution of compressional wave leakage. In addition, the decay rates of the different wave types differ markedly at their respective lowest order coincidence frequencies as shown in Table 2.3. The compressional structural wave field losses energy to the surrounding acoustic medium, radiating in all azimuthal directions ϕ, at a much greater rate. The greater decay rate associated with compressional wave radiation is evident in the time domain rep-

resentation of Figure 2.20, as discussed above, and I have observed similar behavior in the response of the empty shell as will be discussed in Chapter 3.

66 Degree Aspect Angle (φ=24)

The bandlimited time domain representation of the exact normal mode solution computed at an aspect angle of 66 degrees is illustrated in Figure 2.26. The magnitude of the corresponding form function is shown in Figure 2.4. I evaluate the field at this aspect angle as an example of an angle of incidence where only transverse shear (torsional) membrane waves can be excited in the shell. The features of the time domain representation of the specular scatter are similar to those of the backscatter computed for normal incidence, shown in Figure 2.12, where only compressional waves contribute. The initial broadband return from the cylinder is followed by a series of exponentially decaying pulses with a period of 58 μsec produced by radiation from induced transverse shear waves propagating along helical paths on the shell. The period corresponds to the time required for the torsional wave field to circumnavigate the shell. Once again these leaky wave returns are of opposite sense with respect to the geometric portion of the field initially observed, but are of the same sense as the incident field. Destructive interference of these returns with that initially observed produces the nulls shown in the frequency domain representation of Figure 2.4. The observed decay is again a manifestation of radiation losses that occur as the shear waves circumnavigate the shell.

Finally, the form function properties at an aspect angle of 66 degrees are shown in Figures 2.27 - 2.31. Only the leaky wave contributions associated with torsional wave propagation have been included in the asymptotic computation of the form function. Except for low ka, the asymptotic solution compares well with the normal mode series solution as shown in Figure 2.27. The phase of the predicted reflection coefficient, and the geometric portion of the form function, are shown in Figure 2.28. The phase values shown exhibit similar behavior to that observed at normal incidence and at θ = 75 degrees. The magnitudes of the coupling coefficient A_m and the imaginary

wavenumber component δ_m, shown in Figures 2.29 and 2.30, are again related by the approximation $|A_m| \approx 2\delta_m$. The coupling coefficients and the imaginary component of the azimuthal wavenumber v_m decrease as the aspect angle approaches normal incidence as can be seen by comparing Figures 2.29 and 2.30 with Figures 2.23 and 2.24. The form function contributions of the scattered field induced by shear wave excitation and reradiation at this aspect angle are shown in Figure 2.31. The peak levels of the leaky wave field are located at spatial coincidence frequencies which are imposed by the shear wave speed of the shell and phase matching criteria as discussed in Section 2.3.5. The decay rates and form function magnitudes computed at the two lowest coincidence frequencies are listed in Table 2.4. The bandwidths of the radiated field are larger at this aspect angle than at 75 degrees as can be seen by a comparison of Figures 2.31 and 2.25. This increased bandwidth reflects the increased radiation loss of shear waves induced with decreasing aspect angle. I have observed similar behavior in the response of the empty shell as will be discussed in Chapter 3.

Table 2.2: **Computed Membrane Wave Decay Rates and Form Function Values at Beam Aspect**

Membrane Wave Type	Mode $v = n$	Frequency ka	Decay Rate $dB/\mu sec$	Form Function $\|f_f(ka)\|$, dB
Compressional	1	3.71	.112	-1.8
Compressional	2	7.32	.089	-4.1
Compressional	3	10.90	.067	-5.2

Table 2.3: **Computed Membrane Wave Decay Rates and Form Function Values at a 75 degree Aspect Angle**

Membrane Wave Type	Mode $v = n$	Frequency ka	Decay Rate $dB/\mu sec$	Form Function $\|f_f(ka)\|$, dB
Transverse Shear	1	2.54	.040	1.9
Transverse Shear	2	5.01	.037	-1.0
Transverse Shear	3	7.48	.032	-2.6
Transverse Shear	4	9.96	.027	-3.7
Compressional	1	9.12	.090	-3.5

Table 2.4: **Computed Membrane Wave Decay Rates and Form Function Values at a 66 degree Aspect Angle**

Membrane Wave Type	Mode $v = n$	Frequency ka	Decay Rate $dB/\mu sec$	Form Function $\|f_f(ka)\|$, dB
Transverse Shear	1	4.07	.099	-1.1
Transverse Shear	2	8.02	.079	-3.5

2.4 Role of Structural Damping

I have neglected the influence of structural damping throughout the analyses presented thus far. The contribution of leaky wave radiation in the scattered field decreases with increasing levels of structural damping. The influence of structural damping can be seen in Figure 2.32 where I show the magnitude of the form function at normal incidence for four different levels of structural damping. In order to evaluate the influence of structural damping, I have imposed a complex modulus of elasticity $E_s = E(1 - i\eta_d)$ to describe the stiffness of the shell, where η_d is the loss factor of the shell material [11]. This provides a structural damping mechanism and complex propagation velocity $c_{p_d} = \sqrt{E_s/\rho_s(1-\nu^2)}(1 - i\eta_d/2)$. The form function curves shown in Figure 2.32 were computed using normal mode series solutions with constant loss factor values of $\eta_d = 0$ (zero damping), $\eta_d = 0.01$, $\eta_d = 0.05$, and $\eta_d = 0.10$. As can be seen in Figure 2.32, the most significant effect of increased structural damping is an increase in the pressure level at the nulls, i.e. the nulls become more shallow. Moreover, the nulls are broadened as a result of the increased bandwidth associated with the increased damping of the system. The frequency of the nulls remains essentially unchanged and they are located near spatial coincidence frequencies. Peak levels also decrease with increasing damping, but this effect is less pronounced than that observed at the nulls.

These effects occur because the leaky wave radiated field becomes more rapidly attenuated while the geometric field initially observed remains largely unchanged. This can be seen in Figure 2.33 where I show the time domain representation of the field at normal incidence for a loss factor of $\eta_d = 0.10$. A comparison with Figure 2.12, shown for zero structural damping, demonstrates that the peak levels of the initial return from the shell have decreased only minimally while leaky wave levels are significantly attenuated and decay rapidly. The decreased leaky wave pressure levels that result do not produce significant destructive interference between the geometric and leaky fields. Therefore, the nulls shown in the frequency domain become less shallow as discussed above. The geometric, or specularly reflected field

shows little variation with the addition of structural damping, because the effective plane wave reflection coefficient $R_s(v_s, k_z a)$ is insensitive to damping effects. In fact, the asymptotic value of $|R_s|$ equals one regardless of the value of the damping loss factor.

As shown in subsequent chapters, the interference between the geometric and leaky wave backscatter produced by the finite shells away from 5 degrees of beam aspect yields a modulation in the frequency domain. Moreover, initial scattering levels associated with the geometric field are typically much smaller than corresponding levels observed in the specular direction. As a result, peak backscatter levels are measured near spatial coincidence frequencies when coincident radiation is not inhibited by elastic wave scattering at structural discontinuities. Increased structural damping would decrease these peak levels while the bandwidths of the backscatter would increase. However, acoustic radiation appears to be the dominant loss mechanism of the empty and ring stiffened shells as discussed in Chapters 3 and 5. Additional damping provided by the resilient material supporting the internal structures of the complex shell appears to be important at some aspect angles as discussed in Chapter 5.

2.5 The Free Modes of Propagation

I now present analyses of the free modes of propagation of an infinite, fluid loaded cylindrical shell to evaluate the group velocity, decay rate, and cut-off frequencies of the different angular orders of a free membrane wave field. I have calculated the complex axial wavenumber roots $k_{z_m} = k_z a_r + i k_z a_i$ of the fluid loaded dispersion relation over a range of real normalized frequencies $2 \leq ka \leq 12$ and angular orders n. Only the three sets of roots corresponding to propagating waves have been computed, namely compressional, transverse shear, and flexural waves. The phase speed and attenuation of the exponentially decaying wave solutions are quantified by the

wavenumber components using the relations:

$$c_z = c\,ka/k_z a_r \tag{2.60}$$

$$A = 8.686 k_z a_i / a \tag{2.61}$$

where c_z is the axial phase speed, and A is the attenuation expressed in dB for a length equal to the axial wavelength. The shell configuration and material properties listed in Table 1.1 were employed throughout.

The dispersion relation of a fluid loaded cylindrical shell based on Donnell's thin shell equations was introduced in Section 2.2 as equation 2.13. Scott [51] similarly found the complex axial wavenumber roots of a fluid loaded thin shell but employed a different thin shell theory to describe the motions of the shell. Different formulations have been presented in various references, but they give rise to only minor differences in their numerical results [31]. I have found the complex axial wavenumber roots $k_{z_m} a = k_z a_r + i k_z a_i$ with the use of Muller's iterative method [47] for a fixed angular order n and normalized frequency ka. In all cases, I employed a Pekeris branch cut to ensure that estimates of the wavenumber roots associated with different iterations did not cross the branch cut as would often occur with the use of an EJP (Ewing, Jardsky, and Press), or similar branch cut [48].

When calculating membrane wave roots, I employed an initial guess of $k_z a = \sqrt{ka^2 c^2/c_m^2 - n^2} + .01i$ where c_m is the plate speed listed in Table 2.1. In most instances, with some exceptions near the cut-off frequency, this initial guess was found to work well and produce rapid convergence. The behavior of the roots was not studied below the cutoff frequencies of a given angular order. The resulting real and imaginary components of the axial wavenumber associated with compressional waves are shown in Figures 2.34 and 2.35, respectively. The imaginary component of the compressional wave root becomes large near the cut-off frequency for angular orders $n = 1$ and greater as shown in Figure 2.35. Scott [51] attributes this behavior to the inception of a double root near cut-off. The real and imaginary components of the

axial wavenumbers associated with transverse shear waves are shown in Figures 2.36 and 2.35. Both the imaginary and real components of the shear wavenumber rapidly approach zero at the cut-off frequency where torsional waves are uncoupled from the surrounding acoustic medium.

The associated phase and group velocities of compressional and shear waves are shown in Figures 2.38 and 2.39. The group velocity $c_{g_m} = d\omega/dk$ was numerically computed from the roots using a central difference scheme. The resulting membrane wave velocities can be well approximated by the relations:

$$c_{z_m} \simeq c_m / \cos\psi_m \tag{2.62}$$

$$c_{g_m} \simeq c_m \cos\psi_m \tag{2.63}$$

where ψ_m is the helix angle defined by equation 2.56. The phase speeds approach infinity $c_{z_m} \rightarrow \infty$ and the group speeds approach zero $c_{g_m} \rightarrow 0$ near the cut-off frequency of a given angular order $n \geq 1$ as is typical of propagation in a waveguide. In the case of plane wave excitation of a free mode, the axial phase velocity is a constant imposed by the incident field $c_z = c/\cos\theta$ which determines the corresponding imaginary wavenumber components and group velocities of a given mode n.

In the case of flexural wave roots, I first employed an initial guess of $k_z a = \sqrt{\Omega/\beta - n^2}$ at a maximum frequency of interest such that $ka \gg 1$. Once I had obtained the root at this frequency, successive roots were found at lower frequencies using an initial guess based on the previously obtained root and the relation $k_z a_2 = k_z a_1 \sqrt{\Omega_2/\Omega_1}$. This scheme again produced rapid convergence. The resulting wavenumber roots found for the first three non-zero modes n are shown in Figure 2.40. The associated phase and group velocities are shown in Figure 2.41 where the group velocities were again computed numerically using a central difference scheme. Given this frequency range and shell thickness, low order flexural waves are subsonic and do not radiate into the surrounding fluid. Therefore, the axial wavenumbers are real values. The phase speed of these modes does not exceed 500 m/s over this range of frequencies. At high frequencies, the wavenumber roots vary as the square root

of frequency as suggested by Pierce [45] for propagation in a vacuum. In addition, $c_{g_m} \simeq 2c_m$ as for flexural waves in a plate.

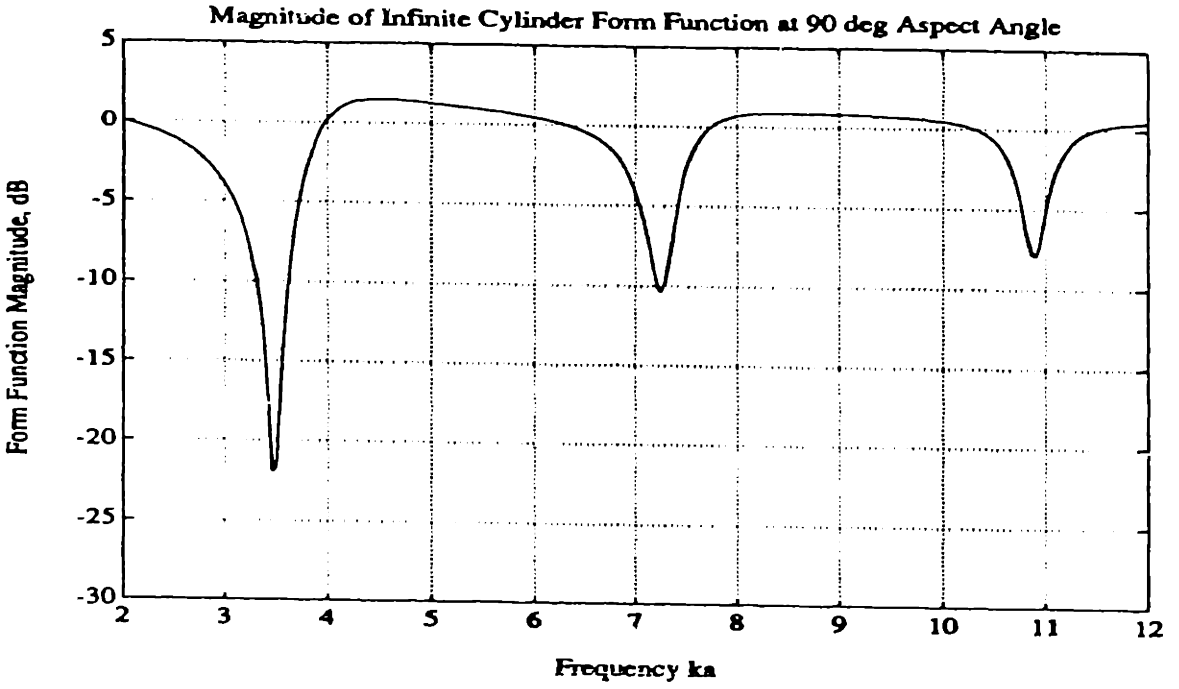

Figure 2.2: The Backscattering Form Function Magnitude of an Infinite Cylinder at Normal Incidence $\theta = 90$ deg

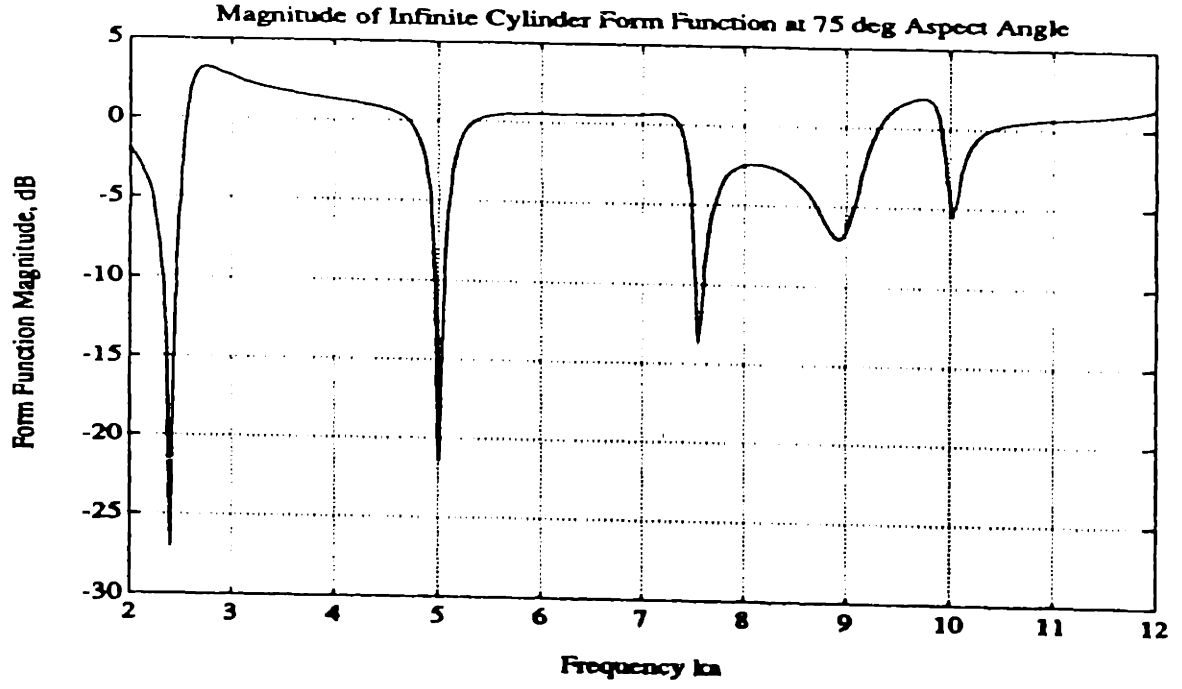

Figure 2.3: Specular Direction Form Function of Infinite Cylinder at a $\theta = 75$ deg Aspect Angle

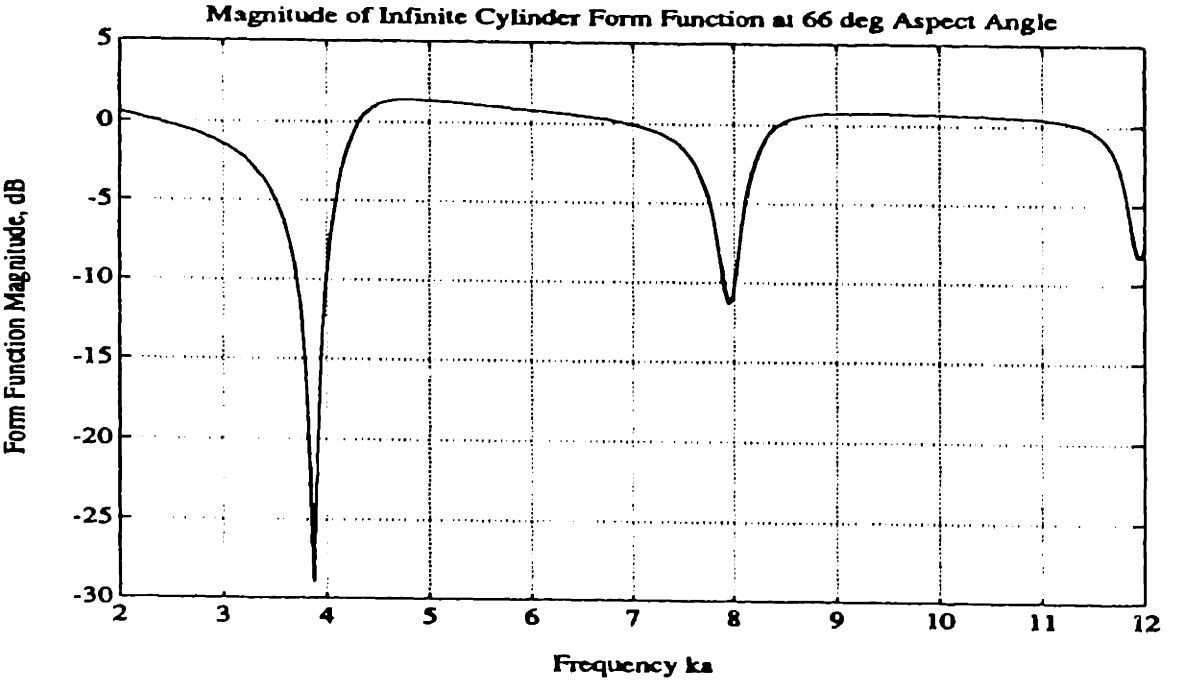

Figure 2.4: Specular Direction Form Function of Infinite Cylinder at a $\theta = 66\,\text{deg}$ Aspect Angle

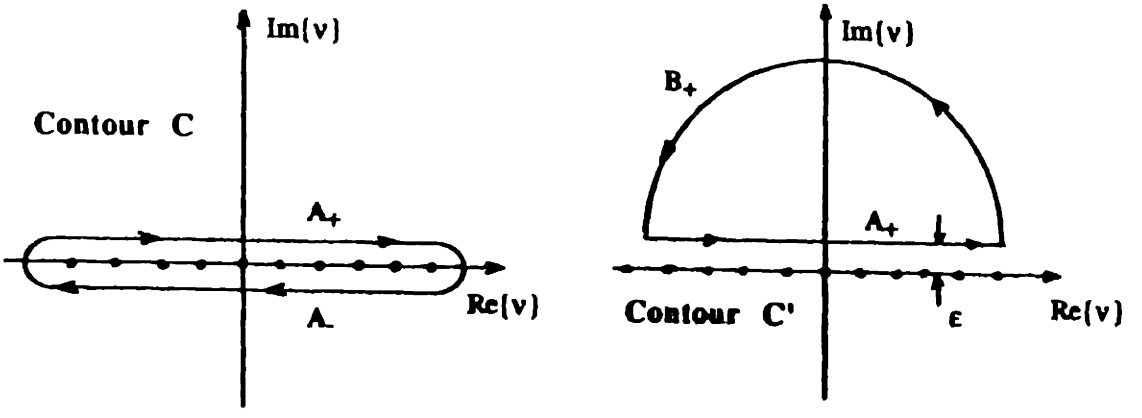

Figure 2.5: Watson Transform Contour C and Deformed Contour $C\prime$ Used to Determine Asymptotic Solutions

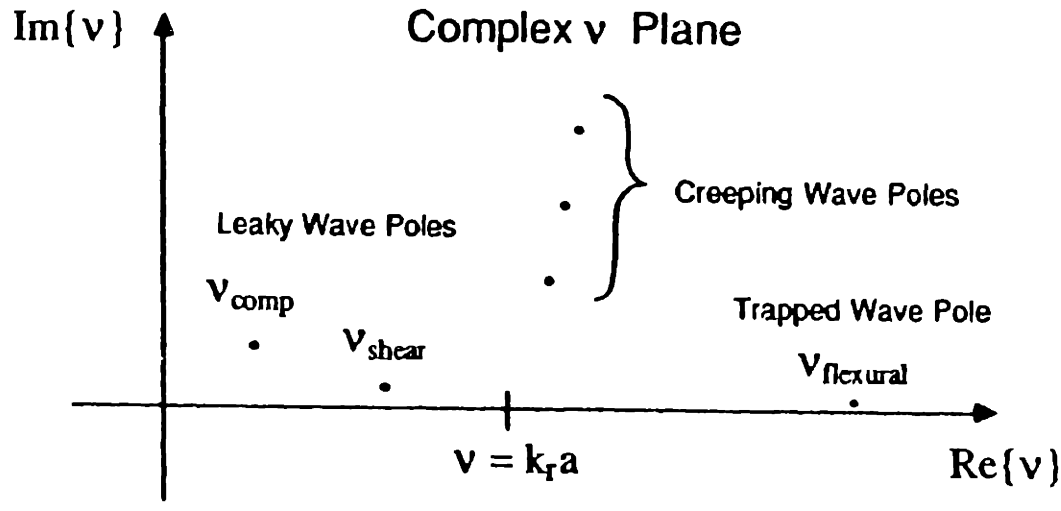

Figure 2.6: Typical Pole Locations in Complex Azimuthal Wavenumber ν Plane for Plane Wave Excitation of a Fluid Loaded Thin Cylindrical Shell

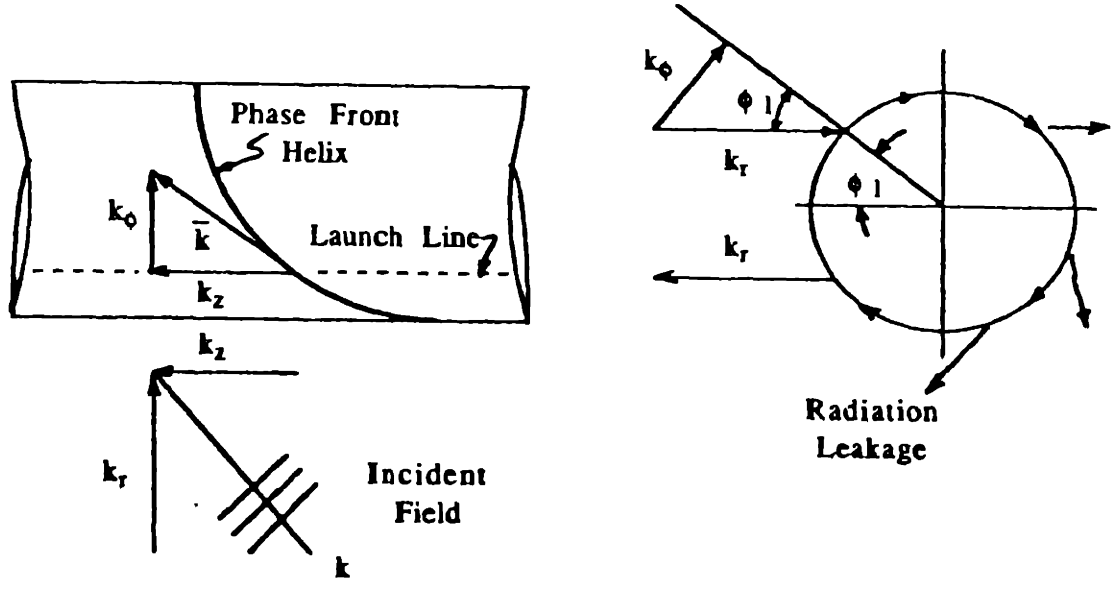

Figure 2.7: Illustration of Phase Matched Launching and Detachment of a Propagating Helical Wave on an Infinite Cylinder

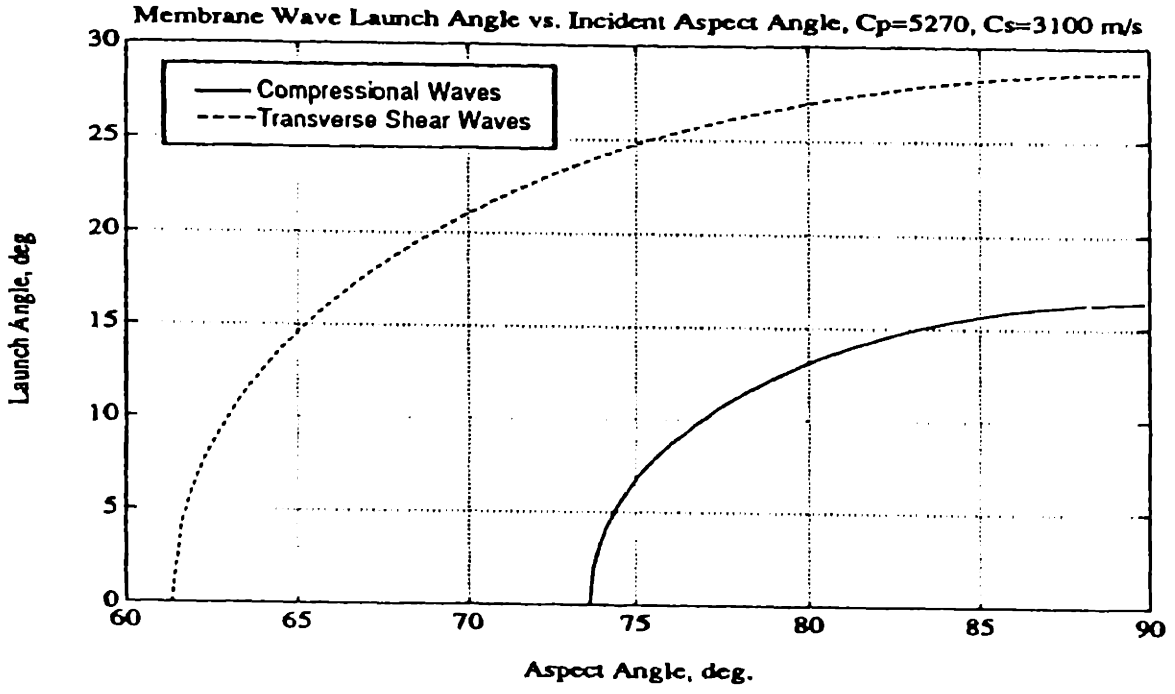

Figure 2.8: Membrane Wave Launch and Detachment Angles ϕ_{l_m} as a Function of Aspect Angle θ

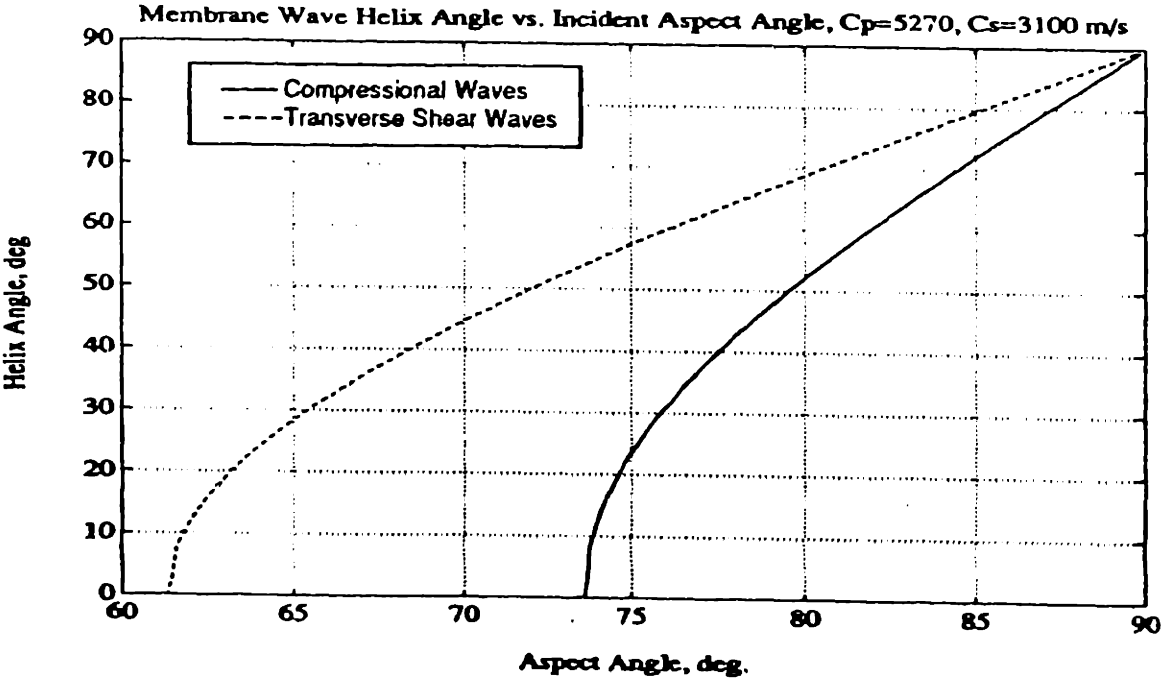

Figure 2.9: Membrane Wave Helix Angle ψ_m, Relative to the Axis of the Cylinder, as a Function of Aspect Angle θ

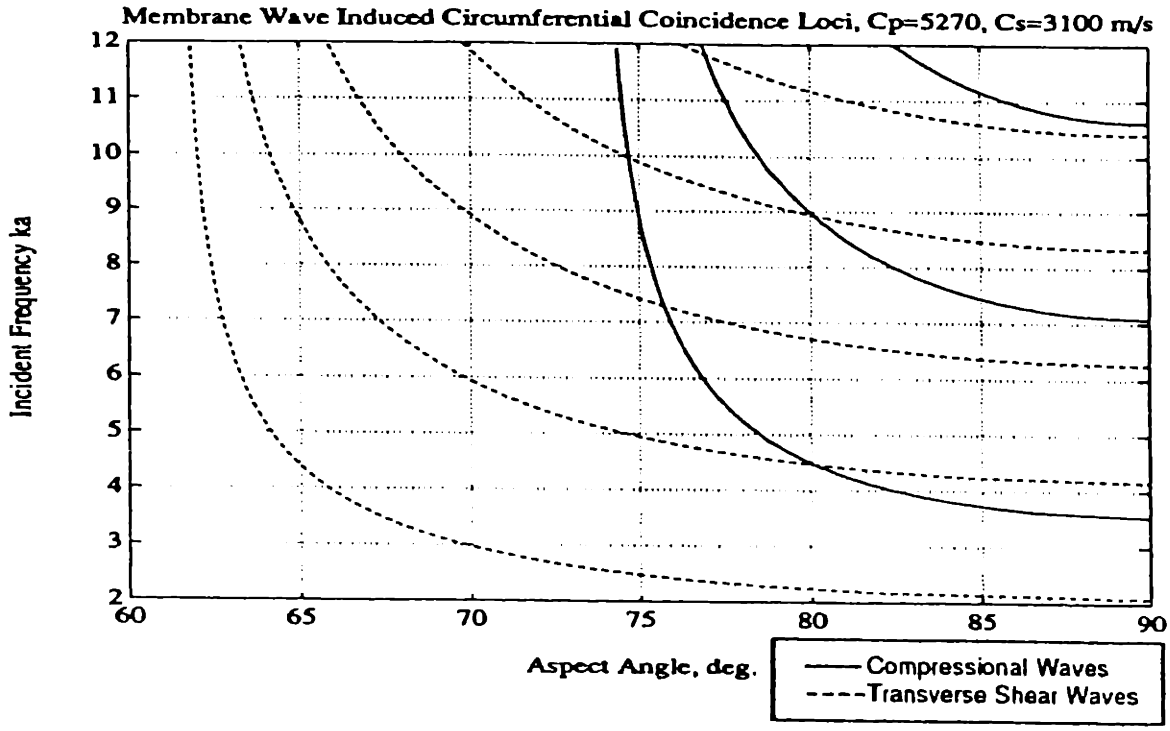

Figure 2.10: Loci of Aspect Angle θ and Frequency ka Where Conditions of Circumferential Spatial Coincidence Exist for Membrane Wave Excitation

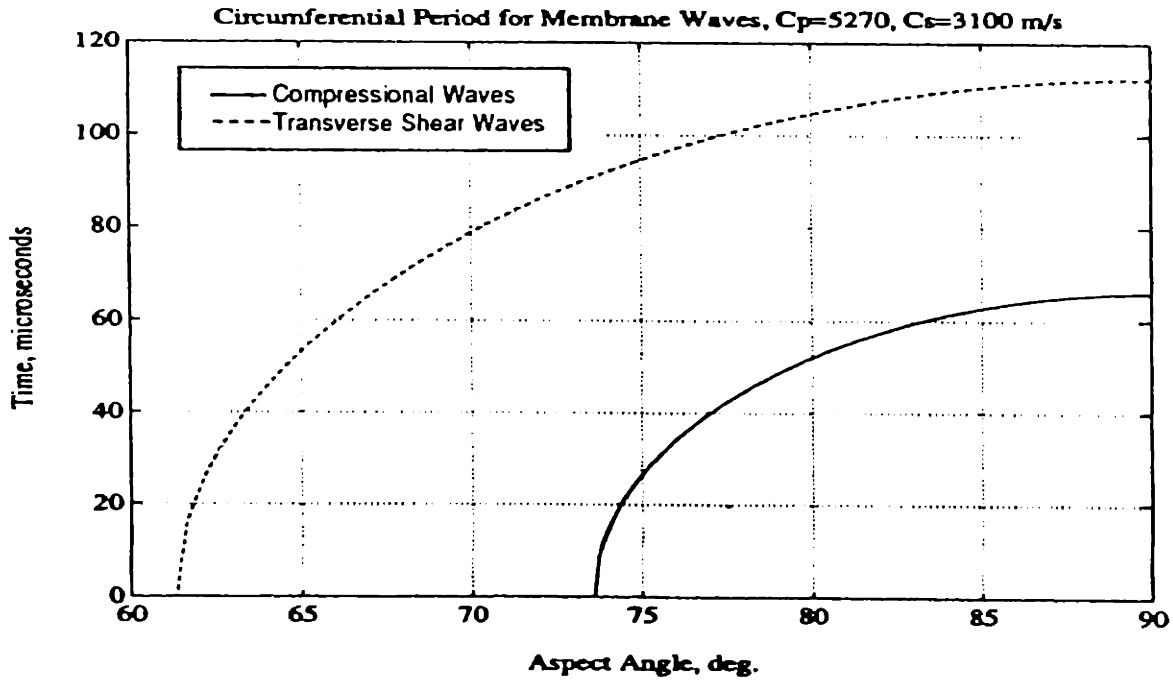

Figure 2.11: Period of Circumferential Component of Phase Matched Helical Membrane Waves

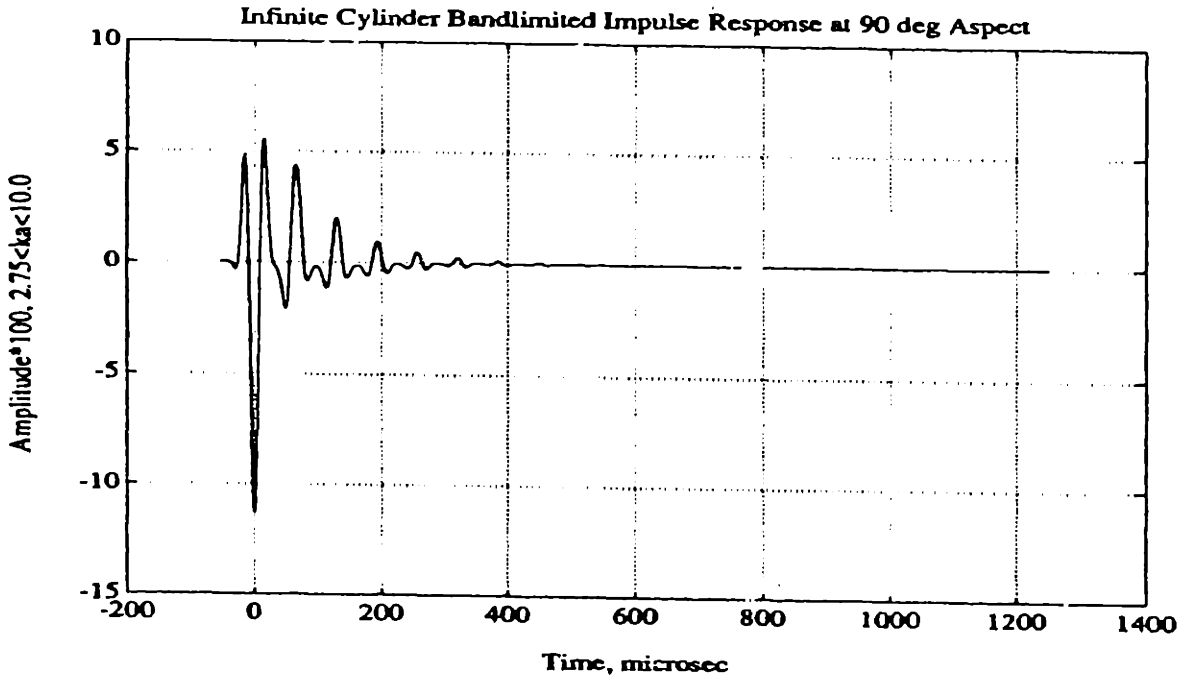

Figure 2.12: Gaussian Bandlimited Time Domain Representation of Backscattered Form Function of an Infinite Cylindrical Shell at Normal Incidence for the Frequency Range $2.75 < ka < 10.0$. Obtained from inverse transform of normal mode series solution.

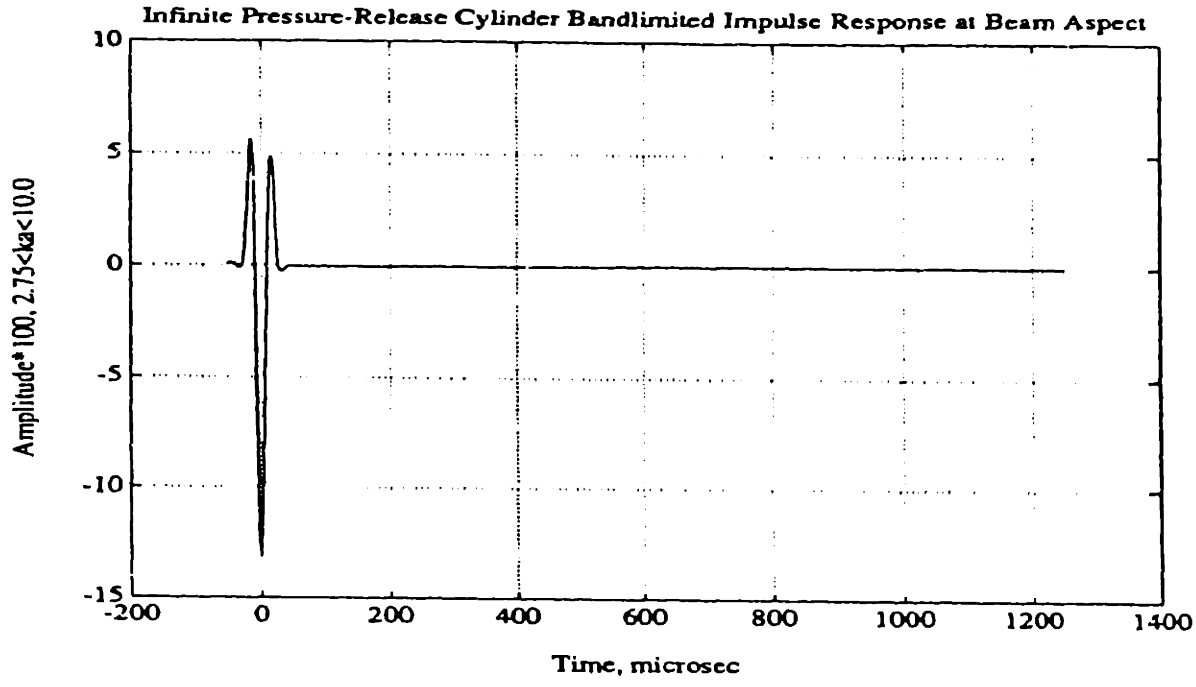

Figure 2.13: Gaussian Bandlimited Time Domain Representation of Backscattered Form Function of an Infinite Pressure Release Cylinder at Normal Incidence for the Frequency Range $2.75 < ka < 10.0$. Obtained from inverse transform of normal mode series solution.

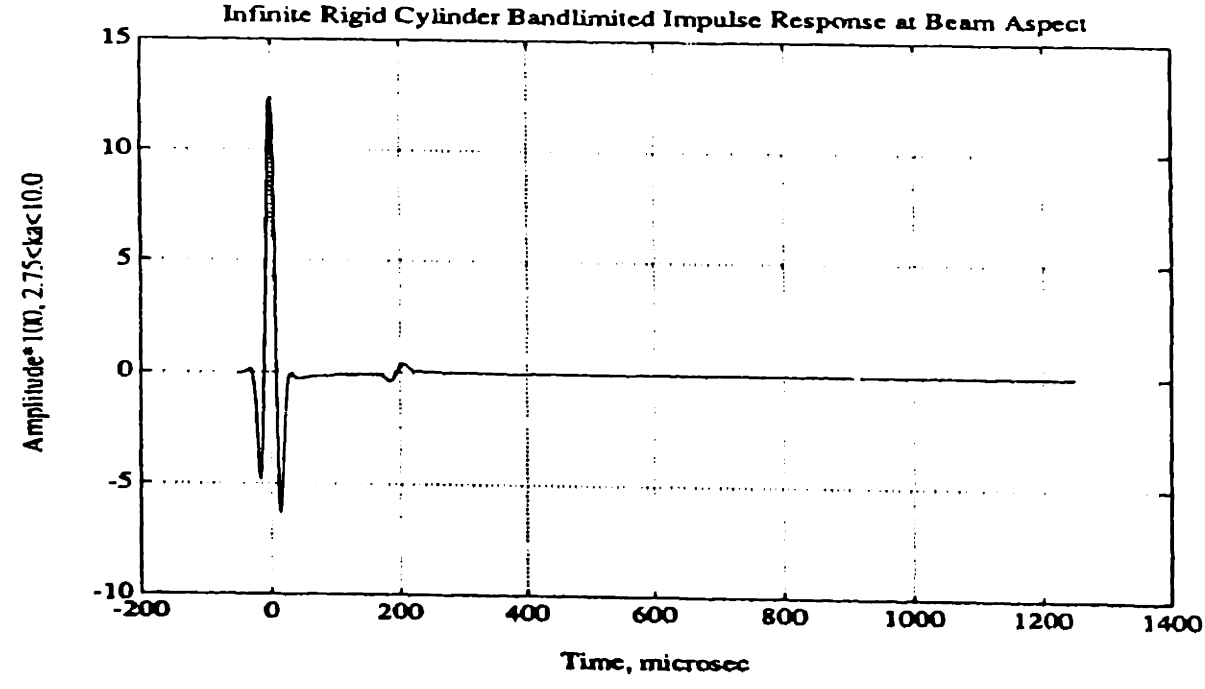

Figure 2.14: Gaussian Bandlimited Time Domain Representation of Backscattered Form Function of an Infinite Rigid Cylinder at Normal Incidence for the Frequency Range $2.75 < ka < 10.0$. Obtained from inverse transform of normal mode series solution.

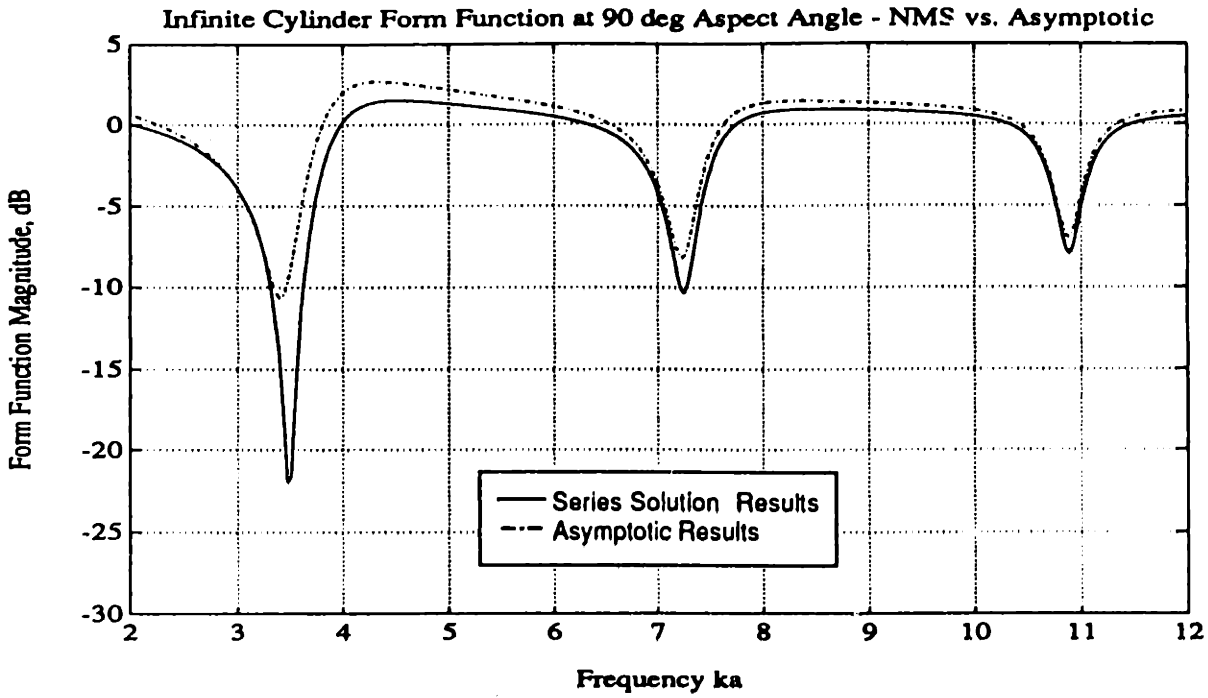

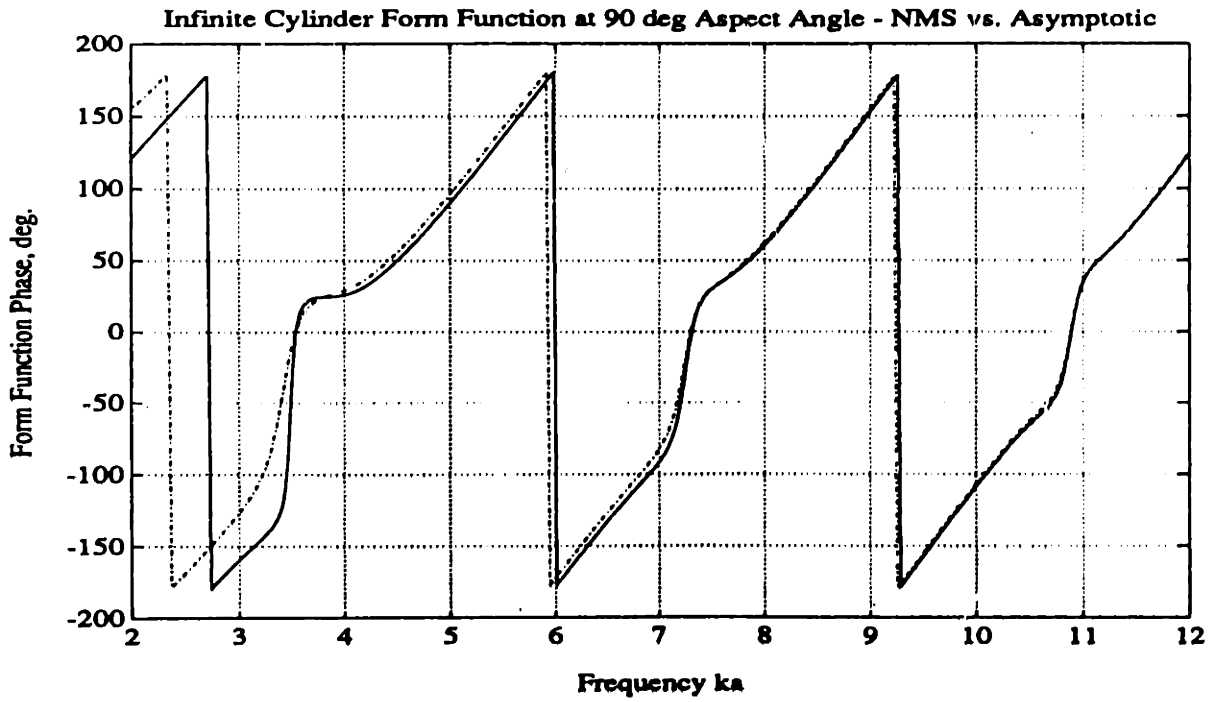

Figure 2.15: Comparison of Normal Mode Series and Asymptotic Solutions for the Backscattered Field Form Function Magnitude and Phase at Normal Incidence

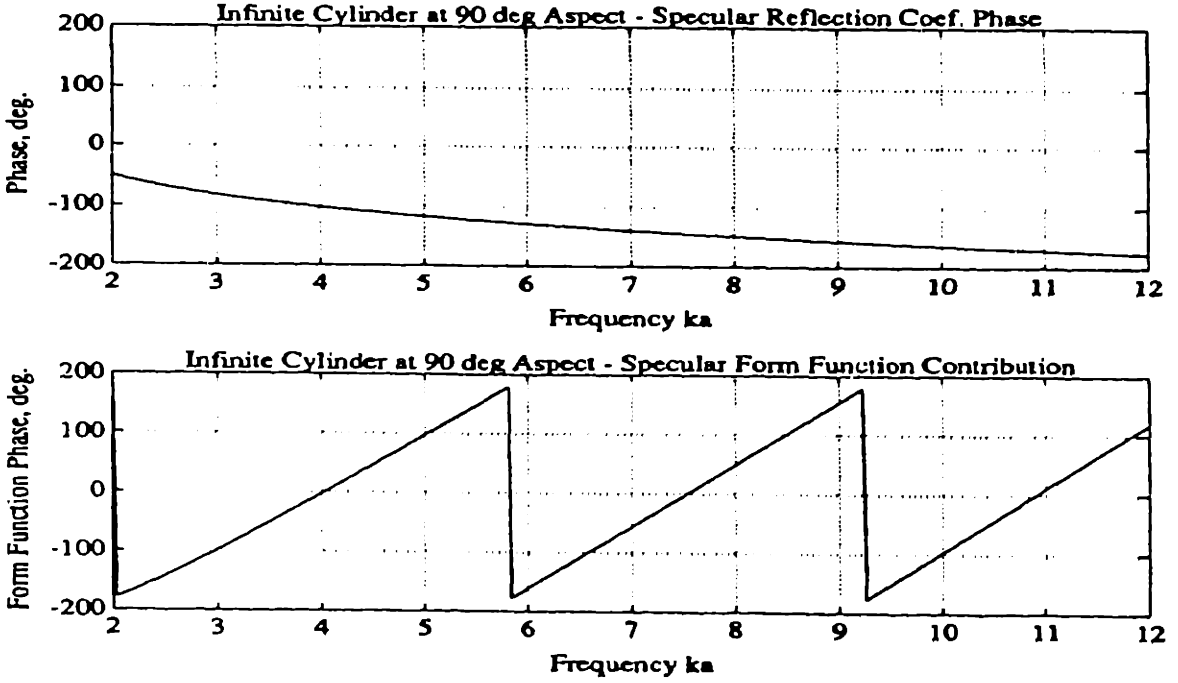

Figure 2.16: Phase of Specularly Reflected Component of the Backscattered Field Form Function at Normal Incidence

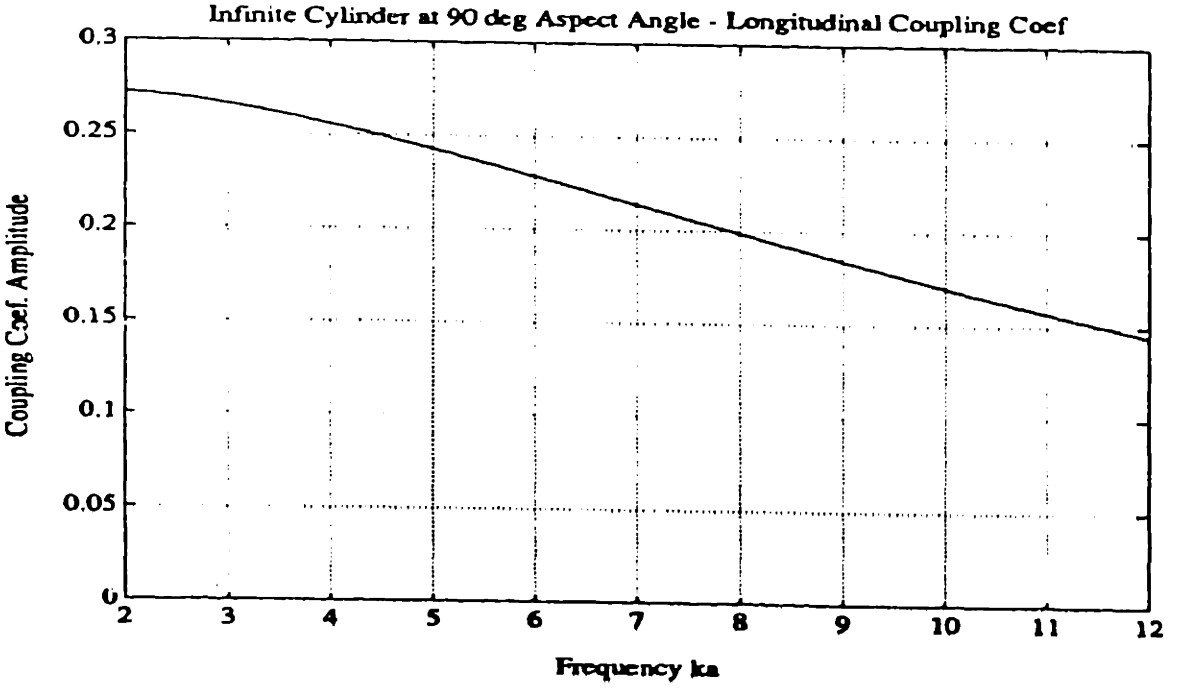

Figure 2.17: Magnitude of Coupling Coefficient A_m Associated with Compressional Wave Excitation at Normal Incidence

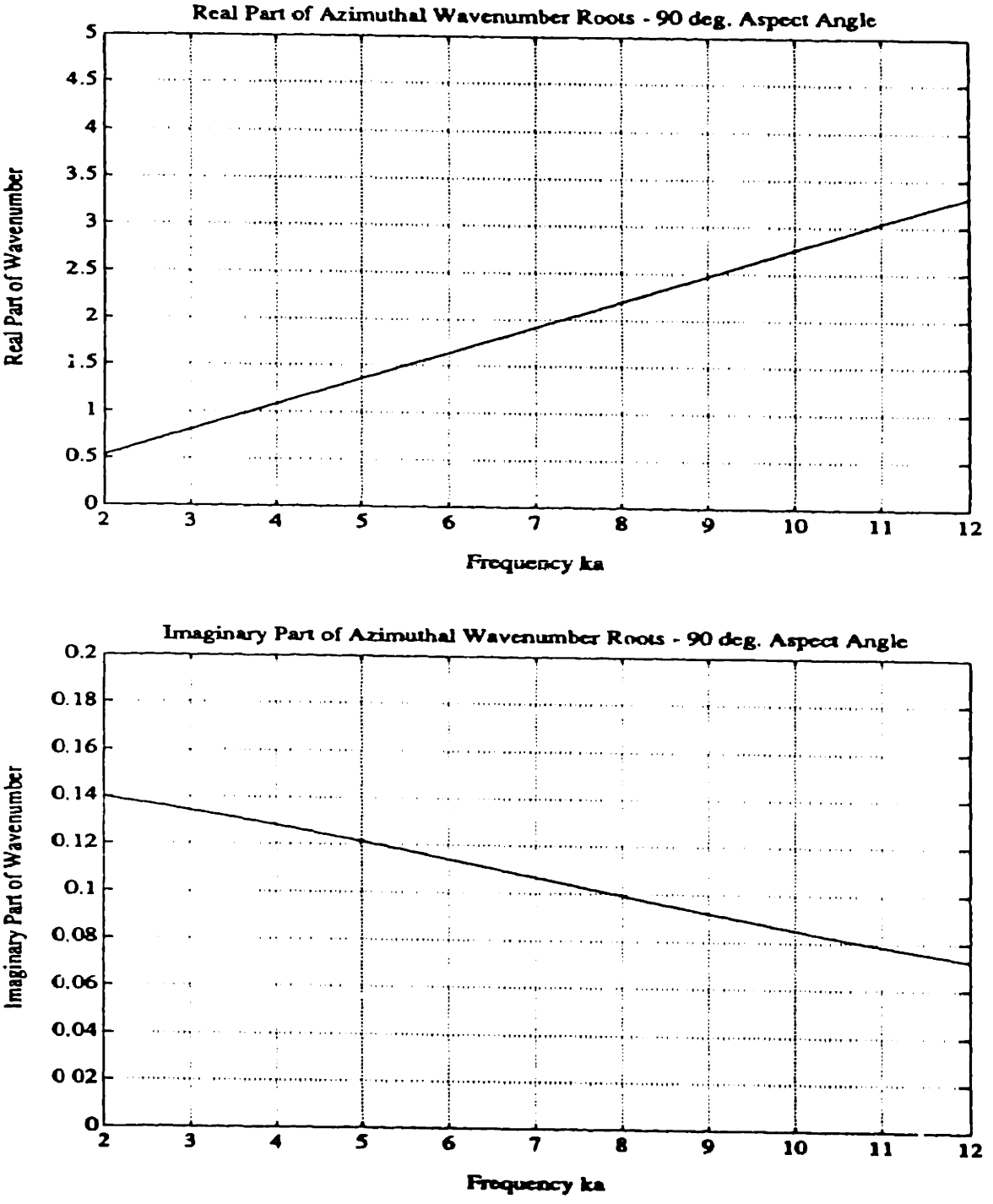

Figure 2.18: Real and Imaginary Components of Azimuthal Wavenumber Poles υ_m Associated with Compressional Wave Propagation and Excitation at Normal Incidence

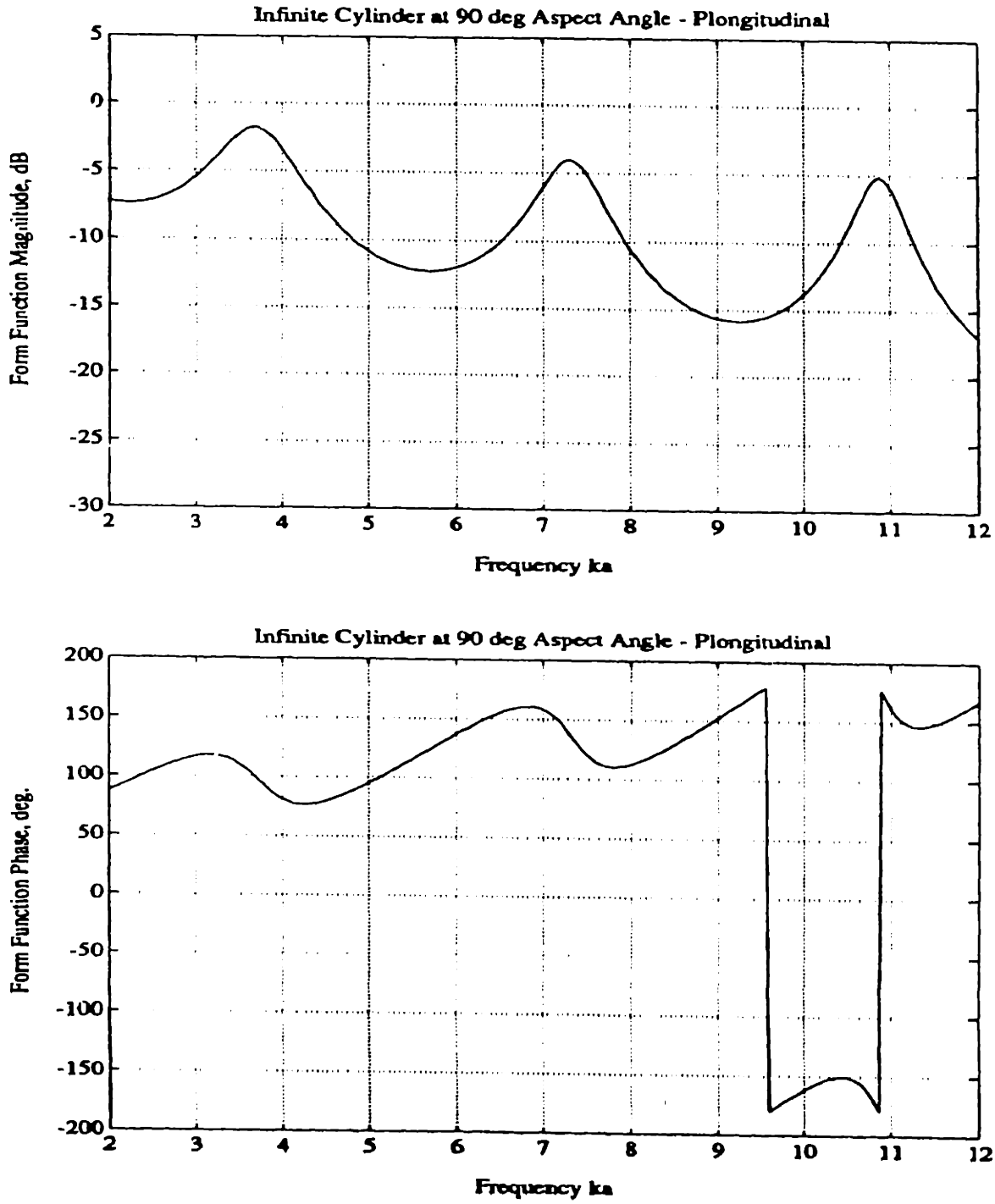

Figure 2.19: Magnitude and Phase of Compressional Leaky Wave Component of Backscattered Field Form Function at Normal Incidence

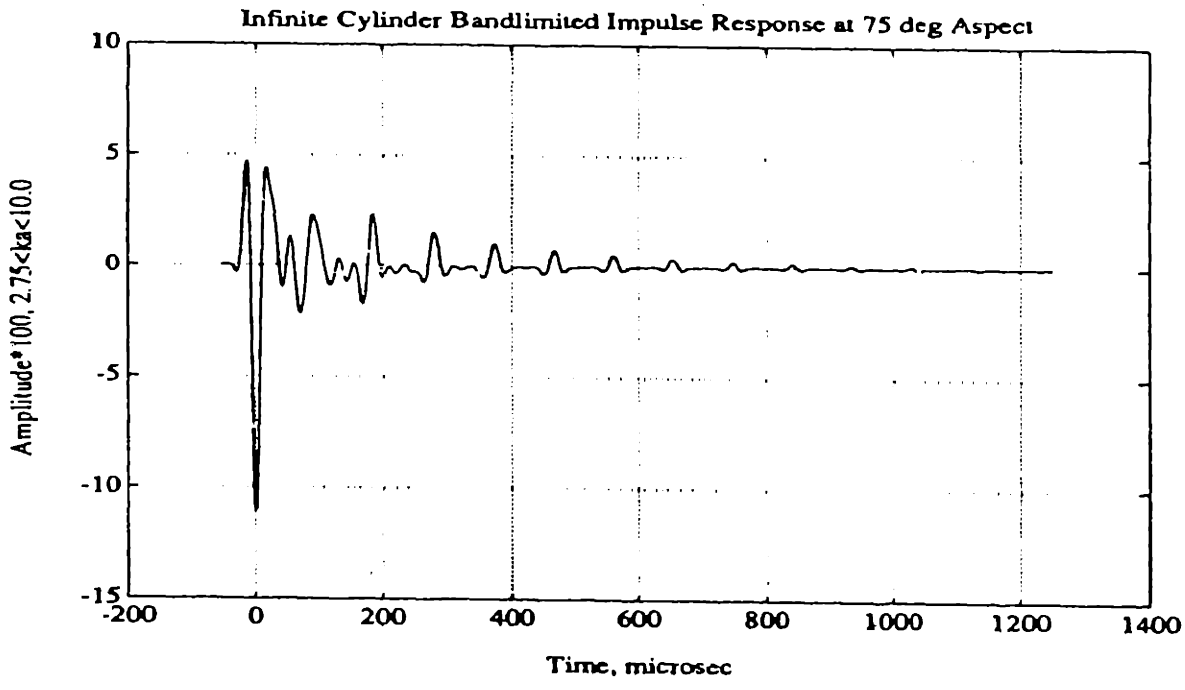

Figure 2.20: Gaussian Bandlimited Time Domain Representation of Specularly Directed Scattered Field Form Function of an Infinite Cylindrical Shell at $\theta = 75$ deg Aspect Angle and the Frequency Range $2.75 < ka < 10.0$. Obtained from the inverse transform of the normal mode series solution.

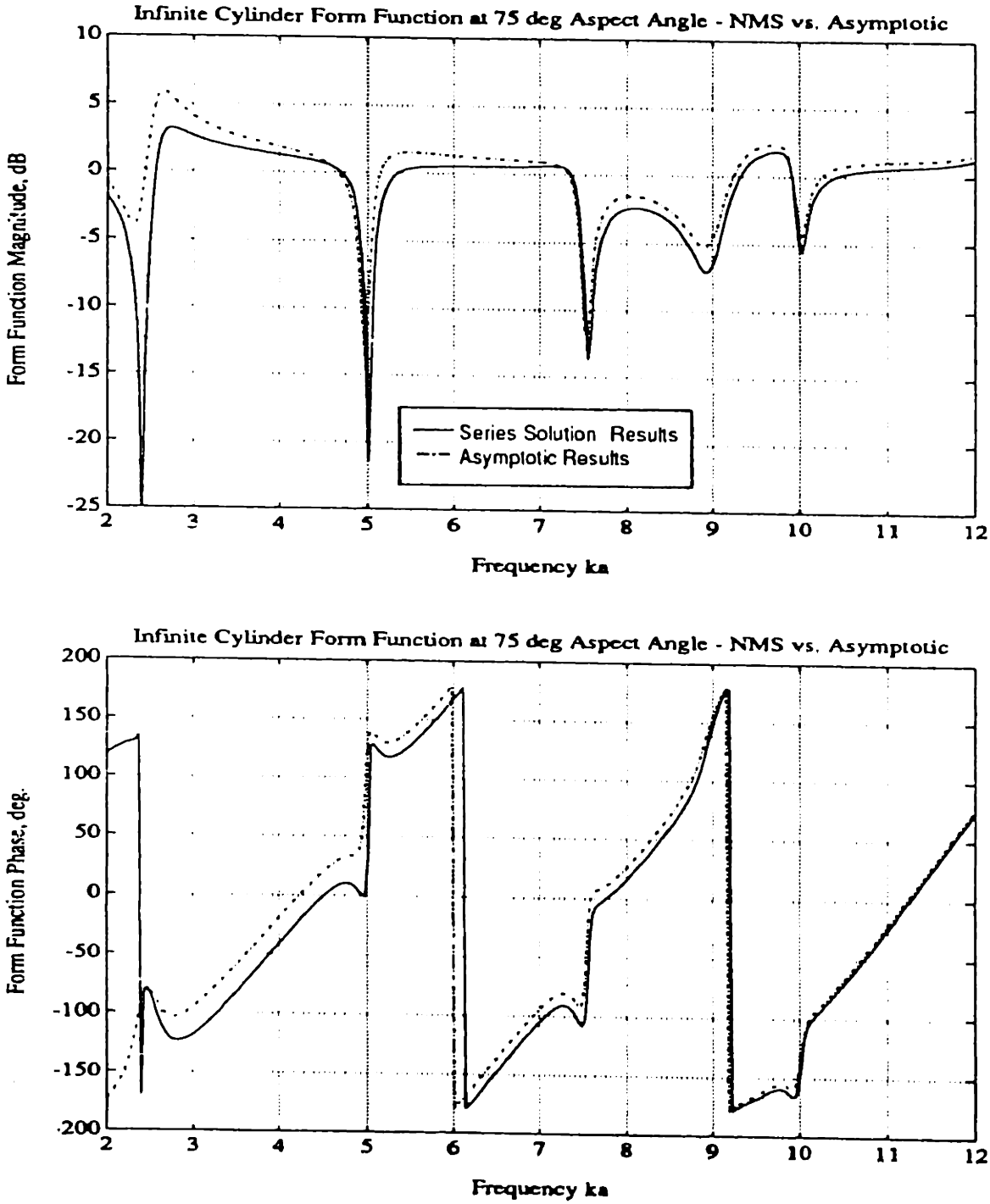

Figure 2.21: Comparison of Normal Mode Series and Asymptotic Solutions for Specular Directed Scattered Field Form Function Magnitude and Phase at a $\theta = 75$ deg Aspect Angle

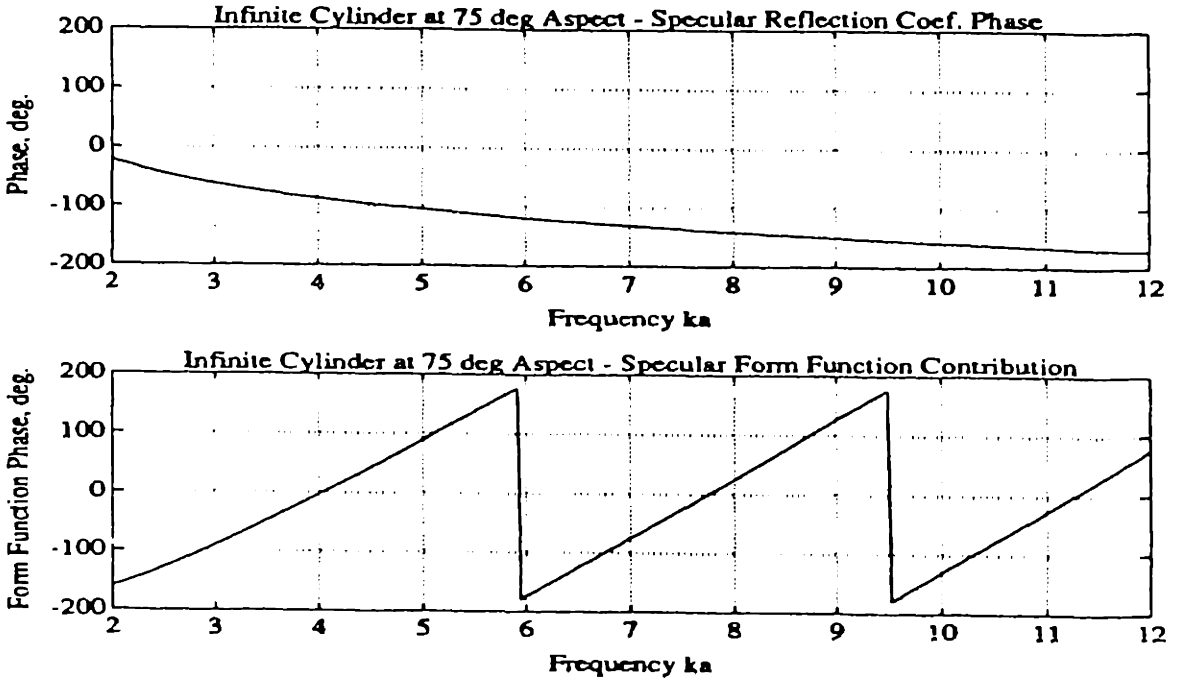

Figure 2.22: Phase of Specularly Reflected Component of Scattered Field Form Function at a $\theta = 75$ deg Aspect Angle

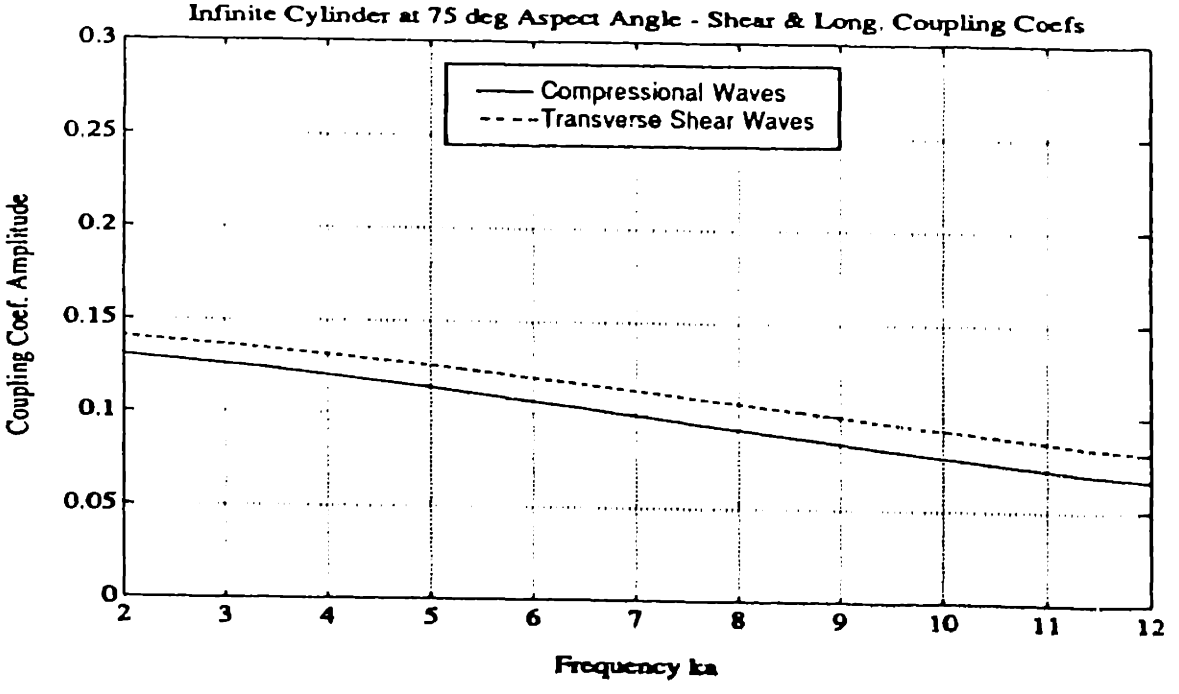

Figure 2.23: Magnitude of Coupling Coefficients A_m Associated with Compressional and Transverse Shear Wave Excitation at a $\theta = 75$ deg Aspect Angle

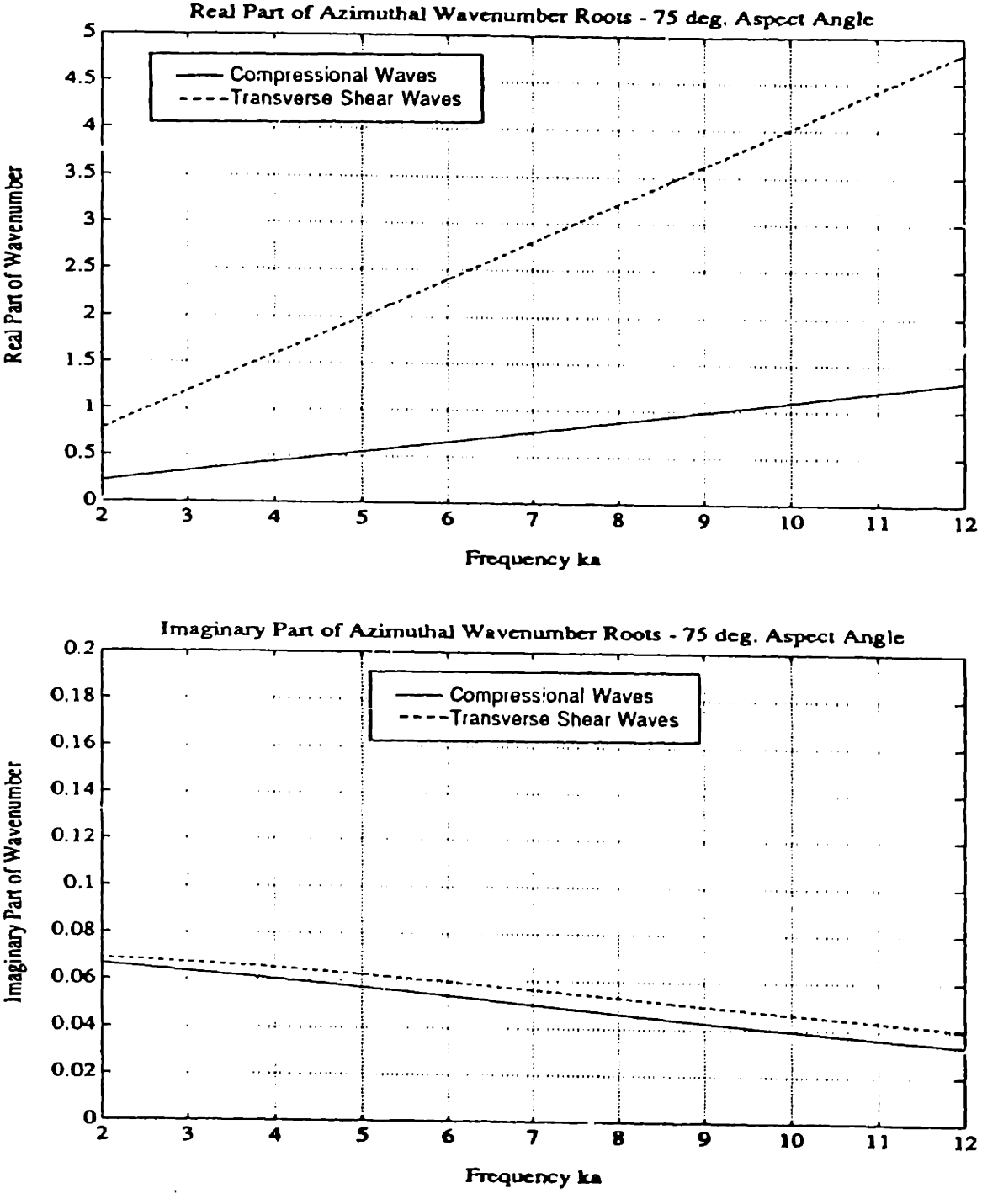

Figure 2.24: Real and Imaginary Components of Azimuthal Wavenumber Poles v_m Associated with Compressional and Transverse Shear Wave Propagation and Excitation at a $\theta = 75$ deg Aspect Angle

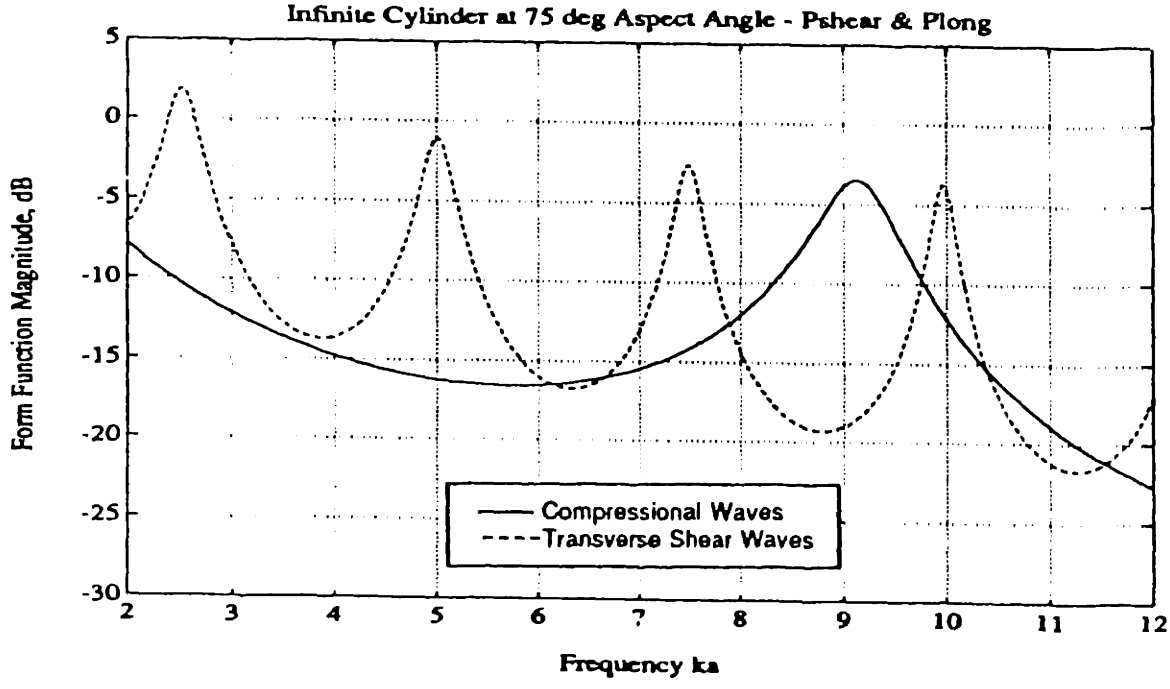

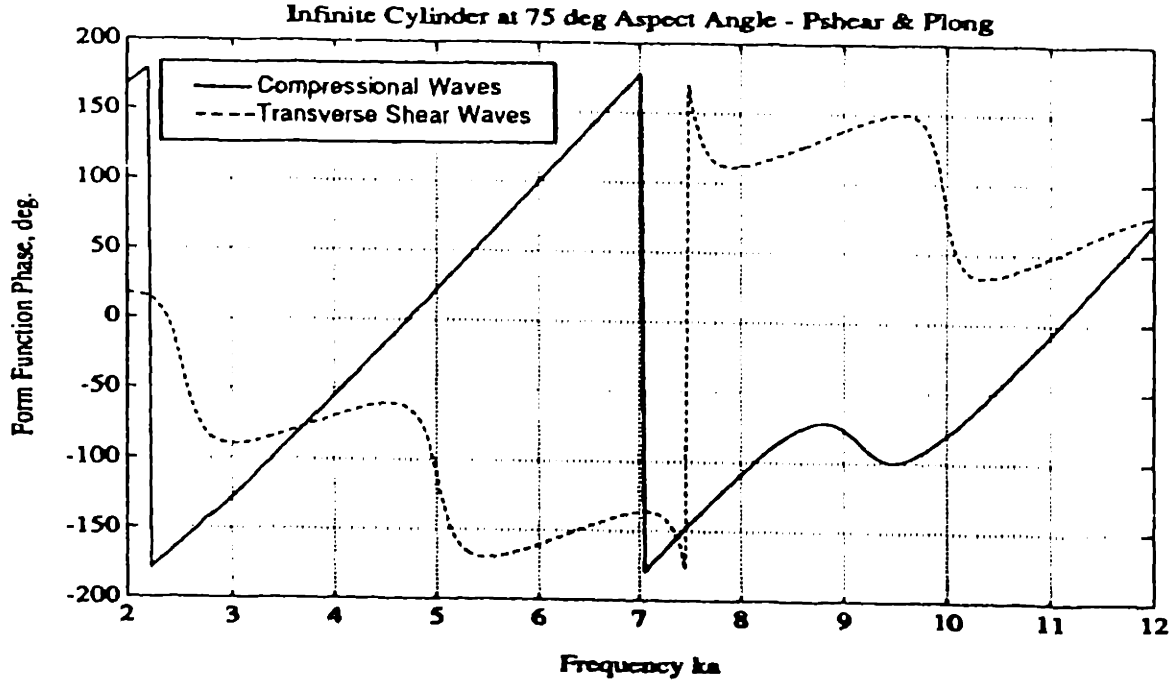

Figure 2.25: Magnitude and Phase of Compressional and Transverse Shear Leaky Wave Component of Specularly Directed Scattered Field Form Function at a θ = 75 deg Aspect Angle

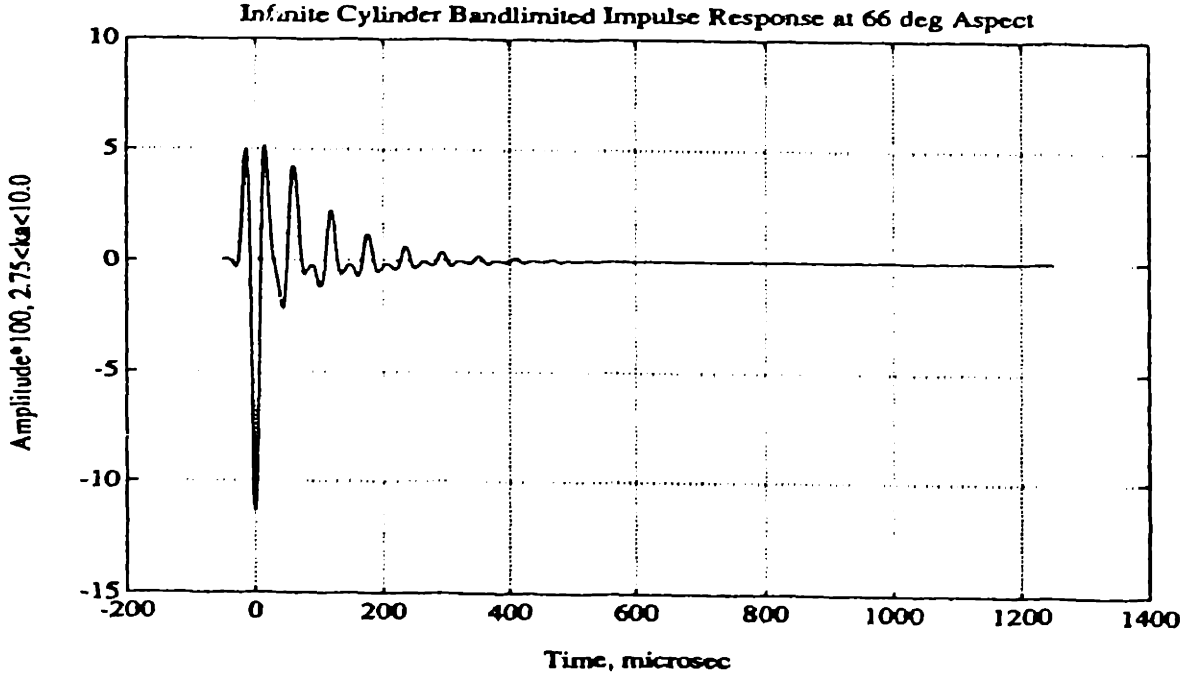

Figure 2.26: Gaussian Bandlimited Time Domain Representation of Specularly Directed Scattered Field Form Function of an Infinite Cylindrical Shell at a $\theta = 66$ deg Aspect Angle and a Frequency Range of $2.75 < ka < 10.0$. Obtained from the inverse transform of the normal mode series solution.

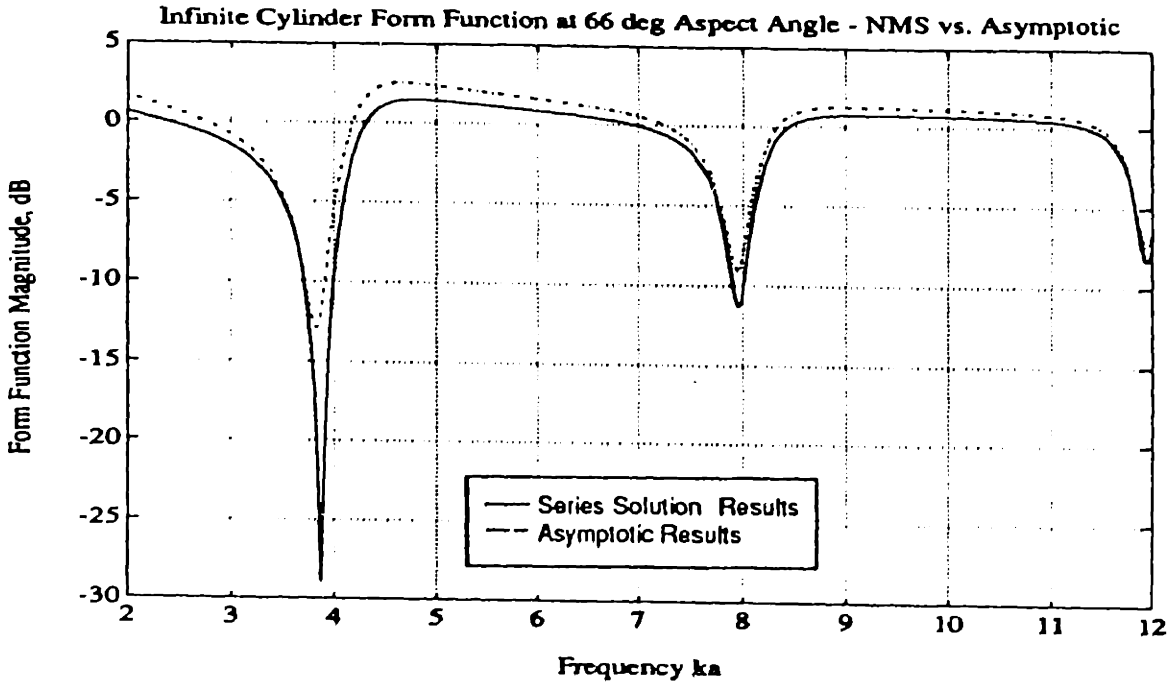

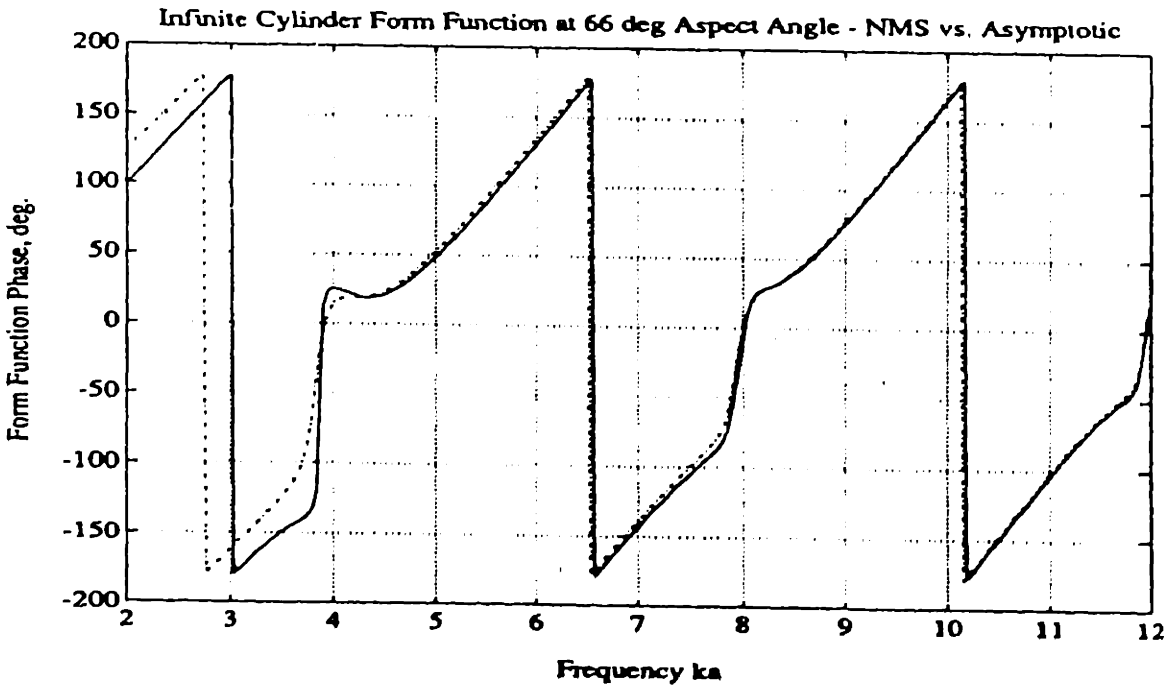

Figure 2.27: Comparison of Normal Mode Series and Asymptotic Solutions for Specular Directed Scattered Field Form Function Magnitude and Phase at a $\theta = 66$ deg Aspect Angle

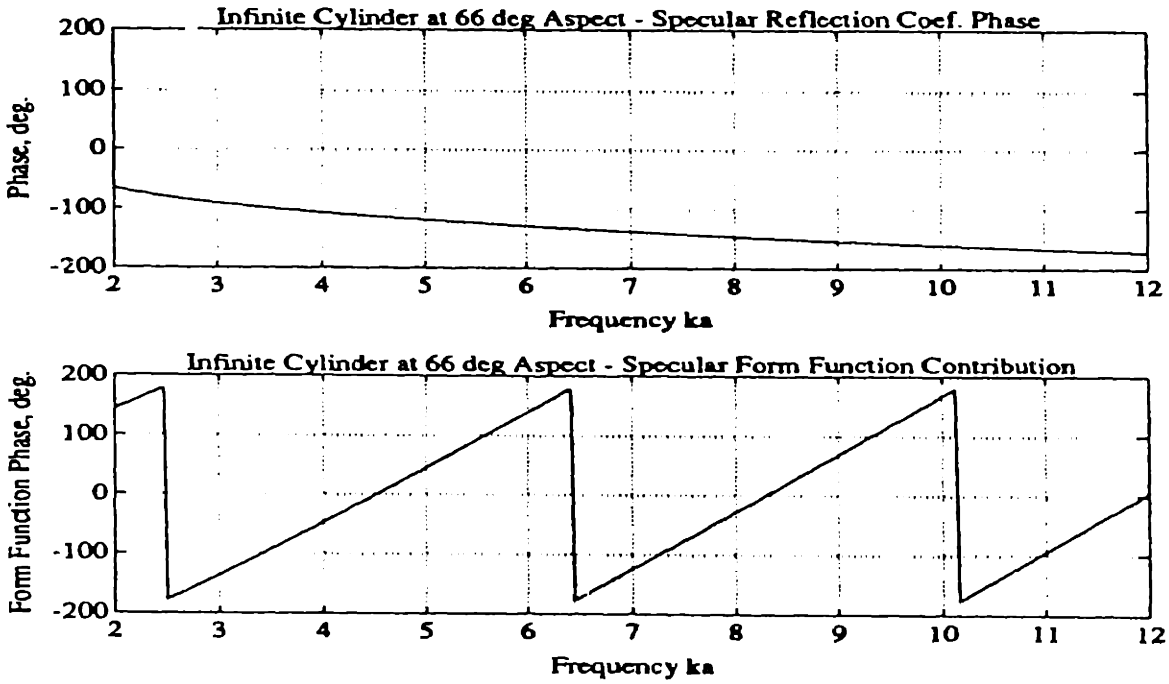

Figure 2.28: Phase of Specularly Reflected Component of Scattered Field Form Function at a $\theta = 66$ deg Aspect Angle

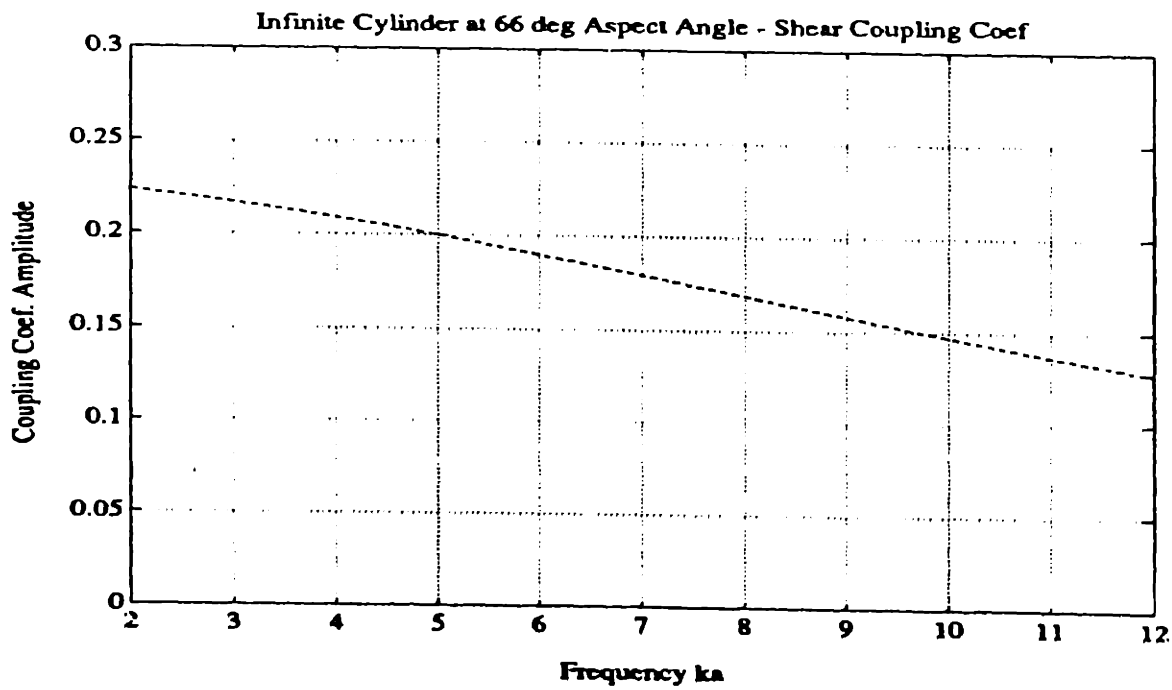

Figure 2.29: Magnitude of Coupling Coefficient A_m Associated with Transverse Shear Wave Excitation at a $\theta = 66$ deg Aspect Angle

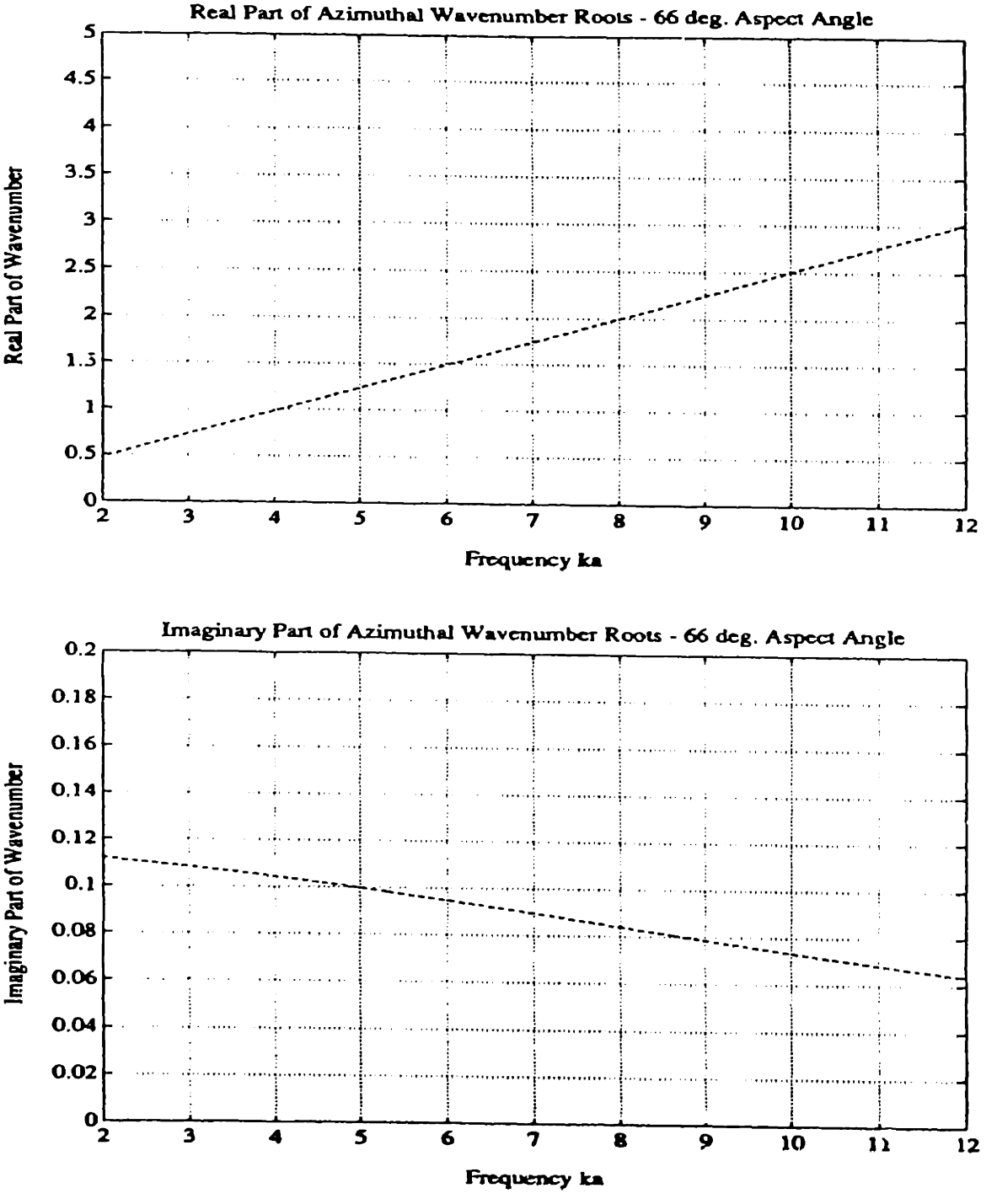

Figure 2.30: Real and Imaginary Components of Azimuthal Wavenumber Poles υ_m Associated with Transverse Shear Wave Propagation and Excitation at a $\theta = 66$ deg Aspect Angle

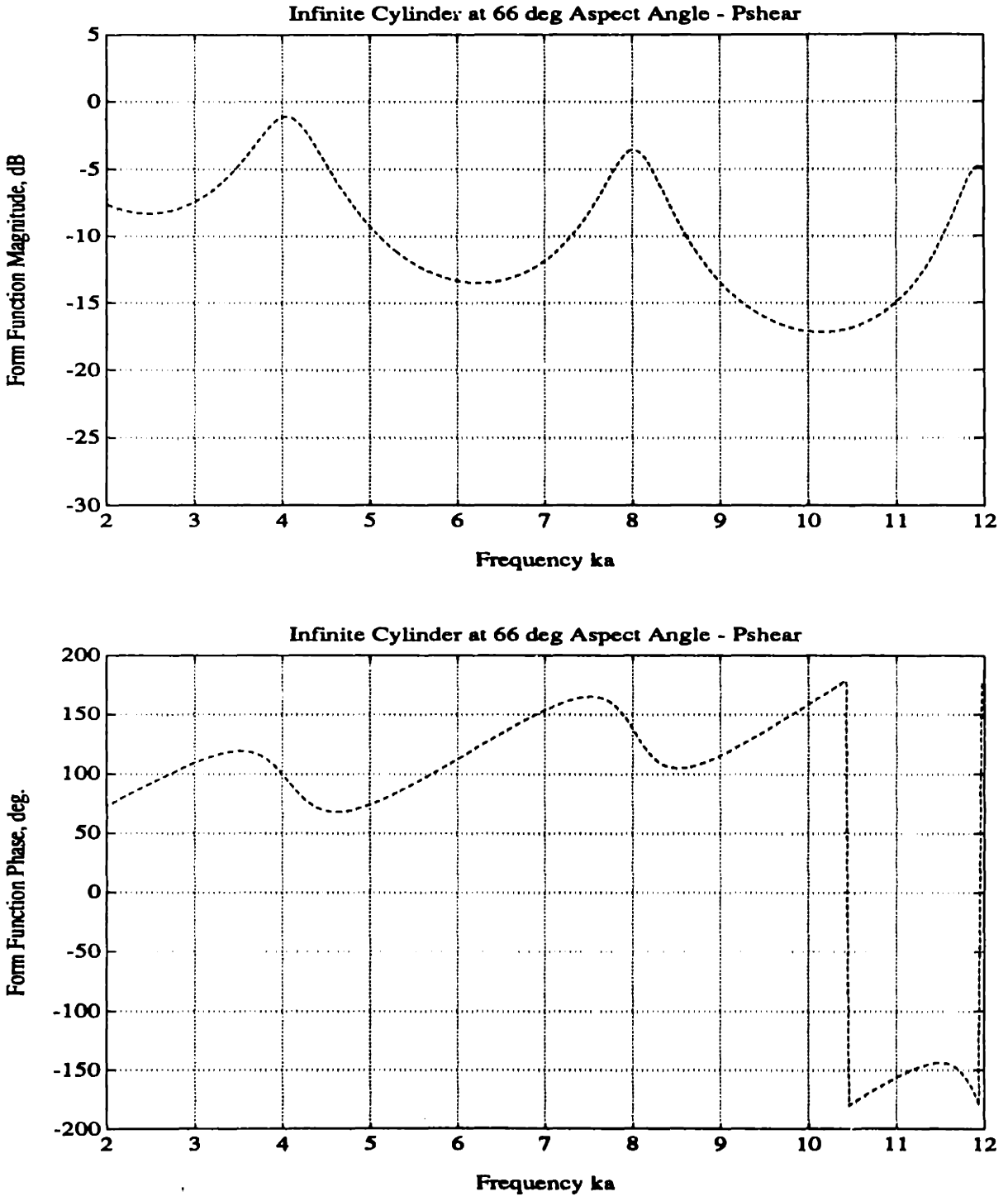

Figure 2.31: Magnitude and Phase of Transverse Shear Leaky Wave Component of Specularly Directed Scattered Field Form Function at a 66 deg Aspect Angle

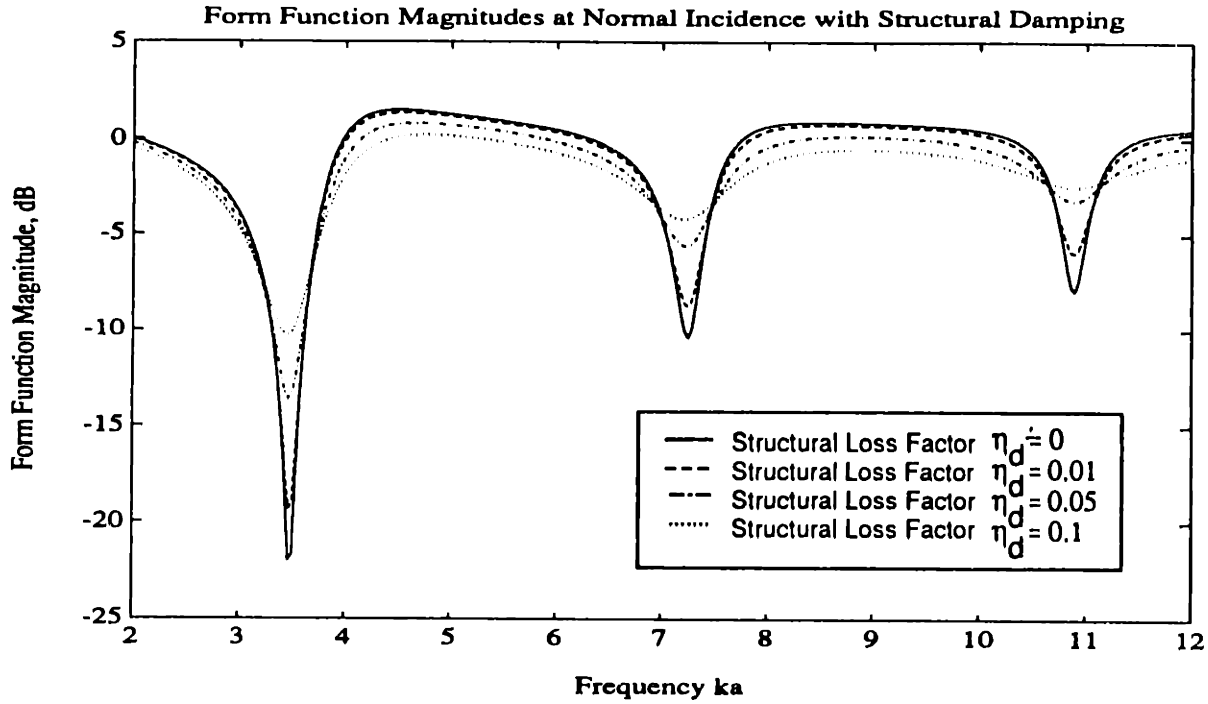

Figure 2.32: Comparison of The Backscattering Form Function Magnitude of an Infinite Cylinder at Normal Incidence with Structural Damping Loss Factors Values of $\eta_d = 0$, 0.01, 0.05, and 0.10

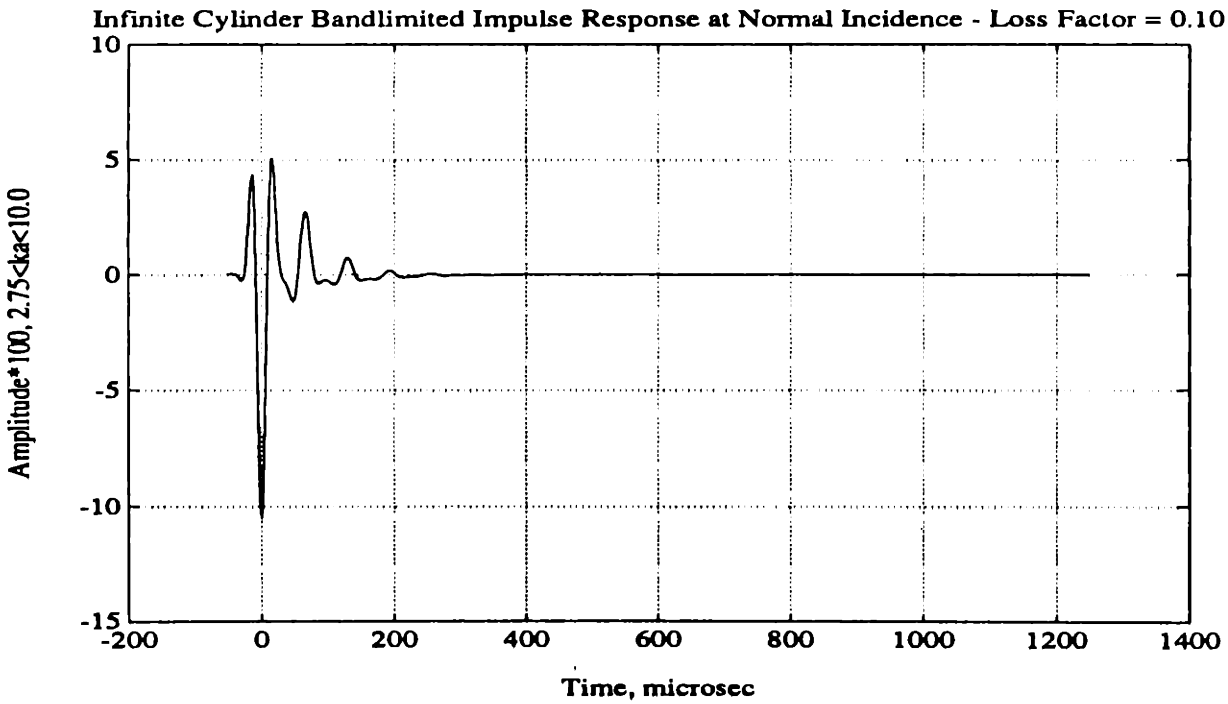

Figure 2.33: Gaussian Bandlimited Time Domain Representation of the Backscattered Form Function of an Infinite Cylindrical Shell at Normal Incidence with a Structural Loss Factor of $\eta_d = 0.10$. Obtained from inverse transform of normal mode series solution for the frequency range $2.75 < ka < 10.0$.

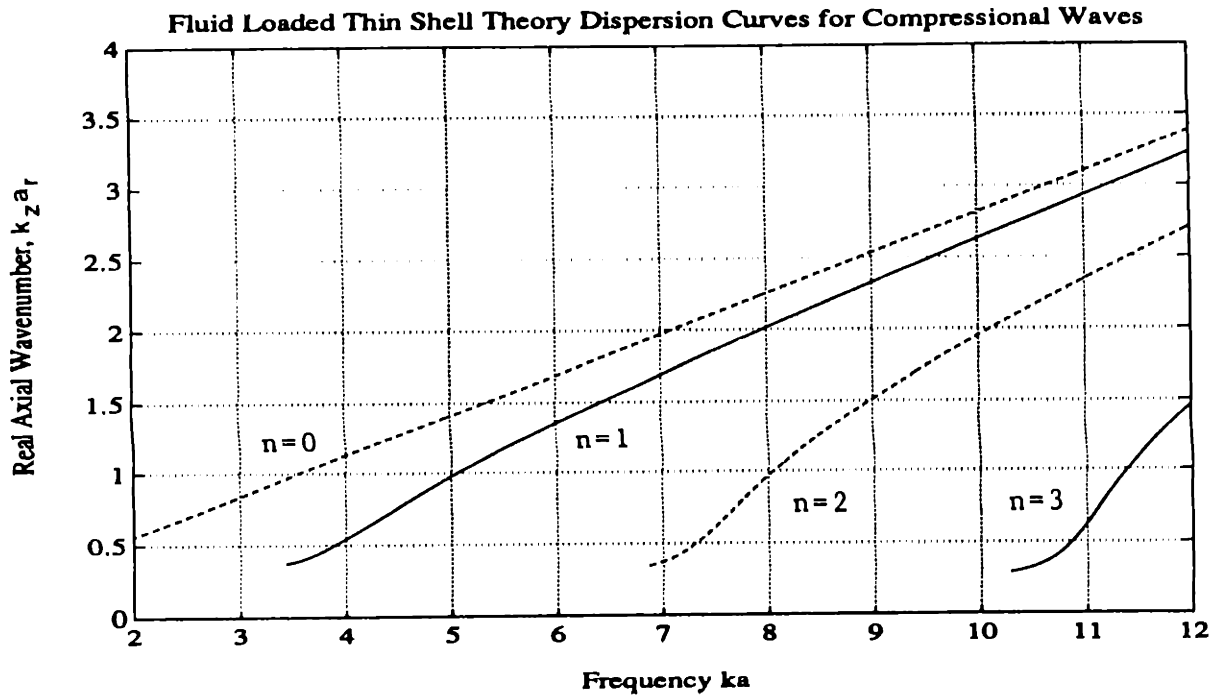

Figure 2.34: Real Part of Axial Wavenumber Roots $k_z a_r$ Associated with Free Compressional Wave Propagation

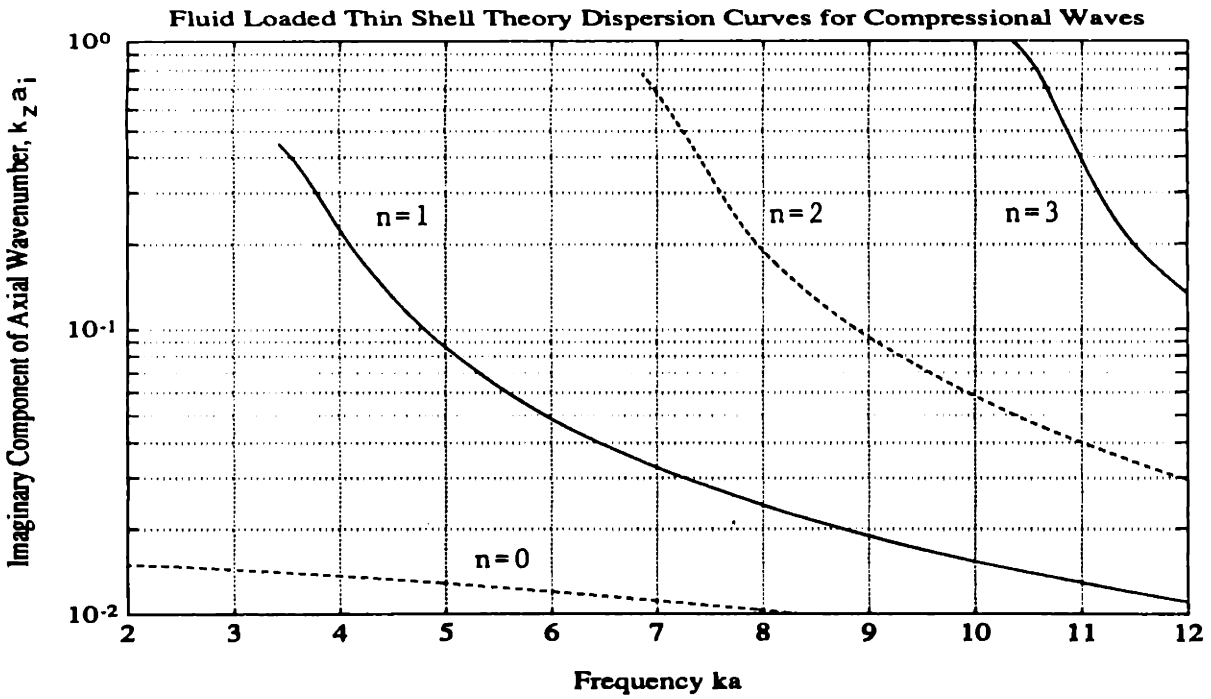

Figure 2.35: Imaginary Part of Axial Wavenumber Roots $k_z a_i$ Associated with Free Compressional Wave Propagation

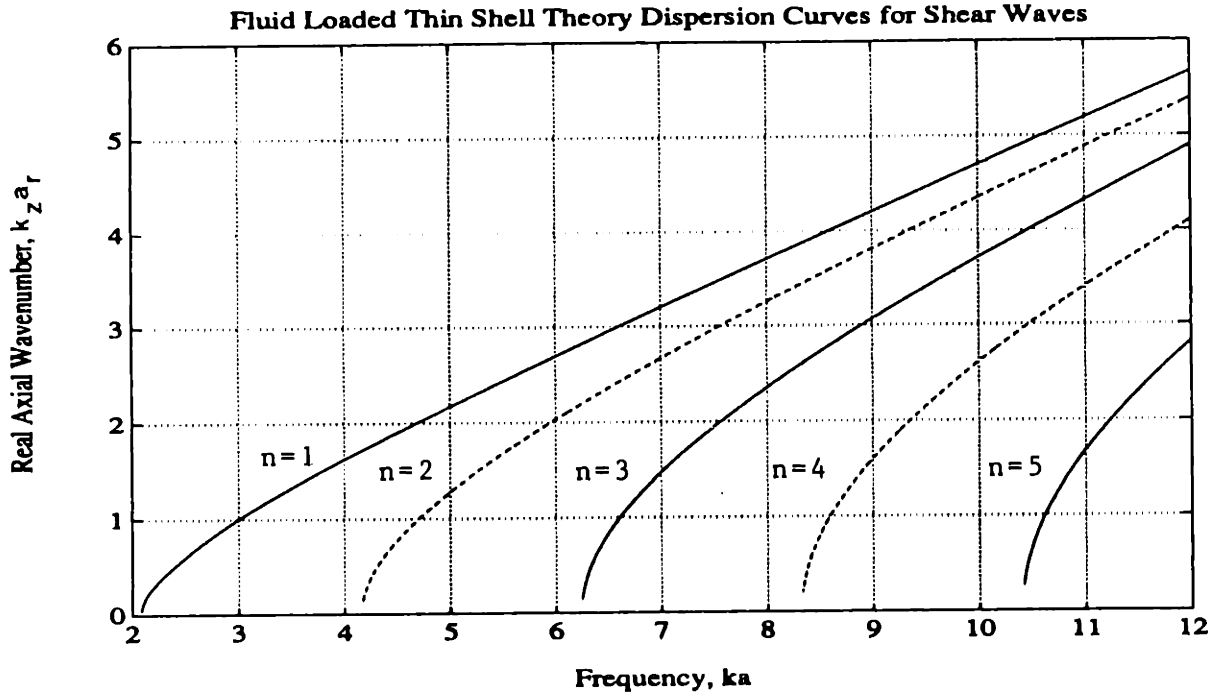

Figure 2.36: Real Part of Axial Wavenumber Roots $k_z a_r$ Associated with Free Transverse Shear Wave Propagation

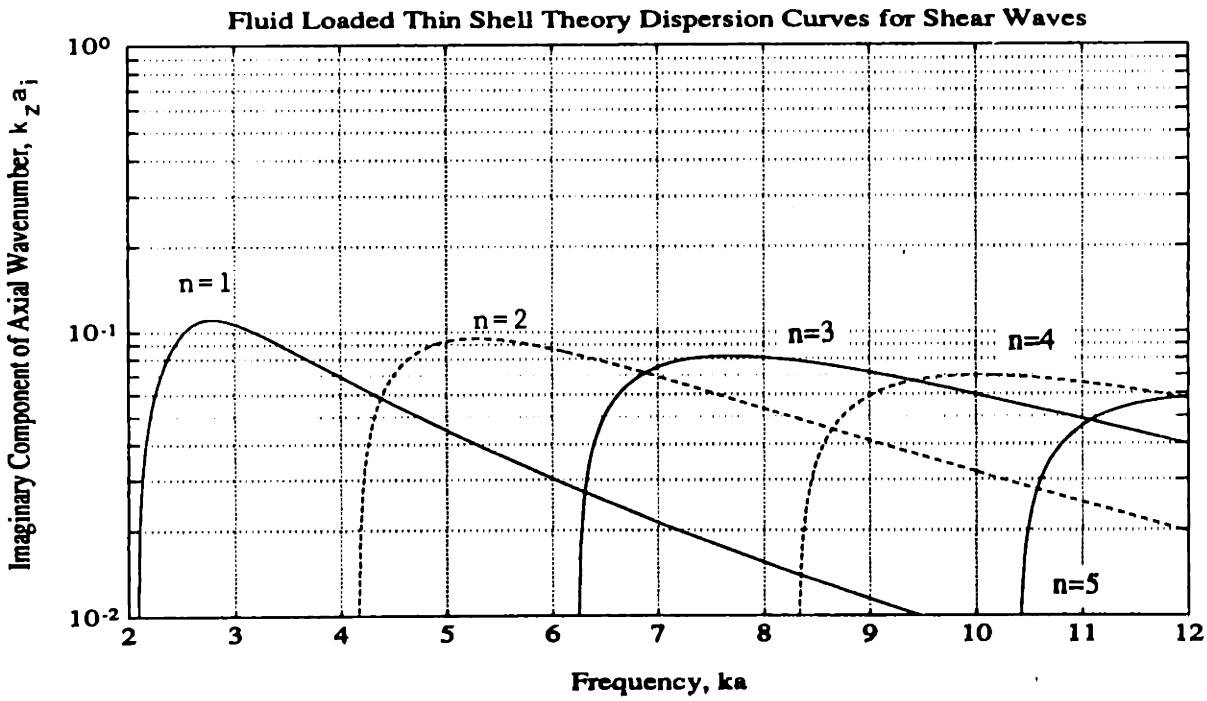

Figure 2.37: Imaginary Part of Axial Wavenumber Roots $k_z a_i$ Associated with Free Transverse Shear Wave Propagation

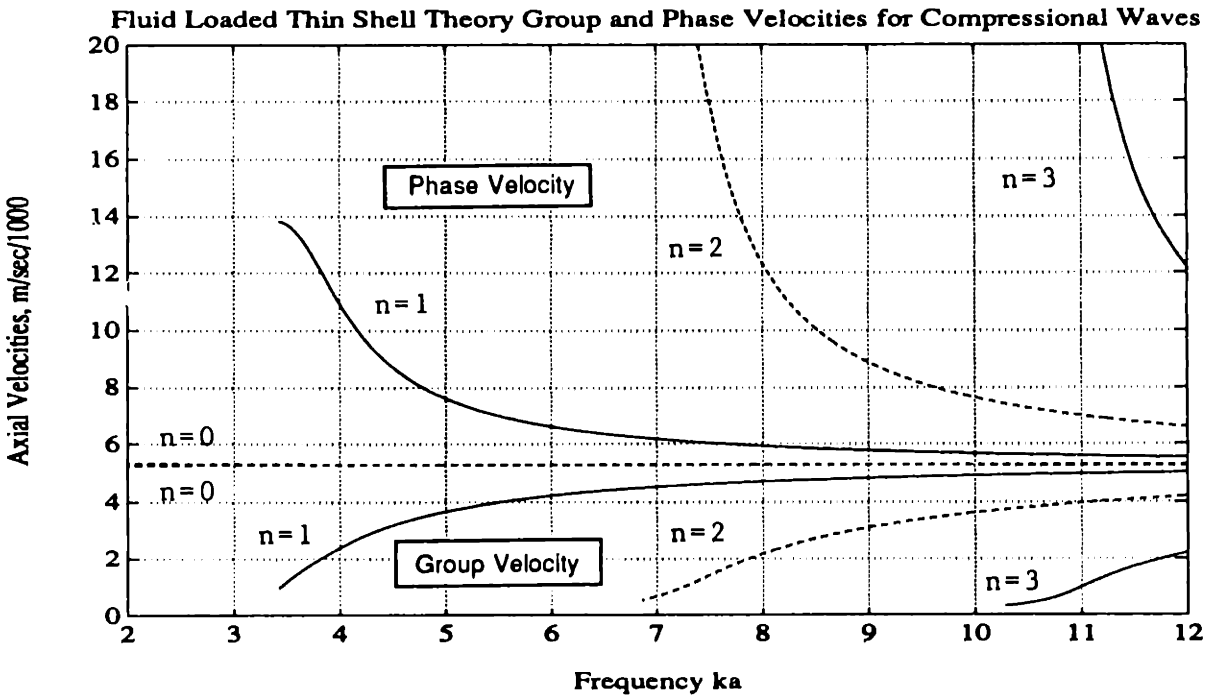

Figure 2.38: Phase and Group Velocities Associated with Free Compressional Wave Propagation

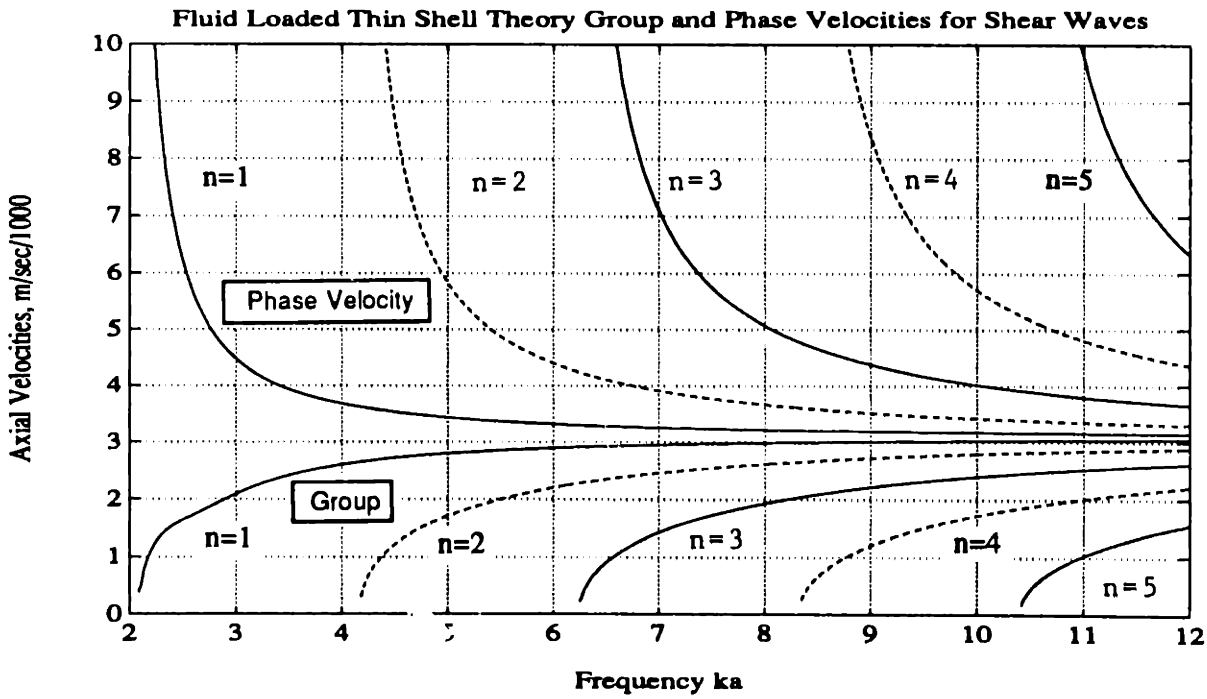

Figure 2.39: Phase and Group Velocities Associated with Free Transverse Shear Wave Propagation

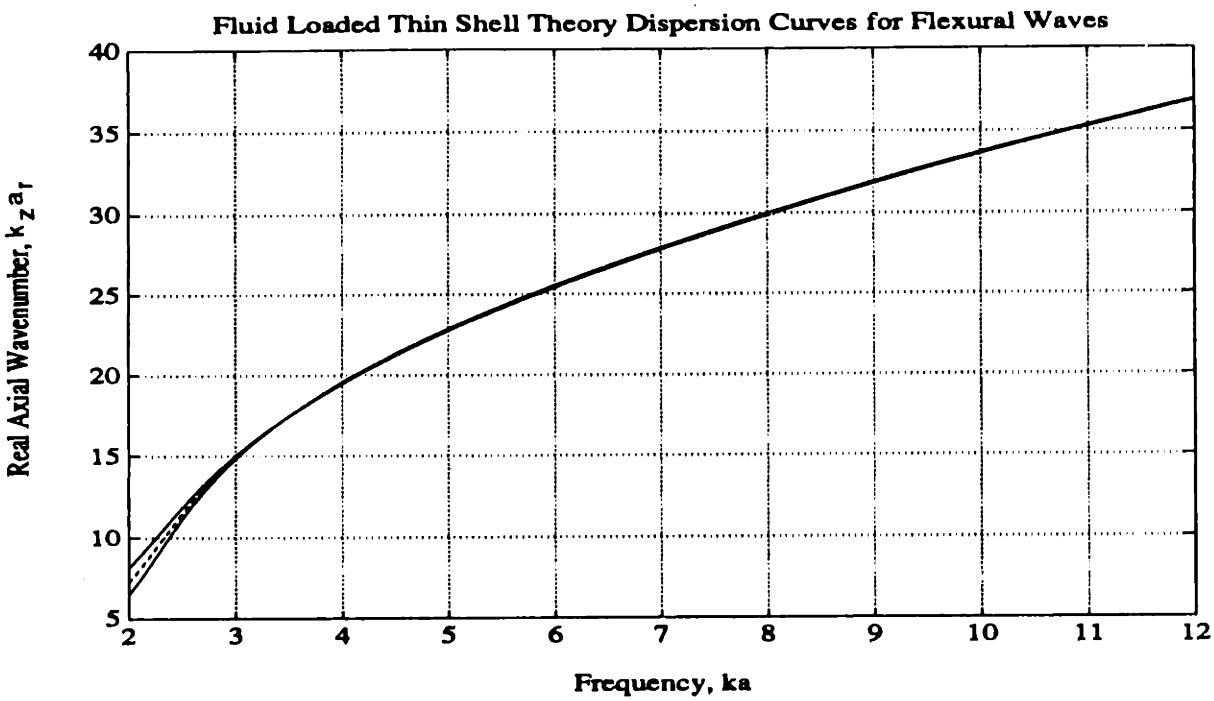

Figure 2.40: Real Part of Axial Wavenumber Roots $k_z a_r$ Associated with Free Transverse Flexural Wave Propagation. These waves are subsonic and the imaginary wavenumber component equals zero.

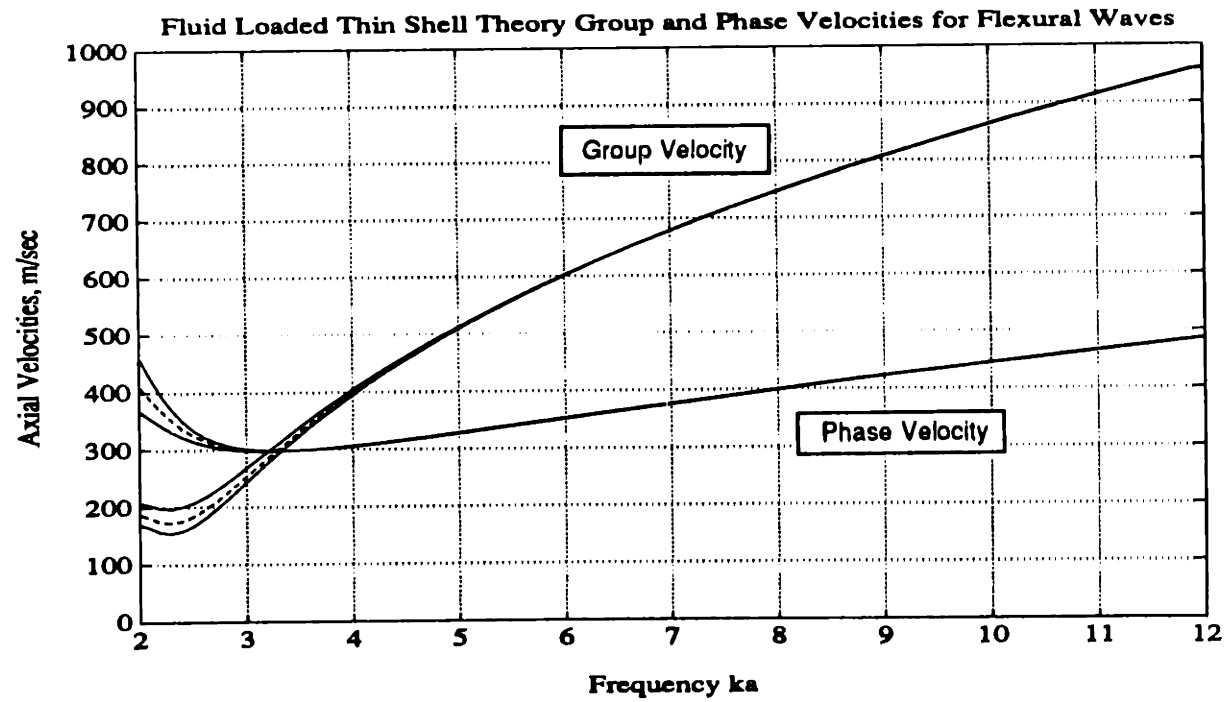

Figure 2.41: Phase and Group Velocities Associated with Free Flexural Wave Propagation

Chapter 3

Empty Shell Backscatter - Measurements and Interpretation

3.1 Introduction

I first describe the measured backscatter of the empty shell because many fundamental scattering processes that are common to the more complicated shells are evident and are more readily interpreted. I briefly review the features of the monostatic field observed over the full range of aspect angles from bow ($\theta = 0\,\mathrm{deg}$) to beam ($\theta = 90\,\mathrm{deg}$) aspect with the intent of contrasting them with the field found within 30 degrees of beam aspect. The focus of the ensuing data interpretation and analysis will be the backscatter measured over a range of aspect angles of $60 < \theta < 90\,\mathrm{deg}$ at a selected roll angle of the model. As previously discussed, this range of aspect angles constitutes the regime where phase matched excitation of membrane waves is generated by the incident field. In addition, I make use of selected bistatic measurements conducted at an aspect angle of 75 degrees to contrast the fields measured in the specular and back directions and to further illuminate the backscattering processes.

The data presented were acquired and processed as discussed in detail in Appendix A. Some asymmetries due to model alignment error and small scale construction defects were observed with changes in model roll angle and at complementary

aspect angles. However, these deviations were found to manifest themselves as small frequency shifts and magnitude errors. The data presented are therefore considered representative of all roll angles and complementary aspect angles.

3.2 Backscattering at Beam Aspect

3.2.1 Interpretation of the Backscatter Features

I begin with a presentation of the field measured at beam aspect which I have found to be similar to the corresponding field of an infinite shell. The magnitude of the measured form function of the empty shell is compared with the infinite cylinder prediction in Figure 3.1. The form function of the empty shell was obtained using the measured transfer function of the scattered and reference source signals, and a gain of 18.6 dB to account for the cylindrical spreading term $\sqrt{2r/a}$ shown in equation 2.17. An additional gain of 0.5 dB was employed to account for the cylindrical spreading of the incident field as discussed in Appendix A.4.2. Given the agreement of the two form functions shown in Figure 3.1, one can conclude that the truncation of the shell must only minimally affect the backscattered field contributions of the geometric and leaky wave components generated at normal incidence.

The nulls in the measured form function shown near harmonics of the ring frequency of the shell $ka = 3.54$ can be interpreted to be the result of destructive interference of the geometric scatter and the compressional leaky wave field. The frequency shift observed in the nulls may be due to small inaccuracies in the computed phase speed of the compressional leaky wave field. Low level excitation and reradiation of torsional waves on the shell may be one source of the measured fluctuations observed in the measured form function. Although only compressional waves contribute to the leaky wave field of an infinite cylinder at normal incidence, transverse shear waves may be induced by small alignment errors and shell imperfections. Phase matching of the incident field on the spherical portions of the endcaps of the finite shell also provides a source of torsional wave excitation. Beamforming analysis

of the measured bistatic field of the complex shell at normal incidence exhibits shear wave propagation of this nature as originally demonstrated by Bondaryk [3].

The bandlimited impulse response of the empty shell at beam aspect is shown in Figure 3.2. This time domain representation of the scatter results from a deconvolution of the source signal from the scattered field measured at a radius of $r = 2\,m$ as discussed in Appendix A.4.3. The time evolution of the field is similar to that computed for an infinite cylinder as readily demonstrated by a comparison of Figures 3.2 and 2.12. The initial return is shown as a bandlimited pulse centered at time $t = 0$ that is of negative sense with respect to the incident field as is consistent with a pressure release surface. The series of bandlimited pulses that follow with a period of 64 μsec correspond to the compressional leaky wave returns and are of opposite sense with respect to the initial return.

The leaky wave returns also exhibit an exponential decay with time that is similar to the decay of the field computed for the infinite cylinder. The logarithm of the magnitude of the analytic signal representation of the backscattered signal is shown as a function of time in Figure 3.3. I have used this representation to calculate the decay rate of the backscattered signal. A least squares linear fit of the envelope, excluding the initial return, yields a broadband amplitude decay rate of .0073 $nepers/\mu sec$ or 0.063 $dB/\mu sec$. The measured value is compared with predicted infinite cylinder radiation decay rates in Table 3.1. The measured and predicted decay rates are close, but it is surprising that the measured decay is 44% less than the predicted decay of mode 1, and 29% less than the predicted decay of mode 2. The decreased decay rates observed indicate that radiation leakage losses, rather than structural damping processes, produce the observed decay. More importantly, this also indicates that the finite shell incorporates additional energy storage mechanisms that are probably produced by the interaction of the cylinder and the endcaps. Although the specific physical origins of this effect are unknown in this case, an impairment of good radiation is consistently observed in all three shells with increasing significance as the shells become more complex. The generation of poorly radiating flexural waves at a

ring discontinuity is addressed in Chapter 4 accordingly.

Table 3.1: **Comparison of Measured and Predicted Decay Rates at Beam Aspect**

Mode $v = n$	Frequency ka	Decay Rate $dB/\mu sec$
1	3.70	0.112
2	7.32	0.089
3	10.39	0.067
Measured	2.75-10.0	0.063

3.2.2 Beam Aspect and Other Specular Target Strength Corrections

The good agreement of the measured and infinite cylinder form functions shown in Figure 3.1 also implies that the measurements were conducted at a radius where the field experiences cylindrical spreading. The measurements conducted at beam aspect were not performed in the Fraunhofer field of the shell. At beam aspect, the field scattered from the cylindrical portions of the finite shell approximates a uniform line array. The amplitude of the effective array is tapered over the relatively small lengths of the endcaps where decreased scattering levels are produced. The monostatic receiver was located at a constant radius $r = 2\ m$ from the center of the target, and therefore, the far field criterion $r > L^2/\lambda$ [13, 54] is not met for the entire frequency range of interest. I have employed a simple discrete array model to numerically estimate the frequency dependent correction $T_{corr}(\omega)$ that is required to calculate the far field target strength from the backscatter data measured at beam aspect. The correction is applied to the spherical spreading based computations of Appendix A.4.2 as shown below:

$$T_c(\omega) = T(\omega) + T_{corr}(\omega) + 20\log 2 + 0.5 \;\; dB \; re \; 1 \; m \tag{3.1}$$

The simulated array consisted of 57 equally spaced point sources separated by a distance of $d = 0.0148\ m$, where the spacing was selected such that $d < \lambda/2$ over the frequency range of interest to prevent spatial aliasing. A total of 51 sources that span a distance of 0.74 m over the center of the array were uniformly shaded, while 3 sources located at each end of the array were Hanning tapered to simulate the decreased scattering contribution of the endcaps. I computed the field at the measurement radius of $r_1 = 2\ m$ and at a far field radius of $r_2 = 50\ m$ and calculated the correction using the following relation:

$$T_{corr}(\omega) = 20\log\left(\left|\frac{P(\omega, r = 50)}{P(\omega, r = 2)}\right|\right) + 20log\,(50/2) \tag{3.2}$$

The resulting corrections $T_{corr}(\omega)$ are shown in Figure 3.4 and the frequency averaged value of the correction equals $T_{corr_{avg}}(2 \leq ka \leq 12) = +8.2\ dB$. The behavior shown above frequencies $ka > 7$ reflects the inception of a fluctuating Fresnel Field that would be observed at the measurement location.

Away from approximately 5 degrees of beam aspect, the coherent radiation length of the backscatter sources of the ring stiffened and complex shells is $O(L/5)$. At an aspect angle of 75 degrees the radiation length of the empty shell is $O(L/4)$. Hence, in these instances this correction is unnecessary because the farfield criterion of L^2/λ is met and the target strength calculations of Appendix A.4.2 with their implicit assumption of spherical spreading are appropriate. The corrections needed to account for the measurement radius become less than 1 dB if the radiation length is smaller than $L/3$, and less than 2 dB for $L/2$. The broadband geometric backscatter initially observed at oblique angles of incidence generally originates from the surfaces that comprise the truncations of all three shells. Hence, the corresponding effective radiation length of this component is $O(L/5)$ or less. In the case of the complex and ring stiffened shell, the effective radiation length of delayed scatter is imposed by

the average spacing of the ring stiffeners, i.e. $L/5$. In the case of the empty shell, I will demonstrate in Section 3.4.1 that the coherent radiation length of the shear wave field is approximately $c_s T_{shear}/2$. Given these coherent radiation lengths of the empty shell, the spherical spreading based target strength computations should be accurate to within 2 dB up to at least an angle of 80 degrees.

In contrast, I believe that this correction should be applied to bistatic target strength computations made in the specular direction. I will demonstrate in Section 3.4.1 and Chapter 5 that the specularly directed form functions measured at aspect angles of 66 and 75 degrees compare closely with corresponding infinite cylinder predictions. Although some variation is induced by the cylindrical spreading of the incident field over the length of the model, the amplitude of the geometric scattering initially observed in the specular direction is uniformly distributed over the full length of the cylindrical portions of the shells. The leaky wave contributions are less uniformly distributed, particularly in the case of the ring stiffened or complex shell, but represent a smaller net contribution to the field. Therefore, although less accurate, these corrections should also be incorporated in these computations.

3.2.3 The Measured Target Strength at Beam Aspect

The peak value of the broadband initial return measured at beam aspect corresponds to a target strength of -13.9 dB re 1 m as computed using the uncorrected methodology described in Appendix A.4.2. In comparison, a geometrical acoustics value [13, 54] of $T = 10\log(aL^2/2\lambda r_{ref}^2) = -5$ dB would be predicted for a finite, perfectly reflecting right circular cylinder of length $0.74m$ (the length of the cylindrical portion of the shell) and radius $a = .05537m$ at the center frequency $ka = 7$. This discrepancy of $+8.9$ dB primarily results because of the small measurement radius employed. If the frequency averaged correction of $+8.2$ dB is applied, the measured target strength of the peak initial return becomes -5.7 dB which is closely approximated by the geometrical acoustics value. The small error that remains may be attributed to measurement inaccuracies and the fact that the incoming wave trans-

fers energy to elastic waves in the shell. The resulting agreement indicates that the asymptotic approximation $|R_s| = 1$ is sufficiently accurate for practical use.

Finally, the corrected far field target strength of the empty shell is shown in Figure 3.5. The basic features of the backscatter of an infinite cylinder remain evident.

3.3 Monostatic Field Properties Observed at Oblique Angles of Incidence

I now briefly examine the monostatic field measured at oblique angles of incidence ranging from bow to beam aspect to contrast measured features with those observed at aspect angles within 30 degrees of beam aspect where helical membrane wave scattering processes are evident. The field measured within 30 degrees of beam aspect is examined in detail later in Section 3.4.

3.3.1 The Initial Scatter From the Empty Shell

Given the broadband shell insonification used throughout the experiments, the geometric portion of the scattered field can be distinguished as a short duration broadband pulse at the beginning of the scattered waveform. The propagation delay of the initial return from the shell changes with aspect angle because the physical location of the origin of the initial return and its distance from the receiver changes. The observed propagation delay of the peak initial return is compared to that measured at bow aspect in Figure 3.6. The target strength associated with the peak initial return is plotted as a function of aspect angle in Figure 3.7. Geometric scattering from the three distinct shell surfaces that comprise the models produces the three local maxima observed in Figure 3.7. Side lobe levels associated with the specularly directed geometric scatter are not apparent in the monostatic field. Hence, backscattering from the various surfaces that comprise the endcap must exceed the side lobe levels of the specularly directed field.

A specularly reflected field generated over the cylindrical surfaces of the shell produces target strength values of -13 dB re 1 m at angles $88 \leq \theta < 90$ deg. The target strength is decreased by 3 dB relative to the peak value at an aspect angle of approximately 86.5 deg. This can be explained as follows. The experimental configuration used provides direct specular ray paths from the cylindrical surfaces of the shell to the receiver for a range of aspect angles ± 3 deg of beam aspect. Hence, the receiver was again located in the cylindrically spreading near field of the shell for measurements conducted at these aspect aspect angles and the frequency averaged correction of $+8.2dB$ calculated at beam aspect should be applied to these aspect angles as well. Moreover, a uniform line array of length $L = 0.74$ m would exhibit a corresponding major lobe beamwidth of 3.5 degrees at the center frequency $ka = 7.0$ [13].

The incident field is nominally perpendicular to the tangential plane of the conical section of the endcap at an aspect angle of $\theta = 63.5$ deg. Hence, scattering from the conical surfaces at a target strength level of -30 dB is observed at aspect angles of $60 \leq \theta \leq 63$ degrees. This compares with a geometrical acoustics prediction of -32 dB. Similarly, scattering from the hemispherical surfaces produces the peak value of -37 dB re 1 m noted within 3 deg of bow aspect. This compares with a geometrical acoustics prediction [13, 54, 41] of $T = 20log(D/4r_{ref}) = -33$ dB for a perfectly reflecting sphere of the same diameter $D = 0.092$ m. The incident field experiences cylindrical spreading over the length of the target. A correction that accounts for the incident pressure level at the bow scattering surface, rather that the acoustic center of the shell, would increase target strength values by 1.4 dB at bow aspect. The remaining discrepancy of nearly 2.6 dB may be attributed to a transfer of energy from the incident field to elastic waves in the shell. However, I have not conducted detailed studies of the field measured near bow aspect.

The target strength of the peak initial return is compared with the target strength computed from a time integration of the squared scattered pressure in Figure 3.8. The integrated target strength values represent the total scattered energy and this

comparison emphasizes the importance of the delayed scatter that is radiated from elastic waves generated on the shell. The integrated target strengths exceed those of the initial return by 5 to 8 dB over an aspect angle range of $63 < \theta < 82$ deg and by as much as 10 dB over the range of $0 < \theta < 40$ deg. The increased levels found over these ranges of aspect angle demonstrate that comparatively large amplitude signal components are observed at later times following the initial return from the shell. The increased levels observed over the range $63 < \theta < 82$ deg result because leaky membrane wave field amplitudes are comparable to, or exceed the amplitude of the initial return over a lengthy time duration. In contrast, the geometric field initially observed at other aspect angles, including the region within about 8 degrees of beam aspect, represents the dominant backscatter.

3.3.2 Time Domain Features of the Monostatic Signals

The time evolution of the monostatic signature of the empty shell is illustrated in Figure 3.9 where contour levels of bandlimited impulse response data are shown as functions of time and aspect angle. The propagation delay of the initial return from the target that is shown in Figure 3.6 has been removed to stack the signals observed at different aspect angles such that the value associated with the peak initial return is shown at time $t = 0$. Before computing the signal envelope, the source signal was deconvolved from the measured scattered signal and Gaussian bandpass filtered as described in Appendix A.4.3.

A large amplitude, periodic field is observed over a range of aspect angles of $62 < \theta < 90$ deg that corresponds to induced membrane wave radiation. Interpretation of these signal components is the focus of Section 3.4. In contrast, no delayed signal components of significant amplitude are observed over the aspect angle range of $40 < \theta < 63$ deg. With the exception of the initial return, signal levels measured over this range of aspect angles are 15 to 20 dB less than peak levels measured within 28 degrees of beam aspect. This decrease is observed because phase matched excitation of transverse shear waves can no longer be accommodated over the cylin-

drical segment of the shell. The integrated target strength values measured within $40 < \theta < 63$ are nearly equal to the target strength of the initial return which is the dominant feature of the monostatic signals. In contrast, more significant delayed signal components are observed near bow aspect and a range of aspect angles of $0 \leq \theta < 40$ deg where increased integrated target strength values are observed. I have not studied the field observed near bow aspect, but it is a current topic of research at MIT (see for example, the work of Conti [16]).

The time delays associated with the onset of scattering from each of the two junctions of the endcaps with the cylinder delineate the temporal regimes where large amplitude signals other than the initial return from the target are observed. These time delays are plotted as a function of aspect angle in Figure 3.10 for comparison with the complex envelope contours shown in Figure 3.9. Their propagation paths are illustrated in Figure 3.11. Near bow aspect, the largest signal levels are observed at times less than that required for the incident planar phase front to propagate to the nearest (bow) endcap and scatter back to the receiver along a direct ray path. In contrast, large amplitude membrane signals observed within 28 degrees of beam aspect occur at times greater than the delay required for the incident phase front to propagate to the farthest (stern) endcap and scatter back to the receiver. This delay results because membrane wave radiation generally cannot be observed at a monostatic receiver until the induced structural wave field has interacted with a structural discontinuity to produce propagation with an axial direction opposite of that of the incident field.

3.3.3 Frequency Dependence of the Total Target Strength

The frequency dependence of the target strength of the empty shell is shown as a function of aspect angle in the contour plot of Figure 3.12. The target strength values $T(\omega, \theta)$ were computed using the methodology discussed in Appendix A.4.2. The largest target strength values are observed within 3 deg of normal incidence where large geometrically scattered fields are generated by the target as discussed earlier.

Significant levels are also found over the range of aspect angles $61 \leq \theta \leq 90$ deg where phase matched excitation of compressional and transverse shear waves is generated by the incident acoustic field. The shear wave spatial coincidence loci $\theta_{coin}(ka, n)$ are clearly evident over this range of aspect angles as will be discussed in detail in Section 3.4. Comparatively weak values are noted at all other aspect angles with the exception of some frequencies and aspect angles within 10 deg of bow aspect. The enhanced target strength values $T(\omega, \theta)$ noted near bow and beam aspect all correspond to angular regimes where particularly large amplitude delayed signal features are observed.

3.4 Interpretation of the Field Observed Over the Range of Aspect Angles of 60-90 Degrees

Once the incident field has traversed the length of the shell, I would expect a back directed leaky wave field to evolve, at least initially, in a fashion similar to that of an infinite shell. I would also expect to observe similar pressure levels given an added correction required to accommodate far field spherical spreading associated with the finite length of the shell. These similarities would only occur given the assumptions previously discussed in Section 1.4 and I expand upon them further here:

- Over this range of aspect angles, the specularly directed scatter of an infinite shell primarily results from radiation of one or both membrane waves propagating in the forward, or positive z direction. Any axial discontinuity in the empty finite shell scatters at least some of these waves in the opposite direction.
- Scattering of wave type 'A' at the discontinuity results in a free wave of type 'A' that propagates in the back, or negative z direction with a greater or lesser amplitude, while other wave types are also energized.
- If the discontinuity is perfectly reflecting the incident wave is reflected with no change in amplitude or phase and the backscatter will be well estimated by

the specularly directed scatter of an infinite shell. Of course the infinite shell estimates would have to be adjusted to account for the spherical spreading of propagation from the finite shell. In fact, the actual discontinuities are not perfectly reflecting and the estimates are degraded but remain useful.

The empty shell backscatter observed over a range of aspect angles of $60 \leq \theta \leq 90$ degrees is predominantly influenced by the leaky membrane wave field, and the geometric field initially scattered from the model. This can readily be seen in the measured target strength $T(\omega, \theta)$ contour plot of Figure 3.13. The nulls induced by the destructive interference of the compressional leaky wave field and the geometric field are strongly evident within 5 degrees of beam aspect. However, the influence of the compressional leaky wave field is not prominent at other aspect angles for a number of reasons addressed later. In contrast, the shear wave spatial coincidence loci previously shown in Figure 2.10 are prominently exhibited as regions of enhanced magnitude throughout this range of aspect angle. Clearly, transverse shear wave excitation is the dominant scattering process found away from beam aspect. In addition, the agreement of the infinite cylinder and measured coincidence frequencies indicates that the truncations do not significantly alter the dispersion of waves on the shell. The magnitudes of the target strength found along the shear wave coincidence loci generally decrease with increasing mode number. This trend is consistent with the frequency dependence of the coincident leaky wave field of an infinite cylinder as quantified in equation 2.57.

The corresponding time domain representation of the monostatic field is illustrated in Figure 3.14 where the contours of the measured signal envelopes are shown for the same range of aspect angles. The first five leaky wave arrival times that would result for broadband plane wave insonification of a simple finite shell with *perfectly reflecting* truncations are shown in Figure 3.15 for comparison with Figure 3.14. The scattering evolution presented in Section 1.4 and the phase matched helical membrane wave period T_m approximation of equation 2.59 were used to derive the time delay predictions of Figure 3.15. The large signal levels shown in Figure 3.14 over the

range of aspect angles of $62 < \theta < 85$ deg primarily correspond to induced transverse shear wave radiation. The first five transverse shear wave radiated pulses are well resolved and the simple time delay predictions of Figure 3.15 compare fairly well. Time delay errors for the transverse shear waves that do show up are small and are due to dispersive effects that are discussed in Section 3.4.1. The predicted arrival times for compressional wave leakage compare less favorably because the compressional wave radiated arrivals noted over the range of aspect angles $86 \leq \theta \leq 90$ do not exhibit a time delay $\Delta t \simeq 2L/c_z$ associated with propagation down the axis of the cylinder. Rather, the compressional wave arrivals are observed at multiples of the circumferential period T_m that decreases with decreasing aspect angle as shown in Figure 2.11. I suspect that this is another manifestation of the small measurement radius of the experimental configuration. The axial propagation delay is probably not observed over this range of aspect angles because within ± 3 degrees of beam aspect, the monostatic receiver is located at a distance from the shell that allows for measurement of the specularly directed field generated at the bow portions of the model. Additional errors associated with compressional wave predictions result because of dispersive effects.

The scattered field associated with a second axial round trip of an induced structural wave is evident in Figure 3.14 over the range of aspect angles $61 \leq \theta \leq 77$ deg. The inception of the second round trip is delayed relative to the first helical shear wave arrival by a nearly constant value of 560 μsec. This corresponds to a velocity of approximately 3100 m/s that is consistent with shear wave propagation. The field observed over this regime may have been generated by a mode conversion process induced at the far (stern) endcap. Individual pulse realizations found over this temporal regime are less well resolved than those found at earlier times. In addition, peak levels exhibited in this regime are 12 to 20 dB less than peak levels measured at earlier times. These effects can be explained by one or more of:

1. As time progresses, the structural waves experience the accumulated influence of membrane wave dispersion which spreads energy in time.

2. Multiple interactions with the impedance discontinuities imposed by the endcaps multiply even small scattering from one wave type to another.

3. Wavenumber filtering enhances certain roundtrip paths and lessons others.

4. Radiation losses from the endcaps alters the decay rates of the shell waves.

The target strength values measured over the range of aspect angles of $60 < \theta < 85\,\text{deg}$ exhibit an axial length-scale dependent modulation. The largest target strength values measured over the range $62 < \theta < 85$ are found where shear wave spatial coincidence conditions and peak modulation levels coexist as shown in Figure 3.13. Length scale effects, together with coincidence excitation and radiation, produces the "string of pearls" [50] pattern observed in the region of the shear wave coincidence loci. The length-scale effects include scatter enhancement provided by axial resonances, and constructive interference of the broadband geometric scatter initially observed and the leaky wave field observed following the axial propagation delay. Axial resonances would produce a similar modulation as defined by the axial wavenumber relation:

$$k_z L_p + \varphi_{end_m}(\omega, \theta) = l\pi \tag{3.3}$$

where L_p is the effective axial propagation length of the shell and l is the axial order. The term $\varphi_{end_m}(\omega, \theta)$ is a phase change induced at each endcap that would potentially be frequency, aspect angle, and wave type dependent. A $\pi/2$ phase term would be required to accommodate the phase change induced by a caustic located at each endcap given the high frequency approximation discussed in Appendix B. The axial component of the wavenumber must equal the axial component of the incident field $k_z = k/\cos\theta$ for phase matched excitation and radiation of helical membrane waves on the cylinder. Therefore, if we employ a simple propagation model that neglects any other phase changes or dispersive effects induced at the endcaps $\varphi_{end_m}(\omega, \theta) = \pi/2$, the axial resonance frequencies ka_{res} are expressed solely as a function of the effective meridian length of the shell L_p and the aspect angle θ:

$$ka_{res} = \frac{\pi a\,(l - 1/2)}{L_p \cos\theta} \tag{3.4}$$

The resulting axial resonance loci are plotted in Figure 3.16 for comparison with the target strength contours of Figure 3.13. The shell length used to compute the axial resonance loci is equal to one half of the perimeter of the shell $L_p = 0.90\ m$. This simple model appears to capture the essential modulation behavior away from beam aspect. However, there is an equally important temporal condition which appears to strongly dictate the length-scale modulation. Observed leaky wave radiation levels associated with multiple axial round trips of the induced structural waves are significantly attenuated relative to those produced during the first round trip. Hence, the observed length-scale modulation often results because of interference of the broadband geometrically scattered field initially observed and the delayed leaky wave field. As illustrated in Figure 1.5, the delay of the first leaky wave return is essentially comprised of the propagation time required for the incident pulse to traverse twice the length of the shell $2L\cos\theta/c$, and a delay Δt_{corr} associated with the different waterborne path lengths of the geometric and leaky wave fields. I will demonstrate in Section 3.4.1 that at an aspect angle of 75 degrees, the observed monostatic leaky wave field is produced by localized axial distribution of the structural wave field. Hence a small correction Δt_{corr} is also needed to account for the actual propagation delay from the stern endcap to the axial point of origin of the effective radiation, and the additional waterborne path length differences encountered. This correction represents the error in the prediction of the arrival time of the first leaky wave return that was demonstrated earlier by a comparison of Figures 3.14 and 3.15. The total delay $2L\cos\theta/c + \Delta t_{wb} + \Delta t_{corr}$ provides the essential modulation resulting from the interference of the initial and leaky wave returns. These effects will be examined in subsequent discussions where the field measured at representative individual aspect angles is interpreted.

In the discussions that follow, I review the monostatic field observed at discrete aspect angles of oblique incidence. Both time and frequency domain representations

of the measured field are examined. Unless otherwise noted, the reference time $t = 0$ refers to the measured delay of the peak value of the initial monostatic return from the model. Frequency domain representations of segments of the observed signals are compared with the target strength of the corresponding leaky wave field of an infinite cylinder. The measured target strength values were computed as discussed in Appendix A.4.2. The target strength of the leaky wave field of an infinite cylinder is computed as:

$$|T_{leaky_m}(\omega,\theta)| = 20\log\left[|p_{leaky_m}(\omega,\theta)|\sqrt{a/2}\right] \tag{3.5}$$

where p_{leaky_m} is the asymptotic value of the specularly directed form function contribution of a given membrane wave type as defined earlier in Section 2.3.4. Again, this comparison implicitly assumes perfectly reflecting endcaps. However, the endcaps are not perfectly reflecting and the elastic wave backscatter of the empty shell is produced by free wave propagation rather than the forced wave processes of the infinite shell scatter. Thus no more than qualitative conclusions can be drawn from the comparisons.

3.4.1 The Monostatic and Specularly Directed Fields Measured at an Aspect Angle of 75 degrees

The bistatic field generated by the empty shell model at an aspect angle of 75 degrees was measured to examine the scatter produced at an angle where both transverse shear and compressional leaky wave fields are expected to contribute. However, large target strength levels measured at this angle are only evident at shear wave coincidence loci as shown in Figure 3.13. In this section, I present selected examples of the bistatic data to illuminate the fundamental processes producing the observed backscatter. All of the bistatic data presented were measured as part of the May 1992 test series and were conducted in a horizontal plane defined by the target and source array, with the receiver located at a constant distance of $r = 2\ m$ from the target

center as discussed in Appendix A. Time domain contours of bistatic levels measured over a range of observation angles of $50 \leq \theta_o \leq 130$ are shown in Figure 3.17. The monostatic and specular directions correspond to observation angles of $\theta_o = 75$ and $\theta_o = 105$, respectively.

I have employed classical focused beamforming of the bistatic data to visualize the time evolution and axial distribution of the scatter. As discussed in Appendix A.4.5, the beamforming operation determines an effective axial distribution of point sources that would produce the bistatic scatter measured over the length of the array. Two arrays were synthesized to evaluate the data shown in Figure 3.17. One array made use of the bistatic data measured over the range of observation angles encompassing $60 \leq \theta_o \leq 120$ to visualize the evolution of the membrane wave field propagating in both axial directions. This array was uniformly amplitude tapered to give equal weight to the full range of observation angles and the resulting envelope of the effective source distribution is shown in Figure 3.18. The second array made use of the data found over $50 \leq \theta_o \leq 100$ to investigate the evolution of the backscatter only and the results are shown in Figure 3.19. In particular, this array was selected to determine the origins of the back directed geometric return and the five large amplitude arrivals that can be seen in the bistatic data of Figure 3.17 at observation locations near the monostatic receiver ($\theta_o \simeq 75$, $300 \leq t \leq 700$).

Comparable source levels computed using the two arrays may differ in some instances because the source strengths are derived from the field measured over different regions in space. However, the beamforming process I employ is an approximate technique intended only to visualize the spatial and temporal evolution of the scatter and it does not render absolute signal levels.

The scatter essentially evolves as discussed in Section 1.4 and my interpretation of the prominent features shown in Figure 3.18 is illustrated in Figure 3.20. One can see that the most of the scattering features shown in both Figures 3.18 and 3.19 exhibit a slope corresponding to phase speed of 5750 m/s. This phase speed equals the trace velocity $c_z = c/\cos\theta$ of the incident field and a positive slope corresponds

to back directed radiation while a negative slope corresponds to specularly directed radiation. The most prominent feature shown in Figure 3.18 is the large amplitude geometrically reflected field produced as the incident field initially passes over the cylindrical portion of the shell at times $0 < t < 129$ μsec. The amplitude of the initial specularly directed return can be seen to taper to much smaller values over the axial extent of the endcaps. In contrast, the initial return observed in the monostatic direction is produced at the junction of the endcap with the cylinder ($\tilde{z}/L = 0.93$) as can be seen at reference time $t = 0$ in Figure 3.19. Phase matched helical membrane waves are excited as the incident field propagates along the length of the shell. Two large amplitude leaky wave fields are initially radiated in the specular direction as shown in Figure 3.19. The first lags the geometric field by approximately 40 μsec and I believe that this corresponds to the second circumnavigation of an induced compressional wave. The first compressional wave circumnavigation would be contained within the pulse width of the initial return. The second resolved leaky wave field lags the geometric field by approximately 95 μsec and corresponds to the first circumnavigation of the phase matched shear field that later produces the coincident backscatter previously seen in the monostatic frequency domain representation of Figure 3.13. Once the membrane wave fields interact with the stern endcap $t > 150$ μsec, they begin to propagate in the opposite axial direction and radiate in the back direction. Thereafter, peak levels generally decay with time and propagation distance. However, compressional wave backscatter is not readily apparent which is consistent with the absence of compressional wave coincidence loci in Figure 3.13 at this aspect angle. In contrast, shear wave radiation is strongly evident with a period of $T = 95$ μsec that produces the enhanced target strength levels observed at the shear coincidence loci.

The shear wave disturbance propagates down the axis with an apparent group velocity that is slower than the phase speed as indicated by the slow axial progression of peak backscatter levels shown in Figures 3.18 and 3.19. The incident field of the experiment occupies a small, but finite axial wavenumber bandwidth at a fixed

frequency. Therefore, once the incident pulse has traversed the length of the cylinder, the energy of the shell disturbance primarily propagates along the cylindrical portions of the shell with an axial group velocity imposed by the incident trace velocity and the coincident modes excited by the incident field. In the case of membrane waves, different circumferential modes of equal phase velocity c_z propagate with nearly equal axial group velocities that can be approximated by the relation $c_{gm} \simeq c_m \cos\psi_m$ as demonstrated in Section 2.5. Thus, the azimuthal distribution of the wavefronts and the associated broadband pulse radiation would remain fairly well resolved over moderate time durations as observed in the experimental data. For an aspect angle of 75 degrees and an axial phase velocity of $c_z = 5750\ m/s$, the predicted shear wave group velocity equals $c_g = 1720\ m/s$ while the group velocity of compressional waves equals $c_g = 4720\ m/s$. Evidence of specularly directed shear wave radiation is not observed again in Figure 3.18 until $t = 650$, or until a time duration of approximately 450 μsec has passed. This corresponds to a speed equal to 1650 m/sec for propagation over a distance of 0.74 m, i.e. the length of the cylindrical portion of the model. Consequently, the energy of the induced shear wave field appears to propagate back towards the bow with a group velocity close to that of a free mode of propagation of an infinite cylinder given an axial phase velocity equal to the nominal trace speed of the incident field. Further evidence of the slow energy propagation of the shear wave field is provided in the bistatic data of Figure 3.17. Periodic shear wave arrivals are not evident in the specular direction ($\theta_o = 105\,\mathrm{deg}$) over the time duration of $400 < t < 800$ μsec although it would only take 150 μsec for a wave to traverse the length of the cylinder at the forced wave speed.

The specularly directed shear wave field shown in Figure 3.18 is first observed at an axial location $\tilde{z}/L \simeq 0.63$. Therefore, the shear wave disturbance must have propagated a distance of 0.26 m, relative to the junction with the endcap, in the time it takes to complete one circumnavigation $T_m = 95$ μsec. This corresponds to a net speed of 2720 m/s which is greater than the group velocity, but less than forced wave speed. Hence, I conclude that the field experiences an initial transition

from the forced wave speed of the transient incident field to the group speed of the coincident mode excited. It is difficult to ascertain the axial location where specularly directed compressional radiation begins because additional scattering that appears to be generated at the bow endcap is also apparent over the same time duration. However, I believe that it must also experience a similar transition associated with the transient nature of the incident field employed in the experiment.

Additional scattering is shown in both Figures 3.18 and 3.19 at axial locations near the bow endcap $\tilde{z}/L = 1.0$ and at times $t < 150\mu sec$. It exhibits a slowly changing circumferential period that is consistent with a phase matched excitation process that would exist over the length of the conical portion of the endcap. However, I have not studied these components in any detail because their contribution to the total field is small compared to the membrane wave field produced over the cylindrical section of the shell.

I have also used a $\tau - p$ transform of the beamformed data of Figure 3.19 to help identify the various constituents of the backscatter. The intercept-slowness representation of Figure 3.21 results from a $\tau - p$ transform of the beamformed data with an axial pivot point located at the center of the shell. Periodic shear wave radiation is evident with a slowness $p = 0.174\ s/km$ corresponding to the trace speed of the incident field. Back directed helical compressional wave radiation cannot be ascertained at this same value of slowness. A field propagating with a slowness of approximately $p = 0.323\ s/km$ is weakly evident in Figure 3.21. This component corresponds to a phase speed nearly equal to the 3100 m/s shear wave speed of the shell. Signal components with this slope are seen in Figure 3.19 at times $t > 200\ \mu sec$ but they are at least 6 dB weaker than the phase matched shear wave field and may be the result of an unknown scattering process induced at the endcaps.

The bandlimited impulse response measured at the monostatic receiver $\theta_o = 75$ is shown in Figure 3.22. The geometric field initially scattered from the model is clearly shown as a well resolved bandlimited pulse centered at time $t = 0$. The initial return from the target is immediately followed by an exponentially decaying

field with a decreasing period near that of the ring frequency. This behavior is observed in other monostatic signals with an increasing initial amplitude as the angle of incidence approached beam aspect $\theta \rightarrow 90\,\text{deg}$. It is induced by an interaction of the incident field and the bow endcap as shown in the beamforming results of Figure 3.19. Large monostatic pressures are observed over the time duration of $300 < t < 700 \mu sec$ that primarily correspond to the coincident shear wave field observed in the target strength and beamforming plots shown earlier. A comparison Figures 2.20 and 3.22 shows that the pulse shapes of the large amplitude signal components found over this duration, because of the interaction with the stern endcap, are not the same as the specularly directed wave. Much of this change can be attributed to a single interaction with a caustic located at the endcap where in the frequency domain a phase change of approximately 90 degrees would be induced as discussed in Appendix B.

The variation of peak levels observed at the monostatic receiver over $300 < t < 700\ \mu sec$ differs markedly from the global variation observed at nearby observation angles. Peak amplitudes observed at the monostatic receiver increase in a nearly linear fashion over the duration $280 \leq t \leq 530\ \mu sec$ and then decrease abruptly near $t = 610$ as shown in Figure 3.22. In contrast, peak levels measured over the range of angles $63 < \theta_o < 87$ degrees increase abruptly with the first shear wave arrival at $t \simeq 300\ \mu sec$ and then remain essentially constant for a total of 3 shear wave arrivals of duration $300 < t < 600\ \mu sec$, and then decay with increasing time. This amplitude variation is more consistent with the behavior that I would expect to observe following the interaction of the structural field with a simple reflecting discontinuity. The peak levels of this component of the scatter can be seen to migrate with increasing time from an observation angle of $\theta_o = 83\,\text{deg}$ at $t \simeq 300$ to an angle $\theta_o = 70$ at $t \simeq 700$, while large amplitude radiation can be seen to migrate over a total range of $63 \leq \theta_o \leq 87\,\text{deg}$. This range of observation angles corresponds to the range that would be insonified by direct phase matched rays emanating at a grazing angle of 75 degrees from the cylindrical portion of the shell as illustrated in

Figure 3.23.

The migration of peak levels over observation angle results because the localized shear wave field on the shell produces a series of acoustic beams with points of origin that propagate down the axis of the shell as illustrated in Figure 3.24. For example, the three regions of large amplitude backscatter shown in the beamforming results of Figure 3.19 at $t \simeq 225$, 325, and 425 μsec each exhibit radiation of uniform amplitude over a length of approximately $L/4$. This corresponds to a coherent radiation length of $c_z T_{shear}/x$ where $x = 2.5$. Hence, each region effectively produces the field of a phase tapered line array with a main lobe beamwidth of approximately $\theta_{3dB} = 12$ degrees [13] at the center frequency $ka = 7$. The span of observation angles where corresponding peak values are shown in the bistatic data of Figure 3.17 (at $t \simeq 310$, 410, 510) is well approximated by this beamwidth. The amplitude of the scatter measured at different observation locations is therefore influenced by their position relative to the beam pattern of back directed shear radiation. For the beamwidths and associated radiation lengths observed here, the monostatic receiver would have to be located at a distance greater than 4 m from the center of the shell to reside within the main lobe of all of the effective beams produced by the back directed shear wave field. The spreading loss associated with the propagation distance from the point of origin to an individual receiver also influences the measured amplitude. However, at this aspect angle the distance to the monostatic receiver ranges from a minimum value of 1.9 m at the bow to a maximum value of 2.1 at the stern and does not appreciably influence the observed amplitudes. Had the measurement been conducted at a distance more representative of the far-field, i.e. $R > 4$ m, the large amplitude arrivals observed at the monostatic receiver over the duration $300 < t < 700$ would exhibit a variation similar to that of the peak values measured at nearby observation angles. When corrected for this effect, the corresponding peaks would form the approximate envelope shown in Figure 3.22.

The monostatic signal components found over this time duration were isolated from the remaining signal and transformed to the frequency domain to evaluate the

relative contributions of its signal constituents A Hamming window was used to isolate the data measured over a slightly increased range of $200 < t < 800$ μsec and it provided a frequency resolution of $\Delta ka_{3dB} = 0.47$. No bandpass filtering was performed. The resulting target strength is shown as a function of frequency in Figure 3.25. The magnitude of the shear and compressional wave contributions to the *specularly directed* target strength of an infinite cylindrical shell are shown in Figure 3.26 for comparison. The peak levels shown in the measured transfer function of Figure 3.25 occur at frequencies of $ka = 2.5$, 4.8, 7.3, and 9.9 that are close to the shear wave coincidence frequencies of modes $n = 1 - 4$ listed in Table 2.3 for an infinite cylinder. Compressional wave scatter is only weakly evident at the first coincidence frequency, $ka = 9.2$. Scattering contributions of unknown origin are also evident at the ring frequency of the shell, but at a level 12 dB less than the shear wave contributions.

The target strength $T(\omega, \theta)$ measured at an aspect angle of 75 degrees is shown in Figure 3.27 to further illustrate the frequency domain representation of the entire monostatic signal. This figure has a frequency resolution of $\Delta ka_{3dB} = 0.08$. The axial propagation delay and decreased geometric backscattering of the finite shell produces a frequency domain representation that differs markedly from that shown in Figure 3.26 for the specularly directed field of an infinite cylinder. This frequency domain representation is modulated with a spacing of $\Delta ka \simeq 0.42$ at frequencies above $ka = 4$. This spacing does not compare favorably with the spacing of $\Delta ka = 0.74$ that would be predicted from the simple axial resonance model of equation 3.4. Rather, it is primarily produced by the interference of the initial return and the delayed leaky field found over the time duration of $300 < t < 700$ μsec. I suspect that this comparison would improve for a receiver at a greater distance from the shell because the effective delay of the leaky wave packet would be decreased and the frequency modulation would therefore be increased. Peak levels are observed at frequencies near the shear wave coincidence frequencies where peak levels of the length-scale modulation exist. Peak levels of -15.3 dB re 1 m at $ka = 2.7$ and

$-17.0\ dB$ at $ka = 4.9$ are observed. Peak measured target strength levels are at most 1 to 3 dB less than the predicted target strength shown in Figure 3.26. The similarity of these shear wave comparisons is quite remarkable given the enormity of the assumptions required to viably compare the specular scatter of an infinite cylinder and the backscatter of a finite shell. Further a smoothed version of the measured curve in Figure 3.27 does compare favorably with Figure 3.26, illustrating the well-known result of dynamics and acoustics that the smoothed frequency response of any finite system is asymptotically that of its infinite model.

However, coincident compressional wave radiation is only weakly evident in measured backscatter. The contribution of compressional scatter measured at the coincidence frequency $ka = 9.2$ over the duration $200 < t < 800$ is $9\ dB$ less than the peak shear wave contribution observed at $ka = 4.8$. In the case of specularly directed scatter from an infinite cylinder, the corresponding shear wave radiation would exceed compressional wave levels by only $2.5\ dB$ as listed in Table 2.3. The lesser contribution of compressional wave backscatter appears to be the result of direct and elastic wave scattering produced at the stern endcap.

The shear wave radiation shown in Figure 3.14 can be seen to persist over long time durations at aspect angles ranging from $73 \leq \theta \leq 85$ deg, and this is caused in part by the greater radiation decay rate of the compressional wave field noted in Chapter 2. However, the greater decay rate of the compressional wave field does not appear to be the cause of the decreased levels of compressional wave scatter. The compressional wave field does experience a radiated energy loss to the specular direction, but both membrane wave types experience similar losses in spite of their different decay rates. The fraction of energy lost to radiation in q circumnavigations of the shell equals $1 - e^{-4\pi q \delta_m}$, where δ_m is radiation loss parameter defined in Chapter 2. As noted earlier, two leaky wave fields are initially radiated in the specular direction and correspond to the second circumnavigation of the compressional field and the first circumnavigation of the shear field. In both cases, the radiation takes place over a distance that is $O(L/2)$. Therefore, the total compressional wave field

experiences an energy reduction of approximately 1.6 dB at $ka = 9.1$, while the shear wave field experiences a reduction of 0.8 dB at $ka = 2.5$. These small reductions cannot account for the diminished levels of compressional wave radiation observed.

Evidence of membrane wave scattering and radiation produced at the stern endcap can be seen in the bistatic data shown in Figure 3.28. In this figure, the specularly directed field ($\theta_o = 105$) consists of geometric scatter from the cylindrical surfaces of the models at $t = 98$ μsec, compressional wave radiation at $t = 138$ μsec, and shear wave radiation at $t = 192$ μsec and $t = 292$ μsec. Large amplitude geometric scatter from the conical surfaces of the endcap is evident near $\theta_o = 155$ degrees. The leaky wave field arrivals can be seen to migrate to larger observation angles θ_o as the structural field traverses the length of the models. The observation angle of $\theta_o = 117$ degrees is the largest that would be insonified by a direct ray emanating from the cylindrical segment of the shell at a grazing angle of 75 degrees and this is seen in Figure 3.28. Radiation can be seen over the range of observation angles of $117 < \theta_o < 150$ with a delay relative to the initial scatter equal to that observed at $\theta_o = 105$. These time delays are indicative of membrane wave scattering and radiation produced over the endcap. As noted previously, I believe that the first incidence of compressional wave radiation is contained within the duration of the initial scatter. Compressional waves may also radiate into the angular space $155 < \theta_o \leq 180$, but his cannot be ascertained from the data. There is evidence of weak levels of shear wave radiation occur over this space as observed near $t = 160 \mu sec$. The magnitude of the compressional wave radiation measured over $117 < \theta_o < 150$ exceeds subsequent shear wave radiation by more than 6 dB. Assuming that this field exhibits the same azimuthal dependence as the incident compressional wave field, this radiation would provide approximately 2 dB of additional loss in compressional wave energy relative to that radiated from 0.74 m segment of an infinite cylinder. I believe that the remaining losses can be attributed to scattering into flexural waves and noncoincident shear waves.

The measured decay rate of the backscatter supports my belief that the interac-

tion of the membrane wave field with the stern endcap must scatter energy to a poorly radiating structural wave field. The magnitude of the analytic signal representation of the backscatter measured at the monostatic receiver is shown in Figure 3.29 to better illustrate its envelope and decay rates. A least squares linear fit of the exponential rate of decay of the signal measured over the time duration $800 \leq t \leq 1400$ exhibits a decay rate of 0.010 $dB/\mu sec$. This decay rate compares with a value of 0.027 $dB/\mu sec$ of a free transverse shear mode of angular order $n = 1$ and phase velocity 5750 m/s. Once again, the measured signal exhibits decay rates considerably less than that of an infinite shell. Over this time duration, the direction of propagation of the remaining shear wave field is primarily back towards the stern and it generates low level radiation in the specular direction as shown in Figure 3.18. However, flexural waves are subsonic and dispersive and would be distributed over the length of the shell at this time radiating only when they encounter a structural discontinuity. In the next chapter, I demonstrate that both membrane wave types scatter energy to subsonic flexural wave at a discrete ring of mass and one can conclude that flexural waves are well excited at structural discontinuities. From these results of the next chapter one cannot conclude that compressional waves would scatter to flexural waves more significantly than shear waves. However, the scattering produced at the slope discontinuity of the endcap may behave quite differently than that produced at a simple ring of mass.

I also demonstrate in the next chapter that compressional waves will scatter to shear waves at the ring, and vice versa. Coincident compressional waves will scatter energy to shear waves at a discontinuity, but at this aspect angle coincident shear waves cannot scatter energy to compressional waves because they are cutoff. Moreover, the shear waves energized at the discontinuity will not be coincident and will propagate with a phase velocity different from that of the incident field and thus radiate in a different direction.

The scattering processes illustrated in Figures 3.18 and 3.19 produce a specularly directed field quite different from that measured in the monostatic direction. The

specularly directed bandlimited impulse response of the field measured at this aspect angle is shown in Figure 3.30. The measured scatter shown in this figure resembles the specular scatter shown in Figure 2.20 for an infinite cylinder over an initial time duration comparable to several circumnavigations of the induced transverse shear wave. However, measured signal levels decrease markedly at times $t > 298\mu sec$ because much of the induced structural wave field is propagating in the opposite axial direction at this time and its radiation is orientated towards the monostatic receiver accordingly. The form function of the signal measured in the specular direction is compared with the corresponding specularly directed form function of an infinite cylinder in Figure 3.31. I employ form function representations in this case because the effective specular radiation length of the empty shell nearly equals its total length and the measurement is again conducted in the near field of the analogous line array. The agreement of the comparison is not as close as that observed at beam aspect in Section 3.2. However, the essential features of the scatter of the infinite cylinder are found in the field of the finite shell, namely the interference of the specular and membrane wave fields. Local minima are located near the predicted spatial coincidence frequencies of Table 2.3. Unlike the frequency domain representation of the the monostatic signal shown in Figure 3.27, the specularly directed field does not exhibit pronounced length-scale dependent modulation. Length-scale effects are relatively unimportant because the specularly directed leaky wave field initially observed does not exhibit a time delay other than that required to complete the first circumnavigation Δt_{l_m}, while the field observed after the first series of interactions with the two endcaps is greatly attenuated by radiation losses.

Some degree of dispersive time spreading must be induced at the endcap. Guo [28] has demonstrated dispersive behavior for both transverse shear wave and compressional wave propagation on a cone. Kargl and Marston [33] demonstrated that the compressional wave becomes significantly dispersive near the breathing frequency of a sphere, $ka = 6.9$ in this case. Therefore, the location of the caustic separating evanescent and propagating regions of the structural wave field on the endcap will

change with frequency. The nature of the caustic is discussed further in Appendix B, but with the use of high frequency approximations valid for frequencies greater than those of interest here.

A Wigner distribution analysis of the Gaussian bandlimited monostatic signal of Figure 3.22 is shown in Figure 3.32. The latter helps identify potential endcap dispersion effects and further evaluates the frequency constituents of the backscatter. The Gaussian smoothing parameters $\sigma_t = 6\ \mu sec$ and $\sigma_{ka} = 0.171$ were selected to provide some inhibition of the cross term amplitudes while maintaining sufficient resolution to evaluate the prominent leaky wave signal properties. The remaining cross terms are artifacts of the analysis technique. The broadband geometric field initially scattered from the model is shown at time $t = 0$. The arrivals induced at the bow endcap and shown at $t = 68\ \mu sec$ and $t = 124\ \mu sec$ in Figure 3.22 manifest themselves as the decreasing frequency components weakly shown over the same time duration in Figure 3.32. Several leaky shear wave arrivals are well resolved in Figure 3.32 over the time duration $330 \leq t \leq 600\ \mu sec$ near the frequencies $ka = 4.9$ and $ka = 7.2$. A frequency decrease with increasing time of the apparent third coincidence frequency is particularly evident, from a maximum value of $ka = 8.3$ to a minimum value of $ka = 7.2$. The larger bandwidths of the monostatic finite shell measurements shown in Figure 3.25, ($\Delta ka = 0.8$) compared to the specular directed field of Figure 3.26 ($\Delta ka = 0.4$), are manifestations of the observed change in the period of the leaky wave field. The observed frequency change with time cannot be attributed to dispersive effects, but rather is an artifact of the small measurement radius employed. Although the variation of the distance from the various points of radiation on the shell to the monostatic receiver does not appreciably influence the measured amplitude, it significantly influences the propagation delay. As a result, an apparent change in frequency is observed and the deviations are greater at higher frequencies. In this instance, membrane wave dispersion effects induced at the endcap are believed to be relatively unimportant.

3.4.2 The Monostatic Field Measured at an Aspect Angle of 66 degrees

I now interpret the scatter measured at an aspect angle of 66 degrees as an example of the angular regime where I would not expect to observe significant levels of compressional wave scattering. This aspect angle exceeds the critical value for phase matched excitation of transverse shear waves by nearly 5 degrees, but is about 7 degrees less than the critical angle for compressional wave excitation. Hence I would not expect compressional wave radiation to contribute to the scattered field unless it is induced by phase matched excitation at the bow endcap, or mode conversion processes occurring at either endcap. The bandlimited impulse response measured at this aspect angle is shown in Figure 3.33 and the magnitude of the analytic signal is shown in Figure 3.34. The large amplitude broadband pulse shown at time $t = 0$ corresponds to the initial geometric scatter of the shell. In addition, two distinct packets of leaky wave radiation are seen with peak amplitudes at times $t = 536$ μsec and $t = 1054$ μsec. Given the simple plane wave scattering evolution described in Section 1.4, I estimate that a back directed shear wave radiated energy packet would be first initiated at $t = 478$ μsec, and a second packet would begin at $t = 948$ μsec. These estimates are based on axial propagation at the trace velocity of the incident field $c_z = 3685$ and include a delay correction for the different waterborne path lengths of the initial and leaky wave fields. Therefore, I conclude that the large amplitude signal components contained within the first packet correspond to radiation from the first axial (length-wise) round trip of the induced shear wave while the latter corresponds to the radiated field of the second round trip.

The signal components observed in the first packet over the time duration of $300 < t < 900$ μsec were isolated from the remaining signal and transformed to the frequency domain to evaluate the relative contributions of the signal constituents. The resulting target strength is shown as a function of frequency in Figure 3.35. The signal components found over this duration were isolated from the remaining signal using a Hamming window providing a frequency resolution of $\Delta ka_{3dB} = 0.47$

and no Gaussian bandpass filtering was performed. The magnitude of the specularly directed shear wave contributions to the target strength of an infinite cylindrical shell are shown in Figure 3.36 for comparison. This comparison is again generally inappropriate unless the assumptions of Chapter 1 are reasonably well met. A comparison of Figures 3.35 and 3.36 indicates that the predominant constituent of the field observed over this duration is the spatial coincidence frequency $ka \simeq 4$ associated with the radiated field of induced transverse shear waves of angular order $n = 1$. Hence, the large amplitude signals observed over this time duration in Figure 3.33 corresponds to radiation from the first axial round trip of an induced shear wave. Although the magnitude of the specular scatter of the infinite shell is only 2 dB less at the second coincidence frequency $ka = 8$, it cannot be discerned in the measured backscatter data and the finite shell must therefore behave differently. I believe that much of this change is induced by scattering of coincident shear waves to noncoincident compressional waves at the slope discontinuity of the endcaps. At this aspect angle, compressional waves are not cutoff at the coincidence frequencies of the shear wave field. The bandwidths of the finite backscatter and infinite shell specular scatter appear comparable with a value of $\Delta ka \simeq 0.9$, but the bandwidths shown in Figure 3.35 are artificially increased by the windowing operation employed to isolated the data segment. Therefore, the decay of the finite shell must again be less than the predicted radiation loss of the infinite shell.

A 595 μsec time delay can be seen to separate the inception of the two distinct energy packets shown in Figures 3.33 and 3.34. This propagation delay corresponds to an apparent group velocity of 2890 m/sec. The apparent group velocity is again closely predicted by the group velocity of a free mode of propagation of a fluid loaded shell $c_g = 2613\ m/sec$ given the trace velocity $c_z = 3658\ m/sec$; see Figure 2.39.

A least squares linear fit of the exponential rate of decay of the overall peak levels found over the duration $528 < t < 1220$ exhibits a decay rate of 0.027 $dB/\mu sec$. A free transverse shear mode of angular order $n = 1$, and the same phase velocity would exhibit a decay rate of 0.028 $dB/\mu sec$ which nicely predicts the overall decay

rate measured. The signal measured over the time duration $528 \leq t \leq 846$ exhibits a larger decay rate of 0.060 $dB/\mu sec$. The decay observed over this duration is probably influenced by the measurement configuration as was observed at an aspect angle of 75 degrees. However, I believe that the small measurement distance tends to increase observed decay rates because measured amplitudes would decrease rapidly as the main lobe of the radiated beam moves beyond the receiver location. In short, one can again see that good coincident radiation has been impaired somewhat by the truncations and the modal behavior induced.

The measured target strength of the empty shell model at 66 degrees is shown as a function of frequency in Figure 3.37. Peak target strength levels are shown near the fundamental shear wave coincidence frequency $ka = 4$. The target strength is also modulated at $\Delta ka \simeq 0.42$ at frequencies $ka > 4.5$. In this case, the frequency spacing is reasonably well approximated by the axial resonance spacing of $\Delta ka = 0.47$ that is predicted by equation 3.4. I believe that this good correlation results because at this aspect angle, the trace speed of the incident field and group velocity of coincident shear field are nearly equal as can be seen in Figure 2.39 at the coincidence frequencies of Table 2.4. Therefore, shear wave dispersive effects are less important.

3.4.3 Evaluation of the Monostatic Signals Measured at Other Representative Aspect Angles

I now examine the monostatic signals measured on the empty shell model at additional discrete aspect angles of 72, 80, and 85 degrees to further evaluate the varying influence of membrane wave scattering processes. The features of the backscatter measured at these aspect angles, together with those previously discussed, are representative of those observed over the full range of angles $63 < \theta < 90$ deg.

The Monostatic Field Measured at an Aspect Angle of 72 degrees

The bandlimited impulse response measured at an aspect angle of 72 degrees is shown in Figure 3.38. Given the phase matched excitation criteria established for

infinite cylinders, I would not expect compressional wave scattering to significantly contribute to the field unless it is induced at the endcaps. The geometric field initially scattered from the shell can be seen as a well resolved symmetric broadband pulse centered at time $t = 0$. Unlike the field observed at an aspect angle of 66 degrees, the initial return from the target is immediately followed by an exponentially decaying field with a period $T \simeq 66\ \mu sec$ corresponding to the ring frequency of the shell. This behavior is observed with increasing amplitude as the aspect angle approaches normal incidence $\theta \rightarrow 90\,\mathrm{deg}$ and appears to be induced by an interaction of the incident field and the shell truncation as noted earlier in Section 3.4.1.

Large amplitude scattered pressures are observed over the time duration of $225 < t < 825\ \mu sec$ shown in Figure 3.38 with peak levels occurring at $t = 470 \mu sec$. These signal components exhibit a period that averages $T_m = 85\ \mu sec$, as would be predicted for coincident shear wave radiation using equation 2.59, but that changes with time ranging from a minimum value of 76 μsec to a maximum of 100 μsec. A similar change in the period with time was also exhibited at an aspect angle of 75 degrees and I believe that this instance is also a manifestation of the small measurement radius employed. The signal components found over this duration were isolated from the remaining signal using a Hamming window as before and the resulting target strength is shown in Figure 3.39. The magnitude of the shear wave contributions to the specularly directed target strength of an infinite cylindrical shell are shown in Figure 3.40 for comparison. Of course this comparison remains somewhat inappropriate, but given the assumptions of Chapter 1 it remains a useful method of identifying membrane wave signal constituents and comparing radiated levels. A comparison of Figures 3.39 and 3.40 indicates that the peak levels measured near $ka = 2.75$, 5.5, and 8.7 correspond to coincident shear wave radiation. Hence, radiation from induced shear waves constitutes the predominant constituent of the field observed over this duration. The bandwidths of the finite shell measurements exceed those of the infinite shell by $\Delta ka = 0.2 - 0.3$. However, the bandwidths shown in Figure 3.39 are artificially increased by the low frequency resolution time window

used to isolate this segment of data. I have found that time windowing a chirp signal with a time dependent period similar to that observed produces a similar increase in the bandwidth. Hence, I believe that the shear wave field experiences radiation damping close to that of a free wave on an infinite cylinder. A null is observed at $ka = 4.2$ which corresponds to destructive interference of the shear wave returns which produces the coincident levels observed at $ka = 2.75$ and $ka = 5.5$. Destructive interference of successive shear wave returns can also be seen in the infinite cylinder scatter results of Figure 3.40 at frequencies centered between pairs of coincidence frequencies. However, in the case of the infinite shell, radiation damping inhibits strong destructive interference and maintains higher levels at these frequencies. I do not believe that the damping of the finite shell is significantly different from that of the infinite shell scatter. Rather, I believe that the interference producing the null is influenced by the amplitude variation of the signal that results because of the small measurement distance employed as discussed in Section 3.4.1.

The anti-symmetric bandlimited pulses observed at times $t \geq 378$ μsec are generated by the back propagating transverse shear waves induced by the incident field as confirmed by the frequency domain analysis discussed above. The anti-symmetric shape of the large amplitude returns observed over this time duration is different from the initial return, as well as the leaky wave specular scatter from an infinite cylinder. Similar behavior is observed at most aspect angles $\theta < 80$ deg as discussed in Section 3.4.1 for the aspect angle of 75 degrees. The anti-symmetric shape is consistent with a phase change of nearly 90 degrees as would be caused by a single interaction with a caustic on the stern endcap as discussed in Appendix B, but interference between successive pulses makes such a conclusion a weak one.

The frequency dependence of the measured target strength representation of the entire measured signal is shown in Figure 3.41. Peak target strength levels are again observed near shear wave coincidence frequencies where peak length-scale modulation levels exist. From Figure 3.38 we see that the large amplitude shear wave radiation is nearly symmetrically located about the peak value shown at $t = 470$. Interference

of two signal components of similar magnitude, but delayed by $\Delta t = 470\ \mu sec$ would produce a cosine modulation with a spacing $\Delta ka = 2\pi a/c\Delta t = 0.50$. Interference of the measured initial and delayed returns produces a target strength modulation with a similar spacing of approximately $\Delta ka = 0.46$ at frequencies $ka > 5$ as shown in Figure 3.41. In contrast, the simple longitudinal resonance model of equation 3.4 would predict a spacing of $\Delta ka = 0.63$. Once again, measured peak target strength levels are close to the values observed for an infinite cylinder and show a trend of decreasing levels with increasing frequency that is similar to the predicted $1/\sqrt{ka}$ dependence. Peak levels range from -17 to $-22\ dB\ re\ 1\ m$ and show little variation from the peak levels observed at aspect angles of 66 and 75 degrees.

Scatter components are noted at $ka = 3.7$ in both Figures 3.39 and 3.41. A similar, but weaker component is observed near the ring frequency at 75 degrees as shown in Figure 3.25. Because they are not evident in the infinite cylinder scatter, I suspect that they are the result of compressional wave ringing of the shell induced at the shell truncations. Shear waves scatter energy to compressional waves when they encounter a structural discontinuity as I demonstrate in the next chapter.

The Monostatic Field Measured at an Aspect Angle of 80 degrees

The bandlimited monostatic impulse response measured at an aspect angle of 80 degrees is shown in Figure 3.42. Given the critical aspect angles for phase matched membrane wave excitation listed in Table 2.1, I would expect both transverse shear and compressional wave radiation to contribute to the scattered field measured at this aspect angle. The geometric field initially scattered from the model is shown as a broadband pulse centered at time $t = 0$ that is less well resolved than that observed at smaller aspect angles. As found at 72 and 75 degree aspect angles, the initial return from the target is immediately followed by an exponentially decaying field with a decreasing period whose average is near that of the ring frequency.

Large scattered pressures of oscillating and then decreasing amplitude are observed over the time duration of $200 < t < 900\ \mu sec$. In spite of these variations, the

amplitude more closely resembles the behavior I would expect given the assumptions of Chapter 1, and the proposed scattering evolution illustrated in Figure 1.5, i.e. an abrupt increase near $t = 2L\cos\theta/c$ and then an exponential decay. The target strength of this portion of the data is shown as a function of frequency in Figure 3.43. The target strength of the corresponding specularly directed leaky wave scatter of an infinite cylinder is shown in Figure 3.44. A comparison of Figures 3.43 and 3.44 indicates that the signal found is once again dominated by shear wave scattering processes. Although less prominent, compressional wave components are also shown in the predicted specular scatter, but not in the measured backscatter. The measured bandwidths of the coincident field exceed those of the infinite cylinder scatter. However, they are largely limited by the resolution of the window employed. Nulls can again be seen that result from destructive interference of the leaky wave returns. Scattering from the shell at the ring frequency is observed as before. However, coincident shear wave levels exceed levels observed at the ring frequency by as much as 16 dB.

The target strength measured at $\theta = 80\,\text{deg}$ is shown in Figure 3.45. The rapid frequency fluctuations of the target strength observed at large aspect angles cannot be described by the simple axial resonance model of equation 3.4. Peak levels are again well predicted by the infinite cylinder results.

The Monostatic Field Measured at an Aspect Angle of 85 degrees

The Gaussian bandlimited monostatic impulse response measured at an aspect angle of 85 degrees is shown in Figure 3.46 for a frequency range of $2.75 < ka < 10.0$. I would again expect both shear and compressional wave radiation to contribute to the scattered field. The geometric field initially scattered from the model shown at $t = 0$ can be seen to be the dominant feature of the signal. The peak amplitude of the initial return is nearly 10 dB greater than the corresponding value measured at 80 degrees. A large amplitude is also evident near $t = 60\ \mu sec$ and this delay corresponds closely to the period T_m of helical compressional wave scatter from an

infinite shell as shown in Figure 2.11.

The target strength measured at $\theta = 85$ degrees is shown in Figure 3.47. A comparison of the target strengths shown in Figures 3.45 and 3.47 indicates that the broadband levels measured at 85 degrees are significantly larger than those measured at 80 degrees or less. This increase in broadband levels, and the absence of significant modulation as observed at the other angles discussed, demonstrates the influence of the increased level of the initial scatter. The target strength of the corresponding specularly directed leaky wave scatter of an infinite shell is shown in Figure 3.48 for comparison. A comparison of Figures 3.47 and 3.48 indicates that coincident radiation of both shear and compressional wave scattering processes are represented. The local minima observed near $ka = 3.7$ and $ka = 7.1$ are the result of destructive interference of the compressional wave radiation and the initial return. The nulls observed near these frequencies deepen as the aspect angle approaches beam aspect $\theta \rightarrow 90$ deg as can be seen in Figure 3.13. The measured bandwidths of coincident shear radiation are again largely limited by the resolution of the time duration of the measured signal. However, as the aspect angle approaches normal incidence $\theta \rightarrow 90^0$, the coupling of the acoustic and shear wave fields decreases and the radiation induced decay rates decrease accordingly. At some aspect angle $85 < \theta < 90$, the observed bandwidth and magnitude of the shear wave radiated field must become limited by structural damping process.

3.4.4 Summary

In this chapter, I have demonstrated that coincident transverse shear wave excitation and reradiation is the dominant scattering process observed in the monostatic direction over a range of aspect angles of $61 \leq \theta \leq 85$ degrees. In contrast, both compressional and shear wave wave scattering processes provide similar contributions to the *specularly directed* field of an infinite cylinder over a range of aspect angles of $73 < \theta \leq 90$ degrees. The effective scattering source distribution derived using beamformed bistatic data measured at an aspect angle of 75 degrees

also exhibits initial compressional wave radiation in the specular direction. However, I believe that radiation and scattering experienced at the stern endcap prohibits comparable levels of compressional wave backscatter at aspect angles less than 85 degrees. Within 5 degrees of beam aspect, compressional wave excitation remains an important backscattering leaky wave constituent. Compressional wave reradiation generated over this range of angles produces nulls near the harmonics of the ring frequency of the shell as can be seen in Figure 3.13.

Although unusual amplitude variations of the leaky wave field are observed in the time domain representations of the monostatic field measured away from beam aspect, the frequency domain representations measured at different aspect angles are remarkably similar. Peak levels are observed near shear wave spatial coincidence frequencies imposed by phase matching criteria. Peak target strength levels generated by shear wave scattering processes consistently fall within the range of $-20 < T(\omega,\theta) < -15$ dB re 1 m at aspect angles $62 < \theta < 85$ degrees. This is consistent with the asymptotic results of equation 2.57 from which it is demonstrated that peak leaky membrane wave levels are primarily governed by the square root of the coincidence frequency and only weakly dependent on the imaginary component of the roots of the dispersion relation. In addition, the frequency domain representations of target strength measured away from beam aspect exhibit fluctuations indicating the interference between the geometrically scattered field initial observed and the delayed leaky wave field, and in some instances, this modulation is well predicted by the spacing of axial resonances. This modulation is a length-scale phenomenon not found in the infinite cylinder computations of Chapter 2.

Finally, I have found that the damping rates of the empty shell are similar to, or less than the predicted values for free wave propagation on an infinite cylinder. The shell truncations represent a means of scattering structural waves to less efficient radiators which must primarily consist of subsonic flexural waves, and thus serve to impair good radiation. These effects are more important for the ring stiffened and complex shells because scattering occurs at each encounter of a structural wave with

a ring as I will demonstrate in the chapters that follow.

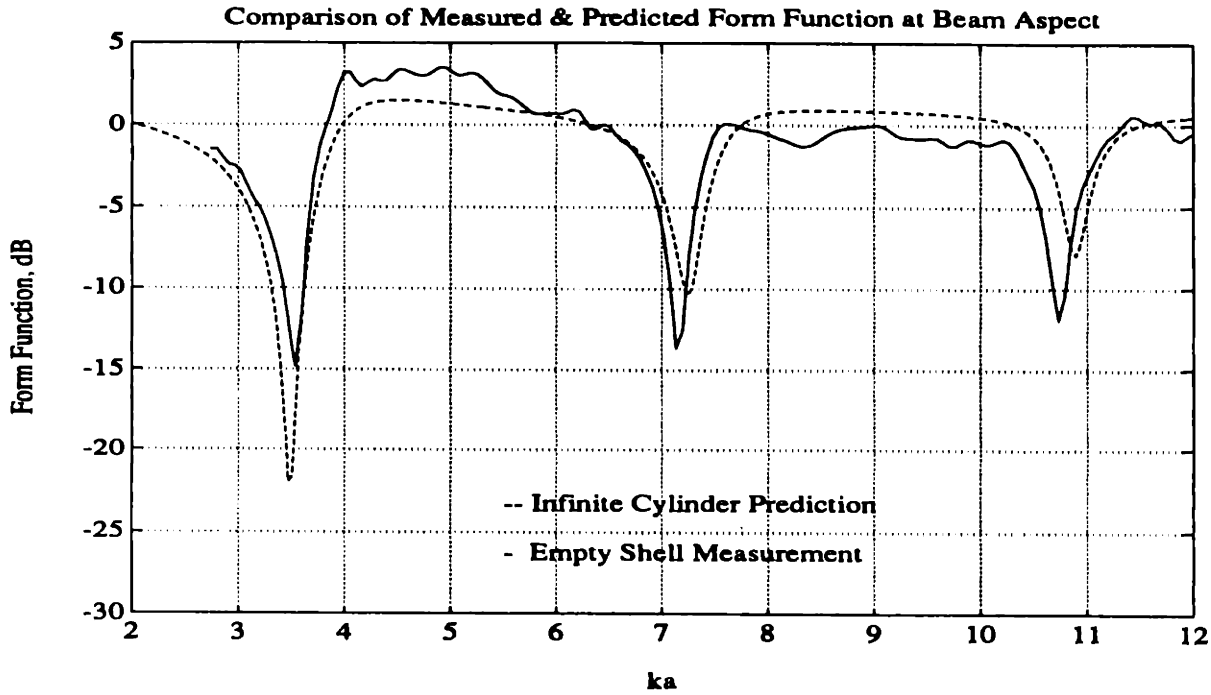

Figure 3.1: Comparison of the Measured Empty Shell and Infinite Cylinder Predicted Beam Aspect Form Functions. The transfer function has a frequency resolution of $\Delta ka_{3dB} = 0.16$.

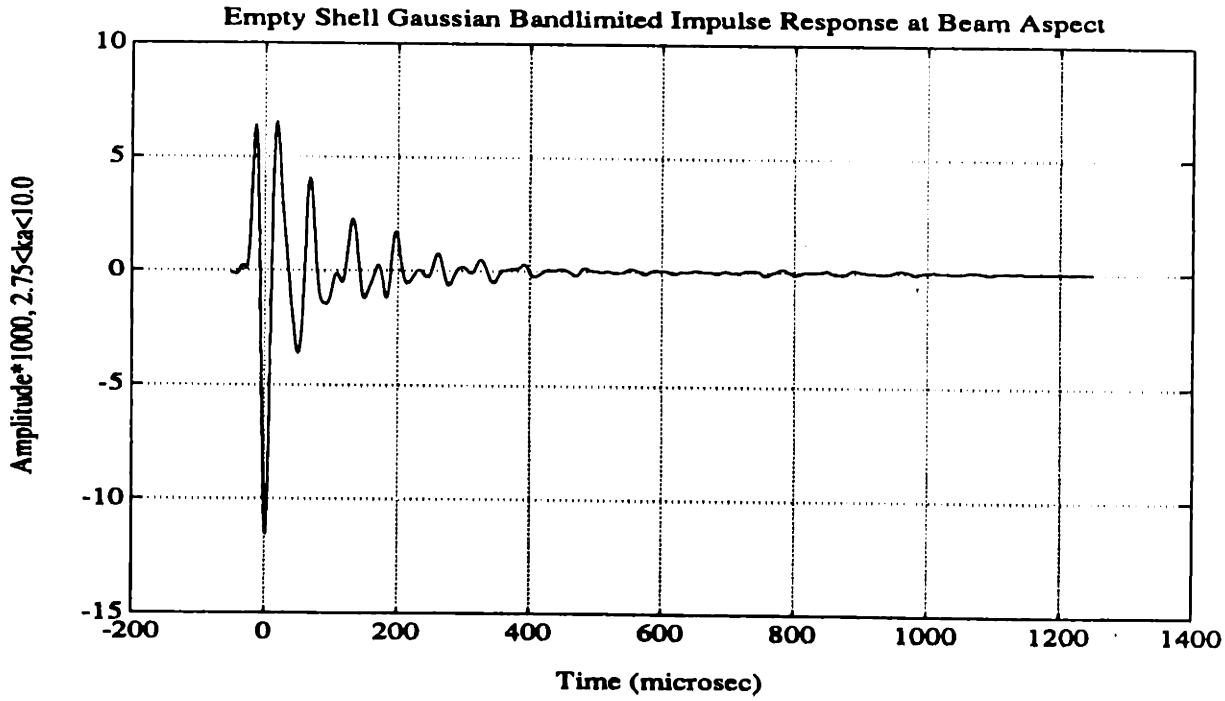

Figure 3.2: Measured Gaussian Bandlimited Monostatic Impulse Response of the Empty Shell at Beam Aspect for a Frequency Range $2.75 < ka < 10.0$ and a Radial Distance of $r = 2\ m$ from the Target Center

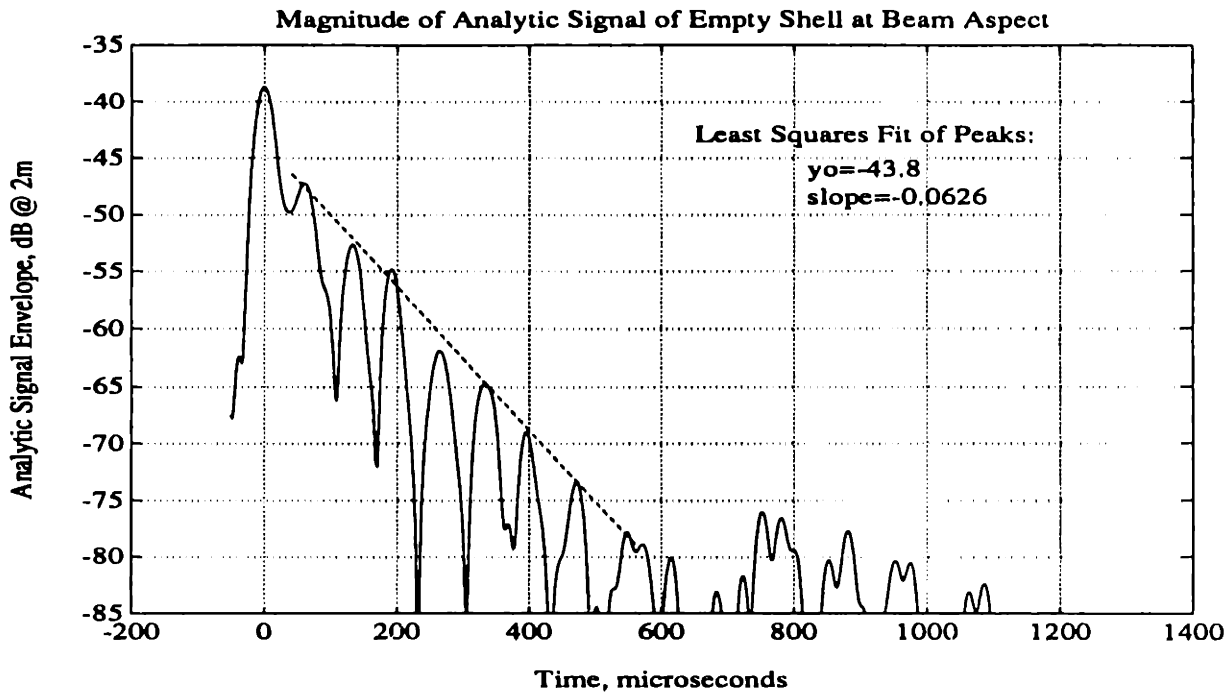

Figure 3.3: Logarithm of the Magnitude of the Envelope of the Gaussian Bandlimited Impulse Response of the Empty Shell at Beam Aspect, $2.75 < ka < 10.0$

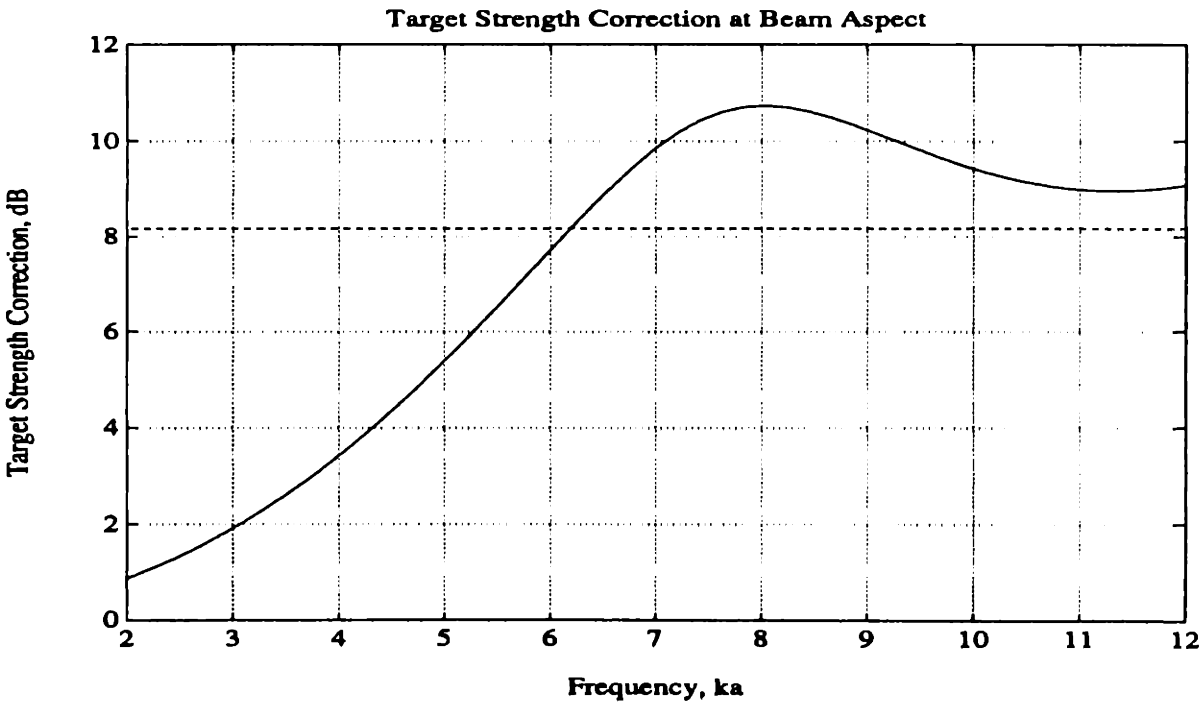

Figure 3.4: Target Strength Correction $T_{corr}(\omega)$. This correction is required to accurately estimate the target strength of the shells when insonified at beam aspect because the receiver is not located in the Fraunhofer field of the shell. This correction is applied to the spherical spreading based computations of Appendix A.4.2.

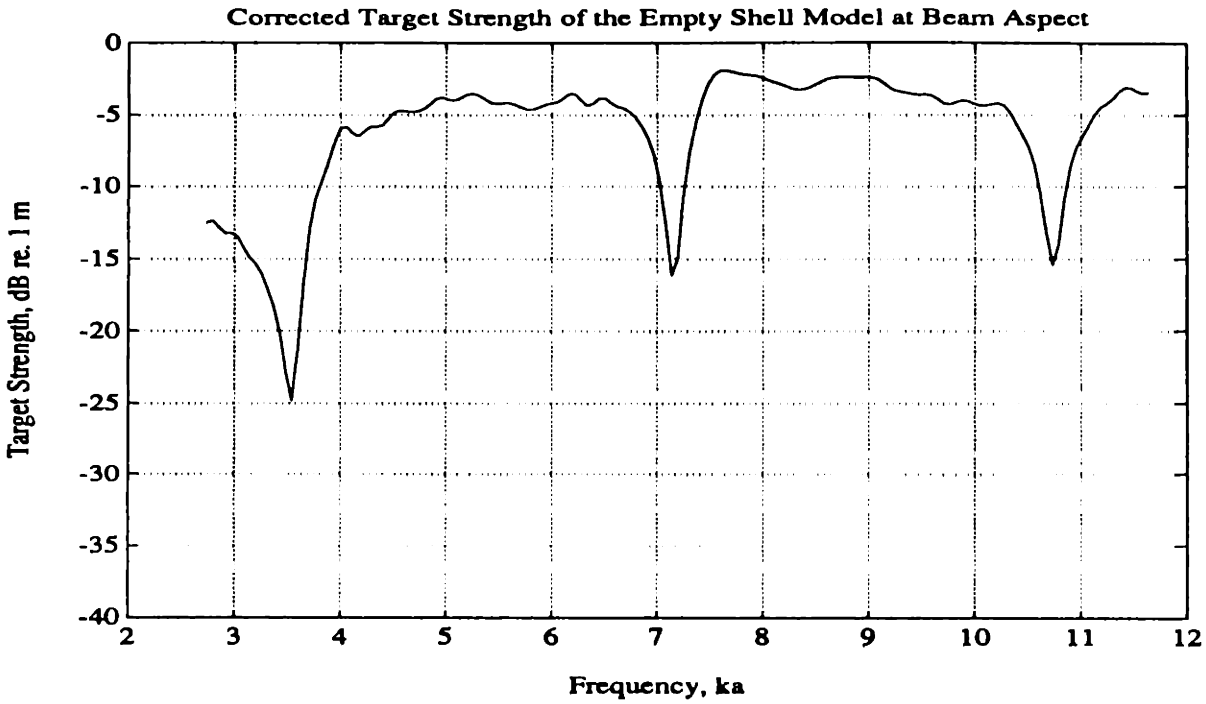

Figure 3.5: Corrected Target Strength of the Empty Shell as Measured at Beam Aspect. The transfer function has a frequency resolution of $\Delta ka_{3dB} = 0.16$.

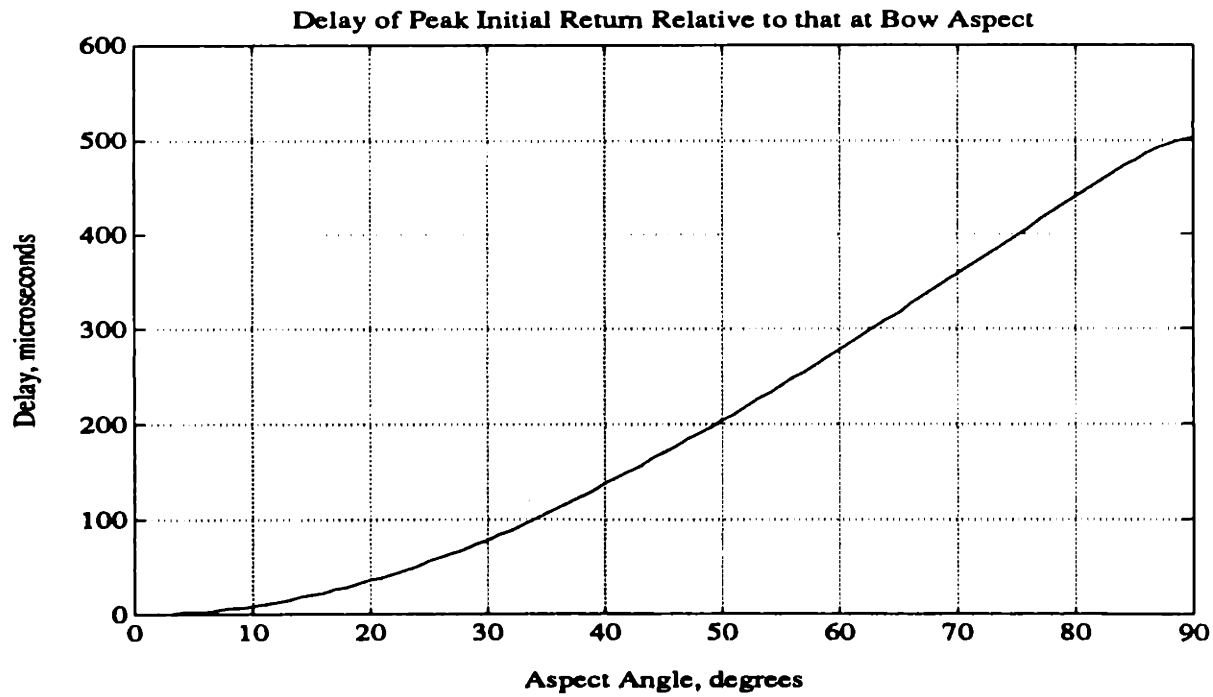

Figure 3.6: Measured Propagation Delay of the Peak Value of the Initial Return from the Empty Shell. Values are referenced to the delay at bow aspect (2231 μsec)

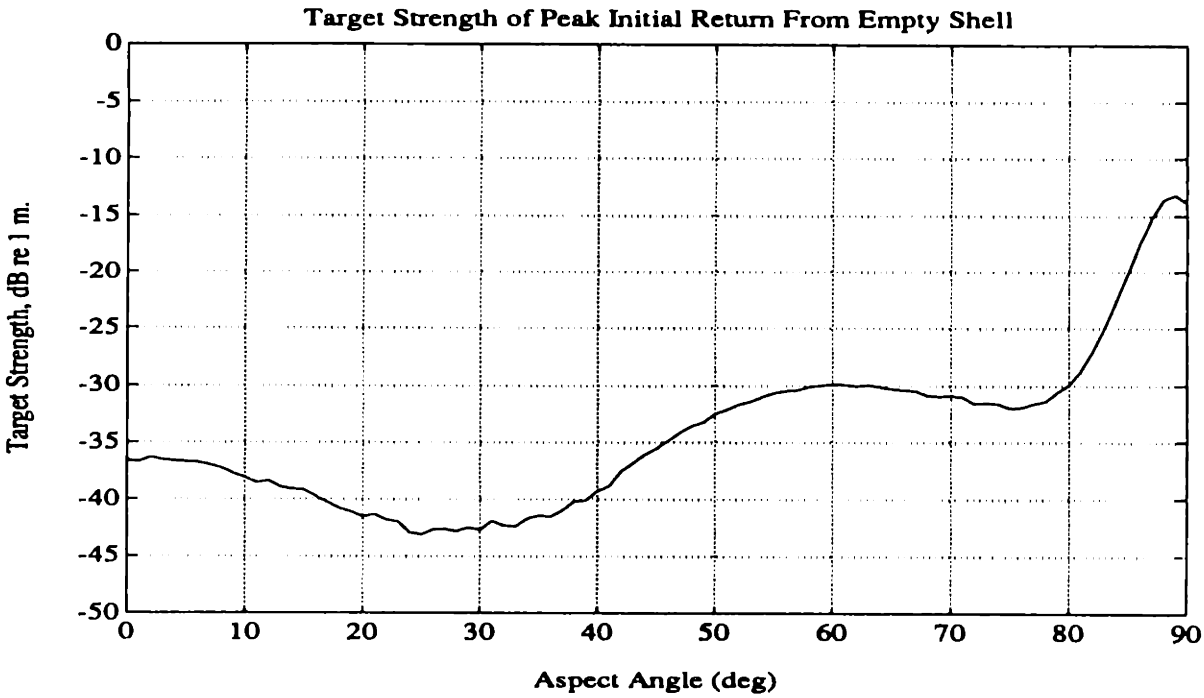

Figure 3.7: Target Strength of the Peak Initial Return $T_{initial}(\theta)$ from the Empty Shell Model. Values are normalized by the pressure level of the incident field at the target center location.

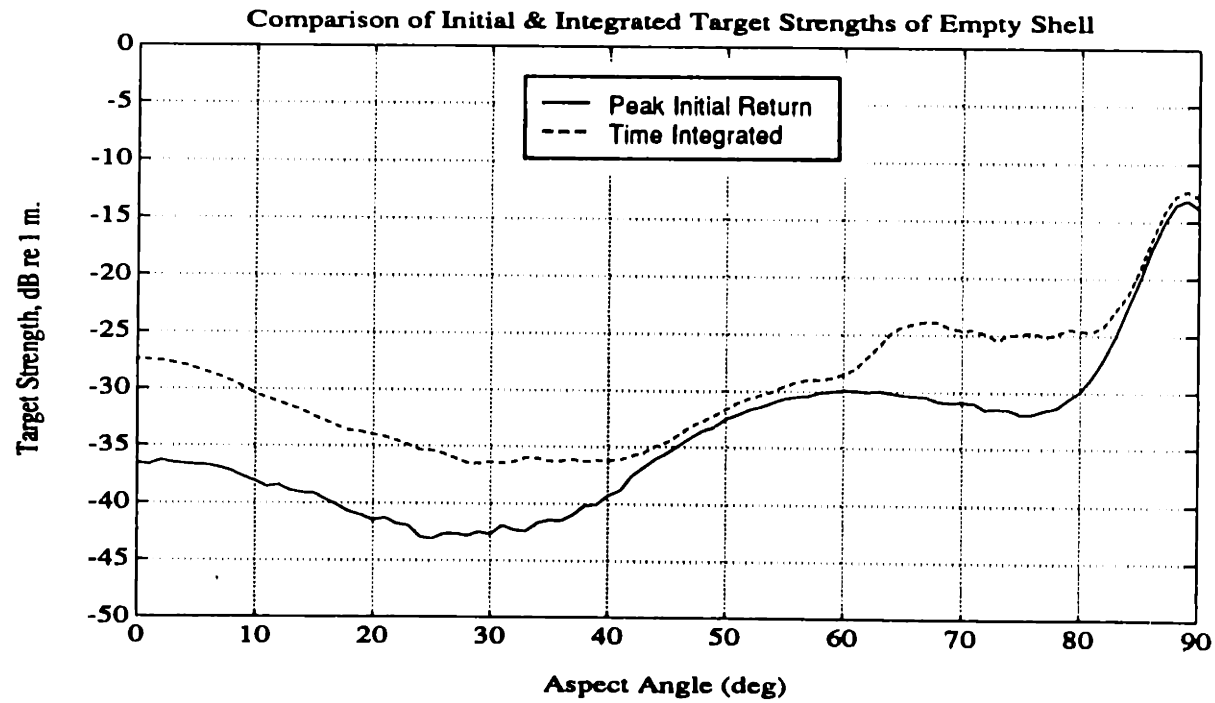

Figure 3.8: Comparison Target Strength Values Computed Using the Peak Initial Return and the Time Integral of the Squared Pressure $p_s^2(t)$

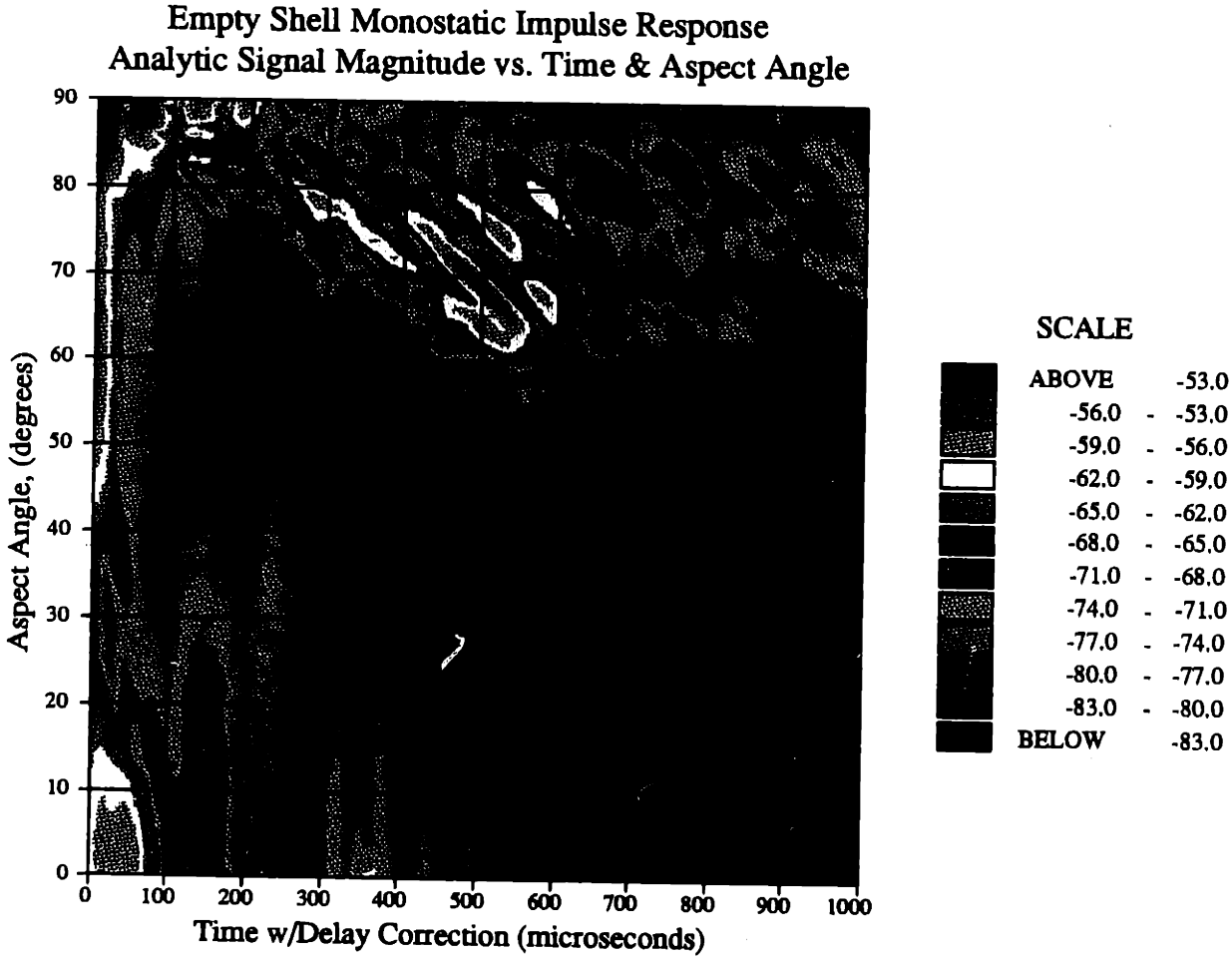

Figure 3.9: Analytic Signal Envelope of the Gaussian Bandlimited Monostatic Impulse Response of the Empty Shell at $r = 2\ m$ for the frequency range of $2.75 < ka < 10.0$ and an aspect angle range of $0 \leq \theta \leq 90\,\text{deg}$. The propagation delay of peak initial return from the target has been removed to stack the signals such that the peak initial return is shown at time $t = 0$ for all θ. The aspect angle $\theta = 0$ corresponds to bow aspect and $\theta = 90$ corresponds to beam aspect or normal incidence. The large amplitude signal components, other than the initial return, observed at angles $\theta > 60$ primarily correspond to helical membrane wave scattering. The predicted critical angle for phase matched shear wave excitation is $\theta_c = 61.3\,\text{deg}$.

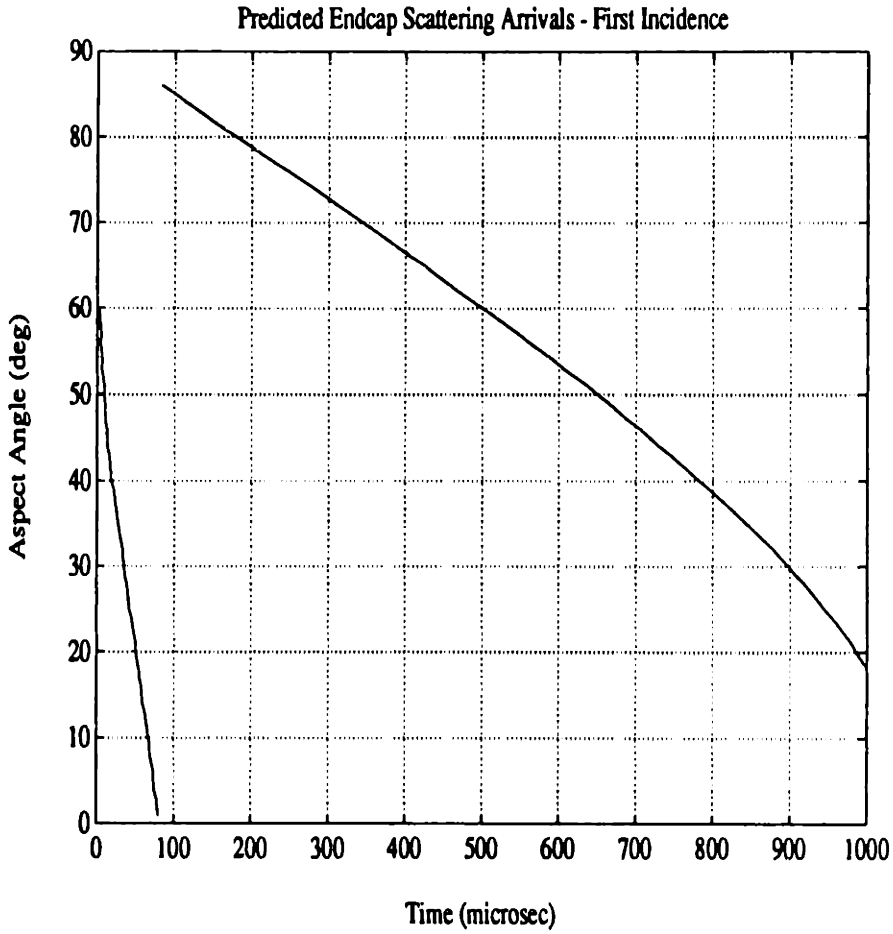

Figure 3.10: Predicted Arrival Times for Scattering from the Slope Discontinuities of the Two Endcaps of the Shell Models with an Axial Propagation Velocity Equal to the Trace Velocity of the Incident Field. This figure is drawn to the same scale as Figure 3.9 for comparison.

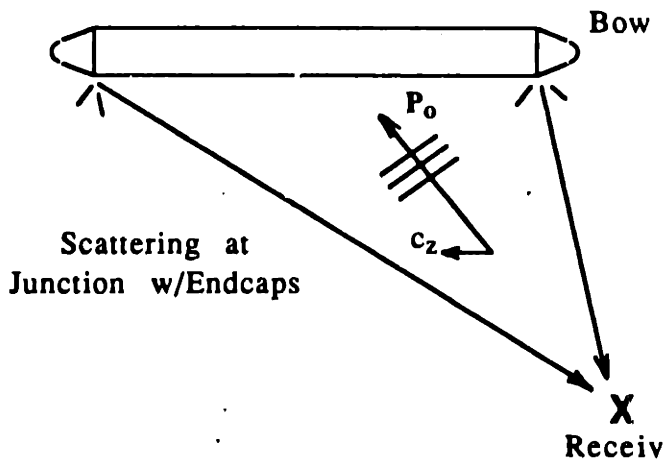

Figure 3.11: Illustration of Propagation Paths of of Scattering from the Slope Discontinuities of the Two Endcaps of the Shell Models

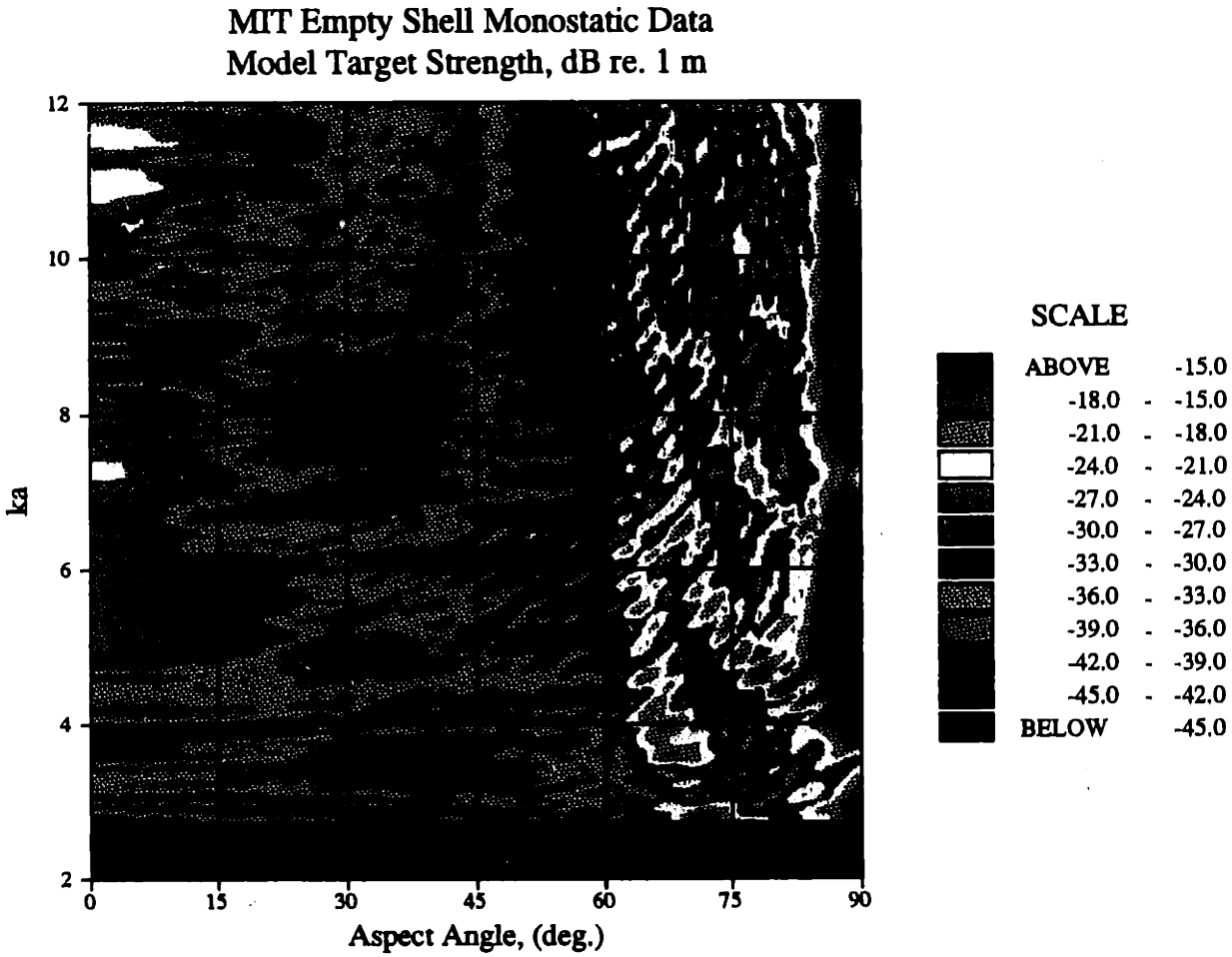

Figure 3.12: Contours of the Measured Target Strength $T(\omega, \theta)$ of the Empty Shell Model over the range of aspect angles $0 \leq \theta \leq 90$ deg. Values are normalized by the pressure level of the incident field at the target center location. The transfer functions have a limiting frequency resolution of $\Delta ka_{3dB} = 0.16$. The aspect angle $\theta = 0$ corresponds to bow aspect and $\theta = 90$ corresponds to beam aspect or normal incidence. The enhanced target strength pattern observed at angles $61 < \theta < 85$ deg correspond to transverse shear coincidence loci. The nulls observed near $\theta = 90$ are the result of destructive interference between the initial and compressional wave scattering components.

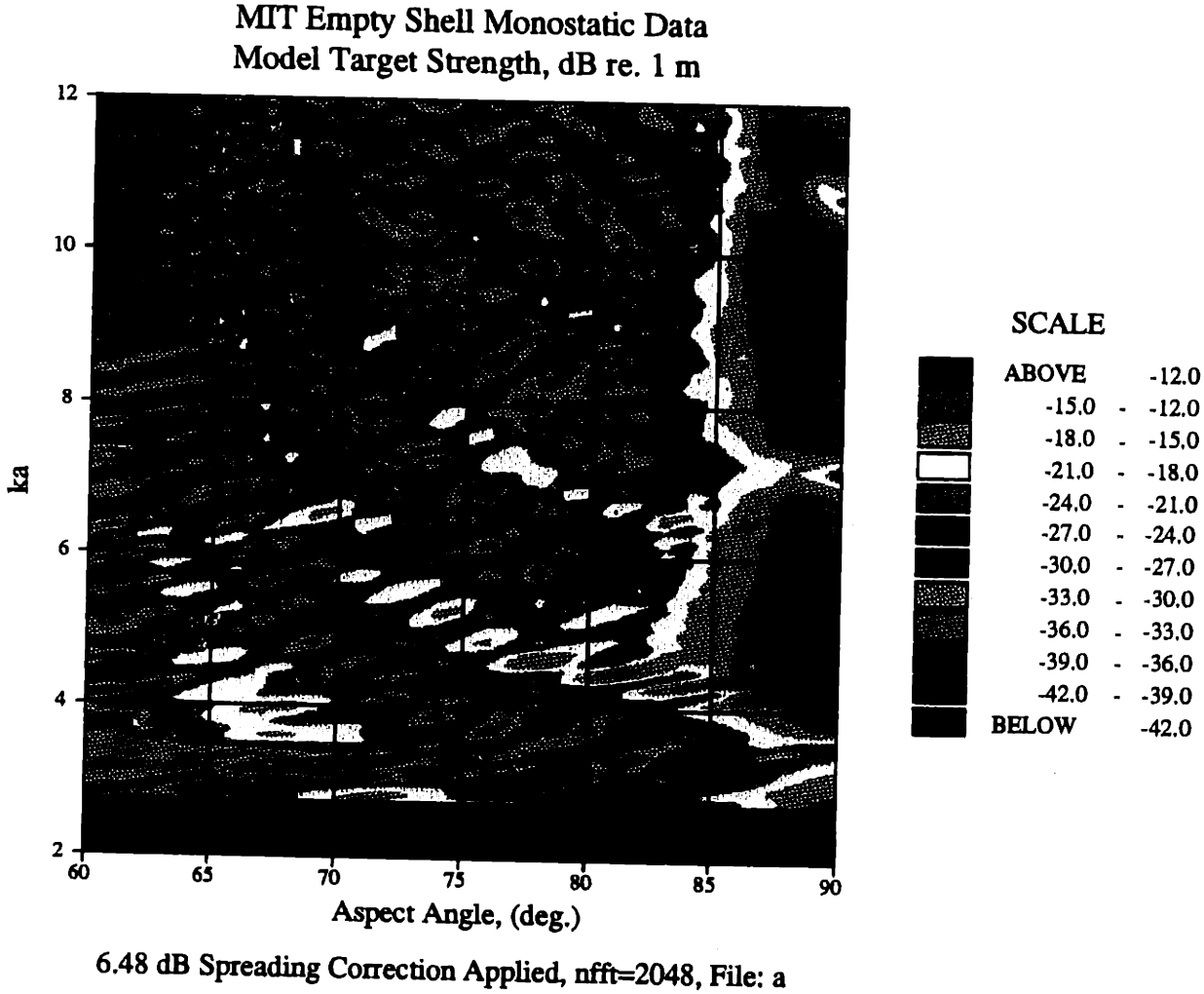

Figure 3.13: Contours of the Measured Target Strength $T(\omega, \theta)$ of the Empty Shell Model over the range of aspect angles $60 \leq \theta \leq 90$ deg. Values are normalized by the pressure level of the incident field at the target center location. The transfer functions have a limiting frequency resolution of $\Delta ka_{3dB} = 0.16$. The aspect angle $\theta = 90$ corresponds to beam aspect or normal incidence. Enhanced target strength can be observed at the transverse shear coincidence loci at all angles $\theta > 61$ deg. The nulls observed near $\theta = 90$ are the result of destructive interference between the initial and compressional wave scattering components.

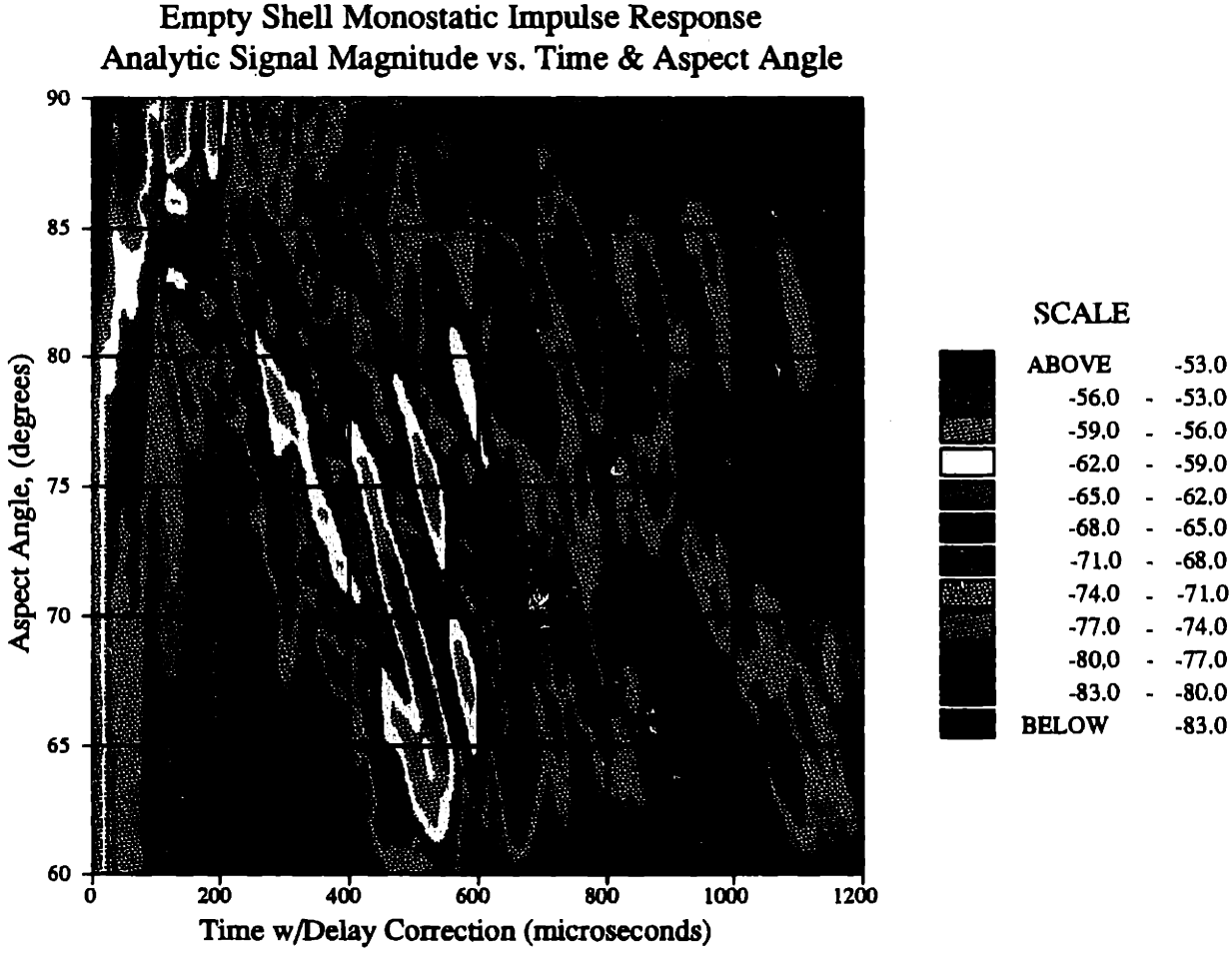

Figure 3.14: Analytic Signal Envelope of the Gaussian Bandlimited Monostatic Impulse Response of the Empty Shell at $r = 2\ m$ for the frequency range of $2.75 < ka < 10.0$ and the range of aspect angles $60 \leq \theta \leq 90$ deg. The propagation delay of peak initial return from the target has been removed to stack the signals such that the peak initial return is shown at time $t = 0$ for all θ. The aspect angle $\theta = 90$ corresponds to beam aspect or normal incidence. The large amplitude signal components, other than the initial return, primarily correspond to helical membrane wave scattering.

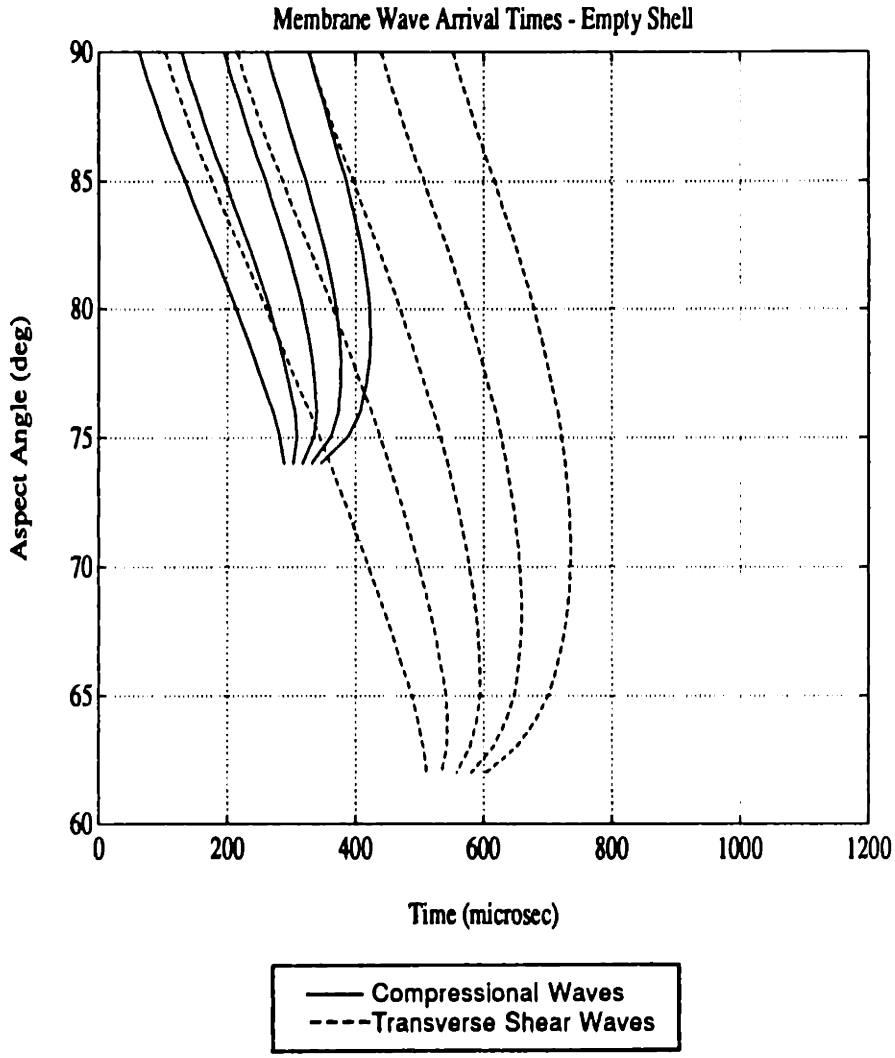

Figure 3.15: Predicted Time Delays of the First 5 Leaky Wave Arrivals Associated with the First Round Trip of the Induced Structural Waves. Predictions are for plane wave insonification of a finite cylinder of length $L = 0.86\ m$ with perfectly reflecting truncations. Propagation delays shown are referenced to the measured delay of the peak initial return. This figure is drawn to the same scale as Figure 3.14 for comparison.

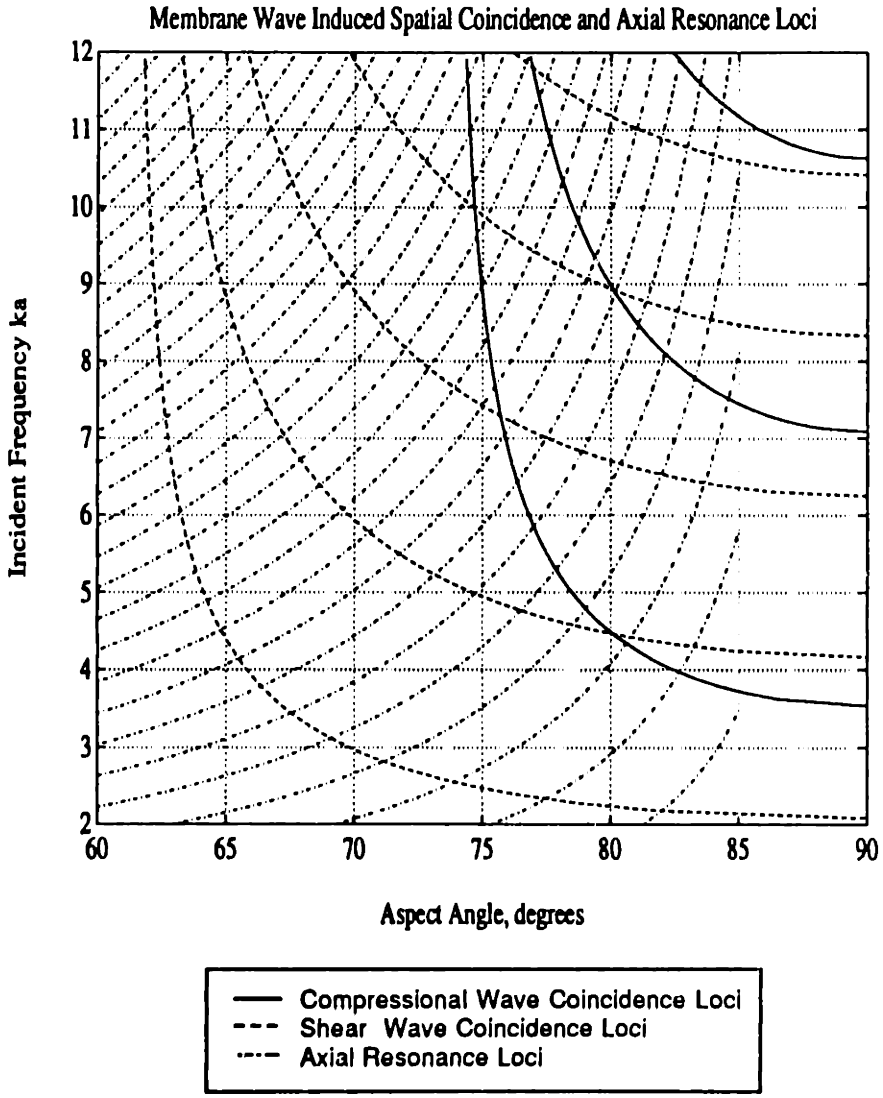

Figure 3.16: Loci of Aspect Angle θ and Frequency ka Where Conditions of Membrane Wave Spatial Coincidence and Axial Resonance Conditions Exist. This figure is drawn to the same scale as Figure 3.13 for comparison.

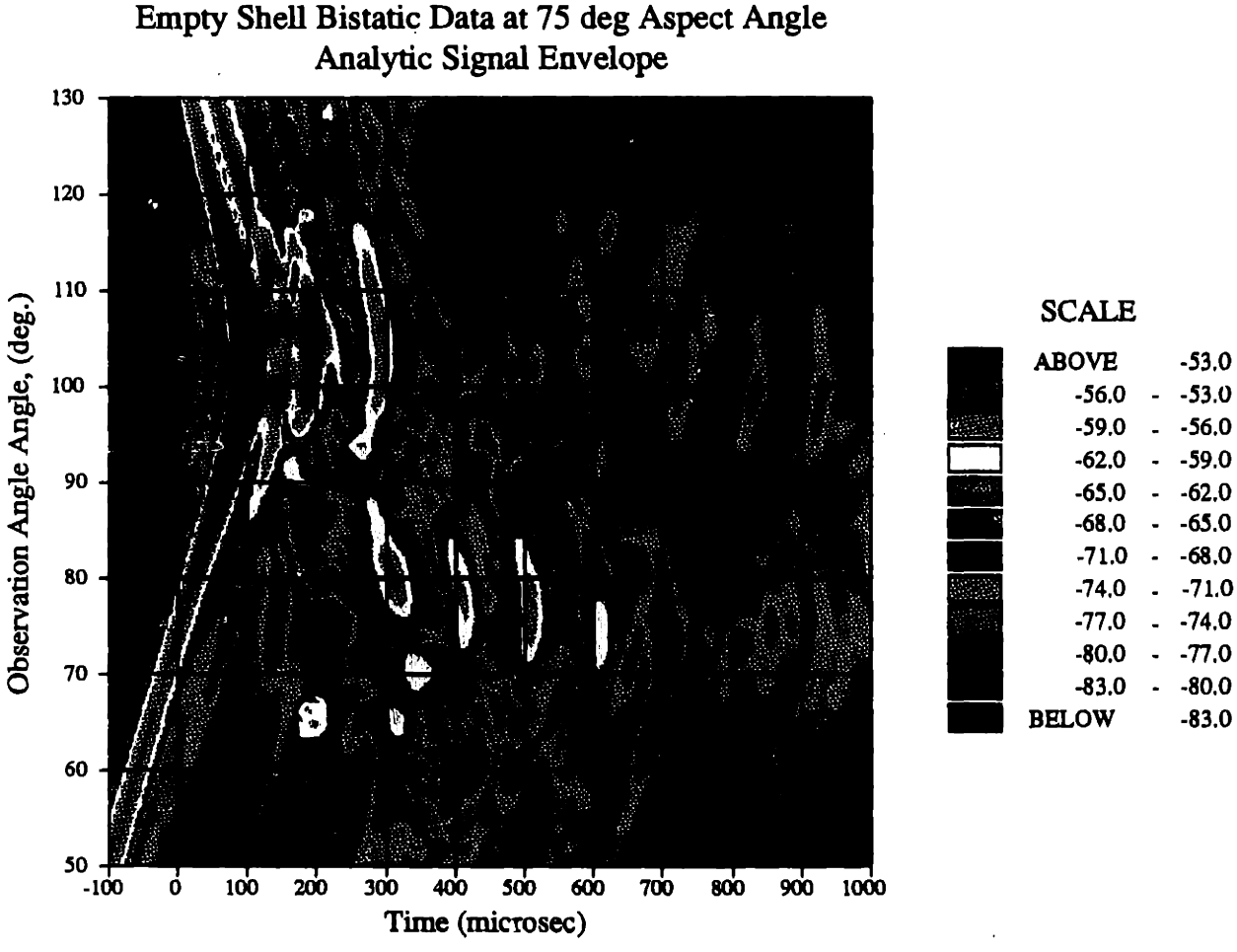

Figure 3.17: Analytic Signal Envelope of the Gaussian Bandlimited Bistatic Impulse Response of the Empty Shell at $r = 2\ m$ for $2.75 < ka < 10.0$ and Observation Angles $50 \leq \theta_o \leq 130$ deg. The time $t = 0$ refers to the time at which the peak initial monostatic return from the target was measured. The observation angle $\theta_o = 75$ corresponds to the monostatic direction, and $\theta_o = 105$ is the specular direction. The periodic field observed near $\theta_0 = 75$ corresponds to induced shear wave radiation.

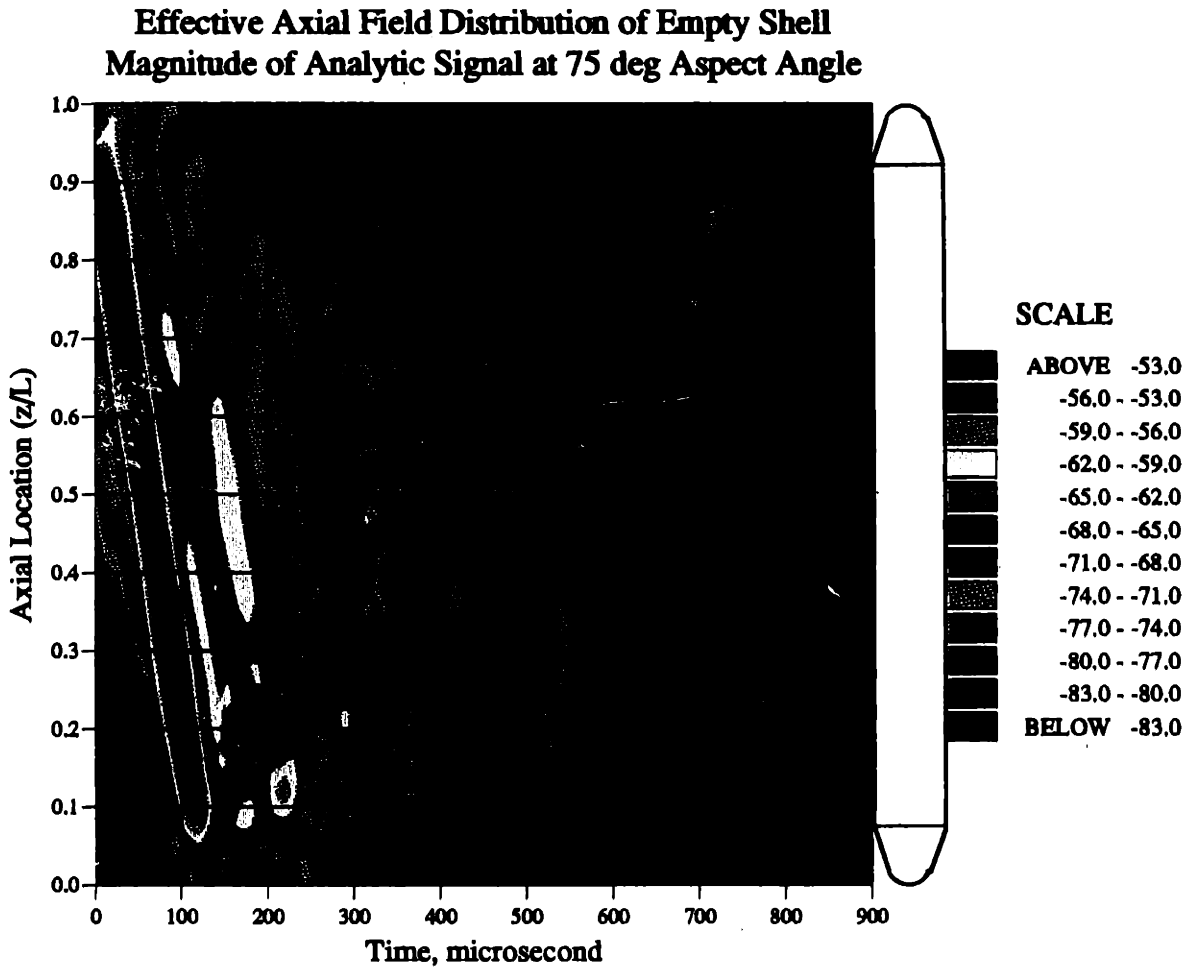

Figure 3.18: Effective Axial Distribution of the Back and Specular Directed Scatter of the Empty Shell Model at an Aspect Angle of 75 degrees. The results were generated using classical focused beamforming of the bistatic data measured over a range of observation angles of $60 \leq \theta_o \leq 120$ deg for the frequency range of $2.75 < ka < 10.0$. The incident field was deconvolved from the distribution to yield a normalized effective point source strength in dB re 1 m. The axial location $\tilde{z}/L = 0$ corresponds to the stern, or far endcap, and $\tilde{z}/L = 1$ is the bow endcap. The beamforming resolution is $\Delta z_{3dB}/L = 0.048$.

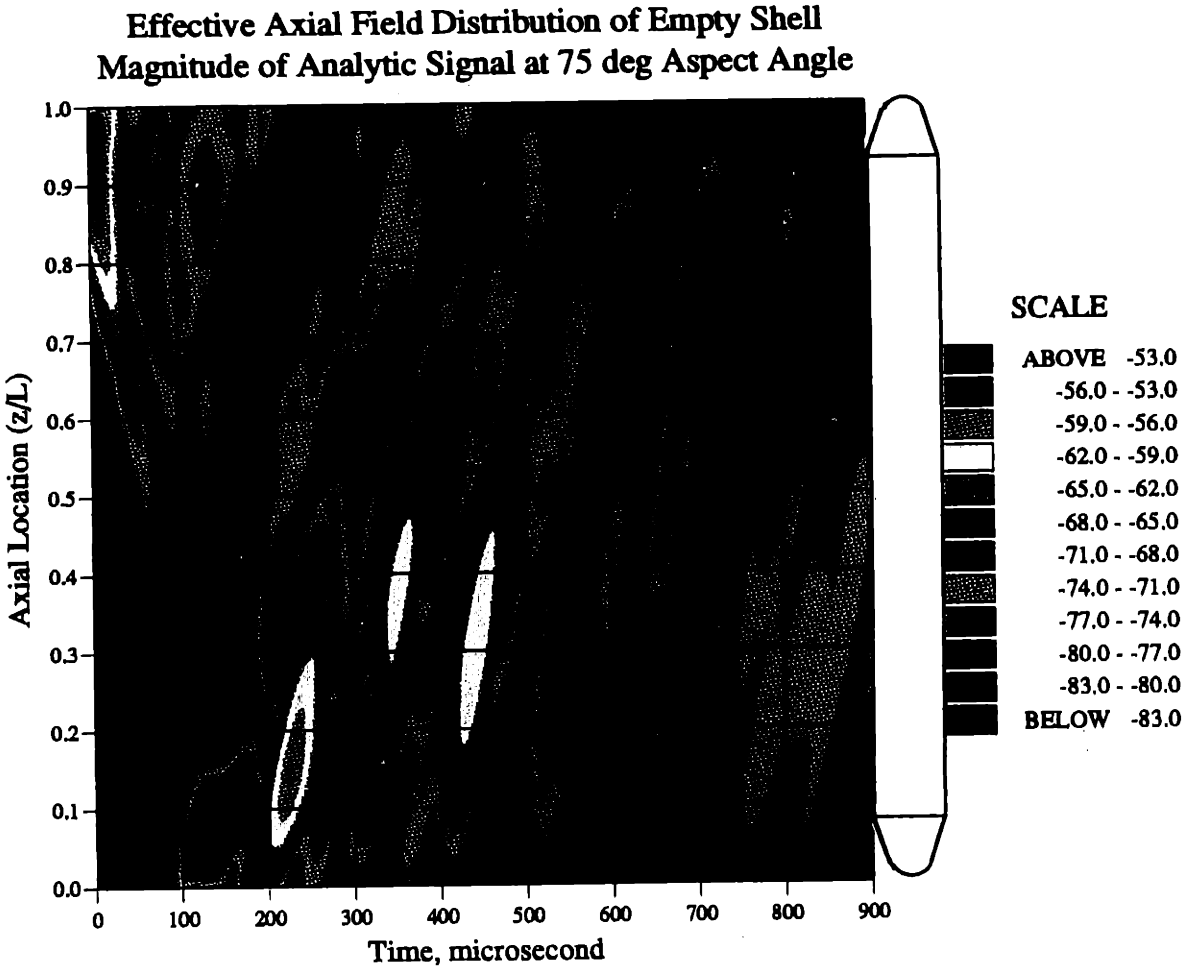

Figure 3.19: Effective Axial Distribution of the Back Directed Scatter of the Empty Shell Model at an Aspect Angle of 75 degrees. The results were generated using classical focused beamforming of the bistatic data measured over a range of observation angles of $50 \leq \theta_o \leq 100$ deg for the frequency range of $2.75 < ka < 10.0$. The incident field was deconvolved from the distribution to yield a normalized effective point source strength in dB re 1 m. The axial location $\tilde{z}/L = 0$ corresponds to the stern endcap and $\tilde{z}/L = 1$ is the bow endcap. The beamforming resolution is $\Delta z_{3dB}/L = 0.085$ and a Hamming amplitude taper was applied over the length of the array.

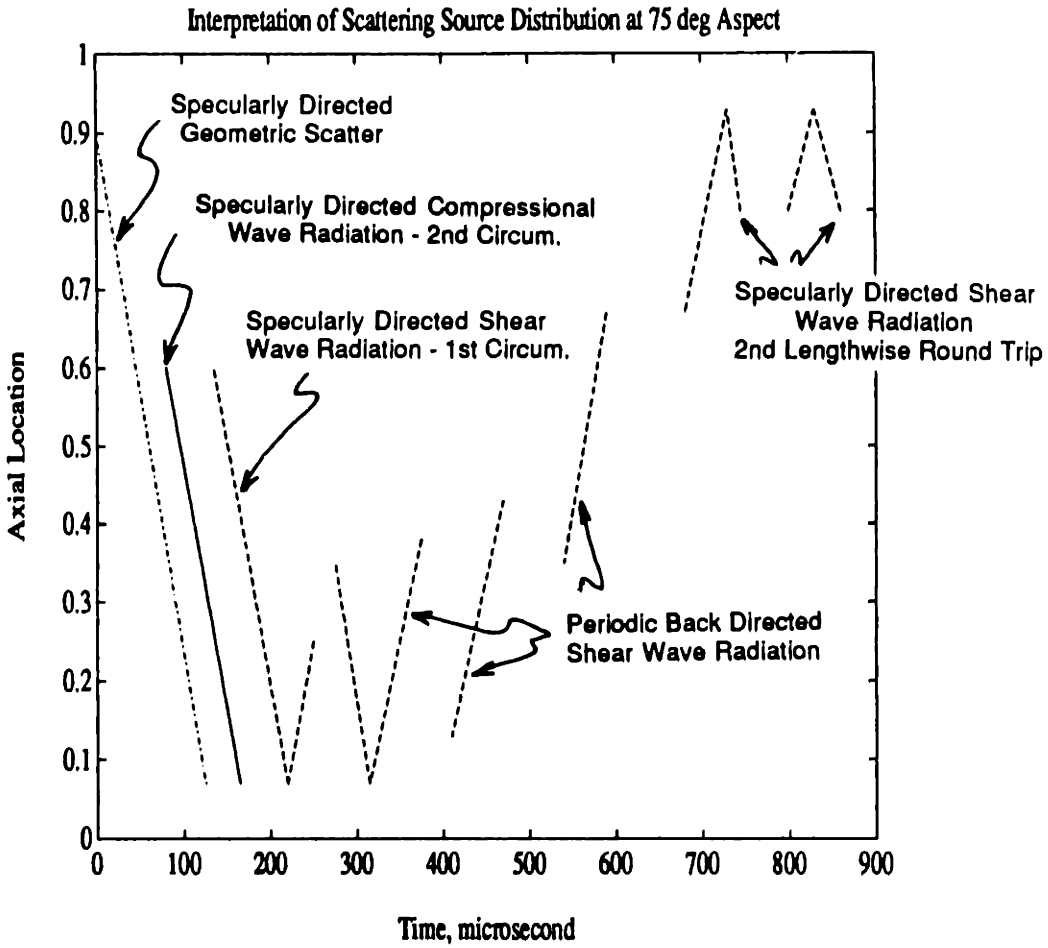

Figure 3.20: Interpretation of the Scatter Produced by the Empty Shell Model at an Aspect Angle of 75 degrees. This illustration corresponds to the effective axial distribution of the back and specularly directed scatter shown in Figure 3.19 and is drawn to the same scale for comparison. The axial location $\tilde{z}/L = 0$ corresponds to the stern, or far endcap, and $\tilde{z}/L = 1$ is the bow endcap.

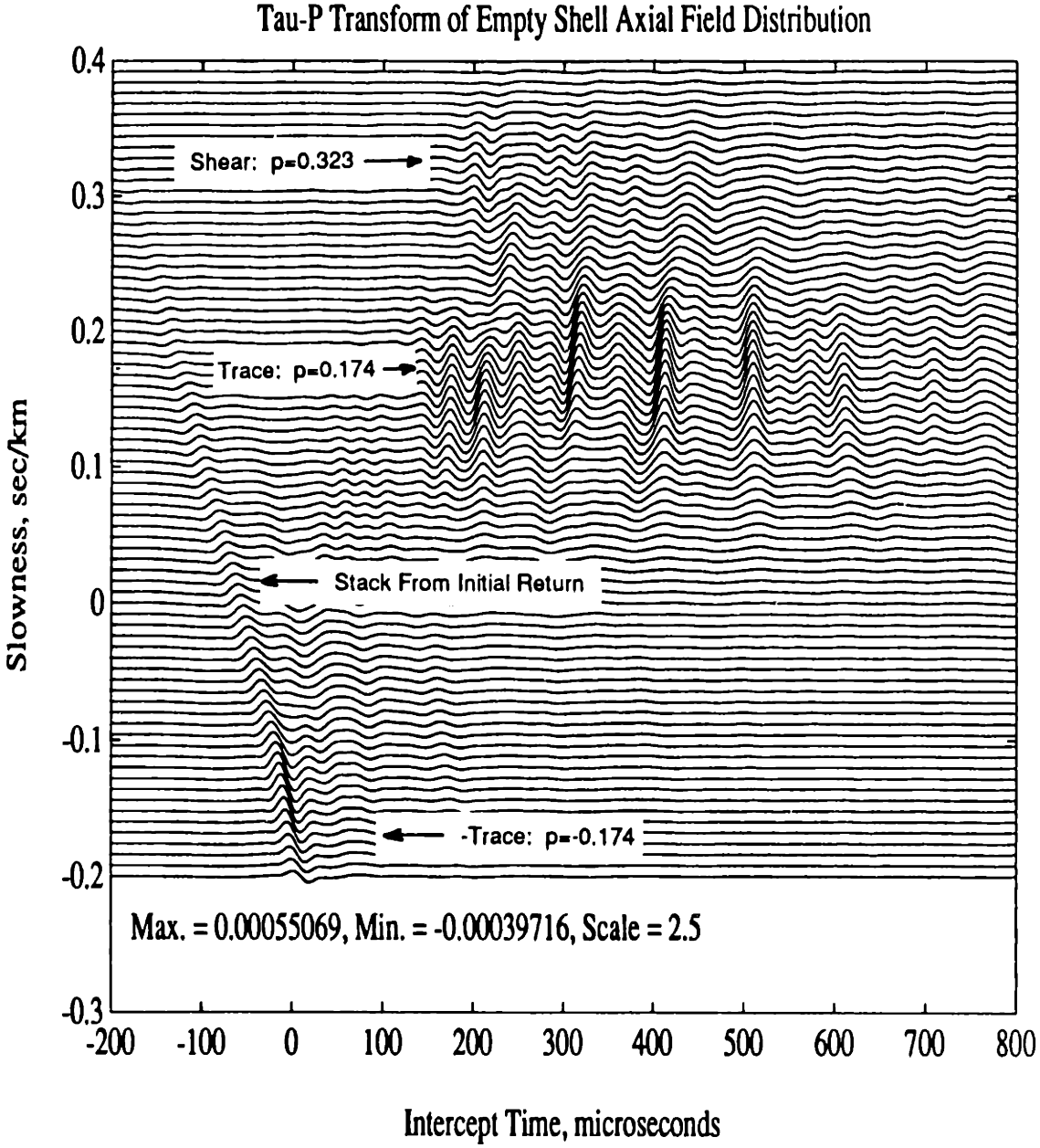

Figure 3.21: $\tau - p$ Transform of the Effective Axial Distribution of Back Directed Scattered Field of the Empty Shell Model at an Aspect Angle of 75 degrees. The results were generated using a discretized Radon transform of the output from focused beamforming of the bistatic data measured over a range of observation angles of $50 \leq \theta_o \leq 100$ deg for the frequency range of $2.75 < ka < 10.0$.

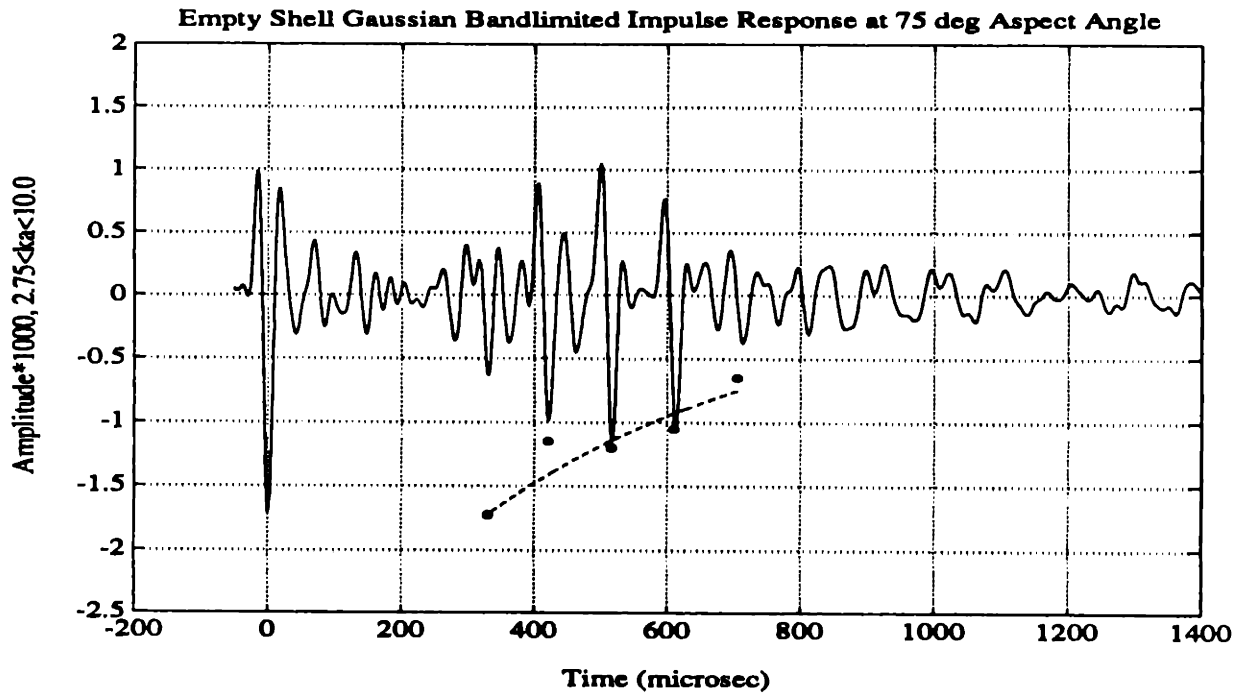

Figure 3.22: Gaussian Bandlimited Monostatic Impulse Response of the Empty Shell at an Aspect Angle of $\theta = 75\,\text{deg}$. The data are bandlimited over the frequency range of $2.75 < ka < 10.0$ and are shown for a distance of $r = 2\ m$ from the target center. The data labeled with a • correspond to the peak values measured at neighboring observation angles shown in Figure 3.17, while the dashed line results from an exponential fit of this data. The dashed line is believed to approximate the signal envelope that would have been observed if the measurement was conducted at a greater distance $R > 4\ m$. At a greater distance, the monostatic receiver would be located in the effective main lobes of the shear wave radiation.

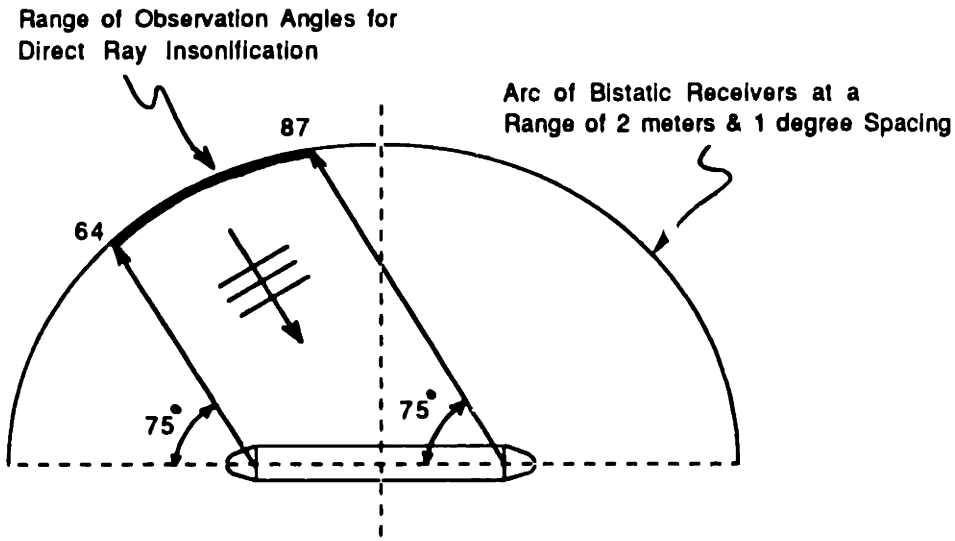

Figure 3.23: Illustration of Phase Matched, Back Directed Ray Paths for Insonification of the Shell at an Aspect Angle of 75 Degrees

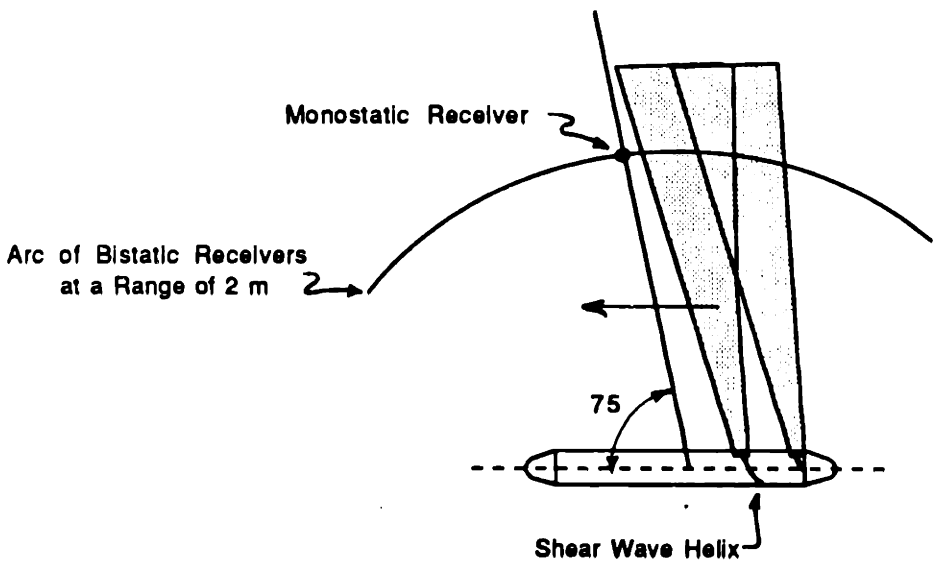

Figure 3.24: Illustration of the Origins of the Variation of Peak Shear Radiation Observed at Observation Angles Near the Monostatic Receiver. The localized shear wave field observed in Figure 3.19 produces a series of acoustic beams with main lobes that insonify different observation angles as the field moves down the axis of the shell.

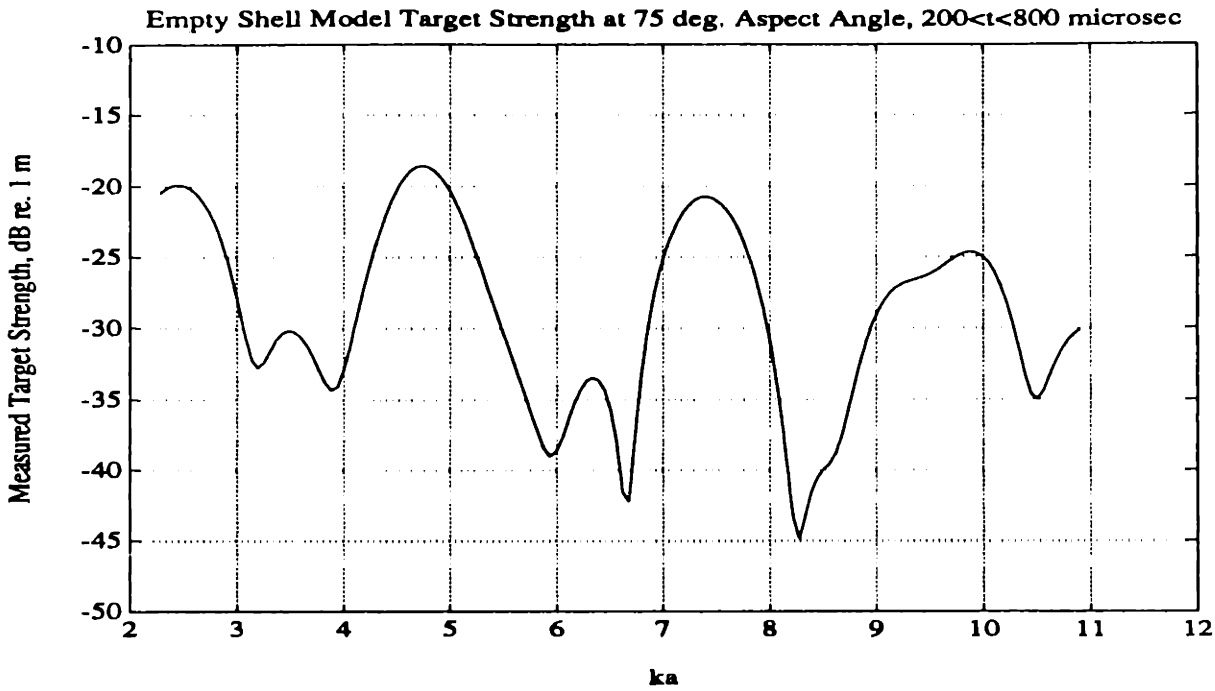

Figure 3.25: Target Strength of the Empty Shell Monostatic Signal Measured Over $200 < t < 800$ and an Aspect Angle of $\theta = 75$ deg. The transfer function shown has a Hamming window frequency resolution of $\Delta ka_{3dB} = 0.47$.

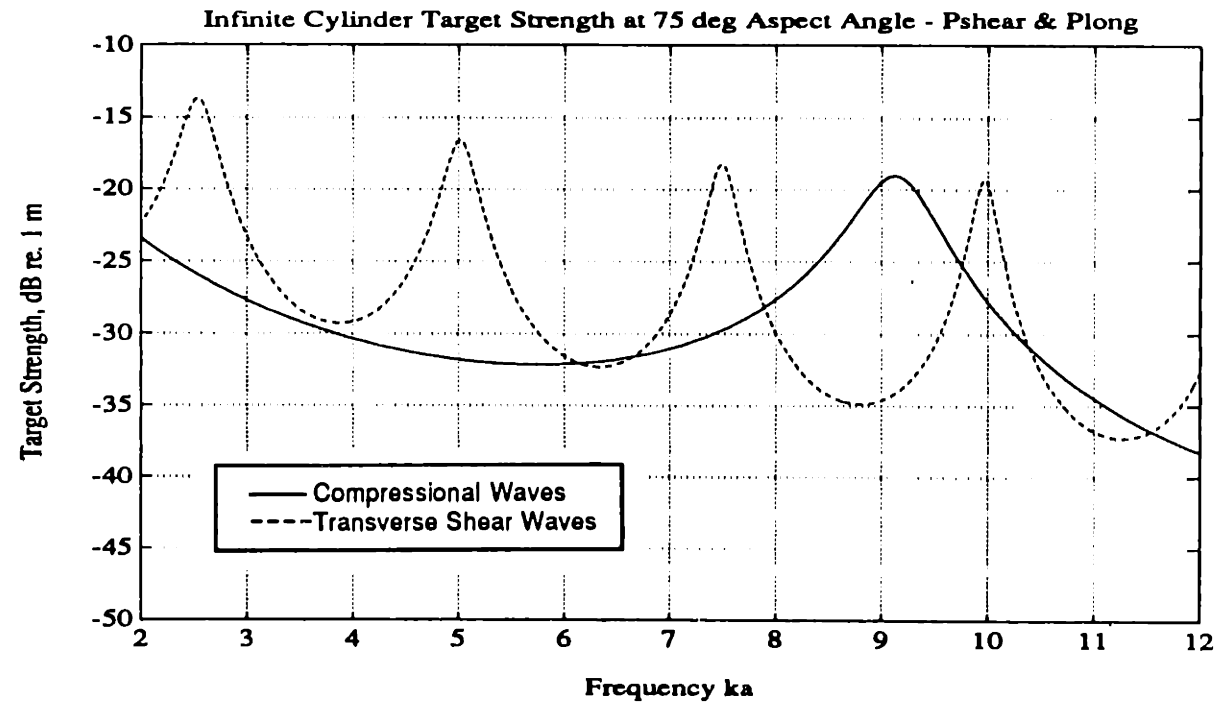

Figure 3.26: Magnitude of Shear and Compressional Leaky Wave Components of Specularly Directed Scattered Target Strength of an Infinite Cylinder at a $\theta = 75$ deg Aspect Angle

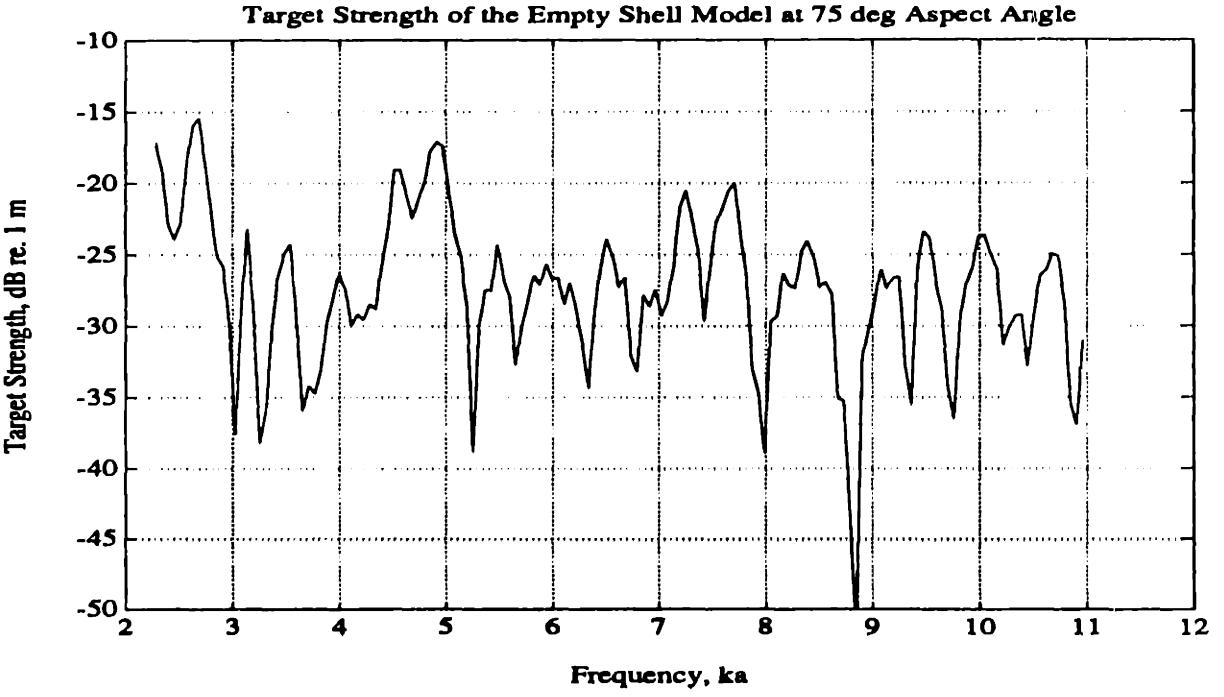

Figure 3.27: Target Strength of the Empty Shell Monostatic Signal Measured at an Aspect Angle of $\theta = 75\,\text{deg}$. The transfer function has a frequency resolution of $\Delta ka_{3dB} = 0.08$.

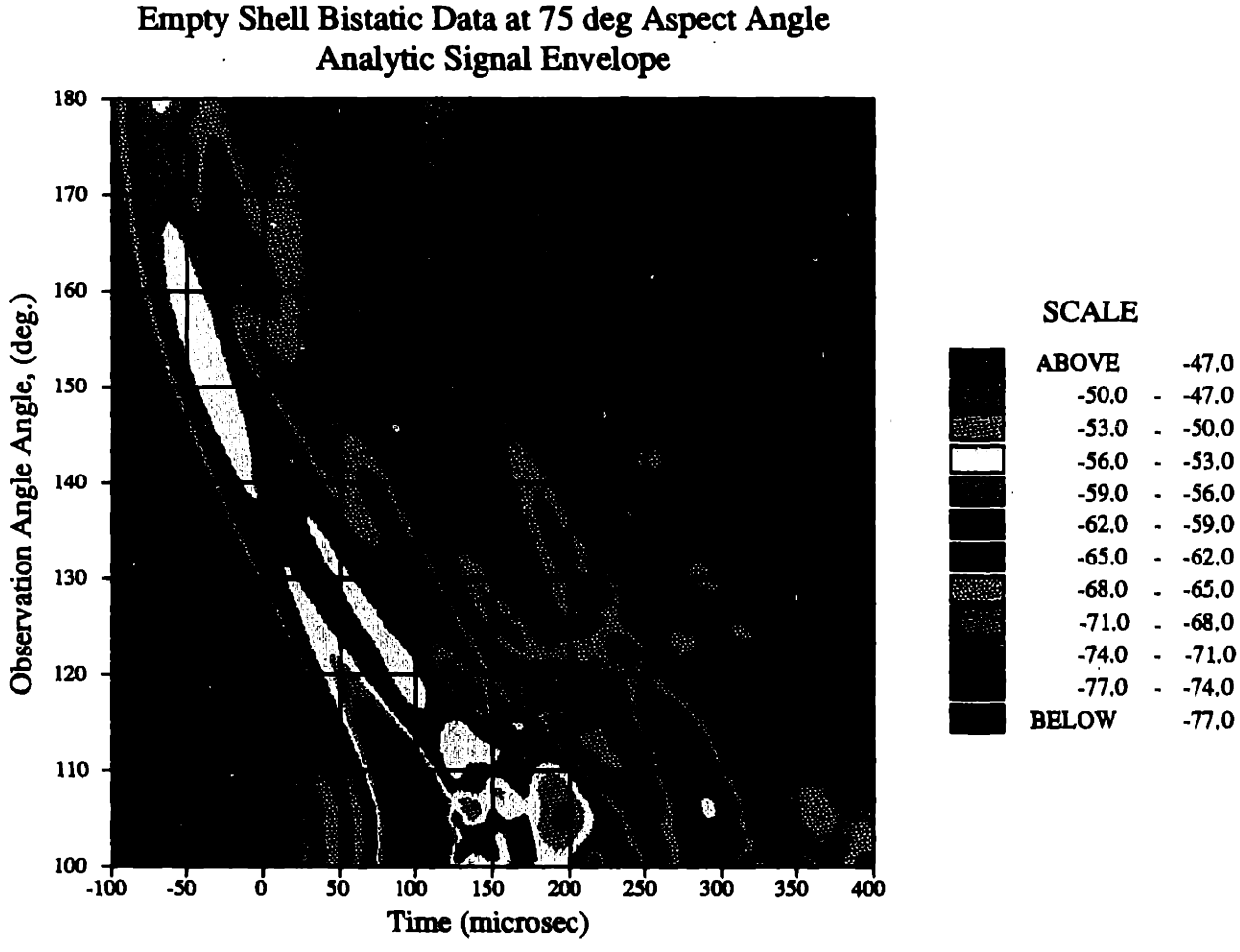

Figure 3.28: Analytic Signal Envelope of the Gaussian Bandlimited Bistatic Impulse Response of the Empty Shell at $r = 2\ m$ for $2.75 < ka < 10.0$ and Observation Angles $100 \leq \theta_o \leq 180$ deg. The time $t = 0$ refers to the time at which the peak initial monostatic return from the target was measured. The observation angle $\theta_o = 105$ corresponds to the specular direction.

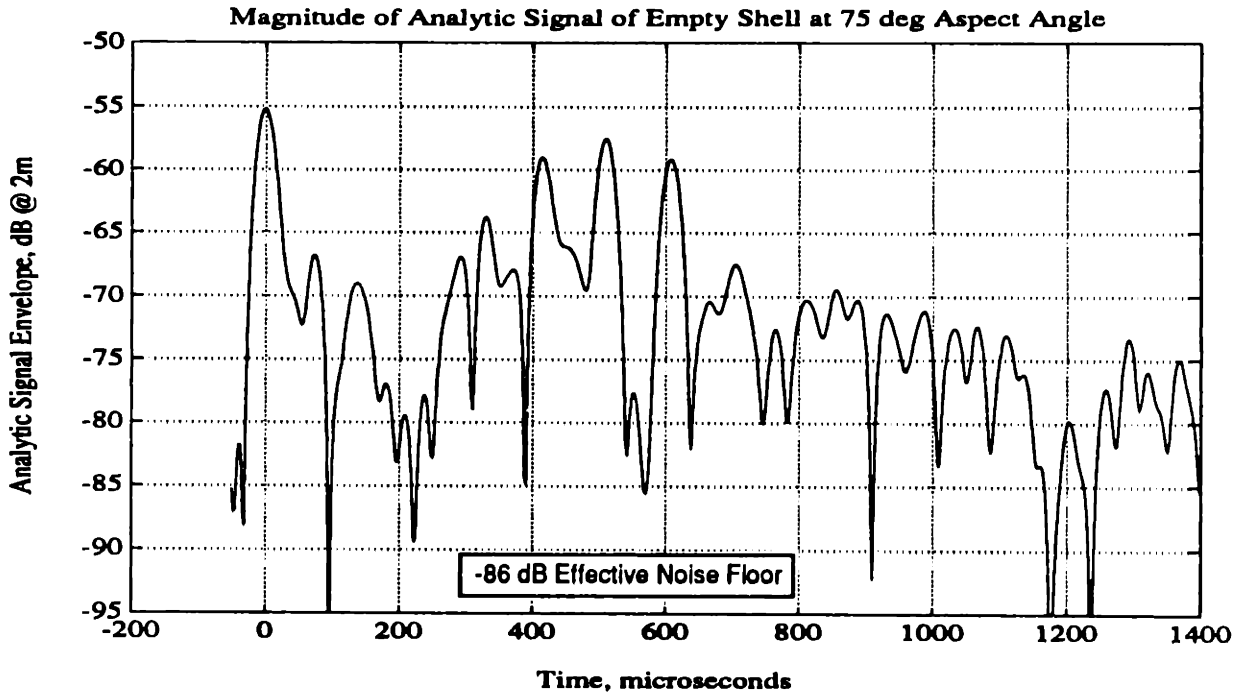

Figure 3.29: Magnitude of the Analytic Signal - Gaussian Bandlimited Time Domain Representation of the Empty Shell at an Aspect Angle of $\theta = 75$ deg for the Frequency Range of $2.75 < ka < 10.0$ and a Distance of $r = 2\ m$ from the Target Center

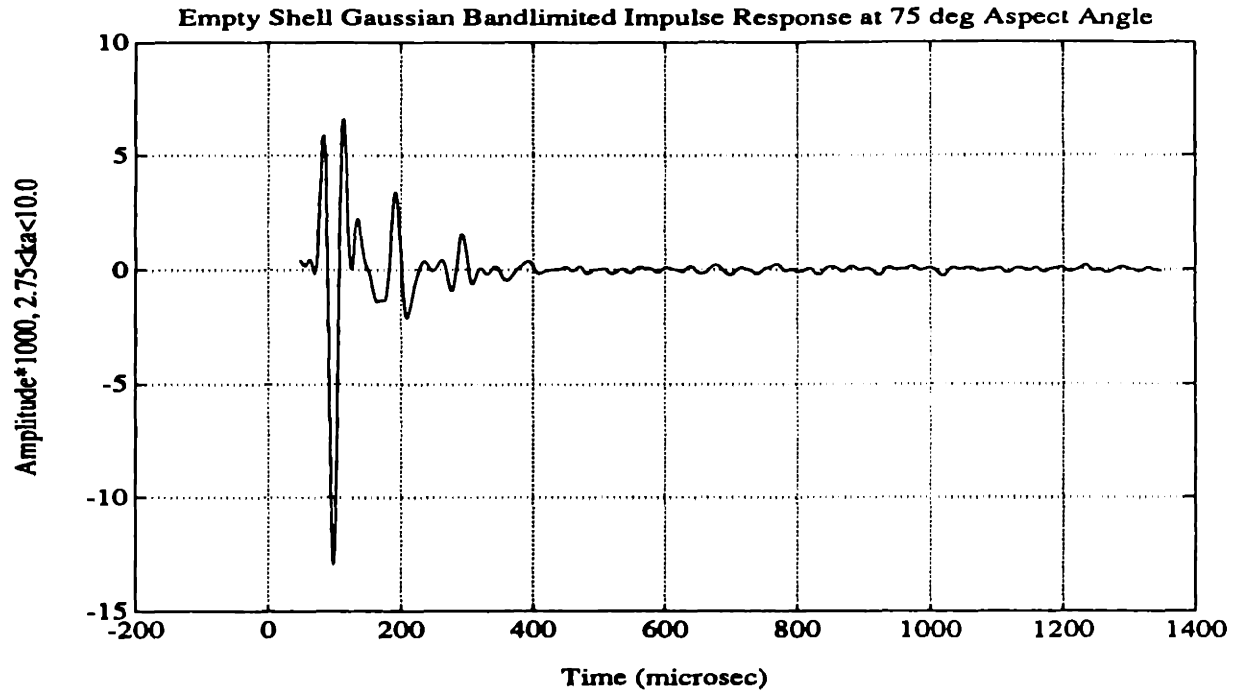

Figure 3.30: Gaussian Bandlimited Specularly Directed Impulse Response of the Empty Shell at an Aspect Angle of $\theta = 75$ deg for the Frequency Range of $2.75 < ka < 10.0$ and a Radial Distance of $r = 2\ m$ from the Target Center

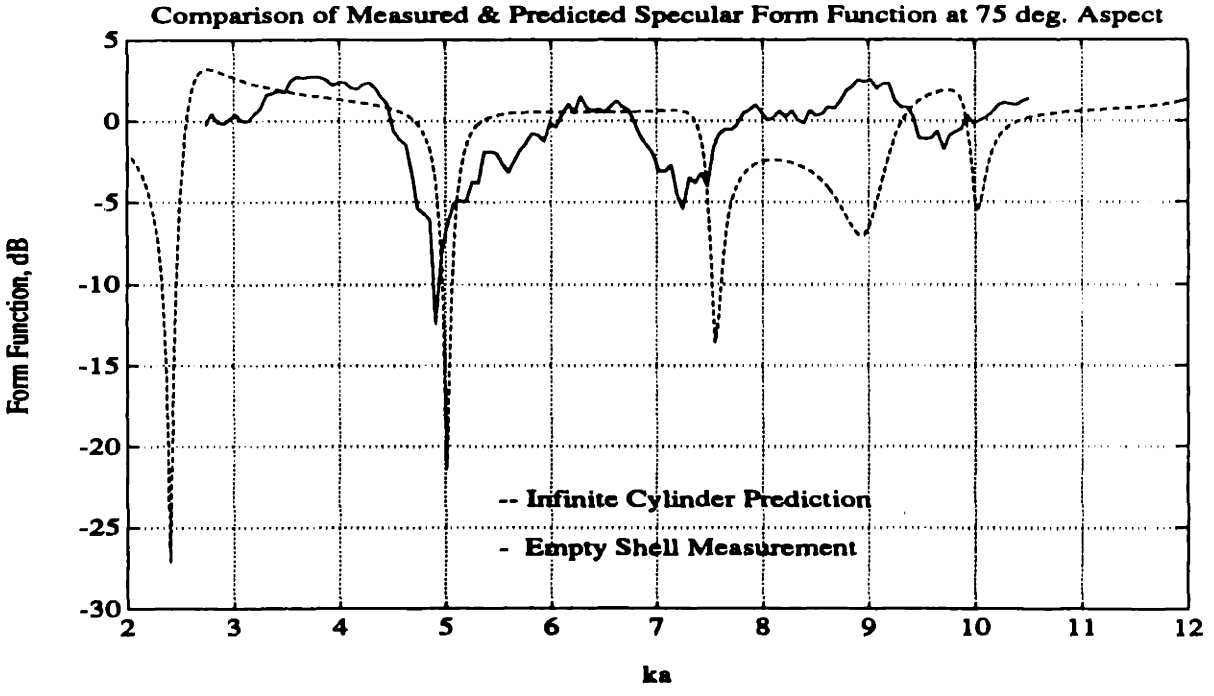

Figure 3.31: Comparison of the Measured Empty Shell and Infinite Cylinder Specularly Directed Form Functions for an Aspect Angle of 75 deg. The measured transfer function has a frequency resolution of $\Delta ka_{3dB} = 0.11$.

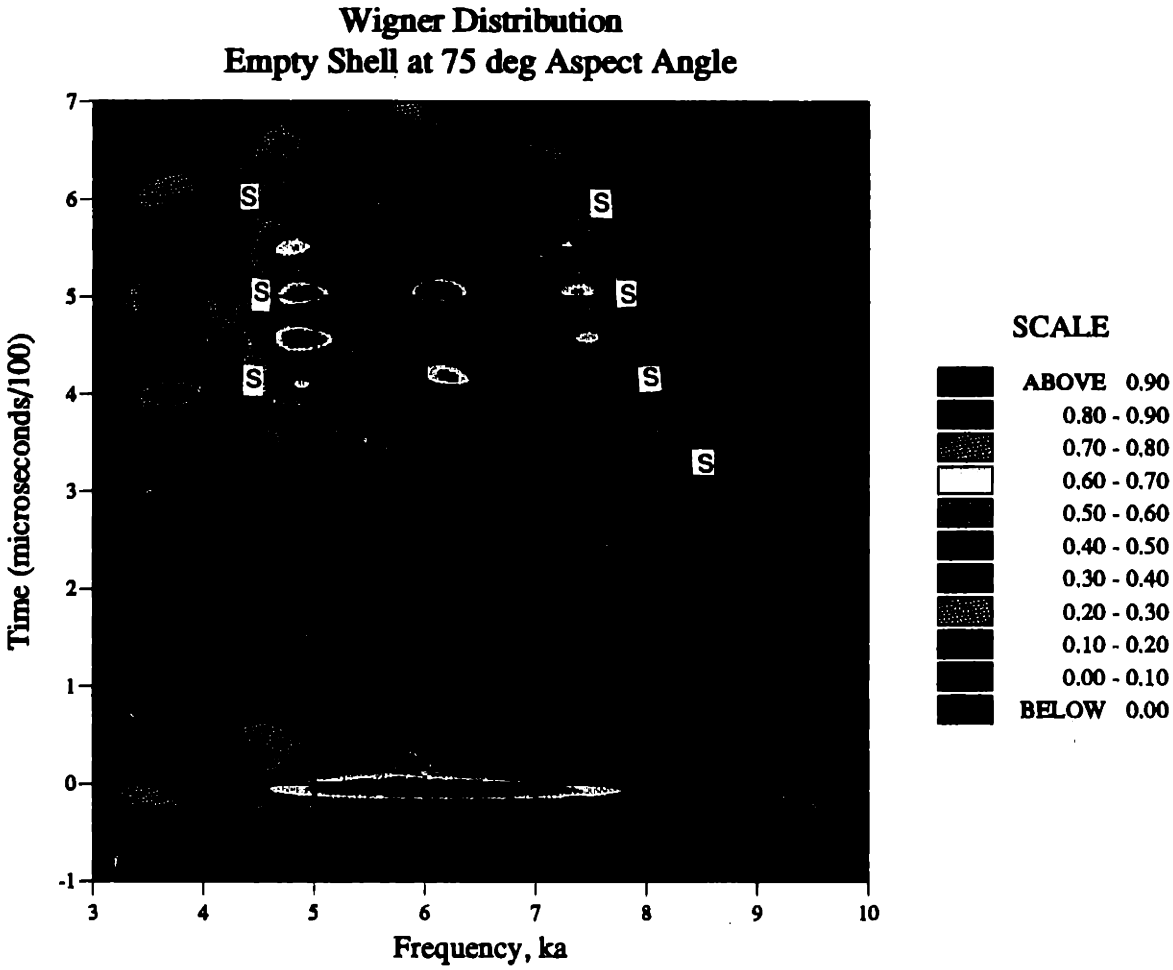

Figure 3.32: Smoothed Wigner Distribution of the Gaussian Bandlimited Monostatic Impulse Response of the Empty Shell at an Aspect Angle of $\theta = 75$ deg, Frequency Range of $2.75 < ka < 11.7$, and a Distance of $r = 2\ m$ from the Target Center. The smoothing was performed with a Gaussian function with $\sigma_t = 6\ \mu sec$ and $\sigma_{ka} = 0.17$. The broadband initial return is seen at $t = 0$. The periodic leaky wave radiation observed at later times near $ka = 5$ and $ka = 7.5$ is labeled with an "s" to distinguish it from signal processing artifacts.

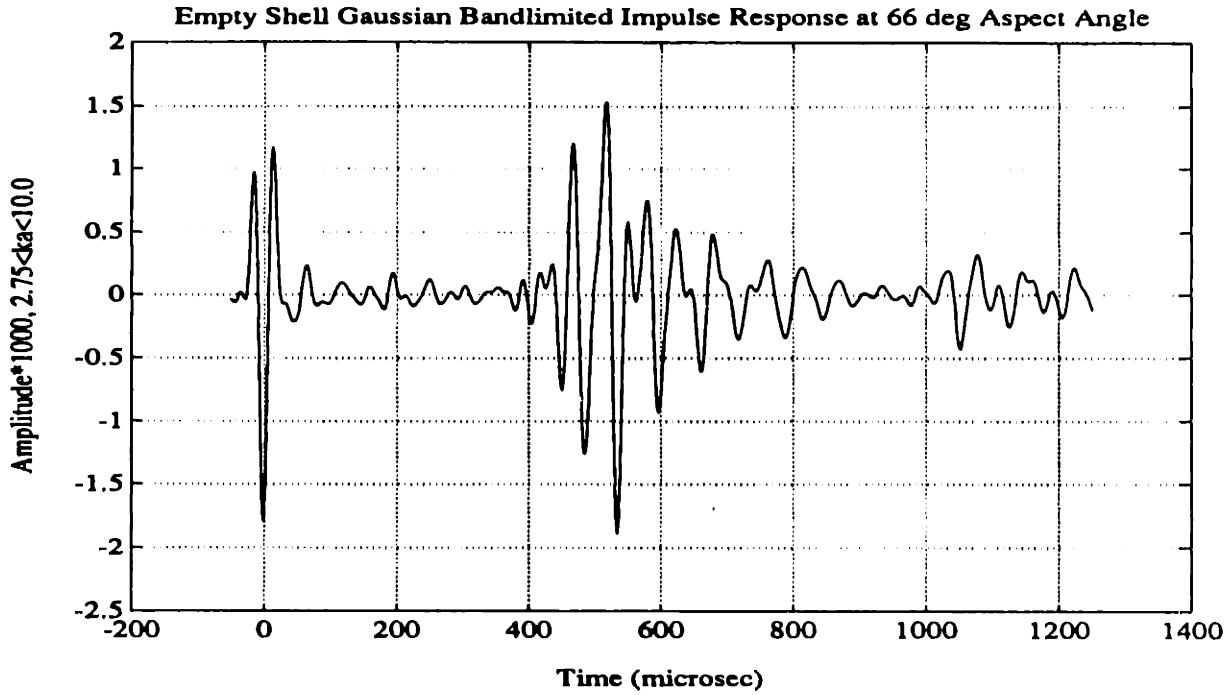

Figure 3.33: Gaussian Bandlimited Monostatic Impulse Response of the Empty Shell at an Aspect Angle of $\theta = 66$ deg for the Frequency Range of $2.75 < ka < 10.0$ and a Radial Distance of $r = 2\ m$ from the Target Center

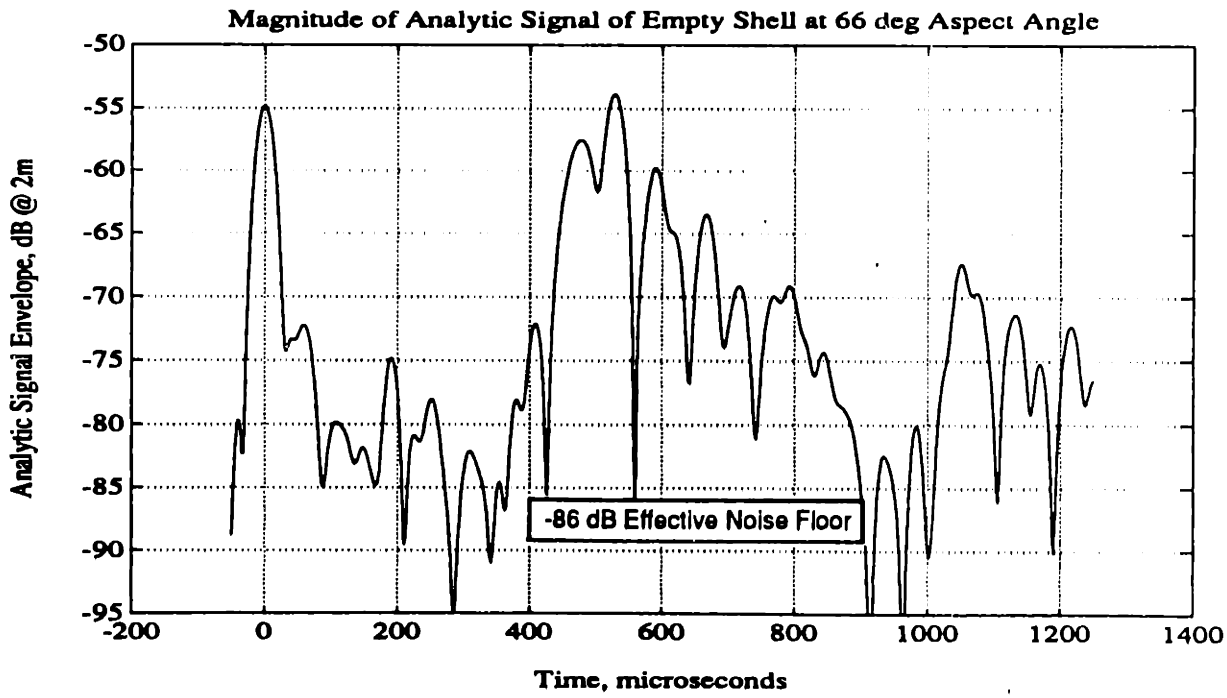

Figure 3.34: Magnitude of the Analytic Signal - Gaussian Bandlimited Time Domain Representation of the Empty Shell at an Aspect Angle of $\theta = 66$ deg for the Frequency Range of $2.75 < ka < 10.0$ and a Distance of $r = 2\ m$ from the Target Center

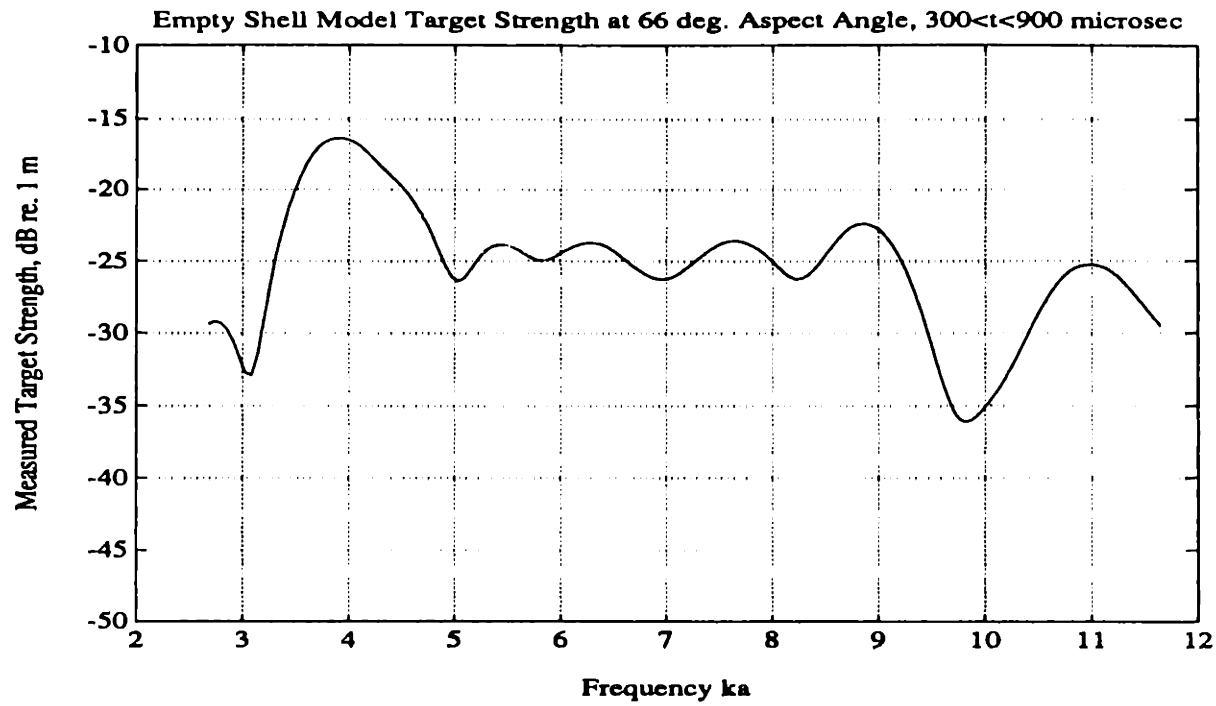

Figure 3.35: Target Strength of the Empty Shell Monostatic Signal Measured Over the duration $300 < t < 900$ μsec and an Aspect Angle of $\theta = 66$ deg. The transfer Function shown has a Hamming window frequency resolution of $\Delta ka_{3dB} = 0.47$.

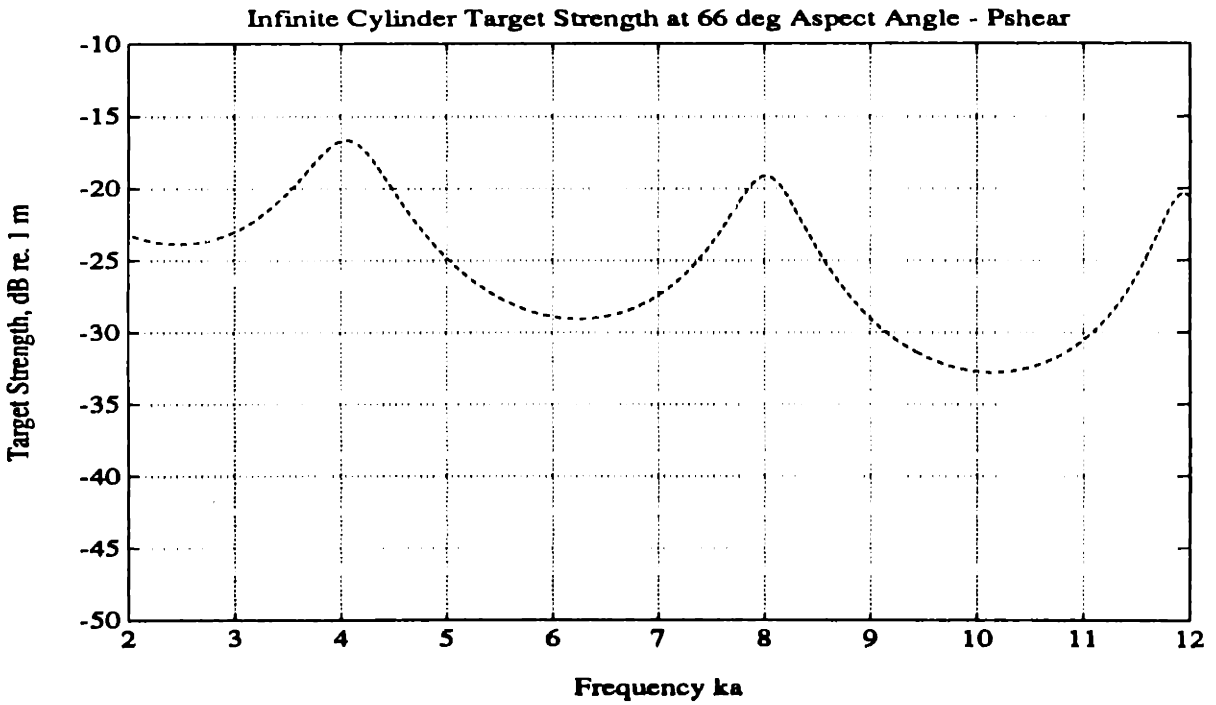

Figure 3.36: Magnitude of Transverse Shear Leaky Wave Component of Specularly Directed Scattered Target Strength of an Infinite Cylinder at $\theta = 66$ deg Aspect Angle

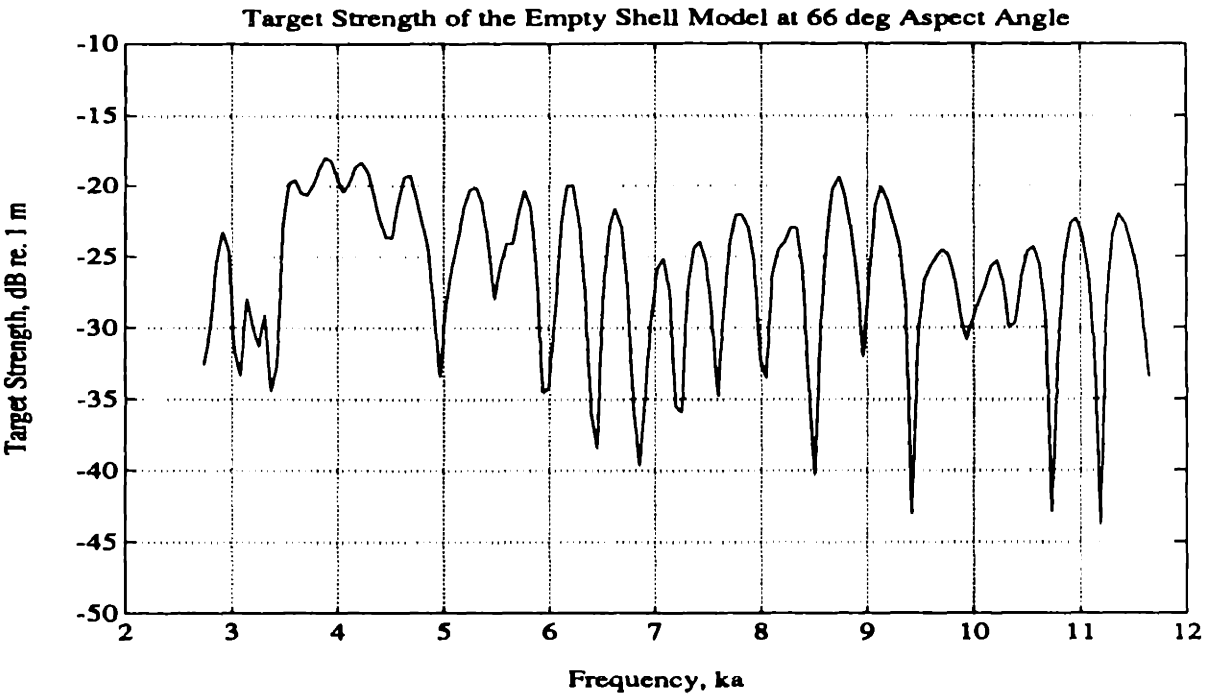

Figure 3.37: Target Strength of the Empty Shell Monostatic Signal Measured at an Aspect Angle of $\theta = 66\,\text{deg}$. The transfer function has a frequency resolution of $\Delta ka_{3dB} = 0.13$.

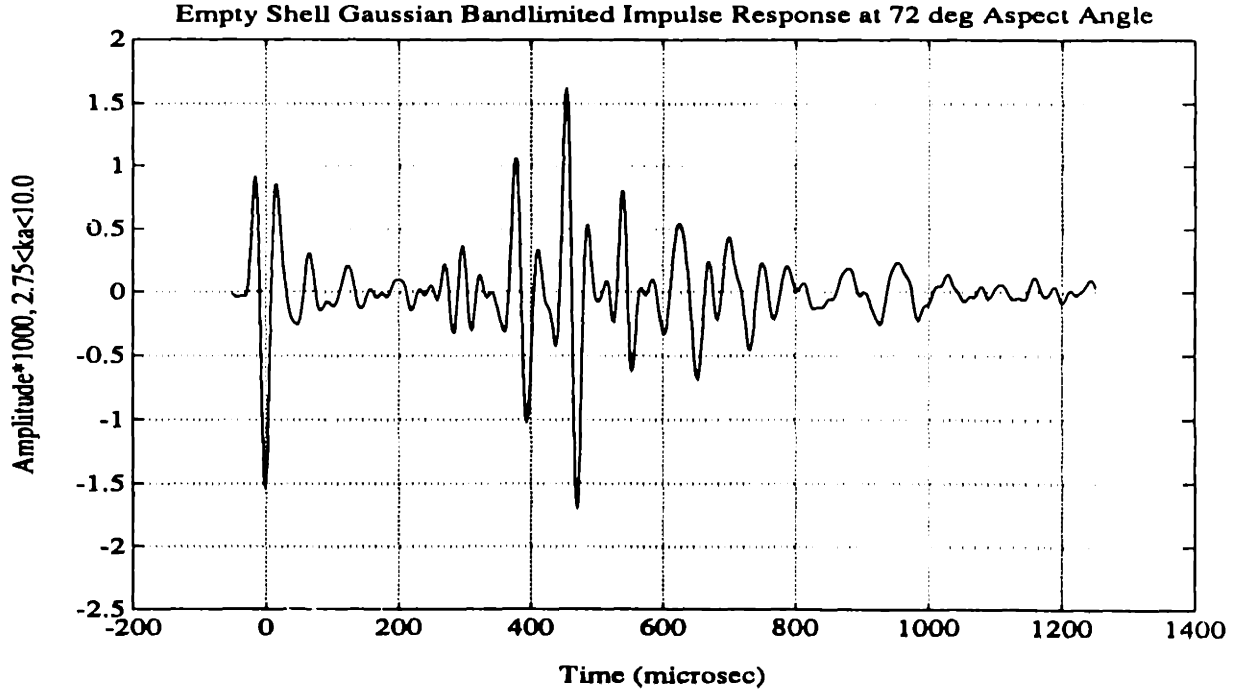

Figure 3.38: Gaussian Bandlimited Monostatic Impulse Response of the Empty Shell at an Aspect Angle of $\theta = 72\,\text{deg}$ for the Frequency Range of $2.75 < ka < 10.0$ and a Radial Distance of $r = 2\ m$ from the Target Center

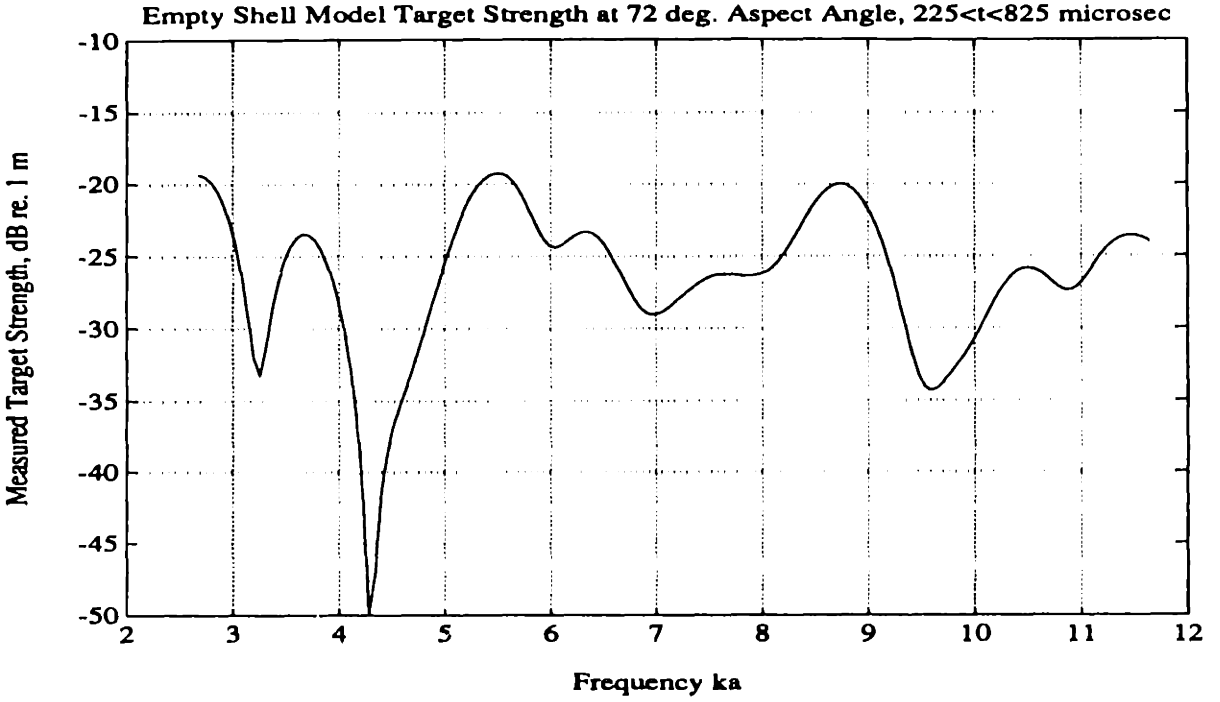

Figure 3.39: Target Strength of the Empty Shell Monostatic Signal Measured Over the Duration $225 < t < 825$ μsec and an Aspect Angle of $\theta = 72$ deg. The transfer function shown has a Hamming window frequency resolution of $\Delta ka_{3dB} = 0.47$.

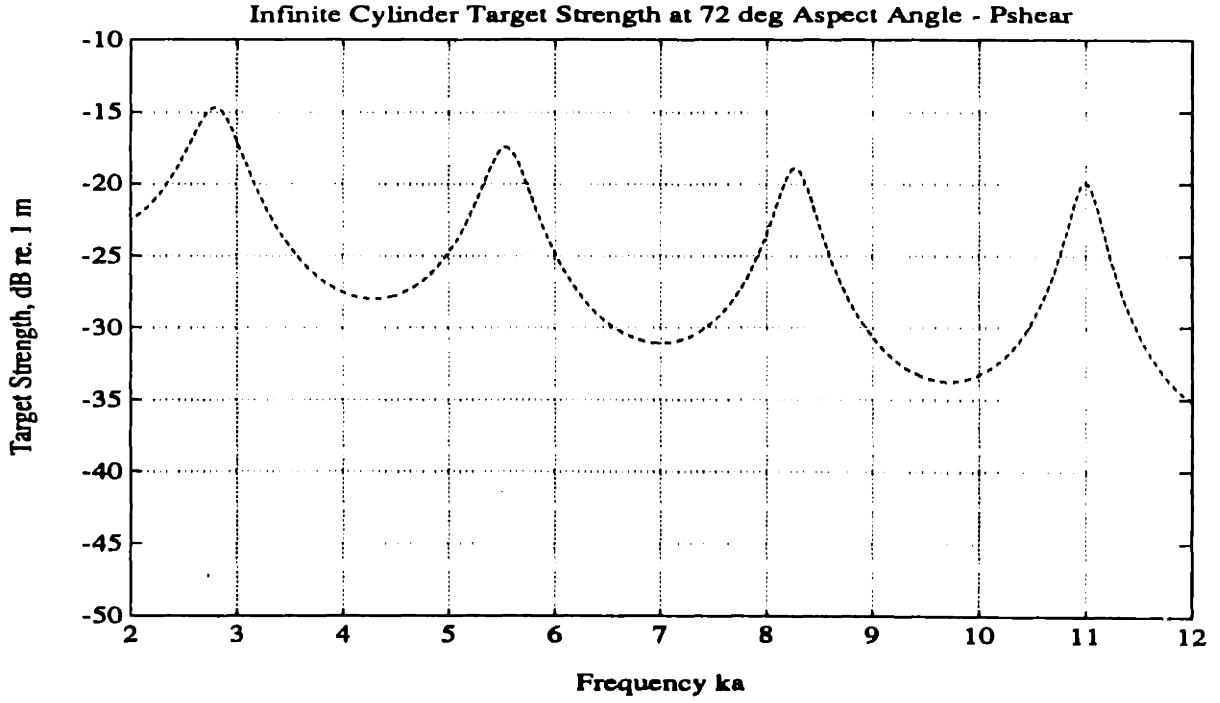

Figure 3.40: Magnitude of Transverse Shear Leaky Wave Component of Specularly Directed Target Strength of an Infinite Cylinder at $\theta = 72$ deg Aspect Angle

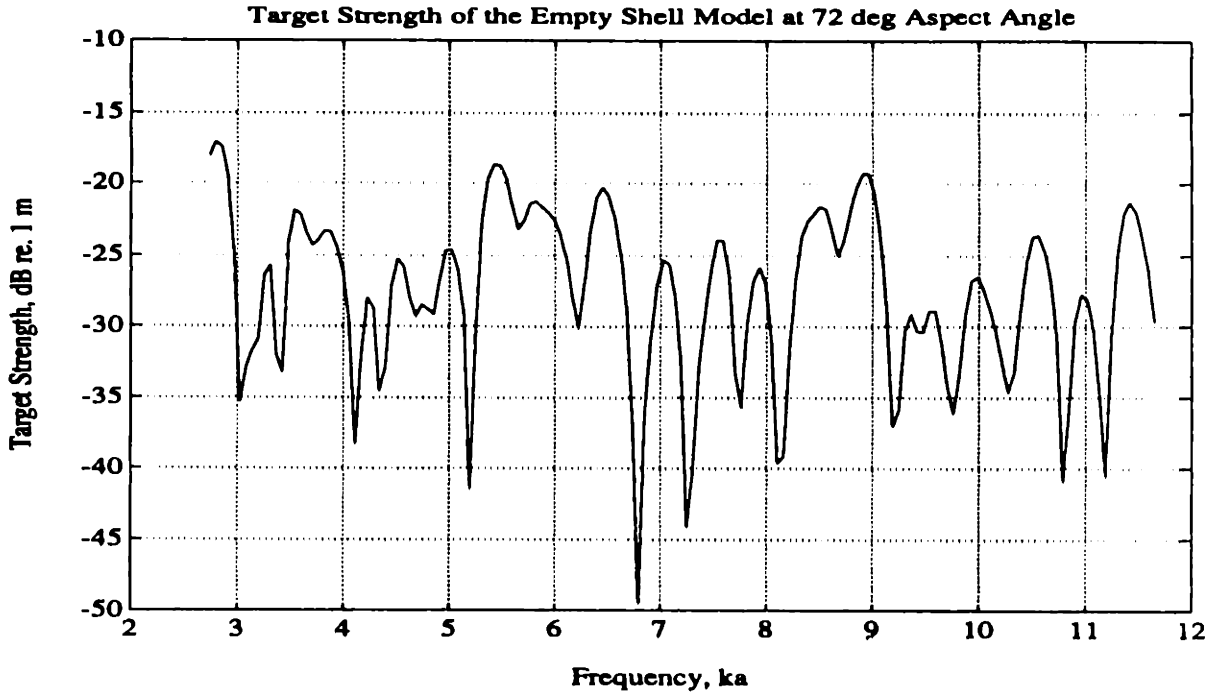

Figure 3.41: Target Strength of the Empty Shell Monostatic Signal Measured at an Aspect Angle of $\theta = 72\,\text{deg}$. The transfer function has a frequency resolution of $\Delta ka_{3dB} = 0.14$.

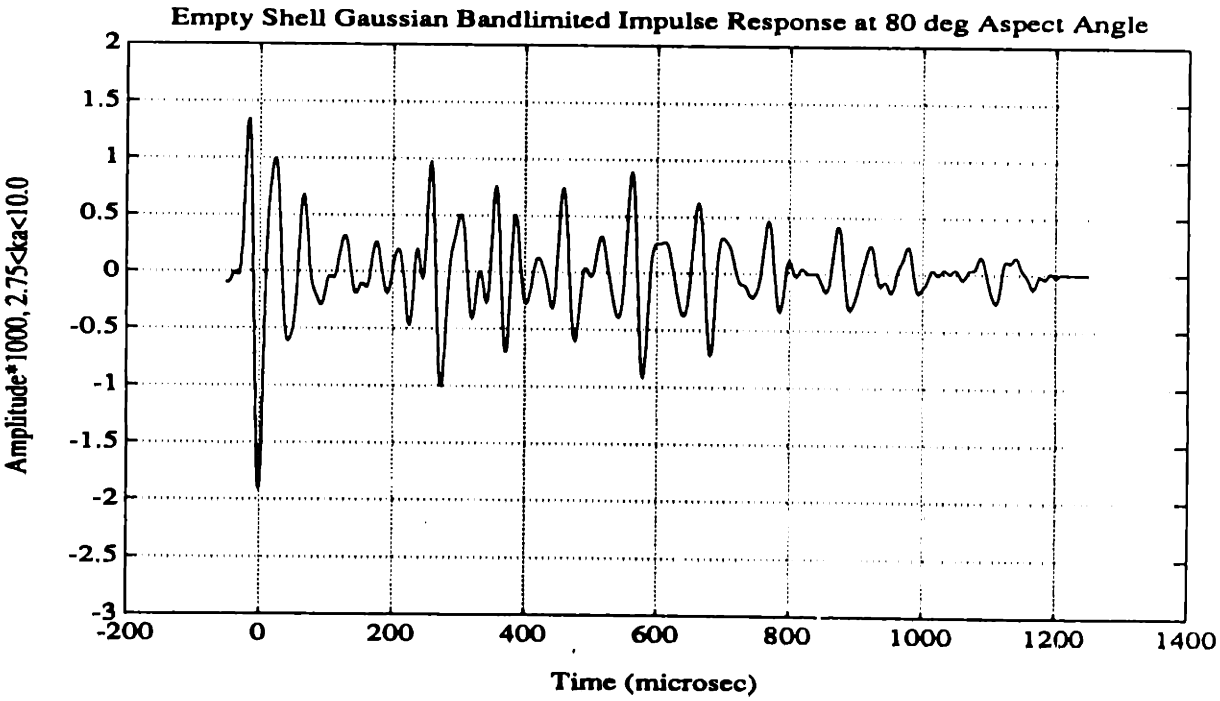

Figure 3.42: Gaussian Bandlimited Monostatic Impulse Response of the Empty Shell at an Aspect Angle of $\theta = 80\,\text{deg}$ for the Frequency Range of $2.75 < ka < 10.0$ and a Radial Distance of $r = 2\ m$ from the Target Center

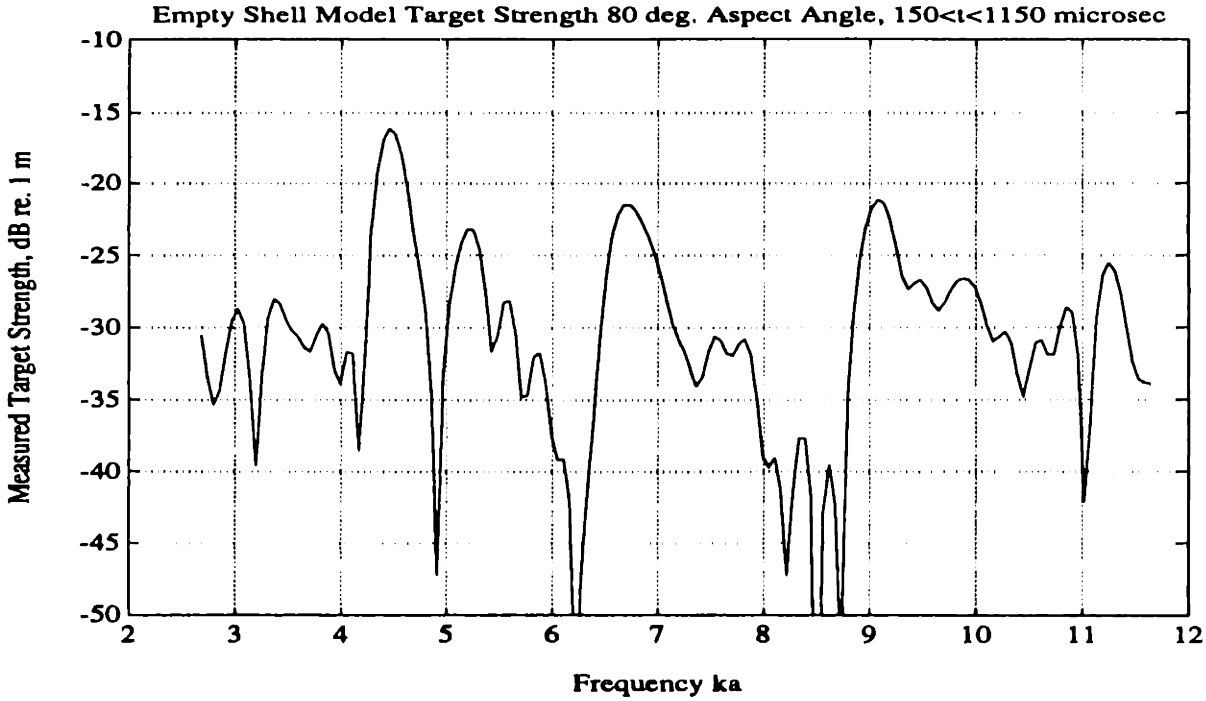

Figure 3.43: Target Strength of the Empty Shell Monostatic Signal Measured Over the Duration $150 < t < 1150$ μsec and an Aspect Angle of $\theta = 80$ deg. The transfer function shown has a Rectangular/Hanning window frequency resolution of $\Delta ka_{3dB} = 0.20$.

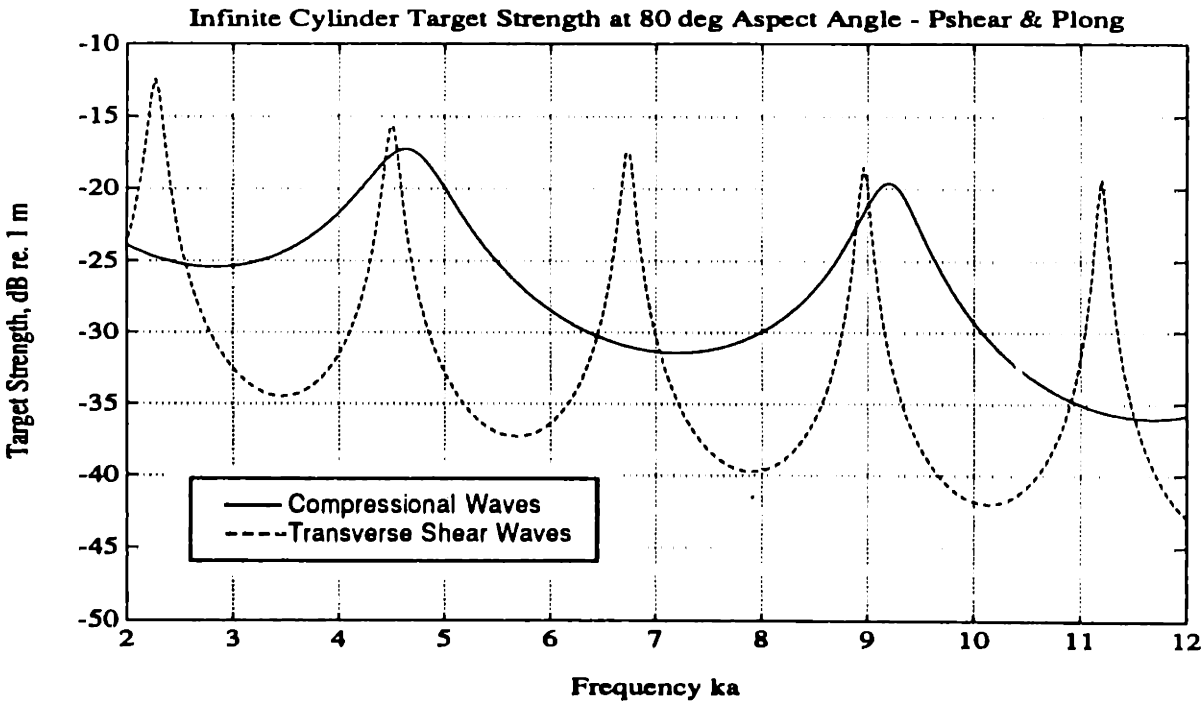

Figure 3.44: Magnitude of Shear and Compressional Leaky Wave Components of Specularly Directed Target Strength of an Infinite Cylinder at an $\theta = 80$ deg Aspect Angle

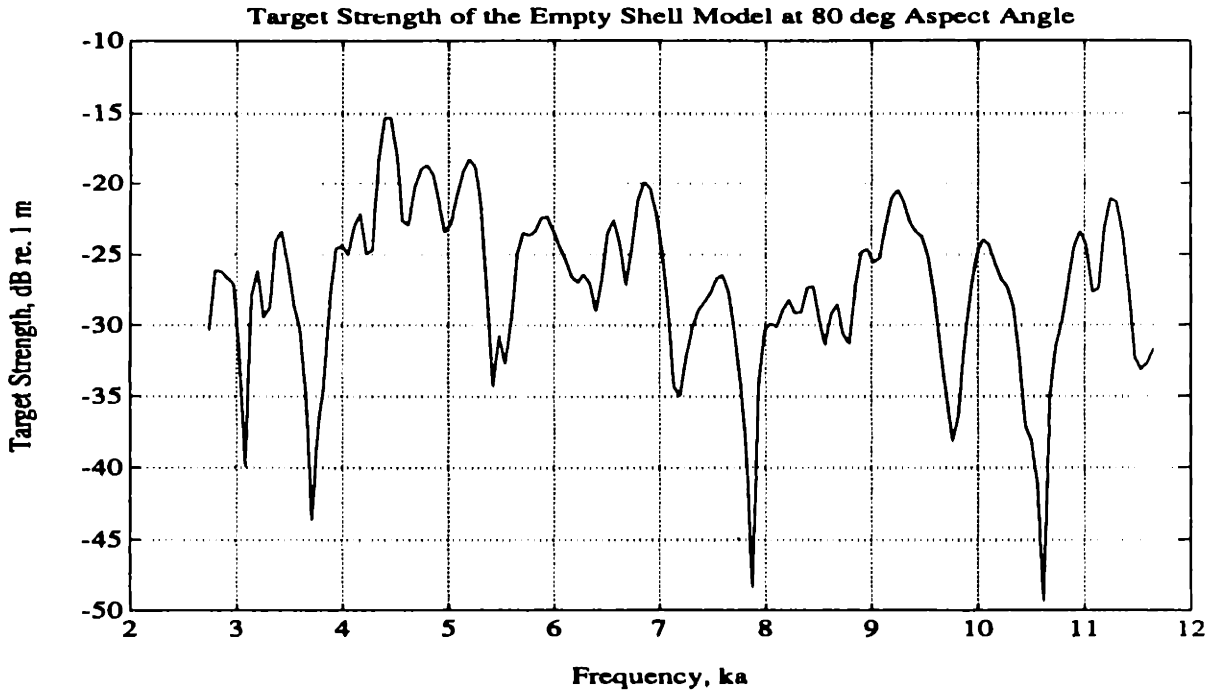

Figure 3.45: Target Strength of the Empty Shell Monostatic Signal Measured at an Aspect Angle of $\theta = 80\,\text{deg}$. The transfer function has a frequency resolution of $\Delta ka_{3dB} = 0.15$.

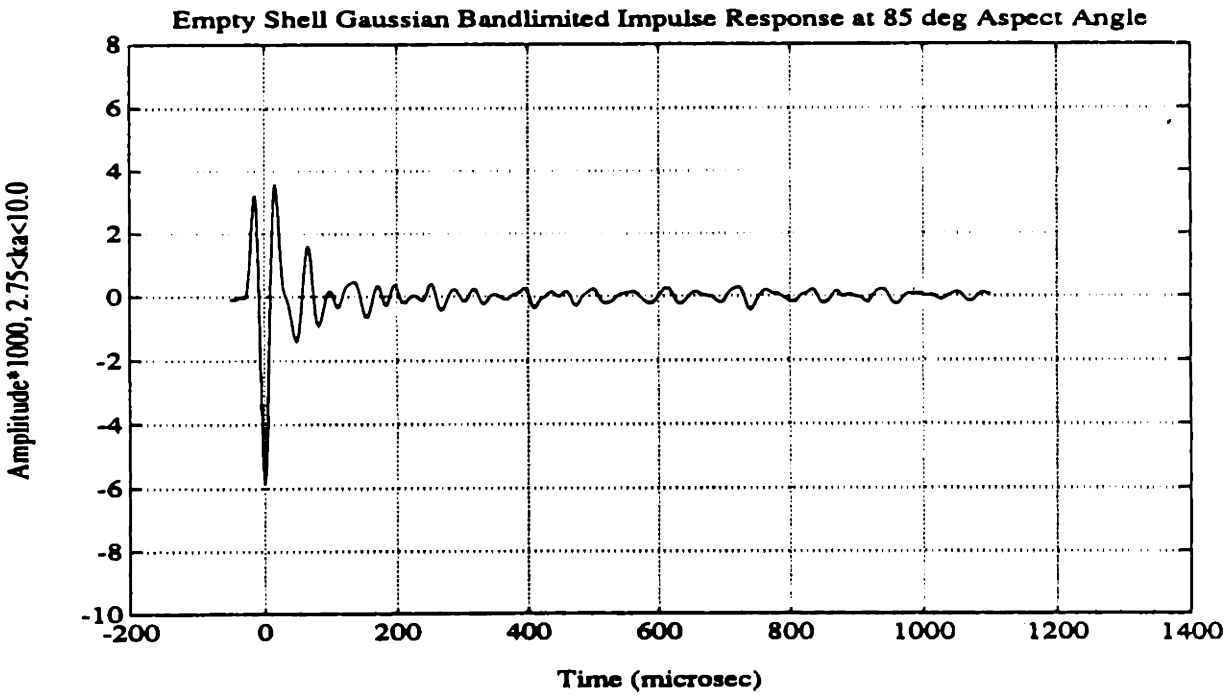

Figure 3.46: Gaussian Bandlimited Monostatic Impulse Response of the Empty Shell at an Aspect Angle of $\theta = 85\,\text{deg}$ for the Frequency Range of $2.75 < ka < 10.0$ and a Radial Distance of $r = 2\ m$ from the Target Center

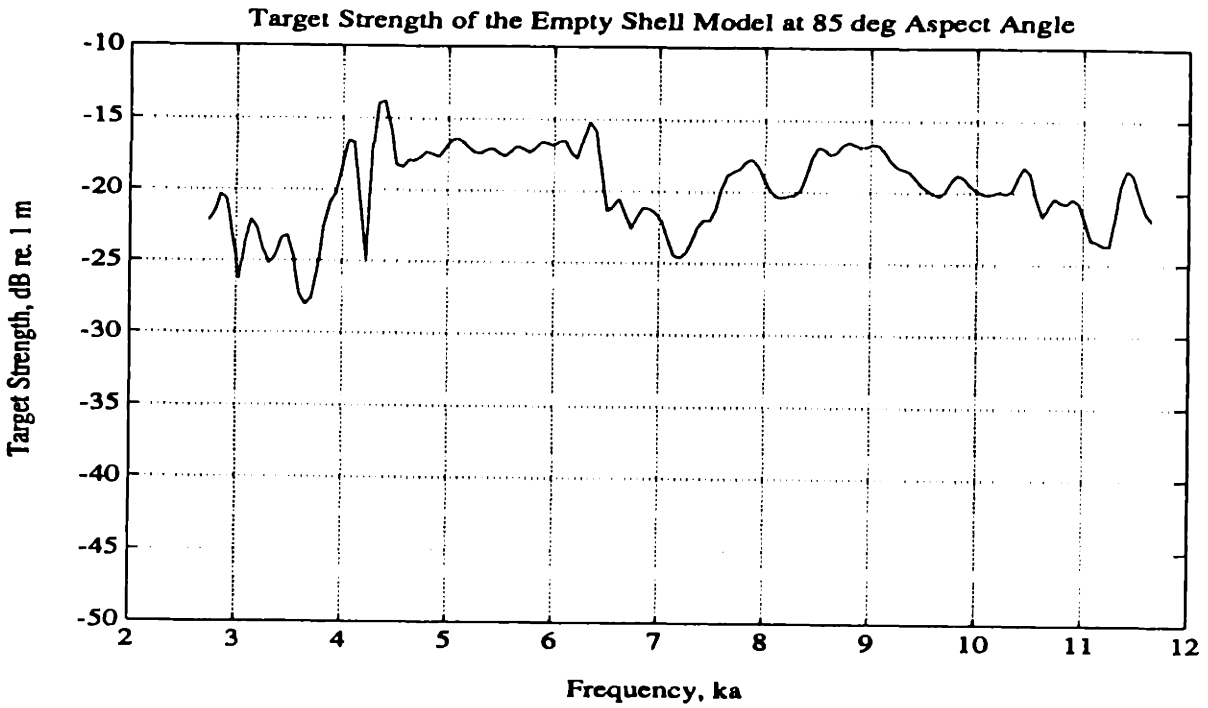

Figure 3.47: Target Strength of the Empty Shell Monostatic Signal Measured at an Aspect Angle of $\theta = 85\,\text{deg}$. The transfer function has a frequency resolution of $\Delta ka_{3dB} = 0.16$.

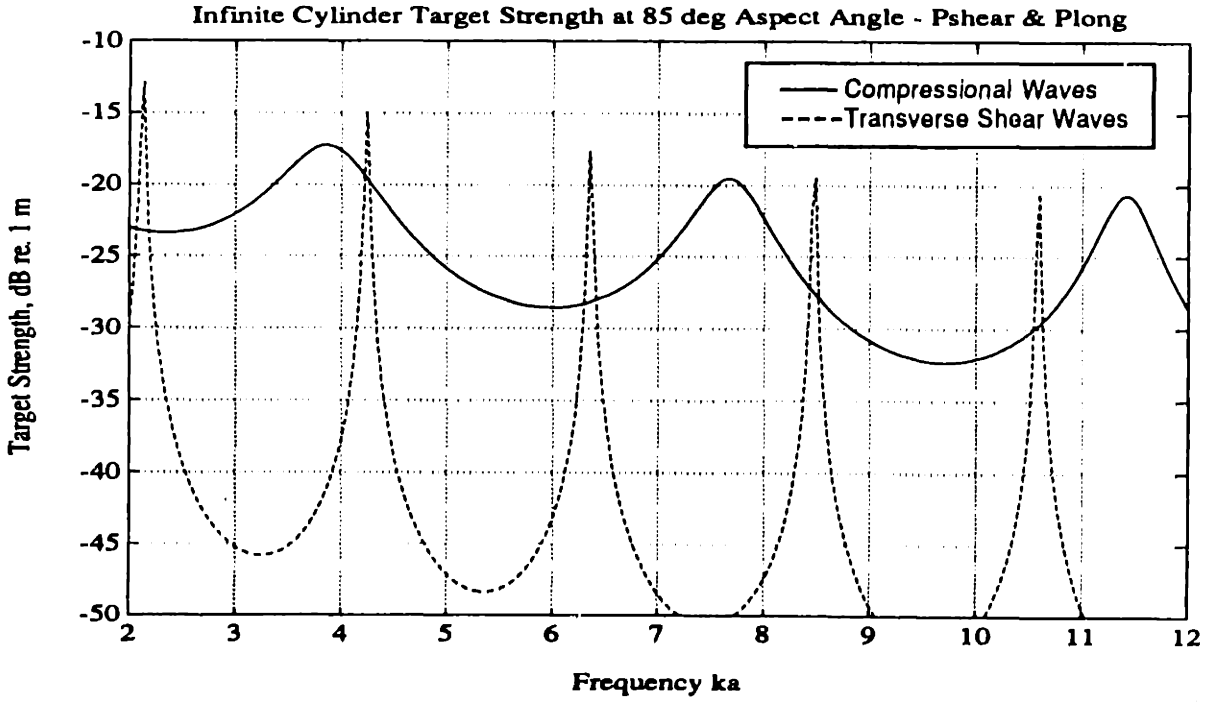

Figure 3.48: Magnitude of Shear and Compressional Leaky Wave Components of Specularly Directed Target Strength of an Infinite Cylinder at $\theta = 85\,\text{deg}$ Aspect Angle

Chapter 4

Scattering of a Structural Wave at a Ring

4.1 Introduction

The stiffeners used in the designs of the ring stiffened and complex shells each represent a means of scattering energy from an incident structural wave to the surrounding fluid and to other structural wave types. In this chapter, I use asymptotic methods to estimate the scattered pressure and the reflection and transmission coefficients generated by the interaction of a given structural wave type with a simplified model of an individual ring. The coupling of shear, compressional, and flexural waves, as well as the fluid loading of the surrounding medium, is incorporated in the analyses.

The ring is modeled as an eccentric continuum of mass of fixed cross section with 1 rotational, and 3 translational degrees of freedom. The ring of mass is located at a discrete axial location ($z = 0$) on an infinite cylinder as shown in Figure 4.1. The elastic properties of the ring are neglected. Admittedly, this is an inaccurate description of the actual dynamics of the ring stiffeners. In particular, I suspect that the inaccuracies associated with this model are greatest near the ring frequency of the shell where compressional wave propagation would be well accommodated in both the shell and the ring. However, the rings are each 10.4 x 12.7 mm in cross section

and represent a significant mass loading of the shell which has a thickness of only 0.53 mm. I believe that at worst, the analyses provide order of magnitude estimates of the scattering behavior. Moreover, the rigorous asymptotic formulation I employ provides a formalism that can be readily adapted with further work to incorporate more accurate descriptions of the dynamics of the ring.

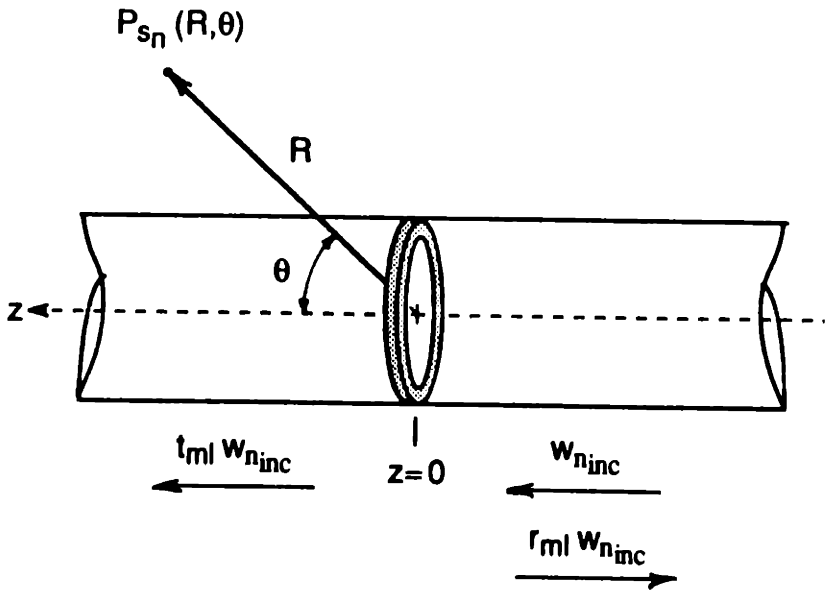

Figure 4.1: Illustration of the Orientation of the Ring Stiffener and the Coordinate System Used to Determine the Scattered Pressure

The method of analysis I employ is adapted from the work of Guo [27] who estimated the scattered pressure produced by the interaction of an elastic disc and an infinite cylindrical shell with plane wave acoustic insonification. I begin with a derivation of the displacement field produced by a ring of forces and moments of arbitrary amplitude that are applied at a discrete axial location along the shell. The equations of motion of the eccentric ring of mass are then presented and used to solve for the forces and moments produced by the interaction of the shell and ring. Given these forces and moments, I then formulate the stationary phase approximation for the scattered pressure and use residue theory to estimate the structural wave reflection and transmission coefficients associated with the radial displacement of the shell. Throughout these analyses, I consider the scattering produced at the ring

by an incident time harmonic structural wave with a fixed integer order azimuthal dependence $e^{in\phi}$. As in Chapter 2, the harmonic time dependence $e^{-i\omega t}$, as well as the azimuthal dependence, is suppressed in the equations that follow.

The asymptotic methods of analysis I use incorporate additional approximations which, with some exceptions, are relatively unimportant and consist of the following:

- I again make use of Donnell's thin shell theory to describe the equations of motion of the shell.

- I compute the reflection and transmission coefficients, and the scattered pressure produced by the interaction of an incident free shear, compressional, or flexural wave with the ring of mass. Use of an incident free wave provided a convenient means of isolating the coupling coefficients associated with the different wave types supported by thin shell theory. However, a more physical realization of the problem would consider the incident field to be generated by a prescribed ring of force, an incident plane wave, or a discrete drive point.

- The method of stationary phase is used to quantify the scattered pressure produced by the interaction of the incident structural wave and the ring. This is a far field, high frequency approximation as noted before in Chapter 2. Once again, I do not incorporate corrections to account for the proximity of a pole to the steepest descent path. Improved accuracy would require modifications similar to those derived by Rumerman [49], as adapted from the work of Felsen and Marcuvitz [22], for the plane wave scattering problem. I compute the scattered pressure in the far field at a location orientated perpendicular to the axis of the shell. With this orientation, the stationary phase approximation is inaccurate near the cut-off frequencies of the different wave types of a given mode n. These effects will be covered in more detail in the discussions that follow.

- The reflection and transmission coefficients are calculated using the sum of the residues that quantify the radial displacement at the poles associated with the

three different wave types. I do not compute the contribution of the branch cut which represents the scattered contribution to the spectral wavenumber continuum.

4.2 Interaction of the Ring and Shell

4.2.1 Displacements of the Shell

The displacements of the shell that are induced by the interaction of the incident structural wave with the ring stiffener are defined by the forced version of the Donnell equations shown below:

$$\frac{\partial^2 u}{\partial z^2} + \frac{1-\nu}{2a^2}\frac{\partial^2 u}{\partial \phi^2} + \frac{1+\nu}{2a}\frac{\partial^2 \vartheta}{\partial z \partial \phi} + \frac{\nu}{a}\frac{\partial w}{\partial z} - \frac{1}{c_p^2}\frac{\partial^2 u}{\partial t^2} = \frac{-f_z}{c_p^2 h \rho_s} \tag{4.1}$$

$$\frac{1+\nu}{2a}\frac{\partial^2 u}{\partial z \partial \phi} + \frac{1-\nu}{2}\frac{\partial^2 u}{\partial z^2} + \frac{1}{a^2}\frac{\partial^2 \vartheta}{\partial \phi^2} + \frac{1}{a^2}\frac{\partial w}{\partial \phi} - \frac{1}{c_p^2}\frac{\partial^2 \vartheta}{\partial t^2} = \frac{-f_\phi}{c_p^2 h \rho_s} \tag{4.2}$$

$$\frac{\nu}{a}\frac{\partial u}{\partial z} + \frac{1}{a^2}\frac{\partial \vartheta}{\partial \phi} + \frac{w}{a^2} + \beta^2\left(a^2\frac{\partial^4 w}{\partial z^4} + 2\frac{\partial^4 w}{\partial z^2 \partial \phi^2} + \frac{1}{a^2}\frac{\partial^4 w}{\partial \phi^4}\right) + \frac{1}{c_p^2}\frac{\partial^2 \vartheta}{\partial t^2} = \frac{f_r - p_s}{c_p^2 h \rho_s} \tag{4.3}$$

Forces and moments of the same azimuthal dependence as the incident structural wave are imparted on the shell at the discrete axial location $z = 0$ and can be expressed as

$$\begin{aligned} f_{z_n} &= F_{z_n}\delta(z) \\ f_{\phi_n} &= F_{\phi_n}\delta(z) \\ f_{r_n} &= F_{r_n}\delta(z) + M_n\delta'(z) \end{aligned} \tag{4.4}$$

I first solve for the displacements in the axial wavenumber domain and make use of the spatial transform pair

$$\hat{f}_n(k_z) = \int_{-\infty}^{\infty} f_n(z) e^{-ik_z z} dz \tag{4.5}$$

$$f_n(z) = \frac{1}{2\pi} \int_{-\infty}^{\infty} \hat{f}_n(k_z) e^{ik_z z} dk_z \tag{4.6}$$

Applying the forward spatial transform of equation 4.5 to the equations of motion yields the following relations for the transform shell displacement variables $\hat{u}_n$, $\hat{\vartheta}_n$ and $\hat{w}_n$

$$\left[\Omega^2 - \alpha^2 - \frac{1-\nu}{2} n^2 - \Omega^2\right] \hat{u}_n - \frac{1+\nu}{2} n\alpha \, \hat{\vartheta}_n + i\nu\alpha \, \hat{w}_n = \frac{-a^2}{c_p^2 h \rho_s} F_{z_n} \tag{4.7}$$

$$\frac{1+\nu}{2} n\alpha \, \hat{u}_n + \left[\omega^2 - \frac{1-\nu}{2}\alpha^2 - n^2\right] \hat{\vartheta}_n + in \, \hat{w}_n = \frac{-a^2}{c_p^2 h \rho_s} F_{\phi_n} \tag{4.8}$$

$$i\nu\alpha \, \hat{u}_n + in \, \hat{\vartheta}_n + \left[1 - \Omega^2 + \beta^2(\alpha^2 + n^2)^2\right] \hat{w}_n = \frac{-a^2}{c_p^2 h \rho_s} \left[\hat{p}_{s_n} - F_{r_n} - ik_z M_n\right] \tag{4.9}$$

where $\Omega = \omega a / c_p$ and $\alpha = k_z a$ are non-dimensional wavenumbers corresponding to the equivalent plate wave speed of the shell and the axial component of the field.

As in Chapter 2, I make use of the momentum equation $\rho_o \partial \dot{w} / \partial t = -\partial p / \partial r$ to relate the radial displacement $\hat{w}_n$ and the scattered pressure $\hat{p}_{s_n}$ at the surface of the shell:

$$\begin{aligned} \frac{a^2}{c_p^2 h \rho_s} \hat{p}_{s_n} &= \frac{a^2}{c_p^2 h \rho_s} \left\{ \frac{\omega^2 \rho_o}{k_r} \frac{H_n^{(1)}(k_r a)}{H_n^{(1)\prime}(k_r a)} \hat{w}_n \right\} \\ &= \overrightarrow{F_\mu} \, E_f k^2 a^2 \, \hat{w}_n \end{aligned} \tag{4.10}$$

Substituting equation 4.10 into equation 4.9 removes the scattered pressure dependence and yields the following system of linear equations for the displacement field on the shell:

Matrix Form of Transformed Donnell Equations (4.11)

$$\begin{bmatrix} \alpha^2 + \frac{1-\nu}{2}n^2 - \Omega^2 & \frac{1+\nu}{2}n\alpha & \nu\alpha \\ \frac{1+\nu}{2}n\alpha & \frac{1-\nu}{2}\alpha^2 + n^2 - \Omega^2 & n \\ \nu\alpha & n & \xi_n \end{bmatrix} \begin{bmatrix} \hat{u}_n \\ \hat{\vartheta}_n \\ -i\hat{w}_n \end{bmatrix} = \begin{bmatrix} F_{z_n} \\ F_{\phi_n} \\ -i(F_{r_n} + ik_z M_n) \end{bmatrix} \frac{a^2}{c_p^2 h \rho_s}$$

where

$$\xi_n = 1 - \Omega^2 + \beta^2 \left(\alpha^2 + n^2\right)^2 + \overrightarrow{F_\mu}\, E_f k^2 a^2$$

The system of linear equations shown above is easily solved to yield the following expressions for the displacements

$$\hat{u}_n = \frac{a^2}{c_p^2 h \rho_s} \frac{1}{D_n} \left\{F_{z_n} y_{11_n} + F_{\phi_n} y_{12_n} - iF_{r_n} y_{13_n} - iM_n y_{14_n}/a\right\} \quad (4.12)$$

$$\hat{\vartheta}_n = \frac{a^2}{c_p^2 h \rho_s} \frac{1}{D_n} \left\{F_{z_n} y_{21_n} + F_{\phi_n} y_{22_n} - iF_{r_n} y_{23_n} - iM_n y_{24_n}/a\right\} \quad (4.13)$$

$$-i\hat{w}_n = \frac{a^2}{c_p^2 h \rho_s} \frac{1}{D_n} \left\{F_{z_n} y_{31_n} + F_{\phi_n} y_{32_n} - iF_{r_n} y_{33_n} - iM_n y_{34_n}/a\right\} \quad (4.14)$$

where the terms $y_{ij_n}(k_z)$ relate the forces and displacements as follows

$$y_{11_n} = -\left\{\xi_n \left(\frac{1-\nu}{2}\alpha^2 + n^2 - \Omega^2\right) - n^2\right\} \quad (4.15)$$

$$y_{12_n} = -\left\{\nu n\alpha - \frac{1+\nu}{2}n\alpha\xi_n\right\} \quad (4.16)$$

$$y_{13_n} = -\left\{\frac{1+\nu}{2}n^2\alpha - \nu\alpha\left(\frac{1-\nu}{2}\alpha^2 + n^2 - \Omega^2\right)\right\} \quad (4.17)$$

$$y_{22_n} = -\left\{\xi_n \left(\alpha^2 + \frac{1-\nu}{2}n^2 - \Omega^2\right) - \nu^2\alpha^2\right\} \quad (4.18)$$

$$y_{23_n} = -\left\{\{\nu\frac{1+\nu}{2}n\alpha^2 - n\left(\alpha^2 + \frac{1-\nu}{2}n^2 - \Omega^2\right)\right\} \tag{4.19}$$

$$y_{33_n} = -\left\{\left(\alpha^2 + \frac{1-\nu}{2}n^2 - \Omega^2\right)\left(\frac{1-\nu}{2}\alpha^2 + n^2 - \Omega^2\right) - \left(\frac{1+\nu}{2}\right)^2 n^2\alpha^2\right\} \tag{4.20}$$

$$y_{14_n} = i\alpha y_{13_n} \tag{4.21}$$

$$y_{24_n} = i\alpha y_{23_n} \tag{4.22}$$

$$y_{34_n} = i\alpha y_{33_n} \tag{4.23}$$

$$y_{ij_n} = y_{ji_n} \tag{4.24}$$

and the term D_n is the dispersion relation of the fluid loaded shell as defined by equation 2.13. Finally, the slope $\hat{w}_n' = \partial\hat{w}_n/\partial x = ik_x\hat{w}_n$ can also be simply expressed as a function of the applied moment M_n and forces F_n:

$$-i\hat{w}_n' a = \frac{a^2}{c_p^2 h\rho_s}\frac{1}{D_n}\left\{F_{z_n}y_{41_n} + F_{\phi_n}y_{42_n} - iF_{r_n}y_{43_n} - iM_n y_{44_n}/a\right\} \tag{4.25}$$

$$y_{44_n} = (i\alpha)^2 y_{33_n} \tag{4.26}$$

Given these relations for the displacements in the axial wavenumber domain, I now apply the inverse wavenumber transform of equation 4.6 to express them in the spatial z-domain and provide a means of equating the displacements of the ring and shell at $z = 0$. The displacements $u_n(z)$, $\vartheta_n(z)$, and $w_n(z)$ are expressed as functions of the shell mobilities $Y_{ij_n}(z|z_O)$ which relate the velocity at location z and direction i to a corresponding ring of force applied in direction j at location z_O:

$$Y_{ij_n}(z|z_O = 0) = \frac{-i\omega}{2\pi}\frac{a^2}{c_p^2 h\rho_s}\int_{-\infty}^{\infty}\frac{y_{ij_n}}{D_n}e^{ik_z z}dk_z \tag{4.27}$$

Application of the inverse wavenumber transform and the mobility relation shown above yields the following expression for the radial displacement at an arbitrary axial location z:

$$-iw_n(z) = \frac{iF_{z_n}}{\omega}Y_{31_n}(z|z_O) + \frac{iF_{\phi_n}}{\omega}Y_{32_n}(z|z_O) + \frac{F_{r_n}}{\omega}Y_{33_n}(z|z_O) + \frac{M_n}{a\omega}Y_{34_n}(z|z_O) - iw_{n_{inc}}(z) \quad (4.28)$$

The residues of the mobility terms shown above will later be used to quantify the reflection and transmission coefficients of the structural wave field. At the location of the ring ($z = 0$), the mobility terms whose integrand is odd in $k_z a$ equal zero and the expressions for the displacements simplify to the following:

$$u_n(z=0) = \frac{iF_{z_n}}{\omega}Y_{11_n}(0|0) + \frac{M_n}{a\omega}Y_{14_n}(0|0) + u_{n_{inc}}(0) \quad (4.29)$$

$$\vartheta_n(z=0) = \frac{iF_{\phi_n}}{\omega}Y_{22_n}(0|0) + \frac{F_{r_n}}{\omega}Y_{23_n}(0|0) + \vartheta_{n_{inc}}(0) \quad (4.30)$$

$$-iw_n(z=0) = \frac{iF_{\phi_n}}{\omega}Y_{32_n}(0|0) + \frac{F_{r_n}}{\omega}Y_{33_n}(0|0) - iw_{n_{inc}}(0) \quad (4.31)$$

$$-iw_n'a(z=0) = \frac{iF_{z_n}}{\omega}Y_{41_n}(0|0) + \frac{M_n}{a\omega}Y_{44_n}(0|0) - iw_n'a_{inc}(0) \quad (4.32)$$

where $u_{n_{inc}}(z)$, $\vartheta_{n_{inc}}(z)$, $w_{n_{inc}}(z)$, and $w'_{n_{inc}}(z)$ are the displacement components of the incident structural wave. I have computed the scattering of an incident free wave of unit radial displacement $w_{n_{inc}}(0) = 1$. The remaining displacement components of the incident field are found from the homogeneous form of matrix equation 4.11 for a given mode n, frequency ω, and axial wavenumber root $\alpha_m = k_z a_m$ of the dispersion relation D_n. The corresponding axial and tangential displacements, and the slope $w_n' = \partial w_n/\partial x$, are found from the relations

$$w'_{n_{inc}}a = i\alpha_m \quad (4.33)$$

$$u_{n_{inc}} = \frac{i}{d_f}\left\{n^2 - \xi_n\left[\alpha_m^2\frac{(1-\nu)}{2} + n^2 - \Omega^2\right]\right\} \tag{4.34}$$

$$v_{n_{inc}} = \frac{i}{d_f}\left\{\xi_n\alpha_m\frac{(1+\nu)}{2}n - \nu\alpha_m n\right\} \tag{4.35}$$

where

$$d_f = \alpha_m\frac{(1+\nu)}{2}n^2 - \nu\alpha_m\left[\alpha_m^2\frac{(1-\nu)}{2} + n^2 - \Omega^2\right]$$

4.2.2 Displacements of the Ring

As discussed earlier, I have modeled the ring stiffener as an eccentric ring of mass of fixed cross section. Reaction forces equal to those applied to the shell, but of opposite sense, are applied to the ring. The ring has a mass per unit length m_R and rotary inertia I_R, and its center of gravity is located at a distance $h_R/2$ from the midsurface of the shell. The displacements of the ring exhibit the same integer order azimuthal dependence $e^{in\phi}$ as the shell and incident structural wave. Having adopted this simple description of the stiffener, the displacements of the ring are related to the applied reaction forces by the equations shown below:

$$u_{R_n} = F_{z_n}\left(\frac{1}{\omega^2 m_R} - \frac{ih_R^2}{4\omega^3 I_R}\right) + \frac{ih_R M_n}{2\omega^3 I_R} \tag{4.36}$$

$$\vartheta_{R_n} = \frac{F_{\phi_n}}{\omega^2 m_R} \tag{4.37}$$

$$w_{R_n} = \frac{F_{r_n}}{\omega^2 m_R} \tag{4.38}$$

$$w'_{R_n} = \frac{1}{\omega^2 I_R}\left(M_n - F_{z_n}h_R/2\right) \tag{4.39}$$

It is equations 4.36 - 4.39 that would be altered with an improved model of the dynamics of the ring stiffener.

4.2.3 Interaction Forces

One can now solve for the interaction forces produced at the ring stiffener by simply equating the displacements and slope of the ring and the shell at the location $z = 0$. The following expressions for the interaction forces result

$$F_{z_n} = \frac{1}{d1}\left\{-u_{n_{inc}}\left(\frac{iY_{44_n}}{\omega} - \frac{a^2}{\omega^2 I_R}\right) + w'_{n_{inc}}\left(\frac{Y_{14_n}}{\omega} - \frac{ih_R a}{2\omega^3 I_R}\right)\right\} \tag{4.40}$$

$$F_{\phi_n} = \frac{1}{d2}\left\{-\vartheta_{n_{inc}}\left(\frac{iY_{33_n}}{\omega} - \frac{1}{\omega^2 m_R}\right) + w_{n_{inc}}\frac{Y_{23_n}}{\omega}\right\} \tag{4.41}$$

$$F_{r_n} = \frac{1}{d2}\left\{-\vartheta_{n_{inc}}\frac{Y_{23_n}}{\omega} - w_{n_{inc}}\left(\frac{iY_{22_n}}{\omega} - \frac{1}{\omega^2 m_R}\right)\right\} \tag{4.42}$$

$$\frac{M_n}{a} = \frac{1}{d1}\left\{-u_{n_{inc}}\left(\frac{Y_{14_n}}{\omega} - \frac{h_R a}{2\omega^2 I_R}\right) - w'_{n_{inc}}\left(\frac{iY_{11_n}}{\omega} + \frac{ih_R^2}{4\omega^3 I_R} - \frac{1}{\omega^2 m_R}\right)\right\} \tag{4.43}$$

where all terms are evaluated at $z = 0$ and

$$d1 = \left(\frac{iY_{11_n}}{\omega} + \frac{ih_R^2}{4\omega^3 I_R} - \frac{1}{\omega^2 m_R}\right)\left(\frac{iY_{44_n}}{\omega} - \frac{a^2}{\omega^2 I_R}\right) + \left(\frac{Y_{14_n}}{\omega} - \frac{h_R a}{2\omega^2 I_R}\right)\left(\frac{Y_{14_n}}{\omega} - \frac{ih_R a}{2\omega^3 I_R}\right)$$

$$d2 = \left(\frac{iY_{22_n}}{\omega} - \frac{1}{\omega^2 m_R}\right)\left(\frac{iY_{33_n}}{\omega} - \frac{1}{\omega^2 m_R}\right) + \frac{Y_{23_n}^2}{\omega^2}$$

Frequency dependent values of the forces and moments induced by a prescribed incident structural wave must be computed prior to estimating the scattered pressure or the reflection and transmission coefficients. Hence, one must first compute frequency dependent values of the mobility terms Y_{ij} shown above. I have numerically computed these values using the extended midpoint integration technique presented by Press et. al. [47]. The integration was performed along a path in the complex wavenumber plane orientated at a $-45°$ angle relative to the positive real axis. This

path was selected to move the integrand away from the poles and thus improve the rate of convergence of the numerical implementation without altering the value of the integral.

4.3 The Scattered Pressure

Having derived expressions for the shell displacements and interaction forces produced by the interaction of the incident structural wave and the ring, I now make use of the method of stationary phase to estimate the scattered pressure. The scattered pressure generated at the ring stiffener is related to the transform of the radial displacement field with the use of the momentum equation as shown below

$$\hat{p}_{s_n}(k_z) = \frac{\omega^2 \rho_o}{k_r} \frac{H_n^{(1)}(k_r a)}{H_n^{(1)\prime}(k_r a)} \hat{w}_n \tag{4.44}$$

Implementation of the inverse transform of equation 4.6 then provides the following spatial domain expression of the scattered pressure:

$$p_{s_n}(z) = \frac{1}{2\pi} \int_{-\infty}^{\infty} \hat{p}_{s_n} e^{ik_z z} dk_z \tag{4.45}$$

while substitution of the radial displacement expression of equation 4.14 and the large argument asymptotic expression for a Hankel function of the first kind [29] yields the following integral expression for the scattered pressure:

$$p_{s_n}(z) \simeq i \frac{E_f k_o^2 a^2}{2\pi} e^{-i(\pi/4 + n\pi/2)} \int_{-\infty}^{\infty} \sqrt{\frac{2}{\pi k_r r}} \frac{e^{i(k_r r + k_z z)}}{H_n^{(1)\prime}(k_r a)} \tilde{w}_n dk_z \tag{4.46}$$

where

$$\tilde{w}_n = F_{z_n} y_{31_n} + F_{\phi_n} y_{32_n} - iF_{r_n} y_{33_n} - iM_n y_{34_n}/a \tag{4.47}$$

I now express the phase term of equation 4.46 in terms of the coordinates R and θ shown in Figure 4.1 to take advantage of the stationary phase approximation.

Recognizing that $k_r = \sqrt{k_o^2 - k_z^2}$, and that the axial and radial coordinates can be expressed as $z = R\cos\theta$ and $r = R\sin\theta$, one can rewrite the expression for the scattered pressure as

$$p_{s_n}(z) \simeq i\,\frac{E_f k_o^2 a^2}{2\pi}\,e^{-i(\pi/4+n\pi/2)}\int_{-\infty}^{\infty}\sqrt{\frac{2}{\pi k_r R\sin\theta}}\,\frac{e^{i\Phi(k_z)}}{H_n^{(1)\prime}(k_r a)}\,\tilde{w}_n\,dk_z \qquad (4.48)$$

and the phase function $\Phi(k_z)$ shown above is given by

$$\Phi(k_z) = R\left(\sqrt{k_o^2 - k_z^2}\sin\theta + k_z\cos\theta\right) \qquad (4.49)$$

Therefore, the axial wavenumber of stationary phase is $k_{z_s} = k_o\cos\theta$ and the corresponding radial wavenumber is $k_{r_s} = k_o\sin\theta$. Application of the general stationary phase solution shown in equation 2.37 yields the following asymptotic approximation for the scattered pressure at a distance R and aspect angle θ:

$$p_{s_n}(R,\theta) \simeq \frac{E_f k_o a}{\pi R}\,e^{-in\pi/2}\,\frac{e^{ik_o R}}{\sin\theta H_n^{(1)\prime}(k_o a\sin\theta)}\,\tilde{w}_n\Big|_{\alpha=k_o a\cos\theta} \qquad (4.50)$$

where the radial displacement variable $\tilde{w}_n$ is evaluated at a discrete axial wavenumber equal to the stationary phase value k_{z_s}.

Three important properties of the scatter produced by the ring are demonstrated by equation 4.50.

1. The pressure field experiences spherical spreading as dictated by the $1/R$ dependence of the amplitude.

2. Having recognized the following relations, one can see that the scattered pressure approaches zero near the surface of the cylinder:

$$\begin{aligned}\sin\theta H_n^{(1)\prime}(k_o a\sin\theta) &= -\sin\theta H_{n+1}^{(1)}(k_o a\sin\theta) + \frac{n}{k_o a}H_n^{(1)}(k_o a\sin\theta)\\ &\rightarrow \infty \;\; as \;\; \theta \rightarrow 0\end{aligned}$$

Hence, the scatter produced at the ring has directivity properties similar to those of a dipole or quadrupole. However, neither model is an accurate representation by itself because the field is generated by a combination of all of the reaction forces generated at the ring.

3. The axial wavenumber of stationary phase $k_{z_s} = k_o \cos\theta$ corresponds to a phase matched condition between the field in the fluid and on the shell. The scattered pressure thus becomes large at angles θ corresponding to the phase matched radiation angle of supersonic shear or compressional waves, i.e. at stationary phase values k_{z_s} equal to the real part of a supersonic root of the dispersion relation D_n. The roots change with frequency, and therefore, the scattering is a frequency selective process. However, the stationary phase approximation I have used becomes inaccurate at frequencies near those where this condition exists. At these frequencies, corrections similar to those of Rumerman [49] are required to account for the proximity of the pole to the steepest descent path. For this study, I have computed the scattered pressure at a far field location orientated perpendicular to the axis of the cylinder ($\theta = \pi/2$) for a range of frequencies beginning just above the cut-off frequency of the given wave type and mode n. Given this observation location and an incident membrane wave, the inaccuracies are only encountered near the cut-off frequencies of compressional waves. In the case of an incident flexural wave, the inaccuracies are encountered at the cut-off frequencies of both membrane wave types.

Finally, the scattered pressure produced at a location orientated perpendicular to the axis of the the cylinder $\theta = \pi/2$ is approximated by

$$p_{s_n}(R, \pi/2) \simeq \frac{E_f k_o a}{\pi R} e^{-in\pi/2} \left. \frac{e^{ik_o R}}{H_n^{(1)\prime}(k_o a)} \tilde{w}_n \right|_{\alpha=0} \tag{4.51}$$

The far field scattered pressure $p_{s_n}(R, \pi/2)$ generated at the ring by an incident shear wave is shown in Figure 4.3, while the pressure generated by an incident compressional wave is shown in Figure 4.4. In both cases, the pressure has been

computed at an angle $\theta = 90$ degrees according to equation 4.51 and the scatter produced by the three modes $n = 1$, 2, and 3 is shown. In addition, the scattered pressure has been normalized by the radiated pressure generated by the incident field at the same radial distance from the shell axis. These figures demonstrate that the scattered field is comparable to the radiated field of the incident wave at the cut-off frequencies of the compressional modes, i.e. at $ka = 3.7$, 7.3, and 10.9. If a different angle θ had been selected, peak values would be observed at other frequencies where the stationary phase point equals the real part of a supersonic root of the dispersion relation $ka\cos\theta = Re\{k_z a_m\}$. For example, peak values would be observed near the frequencies listed in Table 2.3 for $\theta = 75$ degrees.

The far field scattered pressure $p_{s_n}(R, \pi/2)$ generated at the ring by an incident flexural wave is shown in Figure 4.5. In this case, the scattered pressure has been normalized by the radiated pressure generated by a free shear wave field of the same unit radial displacement. This normalization was selected because the incident flexural wave itself does not radiate, and because shear wave radiation is such a prominent source of the observed backscatter over the range of aspect angles of interest here. The resulting transfer functions again show peak values at the cut-off frequencies of compressional wave modes. Peak transfer function values are nearly 40 dB smaller than those produced by incident membrane waves. However, the transfer function shown is based on equal radial displacement values for both flexural and shear waves and a meaningful comparison must include the actual displacement ratio of the waves of interest. Membrane waves generate flexural waves of similar radial displacement when they scatter at a ring as will be demonstrated in the next section. But thereafter, membrane waves propagating on the shell will decay rapidly as they radiate while flexural waves will only loose energy by scattering at a discontinuity. Hence the scattering of flexural waves to the acoustic medium may become significant, particularly at later times in the evolution of the backscatter.

It should be stressed again that the values shown in Figures 4.3 - 4.5 are inaccurate near the peak values.

4.4 Reflection and Transmission Coefficients

I now use the residues of the the wavenumber integrals that define the mobility terms found in equation 4.28 to estimate the reflection and transmission coefficients of the incident structural wave. Although the total radial displacement is quantified by the residues associated with all poles, as well as the contribution of the branch cut, I only consider the contributions of residues at poles associated with propagating wavenumbers. Evanescent poles are characterized by large imaginary wavenumber components and only contribute to the nearfield generated at the ring. The branch cut contributes to the spectral wavenumber continuum. One example of the axial wavenumber dependence of the integrand that defines the radial displacement $w_n(z)$ is shown in Figure 4.6 for an incident free shear wave of mode $n = 1$ and frequency $ka = 7.06$. Peak values are found at the wavenumbers $k_z a = 1.71$, $k_z a = 3.23$, and $k_z a = 28.0$ which correspond to the real part of the compressional, shear, and flexural wave roots of the dispersion relation, respectively. These peak values exceed the neighboring continuum in such a fashion that the branch cut cannot significantly contribute to the value of the integral at these wavenumbers. Although the entire displacement field u_n, v_n, and w_n quantifies the energy carried in the transmitted and reflected waves generated at the ring, I define the transmission and reflection coefficients t_{ml} and r_{ml} in terms of the radial component only. I employ this definition because the radial component determines the amplitude of subsequent radiation. In particular, the coefficients t_{ml} and r_{ml} are defined as the radial displacements generated at $z = 0$ by the interaction of the ring with an incident free structural wave of unity radial amplitude ($w_n = 1$ at $z = 0$). The transmission coefficients t_{ml} correspond to the residues associated with poles defining the wavenumbers of structural waves moving in the same axial direction as the incident wave. These poles are thus located in the upper half of the complex wavenumber plane and are enclosed by the contour of integration shown in Figure 4.2. The selection of this contour ensures physically bounded solutions. The reflection coefficients r_{ml} correspond to the residues of poles enclosed by a similar contour located in the lower half plane.

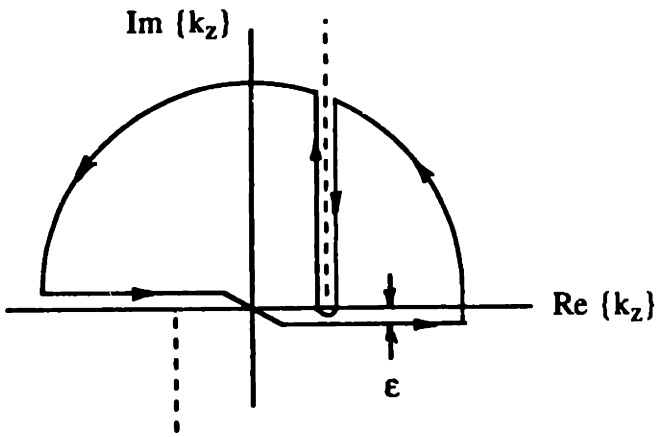

Figure 4.2: The Contour of Integration Used to Determine the Transmission Coefficients for an Incident Wave Propagating in the Positive z Direction. Pekeris branch cuts are shown.

Consider an incident wave moving in the positive z direction with wavenumber $k_z a_{inc}$, such that $Re\{k_z a_{inc}\} > 0$. The resulting radial displacements of a propagating wave generated at the ring are determined by the following relations:

$$w_{n_m}(0^+) = \frac{a^2}{c_p^2 h \rho_s} \left\{ \frac{1}{\frac{\partial D_n}{\partial k_z}} \left[-F_{z_n} y_{31_n} - F_{\phi_n} y_{32_n} + iF_{r_n} y_{33_n} + iM_n y_{34_n}/a \right] \right\} \Bigg|_{a=k_z a_m}$$

$$+\delta(k_z a - k_z a_{inc}) \tag{4.52}$$

$$w_{n_m}(0^-) = \frac{a^2}{c_p^2 h \rho_s} \left\{ \frac{1}{\frac{\partial D_n}{\partial k_z}} \left[F_{z_n} y_{31_n} - F_{\phi_n} y_{32_n} + iF_{r_n} y_{33_n} - iM_n y_{34_n}/a \right] \right\} \Bigg|_{a=k_z a_m} \tag{4.53}$$

where $w_{n_m}(0^+)$ is the radial displacement at $z = 0$ generated by waves moving in the positive z direction and $w_{n_m}(0^-)$ is the displacement generated by waves moving in the opposite direction with the same wavenumber components. Each term contained within the brackets shown above is evaluated at the wavenumber of interest, $\alpha = k_z a_m$ such that $Re\{\alpha\} > 0$, and equals the product of $2\pi i$ and the residue of the wavenumber integral defining the appropriate mobility term of

equation 4.28. The interaction forces shown above are determined as discussed in Section 4.2.3.

Therefore, the coefficients t_{mm} and and r_{mm} that quantify the transmission and reflection of the incident wave are approximated by the following relations:

$$t_{mm} \simeq w_{n_m}(0^+) + 1.0 \tag{4.54}$$

$$r_{mm} \simeq w_{n_m}(0^-) \tag{4.55}$$

Similarly, the transmission and reflection coefficients t_{ml} and r_{ml} that quantify the scattering from an incident wave type with wavenumber $k_z a_m$ to another with wavenumber $k_z a_l$, where both wavenumbers are roots of the dispersion relation D_n, are approximated by the following:

$$t_{ml} \simeq w_{n_l}(0^+) \tag{4.56}$$

$$r_{ml} \simeq w_{n_l}(0^-) \tag{4.57}$$

The reflection and transmission coefficient estimates computed for incident shear, compressional, and flexural waves of circumferential orders $n = 1$, and $n = 2$ are shown in Figures 4.7 - 4.22. One can see from these figures that although the ring is quite massive, significant energy is transmitted to the adjoining length of shell. In addition, one can see that significant levels of wave-type conversion occur when a membrane wave encounters the ring. In contrast, one can see that little scattering to membrane waves occurs when a flexural wave encounters a ring. At high frequencies where the propagation angle becomes primarily axially orientated $\psi \rightarrow 0$, one can see that $r_{cc} \simeq r_{ss}$ and that the ratios r_{sc}/r_{sc} and t_{cs}/r_{sc} are roughly equal to the ratio of the phase speeds c_p/c_s. This behavior is consistent with that observed for simple boundary reflection of shear and compressional waves propagating in an elastic half space [11], but is not found for incident flexural waves.

4.5 Summary of Important Results

Significant levels of scattering to other wave types occurs when a membrane wave encounters a ring as demonstrated in Figures 4.7 - 4.10 and 4.15 - 4.18. Therefore, the strong coincident reradiation of the membrane waves that is observed for an infinite cylinder, as well as the empty shell, will be interrupted by interaction with a series of ring stiffeners. Moreover, because the different wave types each propagate with different phase and group velocities, backscattered energy levels will be smeared in both the time and frequency domains. Of particular importance, both membrane wave types scatter energy to flexural waves with each encounter at a ring. Although less energetic, the flexural waves produced are subsonic and do not radiate until fluidborne scattering occurs with later ring interactions. Hence, I expect the ring stiffened shell to exhibit smaller backscatter decay rates than that of an infinite shell or the empty shell. Interaction of the shell, rings, and internal structures that comprise the complex shell will influence the mode conversion processes produced at the ring. However, I would expect to observe scattering coefficients of the same order of magnitude as those predicted here. In fact, weakened levels of coincident back radiation and decreased decay rates are observed for both the ring stiffened and complex shells as discussed in the next chapter.

It is also particularly important to note that the ring scatters energy from one membrane wave type to another provided it is not cutoff. Therefore, at aspect angles $\theta > 73.6$ degrees, coincidently excited compressional waves will scatter energy to shear waves, but not vice versa. Similarly, while only shear waves are coincidently excited over the range of angles $61.3 \leq \theta < 73.6$, they will scatter energy to compressional waves at the rings. However, the wave energized at the ring will propagate with an axial phase speed different from the incident field and will not be coincident. Hence, coincident compressional wave backscatter will be inhibited at angles $\theta > 73.6$ and coincident shear wave backscatter will be inhibited at smaller angles. In addition, this scattering will smear energy in axial wavenumber and bistatic observation angle. Moreover, I would expect similar effects to occur at any structural

discontinuity located on the exterior portions of the shell, including the slope discontinuity of the endcap design used here. As noted earlier, this may further explain the reduced compressional wave backscatter levels observed for the empty shell.

The magnitude of the transmission coefficients associated with shear or compressional wave propagation, t_{ss} and t_{cc}, are of order $O(0.1)$ over much of the frequency range of interest. In addition, the magnitude of the reflection coefficients r_{ss} and r_{cc} tend to increase with increasing frequency as the propagation helix becomes more axially orientated. As a result, membrane wave vibrations of adjacent shell bays must be weakly coupled, and once several ring interactions have take place, distant bays are virtually uncoupled. Therefore, the aggregate membrane wave radiation from a collection of bays may appear to be largely incoherent, particularly when evaluated at later times in the evolution of the scatter.

Phase matched excitation of membrane waves must remain the primary means of injecting energy into the ring stiffened shell for the range of aspect angles of interest here. Therefore, the flexural wave field of the ring stiffened shell is largely induced by membrane wave scattering at the rings. The magnitudes of the transmission coefficients for flexural waves are of order $O(0.2)$ and one can again expect adjacent shell bays to be weakly coupled. However, low order flexural waves have much slower group velocities than corresponding membrane waves as demonstrated in Chapter 2. Ring interactions of flexural waves occur at a rate that is 4 to 7 times slower than membrane waves and a much greater length of time is required for the flexural wave field to become incoherent. In addition, the disparity between reflected and transmitted flexural wave levels is much smaller when generated by the interaction of an incident membrane wave with a ring. For example, the flexural wave coefficients $r_{sf} \simeq 0.5$ and $t_{sf} \simeq 0.4$ are generated by an incident shear mode $n = 1$ at $ka = 7.0$ as shown in Figures 4.7 and 4.8. As a result, different shell bays will remain moderately well coupled for a lengthy period of time as compared to the membrane wave field.

Finally, the acoustic scattering produced by the interaction of an incident structural wave and a ring stiffener is a frequency selective process. The field produced is

directive and approaches zero along the axis of the cylinder. Peak scattered pressure levels are generated by an incident membrane wave are comparable to the radiated field of the incident wave. The scattering of flexural waves may be important if the radial displacements are large compared with those of existing membrane waves. Therefore, if the scattering is produced in a coherent fashion over a series of rings, the net radiation will be significant and aperture effects will dictate the orientation of the resulting beam pattern.

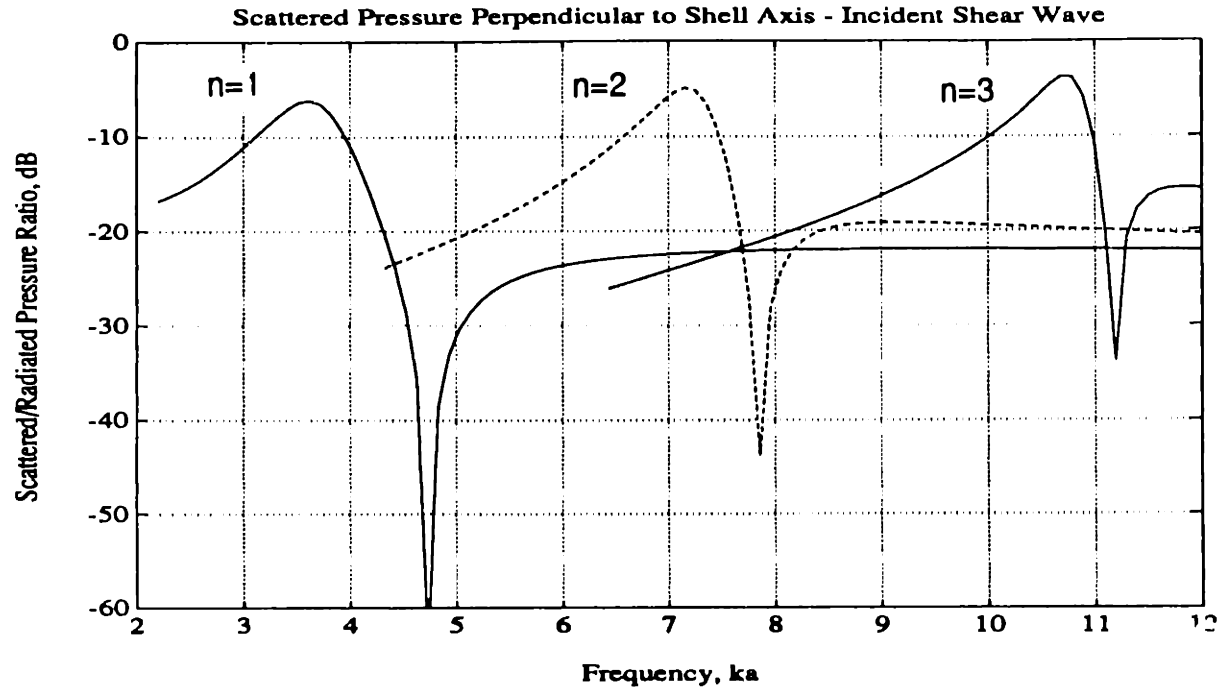

Figure 4.3: The Magnitude of the Far Field Pressure $p_{s_n}(R, \pi/2)$ Scattered at the Ring by an Incident Shear Wave Mode of Unit Radial Amplitude $w_{n_{inc}}(0) = 1$. The scattered pressure is normalized by the field radiated by the incident wave just prior to interaction with the ring.

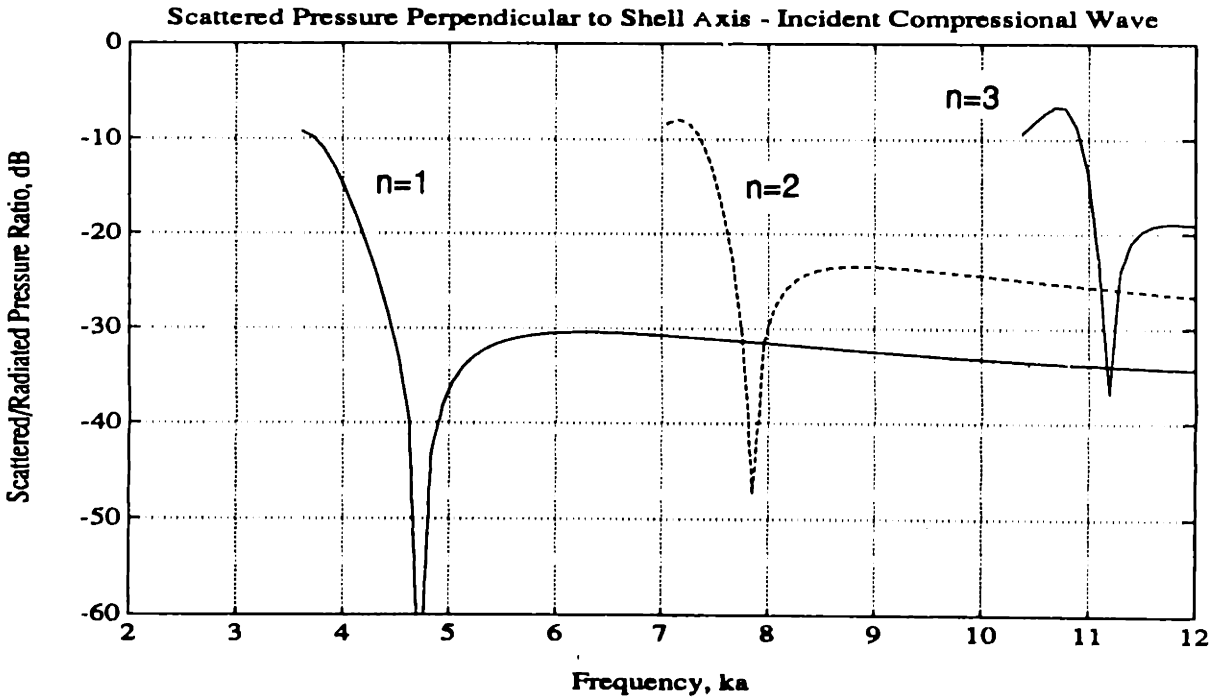

Figure 4.4: The Magnitude of the Far Field Pressure $p_{s_n}(R, \pi/2)$ Scattered at the Ring by an Incident Compressional Wave Mode of Unit Radial Amplitude $w_{n_{inc}}(0) = 1$. The scattered pressure is normalized by the field radiated by the incident wave just prior to interaction with the ring.

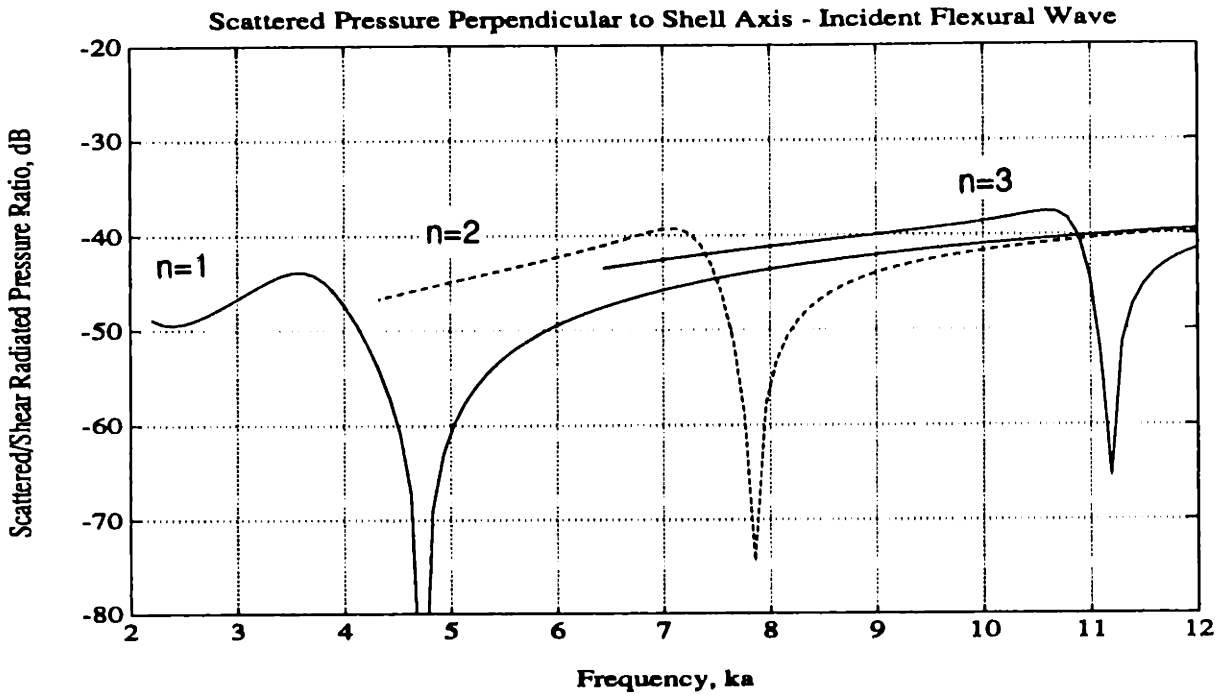

Figure 4.5: The Magnitude of the Far Field Pressure $p_{s_n}(R, \pi/2)$ Scattered at the Ring by an Incident Flexural Wave Mode of Unit Radial Amplitude $w_{n_{inc}}(0) = 1$. The scattered pressure is normalized by the field that would be radiated by a corresponding free shear wave mode of the same radial amplitude.

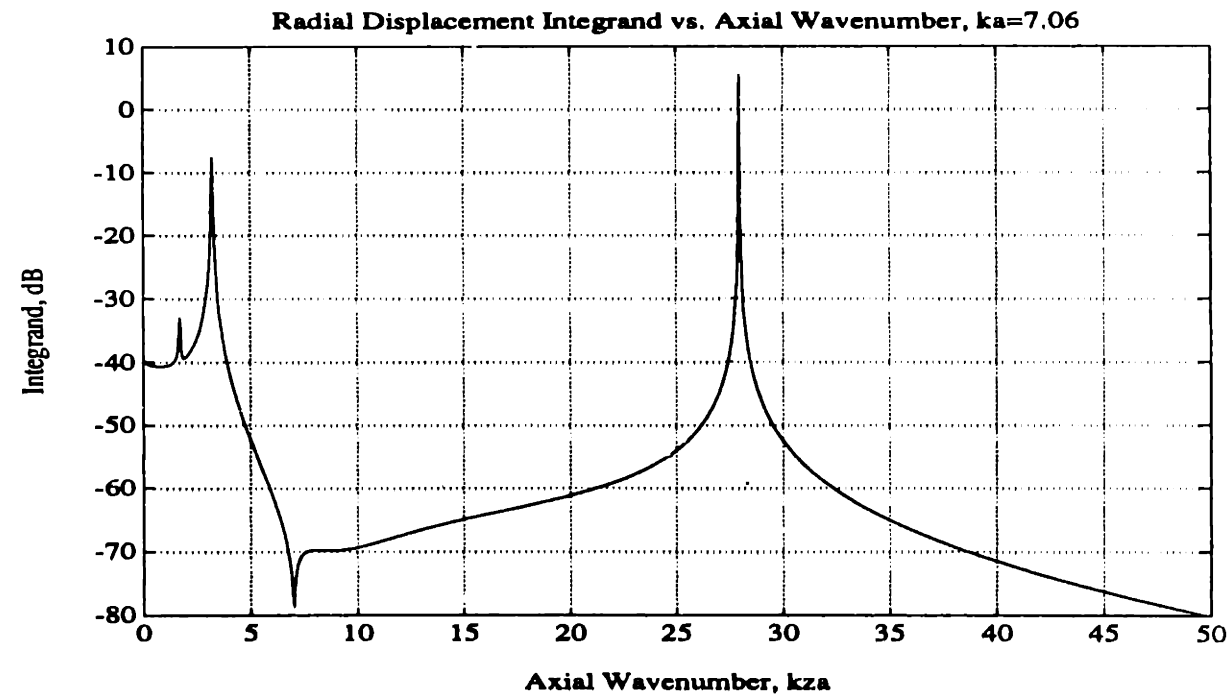

Figure 4.6: The Magnitude of the Integrand Defining the Radial Displacement Produced at the Ring by an Incident Free Shear Wave with Mode $n = 1$ at $ka = 7.06$

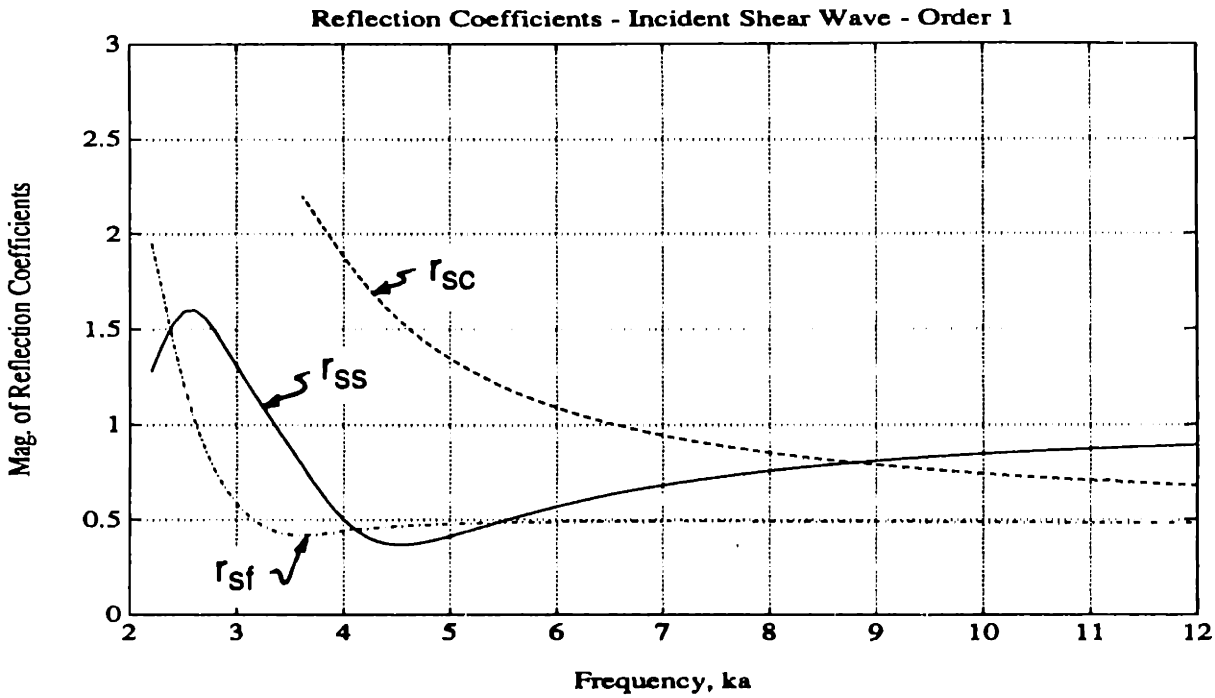

Figure 4.7: The Magnitude of the Reflection Coefficients of an Incident Free Shear Wave with Mode $n = 1$. The subscripts 's', 'c', and 'f' correspond to shear, compressional, and flexural waves respectively.

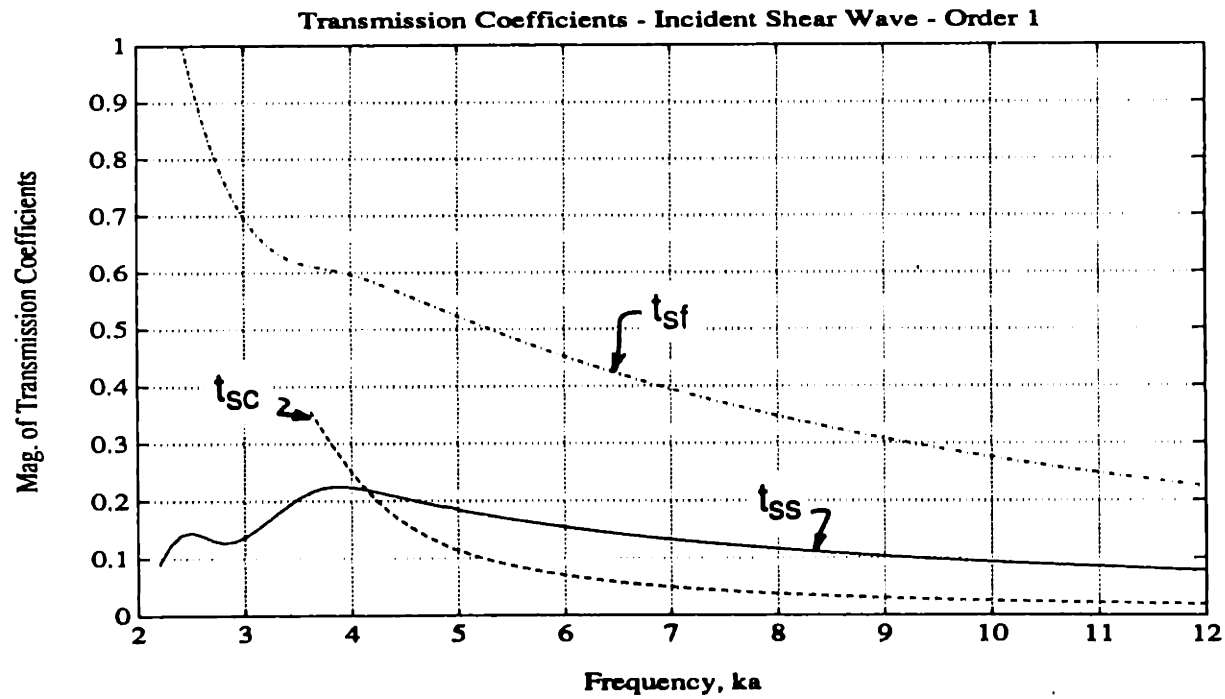

Figure 4.8: The Magnitude of the Transmission Coefficients of an Incident Free Shear Wave with Mode $n = 1$. The subscripts 's', 'c', and 'f' correspond to shear, compressional, and flexural waves respectively.

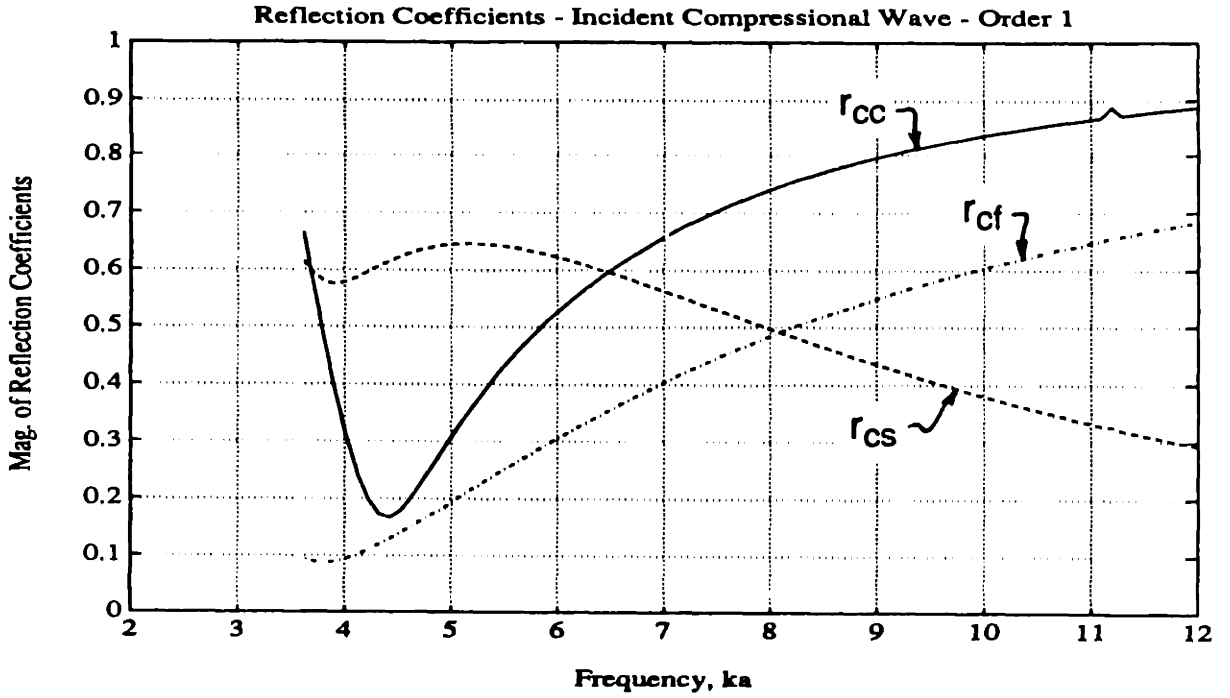

Figure 4.9: The Magnitude of the Reflection Coefficients of an Incident Free Compressional Wave with Mode $n = 1$. The subscripts 's', 'c', and 'f' correspond to shear, compressional, and flexural waves respectively.

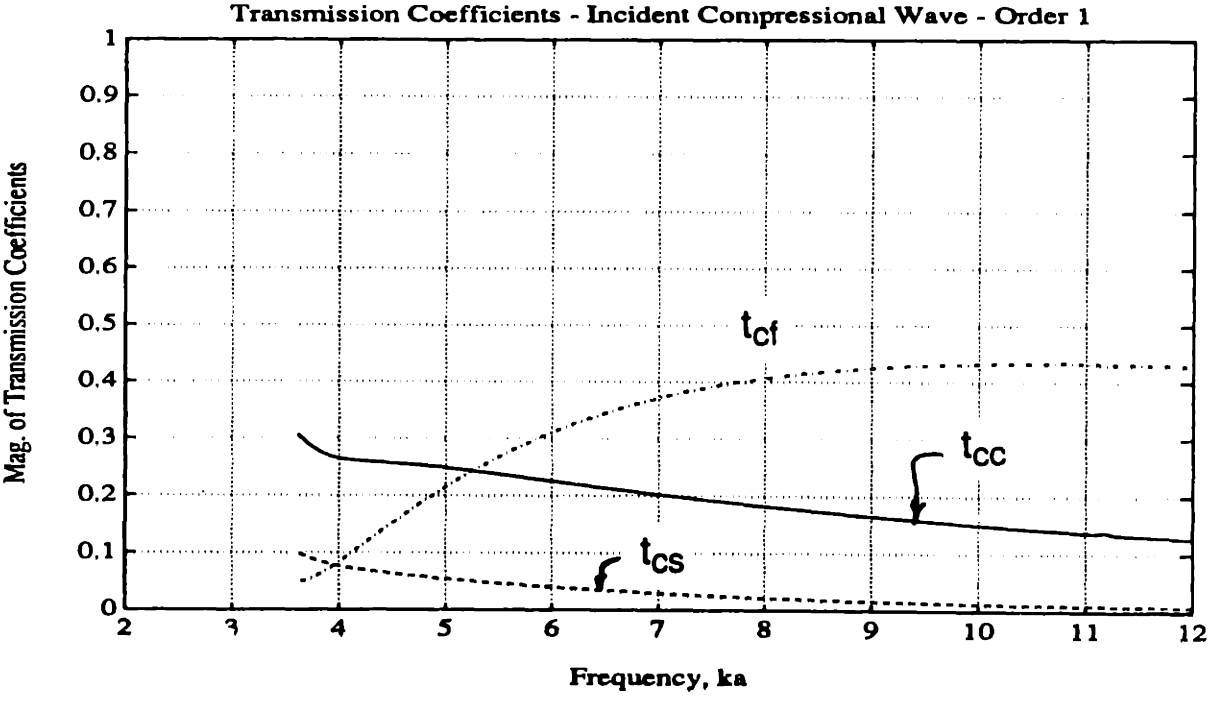

Figure 4.10: The Magnitude of the Transmission Coefficients of an Incident Free Compressional Wave with Mode $n = 1$. The subscripts 's', 'c', and 'f' correspond to shear, compressional, and flexural waves respectively.

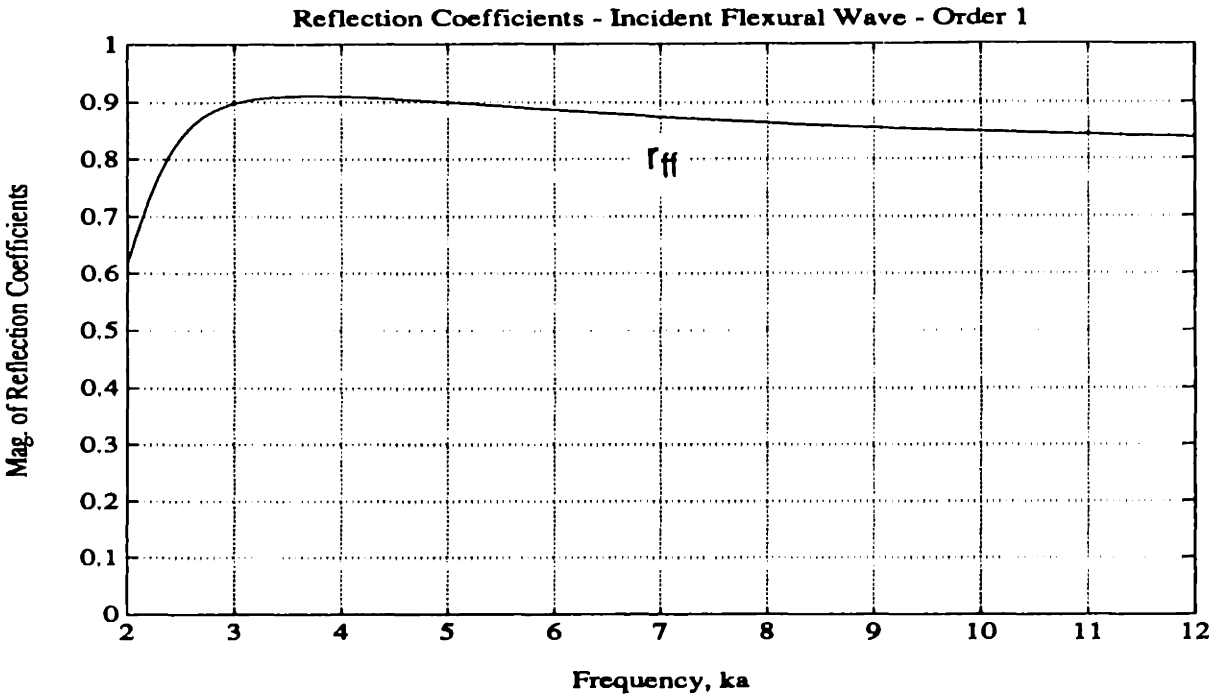

Figure 4.11: The Magnitude of the Reflection Coefficient r_{ff} of an Incident Free Flexural Wave with Mode $n = 1$

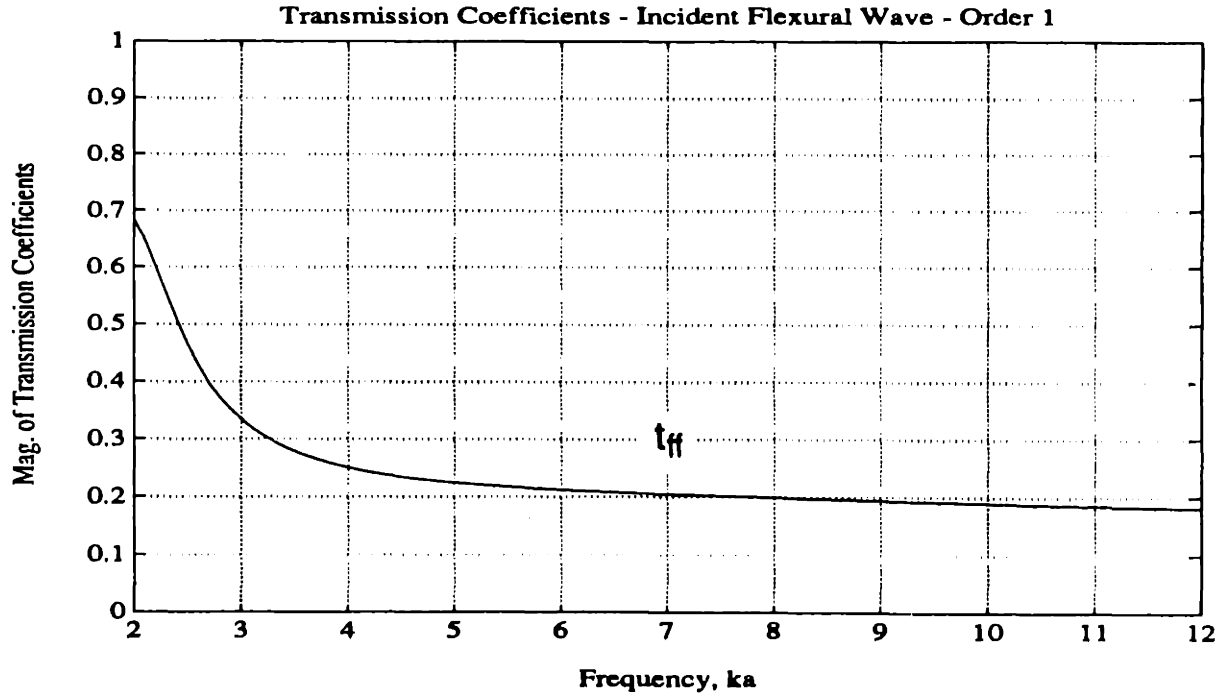

Figure 4.12: The Magnitude of the Transmission Coefficient t_{ff} of an Incident Free Flexural Wave with Mode $n = 1$

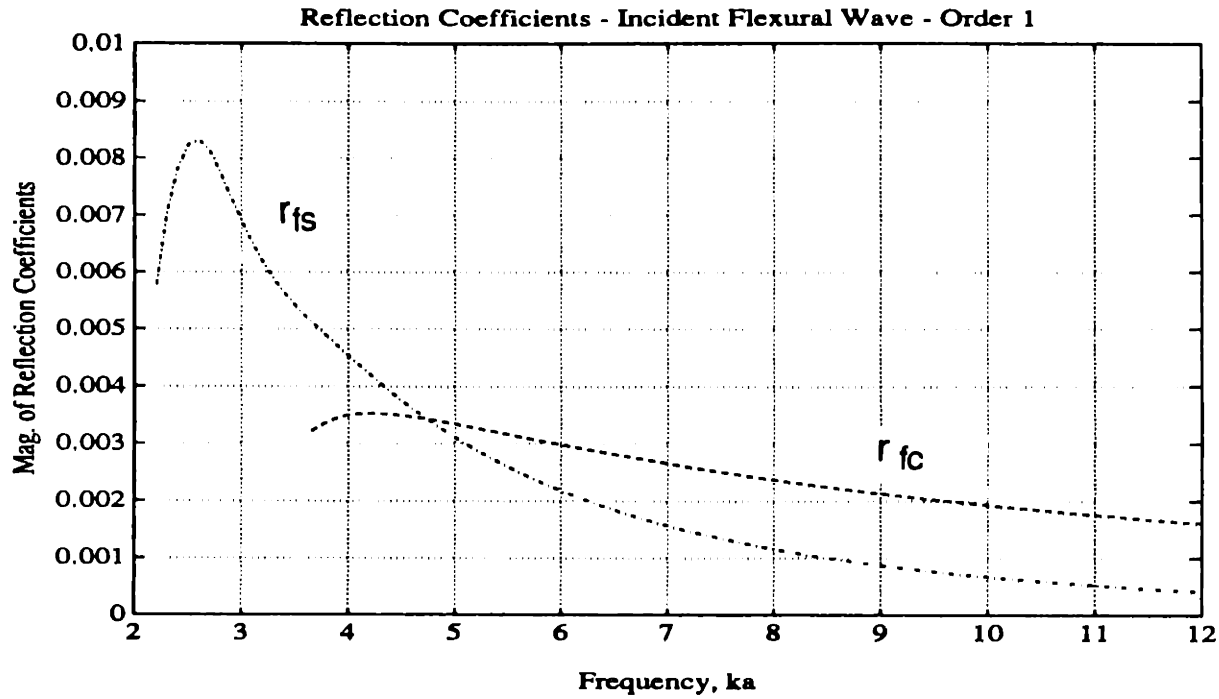

Figure 4.13: The Magnitude of the Coupled Wave Reflection Coefficients of an Incident Free Flexural Wave with Mode $n = 1$. The subscripts 's', 'c', and 'f' correspond to shear, compressional, and flexural waves respectively.

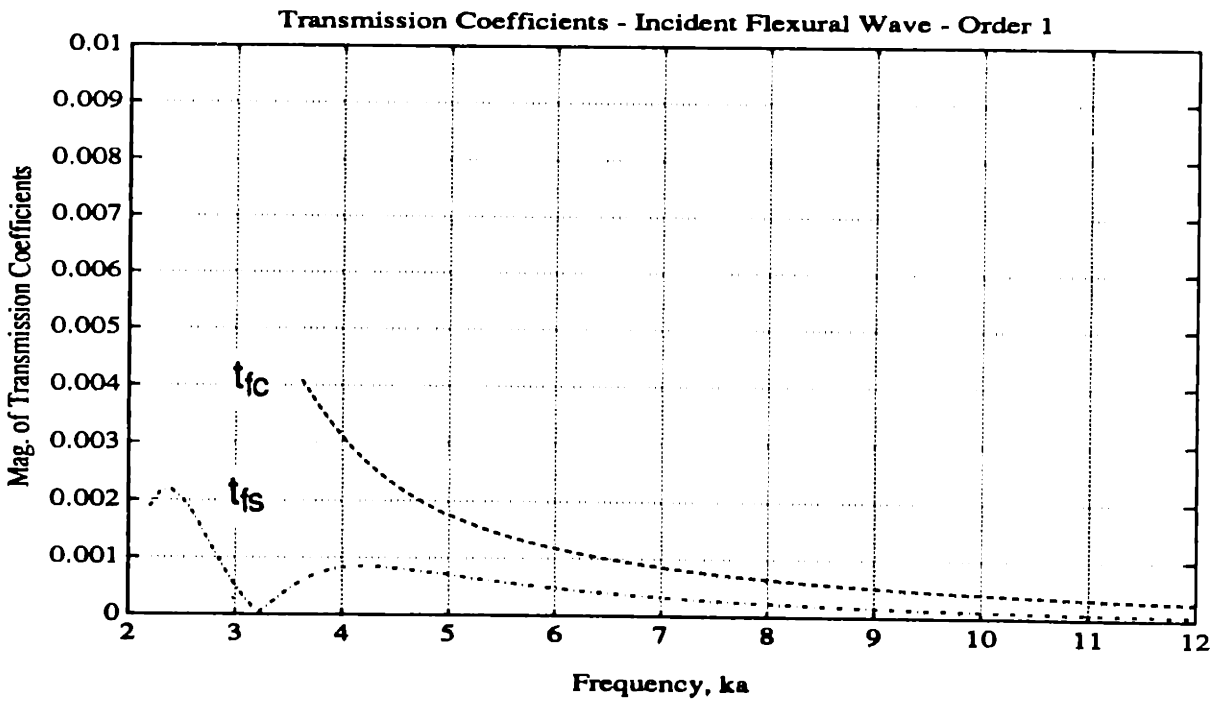

Figure 4.14: The Magnitude of the Coupled Wave Transmission Coefficients of an Incident Free Flexural Wave with Mode $n = 1$. The subscripts 's', 'c', and 'f' correspond to shear, compressional, and flexural waves respectively.

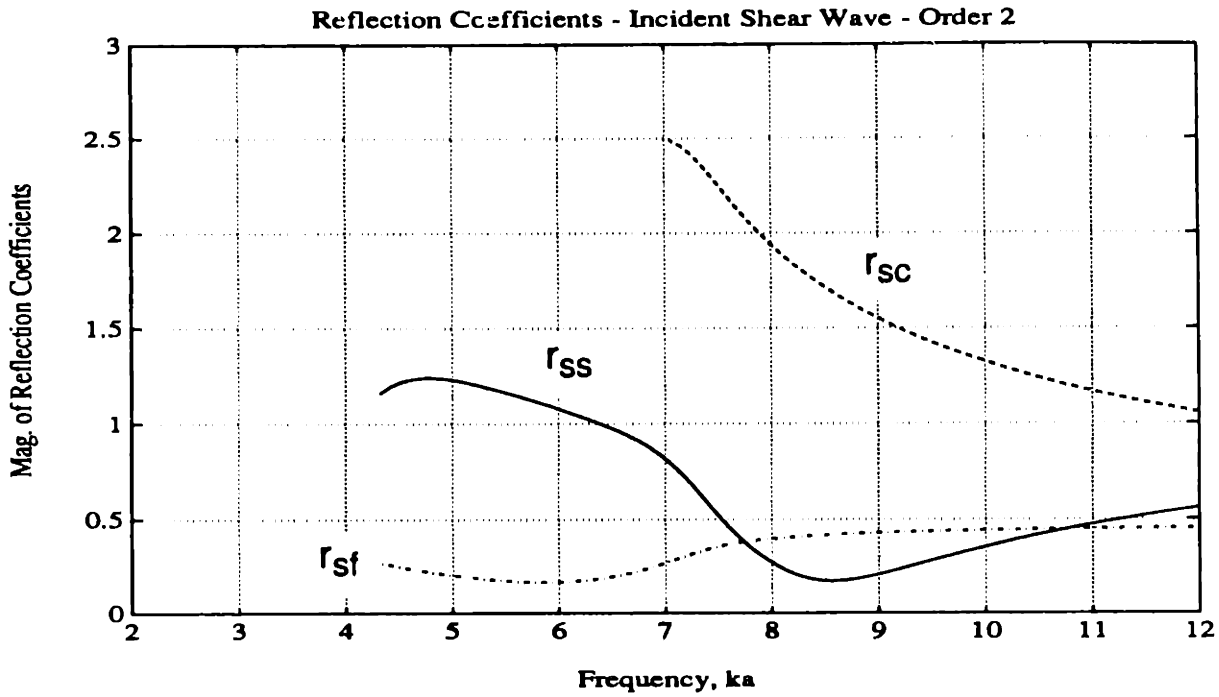

Figure 4.15: The Magnitude of the Reflection Coefficients of an Incident Free Shear Wave with Mode $n = 2$. The subscripts 's', 'c', and 'f' correspond to shear, compressional, and flexural waves respectively.

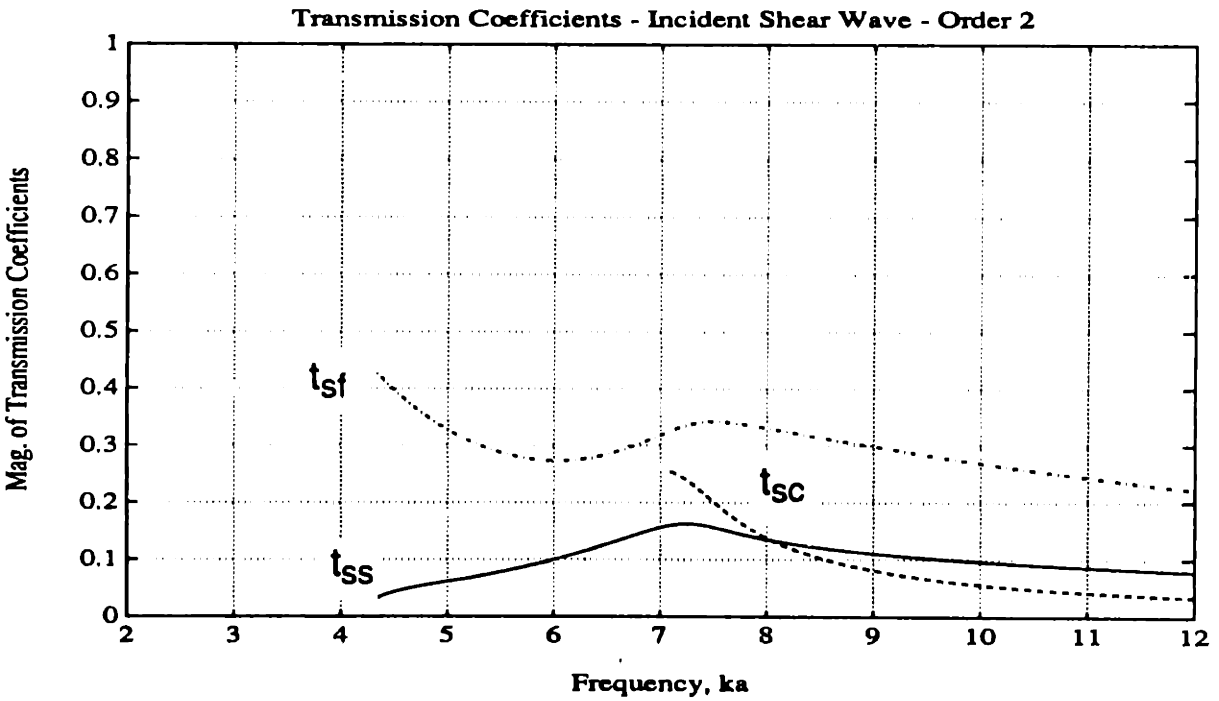

Figure 4.16: The Magnitude of the Transmission Coefficients of an Incident Free Shear Wave with Mode $n = 2$. The subscripts 's', 'c', and 'f' correspond to shear, compressional, and flexural waves respectively.

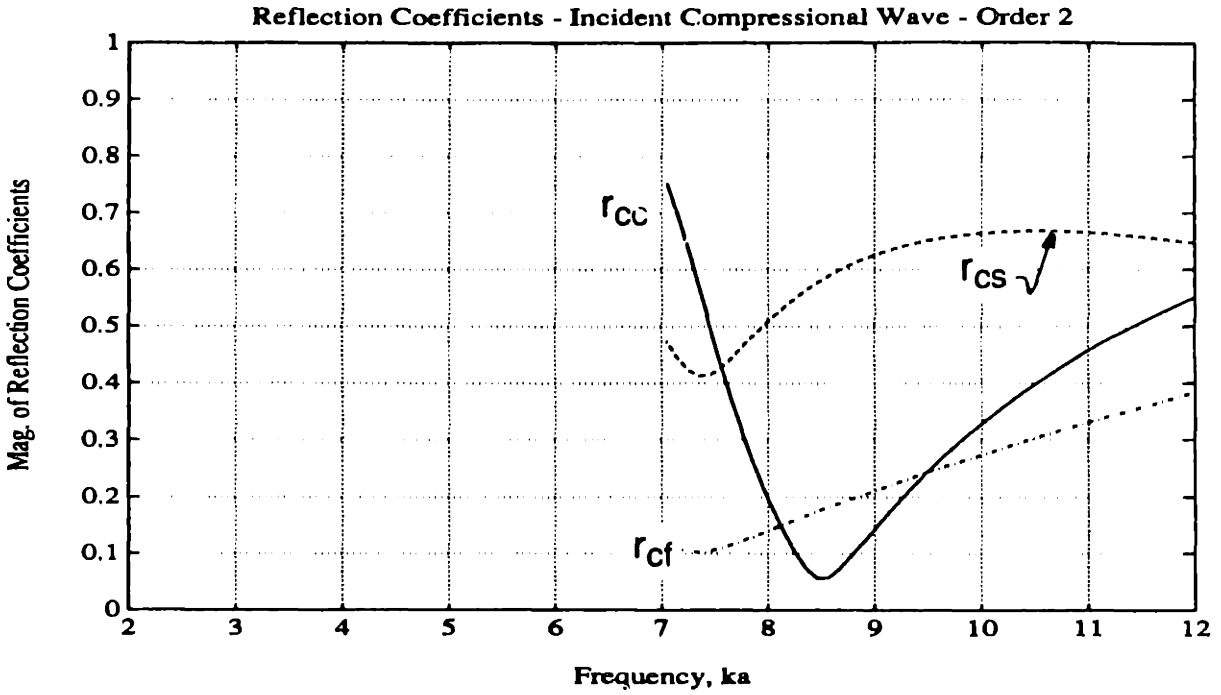

Figure 4.17: The Magnitude of the Reflection Coefficients of an Incident Free Compressional Wave with Mode $n = 2$. The subscripts 's', 'c', and 'f' correspond to shear, compressional, and flexural waves respectively.

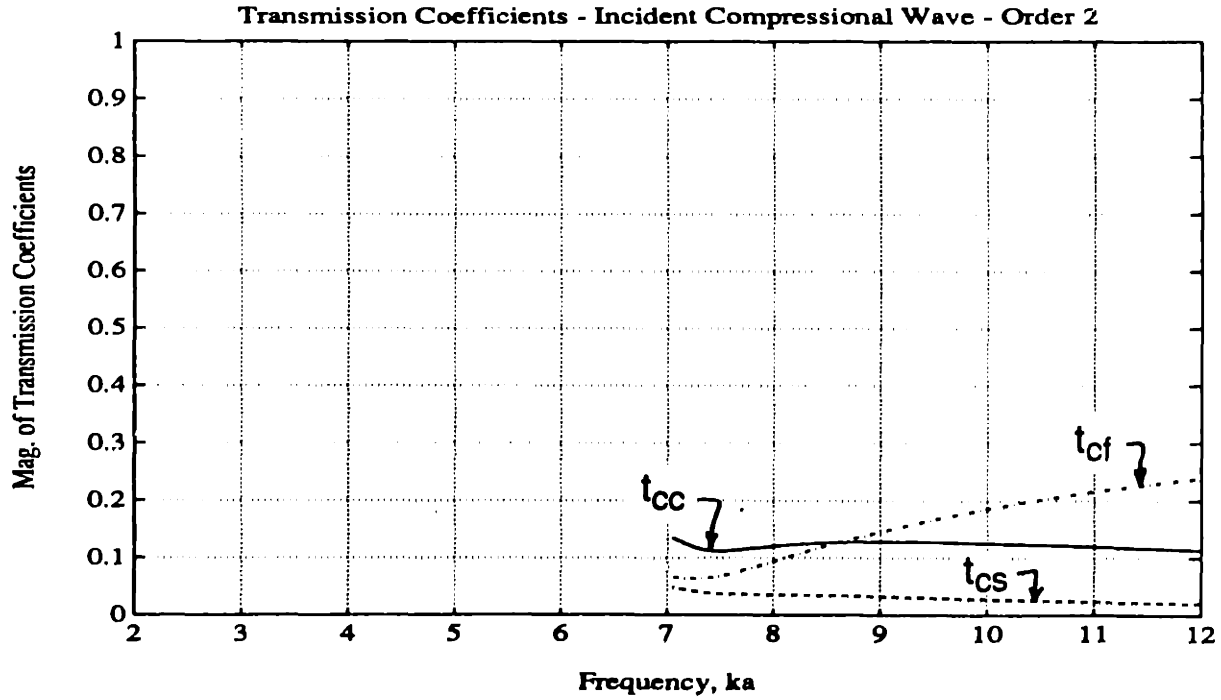

Figure 4.18: The Magnitude of the Transmission Coefficients of an Incident Free Compressional Wave with Mode $n = 2$. The subscripts 's', 'c', and 'f' correspond to shear, compressional, and flexural waves respectively.

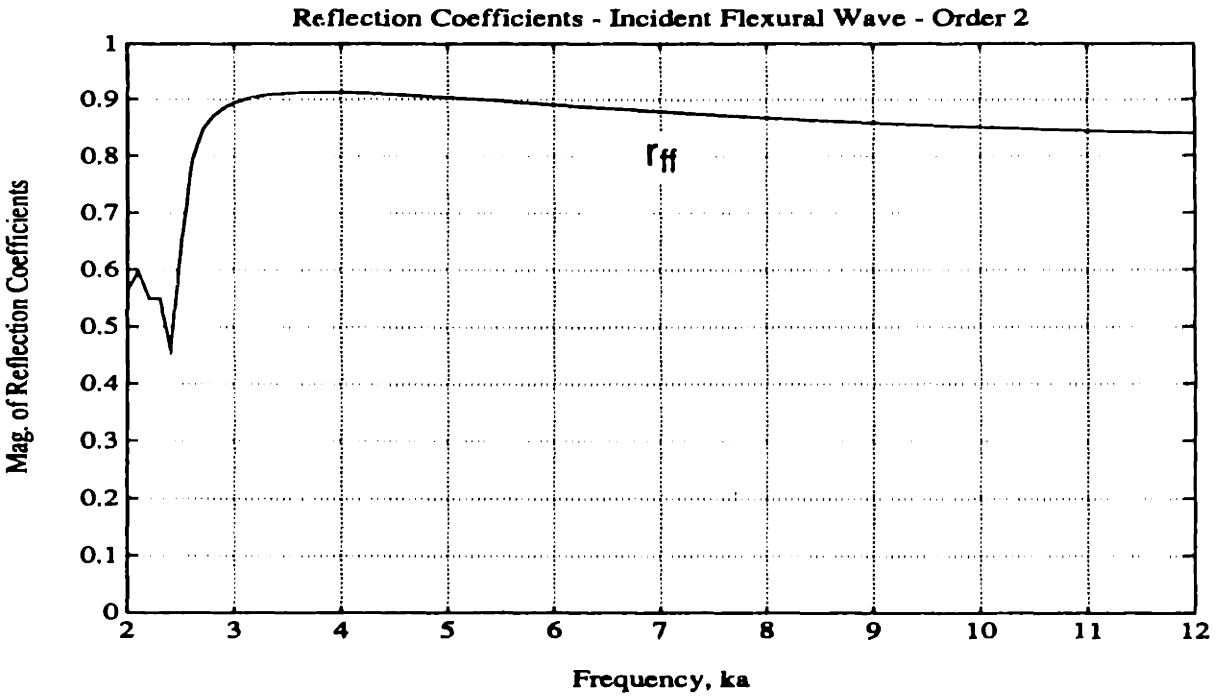

Figure 4.19: The Magnitude of the Reflection Coefficient r_{ff} of an Incident Free Flexural Wave with Mode $n = 2$

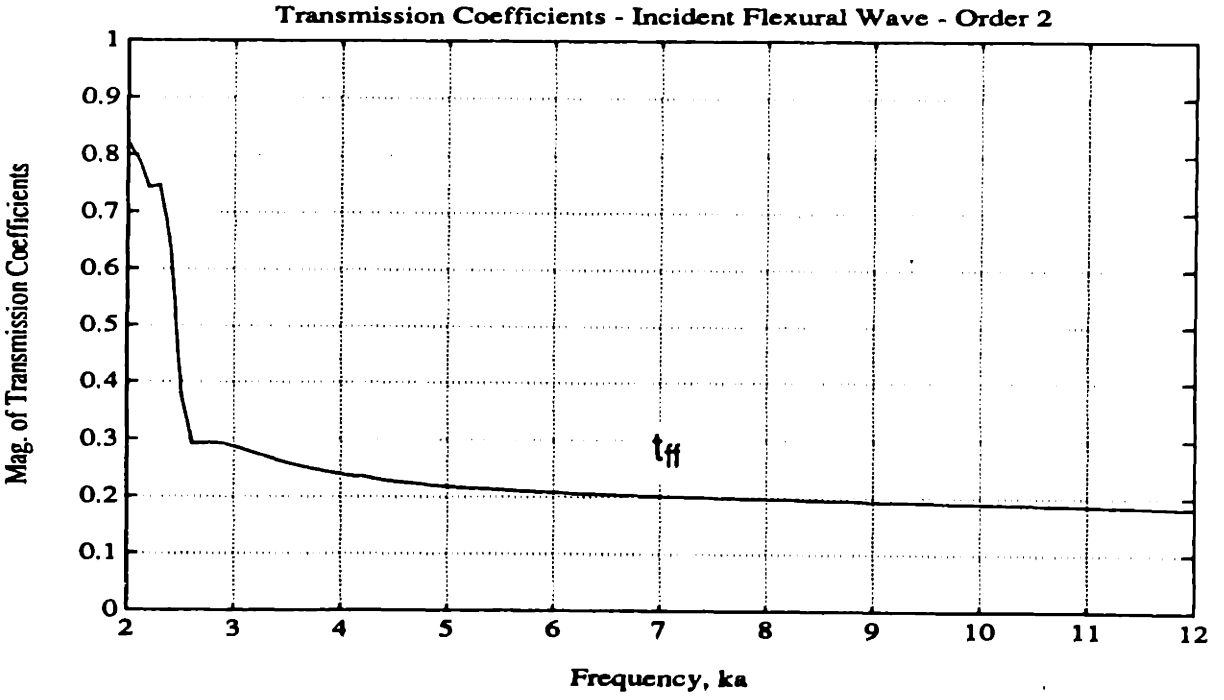

Figure 4.20: The Transmission Coefficient t_{ff} of an Incident Free Flexural Wave with Mode $n = 2$

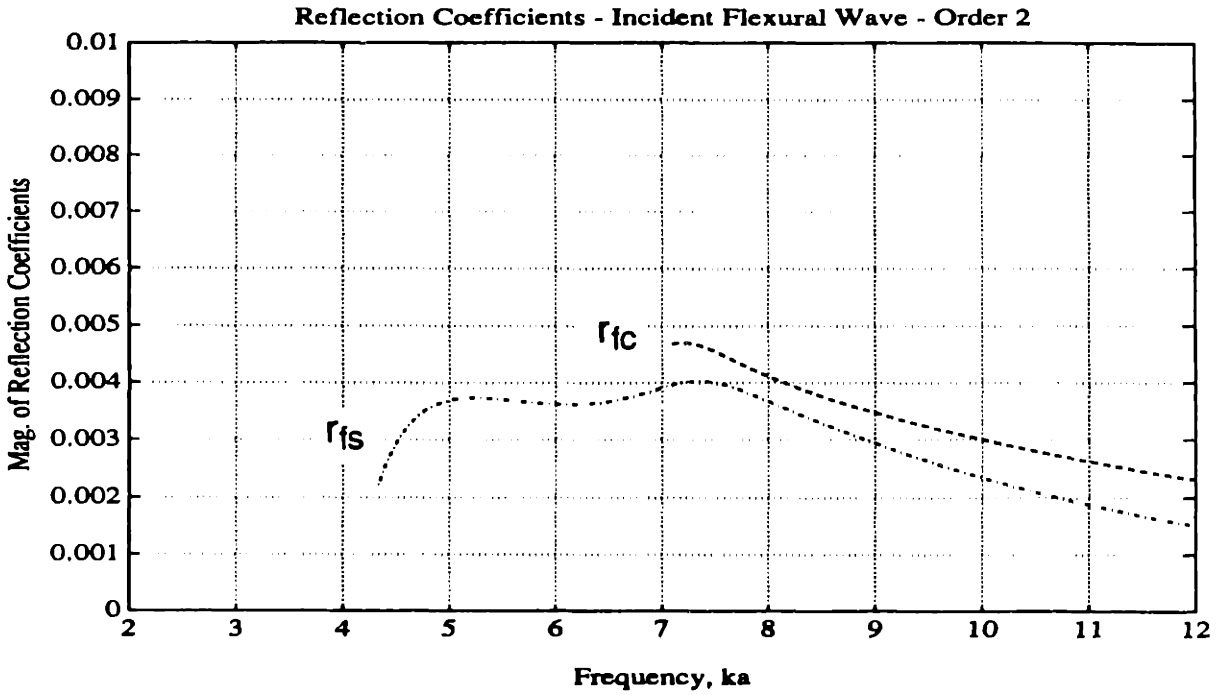

Figure 4.21: The Coupled Wave Reflection Coefficients of an Incident Free Flexural Wave with Mode $n = 2$. The subscripts 's', 'c', and 'f' correspond to shear, compressional, and flexural waves respectively.

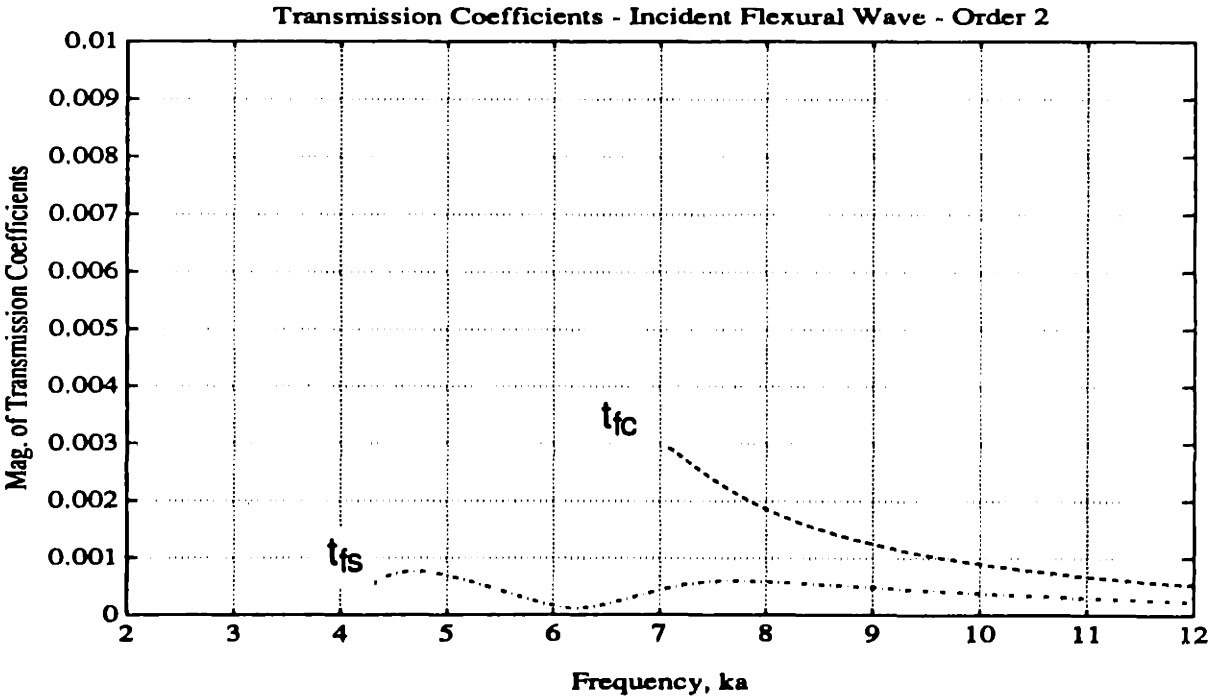

Figure 4.22: The Coupled Wave Transmission Coefficients of an Incident Free Flexural Wave with Mode $n = 2$. The subscripts 's', 'c', and 'f' correspond to shear, compressional, and flexural waves respectively.

Chapter 5

Ring Stiffened and Internally Loaded Shells - Measurements and Interpretation

5.1 Introduction

I evaluate the measured backscatter of the ring stiffened and internally loaded (complex) shells in this chapter. Both shells employ the same configuration of ring stiffeners and the external shell design of the empty shell model. In some instances, both shells produce remarkably similar backscatter, retaining some of the features of the empty shell scatter. However, the structural components that comprise the internal loading of the complex shell provide an additional vibratory energy storage mechanism, as well as an additional transmission path. Therefore, important differences differences among these two shells, and the empty shell, are also evident.

The unequal spacing of the ring stiffeners produces monostatic fields that are not symmetric with respect to beam aspect. For example, the monostatic field measured at an aspect angle of 66 degrees differs from that measured at a complementary angle of 114 degrees. In fact, the use of unequal spacing in the design of the shells allows one to more readily address such issues as the interplay of aperture and axial

resonance effects. However, most of the fundamental physical processes observed can be illustrated with a presentation of the scatter measured at aspect angles ranging from bow ($\theta = 0$) to beam ($\theta = 90$) aspect. Therefore, I primarily present data measured over this range of angles.

Throughout this chapter I make a variety of comparisons of the monostatic field produced by the three different models to highlight the influences of the ring stiffeners and internal loading. The monostatic field observed over the full range of aspect angles from bow to beam incidence will be reviewed. However, the focus of the ensuing data interpretations and analyses will be the monostatic field measured over a range of aspect angles of $60 < \theta \leq 90$ degrees. I also evaluate the results of bistatic measurements of the back and specularly directed scatter generated by the complex shell at aspect angles of 90, 75, and 66 degrees. All of the data presented here were acquired and processed as discussed in detail in Appendix A.

5.2 Influence of Roll Angle

The ring stiffened shell model is an axisymmetric design. Nonetheless, some field asymmetries due to model alignment error and small scale construction defects were observed with changes in roll angle. However, these deviations consist of relatively unimportant frequency shifts and small changes in spectral levels as was noted for the empty shell. Hence, all of the ring stiffened shell data presented are those measured at a constant reference roll angle of 0 degrees.

In contrast, the complex shell design incorporates a quadrant symmetric internal loading configuration as illustrated in Figure 1.4. Monostatic measurements were conducted at roll angles of 0, 22.5, and 45 degrees to investigate potential influences of the internal loading arrangement. The target strength values $T(\omega, \theta)$ measured at all three roll angles are compared with one another in Figure 5.1 for representative aspect angles of 66, 75, and 90 degrees. Changes in roll angle produce changes in target strength no larger than 5 dB, and at most frequencies the changes are quite

smaller than that. The largest changes are generally found at nulls. The influence of the loading that is reflected by the small differences shown in this figure have been neglected since the more significant global influences are the focus of this research. Hence, all of the complex shell data that follows were measured at a constant roll angle of 0 degrees as defined by the reference convention illustrated in Figure A.1.

5.3 Backscattering at Beam Aspect

Even at beam aspect, interaction between the shell, ring stiffeners, and supported internal loading produces scattering sources that vary significantly over the length of the shell. Bondaryk [3] first demonstrated that at beam aspect, the complex shell exhibits an axially distributed field with a temporal variation that is pronouncedly different over the different shell sections bounded by pairs of stiffeners. Bondaryk [3] also employed a $\tau - p$ transform technique to demonstrate the existence of induced shear wave propagation. I have also employed classical focused beamforming to determine the effective axial distribution of the backscattered field. Although the field is not symmetric with respect to the beam aspect plane, I used an array consisting of the bistatic data measured within ± 30 degrees of the monostatic receiver with uniform amplitude taper. This sector includes the shear wave radiation directions of ± 28.7 degrees.

The time domain representation of the resulting axial source distribution is shown in Figure 5.2. The initial geometric scatter is clearly shown at time $t = 0$. Its amplitude is uniformly distributed over the length of the cylindrical portion of the shell, but tapers to smaller values over the length of the endcaps. Three successive compressional wave arrivals can also be discerned by noting that they exhibit a period of approximately 66 μsec corresponding to the ring frequency of the shell. However, the compressional wave sources are not uniformly distributed over the length of the shell and their axial distribution changes with increasing time. The axial dependence is primarily demarcated by decreased amplitudes near stiffener locations and the

junctions of the cylinder with the endcaps. With increasing time, the radiation from the two longest shell bays appears to establish an even order axial resonant dependence while the shorter bay appears to become an odd order resonance. The 0.235 m and 0.189 m lengths of the longer bays would require fundamental even order resonances at $k_z a \simeq 1.5$ and $k_z a \simeq 1.8$ while the odd order resonance of the shorter 0.127 m bay would occur at $k_z a \simeq 1.4$. These resonances are all supersonic over the frequency range of interest here and would radiate.

However, strong radiation from the shell bays can only be observed to exist for a total time duration of about 300 μsec. During this time and thereafter, source levels observed midway between a pair of rings can be seen to decay rapidly and peak amplitudes are then observed at the ring locations themselves suggesting discontinuity radiation. Hence, I believe that the rings provide a means of storing energy in the form of weakly radiating waves.

5.3.1 Aperture Effects

The addition of the ring stiffeners and internal loading not only alters the response parameters of the shell, but it also alters the directivity of the scatter. These effects can be seen in the measured bistatic target strength data shown in Figure 5.3 for the complex shell at beam aspect. The scatter is not symmetric with the respect to the beam aspect plane ($\theta_o = 90$). A strong null is observed near the measured coincidence frequency of the empty shell $ka = 3.6$, but it is located at an observation angle of $\theta_o = 83$ degrees. A strong null can also be seen at the second coincidence frequency $ka = 7.3$ and an observation angle of $\theta_o = 89$ degrees. The axial scattering source distribution behaves like a complicated phase and amplitude tapered line array that generates a directive field different from that produced by the empty shell. Hence, important aperture effects are demonstrated by a comparison of the beam patterns of the two shells. Bistatic measurements of the scatter produced by the empty shell at beam aspect were not conducted. However, I have obtained estimates of its beam pattern using the simple discrete line array discussed in Section 3.2.2 and a frequency

dependent gain correction to equate the predicted on-axis pressure level with the measured monostatic value. This model assumes uniform source strength over the length of the cylindrical portion of the shell and no phase taper. This assumption is supported by the good agreement of the measured and infinite cylinder fields demonstrated in Section 3.2.1. I have limited this prediction to a range of observation angles of $60 \leq \theta_o \leq 120$ degrees because I believe that the endcaps must radiate an axially orientated field that I have not studied. The resulting predictions are shown in Figure 5.4 for the measured coincident frequencies of $ka = 3.6$ and 7.3, and an intermediate frequency of $ka = 5.5$. All of the predictions were computed at a radius of 2 m that equals the distance employed in the actual measurements. The predicted beam patterns do not exhibit the sinc function features of the far-field pattern of a uniform array [13] because as discussed earlier, the receiver is not located in the Fraunhofer field of the array.

The measured beam pattern of the complex shell is shown in Figure 5.5 for the same three frequencies. The beam patterns of the complex and empty shells can be seen to be importantly different at the two coincidence frequencies while no important differences are observed at $ka = 5.5$. The beam patterns measured at $ka = 3.6$ and $ka = 7.3$ exhibit strong asymmetry with respect to the beam aspect plane ($\theta_o = 90$), and deep nulls that are not seen in the corresponding field of the empty shell. The observed beam pattern of the complex shell is the result of interference of the initial geometric scatter and the radiation observed later, each component having different directivity properties. The initial scatter is uniformly distributed over the shell length as shown in Figure 5.2. Therefore, it produces a beam pattern of the same form as the empty shell, but with a frequency dependent gain correction to account for the different scattering source strengths. In contrast, the scattering sources observed later in time are not uniformly distributed in amplitude, or phase, and produce the beam patterns shown in Figure 5.6. I used the beamforming results of Figure 5.2 to estimate of the amplitude and phase taper of these sources for the coincidence frequency $ka = 3.60$. The resulting taper functions are shown in Figure 5.7 and are

subject to the resolution constraints and approximations of the beamforming process. The phase distortions observed near the rings demonstrate important local stiffening effects. This source distribution produces peak scatter levels at an observation angle of $\theta_o = 84$ degrees and appears to destructively interfere with the initial scatter producing the null observed at the same angle in Figure 5.5. Destructive interference also produces the null shown at $\theta_o = 73$ degrees. This interference is analogous to the compressional wave interference observed in the backscatter of the empty shell or an infinite cylinder, but in this case the directive nature of the aggregate compressional wave field produces the interference at an oblique bistatic angle. I am surprised to see that the delayed field is steered to angle so close to the 83 degree angle where a uniform line array would produce a null in the farfield, but I believe this is purely coincidental. I have used the taper estimates to propagate the field back out to a greater distance and found that the delayed scatter was then steered to an angle of approximately 85.5 degrees. Hence, some of the observed interference is a near field aperture effect. Similar effects can also be seen at the second coincidence frequency $ka = 7.3$ with the delayed field steered to an angle of $\theta_o = 87$ degrees.

The complex shell beam pattern observed at the intermediate frequency $ka = 5.5$ is well approximated by the empty shell prediction because weak compressional wave radiation is produced away from coincidence. Peak scattered pressure levels measured at this frequency are 10 dB less than peak levels observed at the two coincidence frequencies as shown in Figure 5.6. These small radiation levels are incapable of providing significant levels of destructive interference with the large amplitude geometric scatter.

5.3.2 Monostatic Time and Frequency Domain Representations

The measured bandlimited impulse response signals and corresponding signal envelopes are shown in Figures 5.8 and 5.9 for the complex shell, and in Figures 5.10 and 5.11 for the ring stiffened shell. Two important effects of the ring stiffeners and

internal loading are revealed by comparisons of these figures with one another and with the corresponding empty shell data shown in Figures 3.2 and 3.3.

- The internal loading has increased the initial scatter produced by the shell.
- The backscatter produced by both the ring stiffened and complex shells at beam aspect does not exhibit exponentially decaying compressional wave radiation over a series of successive circumnavigations as observed for the empty shell.

The initial scatter from the complex shell is 2.5 dB greater than that of the empty and ring stiffened shells. The internal loading increases the mass of the shell and alters the global impedance properties of the shell. Therefore, I am not surprised to see a change in the geometric scattering of the shell. However, I am surprised to see a change of this magnitude, and given this magnitude, I am surprised that no appreciable change was noted for the ring stiffened shell. I have investigated the peak levels of initial scatter produced by a number of different infinite shell models to evaluate the influence of shell stiffness, mass, and internal loadings. The shell models studied included pressure release and rigid cylinders, as well as a shell of increased thickness ($3h$). In addition, I employed a model of a cylindrical shell coupled to a continuous dynamic absorber layer. The dynamic absorber layer consists of many identical springs and masses that are uniformly distributed on the interior surfaces of the shell and act independently of one another. With the addition of the dynamic absorber layer, the Donnell equation for the radial displacement introduced earlier as equation 2.10 is altered to include the added impedance z_{ab} of the layer as shown below:

$$\frac{\nu}{a}\frac{\partial u}{\partial z} + \frac{1}{a^2}\frac{\partial \vartheta}{\partial \phi} + \frac{w}{a^2} + \beta^2\left(a^2\frac{\partial^4 w}{\partial z^4} + 2\frac{\partial^4 w}{\partial z^2 \partial \phi^2} + \frac{1}{a^2}\frac{\partial^4 w}{\partial \phi^4}\right) + \frac{1}{c_p^2}\frac{\partial^2 \vartheta}{\partial t^2} = -\frac{p_s + p_i}{c_p^2 h \rho_s} + \frac{z_{ab}}{c_p^2 h \rho_s}\frac{\partial w}{\partial t} \tag{5.1}$$

The impedance provided at the spring end of a single degree of freedom absorber equals [10]:

$$z_{ab} = -im_{ab}\frac{1 - i\eta_{ab}\omega/\omega_o}{1 - i\eta_{ab}\omega/\omega_o - \omega^2/\omega_o^2} \tag{5.2}$$

where the absorber is defined by the parameters m_{ab}, k_{ab}, and R_{ab}, the per unit area mass, stiffness, and resistance of the attachments; $\omega_o^2 = k_{ab}/m_{ab}$ is the square of the resonance frequency of the oscillator, and $\eta_{ab} = R_{ab}/\omega_o m_{ab}$ is the loss factor. At resonance the impedance of the oscillator is large, being limited only by the resistance of the spring. I computed the scattered field for an absorber layer providing a mass ratio of $\beta_m = m_{ab}/h\rho_s = 3$, and a loss factor of $\eta_{ab} = 0.01$. The internal structures comprising the shell were designed to have fundamental resonances near $ka = 1$, but many different modes would exist at higher frequencies. Therefore, I computed the scatter produced with different system resonance frequencies of $ka_o = 1.0$ and $ka_o = 4.0$. The target strengths of of the peak amplitude of the initial scatter produced by the different cylinders are compared in Table 5.1 for the "Gaussian" filtering bandwidth of $2.75 < ka < 10.0$.

Table 5.1: **Comparison of the Target Strength of the Peak Initial Scatter Produced by Different Infinite Cylinders at Beam Aspect**

Cylinder Description	Target Strength dB re 1 m
Rigid	-33.7
Pressure Release	-33.2
MIT Shell Parameters	-34.5
Increased Thickness $3h$	-35.9
Absorber Layer $ka_o = 1$	-34.7
Absorber Layer $ka_o = 4$	-36.6

Given these results, I would not expect to see the increased mass and altered impedance of the internal loading to produce an increase larger than about 1.5 dB. The small changes in initial scattering levels that are demonstrated in Table 4.1

also support the finding that no appreciable change was noted with the addition of the four ring stiffeners. In any case, the different measurements were probably not conducted with a precision greater than 1 dB and similar measurement deviations may influence the observed increase.

However, I note that Dyer [14] shows the relative strength of the initial beam aspect backscatter to be:

0 dB; empty shell,

1.6 dB; ring stiffened shell,

4.1 dB; complex shell,

a set of values close to those measured (especially when one considers that the precision of the measured data is no better than 1 dB). His theory is based on rigid body motion of the models and their hydrodynamic masses since the elastic pulse in each model travels faster ($\approx 5270/1500$) than the excitation and encompasses a sizable portion of the entire circular cross-section before the excitation ceases. While strictly valid only when this speed ratio $\longrightarrow \infty$, his result for excitation initially of one-half of the cross-section is expressed as

$$20log\left[1+\frac{m_i}{m_s+m_a}\right]$$

where m_i is the internal mass, m_s is the empty shell mass, and m_a is the added hydrodynamic mass.

A comparison of Figures 5.9 and 3.3 indicates that although the initial return on the internally loaded shell has increased by 2.5 dB, the first compressional wave return shown at $t = 66$ μsec has decreased by 6 dB. Over the first 400 μsec, the elastic wave backscatter exhibits an exponential decay of 0.048 $dB/\mu sec$, a value nearly 25% less than that of the empty shell. The decreased level of the first return results because the field is effectively steered away from the monostatic receiver as discussed earlier. The subsequent amplitude variation is indicative of altered impedance properties and energy storage provided by the rings and internal loading. The scattering source distribution and amplitude taper shown in Figure 5.7 demonstrates that de-

creased radiation levels are produced near the rings. However, radiation produced in the region of the rings at later times $t > 300\ \mu sec$ exceeds that of the neighboring shell bays as seen in Figure 5.2. Hence, the ring stiffeners, together with the supported internal structures, must provide energy storage mechanisms of decreased radial amplitude at the exterior shell, and decreased decay rate. This is a locally acting impedance effect that cannot be explained with a simple calculation for a thicker shell that one might think would incorporate similar energy storage mechanisms. A shell with an increased thickness of $3h$ exhibits an increase in the compressional wave speed of approximately 15% at frequencies near $ka = 4$ and the increased speed produces an increase in the decay rate of nearly 70% at this same frequency.

The first incidence of compressional wave scattering produced by the ring stiffened shell is also 6 dB less than that produced by the empty shell as demonstrated by a comparison of Figures 5.11 and 3.3. The compressional wave scatter observed for $t < 200$ is similar to that generated by the complex shell, but radiation from the third circumnavigation is greatly decreased although subsequent ones are not. Given these similarities and the fixed configuration of ring stiffeners, I believe that the ring stiffened shell must exhibit directivity properties similar to the complex shell.

Finally, the beam aspect target strengths $T(\omega, \theta)$ of the three different shells are compared with one another in Figure 5.12. Neither the ringed shell, nor the complex shell, exhibits a pronounced minimum near the ring frequency of the shell. At this frequency, the strong destructive interference of the geometric and compressional wave backscatter produced by the the empty shell is inhibited by the altered directivity of the scatter sources. A less pronounced minimum is generated by both shells near $ka = 3.9$, but this is the result of only weak destructive interference with the directive field producing strong interference near $\theta_o = 83$ degrees at $ka = 3.6$ as noted earlier. Destructive interference remains evident near $ka = 7.3$ for both shells although the minimum value produced by the complex shell is actually located at $\theta_o = 89$ degrees.

The target strengths of the ring stiffened and complex shells nearly equal one another at frequencies below a threshold value of approximately $ka = 5.5$. At higher frequencies, the target strength of the internally loaded shell exceeds that of the empty ring stiffened shell by approximately 4 dB. The target strength of the complex shell also exceeds that of the empty shell at frequencies $ka > 5.5$, but by a smaller value of approximately 2 dB. The increase in target strength can be attributed primarily to the increase in the initial scatter from the complex shell. Similar behavior is also consistently observed at oblique angles of incidence as will be addressed in discussions that follow. In contrast, the target strength of the empty and complex shells both exceed that of the ring stiffened shell over a range of frequencies of $7.4 \leq ka \leq 9.5$, as well as near $ka = 4$. While the ring stiffened shell exhibits no significant change in initial scatter, its compressional wave scattering levels are decreased as noted earlier. This decrease is observed over ranges of frequencies where constructive interference of the initial and compressional wave scatter occurs for the empty shell, but is impaired by decreased compressional wave radiation from the ring stiffened shell.

5.4 Monostatic Field Properties Observed at Oblique Angles of Incidence

I now briefly examine the monostatic data measured at oblique angles of incidence ranging from bow to beam aspect so as to provide context for the main focus of this thesis in the range within 30 degrees of beam aspect. The field measured within 30 degrees of beam aspect is examined in detail in Section 5.5.

5.4.1 The Initial Scatter

The target strength $T_{initial}(\theta)$ associated with the peak initial scatter produced by the ring stiffened and complex shells is compared with that of the empty shell in Figure 5.13. The target strength values were computed as discussed in Appendix

A.4.2. In each case, scattering from the three distinct surfaces that comprise the exterior shells produce local maxima at aspect angles of 90, 60, and 0 degrees. The addition of ring stiffeners does not appreciably alter the initial target strength of the shell surfaces and it differs from the that of the empty shell by less than 1 dB at all aspect angles. These results further confirm that the scatter initially observed is predominantly produced by geometric scattering processes.

The internal loading increases initial scattering by $2-3$ dB over a range of angles within 60 degrees of beam aspect, as was noted at beam aspect, but initial scattering levels are decreased by about 1 dB at aspect angles near bow incidence ($\theta < 30$ degrees). However, while increased initial scatter levels were noted during all of the monostatic measurements of October 1991, less pronounced increases were measured during the bistatic measurements of June 1992, as illustrated in Figure 5.13. An explanation of this 2 dB discrepancy is not yet available. The internal loading provides an apparent change in the impedance of the shell and produces an aspect angle dependent change in the initial scatter. This aspect angle dependence appears to be related to the interrogation lengths of the effective $30\mu sec$ time duration of the incident pulse as recognized by Conti and Dyer [16]. This pulse duration has a waterborne interrogation length of $c_o\tau/2 = 0.022m$ and a compressional wave interrogation length of about $c_p\tau/2 = .079$ that is the maximum value supported by the shell. The incident pulse can initially interrogate about one half of the shell diameter at beam aspect, and it can only interrogate the length of the endcap at bow aspect. Therefore, the internal structures cannot influence the initial scatter amplitudes near bow aspect because they are not interrogated. I suspect that the 1 dB decrease in initial scatter observed at bow aspect is primarily a experimental deviation within the precision of the measurement, which suggests that the difference is, in reality, $3-4$ dB within 60 degrees of beam aspect. This result is consistent with the zero-order impulse theory of Dyer [14].

5.4.2 Time Domain Features of the Monostatic Signals

The elastic wave scattering influences of the ring stiffeners can be made evident in the time domain representations of the monostatic signatures of both the ring stiffened and complex shells. A contour plot of the envelopes of the bandlimited impulse response signals measured over the range of aspect angles of $0 \leq \theta \leq 90$ is shown in Figure 5.14 for the ring stiffened shell, and in Figure 5.15 for the complex shell. The propagation delay of the peak initial return has been removed to stack the signals. A comparison of both figures with the empty shell data shown in Figure 3.9 demonstrates that a significant increase in backscatter is produced by the internal structures and stiffeners at aspect angles within 60 degrees of bow aspect. In addition, both shells exhibit significant backscatter away from bow and beam aspect with time delays less than those of the empty shell. These effects are observed because as noted in Chapter 4, the ring stiffeners directly scatter the forced wave into the surrounding acoustic medium and scatter energy to other wavenumbers. Hence, back propagating structural and acoustic fields are induced at earlier times than observed for the empty shell.

Scattering of the forced wave as it first encounters each individual stiffener can be made evident in both Figures 5.14 and 5.15, particularly over a range of angles $10 < \theta < 60$ degrees, with the use of Figure 5.16. The latter shows the time delays associated with the first incidence of scattering from each ring, and the two junctions of the endcaps with the cylinder. Their propagation paths are illustrated in Figure 5.17 and correspond to simple propagation along the axis of the cylinder at the trace velocity of the incident field and then direct waterborne propagation back to the monostatic receiver at speed c_o.

Additional manifestations of the ring scattering mechanisms presented in Chapter 4 can be seen with further examination of the time domain features shown for the ring stiffened shell in Figure 5.14. Helical membrane wave scattering processes can be seen to produce large amplitude delayed signal components within 30 degrees of beam aspect. However, their features are more diffuse than those of the empty

shell and are observed earlier in time. Periodic torsional wave radiation that is characteristic of the empty shell over the angular range $61 < \theta < 87$ deg is not strongly evident in the monostatic signature of the ring stiffened shell. Moreover, delayed signal levels decrease below the critical aspect angle for shear wave excitation, $\theta = 62$ degrees, but not as abruptly as observed for the empty shell. Scattering of the forced wave at the junction of the bow endcap and ring stiffeners apparently constitutes most of the prominent delayed backscatter shown over the range $20 < \theta < 60$ degrees in Figure 5.14. The time delay of these events is dictated by the axial trace velocity $c_z = c_o/\cos\theta$ of the incident field, as noted previously. Near bow aspect, important levels of delayed backscatter are induced by compressional wave radiation that originates at the bow endcap after experiencing multiple reflections at the individual stiffeners. The approximate time delays associated with the first incidence of these events are listed in Table 5.2 and are referenced to the arrival of the initial scatter. Large amplitude signals are also evident near bow aspect at times $t < 82$. This corresponds to the delay required for the incident field to propagate to the junction of the cylinder and the bow endcap and scatter back to the receiver, as noted for the empty shell.

Table 5.2: **Bow Aspect Time Delays of the First Reflections of Compressional Waves at the Structural Discontinuities**

Discontinuity	Delay (μsec)
Junction w/Bow Endcap	23
Ring Stiffener I	58
Ring Stiffener II	147
Ring Stiffener III	220
Ring Stiffener IV	268
Junction w/Stern Endcap	303
Length of Shell	326

Most of the time domain features of the ring stiffened shell remain evident in the

monostatic signature of the complex, internally loaded shell shown in Figure 5.15. However, the dynamic interaction of the modes of the internal structures and surrounding shell appears to smooth some of the detail of the signature. Additional delayed signal features are particularly evident near bow aspect and up to about $\theta = 50$ deg. Many of these features are possibly generated by induced axial wave propagation in the Delrin rods at a speed of $c_z \simeq 1625\ m/s$, and by multiple reflections at the discrete masses supported at the ring stiffeners by rubber sectors.

Stiffener-induced scattering generally increases backscatter energy levels as quantified in Figure 5.18, where the target strength values derived from the integral of the squared monostatic pressure $T_{integrated}(\theta)$ are compared for each of the three shells. The addition of the ring stiffeners alone increases the backscatter energy by $2-3.5\ dB$ over the range of aspect angles $0 \leq \theta < 63$ degrees and, because the initial scattering is not increased, they must do so via radiation beyond the initial return. But the ring stiffeners do not provide a consistent increase over the range of aspect angles where phase matched membrane wave excitation occurs, namely $63 \leq \theta \leq 90$ degrees.

The comparison of initial and integrated signal levels shown in Figures 5.19 and 5.20 demonstrates that the initial scatter remains the predominant source of backscatter over the angular regime $84 < \theta \leq 90$ degrees. Therefore, I conclude that the ring stiffeners alter the temporal distribution of delayed backscatter generated over the angular regime $63 \leq \theta < 84$ degrees, but only minimally influence the total backscatter.

The internal loading provides an increase of 2 dB in total target strength over that of the ring stiffened shell at nearly all aspect angles as seen in Figure 5.18. While some of this increase represents the increased geometric scattering initially observed, particularly within 55 degrees of beam aspect (see Figure 5.13), it also probably represents an increase in delayed radiation induced by energy storage in the modes of the internal structures. It should be noted once again that this increase was not fully evident at the monostatic receiver locations of the bistatic measurements

conducted in May and June of 1992, but this discrepancy remains to be resolved.

Increased levels of delayed backscatter induced by the ring stiffeners and internal loading are particularly evident over the range of aspect angles $40 < \theta < 63$ degrees. The initial scatter was previously found to dominate the scattered energy of the empty shell over this angular regime as shown in Figure 3.8. In contrast, integrated signal levels shown in Figures 5.19 and 5.20 can be seen to exceed the level of the peak initial return by $2.5-6$ dB for the ring stiffened shell, and by $4-6$ dB (possibly $5-7$ dB) for the complex shell.

5.4.3 Frequency Dependence of the Total Target Strength

The influence of the ring stiffeners and internal loading observed in the time domain is also exhibited in the frequency/angle domain. This is shown for the ring stiffened and complex shells in the contour plots of Figures 5.21 and 5.22. These plots compare with Figure 3.12 for the empty shell. The target strength values $T(\omega, \theta)$ shown in these figures were computed using spherical spreading assumptions as discussed in Appendix A.4.2. The largest target strength values produced by both shells are again located near beam aspect. However, target strength values greater than -24 dB re 1 m are now found within 40 degrees of beam aspect for the ring stiffened shell, and 45 degrees for the complex shell, as opposed to 30 degrees for the empty shell. Increased backscatter is also evident near bow aspect. Scattering processes induced by the ring stiffeners and dynamic interaction with the resiliently mounted internal structures have extended the angular regimes where large backscatter levels are observed.

The ring stiffeners and internal loading have also altered the length scale and spatial coincidence effects evident in the backscatter of the empty shell. These effects are largely influenced by a combination of axial resonance and aperture effects, and elastic scattering produced at the ring stiffeners. These effects are discussed in detail in Section 5.5.

The target strength values $T(\omega, \theta)$ of the ring stiffened and complex shells have

been differenced and shown in Figure 5.23. It is readily apparent from this figure that the internal loading substantially increases the target strength of the ring stiffened shell at discrete combinations of frequency and aspect angles. Increased target strength values are more numerous at frequencies $ka > 6$ which is consistent with the behavior noted near beam aspect, but it is difficult to tell from the figure whether the changes average to zero (they do not; see the next paragraph).

Therefore, I have computed spatial averages of the monostatic backscatter to quantitatively measure the frequency dependent global influences of the ring stiffeners and internal loading. The spatial averages $T_{savg}(\omega)$ were numerically computed from the mean square backscattered pressure data $|P_s(\omega,\theta)|^2$ as discussed in Appendix A.4.2, and were computed over three different regions in angular space. In each case, the results are normalized by the product of the mean square pressure of the incident field and 4π steradians yielding a spatial average expressed in units of target strength. The spatial averages measured over the full range of aspect angles $0 \leq \theta \leq 180$ degrees are shown in Figure 5.24. Although the spatially averaged backscatter of the ring stiffened and empty shells differ near the ring frequency $ka = 3.5$, both shells exhibit similar levels at all frequencies $ka > 4$. The differences noted near the ring frequency are manifestations of altered compressional wave field of the ring stiffened shell near beam aspect as discussed in Section 4.3. In contrast, the internal loading significantly increases levels at frequencies greater than $ka = 5.5$ while exhibiting similar levels at lower frequencies.

The values shown in Figure 5.24 are dominated by the large backscatter produced within approximately ± 8 degrees of beam aspect, where large initial scatter is observed. Therefore, I also computed the spatial average of monostatic data measured over the range of aspect angles encompassing $61 \leq \theta \leq 81$ and $99 \leq \theta \leq 119$ degrees and the resulting values shown in Figure 5.25 better quantify the influence of the stiffeners and internal structures over the angular regime where phase matched membrane wave excitation processes occur. The ring stiffened and empty shell produce similar average levels, but the ring stiffened shell exhibits increased levels of

approximately 2 dB at a series of frequencies ka = 7.7, 8.8, 10.1, and 11.5. The internal structures increased target strengths at frequencies above $ka = 6$.

One can now see that the internal loading does in fact increase backscatter above a threshold frequency of about $ka = 5.5$. Much of the observed increase is the result of increased levels of initial scattering, of which some measurement discrepancies exist. However, as discussed in Section 5.5, the internal structures were also found to increase the decay rates of the backscatter relative to that of the ring stiffened shell. This further indicates that important interaction with the internals must be occurring. The detailed influences of the internal structures are currently a topic of additional study for Hua He [30].

I also computed the spatial average of backscatter measured over a range of aspect angles encompassing ± 60 degrees of bow and stern aspect to quantify the influence of the stiffeners and internal structures over the angular regime where membrane wave excitation is not induced over the cylindrical portions of the shells. The resulting values are shown in Figure 5.26. The ring stiffeners increase average values by at least 2 dB at most frequencies over this angular regime, and the internal structures increase values by as much as 5 dB (possibly 6 dB). These phenomena are currently being studied by Conti [16].

5.5 Interpretation of Backscatter Measured Over the Range of Aspect Angles of 60-90 Degrees

5.5.1 Introduction

The features of the backscatter produced by the ring stiffened and complex shell models over the range of aspect angles of $60 \leq \theta \leq 90$ degrees are highly influenced by the the interaction of the induced leaky membrane wave field with the structural discontinuities and internal loading. The frequency dependence of the target strength measured over this range of aspect angles is shown in the contour plots of Figures 5.27

and 5.28. Some of the features of the empty shell backscatter shown in Figure 3.13 for the same aspect angle range are essentially unchanged. In the case of the ring stiffened shell, regions of enhanced target strength remain located along the spatial coincident loci associated with transverse shear wave excitation, most notably at modes $n = 1$ and $n = 2$. However, coincidence effects in the empty shell are now diffused by the complicated distribution of propagating structural waves caused by interaction with the ring stiffeners. Coincident back radiation is only vaguely evident in the signature of the internally loaded shell. In general, coincidence radiation is impaired with increasing shell complexity as I will demonstrate in more detail later in this section.

Peak values of the target strength of the ring stiffened shell can be seen at aspect angles near $\theta = 88$ degrees, rather than at $\theta = 90$ where a monostatic receiver would measure the specularly directed geometric scatter. The target strength of the empty shell also peaks at similar angles, as does the complex shell although this is not evident in Figure 5.28 because of the contour scale used. This phenomena is largely an artifact of the small measurement radius used. As an example of this effect, I show in Figure 5.29 the beam pattern produced at a distance of 2 m when the discrete array model used earlier is steered to an observation angle of $\theta_o = 92$ deg. This steering angle corresponds to the specular direction of a shell insonified at an aspect angle of $\theta = 88$ and one can see that the pattern peaks near $\theta_o = 87$ and $\theta = 97$ rather than at the steering angle as would occur in the far field. Therefore, I conclude that peak values would generally be located at $\theta = 90$ had the measurements been conducted at a greater distance. However, coincident shear waves are excited and contribute to the backscatter when the shell is insonified just off of beam aspect $\theta = 90 \pm \epsilon$. As a result, shear wave radiation and asymmetric backscatter may produce peaks away from 90 degrees in some instances.

The length scale modulation of the empty shell shell differs from that of the ring stiffened and internally loaded shells. The frequency spacing of peak backscatter levels carries the imprint of length scale effects induced by the ring stiffeners and

internal loading. I show in Figure 5.30 frequency averaged values Δka measured for the three shells at aspect angles of 66, 72, 75, and 80 degrees. The time duration of acquired data limits the frequency resolution the empty and ring stiffened shell data and I believe that the spacings shown for the ring stiffened shell are artificially increased. However one can clearly see that the spacing is significantly reduced by both the ring stiffened and complex shells. However, I expect similar effects because the membrane wave scattering estimates I present in Chapter 4 show sufficiently large reflection coefficients, and levels of radiation to the acoustic field, that a series of rings would alter characteristic radiation lengths and possibly induce aperture effects. Scattering to other wave types with different phase and group velocities would also alter length scales. If the rings were each perfectly reflecting boundaries, axial resonances would occur at frequencies $ka_{res} = n\pi a/(L_i \cos\theta)$ where the distance between the different pairs of stiffeners is L_i and the axial phase speed is equal to the trace velocity of the incident field. The axial resonance loci of this vastly simplified model are shown in Figure 5.31. In comparison with Figure 3.16 for the empty shell, the spacing between the loci of sequential orders are much larger, while the aggregate spacings are often smaller. This simple resonance model does not capture the behavior observed in Figures 5.27 and 5.28, nor should it, since resonances would occur between stiffeners and endcaps that span more than one shell bay. Moreover, the backscatter observed is produced by a convolution of axial resonance and aperture effects. These issues will be addressed in more detail in the discussions that follow.

Evidence of important aperture effects can be seen if one examines the target strength contours of Figures 5.32 and 5.33 where data measured over a range of aspect angles of $60 \leq \theta < 120$ degrees are shown for the ring stiffened and complex shells, respectively. Target strengths shown at complementary aspect angles (e.g. $\theta = 70$ and $\theta = 110$) are similar, but their frequency distributions differ. If only axial resonances determined observed length scales, the target strengths would be symmetric with respect to beam aspect. Therefore, aperture effects induced by the unequal spacing of the rings and internal loading configuration must play a

crucial role in the scattering process. However, aperture effects and the unequally spaced ring configuration does not significantly alter the total backscatter observed at complementary aspect angles. The target strengths derived from time integrals of the squared pressures measured at complementary angles are compared for both shells in Figures 5.34 and 5.35. One can see that the total backscatter generally varies by less than 1 dB, particularly over the range of aspect angles of interest here. Hence, I conclude that the fundamental scattering processes are well represented by data observed over $60 \leq \theta \leq 90$.

The time evolution of the monostatic signatures measured over this range of aspect angles are illustrated in Figures 5.36 and 5.37 for the ring stiffened and complex shells, respectively. Both shells exhibit similar time histories, although with different amplitudes, for delays less than approximately 700 μsec. Hence, given their identical configuration of ring stiffeners, time delays found early in the evolution of the scatter are primarily caused by the spacing of the ring discontinuities. In comparison with Figure 3.14, the regular spacing in time delay is now absent and smaller time delays are evident. The angle-time slope $\theta - \tau$ can still be discerned as in Figure 3.14 which indicates that the delays of scattering processes observed early in time are largely determined by the trace velocity of the incident field. In addition, periodic membrane wave radiation is not as clearly observed at aspect angles $60 < \theta < 85$ which further indicates an impairment of coincidence radiation. One can also see that over a range of aspect angles of $68 < \theta < 80$ degrees, relatively large amplitude backscatter is observed over longer time durations for the ring stiffened shell, than for the empty and internally loaded shells. In fact, the three shells generally exhibit different backscatter decay rates with the ring stiffened shell having the lowest. The different decay rates observed denote important influences of the structural discontinuities and internal loading comprising the shells and are discussed in detail later in this Section.

5.5.2 Time Evolution and Decay Rates

I have again made use of focused beamforming of bistatic data to visualize the time evolution and axial distribution of the scatter produced by the complex shell at aspect angles of 75 and 66 degrees. A synthetic array consisting of the receivers located over a range of observation angles of $60 \leq \theta_o \leq 120$ was used to study the scatter produced at the 75 degree aspect angle. This array encompasses both the back and specular directions and is equivalent to that discussed earlier in Section 3.4.1. Two different arrays, both with uniform amplitude taper, were used to study the scatter produced at 66 degrees. One array consisted of receivers located over a range $50 \leq \theta_o \leq 130$ which was selected to visualize the radiation of membrane waves propagating in both axial directions, as well as discontinuity radiation. A second array consisting of receivers located over a range of $32 \leq \theta_o \leq 100$ deg was used to investigate the sources of back radiation. This array provided good axial resolution as needed to distinguish back directed discontinuity radiation. Similar results could not be obtained at 75 degrees with this simple beamforming algorithm because there is insufficient angular separation between the specular and back directions, and between adjacent sensor locations.

75 Degree Aspect Angle

The envelope of the effective scattering source distribution produced at the 75 degree aspect angle is shown in Figure 5.38. In comparison with Figure 3.18, one can see that the initial geometric scatter remains unchanged, but subsequent scatter is less uniformly distributed over the length of the shell and the periodic back directed coincidence radiation of the empty shell is largely absent. Rather, peak delayed scatter is observed over smaller regions of the shell bays. Peak levels are observed with delays relative to the initial scatter that are nearly equal to the predicted period of membrane waves ($T_{shear} = 92$ $T_{comp} = 26$ μsec). In particular, large amplitude components are observed with a relative delay of approximately 51 μsec which closely approximates the predicted delay of the second circumnavigation of induced com-

pressional waves, and 105 μsec corresponding to the first circumnavigation of shear waves. These altered distributions are consistent with the scattering coefficient estimates of Chapter 4. The shear and compressional reflection coefficients r_{ss} and r_{cc} are estimated as $O(0.75)$, while the transmission coefficients t_{ss} and t_{cc} are $O(0.15)$. Hence, membrane wave propagation in the axial direction opposite of the incident field would be induced with the first encounter of the forced wave with a ring, while the azimuthal dependence of the coincident field would be preserved.

One can also see that the axial distribution rapidly becomes diffuse, and I would expect to see this behavior given the estimates of ring scattering from one wave type to another shown in Chapter 4. For example, the incident field would excite the second coincidence shear mode $n = 2$ at $ka = 5.0$ as listed in Table 2.3. The resulting shear waves cannot scatter to compressional waves because they are cutoff. However, with each ring interaction they will scatter to flexural waves with estimated scattering coefficients of $r_{sf} \simeq 0.2$ and $t_{sf} \simeq 0.3$. The resulting flexural waves would not radiate again until they scatter at another ring. The resulting flexural wave field will tend to limit observed decay rates as I will demonstrate shortly. In contrast, coincidence frequencies of compressional waves exceed the cutoff frequencies of shear waves and scattering to both shear and flexural waves would result. A coincidently excited compressional wave at $n = 1$ and $ka = 9.1$ would scatter to shear waves with estimated coefficients of $r_{cs} \simeq 0.4$ and $t_{cs} \simeq 0.03$, and flexural waves with $r_{cf} \simeq 0.6$ and $t_{cf} \simeq 0.4$. This scattering to shear waves is important because they will propagate with a phase speed different from the incident field, $c_s \simeq 3200m/s$ in this case, and thus will radiate in a different direction. One can see in Figure 5.38, and more prominently in the work of Mackovjak [38], that scatter produced later in time becomes more prominent at the ring discontinuities. Mackovjak attributes this scattering resulting from the interaction of membrane waves with the ring. However, I suspect that much of the discontinuity radiation observed results from the scattering of flexural waves. The estimates of Chapter 4 indicate that the discontinuity radiation resulting from membrane wave interaction is not larger than the radiation produced

as the incident wave propagates over the shells. Thus one would not expect to see larger radiation at the rings than at the shell bays if membrane wave interaction were the primary cause of the radiation.

The bandlimited monostatic impulse response signatures of the empty, ring stiffened, and complex shells are compared in Figure 5.39. All three shells have nearly identical signatures for about the first 80 μsec where the geometric scatter and field induced near the bow endcap are observed. The signatures of the ring stiffened and complex shells differ markedly from the signature of the empty shell at all times shown thereafter, an effect I ascribe to scattering and reflection induced at the stiffeners. In contrast to the distinct energy packet exhibited by the empty shell near $t = 500\mu sec$, the signatures of the other two shells are more uniform. The signatures of the ring stiffened and complex shells themselves are similar with the exception of some amplitude variations.

However, the backscatter decay rates of the three shells are different from one another and these differences are of crucial importance. The envelopes of the signatures of the three shells are compared in Figure 5.40 to illustrate their decay rates and the values I obtained using a least squares fit of the data are compared in Table 5.3.

Table 5.3: **Comparison of the Measured Backscatter Decay Rates of the Shells at an Aspect Angle of 75 Degrees**

Shell Description	Time Duration μsec	Decay Rate $dB/\mu sec$
Empty - Amplitude Corrected	$330 < t < 710$	0.020
Empty	$800 < t < 1400$	0.010
Ring Stiffened	$275 < t < 1075$	0.011
Complex - Internally Loaded	$275 < t < 1200$	0.013

One can see that the leaky wave packet of the empty shell, with the envelope corrections discussed previously in Section 3.4.1, exhibits the greatest decay rate observed and this value exceeds that of the ring stiffened and complex shell by

nearly a factor of two. This decay rate compares well with a predicted decay rate of 0.025 μsec for a free transverse shear mode of angular order $n = 2$ and phase velocity $c_z = 5750\ m/s$. The decay rate of the empty shell signature observed later in time is decreased and compares more closely with that observed for the other two shells. In all three cases, I believe the decreased decay rate is a result of impaired coincident radiation and the influence of flexural wave scattering. As will be addressed in more detail later, back radiation from the ring stiffened and complex shells takes place only partially through coincidence.

Flexural wave scattering at the discontinuities would produce back radiation at a much less efficient rate than membrane waves because they do not radiate from the shell bays and propagate at subsonic speeds. Hence, flexural scattering at the rings would possibly establish a lower bound for the decay observed later in time where membrane waves have experienced several ring interactions and accumulated radiation losses. A flexural wave of order $n = 1$ and frequency $ka = 7.0$ will loose approximately 20% of its energy with each ring interaction as based on reflection and the transmission estimates of $r_{ff} = 0.87$ and $t_{ff} = 0.2$ shown in Figures 4.19 and 4.12. This loss is primarily associated with discontinuity radiation because the estimated values of scattering to membrane waves are $O(.002)$. At this frequency, flexural waves will propagate with a group velocity of 680 m/s as shown in Figure 2.41 and the scatter will therefore decay at a rate of 0.0038 $dB/\mu sec$ for an average ring spacing of $L/5$. This value is less than the observed values and the difference may be attributed to continued loss from non-coincident membrane waves and the approximations of the ring scattering analysis. However, the predicted value does correctly predict the trend of decreased decay rates.

It is also important to note that the decay rate of the complex shell exceeds that of the ring stiffened shell by 18%. This increase was observed over much of the aspect angle range of interest as noted earlier and may be a result of additional damping provided by the resilient supports of the internal structures.

The measured *specularly directed* bandlimited impulse response of the complex

shell is shown in Figure 5.41. In comparison with the specular scatter of the empty shell shown in Figure 3.30, the specular scatter is again dominated by the initial scatter, but the amplitude of shear wave radiation found at $t = 192$ and $t = 292$ μsec is decreased by more than a factor of 2. This can again be attributed to membrane wave reflections induced at the rings which promotes back radiation early in time at the expense of specularly directed radiation.

66 Degree Aspect Angle

Contours of the envelope of the back and specularly directed scattering source distribution produced at the 66 degree aspect angle are shown in Figure 5.42 and contours of the back directed distribution are shown in Figure 5.43. A comparison of Figures 5.38 and 5.42 shows that the scattering sources generated at 75 and 66 degrees evolve in similar fashions, but with different axial phase velocities. The incident field passes over the shell with a slower trace velocity of 3660 m/s at this aspect angle. As noted for the empty shell, specularly directed geometric scatter of uniform amplitude is produced as the incident field initially passes over the cylindrical portions of the shell, while the back directed geometric scatter is produced over the length of the endcap. In contrast with the empty shell, back directed radiation is also generated as the incident field and forced wave encounter each ring stiffener as can be seen in Figure 5.43. Significant levels of radiation are observed following the initial scatter with a relative delay of approximately 60 μsec. This delay agrees well with the circumferential period of the measured shear wave coincidence frequency $ka = 3.9$ of the empty shell. Once again the radiation at the shell bays that is observed early in time quickly becomes diffused, presumably by interaction with the rings and internal structures. Radiation originating at the rings can also be seen later in time where levels in the bay are reduced.

The bandlimited monostatic impulse response signatures of the three shells are compared in Figure 5.44 for this aspect angle. The empty shell shows two distinct packets of energy near $t = 500$ and $t = 1100$ μsec that correspond to two different

Table 5.4: **Comparison of the Measured Backscatter Decay Rates of the Shells at an Aspect Angle of 66 Degrees**

Shell Description	Time Duration μsec	Decay Rate $dB/\mu sec$
Empty - 1st Leaky Wave Packet	$530 < t < 850$	0.060
Empty - Overall Decay	$530 < t < 1220$	0.027
Ring Stiffened	$230 < t < 1220$	0.009
Complex - Internally Loaded	$230 < t < 1220$	0.013

length-wise trips of the shell as noted in Chapter 3. In contrast, one can again see that the signatures of the ring stiffened and complex shells are similar and more uniformly distributed in time because of ring scattering effects. The three shells again exhibit important backscatter decay rate differences as shown in Figure 5.45 and Table 4.4.

The overall decay rate of the empty shell compares well with a predicted decay rate of 0.028 μsec for a free transverse shear wave of order $n = 1$ and phase velocity 3660 m/s, but exceeds the decay rates of the other two shells by a factor of 3. The decay rate of the internally loaded shell is unchanged which further demonstrates that the damping in the resilient materials is important.

The *specularly directed* signature of the complex shell is shown in Figure 5.46 for this aspect angle. Once again the geometric scatter initially observed dominates the measured field and no large amplitude coincident radiation can be seen.

5.5.3 Coincidence Effects and Target Strength

The ring scattering mechanisms discussed in Chapter 4 and the previous subsection can be seen to inhibit coincident radiation, particularly over a range of aspect angles $63 < \theta < 68$ degrees. A comparison of the target strength contour plots of Figures 3.13, 5.27, and 5.28 shows that the shear wave coincidence loci become less

apparent with decreasing aspect angle and increasing order n. As for the empty shell, the compressional wave coincidence loci are not apparent.

I have calculated the target strength of portions of the measured signatures of the ring stiffened and complex shell scatter to evaluate the relative contributions of the signal constituents producing the larger amplitude, "uniform" signal noted earlier. A simple window operation was used to isolate the scatter measured at the 66 and 75 degree aspect angles over a time duration of $30 < t < 1150$ μsec. In Figures 5.47 through 5.50, I compare the results with corresponding empty shell data processed over the time duration where large amplitude coincidence radiation was observed. One can see in Figures 5.47 and 5.48 that coincidence radiation remains evident at 75 degrees. However, coincidence radiation from the complex shell is decreased and is diffused by a decreased frequency spacing of the modulation.

In contrast, one could argue that coincident radiation is evident in the ring stiffened shell of Figure 5.49 for the 66 degree aspect angle, but it is hardly impressive. Moreover, coincidence radiation is completely absent in the complex shell data of Figure 5.50. At this aspect angle compressional waves, are not cutoff at the coincidence frequencies of the shear wave field. Therefore, although the incident field can only excite phase matched shear waves, shear wave scattering at a ring will energize both flexural and compressional waves. The compressional waves excited at the first shear wave coincidence frequency $ka \simeq 4$ will propagate with a phase speed of approximately 11000 m/s and radiate at angles of $\theta_o = 82$ and $\theta_o = 98$ degrees. Hence, the energy of the shear wave field that so dominated the backscatter of the empty shell will be redistributed in the axial wavenumber domain. This redistribution may induce important aperture effects as discussed in the next section.

The target strengths of three shells calculated with the full duration of acquired data are compared in Figures 5.51 and 5.52 for these same aspect angles. In spite of the marked difference in their time signatures and coincidence effects, all three shells exhibit similar peak target strength levels of -20 to -15 dB re 1 m. Therefore, the initial phase matched membrane wave excitation must remain the essential means

of injecting energy into the system for later back radiation. In addition, I will demonstrate in the next section that the beam pattern observed near the monostatic receiver is characterized by high side lobe levels. Hence, while scattering at the ring stiffeners and internal loading effects may alter the fine details of the field, they do not change its broad spectral levels. Moreover, none of the three shells exhibit large enough damping rates to significantly alter peak levels from those determined by free wave radiation damping alone. This is further confirmed by the observation made earlier that over this range of aspect angles, the total backscatter of the three shells are nearly equal.

Finally, the specularly directed target strength of the empty and complex shells are compared in Figure 5.53 for the 75 degree aspect angle measurements. I have applied the target strength corrections of Section 3.2.2 to this data because the receiver is located in the near field of the beam associated with the initial scatter. Although the decay rate of the complex shell data has decreased, the coincidence nulls shown for the empty shell are not produced because insufficient coincident radiation is available to create destructive interference. No bistatic data is currently available to compare with the specular scatter of the complex shell at an aspect angle of 66 degrees. Therefore, I compare its form function with that of an infinite shell in Figure 5.54 and one can see that destructive interference of the initial scatter with coincident shear wave radiation is completely absent.

5.5.4 Aperture Effects

If resonant vibration was the principle source of the observed modulation of the target strength of the ring stiffened and complex shells, the back and specularly directed fields would have to exhibit equal frequency distributions and spacings. This would at least be true later in time where the different geometrically scattered pressures no longer influence the transform, and where numerous ring interactions have taken place to establish the resonant response. However, this crucial behavior cannot be seen in the measured bistatic data of the complex shell.

In order to make this comparison, I have computed the target strength of the back and specularly directed signatures measured at times greater than twice the total time required for the incident field to traverse the length of the shell $t > 2L\cos\theta/c_o$. This should allow sufficient time for several ring interactions to take place and excludes the initial scatter. I transformed the data observed over $700 \leq t \leq 2700$ for the 75 degree aspect angle, and $500 \leq t \leq 2500$ for 66 degrees and these segments where chosen to also exclude large amplitude scatter. The results are shown in Figures 5.55 and 5.56 for 75 degrees, and Figures 5.57 and 5.58 for 66 degrees. One can see from these figures that the late time specular and back directed scatter are not at all similar. Hence, while resonant behavior would establish the axial scattering source distribution, aperture effects are important and must be convolved with the axial source distribution.

I now show portions of the measured beam patterns of the complex shell encompassing the back and specular directions at representative frequencies measured for these same two aspect angles. In Figure 5.59, I show the beam pattern measured over a range of observation angles of $40 \leq \theta \leq 140$ at the 75 degree aspect angle. Beam patterns are shown in this figure for a frequency of $ka = 5.0$, at which apparent coincident radiation can be seen in Figure 5.48, and for $ka = 7.0$ and $ka = 9.3$. The corresponding steered beam pattern of the discrete array model used earlier is shown in Figure 5.60 for comparison. This array has uniform amplitude taper over a length equal to the cylindrical portion of the shells, and hanning amplitude taper at the ends. Similarly, I show in Figure 5.61 the beam pattern measured over the same range of observation angles and for the 66 degree aspect angle. In this figure, beam patterns are shown for a frequency of $ka = 3.9$, at which coincident radiation was observed for the empty shell, and for frequencies of $ka = 6.16$ and $ka = 9.25$. Again the steered beam pattern of the discrete array model is shown in Figure 5.62. Several important properties are readily apparent in these features.

- The beam pattern produced within about 15 degrees of the specular direction is well predicted by the simple discrete array model. This agreement improves

with increasing frequency. It can be attributed to the specularly directed initial scatter that is uniformly distributed over the length of the shell and is large in amplitude.

- The beam pattern shown at observation angles near the monostatic receiver exhibits large side lobe levels. While the side lobe levels of the specular field roll off as predicted, the side lobes of the non-specular field show little roll off. In addition, the beam pattern produced away from the specular direction appears more uniformly distributed in observation angle with increasing frequency. These effects result because the scattering sources are not smoothly distributed over the length of the shell. As discussed in Chapter 4, a directive acoustic field is also scattered with each interaction of a structural wave with a ring, and the ring will also energize other wave types with different phase speeds and radiation angles. Therefore, the phase taper of the scattering distribution is not uniformly distributed over the length of the shell.

- Null depths greater than 10 dB are often observed away from the specular direction. Therefore, coherent aperture effects must be important. Incoherent addition of the radiated field distribution would inhibit the formation of nulls. It is possible that the reflection estimates of Chapter 4 are too large and the different shell bay are better coupled than the results would suggest.

I have computed the amplitude and phase taper functions of the 66 degree back directed scattering source distribution illustrated in Figure 5.43. The resulting taper functions are shown in Figures 5.63 - 5.65 for the same frequencies shown in Figure 5.61. These values are of course subject to the resolution constraints of the beamforming operation. One can see from these figures that amplitude and phase tapers of the scatter are complicated functions of axial location that provide the high side lobe levels observed.

5.6 Summary

It has been demonstrated that the addition of ring stiffeners, as well as resiliently mounted internal loading, significantly influences the details of the time histories of the monostatic and specularly directed scattered fields. Although the details of the time histories of the monostatic field of the empty and ring stiffened shells differed vastly, peak target strength levels showed little variation. An apparent increase in target strength levels of $2-3\ dB$ was observed at frequencies $ka > 5.5$ during the measurements of the complex shell conducted during the October, 1991 test series. Unfortunately, this increase was not evident in the monostatic measurements of the bistatic tests conducted during the May and June of 1992.

Reflection and scattering at the ring stiffeners inhibits radiation of a coherent back or specularly directed leaky wave field over the length of the shell. Hence, coincident back radiation is more important for the empty shell than the ring stiffened and complex shells. Coincidence effects can be seen to become increasing diffuse as the shell configuration becomes more complicated. However, peak levels remain evident near coincidence frequencies for aspect angles $\theta > 67$ degrees where coincident shear waves cannot scatter to compressional waves at the rings because they are cutoff.

In Chapter 4 I demonstrated that scattering of a membrane wave at a mass controlled ring energizes flexural waves and the other membrane wave type if it is not cutoff. I have demonstrated in this chapter that the backscatter decay rates of the empty shell exceed those of the ring stiffened shell by a factor of 2 to 3. This decrease is consistent with the impairment of coincident radiation in the empty shell case and appears to result because the flexural waves excited at the ring propagate with slow group speeds and do not radiate until they scatter at another ring. Thus, the scatter produced later in time will consist of a series of less efficient radiators. My predicted lower bound of the decay rate does not compare well with observed values, but correctly captures the observed trend. The decay rate of the internally loaded shell exceeds that of the ring stiffened shell by 18-44% which is probably a manifestation of the increased damping provided by the resilient material.

The frequency spacing of peak levels of backscatter produced by the ring stiffened and complex shells is considerably less than that of the empty shell. Unfortunately, the frequency resolution of the ring stiffened shell data does not allow a good comparison with the complex shell. This spacing cannot be attributed to resonance effects alone. I have demonstrated that the back and specularly directed scatter of the complex shell is not alike as they would be for resonant scatter in the absence of aperture effects. Moreover, through various examinations of the beam patterns produced at 66, 75, and 90 degree aspect angles I have shown that aperture effects are important and significantly influence observed frequency spacings of the backscatter. The beam patterns produced near the specular direction at oblique angles of incidence are well approximated by the beampattern of an uniform line array with taper truncations. Near the back direction, the scatter has high side lobe levels with little roll off in angle and this results from the complicated amplitude and phase taper of the scattering source distribution. Deep nulls are also observed which is indicative of coherent aperture effects.

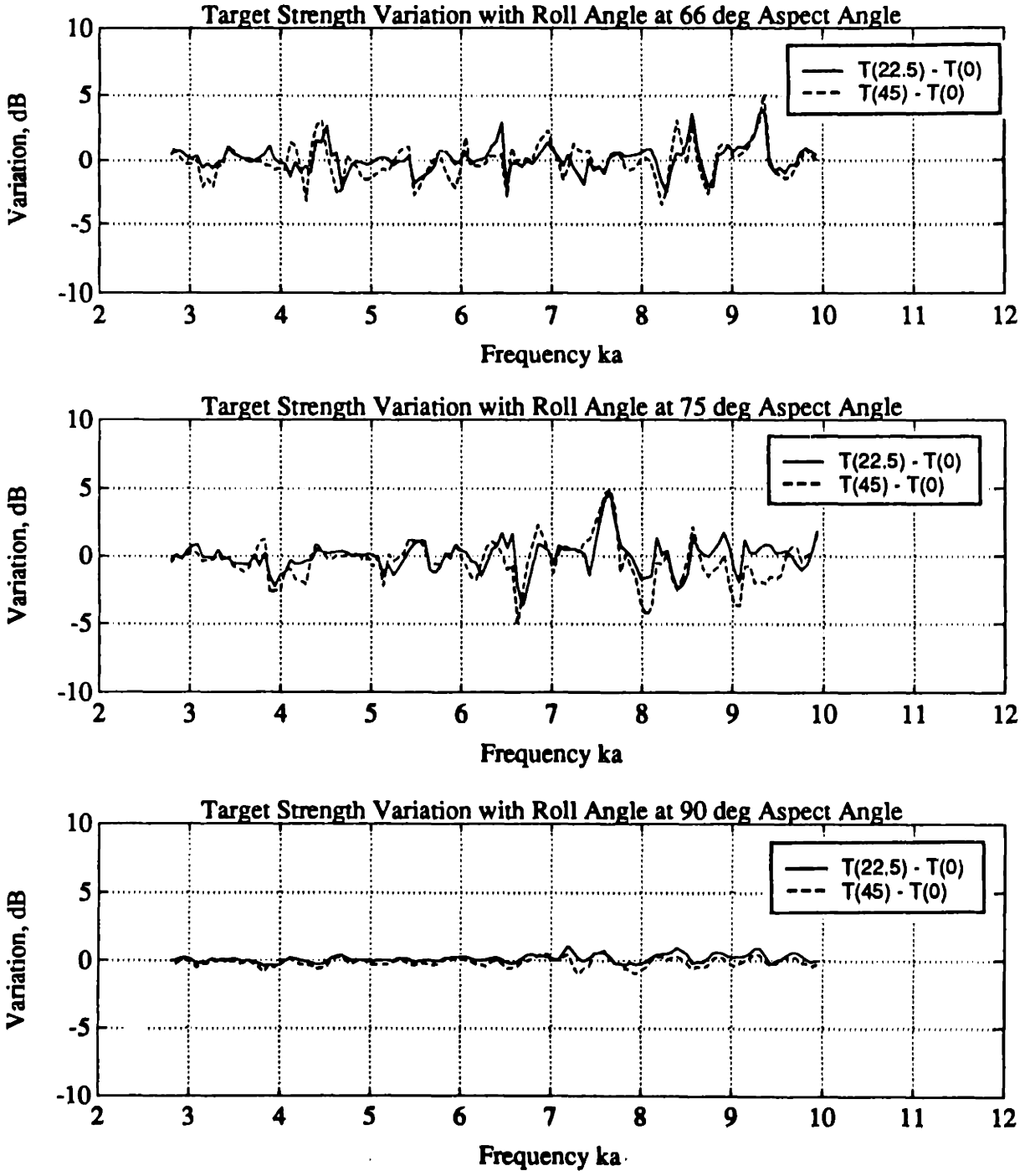

Figure 5.1: Comparisons of the Measured Target Strength $T(\omega, \theta)$ of the Complex, Internally Loaded Shell at Roll Angles of 0, 22.5, and 45 degrees and Aspect Angle of 66, 75, and 90 degrees. The differences shown were computed using averaged values of three neighboring frequency bins to negate the effects of small frequency shifts.

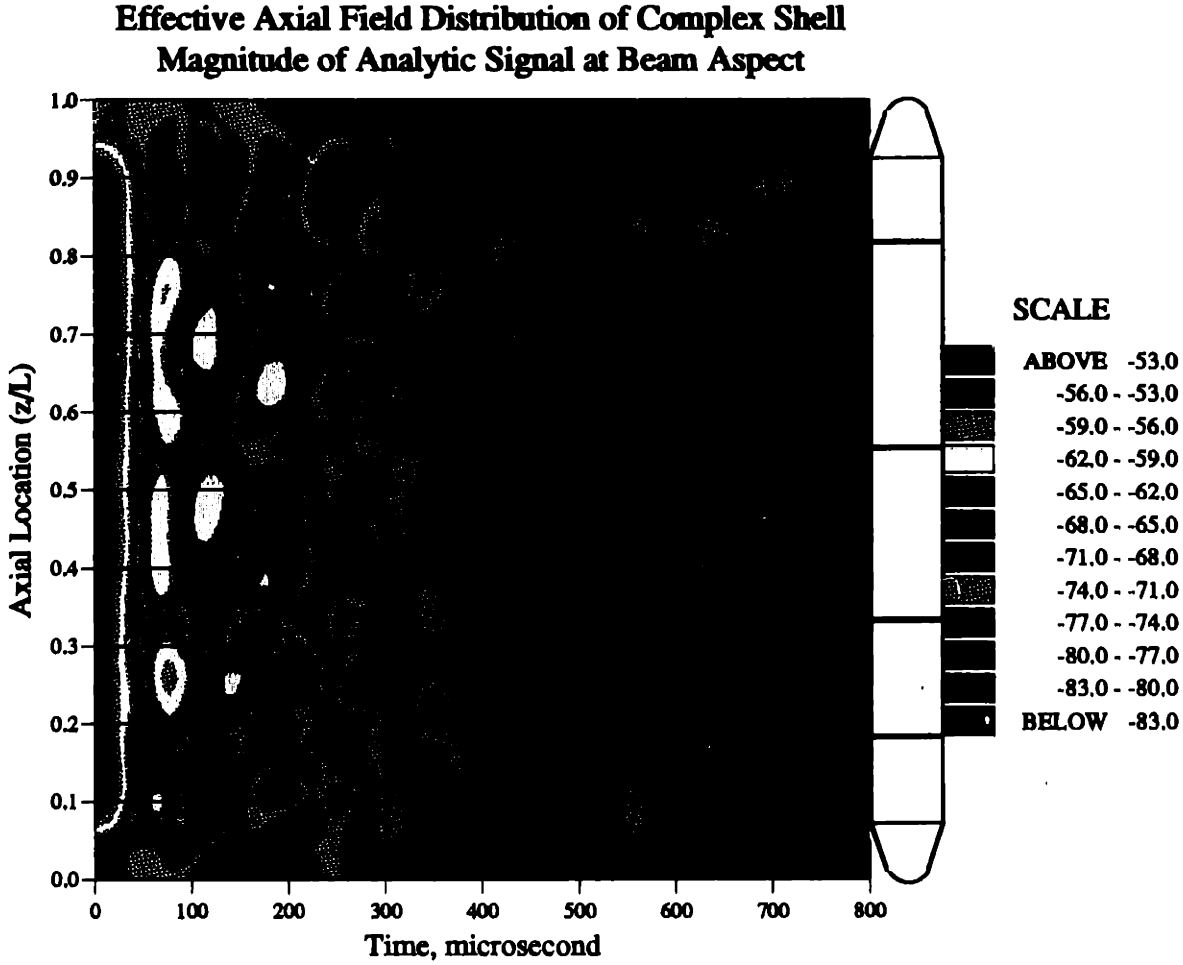

Figure 5.2: Effective Axial Distribution of the Back Directed Scattered Field of the Complex Shell at Beam Aspect. The results were generated using classical focused beamforming of the bistatic data measured over a range of observation angles of $60 \leq \theta_o \leq 120$ deg for the frequency range of $2.75 < ka < 10.0$. The incident field was deconvolved from the distribution to yield a normalized effective point source strength in dB re 1 m. The axial location $\bar{z}/L = 0$ corresponds to the stern, or far endcap, and $\bar{z}/L = 1$ is the bow endcap. The beamforming resolution is $\Delta z_{3dB}/L = 0.048$. Note the non-uniform axial distribution of the scatter sources, and the scatter produced at the rings for times $t > 350$ μsec.

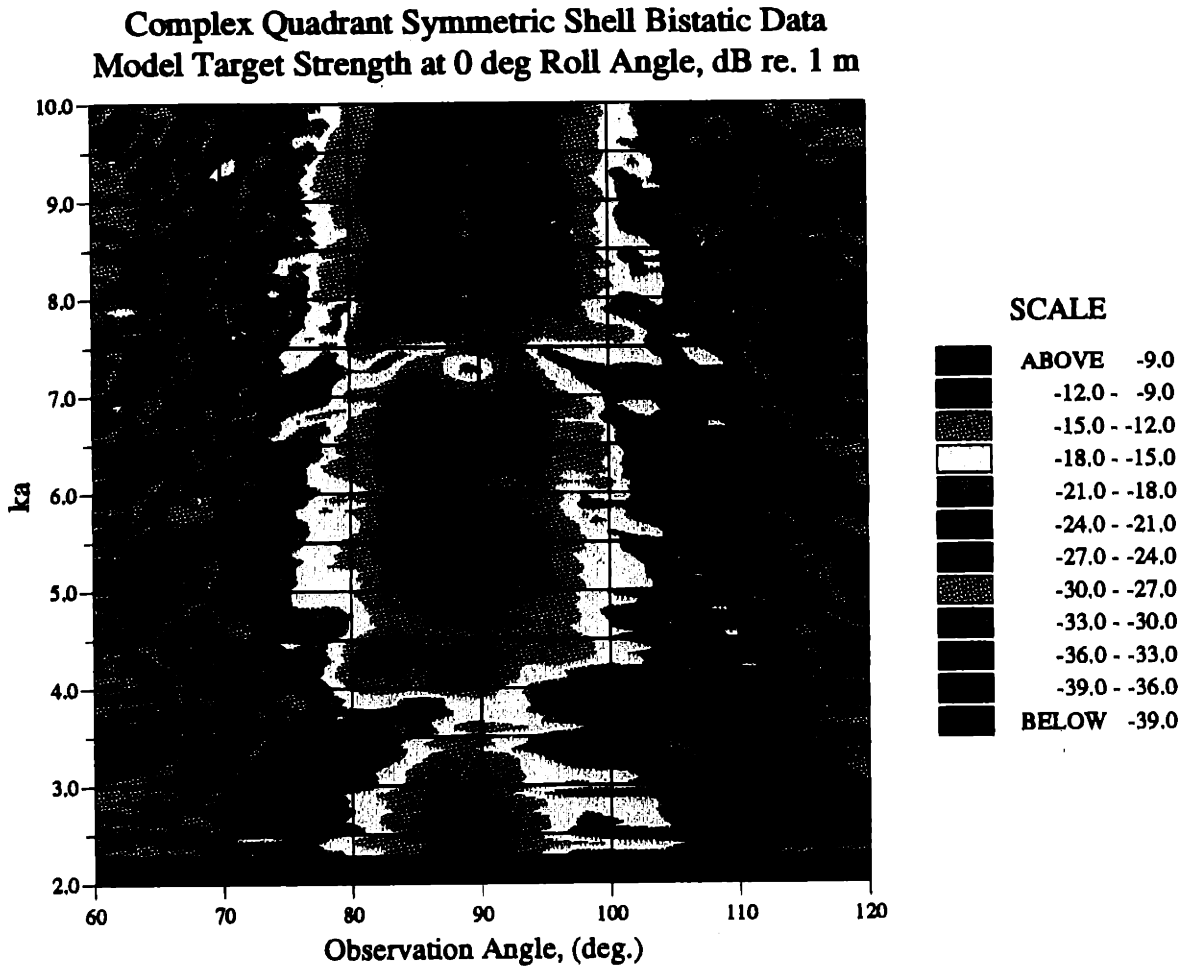

Figure 5.3: Contours of the Bistatic Target Strength $T(\omega, \theta_o)$ of the Complex Shell Measured for Beam Aspect over the range of observation angles $60 \leq \theta \leq 120$ deg. Values are normalized by the pressure level of the incident field at the target center location. The observation angle $\theta_o = 90$ corresponds to a location orientated normal to the axis of the shell and coaligned with its center. The nulls observed near $ka = 3.6$ and $\theta_o = 83$ deg, and near $ka = 7.3$ and $\theta_o = 89$ deg are the result of interference of the initial and compressional wave scattering.

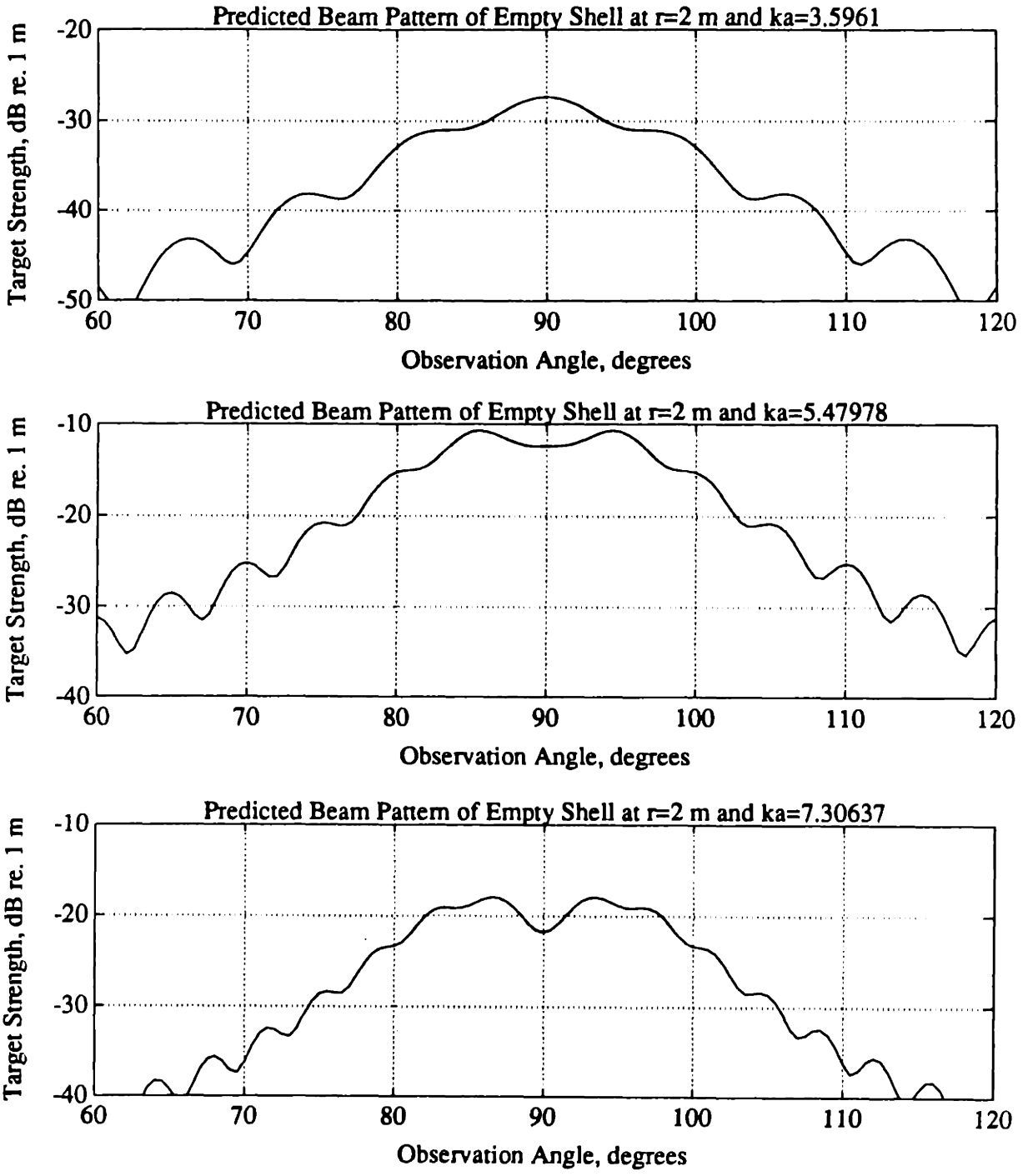

Figure 5.4: Predicted Beam Pattern of the Empty Shell at Beam Aspect and a Distance of $r = 2\ m$. The predictions are shown for the predicted compressional wave coincidence frequencies of $ka = 3.60$ and $ka = 7.31$, and an intermediate frequency of $ka = 5.48$. The magnitude of Target Strength at $\theta_o = 90$ corresponds to the measured monostatic value.

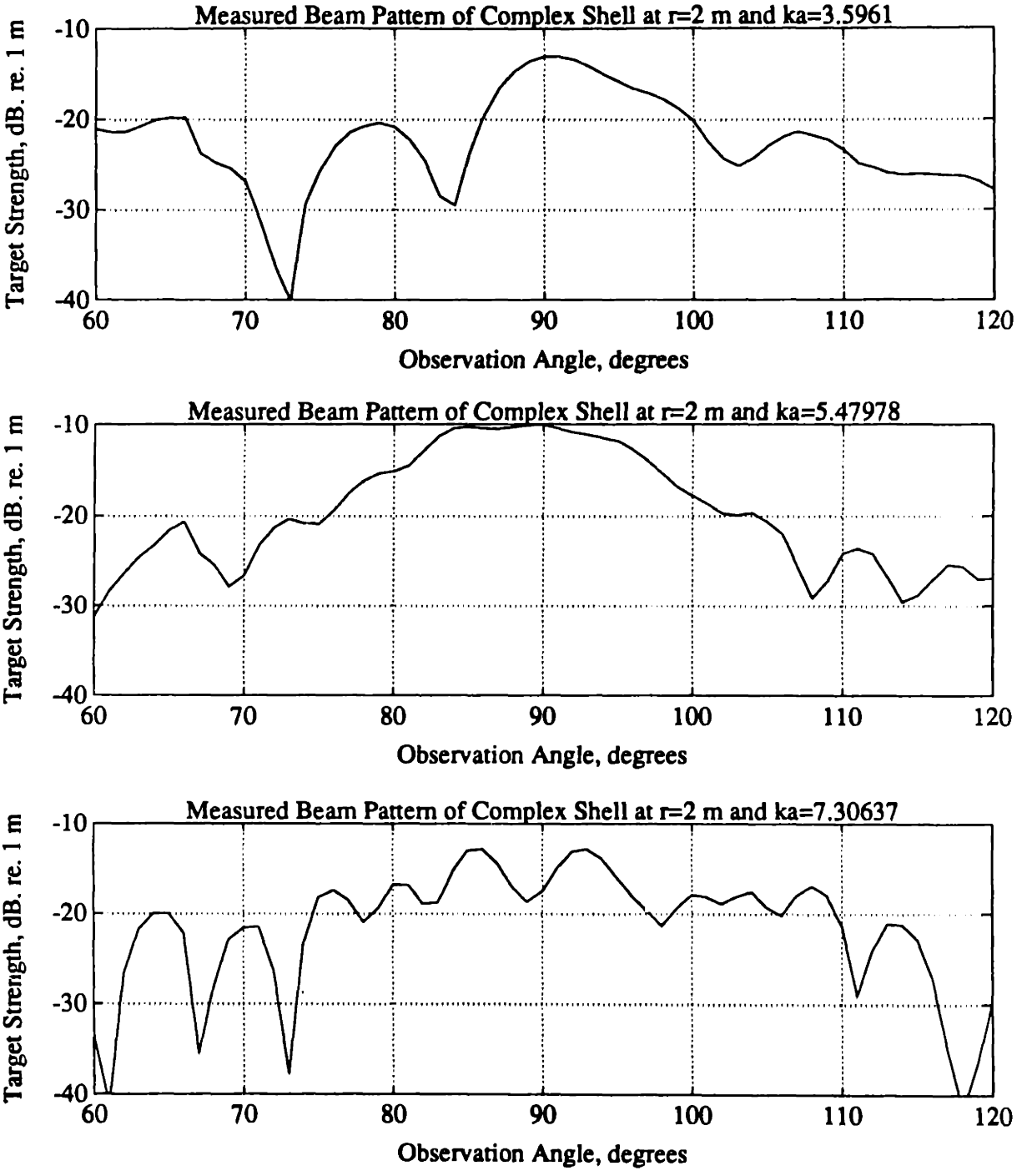

Figure 5.5: Measured Beam Pattern of the Complex Shell at Beam Aspect and a Distance of $r = 2\ m$. The data are shown for the predicted compressional wave coincidence frequencies of $ka = 3.60$ and $ka = 7.31$, and an intermediate frequency of $ka = 5.48$.

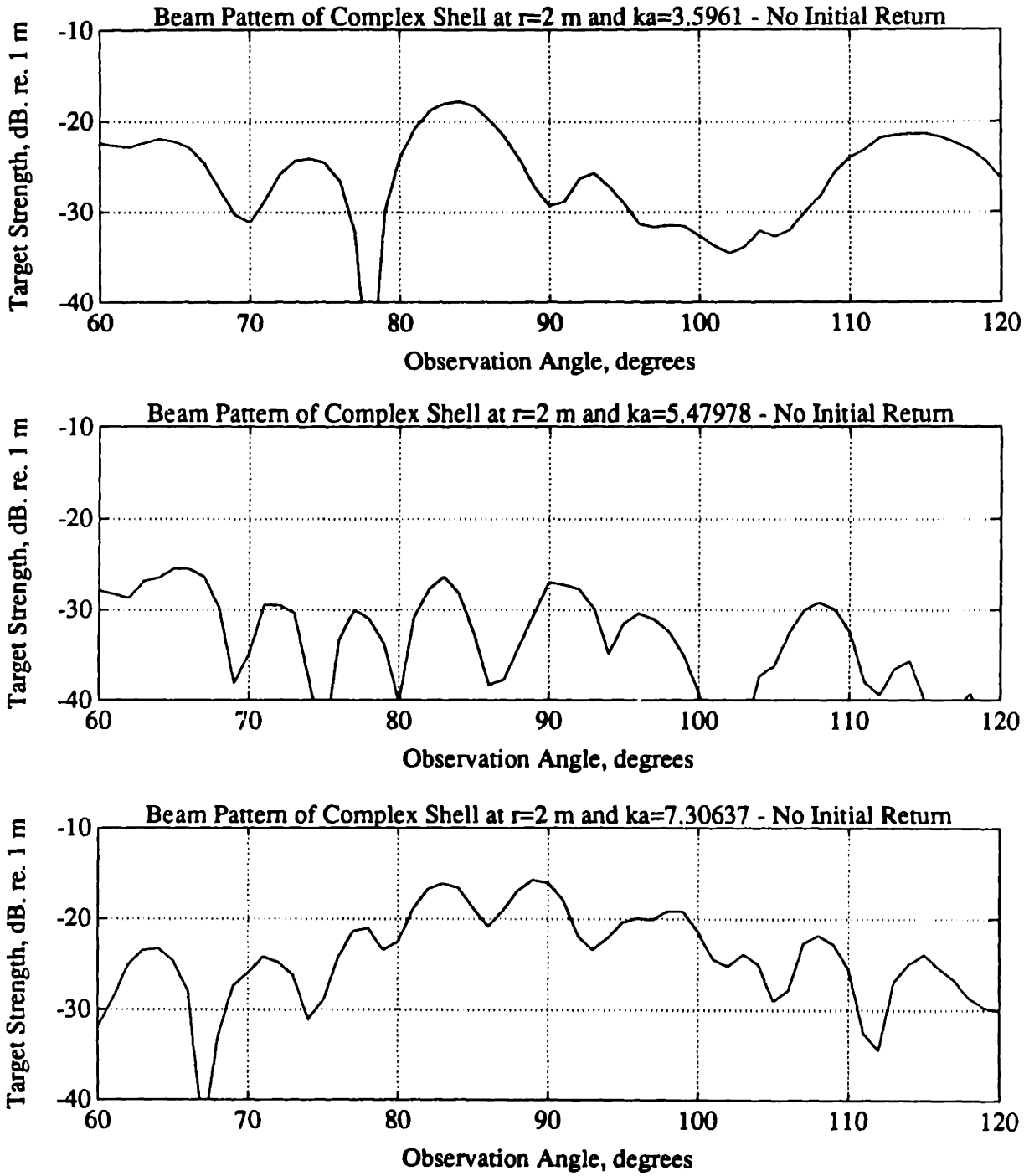

Figure 5.6: Measured Beam Pattern of the Complex Shell at Beam Aspect in the Absence of the Initial Scatter. The initial scatter was removed from the measurement with a simple windowing operation prior to computing the target strength transforms. The data are shown for the predicted compressional wave coincidence frequencies of $ka = 3.60$ and $ka = 7.31$, and an intermediate frequency of $ka = 5.48$.

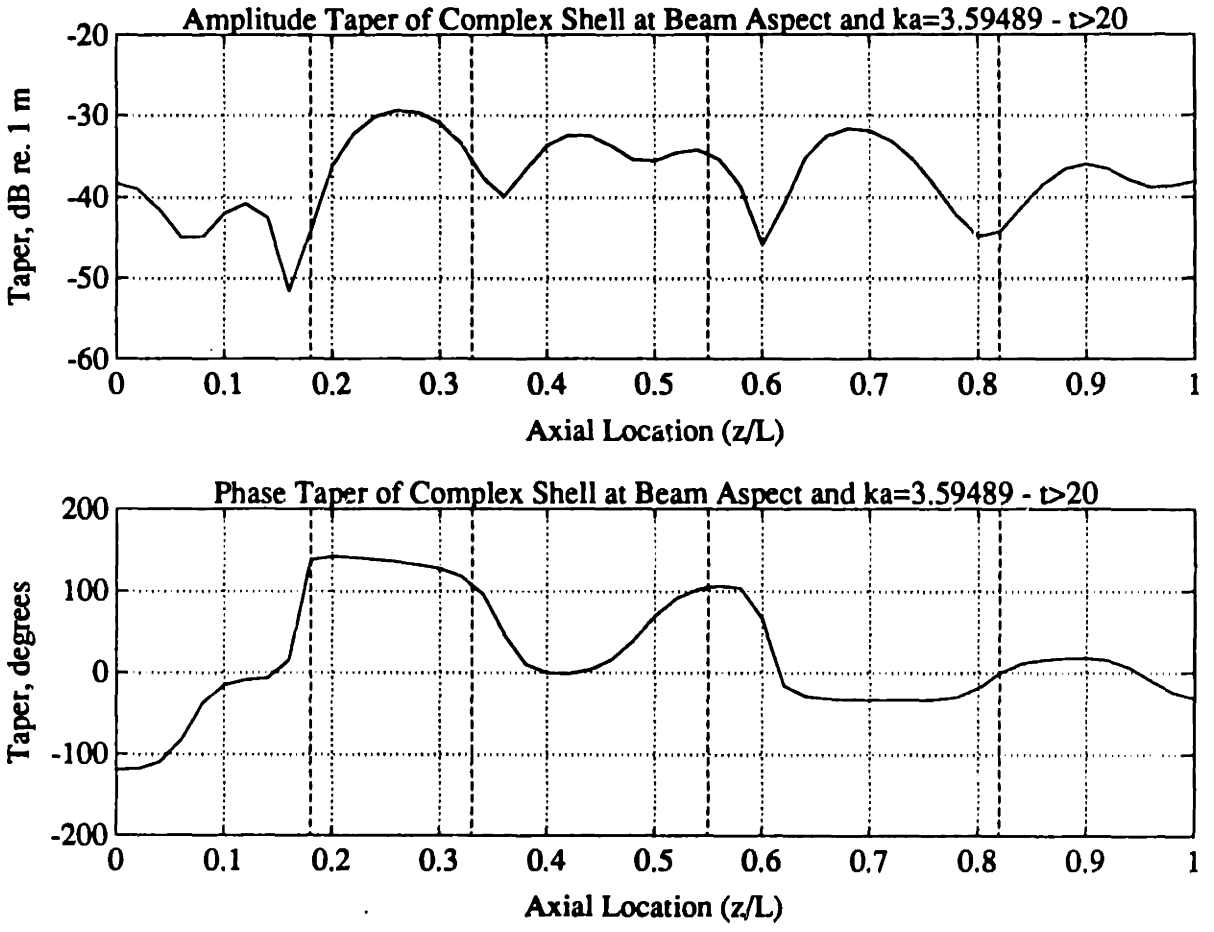

Figure 5.7: Amplitude and Phase Taper of the Complex Shell at Beam Aspect in the Absence of the Initial Scatter. The amplitude taper is shown as a normalized source strength and both are computed from the results of the beamforming operation shown in Figure 5.2. The initial, or geometric scatter, was removed from the measured scatter with a simple windowing operation. The data are shown for the predicted compressional wave coincidence frequency of $ka = 3.60$. The dashed lines show the axial locations of the ring stiffeners.

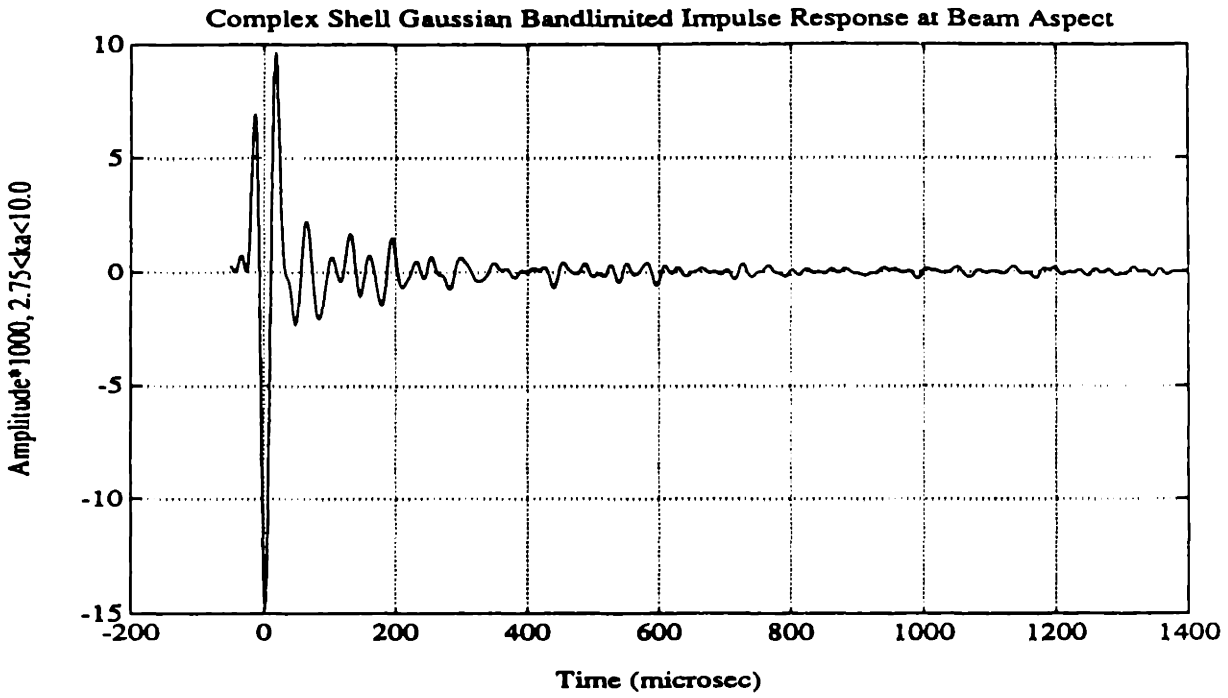

Figure 5.8: Gaussian Bandlimited Monostatic Impulse Response of the Complex Shell at Beam Aspect for the Frequency Range $2.75 < ka < 10.0$ and a Radial Distance of $r = 2\ m$ from the Target Center

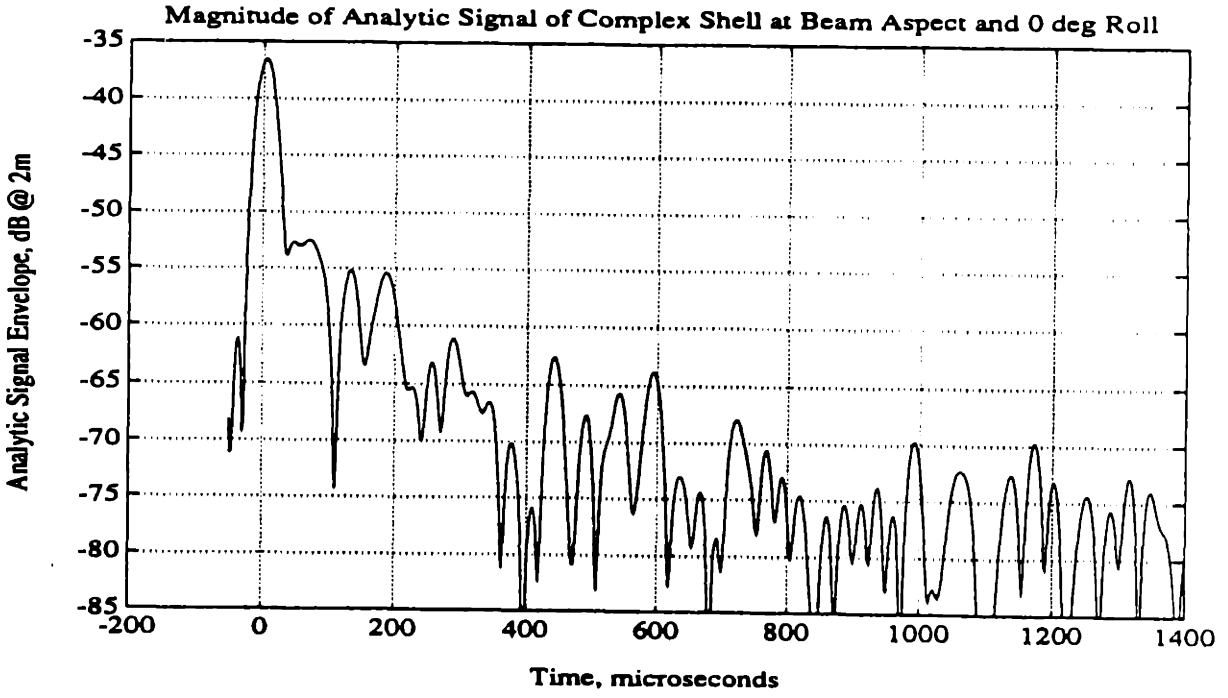

Figure 5.9: Logarithm of the Magnitude of the Envelope of the Gaussian Bandlimited Impulse Response of the Complex Shell at Beam Aspect for the Frequency Range $2.75 < ka < 10.0$ and a Radial Distance of $r = 2\ m$ from the Target Center

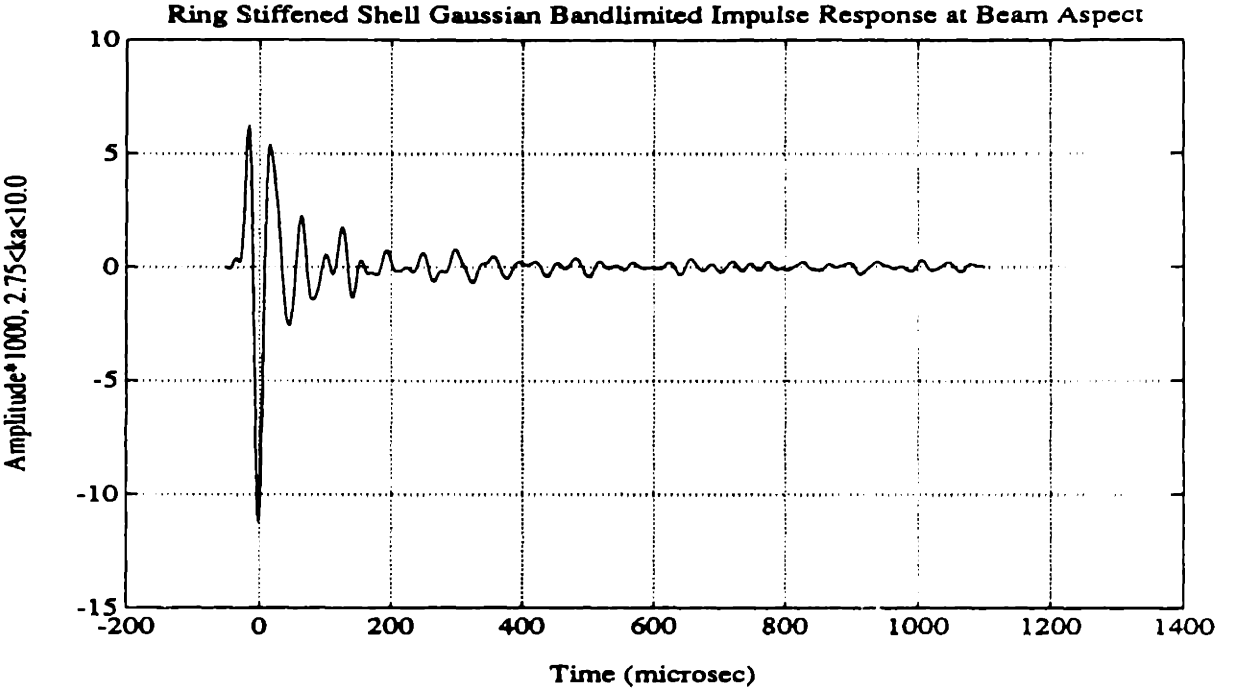

Figure 5.10: Gaussian Bandlimited Monostatic Impulse Response of the Ring Stiffened Shell at Beam Aspect for the Frequency Range $2.75 < ka < 10.0$ and a Radial Distance of $r = 2\ m$ from the Target Center

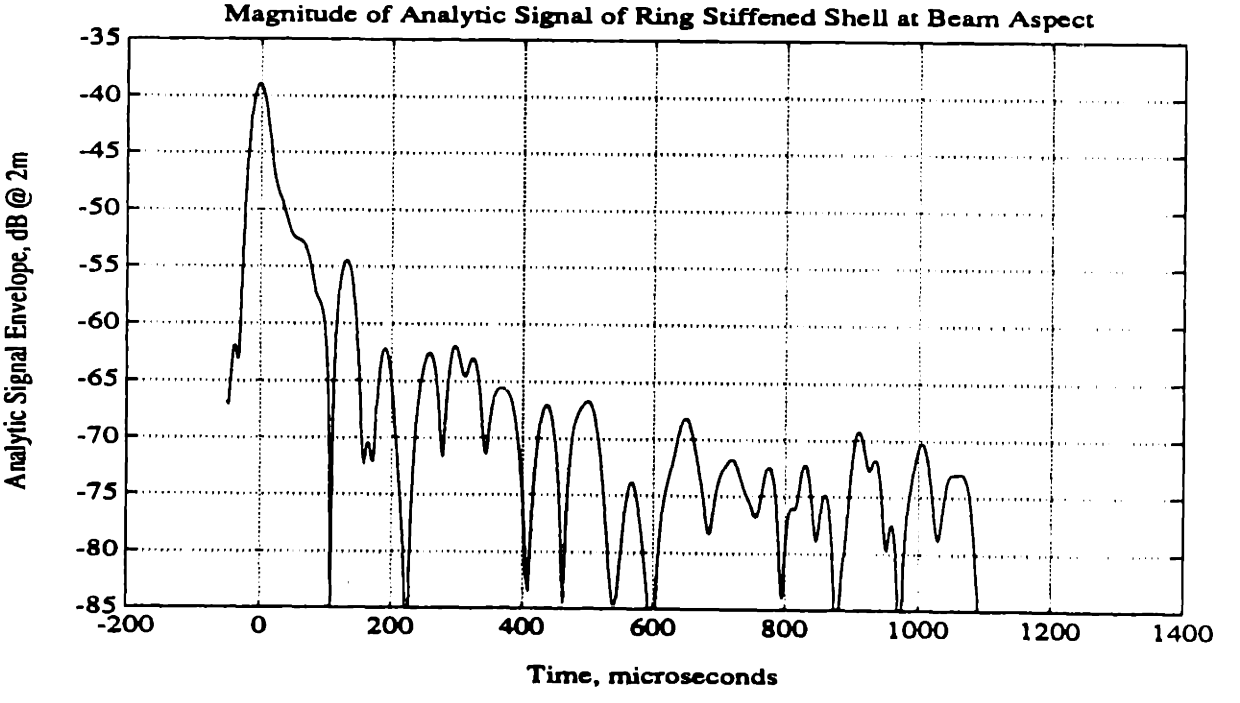

Figure 5.11: Logarithm of the Magnitude of the Envelope of the Gaussian Bandlimited Impulse Response of the Ring Stiffened Shell at Beam Aspect for the Frequency Range $2.75 < ka < 10.0$ and a Radial Distance of $r = 2\ m$ from the Target Center

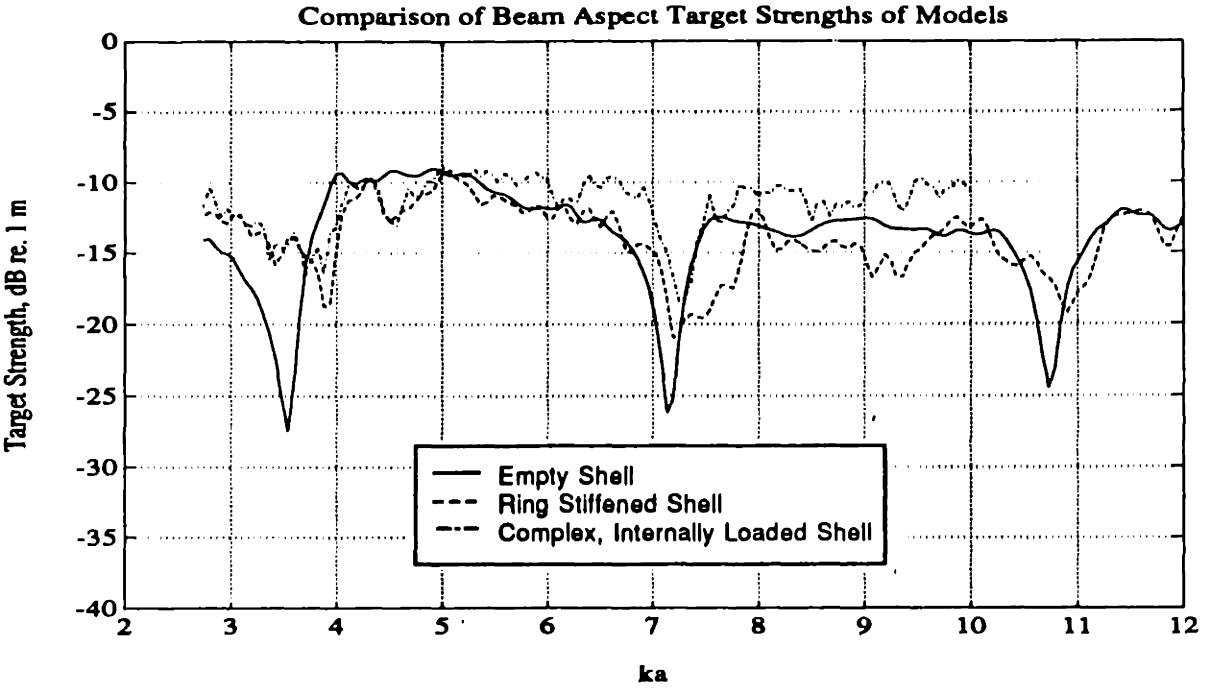

Figure 5.12: Comparison of the Measured Target Strengths $T(\omega, \theta)$ of the Empty, Ring Stiffened, and Complex Shells at Beam Aspect (uncorrected)

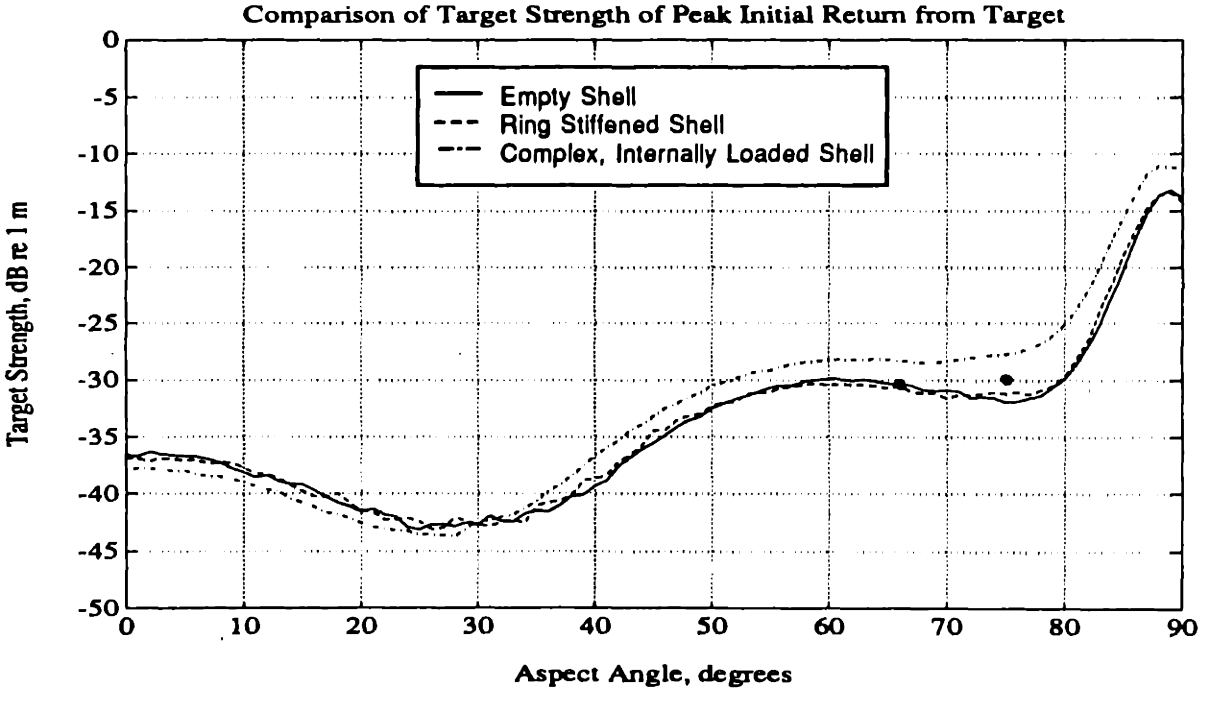

Figure 5.13: Comparison of the Target Strengths Associated with the Peak Initial Return $T_{initial}(\theta)$ from the Empty, Ring Stiffened, and Complex Shells. ($\bullet$ corresponds to data acquired during bistatic measurements of the Complex Shell in May and June, 1992)

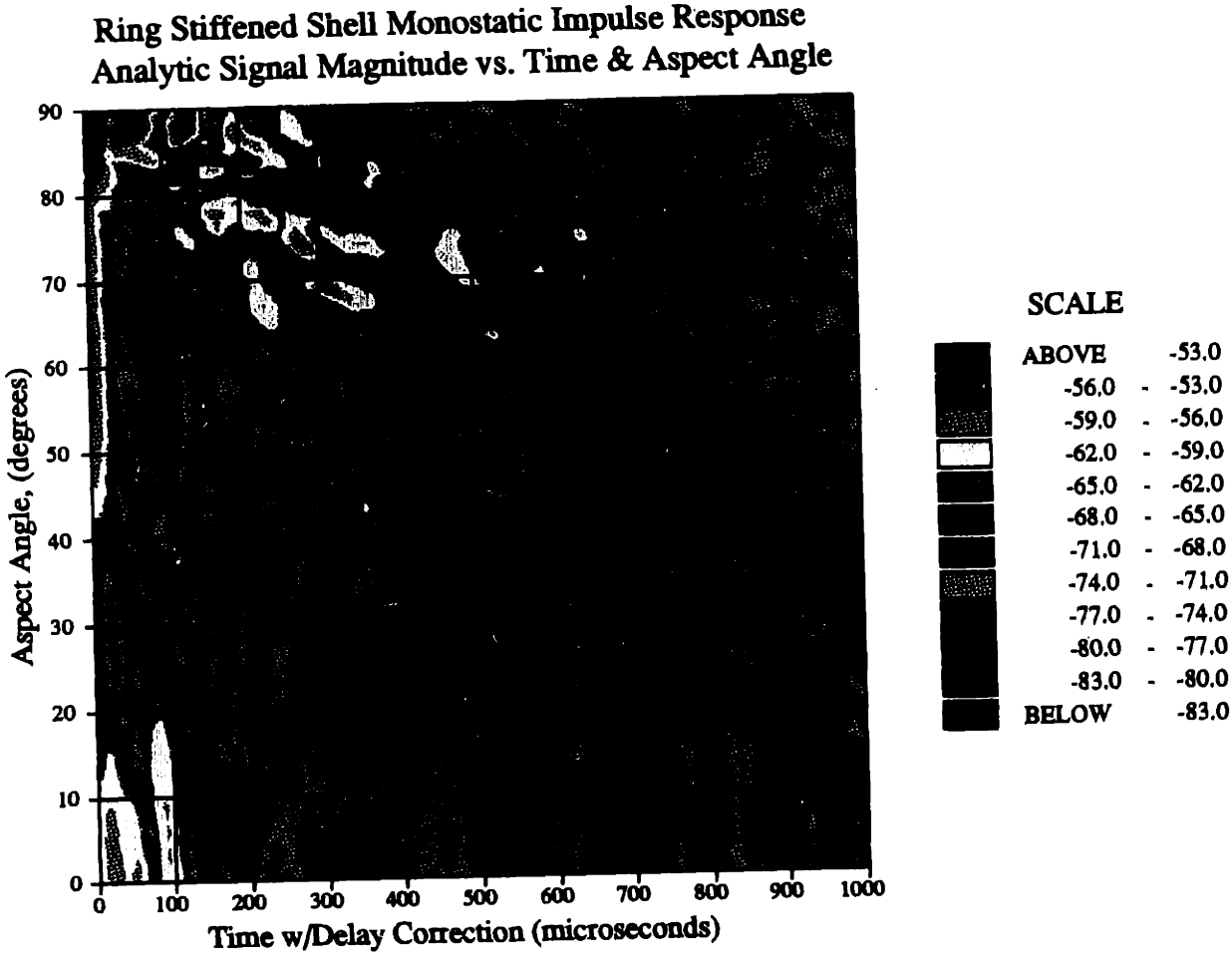

Figure 5.14: Analytic Signal Envelope of the Gaussian Bandlimited Monostatic Impulse Response of the Ring Stiffened Shell at $r = 2\ m$ for the frequency range of $2.75 < ka < 10.0$ and an aspect angle range of $0 \leq \theta \leq 90$ deg. The propagation delay of peak initial return from the target has been removed to stack the signals such that the peak initial return is shown at time $t = 0$ for all θ. The aspect angle $\theta = 0$ corresponds to bow aspect and $\theta = 90$ corresponds to beam aspect.

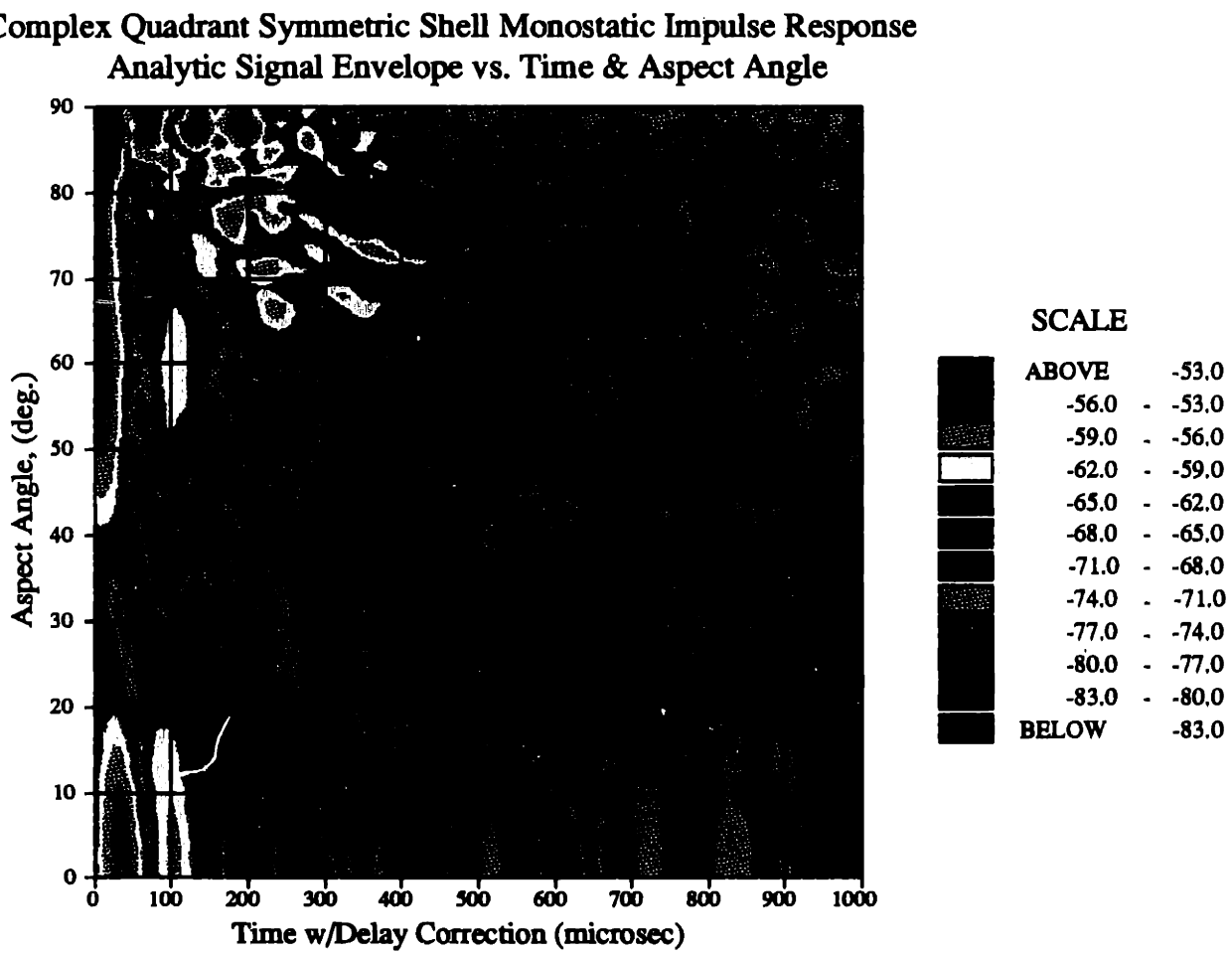

Figure 5.15: Analytic Signal Envelope of the Gaussian Bandlimited Monostatic Impulse Response of the Complex Shell at $r = 2\ m$ for the frequency range of $2.75 < ka < 10.0$ and an aspect angle range of $0 \leq \theta \leq 90$ deg. The propagation delay of peak initial return from the target has been removed to stack the signals such that the peak initial return is shown at time $t = 0$ for all θ. The aspect angle $\theta = 0$ corresponds to bow aspect and $\theta = 90$ corresponds to beam aspect.

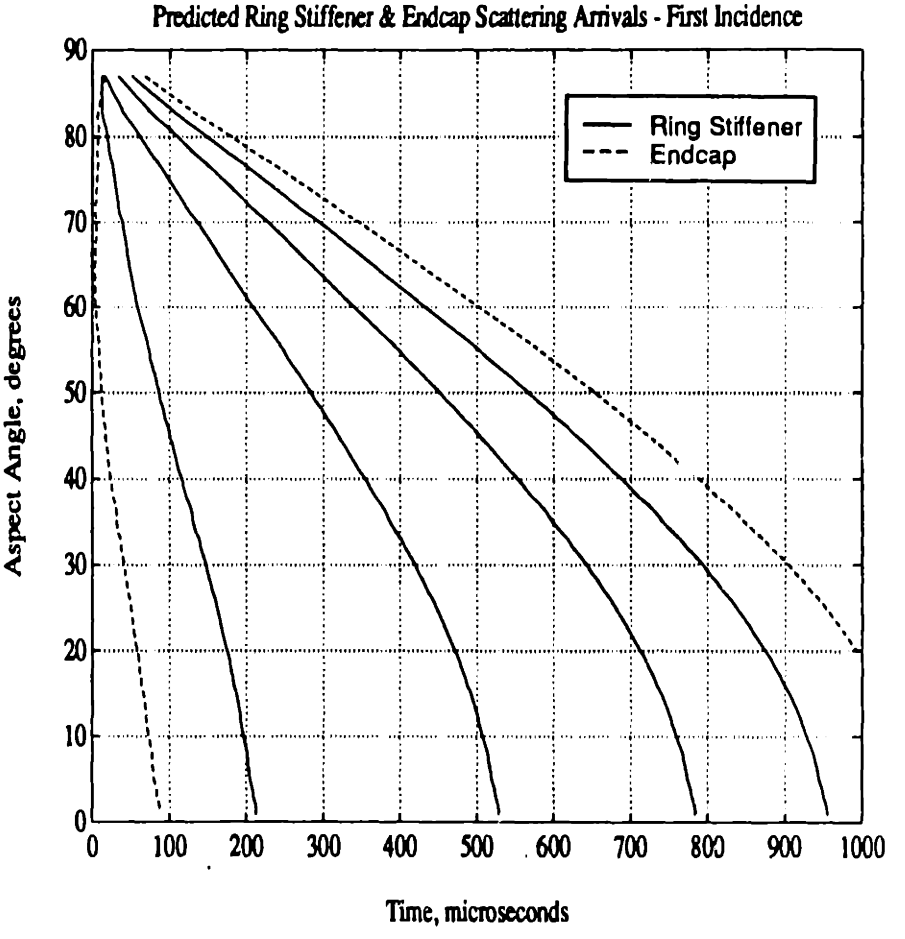

Figure 5.16: Predicted Arrival Times at $r = 2\ m$ for the First Incidence of Scattering from the Ring Stiffeners and Endcaps of the Shell Models. The arrival times are predicted for an axial propagation velocity equal to the trace velocity of the incident field. This figure is drawn to the same scale as Figures 5.14 and 5.15 for comparison.

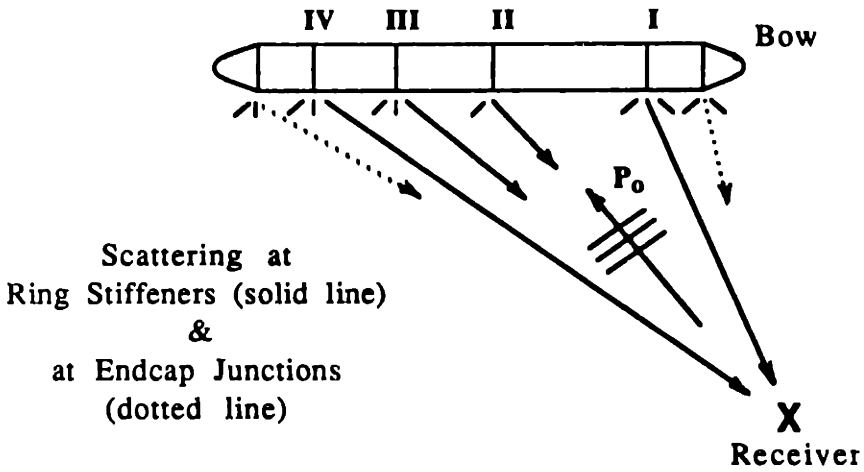

Figure 5.17: Illustration of Propagation Paths of the First Incidence of Scattering from the Ring Stiffeners and Endcaps of the Shell Models

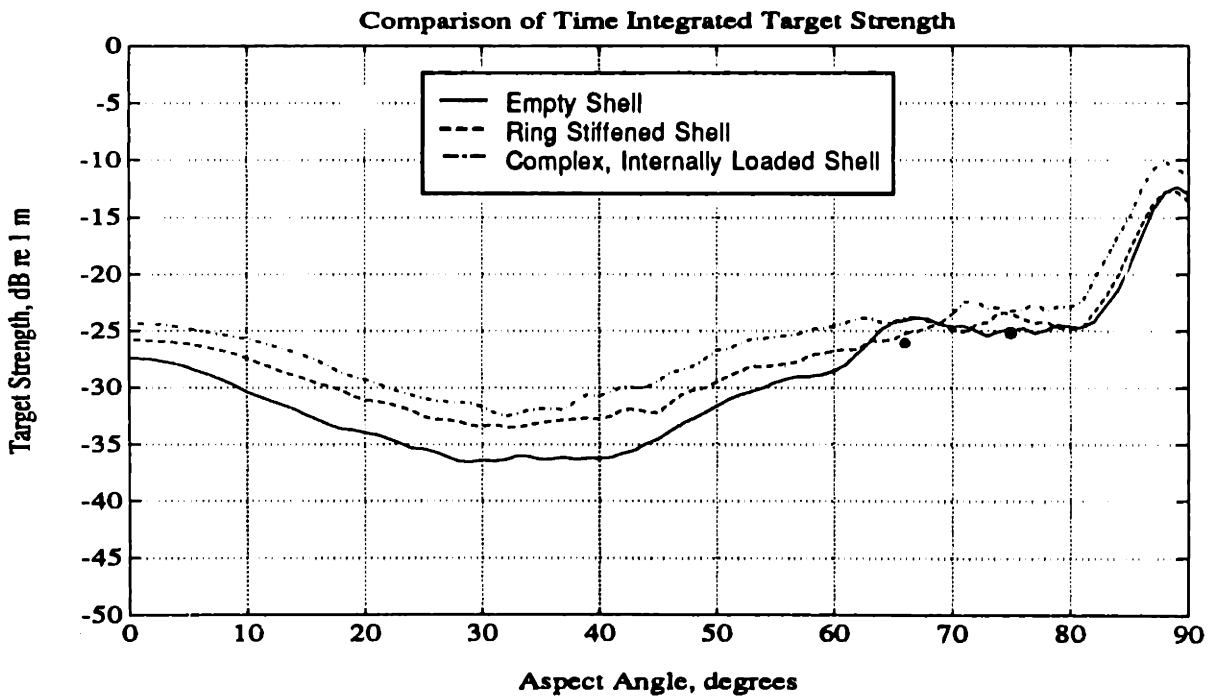

Figure 5.18: Comparison of the Target Strengths Associated with the Integrated Scattered Pressure $p_s^2(t,\theta)$ from the Empty, Ring Stiffened, and Complex Shells. (• corresponds to data acquired during bistatic measurements of the Complex Shell in May and June, 1992)

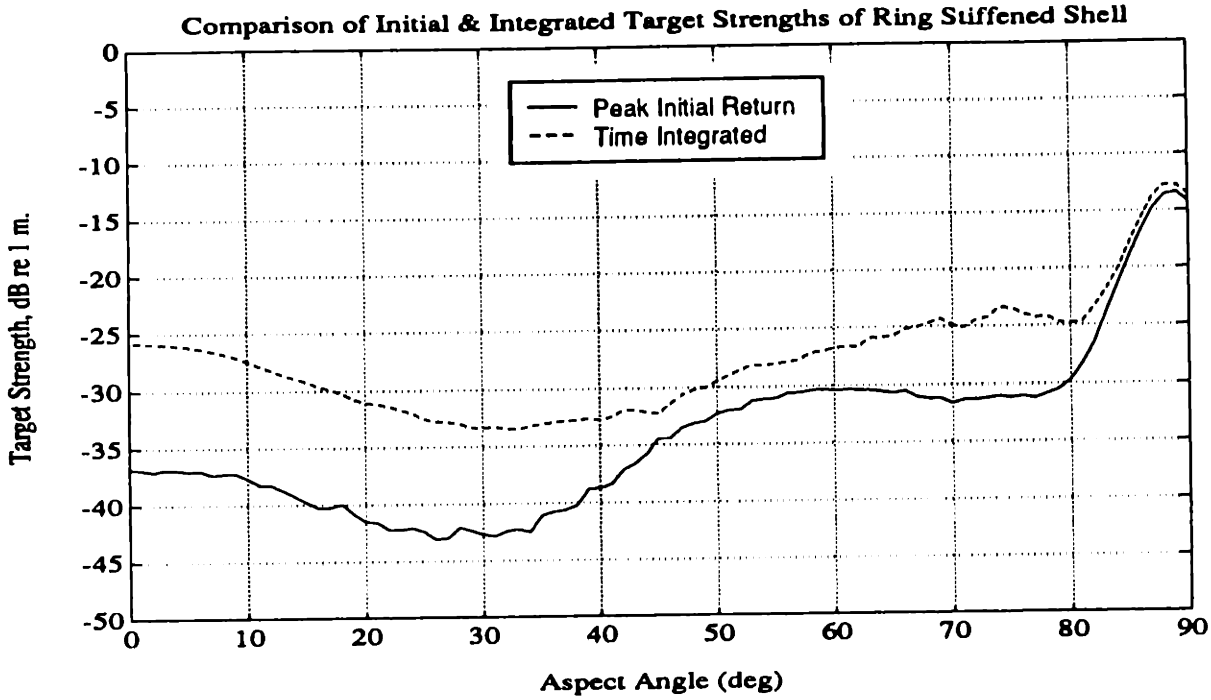

Figure 5.19: Comparison Target Strength Values Computed Using the Measured Peak Initial Return and the Time Integral of the Squared Pressure $p_s^2(t,\theta)$ of the Ring Stiffened Shell

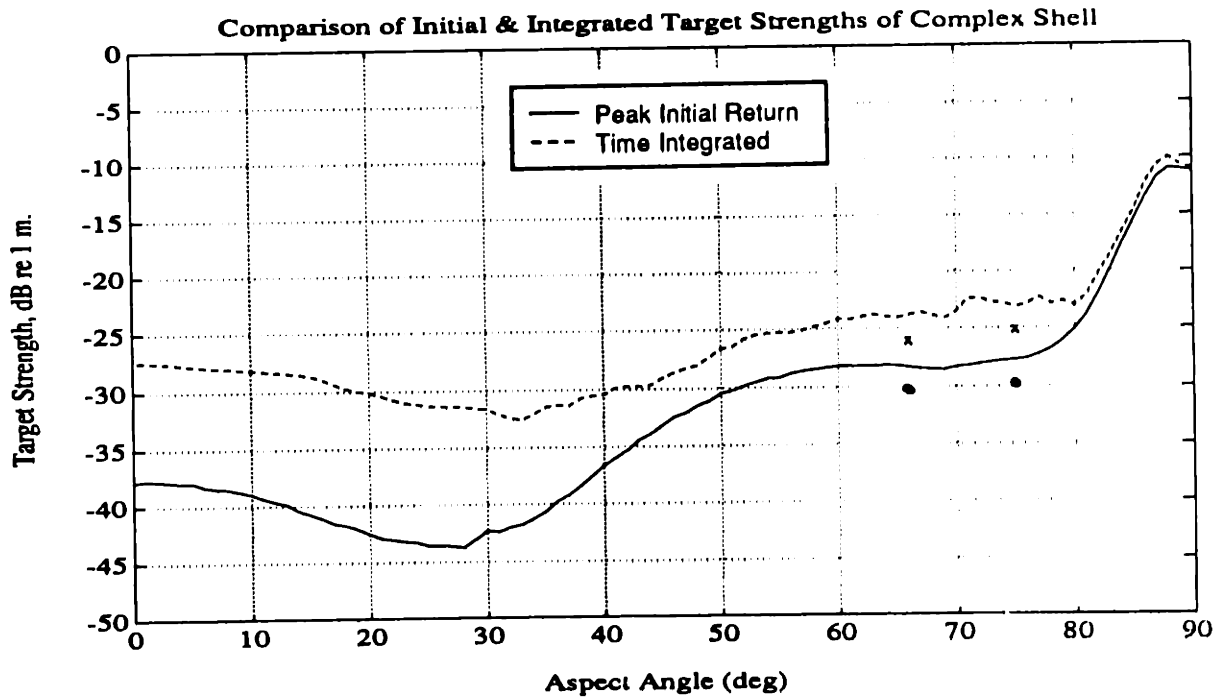

Figure 5.20: Comparison Target Strength Values Computed Using the Peak Initial Return and the Time Integral of the Squared Pressure $p_s^2(t,\theta)$ of the Complex Shell(•-Peak Initial Return & x-Time Integrated - data acquired during bistatic measurements of the Complex Shell in May and June, 1992)

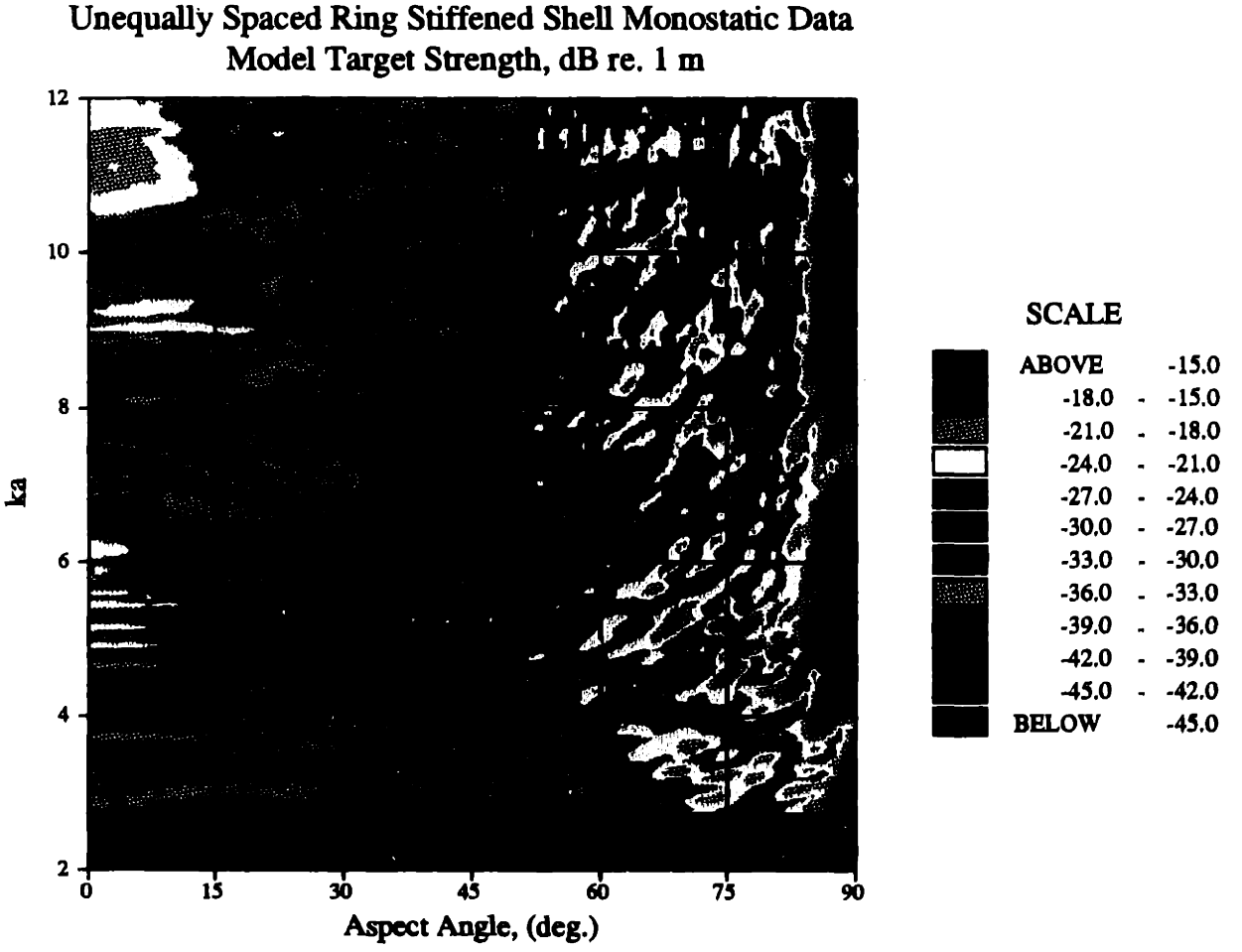

Figure 5.21: Contours of the Measured Target Strength $T(\omega, \theta)$ of the Ring Stiffened Shell Model over the range of aspect angles $0 \leq \theta \leq 90$ deg. Values are normalized by the pressure level of the incident field at the target center location. The transfer functions have a limiting frequency resolution of $\Delta k a_{3dB} = 0.16$. The aspect angle $\theta = 0$ corresponds to bow aspect and $\theta = 90$ corresponds to beam aspect.

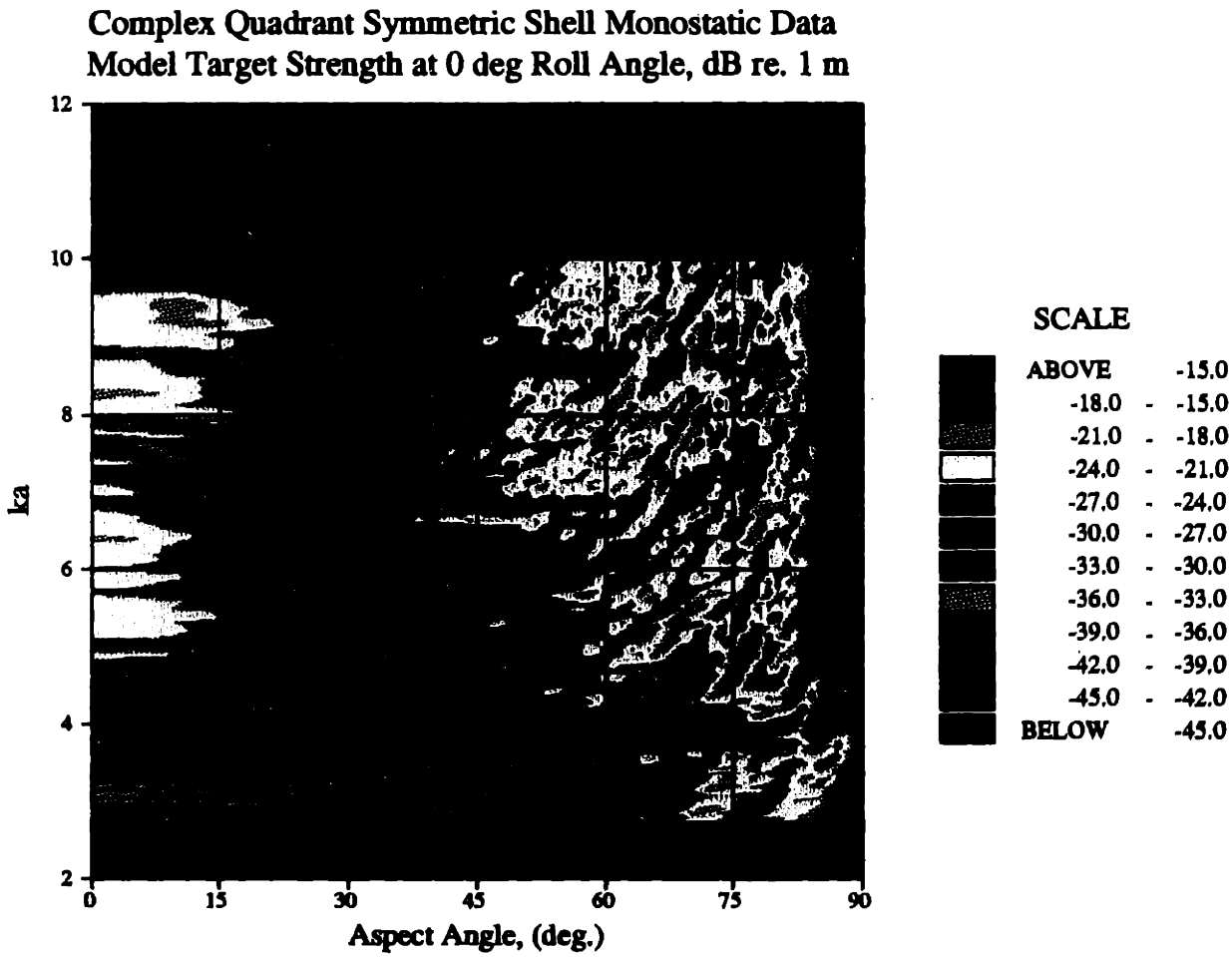

Figure 5.22: Contours of the Measured Target Strength $T(\omega, \theta)$ of the Complex Shell Model over the range of aspect angles $0 \leq \theta \leq 90$ deg. Values are normalized by the pressure level of the incident field at the target center location. The transfer functions have a limiting frequency resolution of $\Delta ka_{3dB} = 0.08$. The aspect angle $\theta = 0$ corresponds to bow aspect and $\theta = 90$ corresponds to beam aspect.

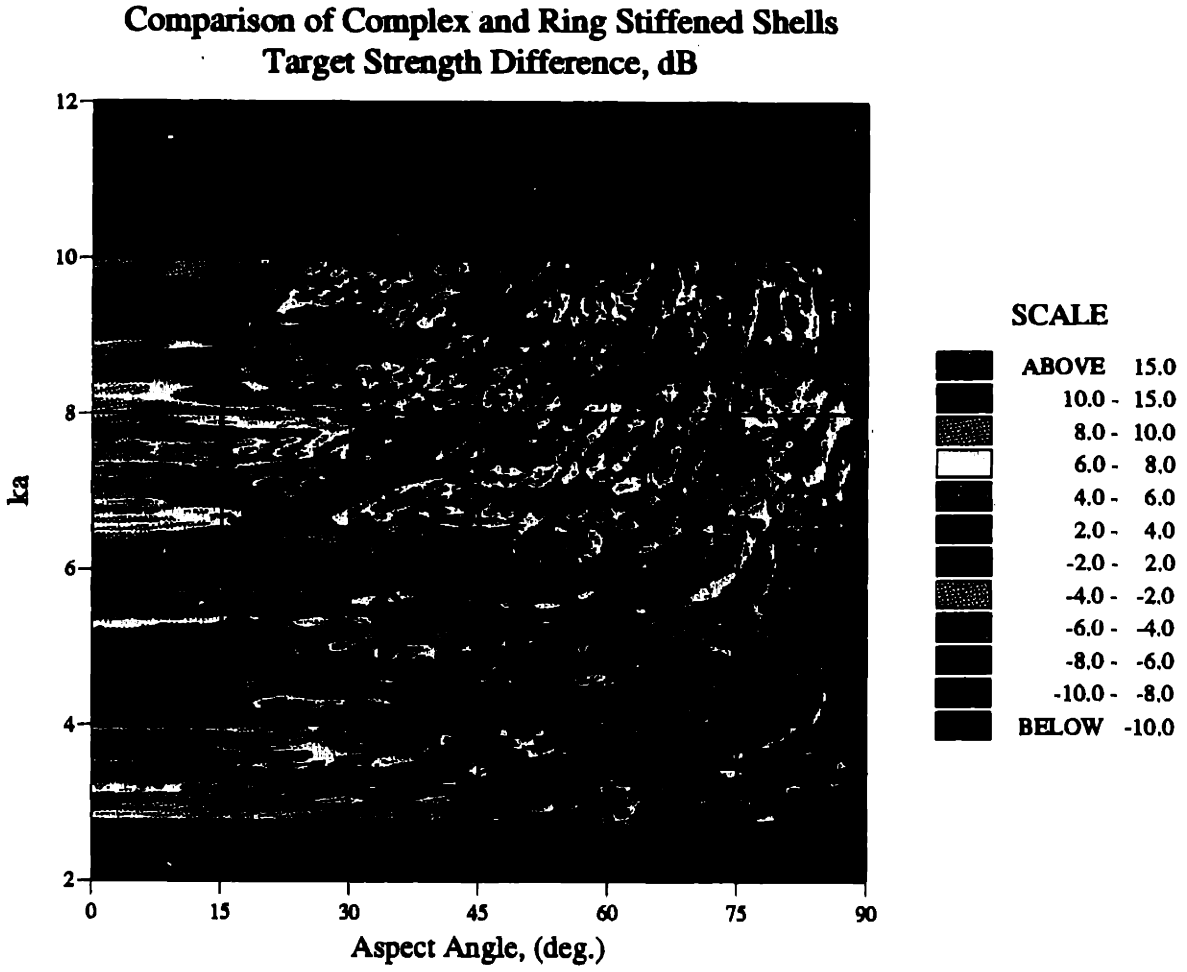

Figure 5.23: Comparison of the Measured Target Strengths $T(\omega, \theta)$ of the Complex and Ring Stiffened Shell Models over $0 \leq \theta \leq 90$ deg, the latter subtracted from the former. The transfer functions have a limiting frequency resolution of $\Delta ka_{3dB} = 0.16$. (Note the nonuniform color scale.)

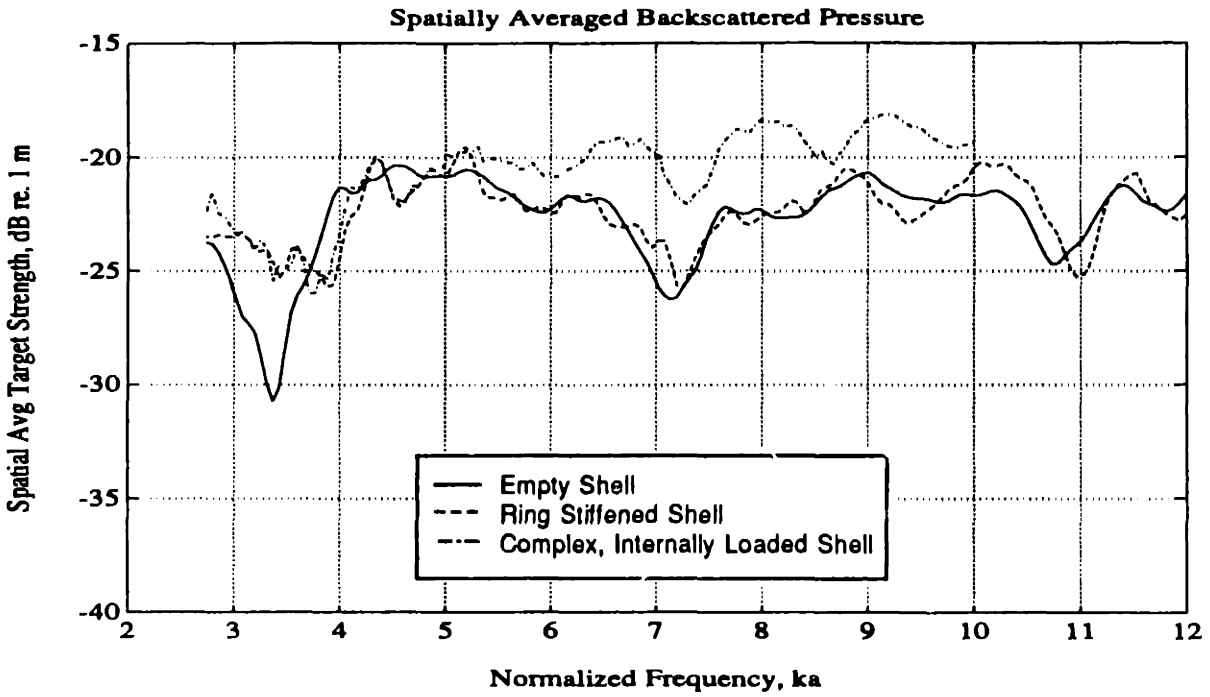

Figure 5.24: Spatial Average of Mean Square Pressure $|P_s(\omega,\theta)|^2$ over the Full Range of Aspect Angles $0 \leq \theta \leq 180$. The average is normalized by the mean square pressure of the incident field $|P_{ref}(\omega)|^2$.

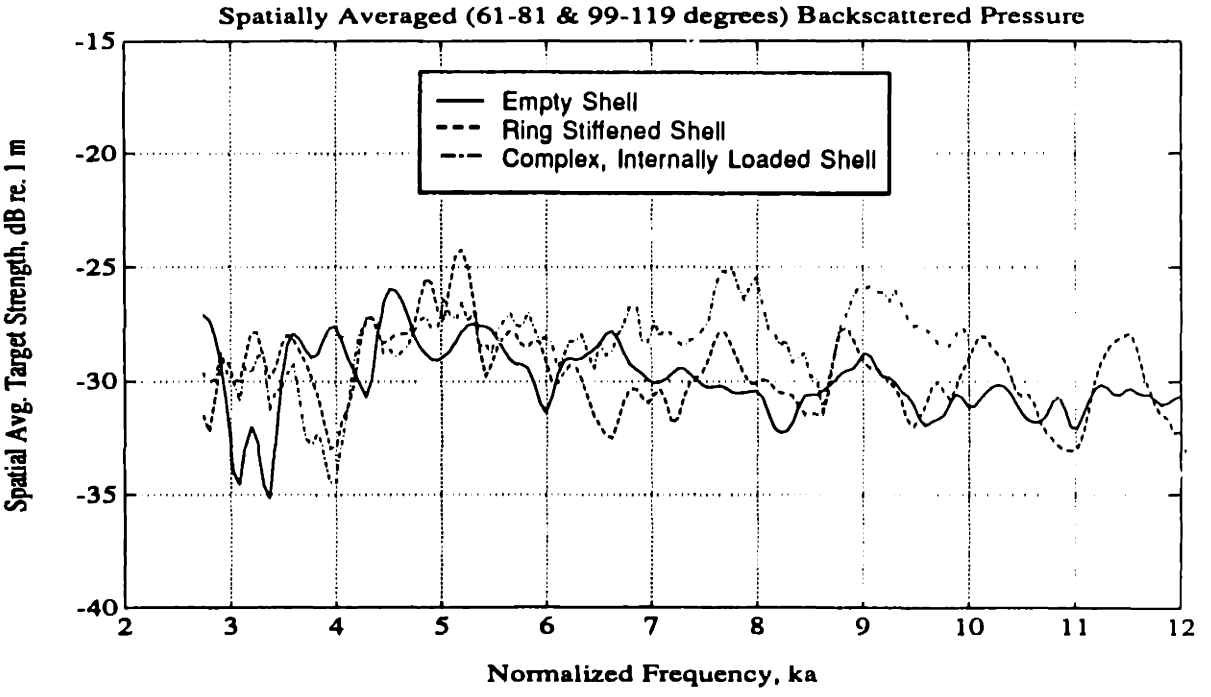

Figure 5.25: Spatial Average of Mean Square Pressure $|P_s(\omega,\theta)|^2$ over the Range of Aspect Angles $61 \leq \theta \leq 81$ and $99 \leq \theta \leq 119$ (Helical Wave Regime). The average is normalized by the mean square pressure of the incident field $|P_{ref}(\omega)|^2$ and 4π steradians.

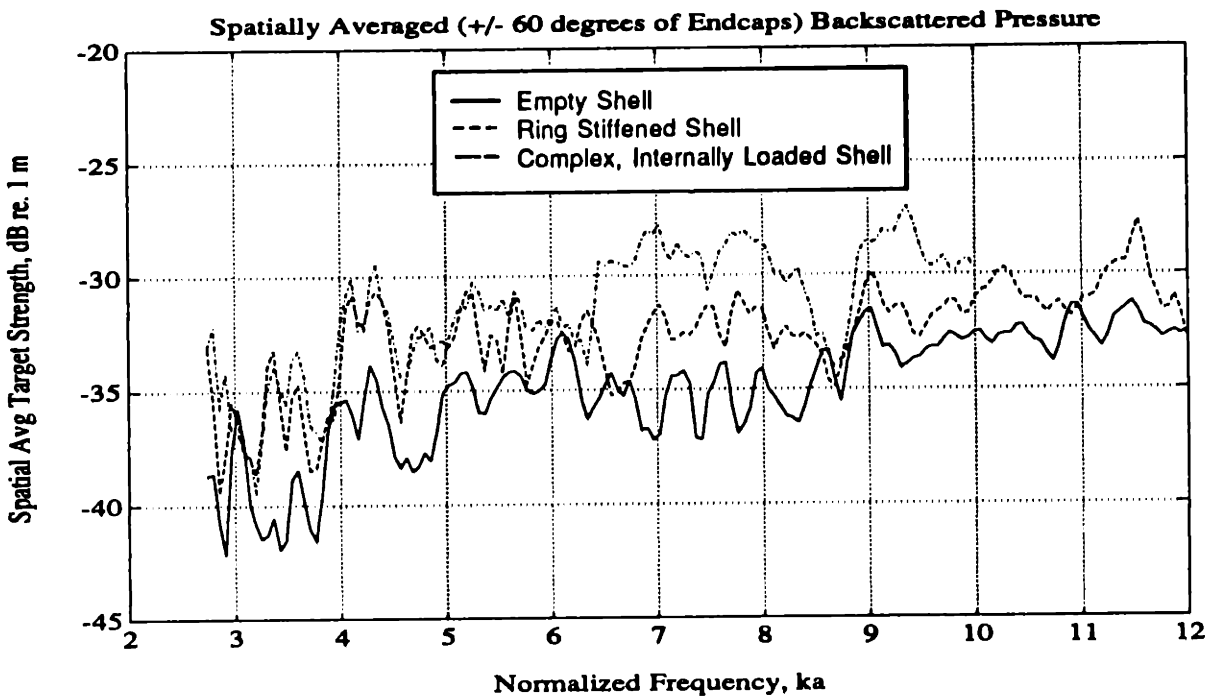

Figure 5.26: Spatial Average of Spatial Average of Mean Square Pressure $|P_s(\omega, \theta)|^2$ over the Range of Aspect Angles within 60 degrees of the Bow and Stern Endcaps. The average is normalized by the mean square pressure of the incident field $|P_{ref}(\omega)|^2$ and 4π steradians.

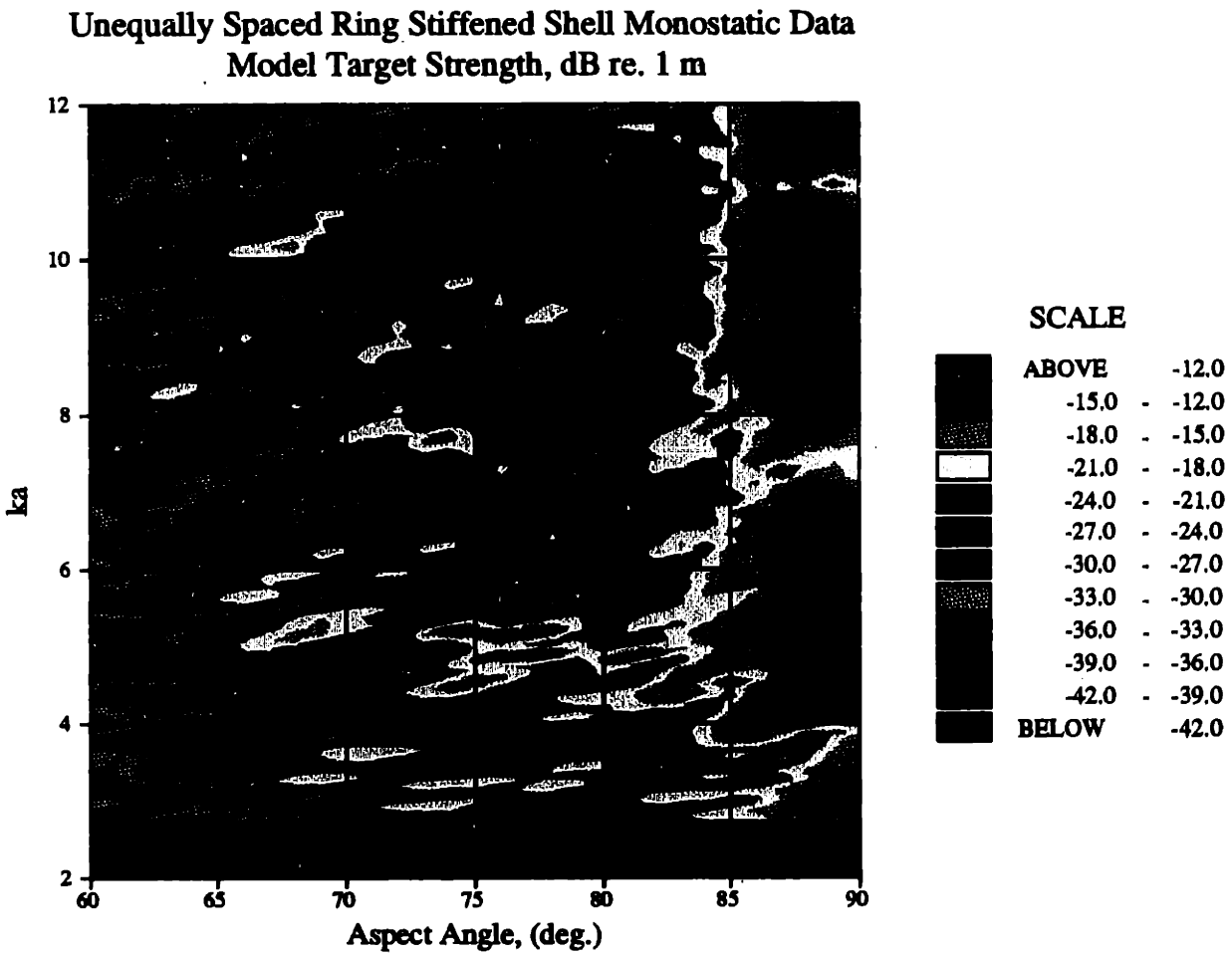

Figure 5.27: Contours of the Measured Target Strength $T(\omega, \theta)$ of the Ring Stiffened Shell Model over the range of aspect angles $60 \leq \theta \leq 90$ deg. Values are normalized by the pressure level of the incident field at the target center location. The transfer functions have a limiting frequency resolution of $\Delta ka_{3dB} = 0.16$. The aspect angle $\theta = 90$ corresponds to beam aspect. The peak values shown near $\theta = 88$ are largely an artifact of the small measurement distance employed. At most frequencies, the peak value of the beam pattern produced 2 m from a uniform line array occurs several degrees away from the steering angle as demonstrated in Figure 5.29.

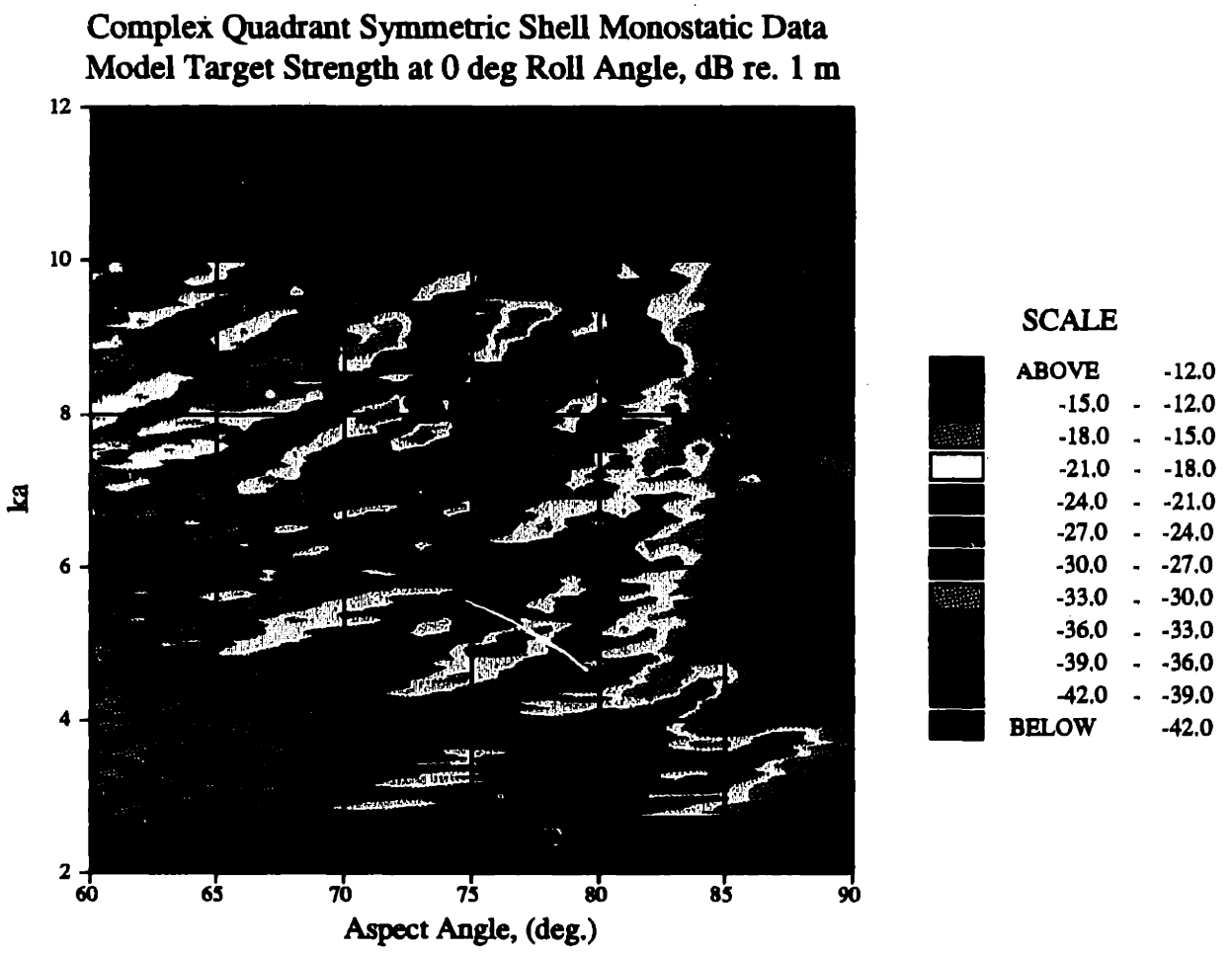

Figure 5.28: Contours of the Measured Target Strength $T(\omega, \theta)$ of the Complex Shell Model over the range of aspect angles $60 \leq \theta \leq 90$ deg. Values are normalized by the pressure level of the incident field at the target center location. The transfer functions have a limiting frequency resolution of $\Delta k a_{3dB} = 0.08$. The aspect angle $\theta = 0$ corresponds to bow aspect and $\theta = 90$ corresponds to beam aspect.

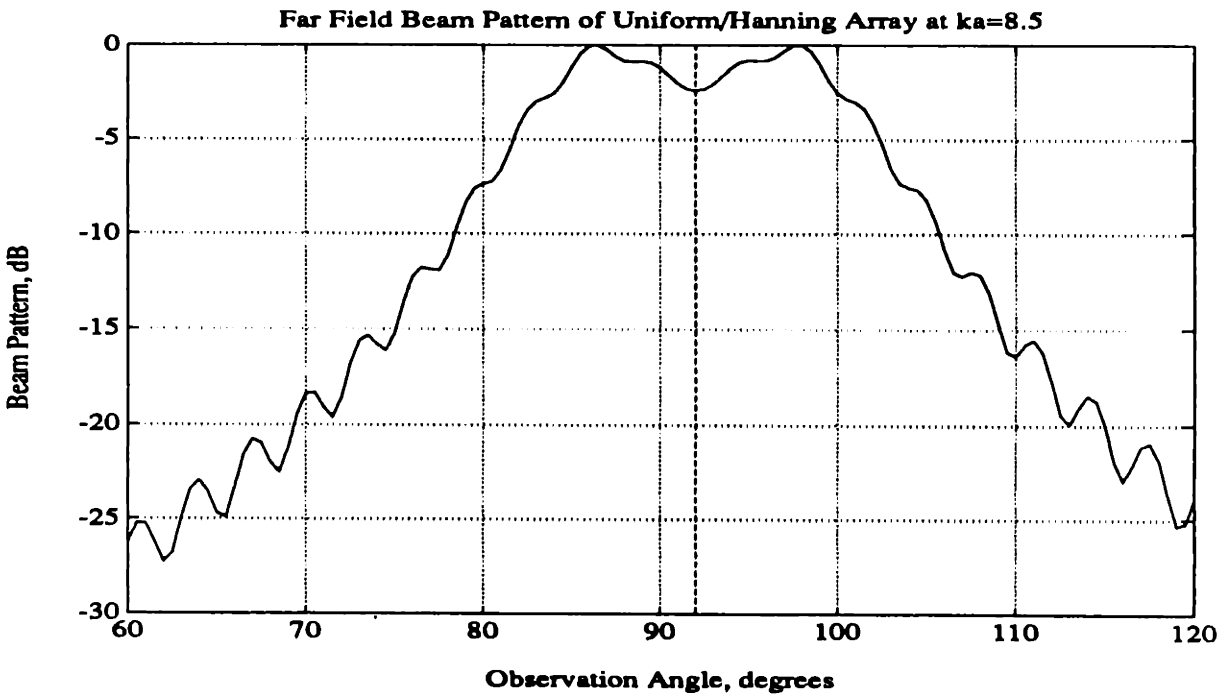

Figure 5.29: Beam Pattern Produced by Simulated Array at a of Distance of 2 m When Steered to $\theta_o = 92$ degrees at $ka = 8.5$. The amplitude of the source distribution of the array is uniform over a length equal to the cylindrical portion of the shells, and is hanning tapered over the length of the endcaps.

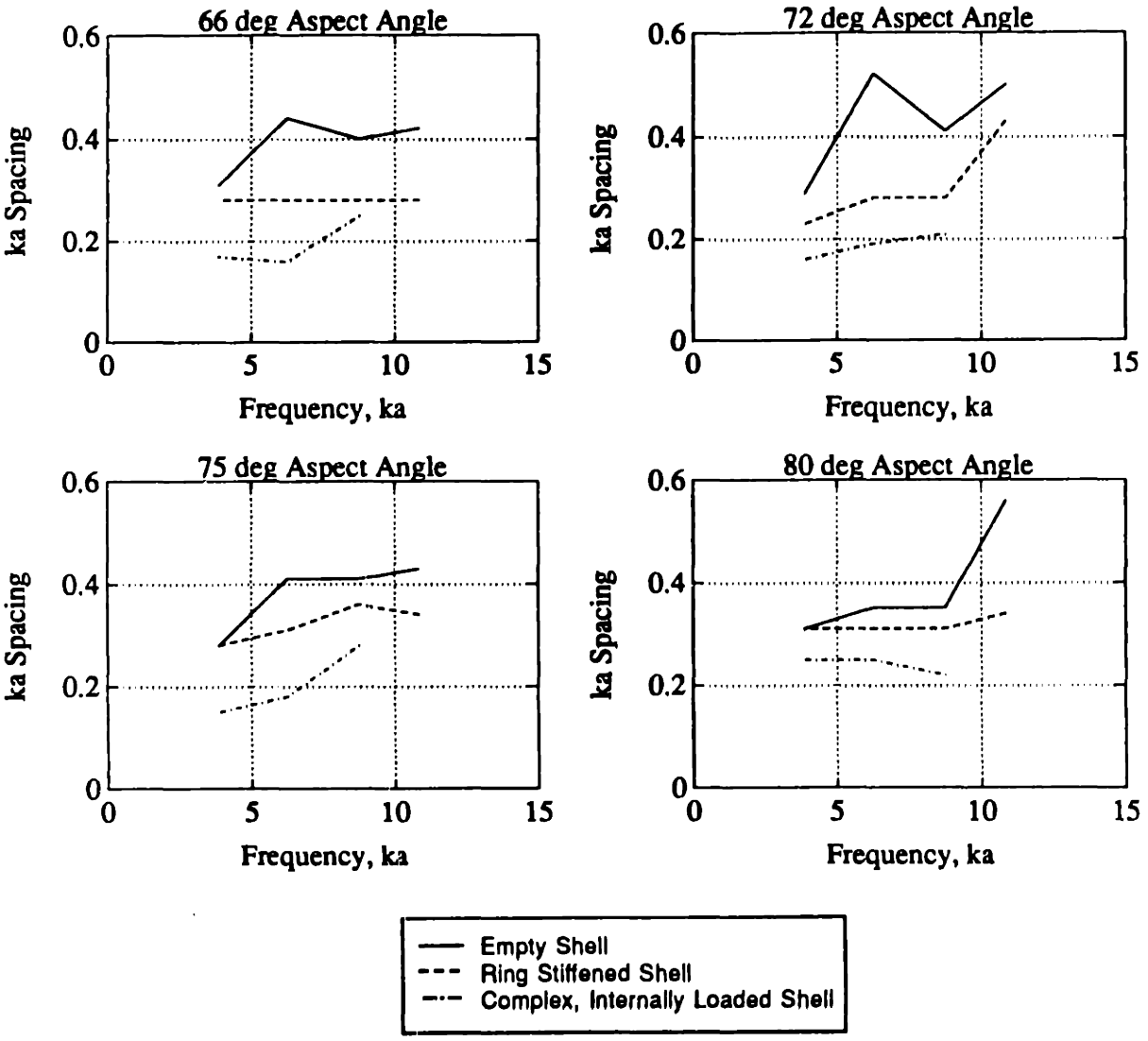

Figure 5.30: Comparisons of the Frequency Spacing Δka of Measured Backscatter at Aspect Angles of 66, 72, 75, and 80 degrees. I believe that the values shown for the ring stiffened shell are limited by the available frequency resolution of the data.

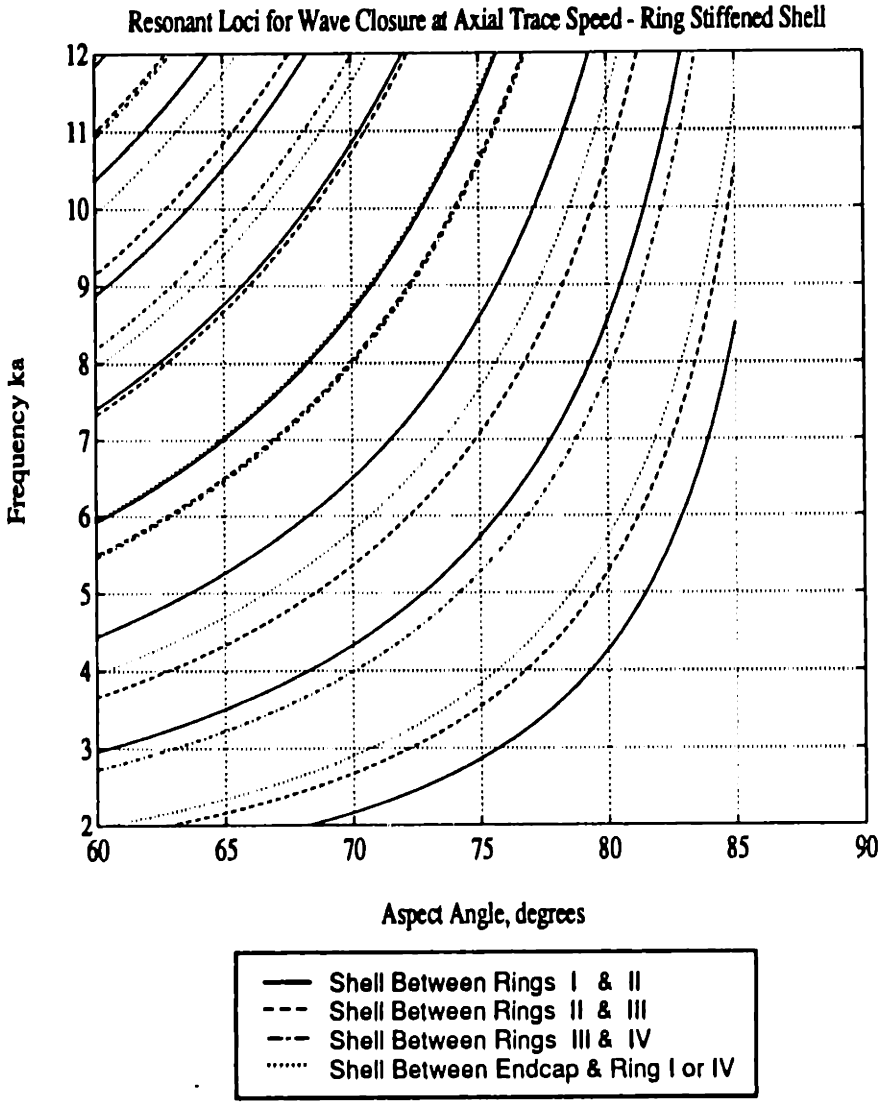

Figure 5.31: Loci of Aspect Angle θ and Frequency ka Where Axial Resonance Occurs for the Four Different Lengths Between Pairs of Stiffeners and the Endcaps. These curves are based on propagation with an axial phase velocity equal to the trace velocity of the incident field, and perfect reflection at the stiffeners. Each order n has four such resonances for wave propagation between the stiffeners, and between a stiffener and endcap. This Figure does no include resononances in which more than one bay participates, i.e. the bays are assumed ideally isolated. The figure is drawn to the same scale as Figures 5.27 and 5.28.

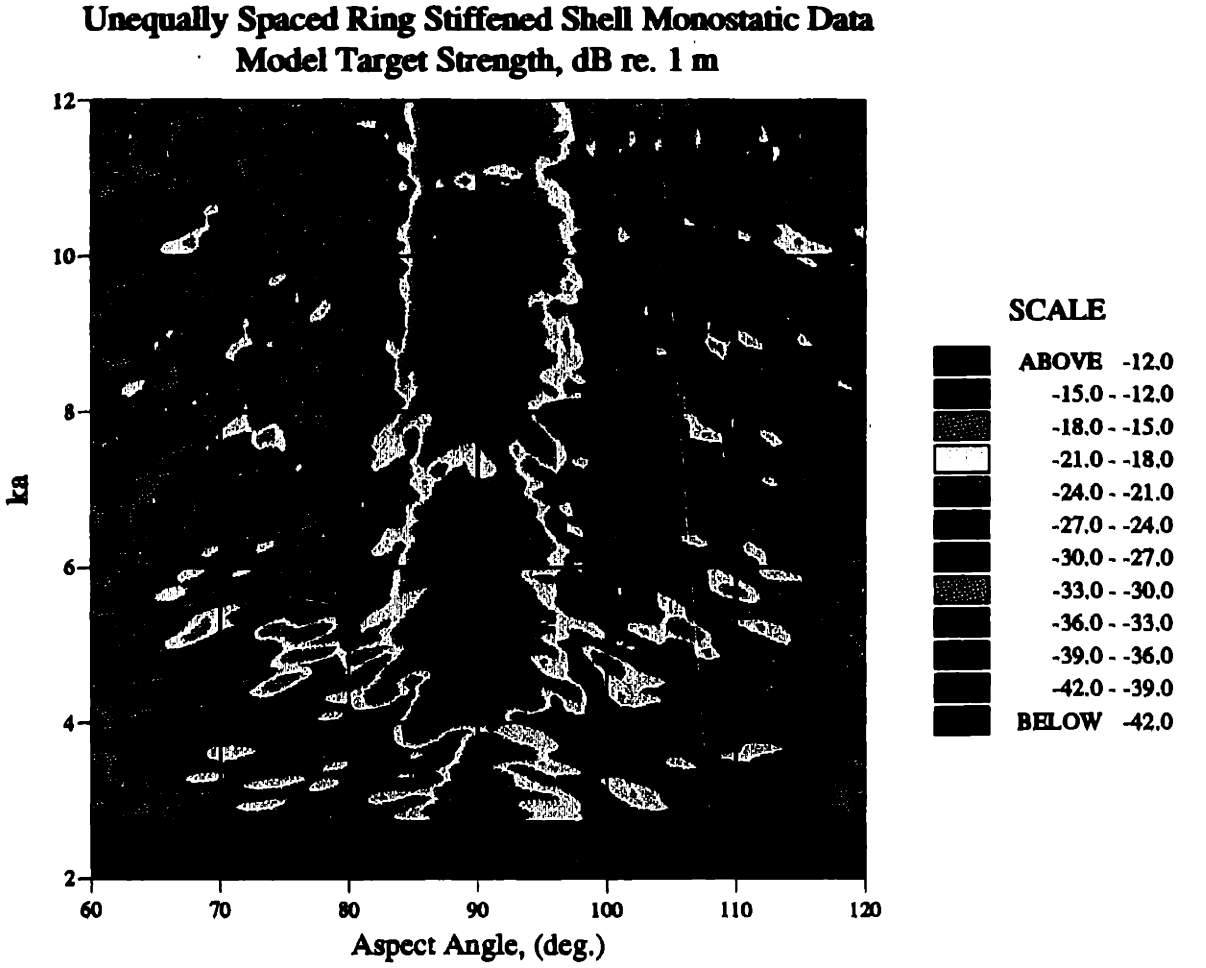

Figure 5.32: Contours of the Measured Target Strength $T(\omega, \theta)$ of the Ring Stiffened Shell Model over the range of aspect angles $60 \leq \theta \leq 120$ deg. Values are normalized by the pressure level of the incident field at the target center location. The transfer functions have a limiting frequency resolution of $\Delta ka_{3dB} = 0.16$. The aspect angle $\theta = 90$ corresponds to beam aspect.

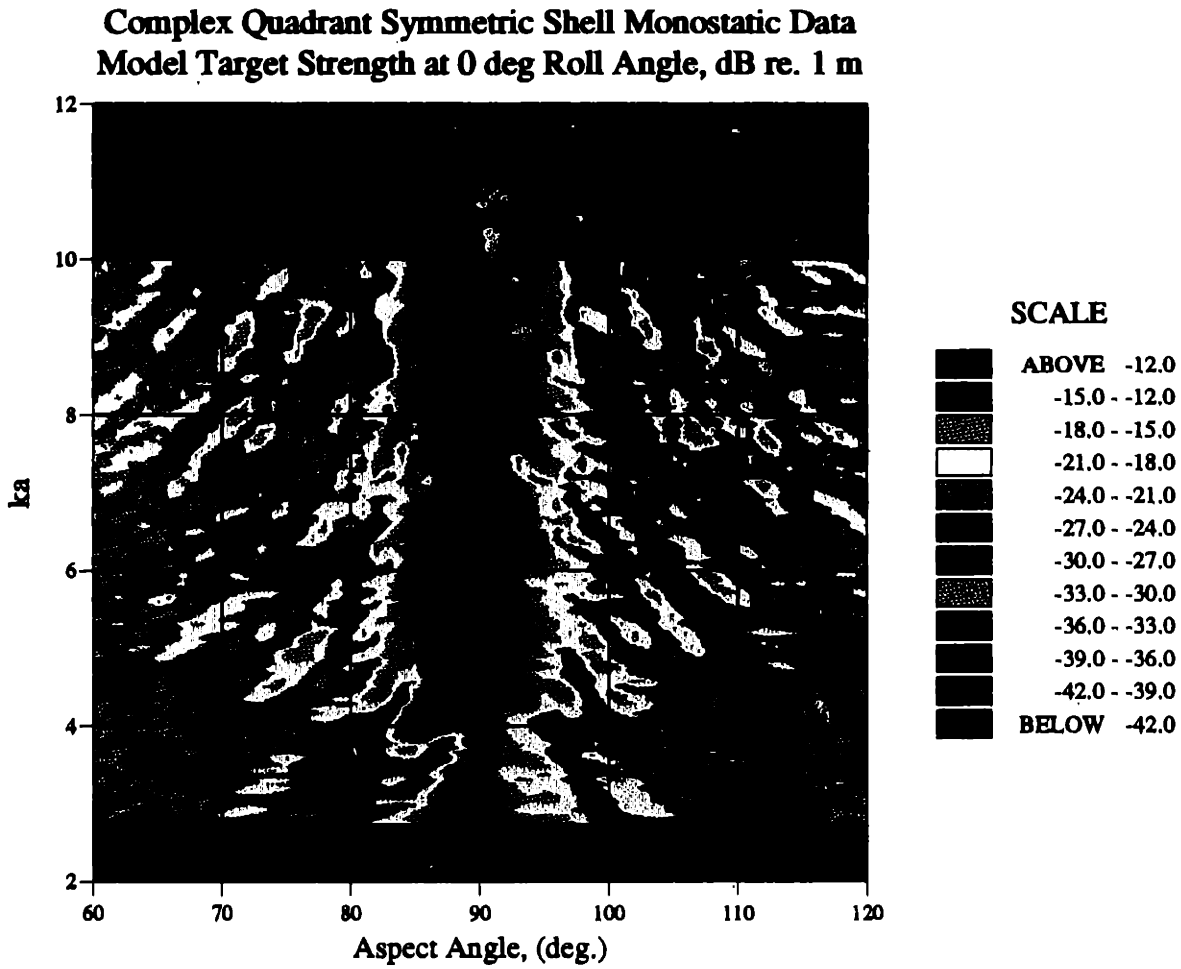

Figure 5.33: Contours of the Measured Target Strength $T(\omega, \theta)$ of the Complex Shell Model over the range of aspect angles $60 \leq \theta \leq 90$ deg. Values are normalized by the pressure level of the incident field at the target center location. The transfer functions have a limiting frequency resolution of $\Delta ka_{3dB} = 0.08$. The aspect angle $\theta = 90$ corresponds to beam aspect.

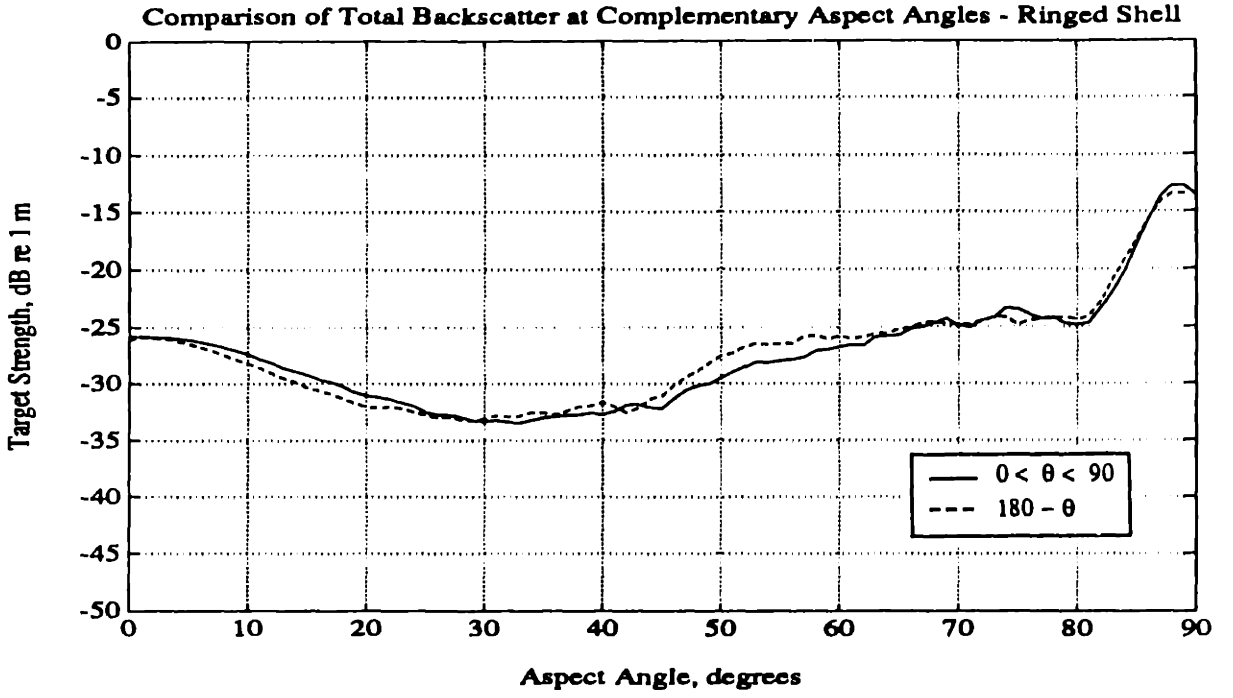

Figure 5.34: Comparison of Total Backscatter Levels Measured at Complementary Aspect Angles for the Ring Stiffened Shell. The target strength values shown were computed using the the time integral of the squared pressure $p_s^2(t,\theta)$.

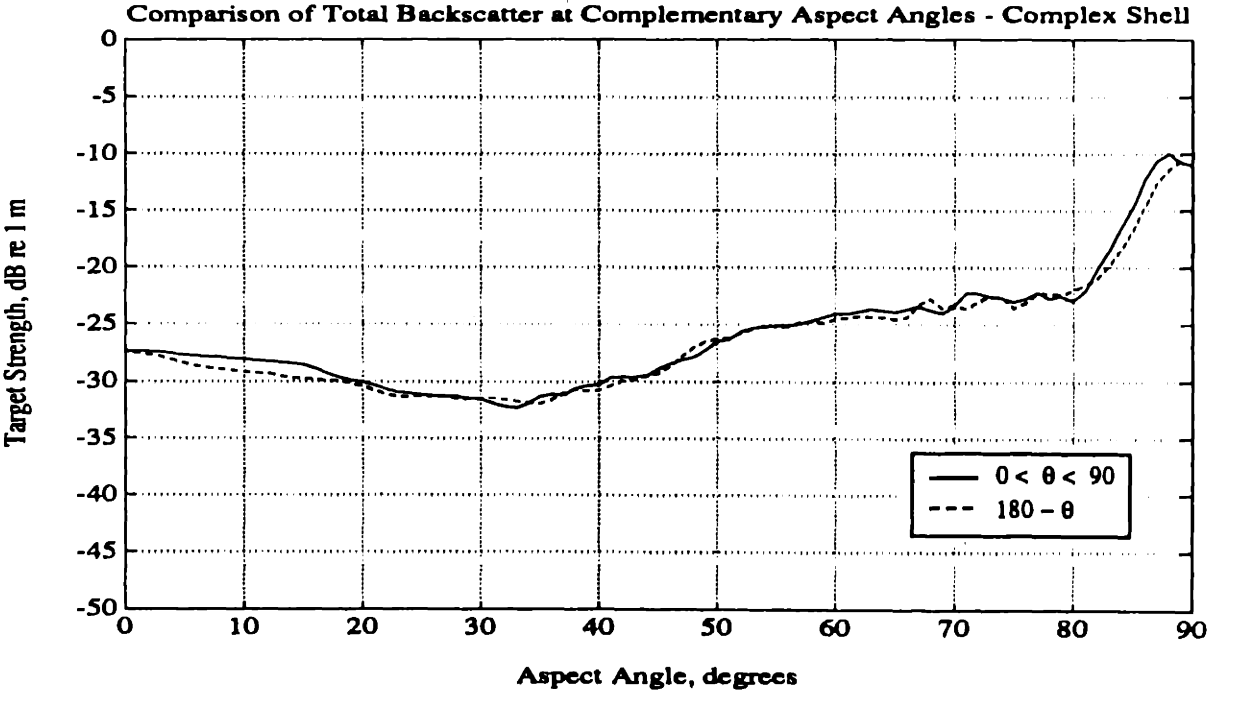

Figure 5.35: Comparison of Total Backscatter Levels Measured at Complementary Aspect Angles for the Complex Shell. The target strength values shown were computed using the the time integral of the squared pressure $p_s^2(t,\theta)$.

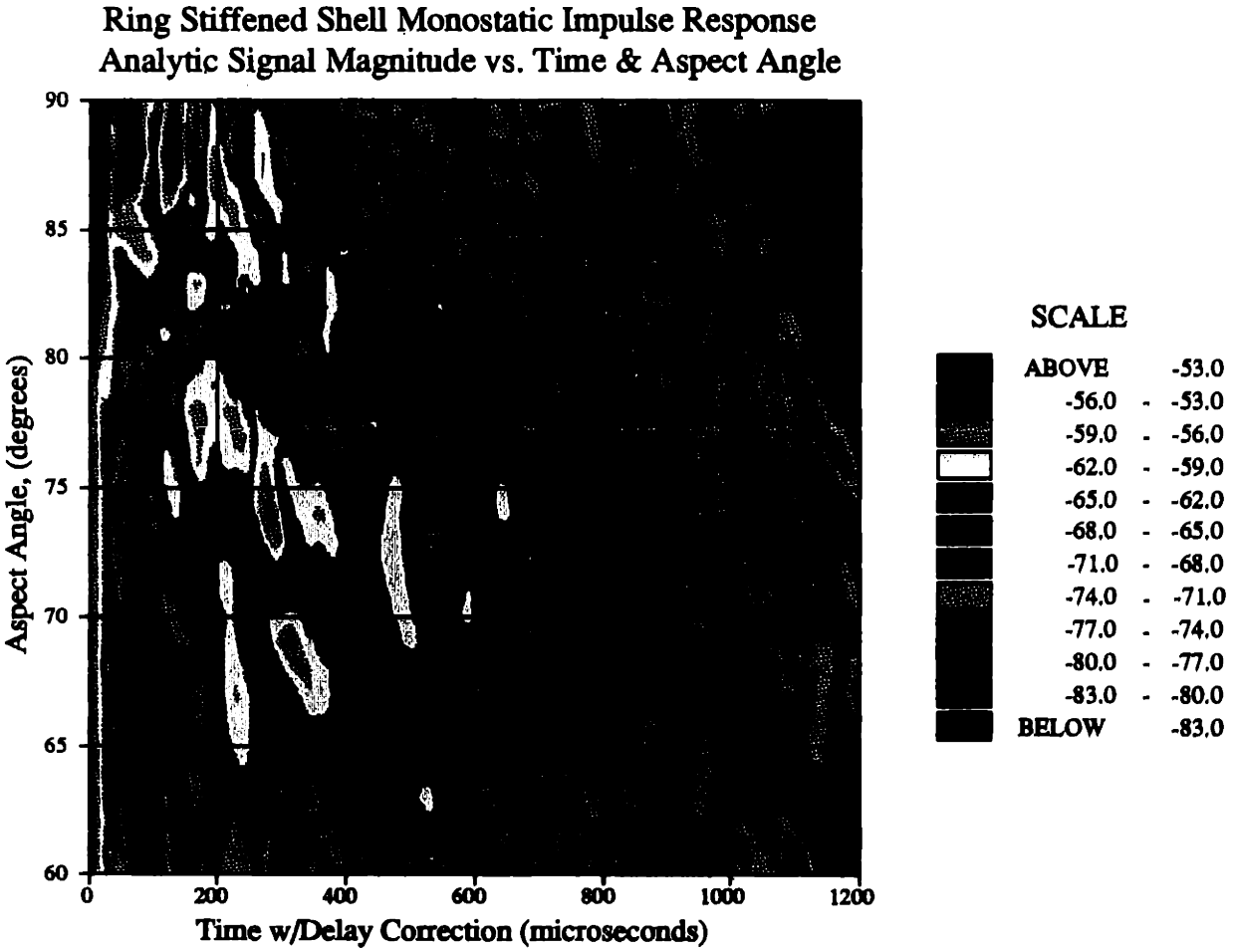

Figure 5.36: Analytic Signal Envelope of the Gaussian Bandlimited Monostatic Impulse Response of the Ring Stiffened Shell at $r = 2\ m$ for the frequency range of $2.75 < ka < 10.0$ and the range of aspect angles $60 \leq \theta \leq 90$ deg. The propagation delay of peak initial return from the target has been removed to stack the signals such that the peak initial return is shown at time $t = 0$ for all θ. The aspect angle $\theta = 90$ corresponds to beam aspect. Note that no data were acquired for $t > 1100\ \mu sec$ near beam aspect.

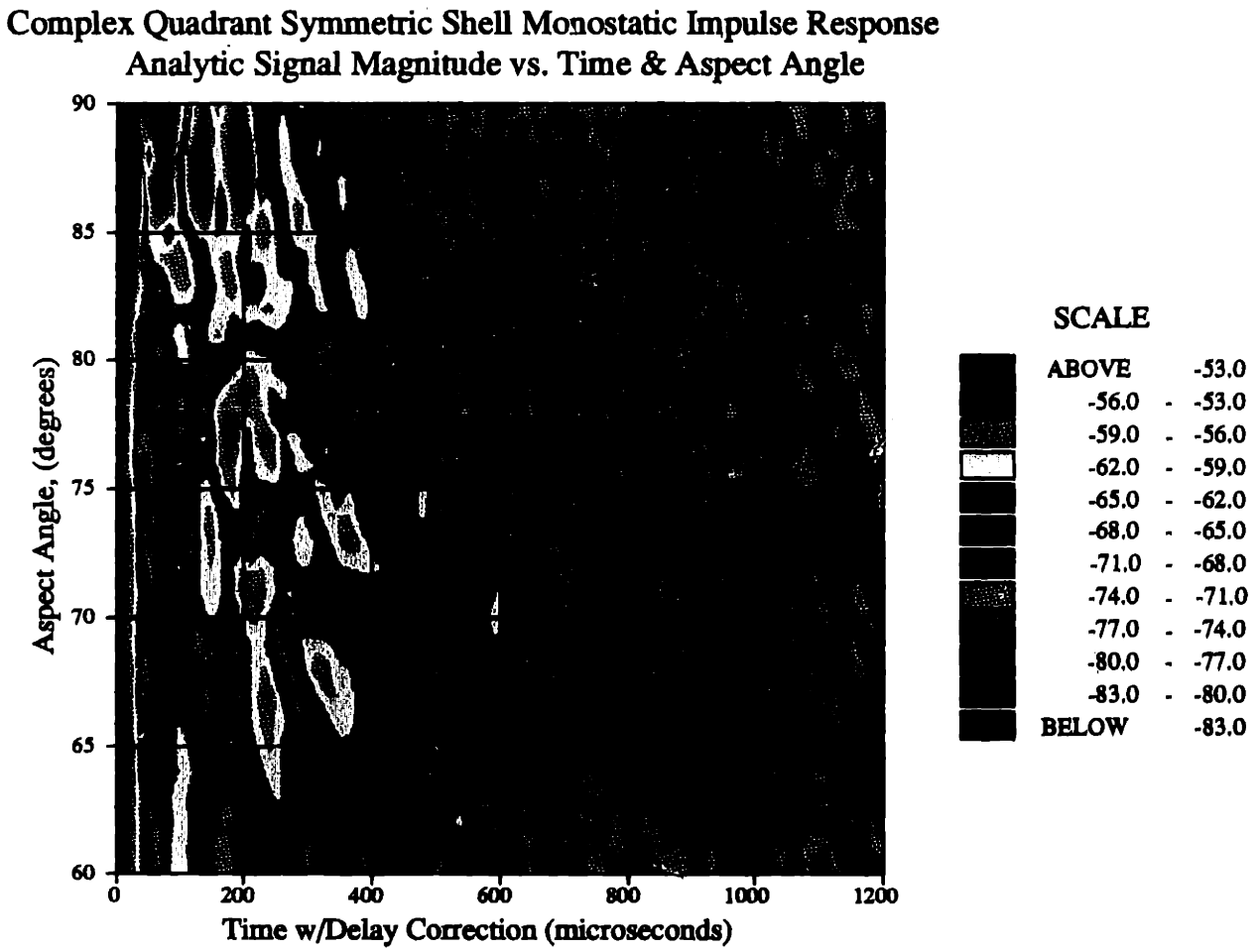

Figure 5.37: Analytic Signal Envelope of the Gaussian Bandlimited Monostatic Impulse Response of the Complex Shell at $r = 2\ m$ for the frequency range of $2.75 < ka < 10.0$ and the range of aspect angles $60 \leq \theta \leq 90$ deg. The propagation delay of peak initial return from the target has been removed to stack the signals such that the peak initial return is shown at time $t = 0$ for all θ. The aspect angle $\theta = 90$ corresponds to beam aspect.

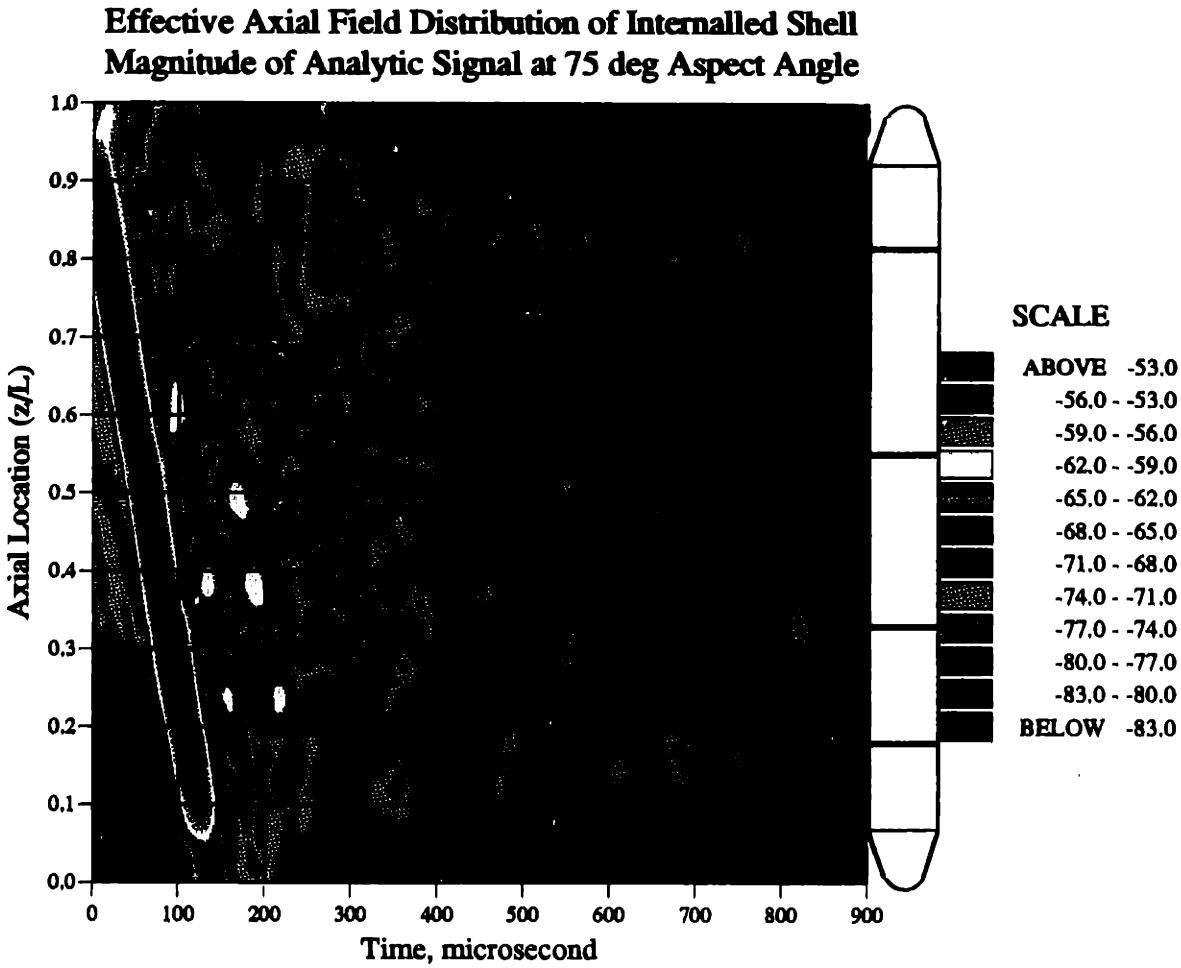

Figure 5.38: Effective Axial Distribution of the Back and Specularly Directed Scatter Sources of the Complex Shell Model at an Aspect Angle of 75 degrees. The results were generated using focused beamforming of the bistatic data measured over a range of observation angles of $60 \leq \theta_o \leq 120$ deg for the frequency range of $2.75 < ka < 10.0$. The incident field was deconvolved from the distribution to yield a normalized effective point source strength in dB re 1 m. The axial location $\tilde{z}/L = 0$ corresponds to the stern endcap, and $\tilde{z}/L = 1$ is the bow endcap. The beamforming resolution is $\Delta z_{3dB}/L = 0.048$.

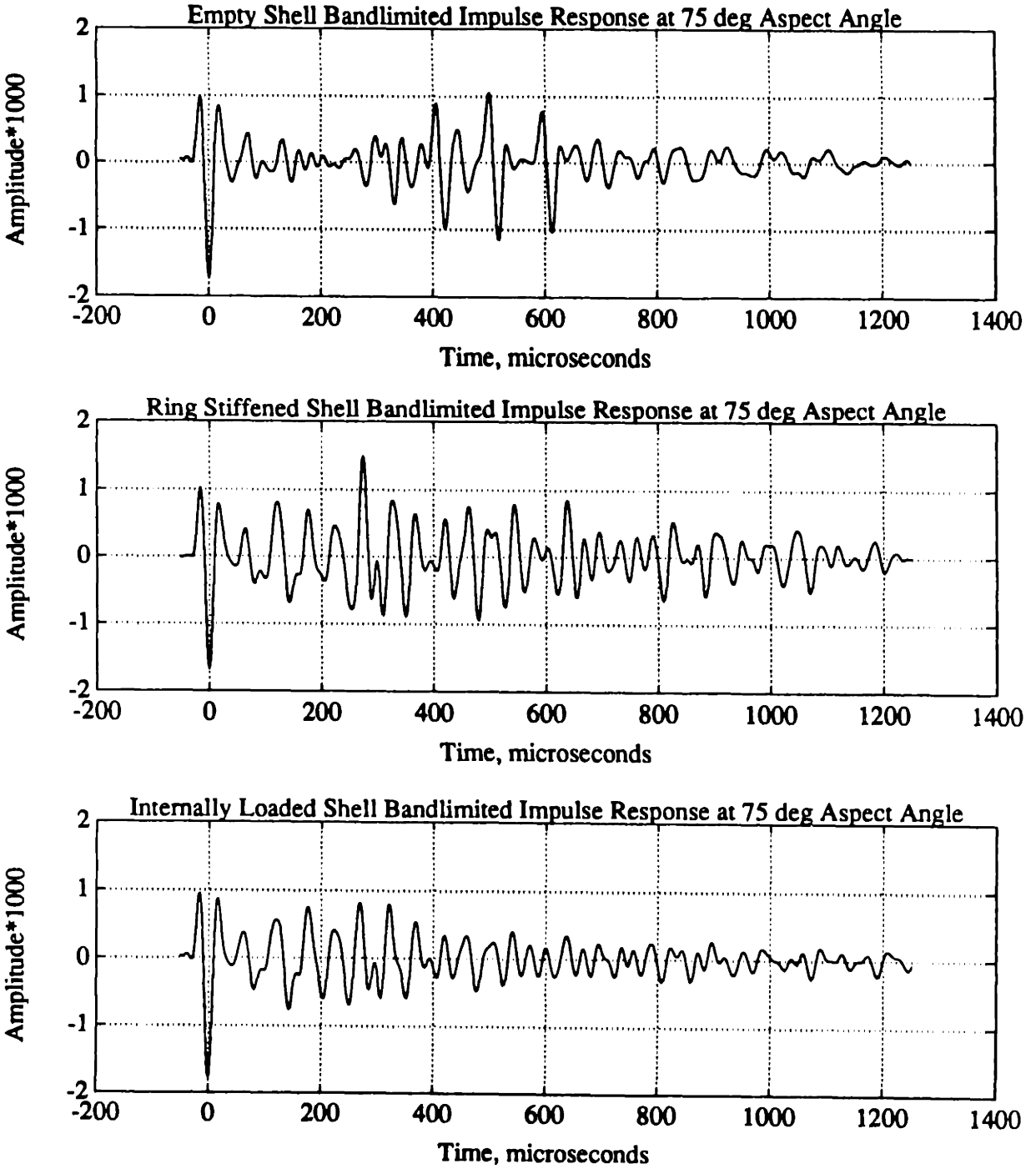

Figure 5.39: Comparison of Bandlimited Monostatic Impulse Response Signatures of the Three Shells at an Aspect Angle of $\theta = 75$ deg. The frequency Range is $2.75 < ka < 10.0$ and the distance from the target center is $r = 2\ m$. The complex shell data shown were measured during the June 1992 test series where increased levels of initial scatter were not measured.

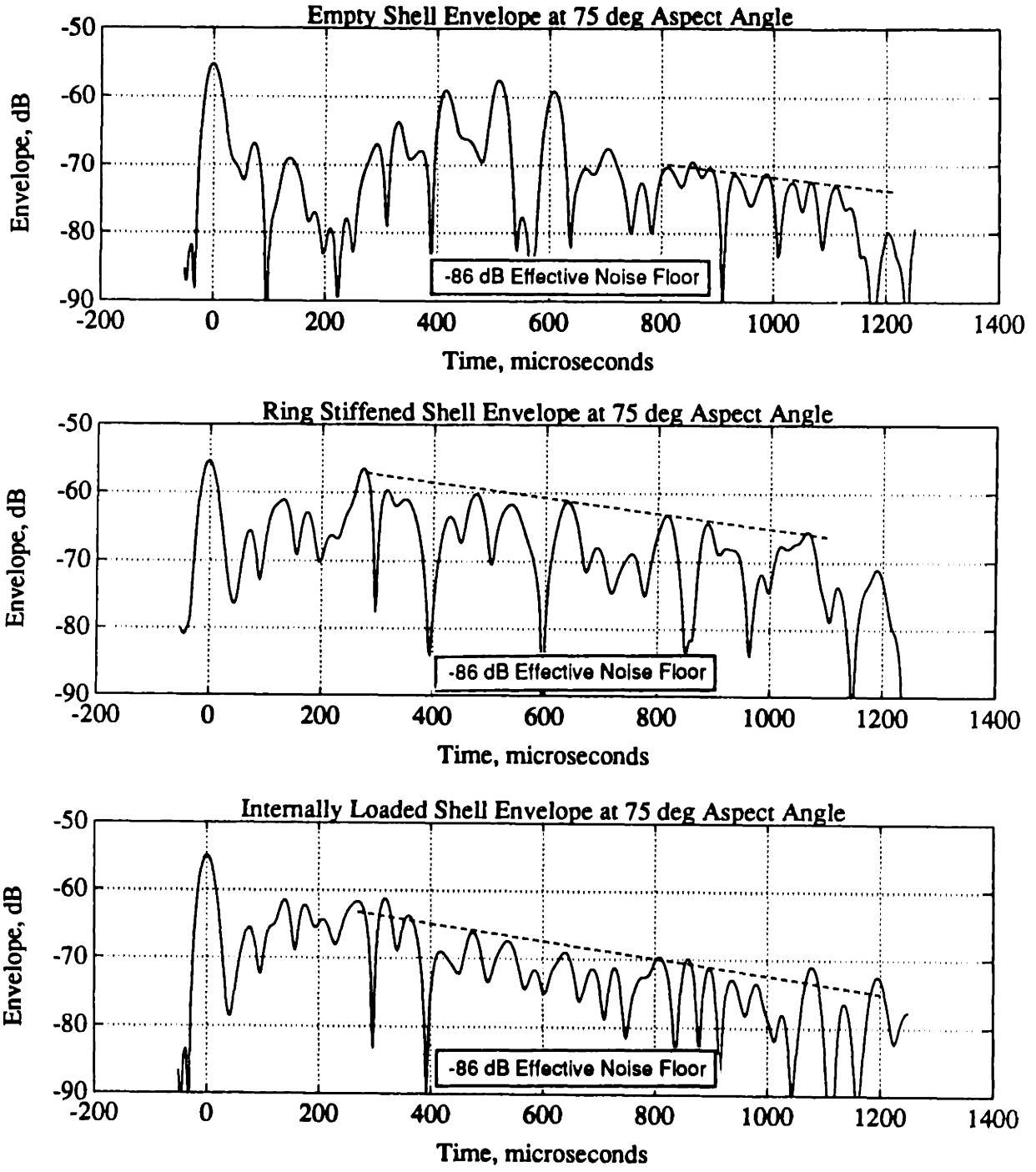

Figure 5.40: Comparison of the Envelopes of the Bandlimited Impulse Response Signatures of the Three Shells at an Aspect Angle of 75 deg. The Frequency Range is $2.75 < ka < 10.0$ and the distance from the target center is $r = 2\ m$. The complex shell data shown were measured during the June 1992 test series where increased levels of initial scatter were not measured.

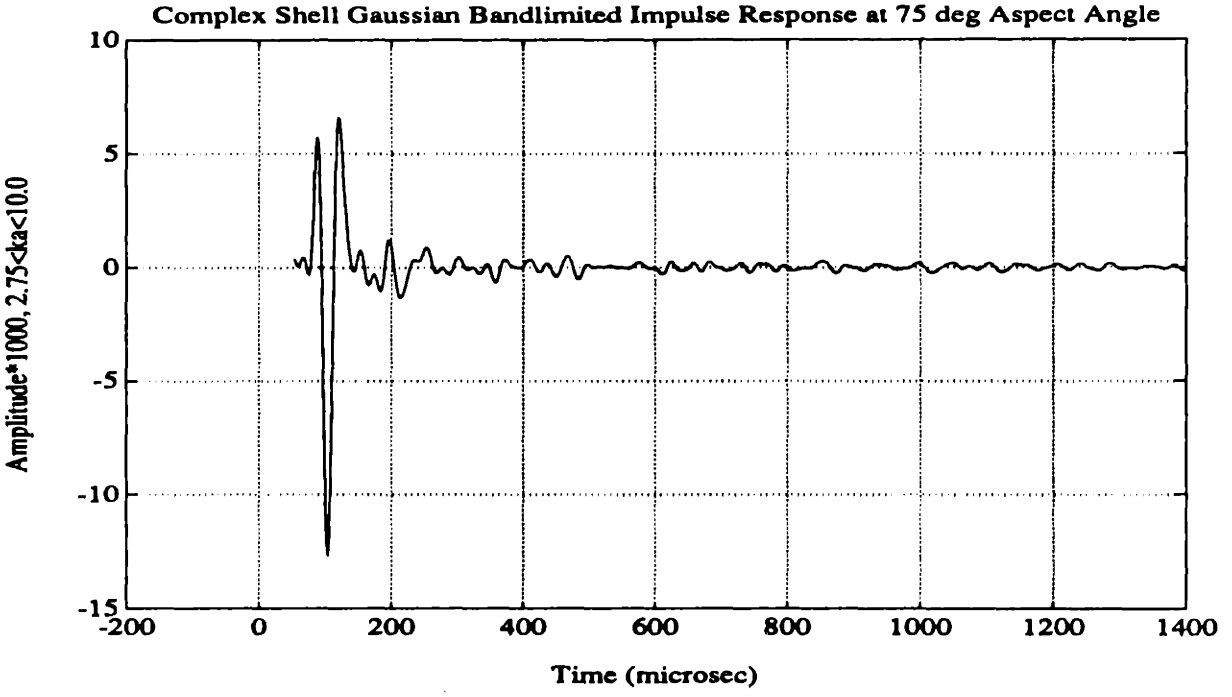

Figure 5.41: Gaussian Bandlimited Specularly Directed Impulse Response of the Complex Shell at an Aspect Angle of $\theta = 75$ degrees. The frequency range is $2.75 < ka < 10.0$ and the distance distance from the target center is $r = 2\ m$.

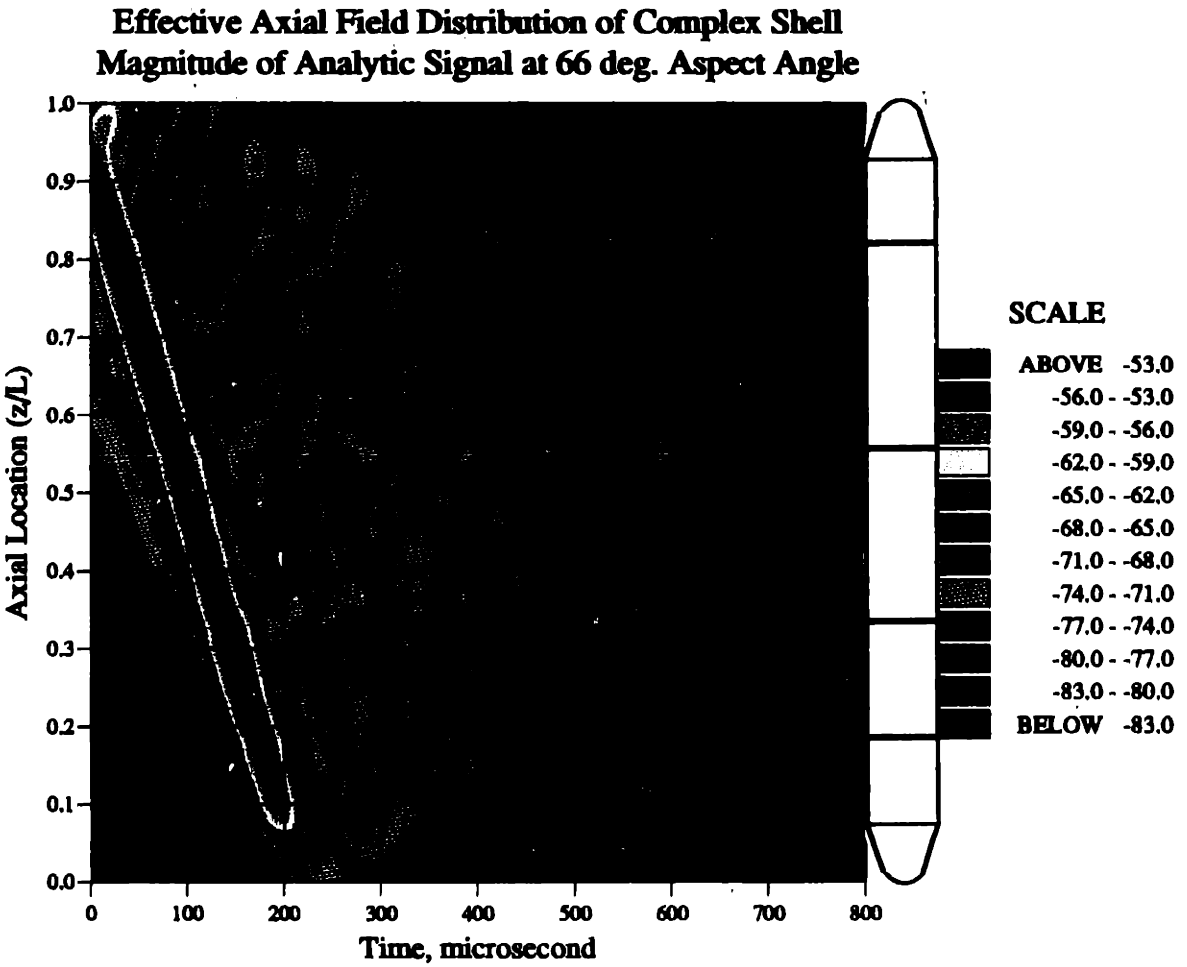

Figure 5.42: Effective Axial Distribution of the Back and Specularly Directed Scatter Sources of the Complex Shell Model at an Aspect Angle of 66 degrees. The results were generated using focused beamforming of the bistatic data measured over a range of observation angles of $50 \leq \theta_o \leq 130$ deg for the frequency range of $2.75 < ka < 10.0$. The incident field was deconvolved from the distribution to yield a normalized effective point source strength in dB re 1 m. The axial location $\tilde{z}/L = 0$ corresponds to the stern endcap, and $\tilde{z}/L = 1$ is the bow endcap. The beamforming resolution is $\Delta z_{3dB}/L = 0.037$.

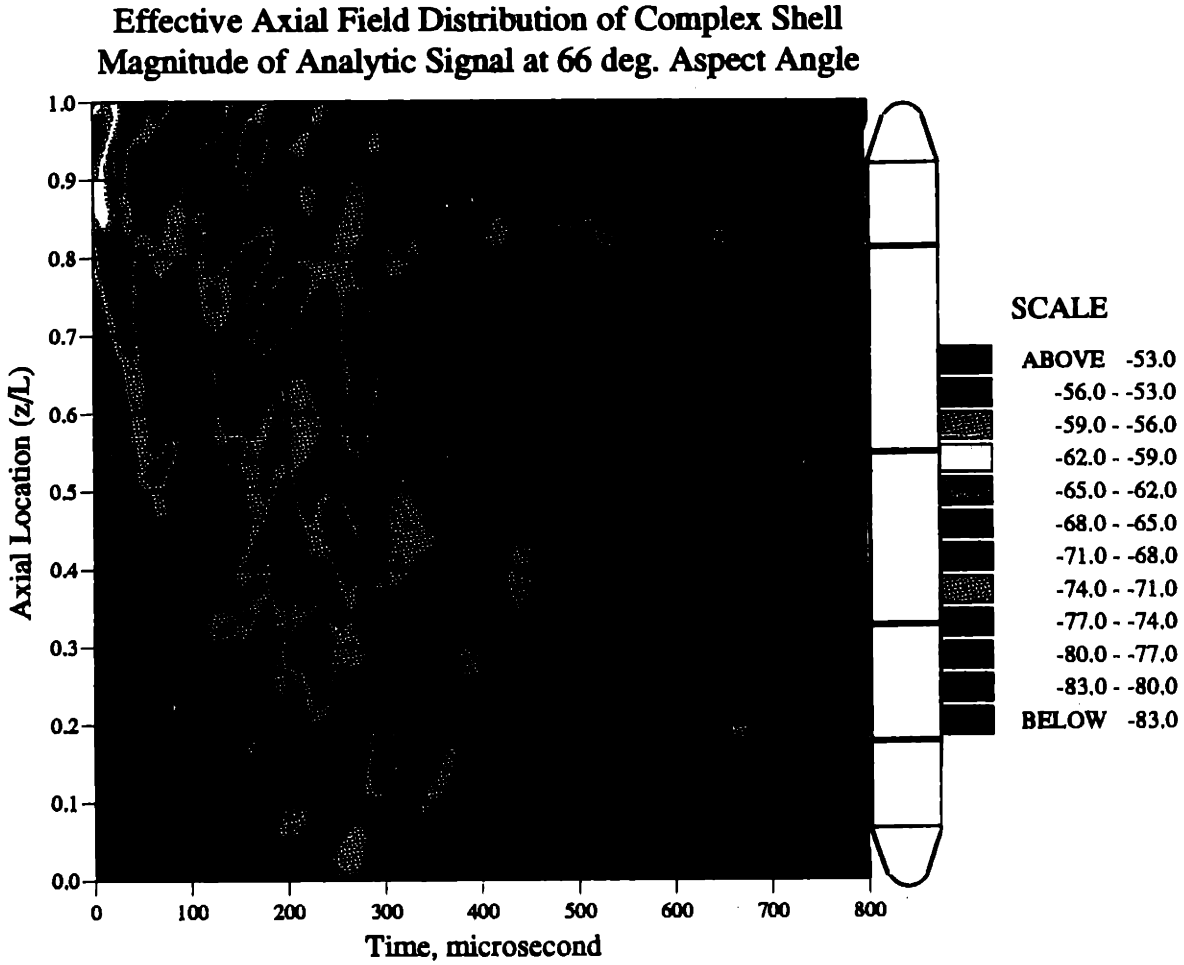

Figure 5.43: Effective Axial Distribution of the Back Directed Scatter Sources of the Complex Shell Model at an Aspect Angle of 66 degrees. The results were generated using focused beamforming of the bistatic data measured over a range of observation angles of $32 \leq \theta_o \leq 100$ deg for the frequency range of $2.75 < ka < 10.0$. The incident field was deconvolved from the distribution to yield a normalized effective point source strength in dB re 1 m. The axial location $\tilde{z}/L = 0$ corresponds to the stern endcap, and $\tilde{z}/L = 1$ is the bow endcap. The beamforming resolution is $\Delta z_{3dB}/L = 0.043$.

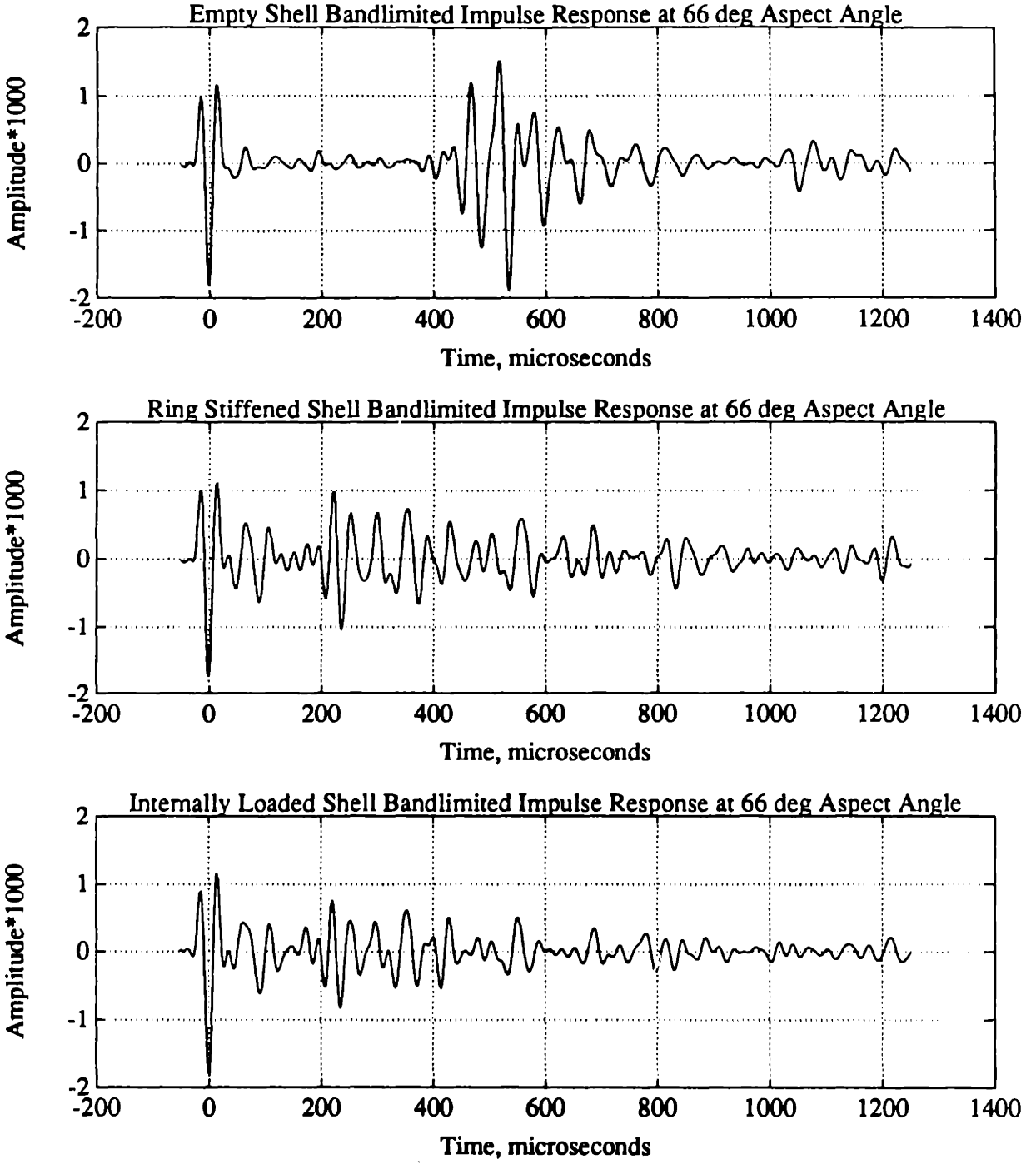

Figure 5.44: Comparison of Bandlimited Monostatic Impulse Response Signatures of the Three Shells at an Aspect Angle of $\theta = 66\,\text{deg}$. The frequency Range is $2.75 < ka < 10.0$ and the distance from the target center is $r = 2\ m$. The complex shell data shown were measured during the June 1992 test series where increased levels of initial scatter were not measured.

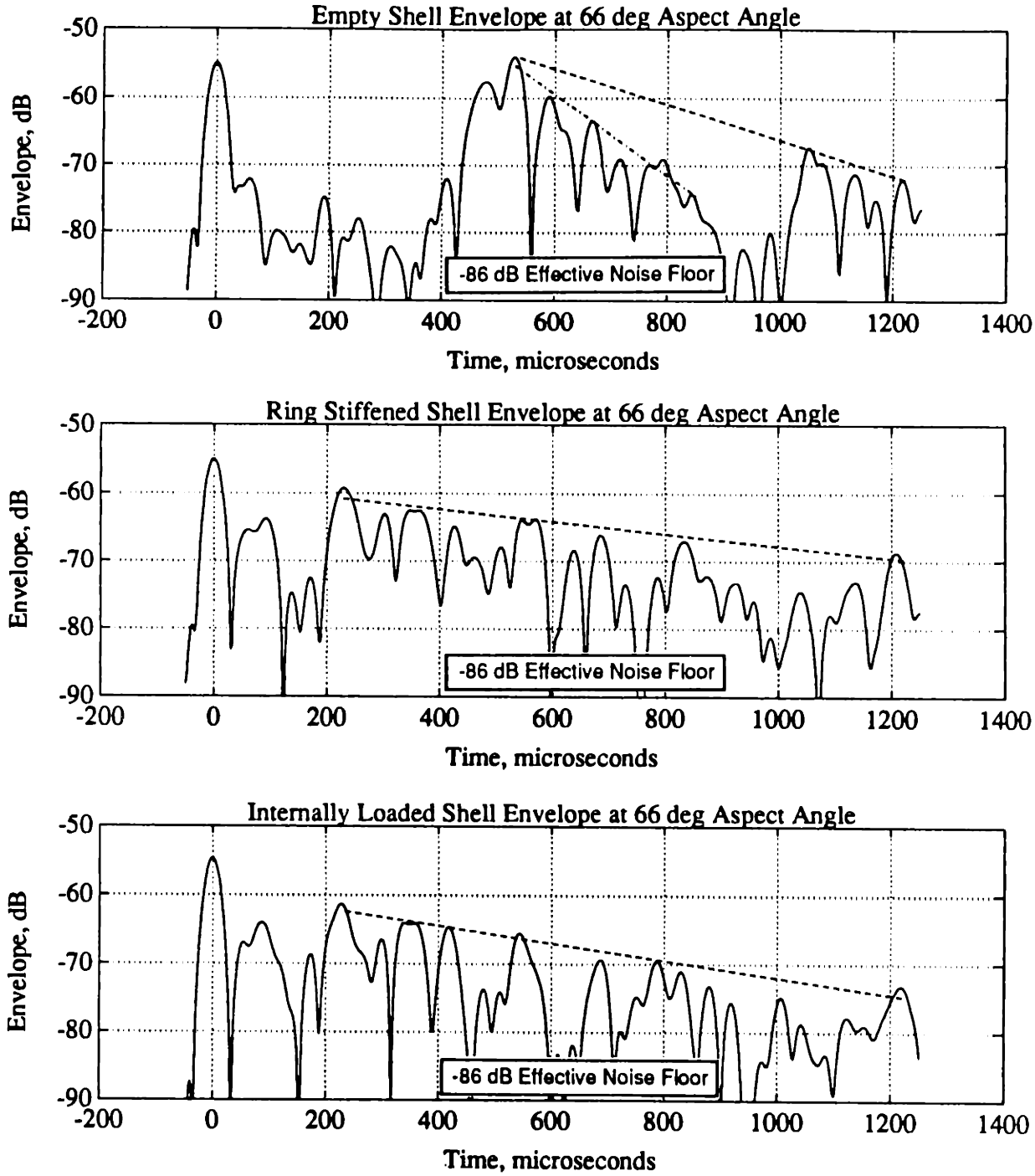

Figure 5.45: Comparison of the Envelopes of the Bandlimited Impulse Response Signatures of the Three Shells at an Aspect Angle of 66 deg. The Frequency Range is $2.75 < ka < 10.0$ and the distance from the target center is $r = 2\ m$. The complex shell data shown were measured during the June 1992 test series where increased levels of initial scatter were not measured.

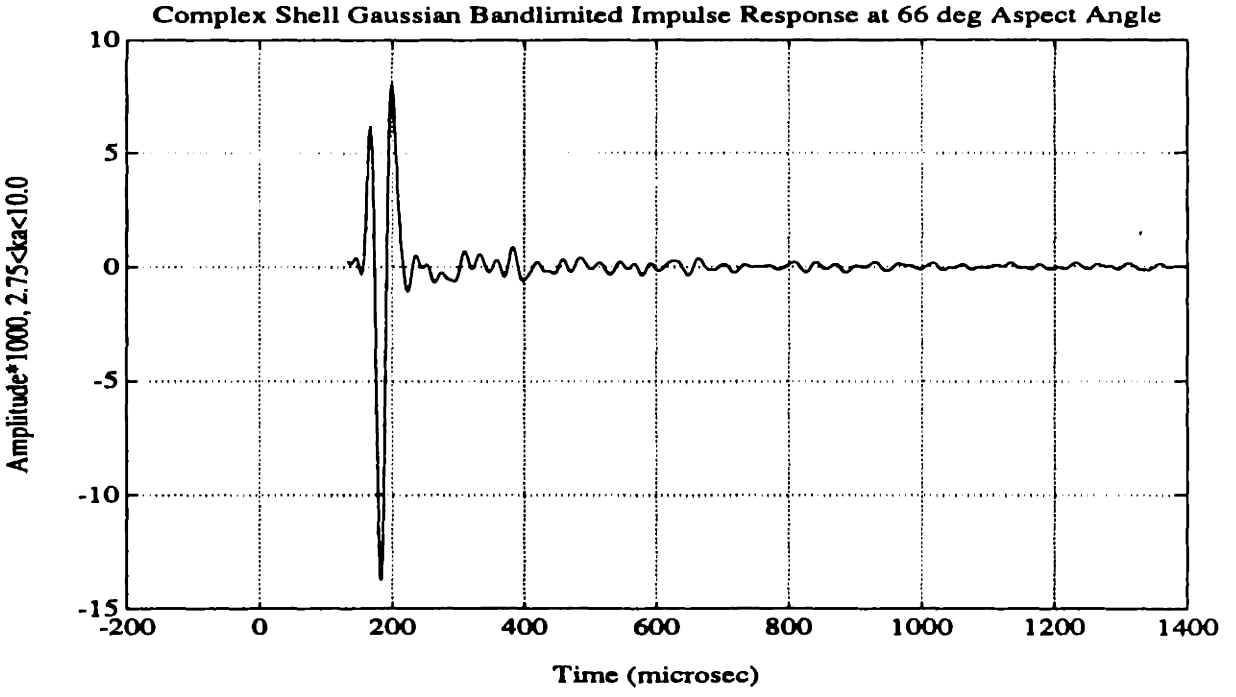

Figure 5.46: Gaussian Bandlimited Specularly Directed Impulse Response of the Complex Shell at an Aspect Angle of $\theta = 66\,\text{deg}$, Frequency Range of $2.75 < ka < 10.0$, and a Radial Distance of $r = 2\,m$ from the Target Center

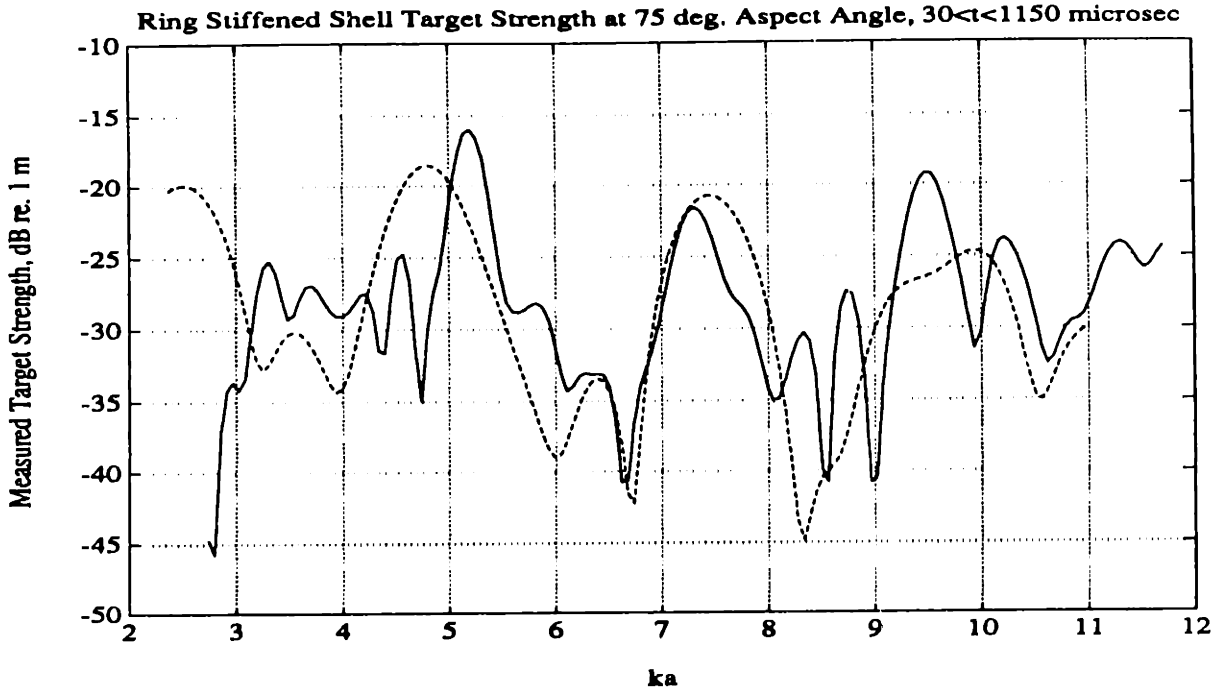

Figure 5.47: Target Strength of the Ring Stiffened Shell Monostatic Signal Measured Over $30 < t < 1150$ and an Aspect Angle of 75 deg. Transfer function shown has a Rectangular/Hanning window frequency resolution of $\Delta ka_{3dB} = 0.19$. The dashed line is the target strength of the empty shell measured over $200 < t < 800$.

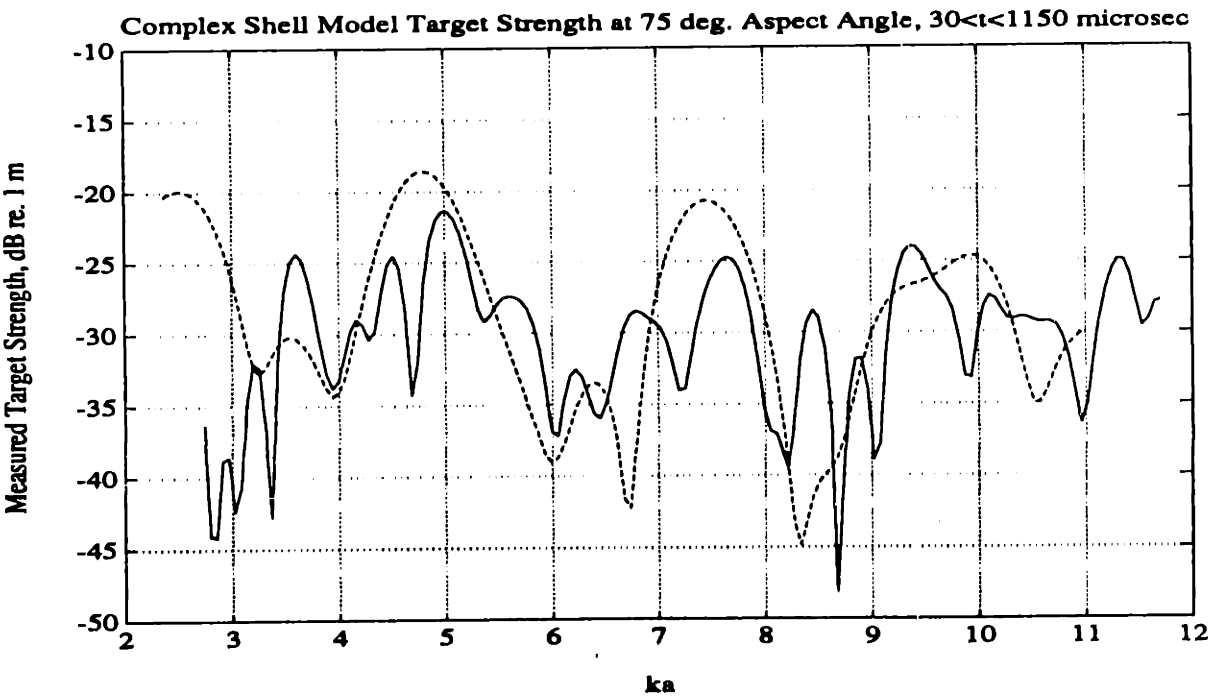

Figure 5.48: Target Strength of the Complex Shell Monostatic Signal Measured Over $30 < t < 1150$ and an Aspect Angle of 75 deg. Transfer function shown has a Rectangular/Hanning window frequency resolution of $\Delta ka_{3dB} = 0.19$. The dashed line is the target strength of the empty shell measured over $200 < t < 800$.

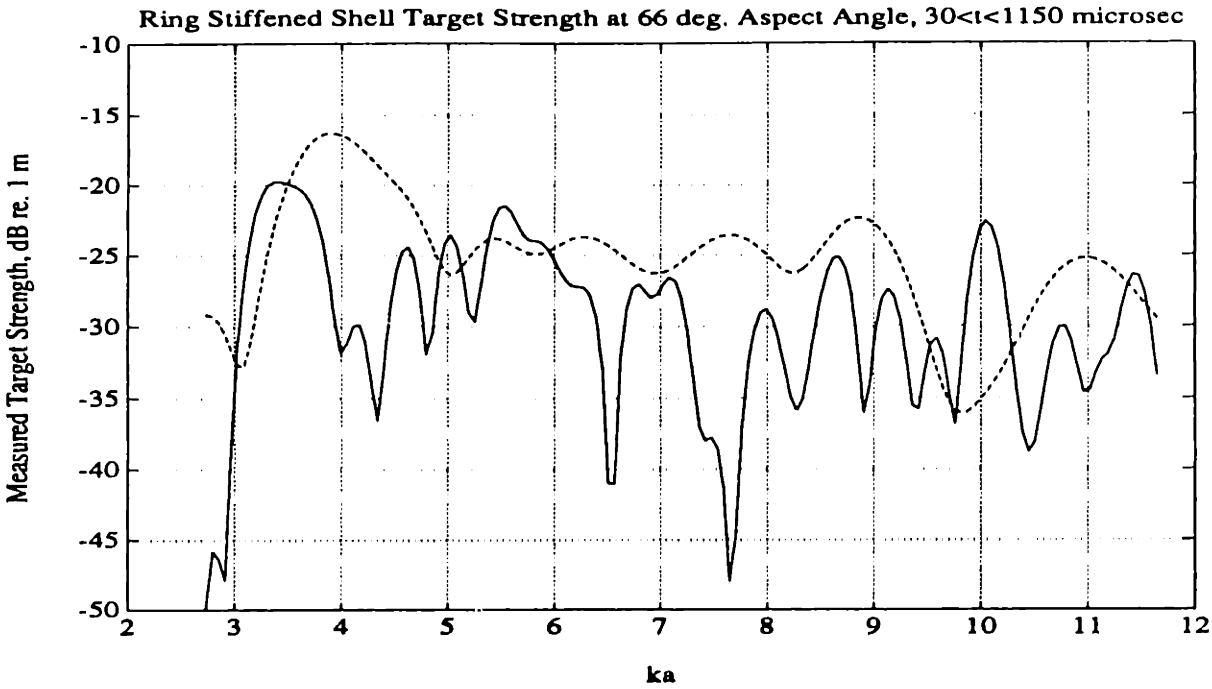

Figure 5.49: Target Strength of the Ring Stiffened Shell Monostatic Signal Measured Over $30 < t < 1150$ and an Aspect Angle of 66 deg. Transfer function shown has a Rectangular/Hanning window frequency resolution of $\Delta ka_{3dB} = 0.19$. The dashed line is the target strength of the empty shell measured over $300 < t < 900$.

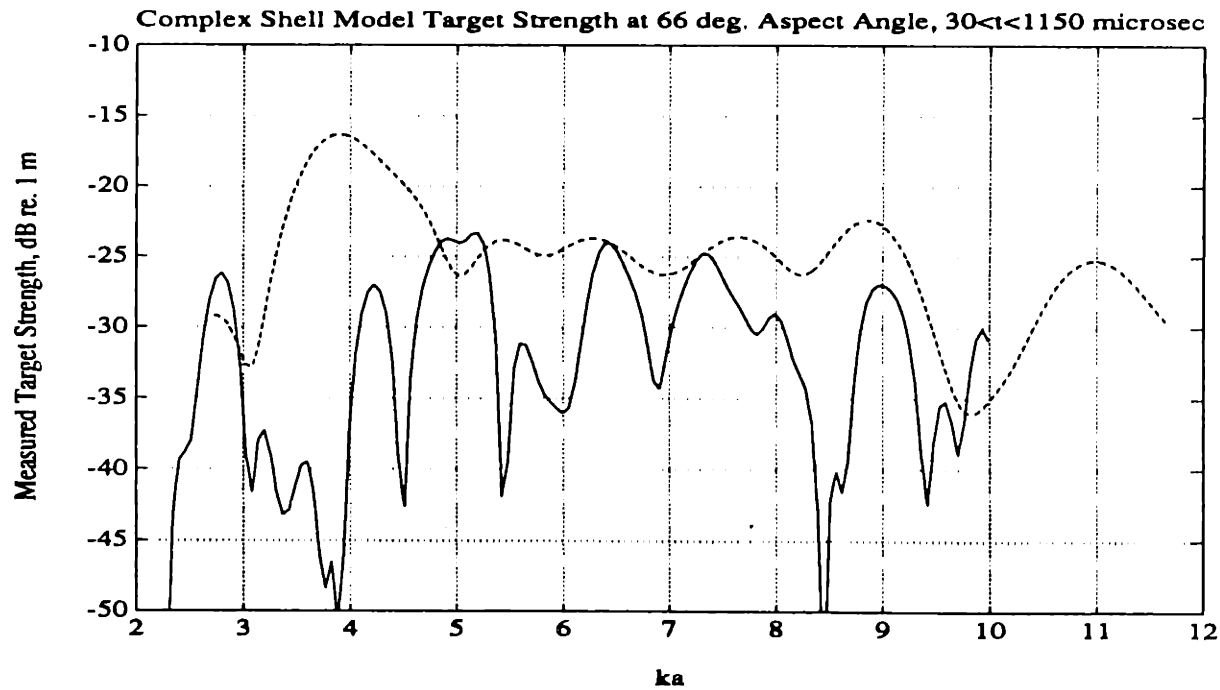

Figure 5.50: Target Strength of the Complex Shell Monostatic Signal Measured Over $30 < t < 1150$ and an Aspect Angle of 66 deg. Transfer function shown has a Rectangular/Hanning window frequency resolution of $\Delta ka_{3dB} = 0.19$. The dashed line is the target strength of the empty shell measured over $300 < t < 900$.

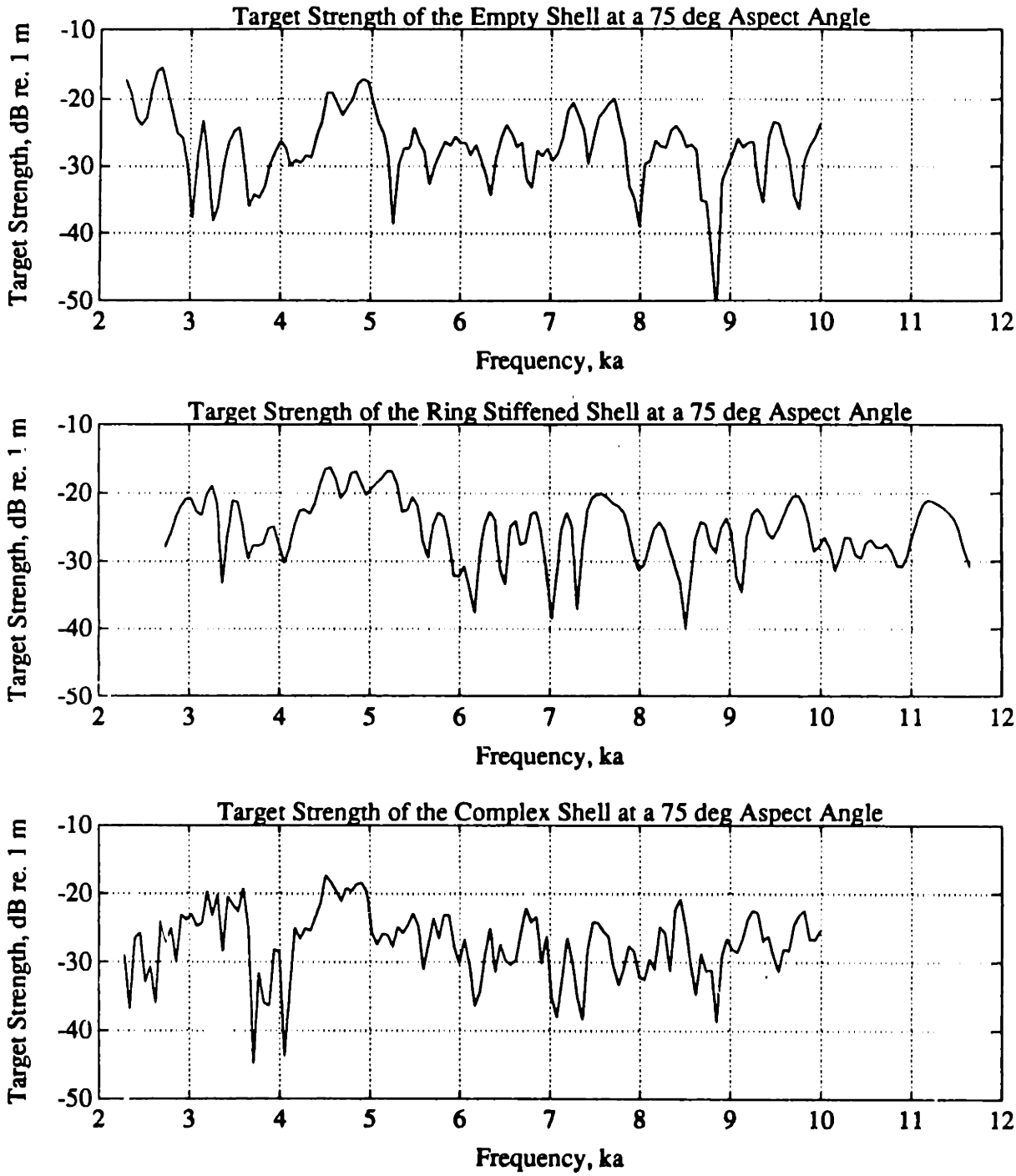

Figure 5.51: Comparison of the Measured Target Strength of the Three Shells at an Aspect Angle of $\theta = 75$ deg. The frequency resolution of the data shown for the empty and complex shells is $\Delta ka_{3dB} = 0.08$, and $\Delta ka_{3dB} = 0.15$ for the ring stiffened shell. The complex shell data shown were measured during the June 1992 test series where increased levels of initial scatter were not measured.

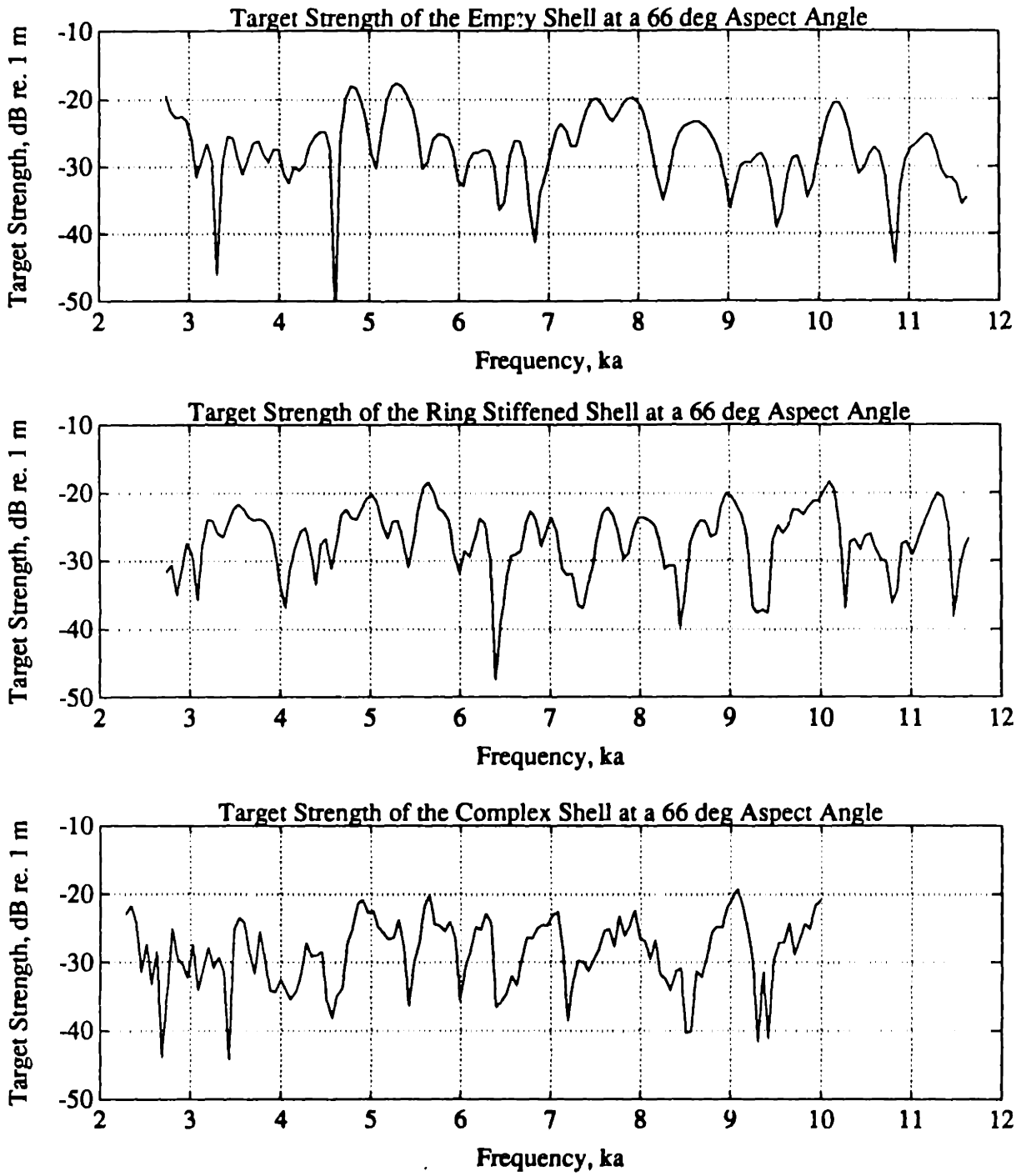

Figure 5.52: Comparison of the Measured Target Strength of the Three Shells at an Aspect Angle of $\theta = 66$ deg. The frequency resolution of the data shown for the empty and complex shells is $\Delta ka_{3dB} = 0.08$, and $\Delta ka_{3dB} = 0.15$ for the ring stiffened shell. The complex shell data shown were measured during the June 1992 test series where increased levels of initial scatter were not measured.

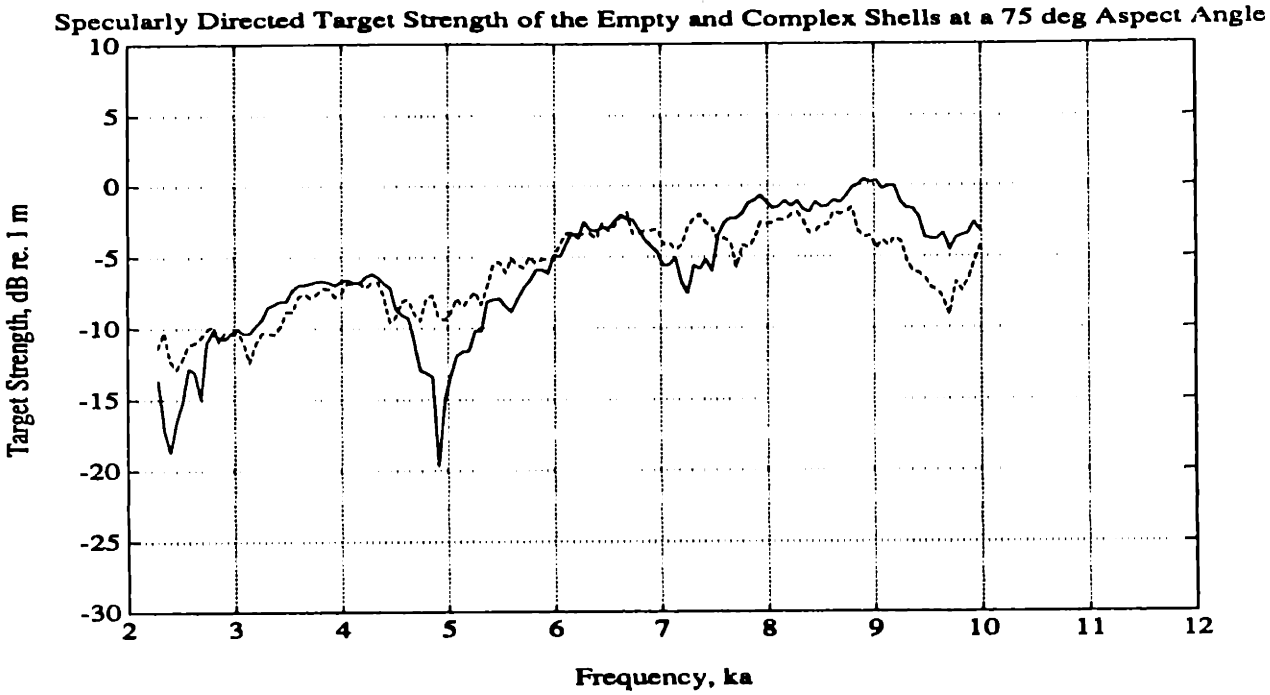

Figure 5.53: Comparison of the Measured Specularly Directed Target Strength of the Complex and Empty Shells for an Aspect Angle of 75 deg. The frequency resolution is $\Delta ka_{3dB} = 0.08$. The values shown include the target strength correction of Figure 3.4.

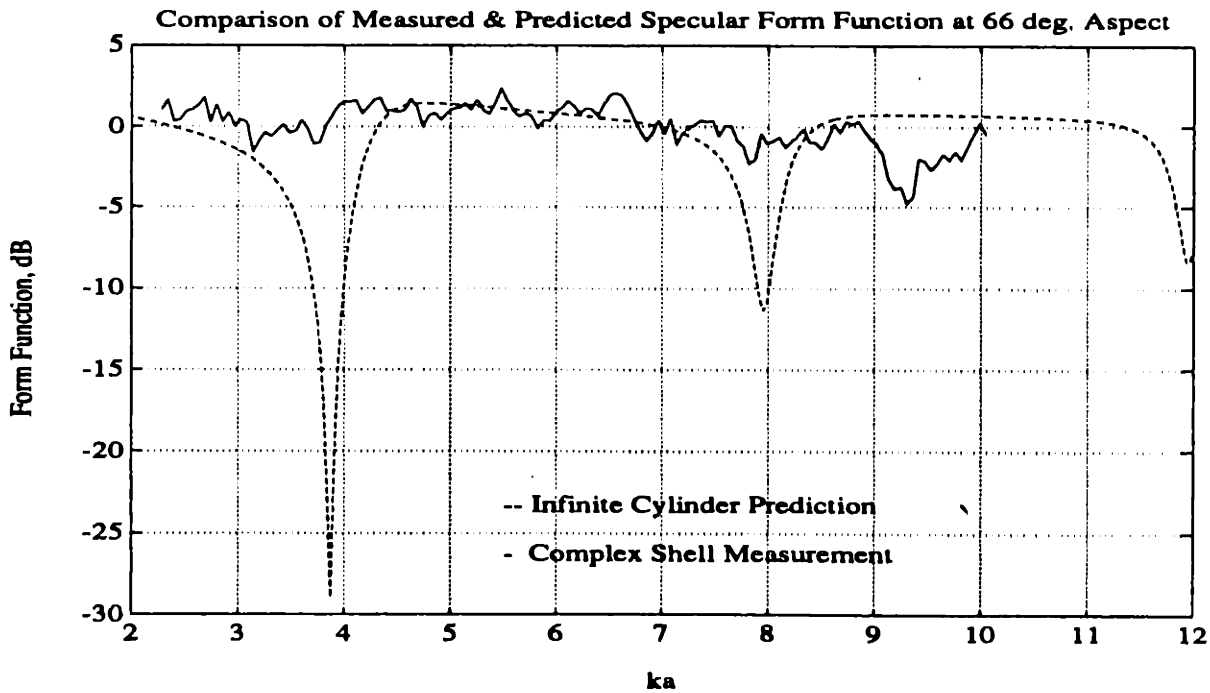

Figure 5.54: Comparison of the Measured Complex Shell and Infinite Cylinder Specularly Directed Form Functions for an Aspect Angle of 66 deg. The frequency resolution of the measured data is $\Delta ka_{3dB} = 0.08$.

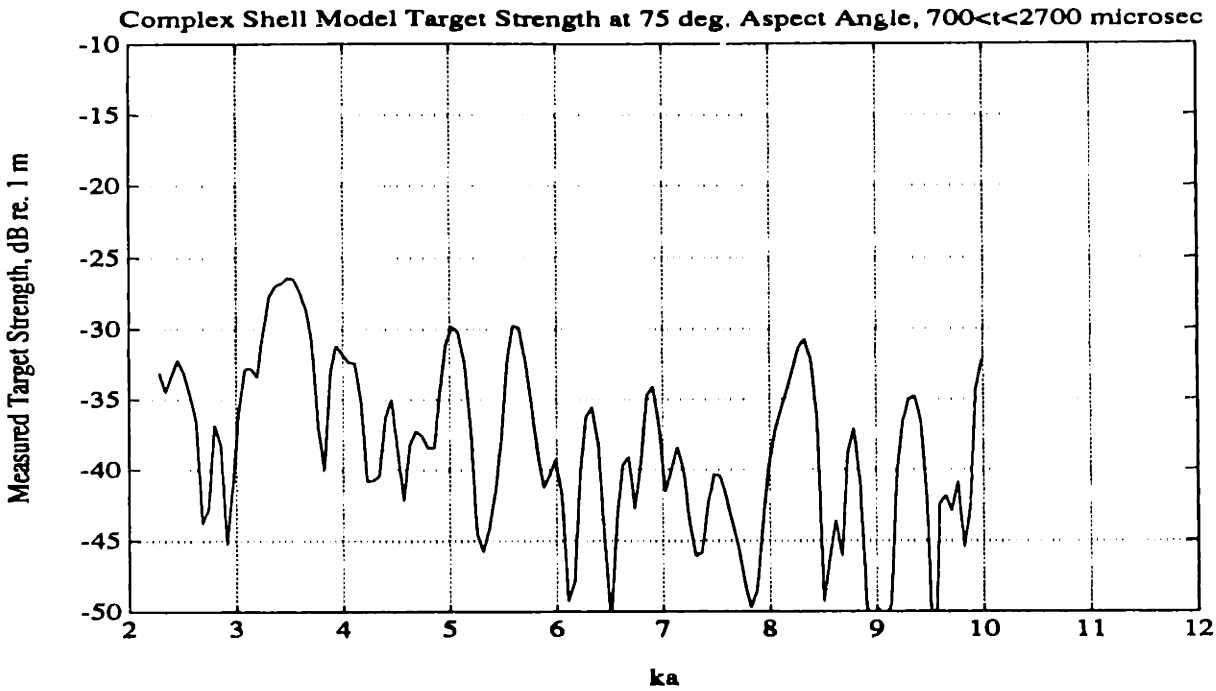

Figure 5.55: Target Strength of the Complex Shell Back Directed Scatter Measured Over $700 < t < 2700\mu sec$ and an Aspect Angle of 75 deg. The transfer function has a Hamming window frequency resolution of $\Delta ka_{3dB} = 0.15$.

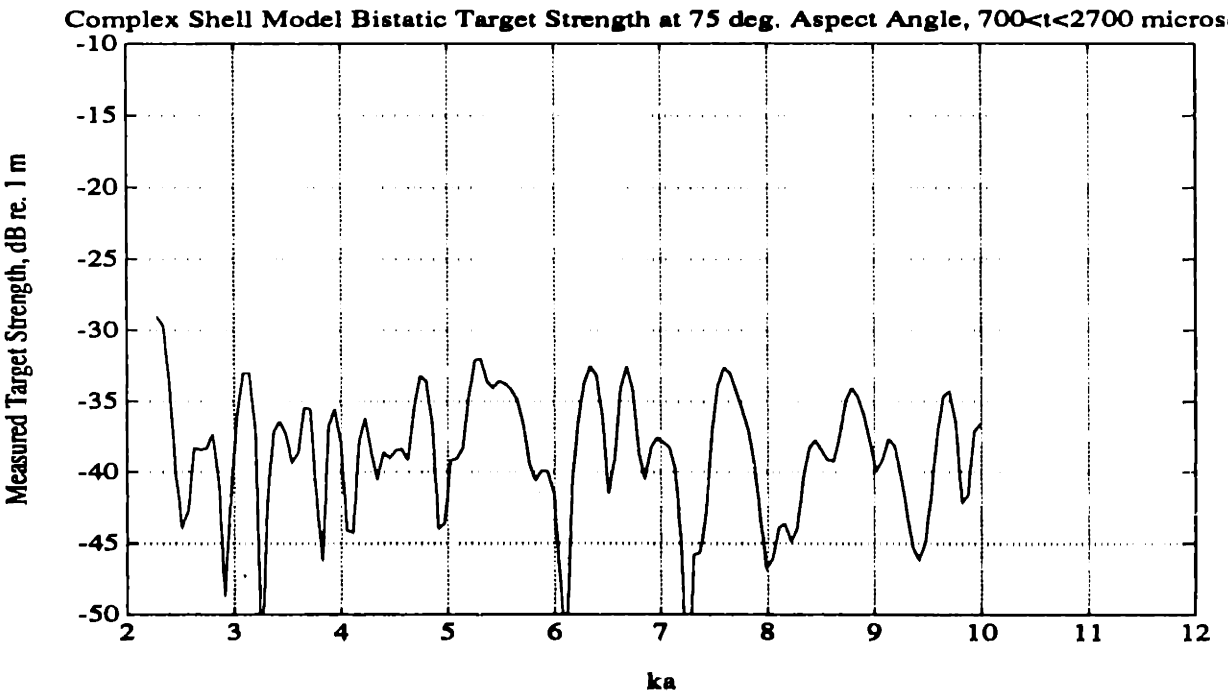

Figure 5.56: Target Strength of the Complex Shell Specularly Directed Scatter Measured Over $700 < t < 2700\mu sec$ and an Aspect Angle of 75 deg. The transfer function has a Hamming window frequency resolution of $\Delta ka_{3dB} = 0.15$.

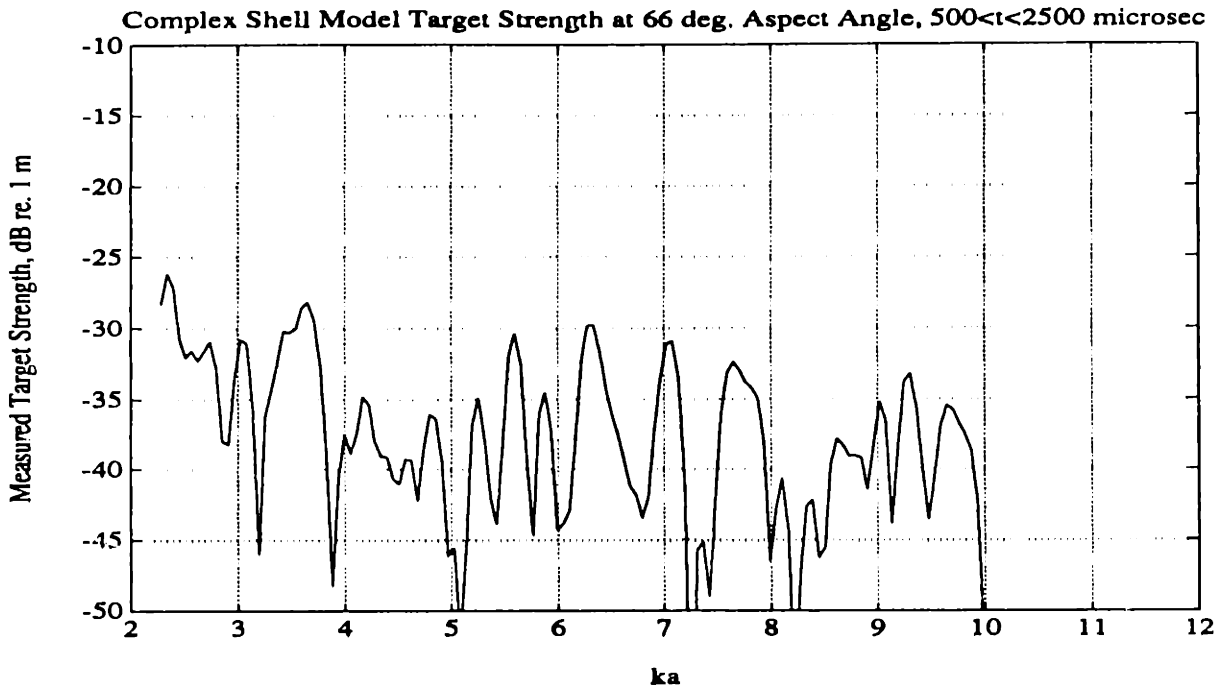

Figure 5.57: Target Strength of the Complex Shell Back Directed Scatter Measured Over $500 < t < 2500\mu sec$ and an Aspect Angle of 66 deg. The transfer function has a Hamming window frequency resolution of $\Delta ka_{3dB} = 0.15$.

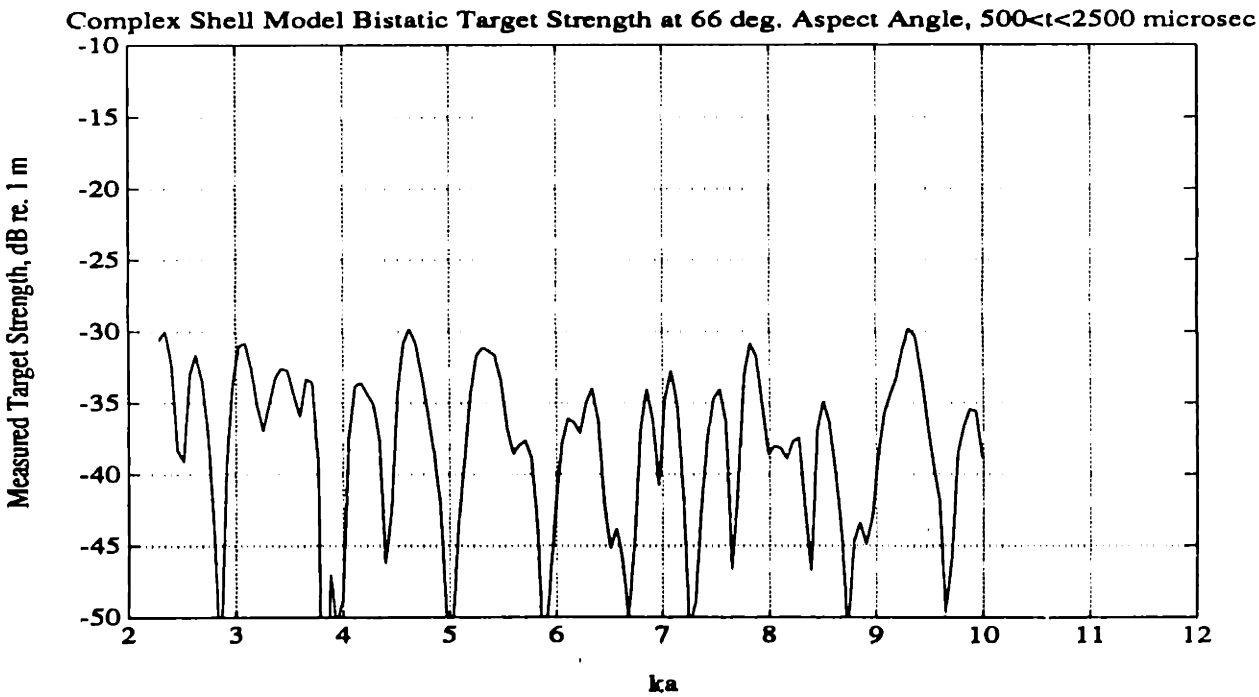

Figure 5.58: Target Strength of the Complex Shell Specularly Directed Scatter Measured Over $500 < t < 2500\mu sec$ and an Aspect Angle of 66 deg. The transfer function has a Hamming window frequency resolution of $\Delta ka_{3dB} = 0.15$.

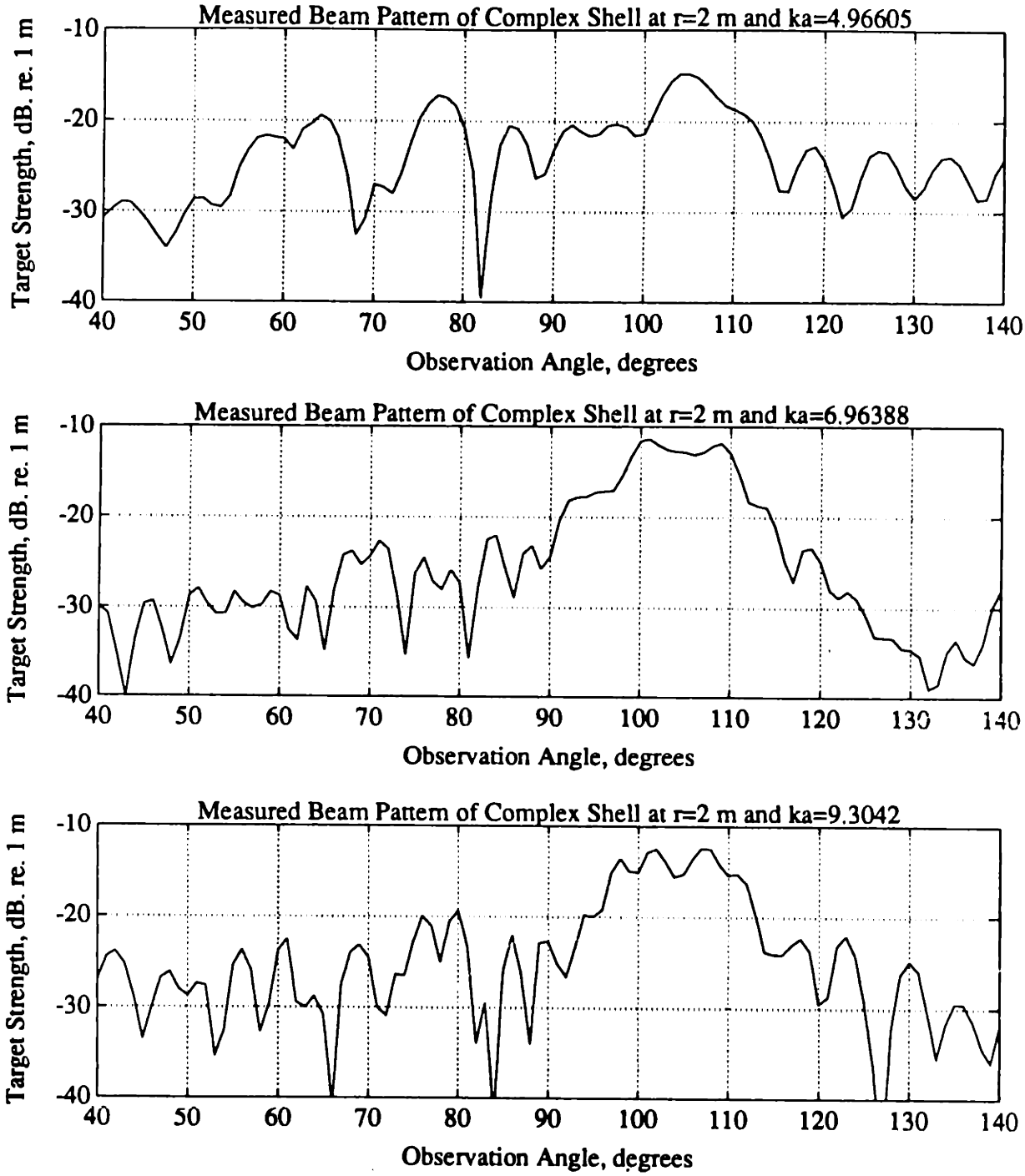

Figure 5.59: Representative Complex Shell Beam Patterns Measured at an Aspect Angle of 75 Degrees and Frequencies of ka = 4.97, 6.96, and 9.30. The observation angle θ_o = 105 corresponds to the specular direction, and θ_o = 75 is the back direction. The receivers were all located at a radial distance of r = 2 m from the target center.

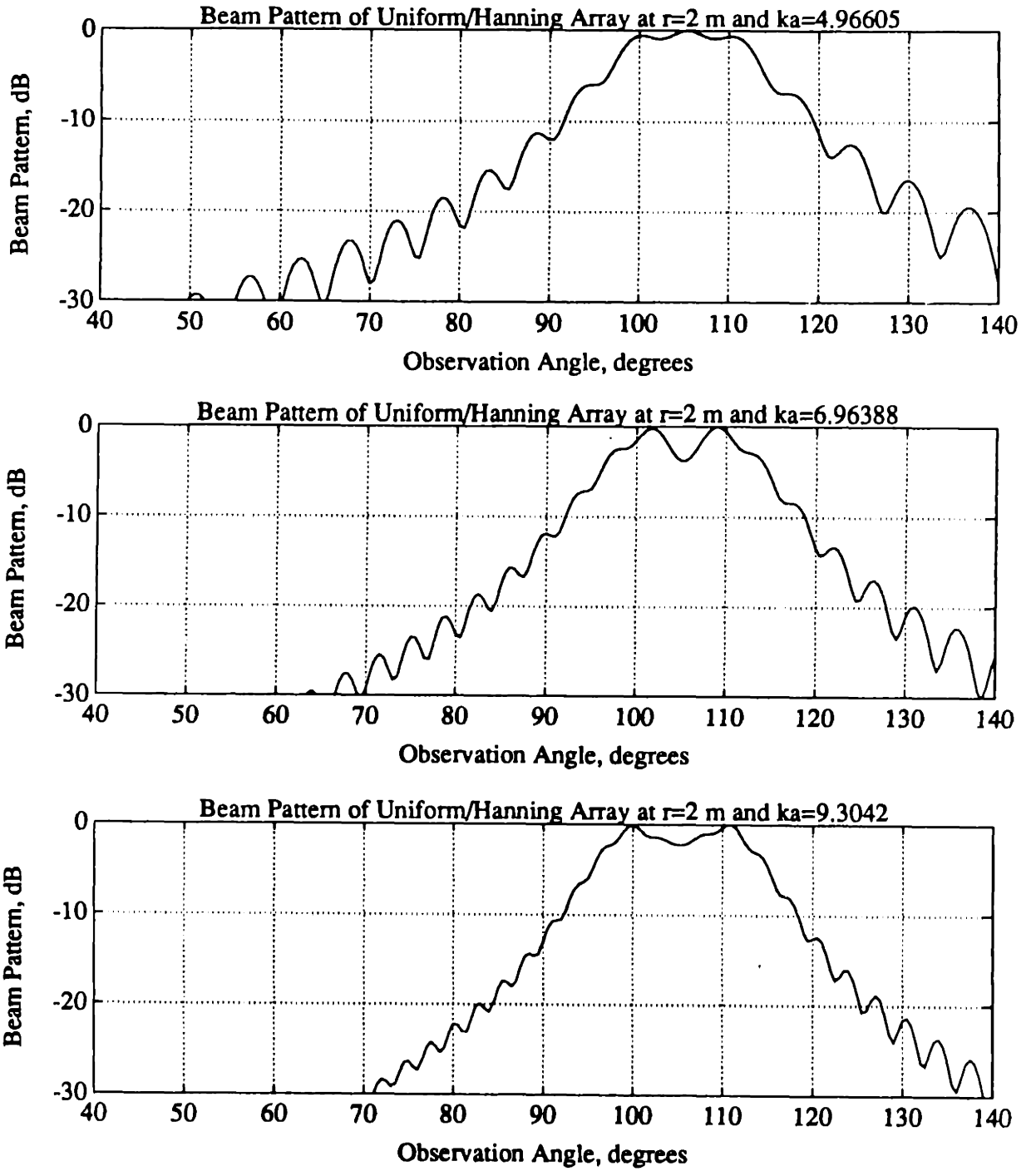

Figure 5.60: Beam Pattern of Discrete Uniform/Hanning Array Steered to θ_o = 105 *deg*. The observation angle $\theta_o = 105$ corresponds to the specular direction, and $\theta_o = 75$ is the back direction. The receivers were all located at a radial distance of $r = 2\ m$ from the target center.

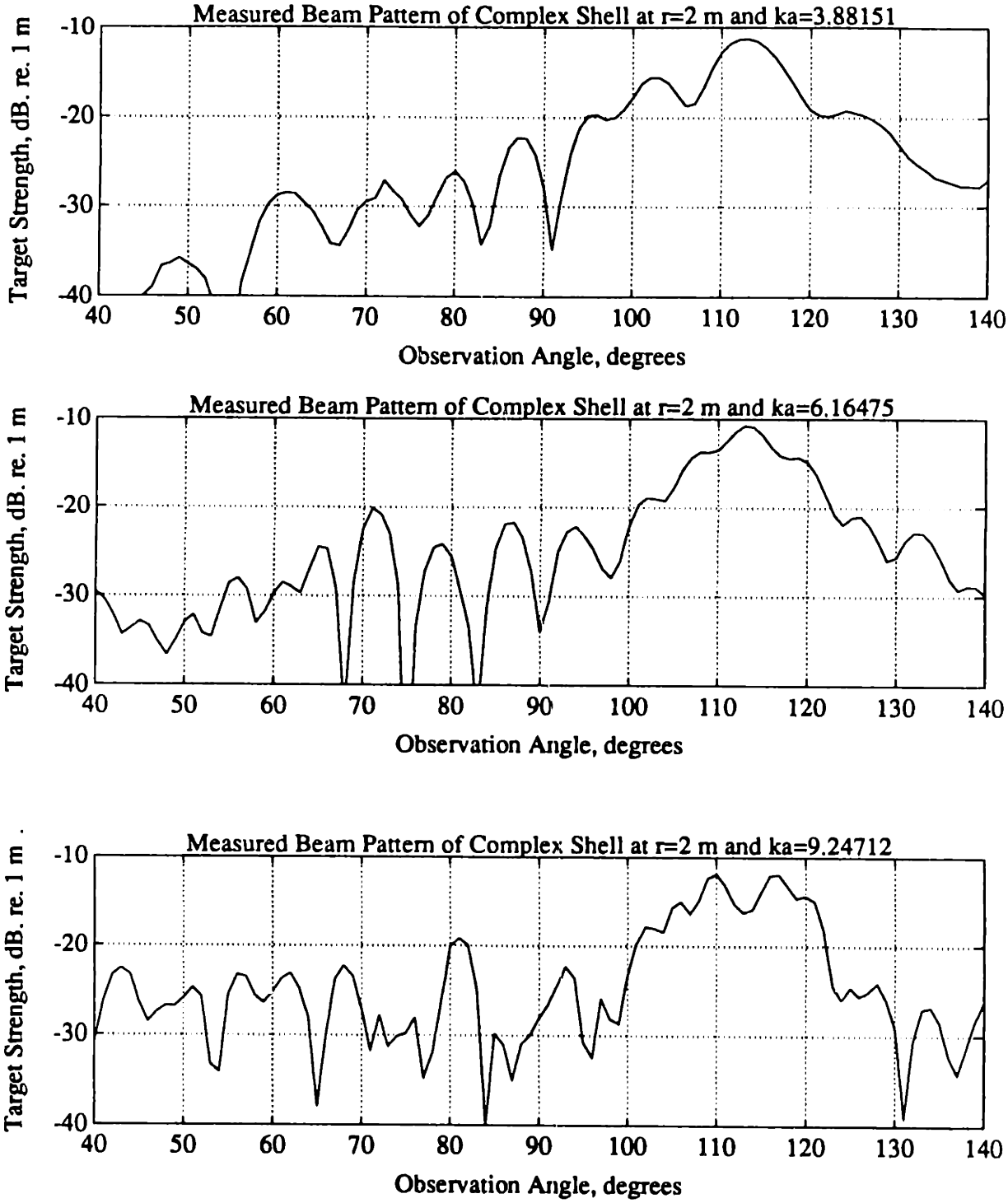

Figure 5.61: Representative Complex Shell Beam Patterns Measured at an Aspect Angle of 66 Degrees and Frequencies of ka = 3.89, 6.15, and 9.24. The observation angle θ_o = 114 corresponds to the specular direction, and θ_o = 66 is the back direction. The receivers were all located at a radial distance of r = 2 m from the target center.

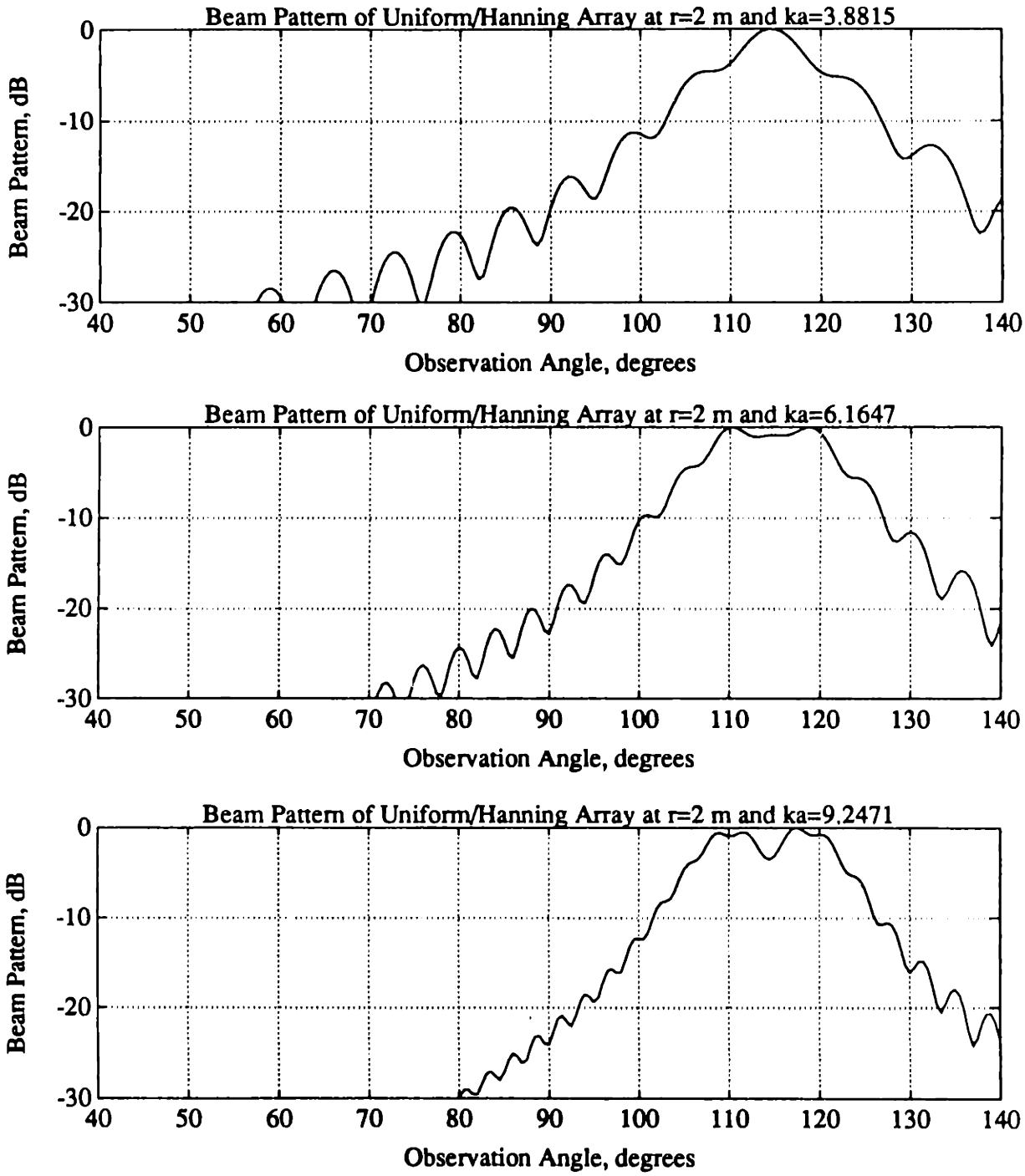

Figure 5.62: Beam Pattern of Discrete Uniform/Hanning Array Steered to θ_o = 114 *deg*. The observation angle $\theta_o = 114$ corresponds to the specular direction, and $\theta_o = 66$ is the back direction of the experiment. The receivers were all located at a radial distance of $r = 2\ m$ from the target center.

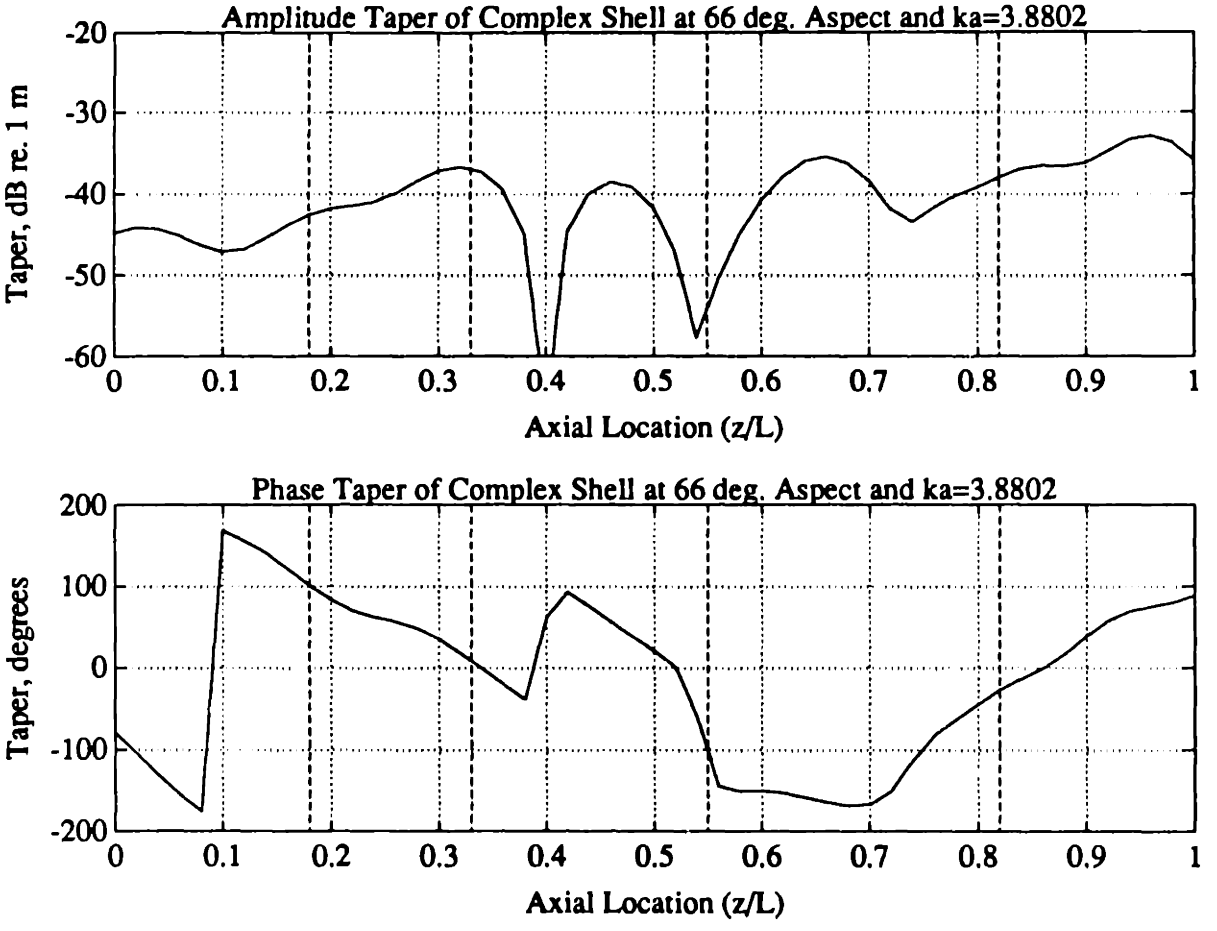

Figure 5.63: Amplitude and Phase Taper of the Complex Shell at an Aspect Angle of 66 degrees. The amplitude taper is shown as a normalized source strength and both are computed from the results of the beamforming operation shown in Figure 5.43. The data are shown for the shear wave coincidence frequency of the empty shell $ka = 3.88$. The dashed lines show the axial locations of the ring stiffeners.

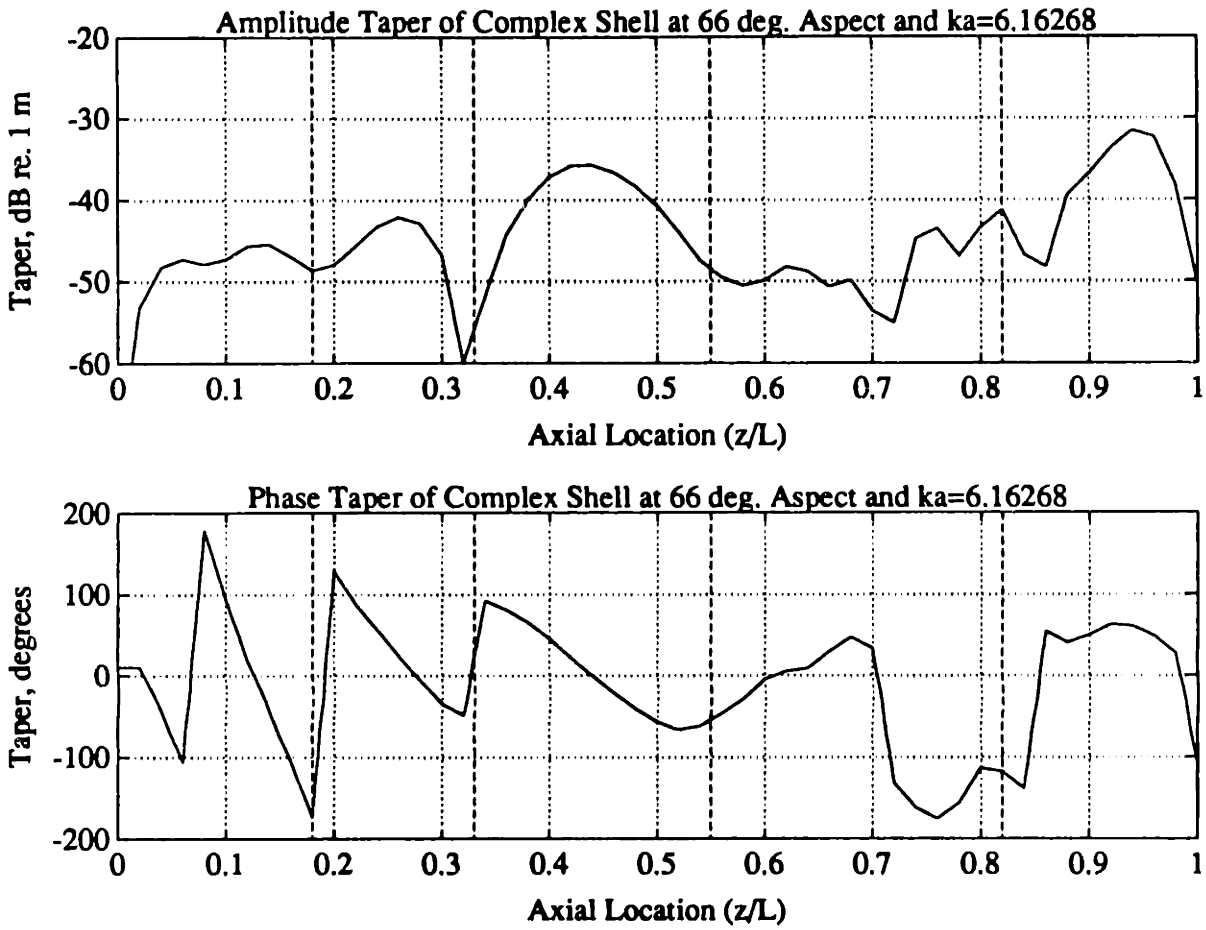

Figure 5.64: Amplitude and Phase Taper of the Complex Shell at an Aspect Angle of 66 degrees. The amplitude taper is shown as a normalized source strength and both are computed from the results of the beamforming operation shown in Figure 5.43. The data are shown for an intermediate frequency of $ka = 6.16$. The dashed lines show the axial locations of the ring stiffeners.

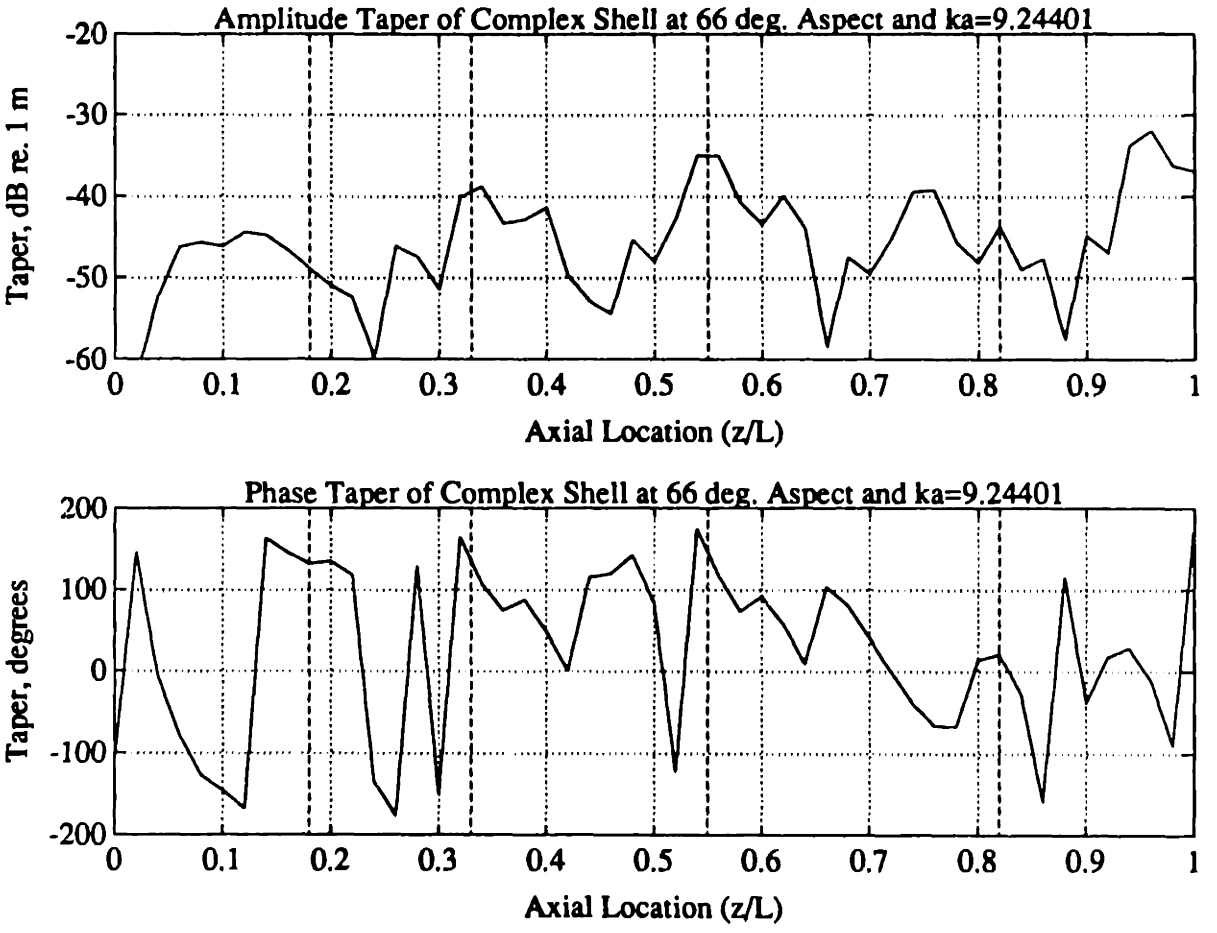

Figure 5.65: Amplitude and Phase Taper of the Complex Shell at an Aspect Angle of 66 degrees. The amplitude taper is shown as a normalized source strength and both are computed from the results of the beamforming operation shown in Figure 5.43. The data are shown for an intermediate frequency of $ka = 9.24$. The dashed lines show the axial locations of the ring stiffeners.

Chapter 6

Conclusion

6.1 Summary and Conclusions

Adapting the Sommerfeld-Watson Transform approach of Rumerman, I have derived an asymptotic formulation of the specularly directed scatter of an infinite cylinder for plane wave insonification at oblique angles of incidence. Membrane wave and geometric scattering processes were found to be the dominant sources of the scattered field over the frequency range of interest, namely $2 < ka < 12$. Given the material properties of the three shells studied, the critical aspect angle for transverse shear wave was found to be $\theta = 61.3$ degrees, while the corresponding angle for compressional wave excitation was found to be $\theta = 73.6$.

I have also examined in detail the monostatic field of the empty shell measured over a range of aspect angles within 30 degrees of beam aspect. Both time and frequency domain representations of the signatures were interpreted. The significant influence of membrane wave backscattering processes was clearly demonstrated over this range of aspect angles. Within 5 degrees of beam aspect, compressional wave excitation and reradiation represents the predominant scatter constituent other than the initial geometric field. Compressional wave scattering produces characteristic nulls in the frequency domain near the harmonics of the ring frequency of the shell.

Away from beam aspect, peak levels of target strength are found at combinations

of frequency and aspect angle where shear wave spatial coincidence and peak length scale effects coexist. Peak levels are not observed at corresponding spatial coincidence frequencies associated with helical compressional wave excitation. I believe that scattering of compressional waves at the slope discontinuity of the stern endcap inhibits the manifestation of back directed radiation at appropriate aspect angles less than 85 degrees. The frequency domain representation of the target strength is modulated with a frequency spacing imposed by axial resonances of the shell and the related delay $\Delta t \simeq 2L\cos\theta/c$ of the back directed leaky wave field. Although the details of the time histories of the monostatic signatures of the empty shell change significantly with changes in aspect angle, peak target strength levels measured away from beam aspect consistently fall within a range of $-20 < T(\omega,\theta) < -15\ dB\ re.\ 1\ m$ with the larger values occurring at lower frequencies. This is consistent with the asymptotic results discussed above.

I have also found that scattering of a structural wave at a mass controlled ring energizes other structural wave types and directly scatters energy to the acoustic medium. Significant scattering from one membrane wave type to another, and to flexural waves is predicted. As a result, the backscatter produced from a shell with a series of rings will be smeared in time and frequency, while scattering to flexural waves has the potential to decrease observed decay rates. Flexural waves are subsonic at this frequency range and do not radiate until they scatter at another ring or similar discontinuity.

I have demonstrated that the influence of the impedance discontinuities imposed by the ring stiffeners is readily evident in the time domain representations of the monostatic signature of the ring stiffened shell. The amplitude of the field initially scattered remains essentially unchanged from that of the empty shell at all aspect angles. However, large amplitude scattered pressures are observed much earlier in the evolution of the scattered field than was observed for the empty shell. The ring stiffeners increased backscattered energy levels by $2-3.5\ dB$ over the range of aspect angles $0 \leq \theta < 63$ degrees.

In contrast, little variation in total backscattered energy levels was observed over the angular regime $63 < \theta < 90$ degrees, although the ring stiffeners and internal loading appear to inhibit or rearrange coincident back radiation. In addition, the ring stiffened shell exhibits backscatter decay rates 2 to 3 times smaller than the empty shell. This decrease appears to be a result of scattering of the supersonic membrane waves to flexural waves at the rings. The decay rates of the internal shell were found to exceed measured values for the ring stiffened shell by a factor of 1.2 - 1.4 which appears to be the result of damping in the resilient material.

Many of the details of the monostatic signature of the ring stiffened shell remain evident in the signature of the complex shell, particularly at times early in the evolution of the field. However, interaction of the internal structures with the surrounding shell induces substantially increased target strength at some discrete combinations of frequency and aspect angle. Spatially averaged target strength values exhibit an apparent increase of $2 - 3$ dB indicating a significant global influence of the internal structures. In addition, the internal structures were also found to increase the initial backscatter at aspect angles $\theta > 30$ degrees. It should be noted, however, that increases of this magnitude were not observed during a set of bistatic measurements conducted at a later date. The origins of this discrepancy remain unresolved. However, the internal structures have altered the response parameters of the ring stiffened shell that supports them. Beamforming analysis of the bistatic field demonstrated that even at beam aspect, interaction between the shell, ring stiffeners, and supported internal loading, produces a field that varies significantly over the length of the shell.

I have also examined the measured bistatic scatter of the complex shell at aspect angles of 66 and 75 degrees. At these angles, a comparison of back and specularly directed scatter demonstrates that aperture effects must be important. The target strength of the scatter observed later in time would be nearly equal in the specular and back directions if axial resonance effects were the sole length-scale process of importance. However, these frequency domain representations are not similar thus

indicating that while resonance effects may be important, aperture effects must significantly influence the observed scatter. In addition, the beampattern produced near the specular direction is well approximated by a uniform line array with hanning amplitude taper at the ends. The beampattern observed near the monostatic receiver exhibits high side lobe levels with little roll off and this is caused by complicated phase and amplitude tapers of the scattering source distribution.

In summary, it has been demonstrated that within 30 degrees of beam aspect, helical membrane waves, and in particular transverse shear waves, serve as a significant means of injecting power into the shell for later reradiation. Depending on the configuration of the shell, the scatter results from a combination of direct phase matched radiation and elastic wave scattering processes induced at the structural discontinuities of the shells.

6.2 Future Work

I made no effort here to use more sophisticated high resolution beamforming techniques such as maximum likelihood methods. The simple classical beamforming employed appears sufficiently adequate to investigate the time evolution of the dominant scattering features found early in the evolution of the field. However, improved techniques would be required to evaluate the low level fields scattered later in time as demonstrated by Mackjovak [38]. In addition, the use of high resolution techniques may provide a feasible method of inferring reflection coefficients and similar parameters that characterize the influence of the structural discontinuities.

I found Wigner distribution analysis of the scattered field measured at oblique angles of incidence to be extremely difficult to interpret and less useful than the work of Yen [65, 66] would suggest. Interpretation of the resulting time-frequency representations was inhibited both by the cross spectra induced by the bilinear transform, and the inherent complexity of the signals themselves. I have presented no Wigner distribution analyses of the signatures of the ring stiffened and complex shells accord-

ingly. However, use of the Wigner distribution may prove more fruitful if applied to the effective source strength $p_{s_z}(z,t)$ associated with a discrete axial location rather than the field measured at a discrete receiver location $p_{s_i}(t)$. The resulting analysis would evaluate the evolution of the field near a stiffener, for example, without the added signal complexity provided by the measurement of the field resulting from the net interference of the axially distributed structural field. Use of the cone-shaped kernal, as developed by Zhao et. al [67], should be investigated as an alternative representation because it inherently inhibits cross spectra resulting from the interference of signal components, while maintaining good time and frequency resolution and finite time support.

Shear wave radiated levels measured with the empty shell insonified at aspect angles ranging from $73 < \theta < 85$ degrees consistently exceeded measured levels associated with compressional wave radiation. As noted earlier, the diminished contribution of the induced compressional wave field appears to result because it is scattered at the endcaps. Analytic and numerical work needs to be performed to better understand the physical origins of this behavior, and in particular, the role of the slope discontinuity of the endcap should be investigated.

To date, no drive point impedance measurements of the empty ring stiffened and internally loaded shells have been conducted. Measurements of this type should be conducted on both shells to identify the resonant frequencies associated with the internal structures and to quantify the increased modal density of the complex shell. It is also essential that measurements of the vibration levels of the internal structures are conducted in the future to better understand their role in the scattering process.

My estimates of scattering at a mass controlled ring demonstrate significant scattering from one membrane wave type to another, and to flexural waves. They also suggest that the rings are highly reflective shell boundaries. However, the elasticity of the rings needs to be addressed. The analyses I present in Chapter 4 can be readily adapted to include these effects. In addition, the fully elastic cylinder model currently under development at M.I.T. should prove to be an effective means

of studying these issues.

Of related interest, nearfield holographic measurements of the ring stiffened and complex shells, although expensive and time consuming, would provide a wealth of useful data that could be used to study the evolution and influence of evanescent waves. Williams [60, 61] has demonstrated the value of this technique for shells of simpler configuration and lower frequencies. Evanescent wave propagation represents a relatively unimportant scattering process of the empty shell when insonified over the range of aspect angles where membrane wave excitation occurs. However, I have found that it must represent an important means of energy transfer between the structural discontinuities of the more complicated shells. In addition, evanescent effects associated with scattering from the empty shell are expected to influence the details of the scattered field observed over the intermediate range of aspect angles of $40 < \theta < 63$ degrees where the initial geometric scatter dominates the monostatic signal.

Finally, transverse shear, or torsional wave scattering processes were found to be of particularly importance within 30 degrees of beam aspect. Dr. Ira Dyer has suggested that the use of concentric cylindrical shells, coupled by a slip or viscoelastic surface, may prove to be an effective means of damping this wave type and reducing its contribution to the scattered field. Detailed analytic and experimental work should be conducted to evaluate the potential attributes of such a design configuration.

Appendix A

Data Acquisition and Signal Processing

A.1 Introduction

The scattering measurements that I have presented in this thesis were all conducted in the facilities located in Building 71 of the U.S. Naval Research Laboratory (NRL) in Washington, D.C.. Monostatic measurements of the empty and unequally spaced ring stiffened shells, NRL model numbers 3600 and 3700, respectively, were performed over the week of 14 July, 1991. Monostatic and bistatic measurements of the complex quadrant symmetric shell (complex), NRL model number 4000, were performed over the week of 10 October, 1991. Bistatic measurements of the empty and complex shell models were also conducted during the months of May and June, 1992. The shells were each insonified at a variety of roll angles as listed in Table A.1 to investigate the potential effects of asymmetries associated with model construction deformations and the internal loading of the complex shell. The roll angle and aspect angle reference conventions I employ are shown in Figure A.1. All of the tests were conducted using broadband pulse insonification of the models with the receiver located at a constant radius of 2 m from the target center. Monostatic measurements were performed at one degree increments of aspect angle while the bistatic

measurements were performed at one degree increments of receiver angle. In both cases, an ensemble of 100 realizations of the scatter was measured for each angle and the results were then averaged and stored. The measurement procedures employed are summarized in Section A.2 and the data acquisition parameters used during each test series are summarized in Tables A.2, A.3, A.4, and A.5. An ensemble measurement of the backscatter of the ring stiffened shell at beam aspect was also conducted with no averaging to evaluate typical statistical properties of the measurements. The resulting statistics and the influence of the clutter subtraction process employed to remove the background field of the tank are evaluated in Section A.3. Finally, the signal processing methods that I have used are summarized in Section A.4.

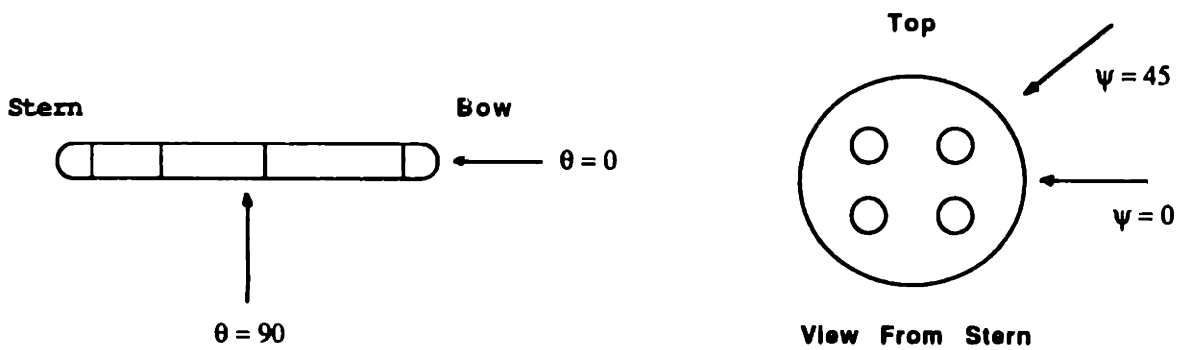

Aspect Angle Convention

Roll Angle Convention

Figure A.1: Roll Angle and Aspect Angle Reference Conventions

Table A.1: **Summary of Tests Performed**

Date	Shell	Measurement Type	Aspect Angle (deg)	Roll Angle (deg)
7/15/91	Empty	Monostatic	0-360	0
7/16/91	Empty	Monostatic	0-180	90
7/16/91	Ring Stiffened	Ensemble	90	0
7/17/91	Ring Stiffened	Monostatic	0-360	0
7/18/91	Ring Stiffened	Monostatic	0-360	45
7/19/91	Ring Stiffened	Monostatic	0-360	90
10/10/91	Complex	Monostatic	0-360	0
10/11/91	Complex	Monostatic	0-360	22.5
10/15/91	Complex	Monostatic	0-360	45
10/16/91	Complex	Bistatic	90	45
5/18/92	Empty	Bistatic	75	0
6/02/92	Complex	Bistatic	66	0
6/03/92	Complex	Bistatic	75	0

Table A.2: **Scattering Measurement Parameters - July 1991**

Receiver Type	Single Hydrophone: B & K 8103
Frequency Range	11.7-50.0 kHz ($2.75 < ka < 11.7$)
Sampling Rate	500 kHz
Analog Filter Cutoff Freq.	A: 3.15/63 kHz B: 0.3/300 kHz
Number of Averages	100
Data Window Length	1820 microseconds
Source Repetition Rate	5 Hz
Target Motion Settling Time	45 seconds
Digitizer	12 Bit
Average Temperature	22.07 ^{o}C

Table A.3: **Scattering Measurement Parameters - October 1991**

Receiver Type	12 Element Vertical Line Array
Frequency Range	11.7-40.0 kHz ($2.75 < ka < 10.0$)
Sampling Rate	500 kHz
Analog Filter Cutoff Freq.	A: 3.15/63 kHz B: 0.3/300 kHz
Number of Averages	100
Data Window Length	2920 microseconds
Source Repetition Rate	5 Hz
Target Motion Settling Time	90 seconds
Receiver Motion Settling Time	45 seconds
Digitizer	12 Bit
Average Temperature	21.81 ^{o}C

Table A.4: **Empty Shell Scattering Measurement Parameters - May 1992**

Receiver Type	12 Element Vertical Line Array
Frequency Range	10.0-42.8 kHz ($2.33 < ka < 10.0$)
Sampling Rate	500 kHz
Analog Filter Cutoff Freq.	A: 10/50 kHz B: 3/100 kHz
Number of Averages	100
Data Window Length	>2580 microseconds
Source Repetition Rate	5 Hz
Receiver Motion Settling Time	45 seconds
Digitizer	10 Bit
Average Temperature	21.57 $^{\circ}C$

Table A.5: **Complex Shell Scattering Measurement Parameters - June 1992**

Receiver Type	12 Element Vertical Line Array
Frequency Range	10.0-42.8 kHz ($2.33 < ka < 10.0$)
Sampling Rate	500 kHz
Analog Filter Cutoff Freq.	A: 10/50 kHz B: 3/100 kHz
Number of Averages	100
Data Window Length	>2420 microseconds
Source Repetition Rate	5 Hz
Receiver Motion Settling Time	45 seconds
Digitizer	12 Bit
Average Temperature	21.54 $^{\circ}C$

A.2 Test Procedure

A.2.1 Test Configuration

The scattering measurements were conducted in NRL's measurement tank as illustrated in Figure A.2. The gross dimensions of the tank and their associated acoustic reflection travel times effectively limit the duration of viable scattering data. The tank is roughly 7.9 x 11.4 m in cross section while its depth is 7.3 m in the region of the target and 6.1 m elsewhere. The target is suspended from an alignment cross at a depth of 3.0 m and is located 2.0 m from the receiver and 2.18 m from the source array. The source, target, and single hydrophone receiver all lie within the same horizontal plane. When a single hydrophone is used to measure the scattered field, the limiting signal duration is imposed by the propagation time required for a ray emanating from the source to reflect off the water surface and travel to the receiver. A single hydrophone of the type used during the July, 1991 measurement series provides no means of adequately rejecting this signal. In addition, the clutter subtraction process discussed in Sections A.2.3 and A.3 becomes ineffective because the reflected source field is too large in amplitude. Given the configuration of the measurement facility, the backscattered signal duration is limited to 1300 microseconds for a shell at beam aspect and 1803 microseconds at bow or stern aspect. The vertically oriented line array receiver used during the October 1991, and the May and June, 1992 measurements provides an effective means of rejecting many reverberant signals originating at the tank surface and bottom and thus extends the duration of viable data at the expense of a reduced frequency range. For these measurements the signal duration is limited to approximately 3000 microseconds by reflections off the tank side walls. Other limits are imposed by different reverberant paths for bistatic measurements away from the backscattering direction.

Prior to testing the models were cleaned and treated with a detergent based wetting solution. The models were then submerged and maintained at test depth for a minimum of 6 hours to provide pressure equalization, and more importantly,

dispersion of air bubbles at the model surfaces. For most of the tests, more than 24 hours of wetting time was employed prior to data acquisition. Each model is suspended from 4 narrow gauge steel wires attached at the endcaps and the alignment cross. A weight is suspended several meters below the target by 4 additional steel wires to provide near neutral buoyancy.

The average water temperatures measured in the tank over the duration of a given measurement series are listed in Tables A.2-A.5. Temperatures measured at a discrete location in the tank were found to vary by less than 0.05 $°C$ over the duration of a given measurement. Given an average temperature of 22.0 $°C$ and the composition of the water found in the tank, a constant sound speed of $c = 1488.5\ m/sec$ has been employed for all analyses.

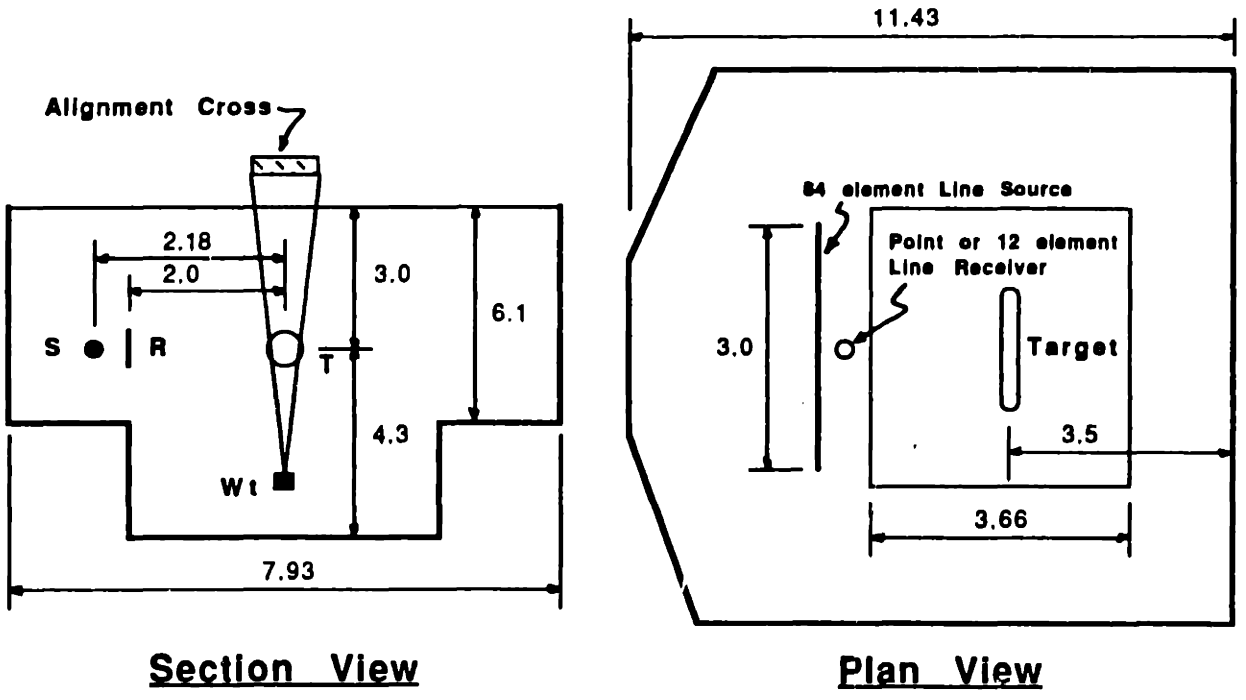

Figure A.2: NRL Building 71 Scattering Measurement Tank

A.2.2 The Source and Incident Field Properties

An 84 element shaded line array [17] was used as a source for all of the tests to provide a cylindrically spreading incident field with near linear phase fronts over the length of the target. The center of the target is located 2.18 m from the center of the source array. The magnitude and phase of the field generated at 30 kHz along a line parallel to the source at the target center location is illustrated in Figure A.5. A suitable waveform, given the impulse response of the source system, is applied to the array to produce a flat spectrum over the desired frequency range.

Before moving the target to the insonification region and conducting target scattering measurements, reference source levels are first measured. The structure supporting the receiver physically prohibits movement to the actual target center location, and therefore, the reference source levels are measured at a location 0.22 m from the target center position (1.96 m from the source). A cylindrical spreading correction is applied to target strength calculations to accommodate this discrepancy as noted in Section A.4.2. The spectral and time domain representations of the reference source signals used during the July test series are shown in Figures A.3 and A.4.

A.2.3 Scattering Data Measurement

Measurement of the scattered field primarily consists of measuring the highly repeatable background field, or 'clutter signal', and the total pressure field produced by insonification of the target. The clutter signal is then numerically subtracted from the raw monostatic or bistatic data to reveal the 'true' scattered field.

Once the wetting period is complete and the reference source level has been measured, the target is temporarily moved to the measurement location for preliminary alignment and to set amplifier gains. Data acquisition is delayed as specified in Tables A.2-5 to allow the incident pulse to pass by the monostatic receiver location before any data is digitized. This delay provides for a better use of the dynamic range of the acquisition system and prevents amplifier saturation. In the case of

bistatic data, data acquisition is delayed by the time required for the source pulse to reach a location near the target center. This delay is selected to allow measurement of the incident field during clutter signal acquisition as needed to properly account for the scattered field component needed to produce the forward scattering shadow region.

The target is then moved back to the corner of tank and the clutter signal is measured and averaged over a 100 shot ensemble. Clutter signal measurements are made over the full range of receiver locations that will comprise the bistatic measurement collection. An example of the time domain representation of the average clutter signal at the monostatic receiver location is shown in Figure A.6 for a measurement of the ring stiffened shell. In Figure A.6, zero time refers to the start of data acquisition with a delay of 980 microseconds after the source is triggered. The large burst of energy shown over the time range of 3100-3500 microseconds is produced by reflections of the incident pulse off the free surface and the tank bottom. If the target was in place, additional target dependent contributions would result in this time range from energy scattered off the shell and subsequently reflecting off the surface back to the receiver. Energy found at other times consists of a highly repeatable field generated by interaction of the source wave field and the tank boundaries. The averaged clutter signal spectrum is shown in Figure A.7 and clearly occupies the band of energy of the source wave field.

Following the completion of the clutter signal measurement, the target is moved to its measurement location for final alignment and scattering data measurement. The ambient noise levels of the tank in the absence of source excitation are first measured and stored. The target is then insonified with the source firing at a rate of 5 Hz and the resulting raw scattering data is averaged over 100 shots and stored. The target or receiver is then rotated to a new position. Data acquisition is commenced again after a delay deemed sufficient to allow target and receiver vibrations to dissipate. Clutter and ambient noise measurements are repeated following the completion of the target insonification measurements. The averaged clutter signal is then numerically

subtracted from the averaged target scattered signal for each aspect or receiver angle to remove the background component of the original scattered signal measurements. Typical time domain representations of monostatic data before and after clutter subtraction are shown in Figure A.8 for the ring stiffened shell at an aspect angle of 75 degrees. The level of clutter reduction is significant, but not perfect as made evident by the non-zero signal levels shown in Figure A.8 over the time duration of $1200 < t < 1600$ microseconds. Details of the effectiveness of the clutter subtraction process and its statistics are discussed in more detail in Section A.3.

Finally, the resulting data is multiplied by a time window to remove the portions of the data where the clutter subtraction process breaks down. Target induced clutter signals and large amplitude tank boundary reflections such as those found near $t = 3100$ microseconds in Figure A.6 cannot be accurately subtracted from the raw scattered field measurement. The 'cleaning' windows used consist of a rectangular portion with Hanning tapering at the ends to provide no discontinuities in amplitude and a high frequency rolloff of 18 dB per octave. The window used for the July measurement series is shown in Figure A.6. The resulting signals measured during the July and October test series were then high pass filtered by NRL with a high order finite impulse filter (FIR) to inhibit presentation of potentially classified low frequency information that is of no interest to my work. The data collected during May and June of 1992 did not require high pass filtering.

A.3 Influence of the Clutter Subtraction Process

Residual signal levels induced by imperfect clutter subtraction, rather than ambient noise, comprises the effective noise floor of the measurements presented here. Example comparisons of the envelopes of the clutter signal and 'true' backscatter signals are shown in Figures A.9 and A.10 for insonification of the ring stiffened at 30 degrees and beam aspect, respectively. The clutter signal itself is of similar magnitude or exceeds the true backscattered signal over much of the signal duration observed

at most aspect angles. Therefore, phase errors induced by temperature and sound speed changes, target or receiver movement, and electronic phase drifts must be kept minimal to ensure accurate measurement of the 'true' scatter signal. Two clutter signals measured 9 hours apart on 18 July, each resulting from the average of 100 individual realizations, have been subtracted from one another to illustrate typical residual levels. The level of clutter signal reduction observed over this lengthy time duration is shown as a function of frequency ka in Figure A.11. An average reduction level of 27 dB was measured over the frequency range of interest. Although smaller levels of reduction are noted at many discrete frequencies, decreased levels of reduction are generally found at frequencies where low level clutter signal levels exist. However, the level of clutter signal reduction generally decreases with increasing frequency. The power spectral density of the resulting residual signal is shown in Figure A.12. The spectrum of the residual signal is dominated by a peak level of -67 dB at 49 kHz where a peak clutter signal level of -53 dB was measured as shown in Figure A.7. The contrasting power spectral density of an averaged measurement of 100 realizations of the ambient noise field is shown in Figure A.14. Peak spectral levels of the residual clutter signal exceed those of the ambient field by 10 dB or more at numerous frequencies.

A plot of the magnitude of the complex envelope of this residual clutter signal is shown in Figure A.13. An effective residual signal level of -30 dB re. 1 Pa is shown in Figure A.13. Improved clutter subtraction results were observed when the time duration separating clutter and scattering measurements was decreased. For example, an effective noise floor of -33 dB can be seen in Figure A.10 where the two measurements shown were separated by approximately 2 hours. However, given the lengthy time durations required to complete a full measurement series (more than 10 hours was typical), I consider a clutter subtraction residual level of -30 dB re. 1 Pa to be a conservative value of the effective noise floor. This corresponds to an effective noise floor of -86 dB for the Gaussian bandlimited impulse response functions shown throughout the thesis.

An ensemble measurement of 100 realizations of the backscatter from the ring stiffened shell was measured at beam aspect to evaluate typical statistical properties of the measurements. The ensemble mean values of the corresponding spectral magnitude $m(\omega) = \langle |P_s(\omega)| \rangle$, as well as the mean values plus or minus the standard deviation of the magnitude $m(\omega) \pm \sigma(\omega)$, are shown in Figure A.15. In this case, I have found the standard deviation of the magnitude to be less than 1 dB re. 1 Pa over the frequency range of insonification. The corresponding standard deviation of the phase, calculated in the absence of the propagation delay, is shown in Figure A.16. The standard deviation of the phase averages 4.9 degrees over the frequency range of interest, while values approach 10 degrees at nulls of the spectrum. These values are consistent with the established noise floor.

A.4 Signal Processing Methods

A.4.1 Spectral Density Estimates

The spectral density estimates that I have presented here were all computed using direct FFT transform techniques as presented by Newland [43], Oppenheim and Schaffer [44], and Kay and Marple [34]. In all cases, the results have been averaged over an ensemble of 100 measurements to limit the variance of the estimates. Consider the discrete Fourier transform of a sequence of N samples of a signal sampled at equispaced time intervals Δt:

$$X(\omega_k) = \Delta t \sum_{n=0}^{N-1} x_n e^{-i2\pi kn/N} \tag{A.1}$$

Spectral analyses of essentially deterministic finite energy waveforms, such as the reference source signal, consisted of computations of the discrete energy spectral density S_{ESD}. I have computed energy spectral density estimates using the relation:

$$S_{ESD}(\omega_k) = |X(\omega_k)|^2 \tag{A.2}$$

Spectral analyses of locally stationary stochastic signals, such as residual clutter and ambient noise measurements, have consisted of computations of the discrete power spectral density S_{PSD}. Power spectral density estimates have been computed using the relation

$$S_{PSD}(\omega_k) = \frac{1}{W_g N \Delta t} |X_w(\omega_k)|^2 \tag{A.3}$$

where X_w is the transform of a windowed time sequence and $W_g = \sum w_n^2/N$ is a correction to provide for a unbiased estimate given the amplitude taper of the window w_n.

A.4.2 Target Strength Calculations

Target Strength relates the acoustic intensity reradiated from the target at a reference radius of 1 m, to the incident intensity at the target as discussed by Dyer [13]. I have calculated the target strength of the three models as a function of frequency and aspect angle $T(\omega, \theta)$ by computing the transfer function of the measured monostatic pressure $P_s(\omega, \theta)$ and the reference source signal $P_{ref}(\omega)$. A cylindrical spreading correction of $+20 \log \sqrt{2.18/1.96} = 0.5$ dB has been employed to ascertain the level of the incident field at the target center, as opposed to the actual reference source measurement location. In addition, a 2 m transmission loss correction of 6 dB was applied to account for spreading losses from the target center to the receiver location.

$$P_s(t, \theta) \xrightarrow{F.T.} P_s(\omega, \theta) \tag{A.4}$$

$$P_{ref}(t, \theta) \xrightarrow{F.T.} P_{ref}(\omega) \tag{A.5}$$

$$T(\omega, \theta) = 20 \log \left[|P_s(\omega, \theta)| \, / \, |P_{ref}(\omega)| \right] + 6.5, \; dB \; re. \; 1 \; m \tag{A.6}$$

I have also performed calculations to evaluate the target strength associated with the time integrated pressures of the scattered and incident fields. The resulting

target strength values $T_{integrated}(\theta)$ represent the ratio of the total energies of the monostatic scatter and the incident source signal. The integration was performed over the time duration of the measurements and was performed numerically using a simple Simpson's rule technique.

$$T_{integrated}(\theta) = 10\log\left[\int P_s^2(t,\theta)\,dt \;/\; \int P_{ref}^2(t)\,dt\right] + 6.5,\ dB\ re.\ 1\ m \qquad (A.7)$$

The target strength associated with the amplitude of initial return from the target was also computed to demonstrate the significance of delayed signal returns.

$$T_{initial}(\theta) = 20\log\left[P_{s_{peak}}(t=0,\theta)/ - P_{ref_{peak}}(t=0)\right] + 6.5,\ dB\ re.\ 1\ m \qquad (A.8)$$

The reference signal level has been multiplied by -1 in equation A.8 to account for the pressure release nature of the initial scatter from the target.

I have also computed the average value of back directed target strength in angular space $T_{savg}(\omega)$ as a function of frequency to provide a simple means of comparing the gross scattering features of the different models. The spatial average was computed over various angular ranges $\theta_1 \leq \theta_2$ and normalized by a constant 4π steradians. The spatial integral was computed from the discrete angular measurements using a simple Simpson's Rule technique. Variations in target strength associated with model roll angle are minimal and were neglected accordingly.

$$T_{savg}(\omega) = 20\log\left[\frac{1}{4\pi r^2\,|P_{ref}(\omega)|}\int_{\theta_1}^{\theta_2} 2\pi r^2\,|P_s(\omega,\theta)|\sin\theta\,d\theta\right] + 6.5,\ dB\ re.\ 1\ m \qquad (A.9)$$

A.4.3 Method of Deconvolution

In many instances, I have deconconvolved the measured source signal from the scattered signals, and then bandpass filtered the results to better interpret their time domain representations. The resulting signal representations do not exhibit the ringing

behavior observed in the source wave form as seen in Figure A.4. These operations were performed numerically following completion of the windowing and high pass filter operations done at NRL.

The scattered pressure measured at a given aspect angle $P_s(t)$ and the reference source signal $P_{ref}(t)$ were first transformed to their frequency domain representations $P_s(\omega)$ and $P_{ref}(\omega)$. In the frequency domain, the deconvolved signal consists of the transfer function defined by the measured scattered spectrum $P_s(\omega)$ divided by the source spectrum $P_{ref}(\omega)$. However, noise dominates the measured spectra outside the band of insonification producing non-physical transfer function levels as well as potential division by zero numerical difficulties. White noise $n(\omega)$, characterized by constant spectral levels, but random phase, was added to the out of band portion of the reference source spectrum to prohibit these numerical problems. This further ensures that the transfer function describes the bandlimited physical processes of interest.

$$\tilde{P}_{ref}(\omega) = P_{ref}(\omega) + n(\omega) \tag{A.10}$$

$$H(\omega) = P_s(\omega)/\tilde{P}_{ref}(\omega) \tag{A.11}$$

The resulting transfer function $H(\omega)$ was then bandpass filtered with a "Gaussian" filter $G(\omega)$, as described in Chapter 1, to attenuate out of band noise, limit ringing associated with the sharp band edges employed, and attenuate levels located near 76 kHz ($ka = 17.8$) where coherent energy is observed in both the scattered and source signals. Moreover, this filter was employed in the infinite cylindrical shell analyses of Chapter 2 to produce a tractable analytic pulse waveform. The bandpass filter used occupies the limiting bandwidth of the different measurement series, i.e. $2.75 < ka < 10.0$. The resulting time domain representations associated with any given data set can be compared with one another. The time domain representation of the resulting bandlimited pulse is shown in Figure 1.6. The mean and standard deviation parameters used to create the filter, such that the 6 dB down points are

located the band edges, are shown in Table A.5.

$$\tilde{H}(\omega) = G(\omega)H(\omega) \tag{A.12}$$

The deconvolved signal $P_{s_{dec}}(t)$ is then computed using an inverse discrete Fourier transform of the transfer function $\tilde{H}(\omega)$.

$$P_{s_{dec}}(\omega) \xrightarrow{I.F.T.} \tilde{H}(t) \tag{A.13}$$

Table A.6: **Bandpass Filter Parameters Used**

Band kHz (ka)	Mean kHz (ka)	Standard Deviation kHz (ka)
11.7 - 42.8 (2.75 - 10.0)	27.3 (6.4)	13.2 (3.1)

A.4.4 Calculation of Signal Envelopes

Signal envelopes have been presented at some aspect angles to evaluate decay rates and the time evolution of signal energy levels. The magnitude of the envelope of a given scattered signal $p_s(t)$ was computed as the magnitude of its complex analytic signal representation $p_{analytic}(t)$ as suggested by Lyon [37]. A complex sequence approximating the analytic signal was generated from the original real sequence using a 255 point FIR filter to approximate the Hilbert transform relation of Oppenheim and Schafer [44] shown below

$$P_{analytic}(\omega) = \begin{cases} 2P_s(\omega), & 0 \leq \omega < \pi, \\ 0, & -\pi \leq \omega < 0 \end{cases} \tag{A.14}$$

The FIR filter was generated using a Hanning window method. The time domain representation of the analytic signal was then computed as the inverse transform

$$p_{analytic}(t) = p_r(t) + ip_i(t) \xleftarrow{I.F.T.} P_{analytic}(\omega) \tag{A.15}$$

The signal envelope $E(t)$ then equals the magnitude of the resulting complex analytic signal as shown below:

$$E(t) = \sqrt{p_r^2(t) + p_i^2(t)} \tag{A.16}$$

The resulting signal envelope $E(t)$ equals the magnitude of the complex envelope $|\tilde{f}(t)|$ of the original signal $p_s(t)$, where $p_s(t) = Re\{\tilde{f}(t)e^{i2\pi f_c t}\}$ [5]. However, it should be noted that the analytic signal representation $p_{analytic}(t)$ does not equal the complex envelope itself, but rather, $p_{analytic}(t) = \tilde{f}(t)e^{i2\pi f_c t}$.

A.4.5 Bistatic Aperture Imaging

I have used classical focused beamforming techniques in various sections of the thesis to steer beams from a selected arc of measured bistatic data and estimate an effective axial distribution of point sources that would produce the scatter measured over the length of the array. Fundamental beamforming techniques of the type used here have been formulated in a variety of references, see for example the work of Dyer [13] and Baggeroer [4, 5]. Following the basic approach of Bondaryk [3] and Duckworth [12], I have employed various synthetic arrays comprised of bistatic sensor locations spaced at 1 degree increments to analyze the spatial and temporal distribution of the measured scatter. The beamforming process is graphically illustrated in Figure A.17.

The beamforming was performed in the frequency domain to take advantage of the speed of FFT algorithms, and to accurately provide the phase taper of the array. The output of the focused beam $P_{ss}(z, \omega)$ was calculated for each discrete frequency and associated fluidborne wavenumber $k = \omega/c$ as shown below in equation A.17.

$$P_{sz}(z,\omega) = \frac{1}{\sum_{j=1}^{n} w_j}\left[w_1 r_1 e^{ikr_1}\ w_2 r_2 e^{ikr_2} \cdots w_n r_n e^{ikr_n}\right]\begin{bmatrix} P_{s_1}(\omega) \\ P_{s_2}(\omega) \\ \vdots \\ P_{s_n}(\omega) \end{bmatrix} \tag{A.17}$$

where P_{s_j} is the pressure measured at sensor j, and w_j is an amplitude taper function applied over the length of the array to limit side lobe levels of the beamforming process. The term r_j is the distance from the axial point of interest on the shell to each individual sensor location. The axial resolution $\Delta z_{3\,dB}$ of the various beamforming operations I present in this thesis are summarized below in Table A.7.

Table A.7: **Axial Resolution of Beamforming Operations**

No. Sensors	Amplitude Taper	$\Delta z_{3\,dB}$ (m)
51	Hamming	0.073
61	Uniform	0.041
69	Uniform	0.037
81	Uniform	0.032

Finally, the source signal was deconvolved from the distribution $P_{sz}(z,\omega)$ using the methods of Section A.4 and inverse transformed to the time domain for further evaluation.

$$P_{sz_{dec}}(z,\omega) \xrightarrow{I.F.T.} P_{sz_{dec}}(z,t) \tag{A.18}$$

The deconvolution and "Gaussian" bandpass filtering process makes the scattering features more readily observable.

A.4.6 The $\tau - p$ Transform

The $\tau - p$ transform is a discretized Radon transform that I have employed to quantify the slowness properties of the axial distribution of the back directed scatter of the

empty shell at an aspect angle of 75 degrees. It was used to transform the space-time data $P_{sz_{dec}}(z,t)$ resulting from the bistatic beamforming operations of Section A.4.5 into apparent slowness-intercept time data $P_{sz_{dec}}(p,\tau)$. Fricke and Baggeroer [24] made similar use of the $\tau - p$ transform to elicit the modal structure excited by transient broadband insonification of elastic plates and discuss its use in detail. The $\tau - p$ transform effectively steers the linear array about a designated pivot point z_o and sums the results along the length of the array providing a slant stack of the data. The $\tau - p$ transform of a signal $s(z,t)$ is defined by the equation:

$$\tilde{s}(\tau,p) = \sum_{j=1}^{n} s(z_j, \tau + pz_j) \tag{A.19}$$

where $s(z_j,t)$ corresponds to a time trace measured at the discrete location z_j. A z-coordinate system was chosen such that the origin is located at the center of the array, i.e. the center of the shell. The axial slowness parameter $p = 1/c_z$ quantifies the apparent phase speed along the axis while the parameter τ quantifies the intercept time at the origin.

The computation of the transform was done in the frequency domain to take advantage of the efficiency of the Fast Fourier Transform. The effective delay of the stacking operation can be expressed as a simple modulated transform in the frequency domain yielding:

$$s(z_j, \tau + pz_j) \xrightarrow{\mathcal{F}.\mathcal{T}.} S(z_j,\omega)e^{i\omega pz_j} \tag{A.20}$$

The $\tau - p$ transform at a given slowness value p can then be expressed as the inverse transform of the resulting frequency domain representation

$$\tilde{s}(\tau,p) \xleftarrow{\mathcal{I}.\mathcal{F}.\mathcal{T}.} \sum_{j=1}^{n} S(z_j,\omega)e^{i\omega pz_j} \tag{A.21}$$

Aliasing criteria associated with the use of the discretized form of the Radon transform have been evaluated by Turner [53]. The required slowness sampling in-

terval is defined by the relation $\Delta p < 1/Lf_{max}$ while the sampling interval must obey $\Delta z < 1/2p_{max}f_{max}$, where L is the total length of the array (0.86 m), f_{max} is the largest frequency of appreciable signal energy (50 kHz), and p_{max} is the largest slowness of interest. I employed sampling intervals of $\Delta z = 0.0172\ m$ and $\Delta p = 0.004\ sec/km$, accordingly. In addition, the array was amplitude tapered using a Hamming window function to limit side lobe leakage affects associated with the beamforming operation.

Use of the inverse $\tau - p$ transform was not employed here and its implementation is well documented by Fricke [24] and Turner [53].

A.4.7 Wigner Distribution Analysis

I have also made use of Wigner distribution (WD) analysis to provide a high resolution time-frequency representation of the empty shell backscatter that was measured at an aspect angle of 75 degrees. The properties and implementation of continuous and discrete time Wigner distribution analysis have been studied in detail by Claasen and Mecklenbrauker [7, 8, 9]. The auto-Wigner distribution of a continuous time representation of a signal is defined by the following bilinear transformation:

$$W(t,\omega) = \int_{-\infty}^{\infty} e^{-i\omega\tau} f(t+\tau/2) f^*(t-\tau/2) d\tau \qquad \text{(A.22)}$$

Given this formal definition, the WD of a chirp signal $f(t) = Ae^{i\alpha t^2}$ with instantaneous frequency $\omega(t) = \alpha t$ equals:

$$W_{chirp}(t,\omega) = |A|^2 2\pi\delta(\omega - \alpha t) \qquad \text{(A.23)}$$

The Wigner distribution of a chirp function is non-zero only at the instantaneous frequency of the signal thus demonstrating an instance where use of the transformation is attractive. Claasen and Mecklenbrauker further demonstrate that the first order moment, or average frequency of the distribution at a fixed time coincides with the instantaneous frequency of the signal while integration over the frequency yields the

instantaneous power. They also demonstrate that the average time at a fixed frequency equals the group delay and integration over time yield the energy density at the selected frequency. However, the bilinear nature of the transformation inherently provides several significant disadvantages. The Wigner distribution of a sum two signals does not equal the sum of the Wigner distributions of the individual signals. Furthermore, the distribution is not semi-positive definite. These disadvantages are clearly demonstrated by the WD of a simple sinusoidal signal $f(t) = \cos(\omega_o t)$ as shown below:

$$W_{sinusoid}(t,\omega) = |A|^2 \frac{\pi}{2} [\delta(\omega + \omega_o) + \delta(\omega - \omega_o) + 2\delta(\omega)\cos(2\omega_o t)] \qquad (A.24)$$

The additional contributions, or cross spectra found at $\omega = 0$ are manifestations of the bilinear transformation. The cross spectra resulting from interference among the constituents of a signal can be inhibited with the use of smoothing window function with an associated loss of resolution. However, because the WD is not positive semi-definite, it does not directly evaluate signal energy levels. In contrast to a spectrogram, the WD can only be used to provide rough insight into how signal energy is distributed in time and frequency.

The discrete version of the WD of a sampled signal $x(n)$ of a finite duration of $N\Delta t$ has been implemented as follows:

$$W(n\Delta t, k\Delta\Omega) = 2\Delta t \sum_{m=0}^{N-1} x(n+m)x^*(n-m)e^{-i2\pi mk/N} \qquad (A.25)$$

As demonstrated by Claasen and Mecklenbrauker [8], this discrete time implementation is periodic in frequency ω with period π. Therefore, the frequency samples of the continuous signal are found at $\Delta\Omega = \pi/(N\Delta t)$. Moreover, in order to prevent frequency aliasing, the signal must not have any significant energy content at frequencies above one quarter of the sampling frequency. This is a more restrictive requirement than the Nyquist sampling criteria associated with simple discrete

Fourier transforms. However, aliasing was not a restrictive issue for the WD analyses presented here because all the data acquired was oversampled by a factor of at least 4.5.

The resulting discrete time WD results were smoothed by convolving the WD with a truncated two dimensional Gaussian window function as shown below:

$$\tilde{W}(n,k) = \sum_{m=n-2\sigma_t}^{n+2\sigma_t} \sum_{j=k-2\sigma_\omega}^{k+2\sigma_\omega} W(j,k) e^{-\frac{1}{2}[(m-n)^2/\sigma_t^2 + (j-k)^2/\sigma_\omega^2]} \qquad \text{(A.26)}$$

This smoothing technique was implemented by Wahl and Bolton [58]. I selected this technique because it provides varying levels of inhibition of the cross term amplitudes while readily providing independent control of time and frequency resolutions through the use of the discrete parameters σ_t and σ_ω. Finally, the smoothed WD $\tilde{W}$ was normalized by its peak value for plotting purposes.

Yen [65, 66] successfully employed a discrete time version of the WD to evaluate the scattered signals of spherical shells and solids, and simple cylindrical shell and solids at bow aspect. However, I found that implementation of the WD for the more complicated scattered pressure signals studied here produced results that were extremely difficult to evaluate and interpret. These difficulties were primarily induced by increased number of cross spectra and the fundamental complexity of the signals themselves. The scattered pressure signals generated by the ring stiffened and complex shells, in particular, were difficult to interpret. Therefore, I have only presented the results corresponding to the empty shell data measured at 75 degrees.

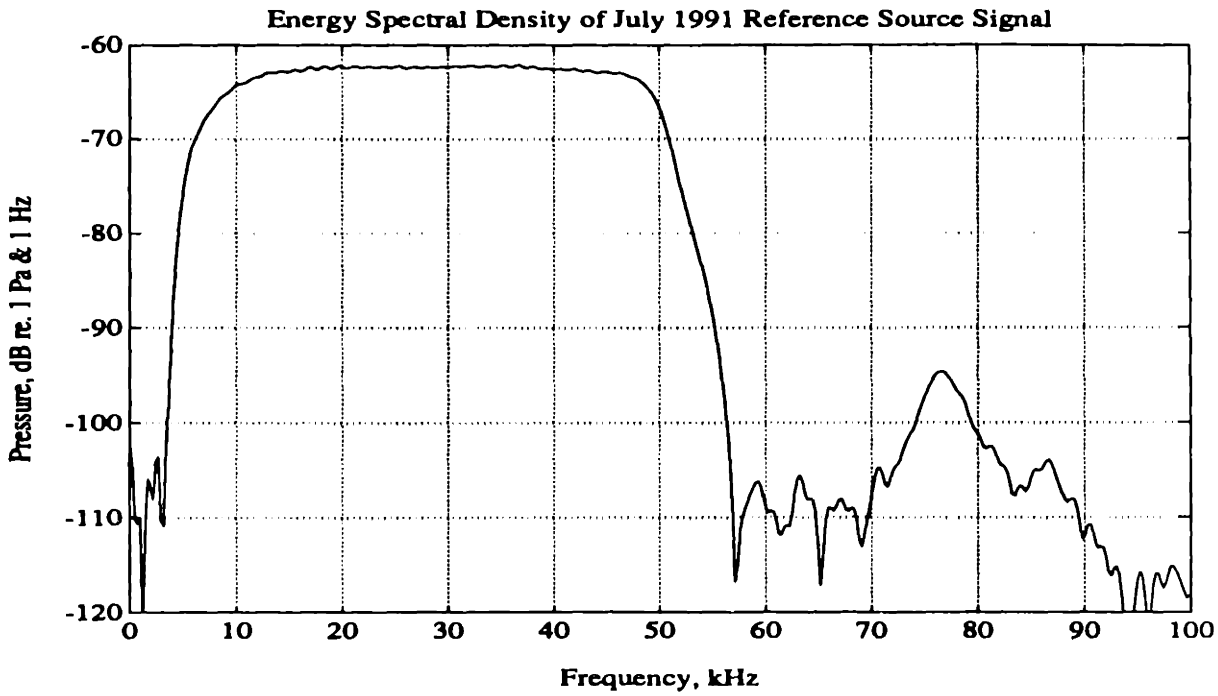

Figure A.3: Energy Spectral Density of the Reference Source Signal used for July 1991 Measurements. Data measured 1.96 m from the source array.

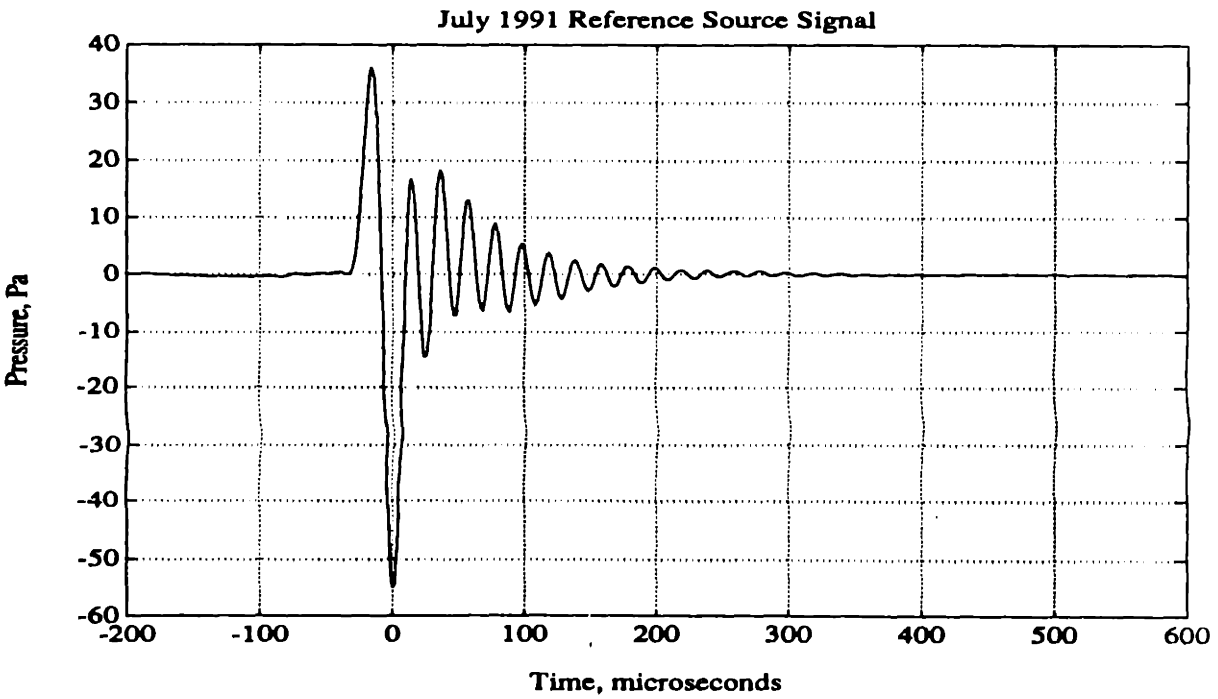

Figure A.4: Measured Reference Source Signal of the July 1991 Measurements. Data measured 1.96 m from the source array.

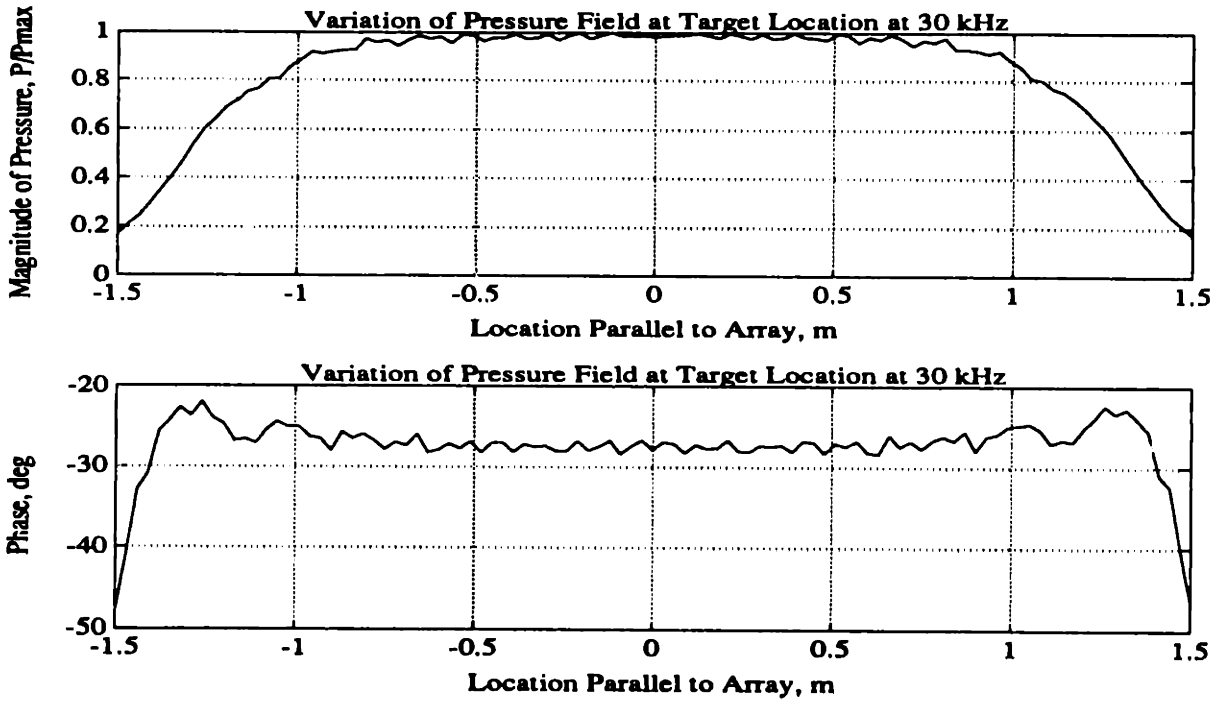

Figure A.5: Variation of the Source Pressure Field Generated at 30 kHz Along a Line Parallel to the Source at the Target Center. Target Center at $x = 0$.

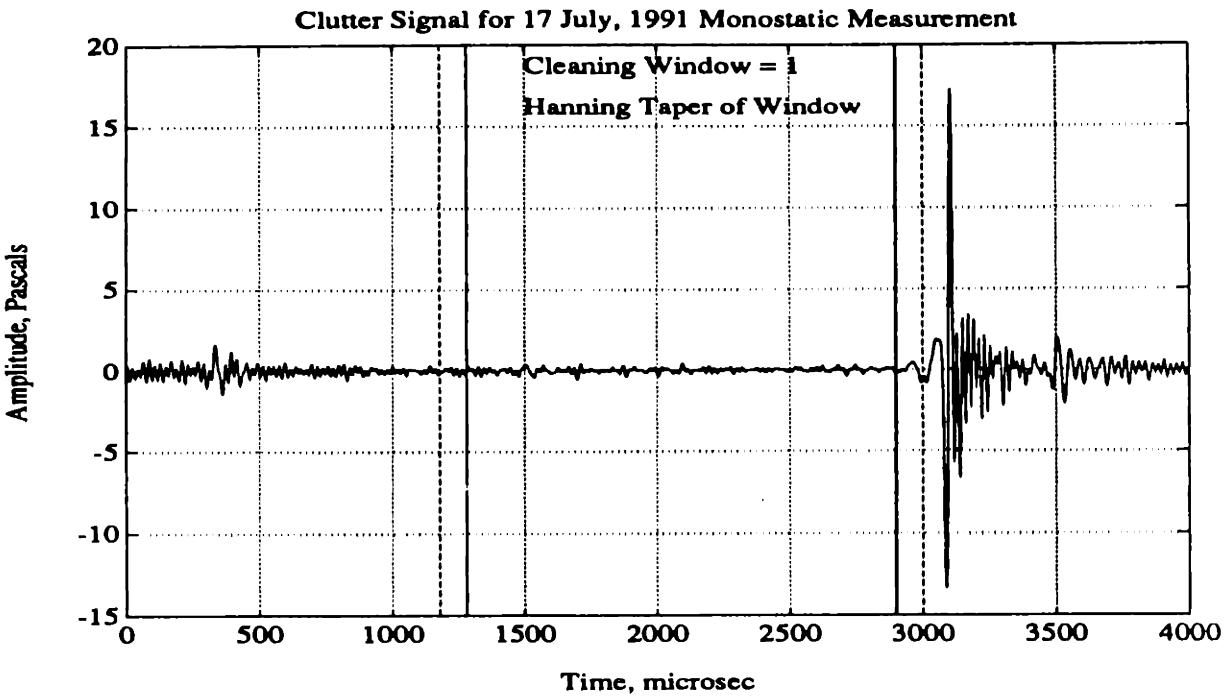

Figure A.6: Measured Average Clutter Signal of 17 April, 1991, 100 averages, $t = 0$ Corresponds to start of data acquisition $980\mu sec$ after source onset

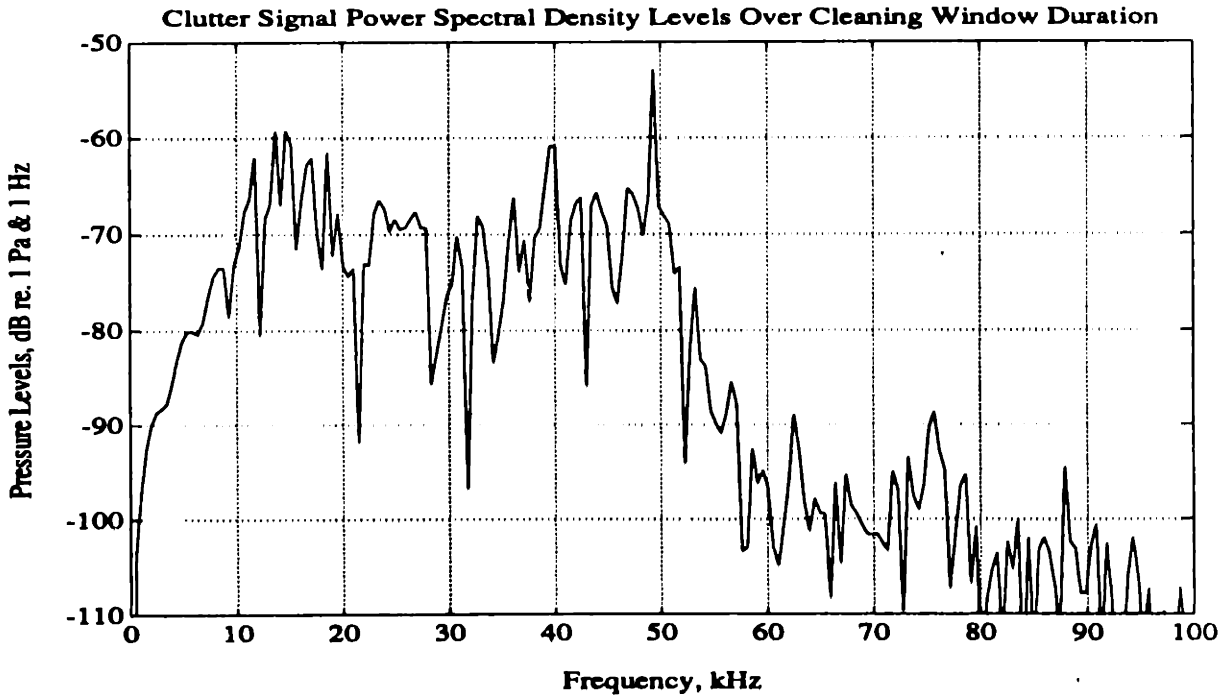

Figure A.7: Clutter Signal Power Spectral Density Measured Over the Cleaning Window Duration on 17 April, 1991 , 100 averages

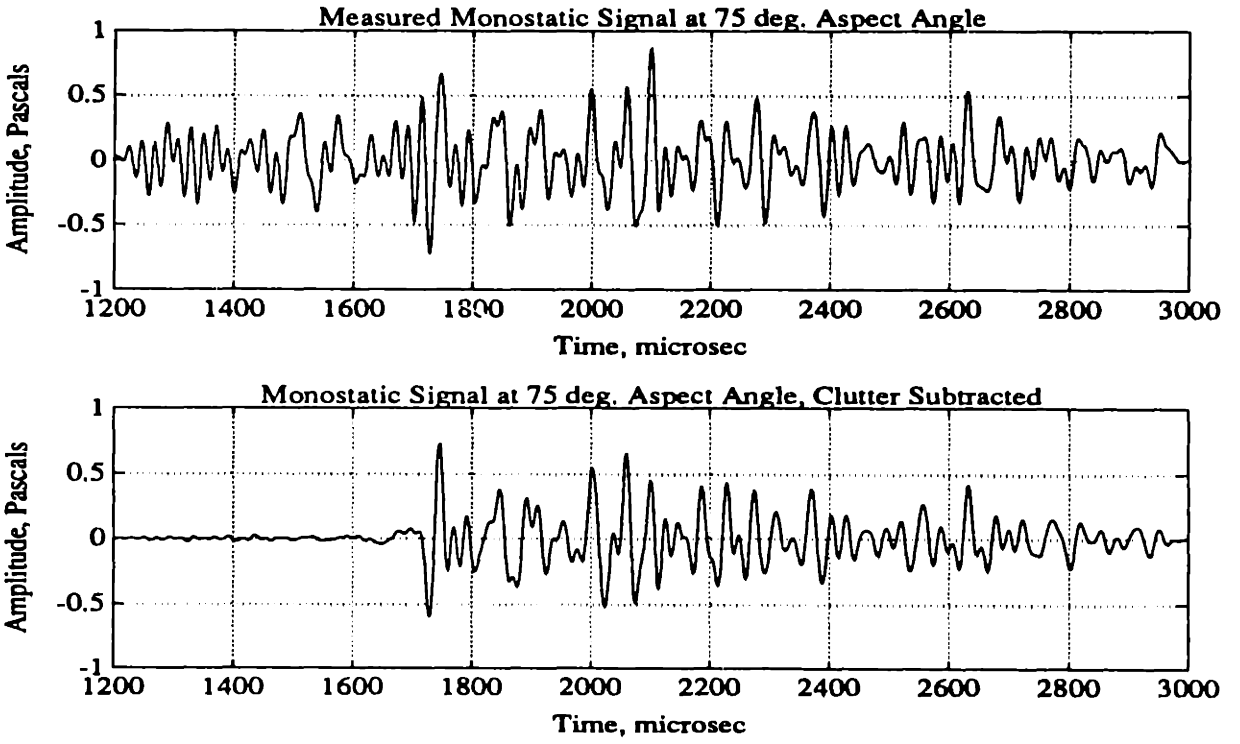

Figure A.8: Typical Clutter Subtraction Process Results, Unequally Spaced Ring Stiffened Shell at 75 degree Aspect Angle, $t = 0$ Corresponds to start of data acquisition

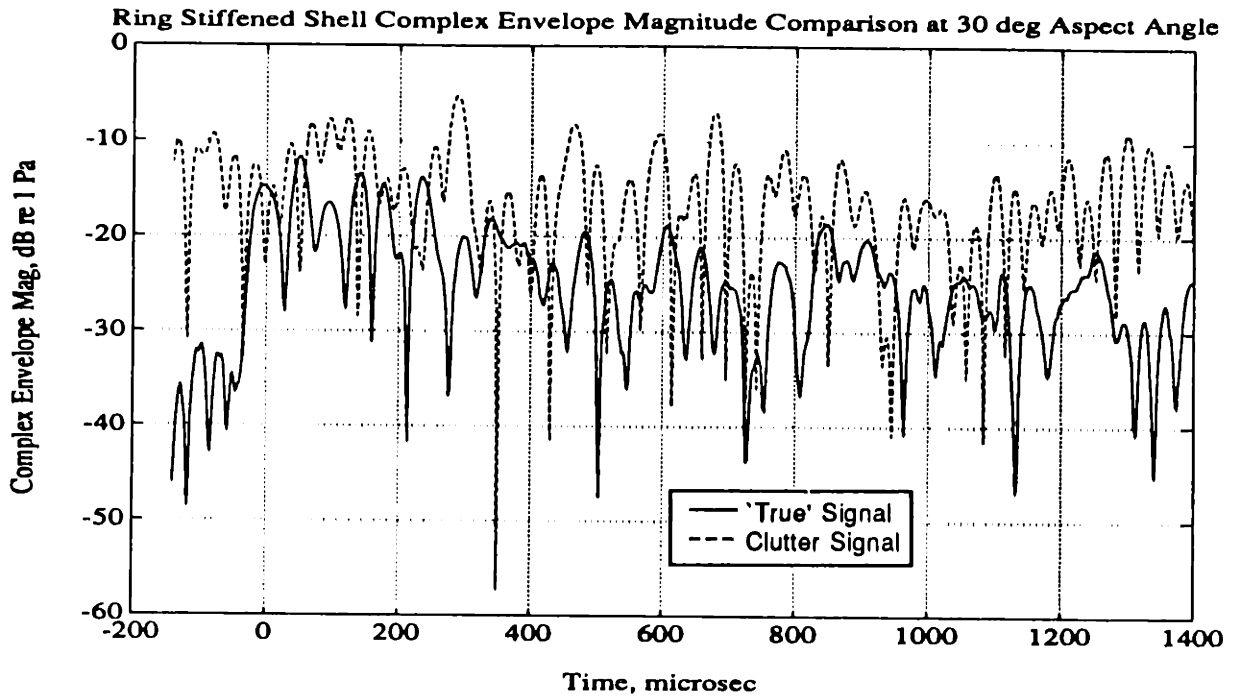

Figure A.9: Comparison of 'True' Backscattered Signal ($r = 2\ m$) and Clutter Signal Envelopes, Unequally Spaced Ring Stiffened Shell at 30 degree Aspect Angle. $t = 0$ Corresponds to time of initial scattered return

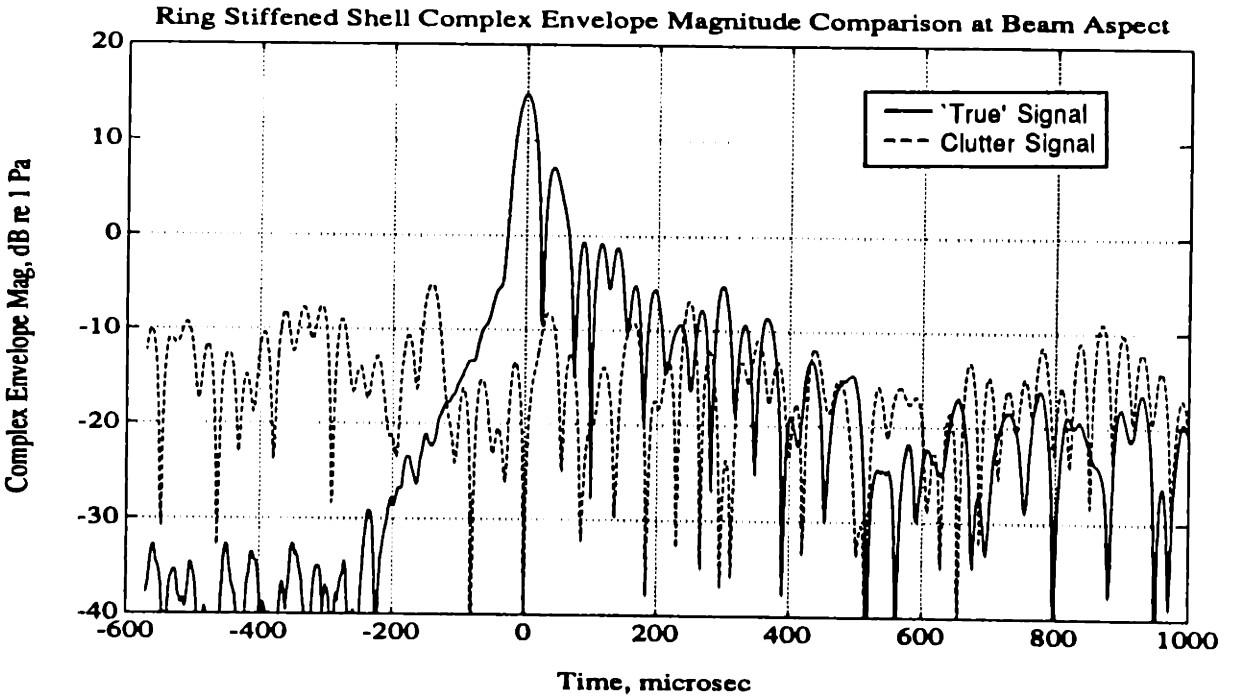

Figure A.10: Comparison of 'True' Backscattered Signal ($r = 2\ m$) and Clutter Signal Envelopes, Unequally Spaced Ring Stiffened Shell at Beam Aspect. $t = 0$ Corresponds to time of initial scattered return

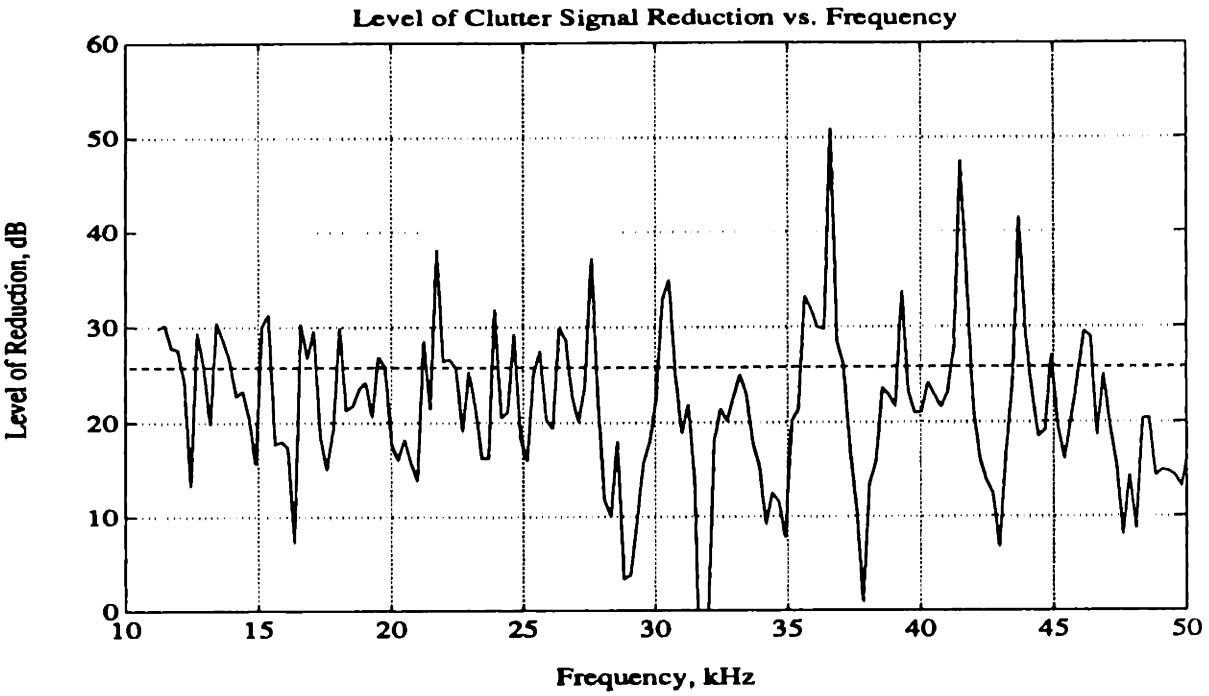

Figure A.11: Typical Levels of Clutter Signal Reduction, Results obtained from the subtraction of 2 averaged clutter measurements taken 9 hours apart on 18 July, 1991, 100 averages.

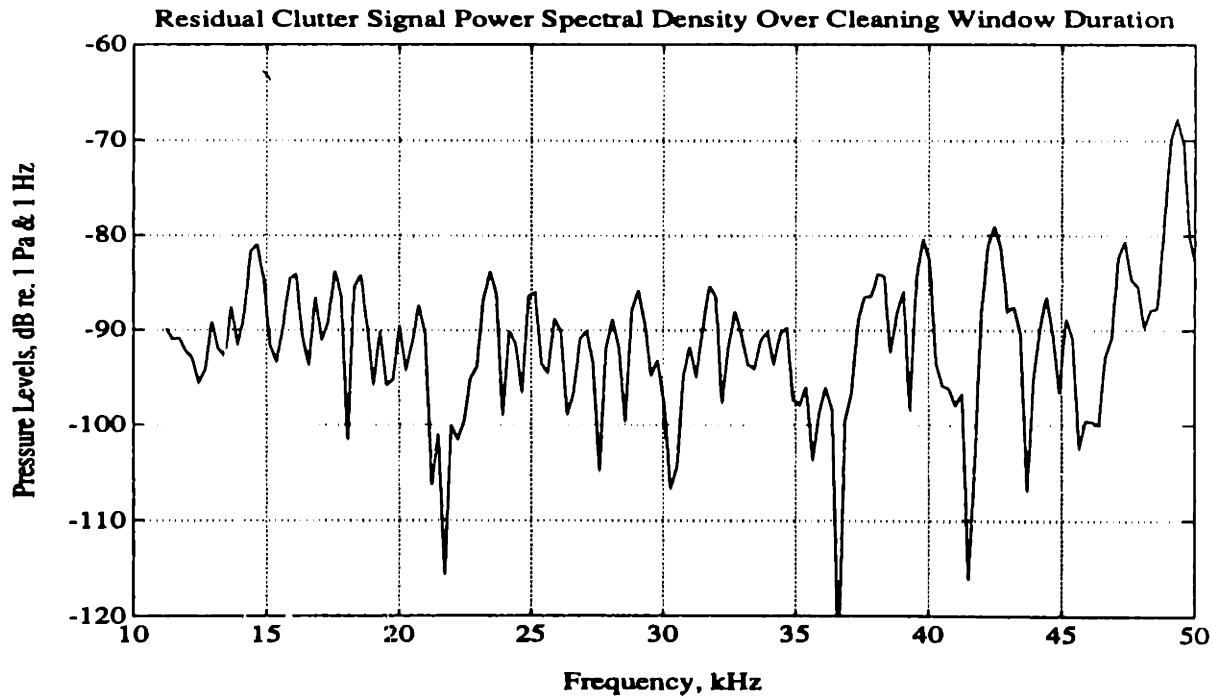

Figure A.12: Typical Residual Clutter Signal Power Spectral Density, Results obtained from the subtraction of 2 averaged clutter measurements taken 9 hours apart on 18 July, 1991, 100 averages.

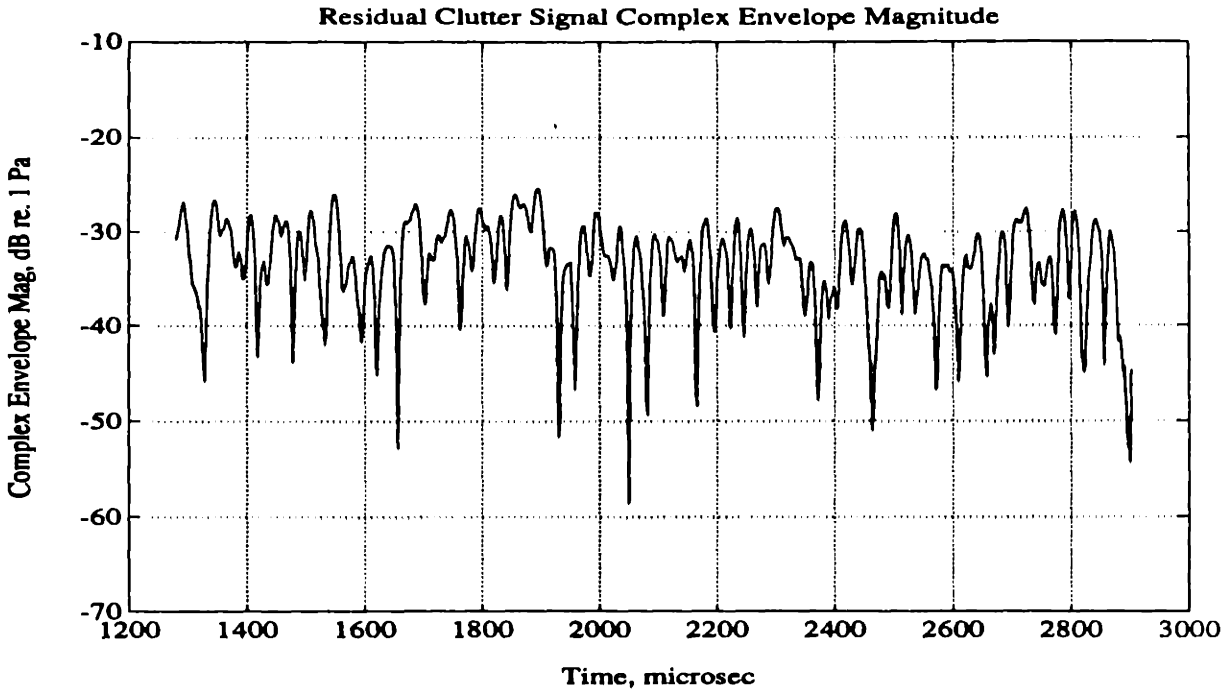

Figure A.13: Typical Residual Clutter Signal Envelope Magnitude. Results obtained from the subtraction of 2 averaged clutter measurements taken 8 hours apart on 18 July, 1991. $t = 0$ Corresponds to the start of data acquisition.

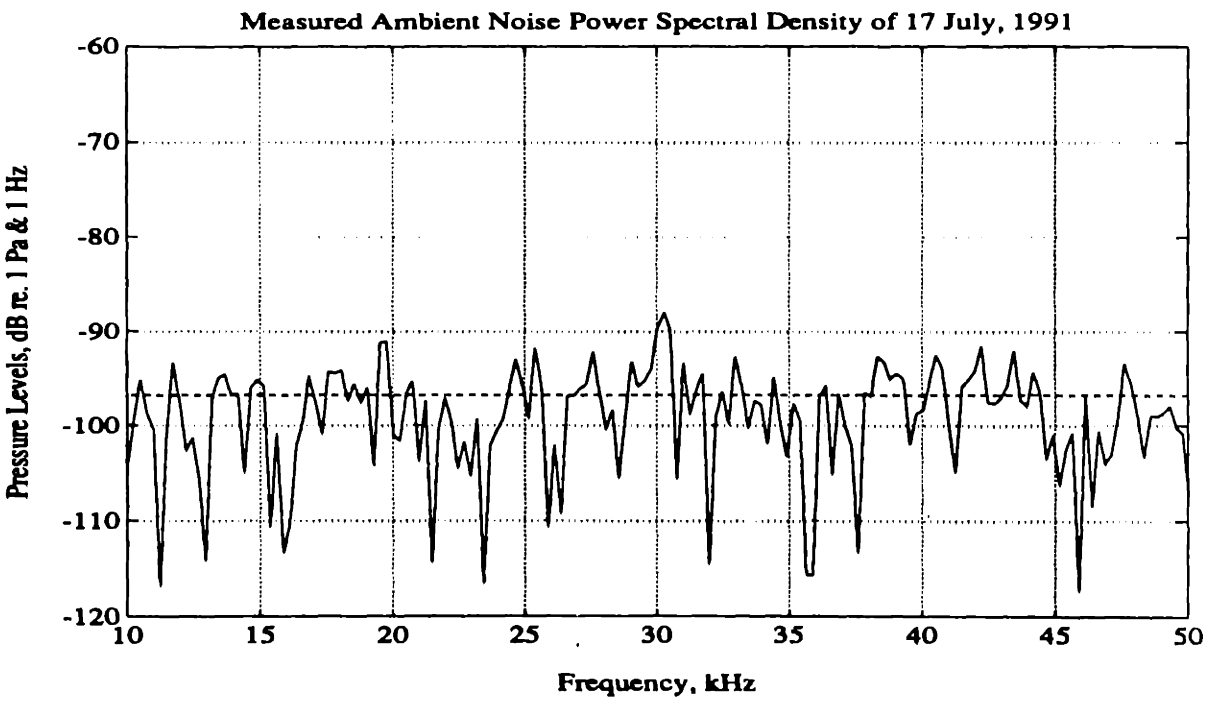

Figure A.14: Ambient Noise Power Spectral Density Measured on 17 July, 1991, 100 Averages

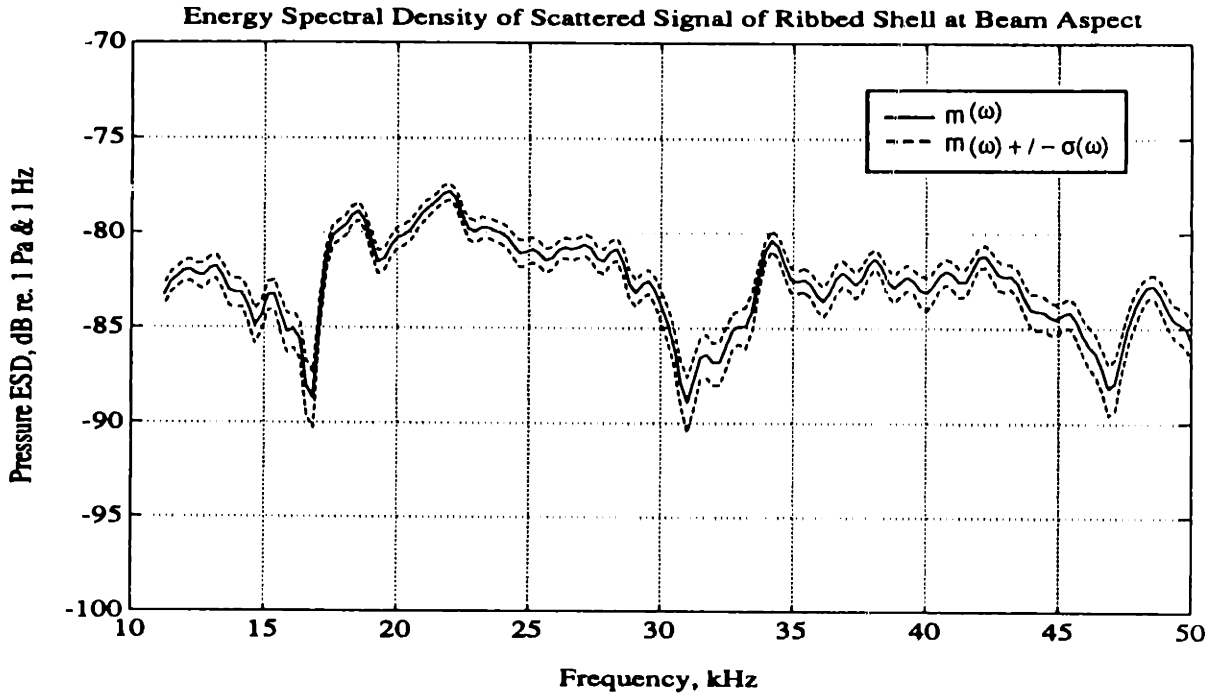

Figure A.15: Statistical Properties of the Spectral Magnitude of 100 Shot Ensemble Measurement of the Unequally Spaced Ring Stiffened Shell at Beam Aspect

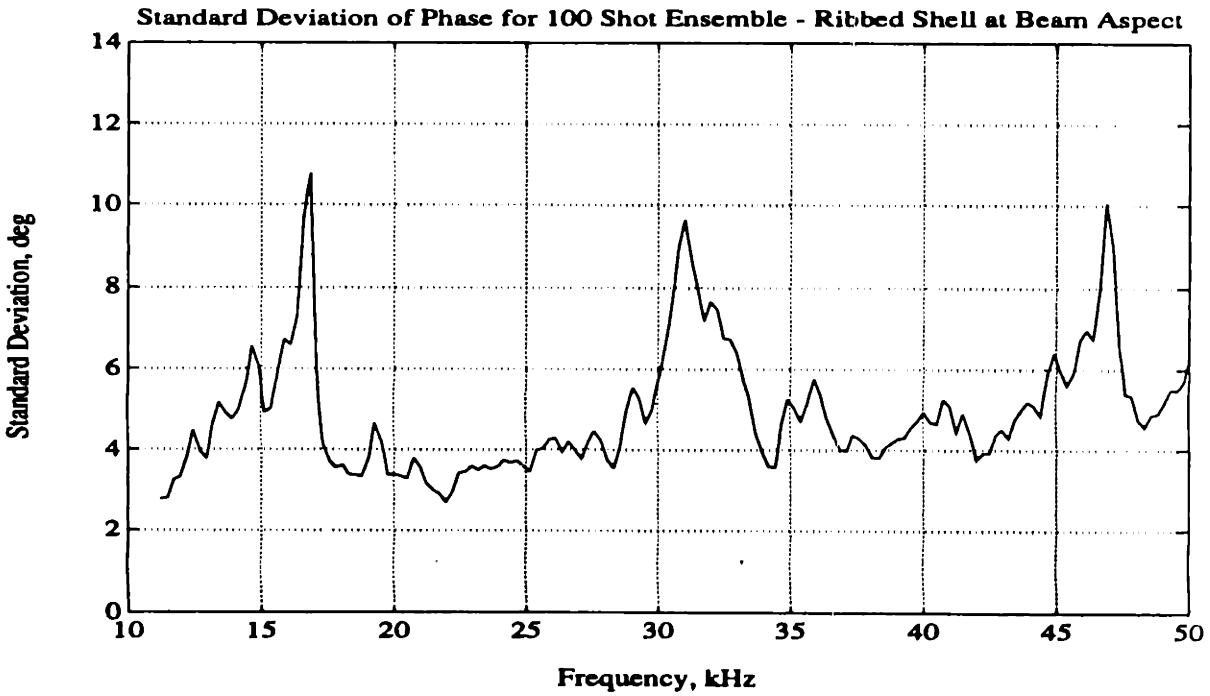

Figure A.16: Standard Deviation of the Phase (2 m Propagation Delay Removed) of a 100 Shot Ensemble Measurement of the Unequally Spaced Ring Stiffened Shell at Beam Aspect

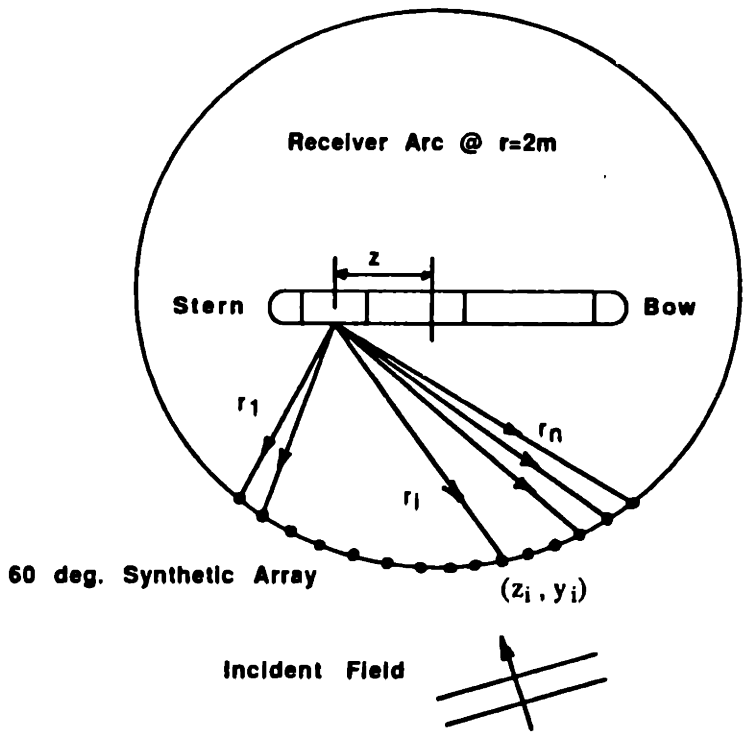

Figure A.17: Illustration of Classical Beamforming of Bistatic Data for Analysis of the Complex Shell at an Aspect Angle of 75 degrees

Appendix B

Generation of Membrane Wave Caustics at the Endcaps

The membrane wave helices generated on the shell by an incident plane wave at oblique incidence encounter caustics on either the conical or hemispherical surfaces of the the endcaps. The caustics separate the propagating region of the induced membrane wave field from an evanescent region. A caustic occurs at an axial position where the helix angle of a propagating wave equals the value $\psi = \pi/2$, i.e. $k_{az} = 0$, and the wave begins to propagate in the opposite axial direction. The wavenumber k_{az} is axially orientated, but located in a plane tangent to the surface of the cone. Consider a membrane wave traveling along an axially varying helix on a right circular cone as shown in Figure B.1. A membrane wave traveling on the cylinder encounters the cone of the endcap with an azimuthal field dependence v and a helix angle ψ_{cyl} that is prescribed by the aspect angle of the incident field and the wave speed c_m according to equation 2.56. At high frequencies, membrane wave waves essentially remain dispersionless on the conical and spherical surfaces of the endcaps and their wave speeds c_m can be approximated using the constant values listed in Tables 1.1 and 2.1. I want to stress that this is a high frequency approximation that is not appropriate for the frequencies of interest here. For the frequencies of interest, membrane waves do experience significant dispersion on the

conical sections of the endcap as demonstrated by Guo [28]. In addition, dispersive effects are expected on the hemispherical sections of the shell as demonstrated for the first symmetric Lamb mode on a spherical shell by Kargl and Marston [33]. However, I present this approximation here to simply demonstrate the processes governing the formation of caustics. This simple analysis does not preclude mode conversion or reflection of the incident structural wave components at the endcap.

The azimuthal field dependence v is a constant value over the entire length of the model as required to meet continuity conditions (Snell's Law). However, the azimuthal wavenumber component k_ϕ of the propagating wave changes as the radius of the cone changes

$$k_\phi(z) = v/r(z) \tag{B.1}$$

Therefore, the helix angle ψ_{cone} of the wave changes as it propagates down the longitudinal axis of the cone as required to maintain a fixed wavenumber k_m and a fixed azimuthal dependence v.

$$k_m^2 = k_{az}(z)^2 + k_\phi(z)^2 \tag{B.2}$$

$$v \;=\; a\, k_{\phi_1} \;=\; r(z)\, k_\phi(z) \tag{B.3}$$

$$\cos\psi_{cone}(z) \;=\; \frac{k_{az}(z)}{k_m} \;=\; \sqrt{1 - \frac{k_{\phi_1}^2}{k_m^2}\frac{a^2}{r(z)^2}} \tag{B.4}$$

where the azimuthal wavenumber component of the wave on the cylinder is $k_{\phi_1} = v/a$. The helix angle ψ_{cone} at an axial location z on the cone can be further related to the the helix angle of the wave on the cylinder ψ_{cyl} using the following relations:

$$k_{\phi_1} = k_m \sin\psi_{cyl} \tag{B.5}$$

$$\psi_{cone}(z) = \cos^{-1}\sqrt{1 - (a^2/r(z)^2)\,\sin^2\psi_{cyl}} \tag{B.6}$$

Finally, the axial location of the caustic on a right circular cone can be shown to be

$$z_c = l_{cone} \frac{1 - \sin \psi_{cyl}}{1 - b/a} \tag{B.7}$$

where b is the radius of the cone at the junction with the hemisphere, and l_{cone} is its overall length.

If the required location z_c exceeds the length of the cone, $\sin \psi_{cyl} < b/a$, the caustic occurs on the hemispherical surfaces of the endcap. The phase fronts then follow a great circle path on the hemisphere and the caustic is located at the axial location

$$\begin{aligned} z_c &= l_{cone} + b \cos \psi_{cone}(z = l_{cone}) \\ &= l_{cone} + b \sqrt{1 - (a^2/b^2) \sin^2 \psi_{cyl}} \end{aligned} \tag{B.8}$$

The caustic associated with a given membrane wave type is located at the end of the shell $z_c = l_{cone} + b$ when the aspect angle of the incident field equals the critical angle θ_c listed in Table 2.1 and the helix angle on the cylinder equals zero $\psi_{cyl} = 0$. The locations of the caustic associated with both membrane wave types are shown as a function of aspect angle in Figure B.2.

A 90 deg phase shift is introduced as a given waveform passes through a caustic location. A phase shift of $e^{-i\pi/2}$ is introduced for positive frequencies, and $e^{+i\pi/2}$ for negative frequencies as formulated by Felsen and Marcuvitz [22], and Marston [33, 39]. This phase shift transforms the symmetric bandlimited pulse of the incident field into an asymmetric pulse as illustrated in Figure B.3. I have observed this phase shift in the scattered leaky wave field of the empty shell model at some aspect angles as presented in the Section 2.3.

Given the assumption of dispersionless propagation employed here for membrane waves, the helix angle ψ_{cone} and caustic location z_c are not functions of frequency

or mode number $v = n$. Both parameters are functions of the cone geometry and the helix angle of the incident structural wave at the junction of the cone with the cylinder. Therefore, the location of the caustic is prescribed solely by the wave type and aspect angle of the incident field.

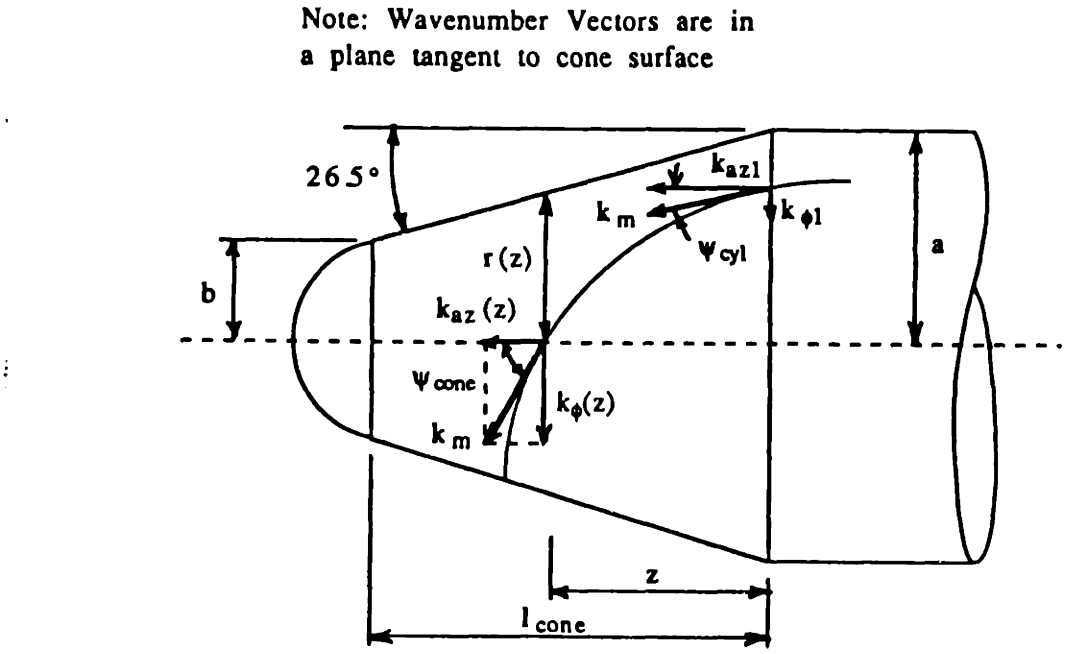

Figure B.1: Illustration of Helix Wavenumber Components on the Conical Section of the Endcaps Used on All Three Shell Models

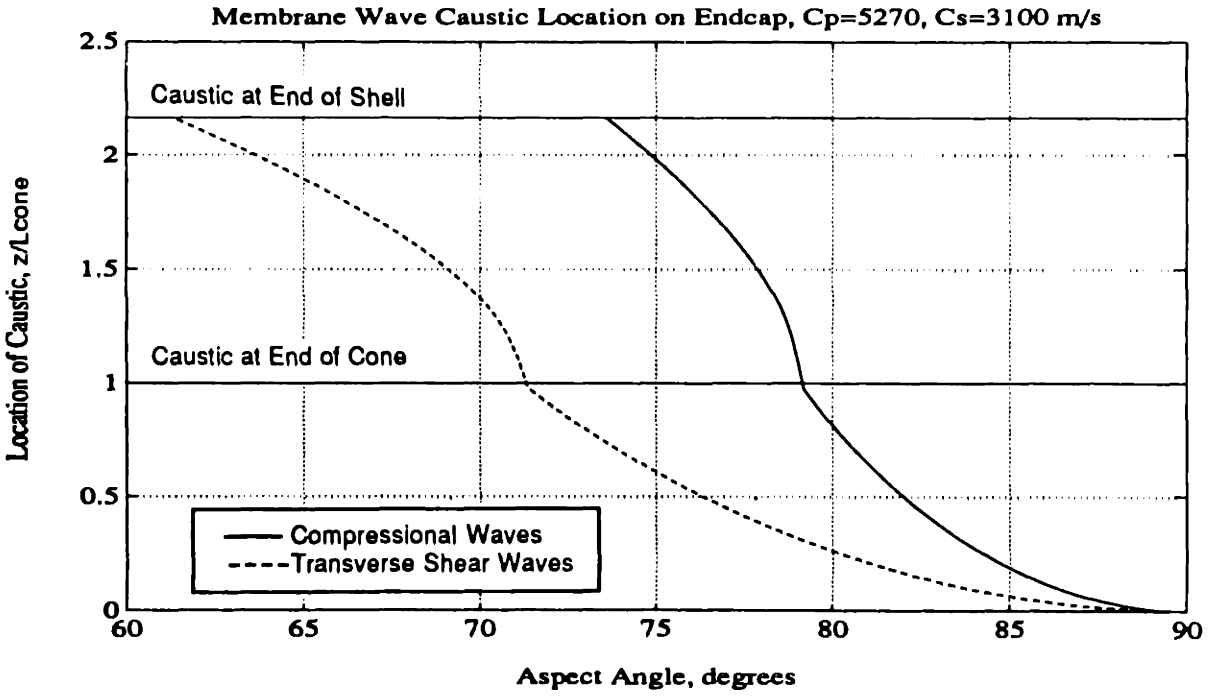

Figure B.2: Location of Caustic on Endcap for Transverse Shear and Compressional Waves, $b/a = 0.75$, $b/l_{cone} = 1.16$

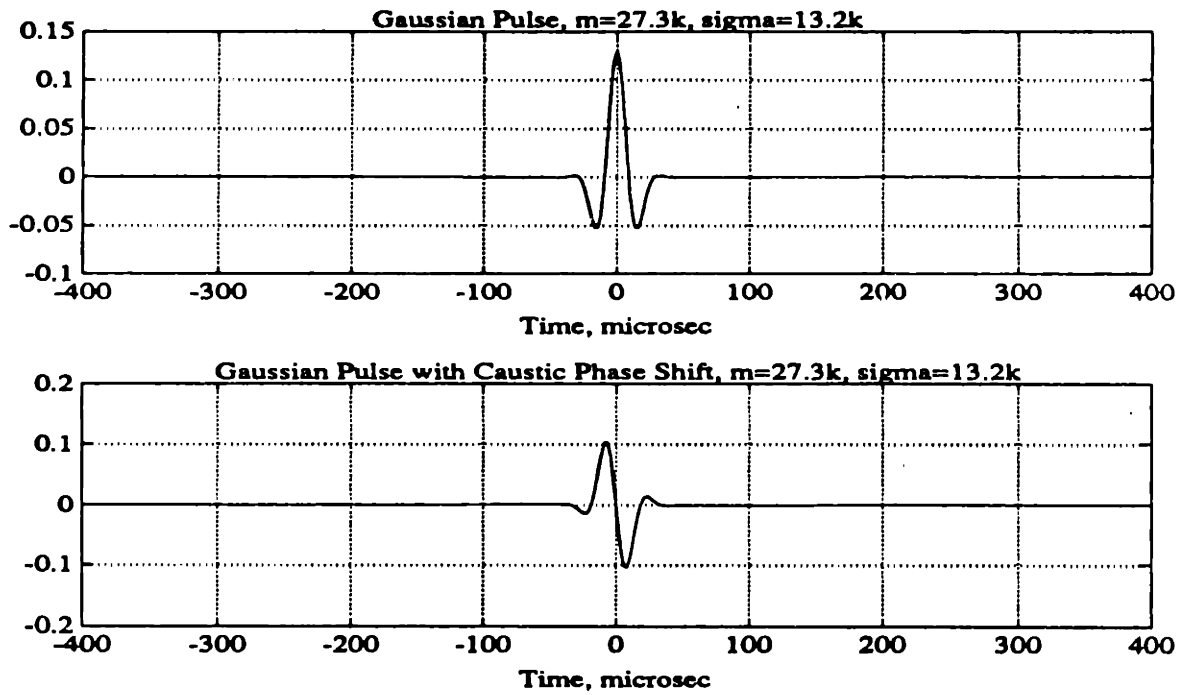

Figure B.3: Illustration of Gaussian Pulse Waveform Before and After Interaction with Caustic at Endcap, $2.75 < ka < 10.0$

Bibliography

[1] M. Abramowitz and I. A. Stegan, *Handbook of Mathematical Functions* (Dover Publications, New York, NY 1972).

[2] J. D. Achenbach, J Bjarnason, and T. Igusa, "Effect of Vibrating Sub-Structure on Acoustic Radiation from a Cylindrical Shell", ASME Winter Annual Meeting, 1990, 90-WA/NCA-7.

[3] A. B. Baggeroer, H. Schmidt, J. R. Fricke, and J. Bondaryk,"Time Domain Processing in Mid-Frequency Structural Acoustics", ASA Meeting, 13 May, 1992.

[4] A. B. Baggeroer, "Space/time random processes and optimum array processing", Naval Undersea Center Technical Report 506, (1976).

[5] A. B. Baggeroer, "Sonar Signal Processing", *Applications of Digital Signal Processing*, edited by A. V. Oppenheim, (Prentice-Hall, Englewood Cliffs, NJ 1978).

[6] C. M. Bender and S. A. Orszag, *Advanced Mathematical Methods for Scientists and Engineers*, (McGraw-Hill,New Yourk, NY 1978).

[7] T. A. C. M. Claasen and W. F. G. Mecklenbrauker, "The Wigner Distribution - A tool for Time-Frequency Signal Analysis, Part I: Continuous-Time Signals", Phillips Journal of Research, **35** (3), 217-250 (1980).

[8] T. A. C. M. Claasen and W. F. G. Mecklenbrauker, "The Wigner Distribution - A tool for Time-Frequency Signal Analysis, Part II: Discrete-Time Signals", Phillips Journal of Research, **35** (4/5), 276-300 (1980).

[9] T. A. C. M. Claasen and W. F. G. Mecklenbrauker, "The Wigner Distribution - A tool for Time-Frequency Signal Analysis, Part III: Relations with other Time-Frequency Signal Transformations", Phillips Journal of Research, **35** (6), 372-389 (1980).

[10] C. Corrado, I. Dyer, R. Zavistoski, "Coupled Wave Complexity in Structural Acoustics", Presented at the Winter Annual Meeting of the ASME, Nov., 1990, Paper No. 90-WA/NCA-8.

[11] L. Cremer and M. Heckl, *Structure-Borne Sound*, Translated and Revised by E. E. Ungar, (Springer-Verlag, Heidelberg, Germany 1988).

[12] Private Conversation with Dr. G. L. Duckworth and Dr. N. Martin, Winter of 1991.

[13] I. Dyer, "Fundamentals of Underwater Sound", MIT course notes (unpublished).

[14] Personal Communication with I. Dyer during January 1993.

[15] I. Dyer and M. Conti, Memorandum dated 25 June, 1990, Subject: Scale Model Experiments on an Internally Loaded Cylinder.

[16] M. Conti is currently pursuing a Doctoral Degree at MIT and the focus of his research is interpretation of the scatter observed near bow aspect.

[17] Element Shading Coefficients for Transmitting Line Array Received from NRL, October 1991.

[18] F. Fahy, *Sound and Structural Vibration: Radiation, Transmission, and Response*, (Academic Press, San Diego, CA, 1985).

[19] L. B. Felsen, J. M. Ho, and I.T. Lu, "Three-Dimensional Green's Function for Fluid-Loaded Thin Elastic Cylindrical Shell: Formulation and Solution", J. Acoust. Soc. Am., **87** (2), 543-553 (1990).

[20] L. B. Felsen, J. M. Ho, and I.T. Lu, "Three-Dimensional Green's Function for Fluid-Loaded Thin Elastic Cylindrical Shell: Alternative Representations and Ray Acoustic Forms", J. Acoust. Soc. Am., **87** (2), 554-569 (1990).

[21] L. B. Felsen, J. M. Ho, and I.T. Lu, "Erratum: Three-Dimensional Green's Function for Fluid-Loaded Thin Elastic Cylindrical Shell: Alternative Representations and Ray Acoustic Forms", J. Acoust. Soc. Am., **89** (3), 1463-1464 (1991).

[22] L. B. Felsen, and N. Marcuvitz, *Radiation and Scattering of Waves*, (Prentice-Hall, Englewood Cliffs, NJ 1973).

[23] J. M. Ho and L. B. Felsen, "Nonconventional Traveling Wave Formulations and Ray-Acoustic Reductions for Source-Excited Fluid Loaded Thin Elastic Spherical Shells", J. Acoust. Soc. Am., **88** (5), 2389-2414 (1990).

[24] J. R. Fricke and A. B. Baggeroer, "Modal-Slowness Analysis of Plate Vibrations", Submitted for publication Sept., 1991.

[25] Y. P. Guo, "Sound Scattering from an Internally Loaded Cylindrical Shell", J. Acoust. Soc. Am., **91** (2), 926-938 (1992).

[26] Y. P. Guo, "Sound Scattering from Cylindrical Shells with Internal Elastic Plates", April 1992, to be published in J. Acoust. Soc. Am..

[27] Y. P. Guo, "Scattering of Impulse Signal by Elastic Shells with Internal Structures", ASA Meeting, 13 May, 1992, Session 4SA9.

[28] Private conversations with Y.P. Guo, July, 1992 where Guo has determined dispersive properties of right circular cones.

[29] F. B. Hildebrand, *Advanced Calculus for Applications*, (Prentice-Hall, Englewood Cliffs, NJ 1976).

[30] Hua He is currently pursuing a Doctoral Degree at MIT and the focus of his research is group delay and related effects of the internal structures.

[31] M. C. Junger, and D. Feit, *Sound, Stuctures, and Their Interaction*, (MIT Press, Cambridge, MA 1986).

[32] S. G. Kargl and P. L. Marston, "Observations and Modeling of the Backscattering of Short Tone Bursts from a Spherical Shell: Lamb Wave Echoes, Glory, and Axial Reverberations", J. Acoust. Soc. Am., **85** (3), 1014-1028 (1989).

[33] S. G. Kargl and P. L. Marston, "Ray Synthesis of Lamb Wave Contributions to the Total Scattering Cross Section for an Elastic Spherical Shell", J. Acoust. Soc. Am., **88** (2), 1103-1113 (1990).

[34] S. M. Kay and S. L. Marple, "Spectrum Analysis - A Modern Perspective", Proceedings of the IEEE, **69** (11), 1380-1414 (1981).

[35] A. Klauson and J. Metsaveer, "Sound Scattering by a Cylindrical Shell Reinforced by Lengthwise Ribs and Walls", J. Acoust. Soc. Am., **91** (4), 1834-1843 (1992).

[36] F. Leon, F. Lecroq, D. Decultot, and G. Maze, "Scattering of an Obliquely Incident Acoustic Wave by an Infinite Hollow Cylindrical Shell", **91** (3), 1388-1397 (1992).

[37] R. H. Lyon, *Machinery Noise and Diagnostics*, (Butterworths, Stoneham, MA 1987).

[38] D. P. Mackovjak, "Array Measurements of Backscattered Data From Internally Loaded Cylindrical Shells", Master's Thesis, Draper Report No. CSDL-T-1157, February, 1993.

[39] P. L. Marston, "GTD for Backscattering from Elastic Spheres and Cylinders in Water and the Coupling of Surface Elastic Waves with the Acoustic Field", J. Acoust. Soc. Am., **83** (1), 25-37 (1988).

[40] G. Maze, F. Lecroq, D. Decultot, J. Ripoche, S. Numrich, and H. Uberall,"Acoustic Scattering from Finite Cylindrical Elastic Objects",J. Acoust. Soc. Am., **90** (6), 3271-3287 (1991).

[41] P. M. Morse and K. U. Ingard, *Theoretical Acoustics*, (Princeton University Press, Princeton, New Jersey, 1968).

[42] V. V. Muzychenko, A. P. Paniklenko, and S. A. Rybak, "Dispersion Curves for Normal Modes in Cylindrical Shell and Conditions for Spatial Coincidence in the Vacinity of the Critical Frequencies", Sov. Phys. Acoust., **30** (1), 47-51 (1984).

[43] D. E. Newland, *Random Vibrations and Spectral Analysis* (Longman, Essex, England 1985).

[44] A. V. Oppenheim and R. W. Schafer, *Discrete Time Signal Processing*, (Prentice Hall, Englewood Cliffs, NJ 1989).

[45] A. D. Pierce, "Wave Propagation on Thin-Walled Cylindrical Shells", *Elastic Wave Propagation*, edited by M. F. McCarthy and M. A. Hayes, (Elsevier, New York, 1989), 205-210.

[46] A. D. Pierce, *Acoustics, An Intoduction to its Physical Principles and Applications*, (McGraw-Hill, New York, NY 1981).

[47] W. H. Press, B. P. Flannery, S. A. Teukolsky, and W. T. Vetterling, *Numerical Recipes in C*,(Cambridge University Press, New York, NY 1988).

[48] D. Ricks and H. Shmidt have developed a fully elastic global matrix analysis technique for cylindrical shells and plan to submitted several papers to JASA that will discuss its derivation and important results during 1993. winter, 1993.

[49] M. L. Rumerman,"Increased Accuracy in the Application of the Sommerfeld-Watson Transformation to Acoustic Scattering from Cylindrical Shells", J. Acoust. Soc. Am., **90** (5), 2739-2750 (1991).

[50] M. L. Rumerman used the expression "String of Pearls" to describe the enhanced target strength pattern found in the region of the coincidence loci during a presentation at the ONR/DARPA Program Review Meeting of July, 1991 at MIT.

[51] J. F. M. Scott,"The Free Modes of Propagation of an Infinite Fluid-Loaded Thin Cylindrical Shell", J. Acoust. Soc. Am., **125** (2), 241-280 (1988).

[52] M. Talmant and G. Quentin, "Study of the Pseudo - Lamb Wave S_o Generated in Thin Cylindrical Shells Insonified by Short Ultrasonic Pulses in Water".

[53] G. Turner, "Aliasing in the Tau-p Transform and the Removal of Spatially Aliased Coherent Noise", Geophysics, **55** (11), 1496-1503 (1990).

[54] R. J. Urick, *Principles of Underwater Sound for Engineers*, (McGraw-Hill, New York, NY 1967).

[55] P. Ugincius and H. Uberall, "Creeping-Wave Analysis of Acoustic Scattering by Elastic Cylindrical Shells", J. Acoust. Soc. Am., **43** (5), 1025-1035 (1968).

[56] N. D. Veksler, V. M. Korsunskii, and S. A. Rybak, "Scattering of an Obliquely Incident Plane Wave by a Circular Cylindrical Shell", Sov. Phys. Acoust., **36** (1), 5-7 (1990).

[57] N. C. Veksler, "The Analysis of Peripheral Waves in the Problem of Plane Acoustic Pressure Wave Scattering by a Circular Shell", ACUSTICA, **69**, 63-72 (1989).

[58] T.J. Wahl and J. S. Bolton, "The Use of the Wigner Distribution to Analyze Structural Impulse Responses", Int. Congress on Recent Developments in Air and Structure-borne Sound and Vibration, March 6-8, 1990, Auburn University.

[59] G. B. Warburton, "Vibration of a Cylindrical Shell in an Acoustic Medium", J. Mech. Eng. Sci., **3** (1), 69-79 (1961).

[60] E. G. Williams, H. D. Dardy, and K. B. Washburn,"Generalized Nearfield Acoustic Holography for Cylindrical Geometry: Theory and Experiment", J. Acoust. Soc. Am., **81** (2), 389-407 (1987).

[61] E. G. Williams, B. H. Houston, and J. A. Bucaro,"Broadband Nearfield Acoustical Holography for Vibrating Cylinders", J. Acoust. Soc. Am., **86** (2), 674-679 (1989).

[62] K. L. Williams and P. L. Marston, "Axial Focused (Glory) Scattering Due to Surface Waves Generated on Spheres: Model and Experimental Confirmation Using Tungsten Carbide Spheres", J. Acoust. Soc. Am., **78** (2), 722-728 (1985).

[63] K. L. Williams and P. L. Marston, "Backscattering from an Elastic Sphere: Sommerfeld Watson Transformation and Experimental Confirmation", J. Acoust. Soc. Am., **78** (3), 1093-1102 (1985).

[64] K. L. Williams and P. L. Marston, "Synthesis of Baackscattering from an Elastic Sphere Using the Sommerfeld-Watson Transformation and Giving a Fabry-Perot Analysis of Resonances", J. Acoust. Soc. Am., **79** (6), 1702-1708 (1986).

[65] N. Yen, "Time and Frequency Representation of Acoustic Signals by Means of the Wigner Distribution Function: Implementation and Interpretation", J. Acoust. Soc. Am., **81** (6), 1841-1850 (1987).

[66] N. Yen, L. R. Dragonette, S. K. Numrich, "Time-Frequency Analysis of Acoustic Scattering From Elastic Objects", J. Acoust. Soc. Am., **87** (6), 2359-2370 (1990).

[67] Y. Zhao, L. E. Atlas, and R. J. Marks, "The Use of Cone-Shaped Kernals for Generalized Time-Frequency Representations of Nonstationary Signals", IEEE Transactions on Acoustics, Speech, and Signal Processing, **38** (7), 1084-1091 (1990).